LECTURE NOTES IN NANOSCALE SCIENCE AND TECHNOLOGY 3

Zhiming M. Wang

Editor

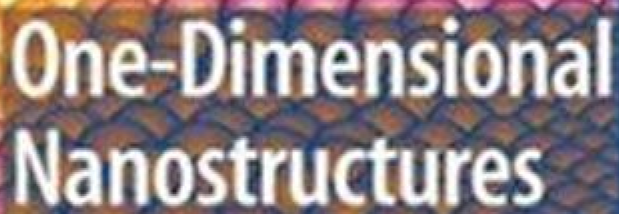
One-Dimensional Nanostructures

Springer

One-Dimensional Nanostructures

LECTURE NOTES IN NANOSCALE SCIENCE AND TECHNOLOGY

Series Editors:
Zhiming M. Wang, Department of Physics, University of Arkansas, Fayetteville, AR, USA
Andreas Waag, Institut für Halbleitertechnik, TU Braunschweig, Braunschweig, Germany
Gregory Salamo, Department of Physics, University of Arkansas, Fayetteville, AR, USA
Naoki Kishimoto, Quantum Beam Center, National Institute for Materials Science, Tsukuba, Ibaraki, Japan

Volumes Published in this Series:
Volume 1: Self-Assembled Quantum Dots, Wang, Z.M., 2008
Volume 2: Nanoscale Phenomena: Basic Science to Device Applications, Tang, Z., and Sheng, P., 2008
Volume 3: One-Dimensional Nanostructures, Wang, Z.M., 2008

Forthcoming Titles:
B-C-N Nanotubes and Related Nanostructures, Yap, Y.K., 2008
Towards Functional Nanomaterials, Wang, Z.M., 2008
Epitaxial Semiconductor Nanostructures, Wang, Z.M., and Salamo, G., 2008

One-Dimensional Nanostructures

Zhiming M. Wang
Editor

University of Arkansas
Fayetteville, AR, USA

Series Editors:
Zhiming M. Wang
Institute of Nanoscale Science
and Engineering
University of Arkansas
Fayetteville, AR
USA

Gregory Salamo
Department of Physics
University of Arkansas
Fayetteville, AR
USA

Andreas Waag
Institut für Halbleitertechnik
TU Braunsweig
Braunschweig
Germany

Naoki Kishimoto
Quantum Beam Center
National Institute for Materials Science
Tsukuba, Ibaraki
Japan

ISBN 978-0-387-74131-4 e-ISBN 978-0-387-74132-1

Library of Congress Control Number: 2008927188

© 2008 Springer Science+Business Media, LLC
All rights reserved. This work may not be translated or copied in whole or in part without the written permission of the publisher (Springer Science+Business Media, LLC, 233 Spring Street, New York, NY 10013, USA), except for brief excerpts in connection with reviews or scholarly analysis. Use in connection with any form of information storage and retrieval, electronic adaptation, computer software, or by similar or dissimilar methodology now known or hereafter developed is forbidden.
The use in this publication of trade names, trademarks, service marks, and similar terms, even if they are not identified as such, is not to be taken as an expression of opinion as to whether or not they are subject to proprietary rights.

Printed on acid-free paper

9 8 7 6 5 4 3 2 1

springer.com

Preface

One-dimensional (1D) nanostructures represent a group of nanomaterials with highly anisotropic morphologies, the smallest dimension falling in the range of 1–100 nm. Typical examples of 1D nanostructures include nanowires and nanotubes. Semiconductor nanowires are characterized by the efficient transport of electrons and excitons, and have been regarded as the most promising building block for nanoscale electronic and optoelectronic devices. Nanosystems can be built from these elements using metallic nanowires as interconnects. Carbon nanotubes, either semiconducting or metallic, are mechanically robust and chemically stable, suggesting numerous potential applications in nanoelectronics. The growth, characterization, and applications of 1D nanostructures invoke all disciplines of science and engineering. As a result, scientists working in one area need to go beyond their own expertise to obtain a broad view of the whole field. The objective of this book is to elucidate the fundamental, underlying science common to 1D nanostructures and their applications. The result is a representative snapshot of the latest developments from diverse perspectives in a series of chapters from highly engaged scientists.

In Chaps. 1–4, particular emphasis is placed on synthesis of nanowires. Chap. 1 summarizes the controversy regarding nanowire growth mechanisms and proposes a Si-assisted growth model. Chap. 2 reviews the synthesis and properties of SiC 1D nanostructures, in both experiments and theories. Chap. 3 deals with self-organization of Si-based nanowires. Chap. 4 demonstrates the formation of large-scale arrays of addressable Si nanowires, with controllable dimension, placement, and orientation, showing the promise for integration of nanowires into device architectures.

Chaps. 5–7 focus on the property characterization of nanowires. Chap. 5 reveals the extreme optical anisotropy of individual nanowires and of nanowire ensembles. Chap. 6 offers a numerical method for a better description of the plasmonic properties of silver nanowires. Chap. 7 investigates electromagnetic nanowire resonances for field-enhanced spectroscopy.

The progress made toward applications is discussed in Chaps. 8–10. Chap. 8 is devoted to detailed analysis of engineering contact barriers and their impact on the electrical transport properties of carbon nanotube field-effect transistors. Chap. 9

presents a comprehensive overview on the current status of low dimensional nanomaterials for spintronics. Chap. 10 reports on 1D phase-change nanomaterials for information storage applications.

Chap. 11 is a theoretical contribution in nature and studies the melting behavior, thermal conductivity, and mechanical properties of crystalline GaN nanotubes through molecular dynamics methods.

While the above chapters deal with freestanding properties of 1D nanostructures, buried semiconductor nanowires – commonly referred to as quantum wires – are the subjects of the last chapter. Chap. 12 reviews the self-assembly of InAs/InAl(Ga)As quantum wires on InP substrates and demonstrates how the lateral composition modulation in InAlAs buffer layers plays an important role in determining their structural and optical properties.

Finally, the editor wishes to thank his wife, Yanze Xie, for her support and understanding. The editor himself is highly involved in many research projects, and therefore, is forced to perform nearly all editorial work at home, often at night and on weekends. This means many sacrifices for Yanze as a mother of two young kids. The editor is honored that she has accompanied him in the past from China to Germany to the United States, and looks forward to spending the rest of his life with her.

Fayetteville *Zhiming M. Wang*
February 2008

Contents

1 Study of Nanowire Growth Mechanisms: VLS and Si Assisted 1
Hyun D. Park and S.M. Prokes

2 One-Dimensional SiC Nanostructures: Synthesis and Properties 17
Weimin Zhou, Yafei Zhang, Xiaoming Niu, and Guoquan Min

3 Self-Organized Nanowire Formation of Si-Based Materials 61
Hideo Kohno

4 Controlled Formation of Individually Addressable Si Nanowire Arrays for Device Integration 79
Ying-Lan Chang and Sung Soo Yi

5 Physical Properties of GaN Nanotubes as Revealed by Computer Simulation 97
Zhiguo Wang, Fei Gao, Xiaotao Zu, and William J. Weber

6 Optical Anisotropy of Semiconductor Nanowires 127
Jaime Gómez Rivas, Otto L. Muskens, Magnus T. Borgström, Silke L. Diedenhofen, and Erik P.A.M. Bakkers

7 FDTD Spectroscopic Study of Metallic Nanostructures: On the Pertinent Employment of Tabulated Permittivities 147
Thierry Laroche and Alexandre Vial

8 Electromagnetic Nanowire Resonances for Field-Enhanced Spectroscopy 175
Annemarie Pucci, Frank Neubrech, Javier Aizpurua, Thomas Cornelius, and Marc Lamy de la Chapelle

9 Designing the Carbon Nanotube Field Effect Transistor Through Contact Barrier Engineering 217
Byoung-Kye Kim, Hyo-Suk Kim, Hye-Mi So, Noejung Park, Suklyun Hong, Ju-Jin Kim, and Jeong-O Lee

10 Low Dimensional Nanomaterials for Spintronics 247
Jinlong Yang and Hongjun Xiang

11 One-Dimensional Phase-Change Nanomaterials for Information Storage Applications 273
Xuhui Sun, Bin Yu, Garrick Ng, and M. Meyyappan

12 Ordering of Self-Assembled Quantum Wires on InP(001) Surfaces . . 291
W. Lei, Y. H. Chen, and Z. G. Wang

Index 323

Contributors

Javier Aizpurua
Donostia International Physics Center and Joint Center of Materials Physics CSICUPV/EHU,
Paseo Manuel de Lardizabal 4,
Donostia-San Sebastian 20018
Spain

Erik P.A.M. Bakkers
Philips Research Laboratories,
High-Tech Campus 4,
5656 AE Eindhoven,
The Netherlands

Magnus T. Borgström
Philips Research Laboratories,
High-Tech Campus 4,
5656 AE Eindhoven,
The Netherlands

Ying-Lan Chang
Agilent Laboratories, Agilent Technologies, 5301 Stevens Creek Blvd, Santa Clara, CA 95051, USA
and
Nanomix, Inc., 5980 Horton Street, Suite 600, Emeryville, CA 94608, USA

Marc Lamy de la Chapelle
Laboratoire de Nanotechnologie et Instrumentation Optique,
Institut Charles Delaunay,
CNRS FRE 2848, Pôle Physique,
Matériaux et Nanotechnologie,
Université de Technologie de Troyes,
12 rue Marie Curie, BP-2060,
10010 Troyes Cedex, France

Y. H. Chen
Key Laboratory of Semiconductor Materials Science, Institute of Semiconductors, Chinese Academy of Sciences, PO Box 912, Beijing 100083, P.R. China

Thomas Cornelius
Department of Materials Research, Gesellschaft für Schwerionenforschung (GSI), Planckstr. 1, 64291 Darmstadt, Germany

Silke L. Diedenhofen
FOM Institute for Atomic and Molecular Physics, AMOLF,
c/o Philips Research Laboratories,
High-Tech Campus 4, 5656 AE Eindhoven, The Netherlands

Fei Gao
Pacific Northwest National Laboratory,
PO Box 999, Richland, WA 99352,
USA

Suklyun Hong
Department of Physics and Institute of Fundamental Physics, Sejong University, Seoul 143–747, Korea

Byoung-Kye Kim
Department of Physics, Chonbuk National University, Jeonju, Korea

Hyo-Suk Kim
Department of Physics, Chonbuk National University, Jeonju, Korea

Ju-Jin Kim
Department of Physics, Chonbuk National University, Jeonju, Korea

Hideo Kohno
Graduate School of Science, Osaka University 1-1 Machikaneyama, Toyonaka, Osaka 560-0043, Japan

Thierry Laroche
Institut Charles Delaunay, Université de technologie de Troyes, CNRS FRE 2848 Laboratoire de Nanotechnologie et d'Instrumentation Optique 12, rue Marie Curie BP-2060, 10010 Troyes Cedex, France

Jeong-O Lee
Fusion-Biotechnology Research Center, Advanced Materials Division, Korea Research Institute of Chemical Technology, Daejeon 305–600, Korea

W. Lei
Key Laboratory of Semiconductor Materials Science, Institute of Semiconductors, Chinese Academy of Sciences, PO Box 912, Beijing 100083, P.R. China

M. Meyyappan
NASA Ames Research Center, Moffett Field, CA 94035, USA

Guoquan Min
Shanghai Nanotechnology Promotion Center, Shanghai 200037, China

Otto L. Muskens
FOM Institute for Atomic and Molecular Physics, AMOLF, c/o Philips Research Laboratories, High-Tech Campus 4, 5656 AE Eindhoven, The Netherlands

Frank Neubrech
Kirchhoff Institute for Physics, University of Heidelberg, Im Neuenheimer Feld 227, 69120 Heidelberg, Germany

Garrick Ng
NASA Ames Research Center, Moffett Field, CA 94035, USA

Xiaoming Niu
Shanghai Nanotechnology Promotion Center, Shanghai 200037, China

Hyun D. Park
US Naval Research Lab, 4555 Overlook Ave., SW, Washington, DC 20375, USA

Noejung Park
Department of Applied Physics, Dankook University, Yongin 448–701, Korea

S.M. Prokes
US Naval Research Lab, 4555 Overlook Ave., SW, Washington, DC 20375, USA

Annemarie Pucci
Kirchhoff Institute for Physics,
University of Heidelberg,
Im Neuenheimer Feld 227,
69120 Heidelberg, Germany

Jaime Gómez Rivas
FOM Institute for Atomic
and Molecular Physics, AMOLF,
c/o Philips Research Laboratories,
High-Tech Campus 4, 5656 AE
Eindhoven,
The Netherlands

Hye-Mi So
Fusion-Biotechnology Research
Center, Advanced Materials Division,
Korea Research Institute
of Chemical Technology,
Daejeon 305–600, Korea

Xuhui Sun
NASA Ames Research Center,
Moffett Field, CA 94035, USA

Alexandre Vial
Institut Charles Delaunay,
Université de technologie de Troyes,
CNRS FRE 2848 Laboratoire de
Nanotechnologie et d'Instrumentation
Optique 12, rue Marie Curie BP-2060,
10010 Troyes Cedex, France

Z.G. Wang
Key Laboratory of Semiconductor
Materials Science,
Institute of Semiconductors,
Chinese Academy of Sciences,
PO Box 912, Beijing 100083, P.R.
China

Zhiguo Wang
Department of Applied Physics,
University of Eletronic Science
and Technology of China,
Chengdu 610054, P.R. China

William J. Weber
Pacific Northwest National
Laboratory, PO Box 999, Richland,
WA 99352, USA

Hongjun Xiang
Hefei National Laboratory for Physical
Sciences at the Microscale, University
of Science and Technology
of China, Hefei, Anhui 230026, P.R.
China

Jinlong Yang
Hefei National Laboratory for Physical
Sciences at the Microscale,
University of Science and Technology
of China, Hefei, Anhui 230026,
P.R. China

Sung Soo Yi
Philips Lumileds Lighting, 370 West
Trimble Road, San Jose, CA 95131,
USA

Bin Yu
NASA Ames Research Center,
Moffett Field, CA 94035, USA

Yafei Zhang
Research Institute of Micro/Nano
Science and technology,
Shanghai Jiaotong University,
Shanghai 200030, China

Weimin Zhou
Shanghai Nanotechnology Promotion
Center, Shanghai 200037, China

Xiaotao Zu
Department of Applied Physics,
University of Eletronic Science
and Technology of China,
Chengdu 610054,
P.R. China

Chapter 1
Study of Nanowire Growth Mechanisms: VLS and Si Assisted

Hyun D. Park and S.M. Prokes

Abstract In this chapter, we have examined several of our recent results on InAs nanowires that have implications to the vapor–liquid–solid (VLS) growth mechanism as well as the newly proposed Si-assisted growth mechanism. In summary, the study on the effect of oxygen during the nanowire growth showed the inhibiting effect of oxygen on the VLS growth mechanism. The results on the observation of size-dependent liquidus depression, more importantly, do not seem applicable on the results of Ti-catalyzed grown Si nanowires, but bring into question the validity of the vapor–solid–solid (VSS) growth mechanism in the Au-catalyzed grown GaAs and InAs nanowires. In the newly proposed nanowire growth mechanism, namely the Si-assisted mechanism using SiO_x, a growth model is proposed based on the phase separation of SiO at higher temperature, which forms a stable SiO_2 and reactive, nanometer-sized Si clusters. It is suggested that these clusters consequently serve as the nucleating/catalyst sites for the growth of InAs nanowires with the growth mechanism different from VLS, VSS, and OA.

1.1 Introduction

Two primary nanowire growth mechanisms have been reported in the literature: vapor–liquid–solid (VLS) and oxide assisted (OA). On the one hand, the OA growth mechanism does not use any metal catalyst, but somehow utilizes the reaction of the metastable oxide. Previously, nanowires such as Ge [1], C [2], GaAs [3], and Si [4] have been grown using GeO, CO, Ga_2O_3, and SiO, respectively. Based on these results, it has been suggested that the metastable oxides serve as a nucleating center for subsequent growth of the nanowires, but much work is still needed to fully understand this growth mechanism. On the other hand, the VLS growth mechanism utilizes a metal catalyst (such as Au, Ni, and Fe) to enhance the nanowire growth. The key feature of this growth mechanism is the liquid state of the metal alloy tip during the nanowire growth, which occurs by the formation of a eutectic alloy. Once the

alloy tip forms a eutectic, any excess material that is adsorbed from the vapor precipitates out in the form of a nanowire. Over the years, numerous nanowires such as Si [5,6], Ge [7], and InAs [8–10], to name a few, have been successfully grown using this growth mechanism. Recently, however, a different growth mechanism, namely the vapor–solid–solid (VSS) (where the metal alloy tip is supposedly in solid state during the nanowire growth, unlike the VLS) was proposed to explain the growth of Au-catalyzed GaAs [11] and InAs [12] nanowires in the CBE and MOVPE growth systems, respectively. The growth of InAs nanowires in the MOVPE system, in particular, was shown to occur at temperatures up to 480°C when using an Au catalyst (this is near the Au–In eutectic temperature of 450°C), but no growth was noted at higher temperatures. However, when a 13-Å SiO_x layer was deposited along with the Au catalyst, the growth of InAs nanowires at temperature of 580°C was reported. Based on this preliminary work, it was suggested that the growth at higher temperature was possible only with the presence of the oxide, where its effect was to prevent the Au–In tip from melting, thereby extending the VSS growth process. Our own recent results (where we observed a size-dependent liquidus depression of Au–In alloy tip) [13], however, reported InAs nanowire growth up to 660°C (with no SiO_x), and the Au–In tip retained its liquid feature down to 400°C. Since our results confirmed that the VLS is valid in the InAs system, there is some question as to the validity of the VSS growth mechanism in the Au-catalyzed grown GaAs and InAs nanowires as well as the real role of the oxide employed in the work of Dick et al.

In addition, in the work of Kolb et al. [14], SiO evaporation and VLS were combined to grow Si nanowires. In this case, the suggested growth model included the VLS mechanism to grow Si nanowires, and the oxide was thought to deposit only around the Si core but not on the Au catalyst. In this chapter, we review some of our recent work, which includes the effect of oxygen in the VLS growth mechanism, the controversy regarding the VSS–VLS growth mechanisms, and the newly proposed Si-assisted growth mechanism that was used to explain the nanowire growth using SiO_x. The outline of the chapter is as follows. In Sect. 1.2, the VLS growth mechanism is discussed, which includes the basic description (Sect. 1.2.1), the effect of oxygen on VLS (Sect. 1.2.2), and the controversy regarding VSS and VLS (Sect. 1.2.3). In Sect. 1.3, the Si-assisted growth mechanism is discussed. Concluding remarks are given in Sect. 1.4.

1.2 VLS Growth Mechanism

1.2.1 Basic Description

In its simplest term, the VLS growth mechanism is a nanowire growth process, which utilizes a nanometer-sized metal alloy that is in liquid state during the nanowire growth. It is perhaps the most well-known nanowire growth mechanism,

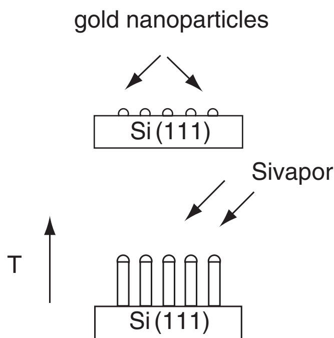

Fig. 1.1 VLS growth process of Si nanowires using Au nanoparticles on a Si(111) substrate

first put forward by Wagner and Ellis [15] and subsequently reviewed in detail by Wagner and Givargizov [16, 17]. The primary feature of this growth mechanism is the liquid metal alloy droplet which serves as the preferred site for nucleation due to its large accommodation coefficient compared with the surrounding solid surface. It should be noted that the dimension of the nanometer-sized droplet also serves to determine the diameter of the nanowire.

The schematic of the basic steps involved in the VLS growth mechanism is shown in Fig. 1.1 in the epitaxial growth of Si nanowires using Au nanoparticles on a Si(111) substrate. The growth proceeds with the initial deposition of Au nanoparticles (Au thin film can also be deposited instead) on an oxide-free Si(111) substrate using poly-L-lysine. The Au-deposited Si(111) substrate is then placed inside the reaction zone and the temperature is raised above the Au–Si eutectic, where the Au nanoparticles form nanometer-sized Au–Si liquid alloy droplets. At the nanowire growth temperature, the Si vapor (from such sources as silane, $SiCl_4$, or laser ablation of Si target) impinging on these droplets allows supersaturation to occur. Further incorporation of Si vapor into the droplet then causes the nanowire to grow by precipitation above the substrate in the $\langle 111 \rangle$ growth direction, with the liquid alloy droplet remaining at the top. When the nanowire growth is finished and cooled to room temperature, the alloy droplet still remains at the tip of the nanowire, but in solid form. The remnant of this metallic alloy nanoparticle found at the tip of the nanowire is typically used as evidence of the VLS growth mechanism. Over the years, numerous types of nanowire growths have been successfully attributed to this growth mechanism [5, 18–20].

1.2.2 Effect of Oxygen on VLS

Recently, we have examined the effect of oxygen on the VLS growth mechanism in the growth of InAs nanowires inside a torch-sealed quartz tube [21]. The details of the experimental procedure for this work can be found elsewhere, but the

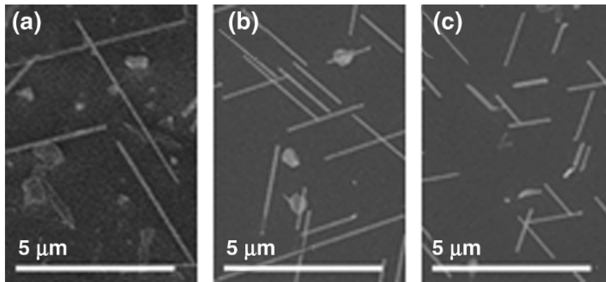

Fig. 1.2 Growth on InAs(111) with 5° miscut as seen from the top with (**a**) 50 mTorr (no oxygen backfill). Parts (**b**) and (**c**) are with 200 and 800 mTorr of oxygen backfill, respectively (reprinted with permission from [21], Copyright 2006, American Institute of Physics)

experiment essentially consisted of a quartz tube (initially filled with bare and Au-deposited InAs substrates) evacuated to 50 mTorr and then backfilled with 200 and 800 mTorr of oxygen and torch sealed. The quartz tube was then annealed inside the open-end furnace for the nanowire growth time of 30 min. The InAs nanowires were grown on InAs(111) substrate with 5° miscut with Au catalyst. The results are shown in the scanning electron microscope (SEM) images in Fig. 1.2a–c, where there was a corresponding decrease in the nanowire lengths with the increase in the oxygen level, clearly indicating the deleterious effect of oxygen on the VLS growth mechanism.

To further ascertain the effect of oxygen on the VLS nanowire growth, nanowires were first grown for only 5 min using an Au catalyst on InAs(111)B substrate. These nanowires were then oxidized in air at room temperature for 3 days, placed back into the quartz tube, and then grown for an additional 25 min. The quartz tubes were all sealed at 50 mTorr. The results are shown in Fig. 1.3a and b for 5 min and additional 25 min (after room temperature air oxidation), respectively. The nanowires grown on InAs(111)B substrate under identical, nonoxidized growth condition typically yielded a length greater than 2 μm (not shown), but as can be seen in the SEM images, we only observed a small change in the length of the nanowires from 5 min (250–300 nm) to 25 additional minutes (300–600 nm). This result indicates a noticeable decrease in the growth rate after the oxidation step.

From the growth experiments performed at various vacuum pressures, these results suggest that the presence of oxygen inhibits nanowire growth in the VLS growth mechanism. Although some nanowires were still seen growing even at 800 mTorr, the inhibiting effect of oxygen was quite evident and it was more pronounced with worsening vacuum conditions. The room temperature oxidation of the Au–In tips in the air offers additional proof of the deleterious effect of oxygen on the nanowire growth. For the Au–In alloy, the interdiffusion of Au and In occurs quickly even at room temperature, and various intermetallic compounds are formed depending on the wt% of In and Au. After 1 day, intermetallic compounds such as $AuIn_2$, AuIn, and Au_7In_3 have been identified [22]. As In readily oxidizes, the In in the Au–In alloy will be subjected to oxidation. Although the literature on the

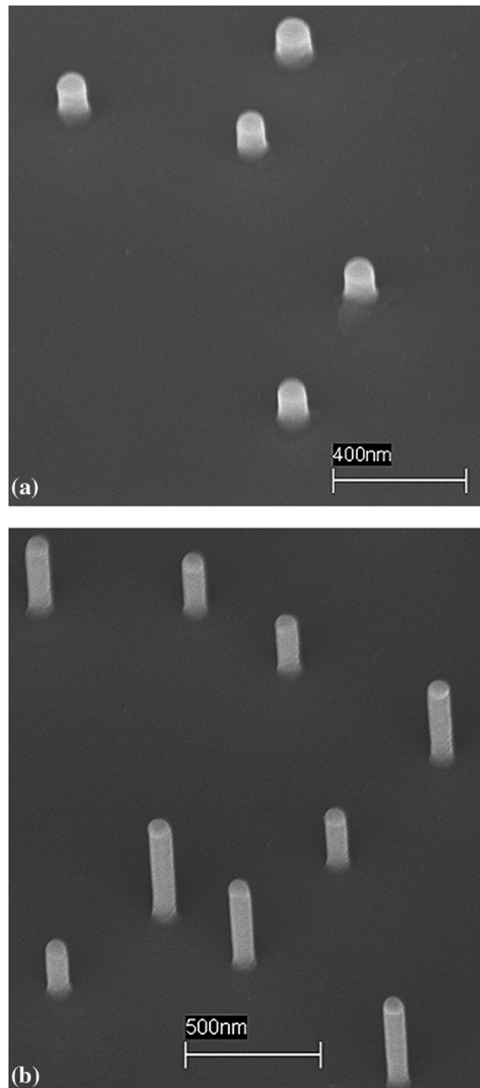

Fig. 1.3 SEM images showing growth at (**a**) 5 min and (**b**) 25 additional minutes after 3 days room temperature oxidation

oxidation of Au–In alloy is scarce, the work of Pasquevich et al. [23] has shown that In oxidation occurs primarily on the surface, not internally, regardless of the In content in the Au–In alloy. Consequently, the surface oxide, which forms either at room or at higher temperature (at 580°C during the growth at poor vacuum pressures), will then serve as a diffusion barrier for impinging In and As atoms, which are in the vapor state, thus inhibiting the nanowire growth. This is consistent with our reported growth results.

1.2.3 VLS and VSS

A recent and more debated development regarding the VLS growth mechanism is the newly proposed VSS growth mechanism that was used to explain the Au-catalyzed growth of GaAs nanowires in CBE by Persson et al. [11] (and subsequently by Dick et al. [12] in the Au-catalyzed growth of InAs nanowires in MOVPE). The basis of the VSS growth mechanism is the solid state of the metal alloy tip used during the nanowire growth, and not liquid as in the case of VLS. Generally, the VLS growth mechanism had been quite successful over the years in explaining the nanowire growth process that used metal catalysts in the growth. Recently, however, there was one result, namely the growth of Ti-catalyzed Si nanowires by Kamins et al. [24], that did not seem consistent with the VLS growth mechanism. In their work, Kamins et al. found the growth of Ti-catalyzed Si nanowire at approximately 600°C, much below the Si–Ti eutectic temperature (the lowest published Ti–Si eutectic temperature is about 1,300°C). Because the growth temperature was considerably lower than that required for the metal alloy tip to be in liquid state, and with the size-dependent melting point depression interpretation insufficient, the authors then concluded that the nanowire should have grown with the metal alloy tip in solid state. Subsequently, Persson et al. investigated the growth of GaAs nanowires by CBE using an Au catalyst, where Au–Ga alloy is formed. Then, through in situ transmission electron microscope (TEM) analysis and X-ray energy dispersive spectroscopy (EDS) of the GaAs nanowires, Persson et al. observed not only the crystallinity of the Au–Ga seed alloy particle at the growth temperature, but also a low Ga concentration in the Au–Ga alloy below the level required for the eutectic melt.

Based on these observations, VSS growth mechanism was then proposed. Soon thereafter, Dick et al. [12] used this growth mechanism to explain the growth of InAs nanowires by MOVPE as well (with Au–In alloy particle), suggesting the failure of the VLS growth mechanism. In their work, the authors also concluded that the growth of Au-catalyzed InAs nanowires was possible only when the metal alloy tip of Au–In was in solid state during the nanowire growth, which limited the growth of InAs nanowires below the eutectic temperature. It should be mentioned that for both Au-catalyzed GaAs and InAs nanowires, the element As is not present (or present only in trace amount) in these metal alloy tips and thus only a binary phase diagram is necessary.

Since then, several contradicting works by Harmand et al. [25] and by us [13,21] have been published, reexamining the validity of the VSS growth mechanism. In the work of Harmand et al., the elemental composition of the Au–Ga seed alloy particle was examined at different growth durations in the case of GaAs nanowires grown in MBE. From their analysis, the authors have identified three different metallic compounds at room temperature: the hexagonal $\beta' Au_7Ga_2$ structure, the orthorhombic AuGa structure, and an almost pure Au face-centered cubic structure, and observed that the final composition of the metallic particle (determined at room temperature) depended on the growth history of the wire. Thus, it was suggested that the Au–Ga seed alloy particle was indeed in liquid state during the nanowire growth and

that GaAs nanowires grew via the VLS mechanism in contrast to the VSS growth mechanism of CBE-grown nanowires.

In our recent work, we studied the size-dependent melting point depression of a metallic binary system undergoing the VLS growth mechanism. In our work, a point elemental composition EDS was performed on various Au–In tip sizes (20–100 nm) in the InAs nanowires that were grown in the temperature range 400–660°C (not shown). The highest growth temperature reported was approximately 100°C higher than the temperature (which is above the eutectic temperature) at which InAs nanowires were grown in the MOVPE system of Dick et al. The results of EDS analysis are shown in Table 1.1, where tips having diameters approximately 60 nm and below showed decreased In content compared with diameters larger than 60 nm. The results show a 30% decrease in the In content in all nanowires with diameters 60 nm or less, as compared with the 100-nm nanowires. Interestingly, in the Au–In phase diagram (not shown), the measured In content for the tip size 100 nm is within the liquid region above the liquidus line, while the tip sizes 60 nm or less are in the solid plus liquid region. These observations suggest the occurrence of size-dependent melting point depression, but to support this claim, the InAs nanowires were also grown below the Au–In eutectic at 400°C using 20 and 60-nm-sized Au nanoparticles. The results, as shown in Fig. 1.4, show the liquid-like migration of Au–In alloy particle (as well as subsequent nanowire growth) despite the temperature being below the level required for the eutectic melt, thereby confirming the occurrence of size-dependent melting point depression as well as the nanowire growth via VLS growth mechanism.

One possible origin of the melting temperature depression is the Gibbs–Thomson effect owing to the finite size of a crystal [26]. To illustrate the order of magnitude associated with this effect [13], consider a single-component spherical crystal of radius r. The melting temperature T_r of the finite size crystal is given by the expression

$$T_m - T_r = 2\gamma\Omega / r\Delta S,$$

Table 1.1 Summary of EDS elemental composition analyses on the gold alloy tip of various nanowires

Size (nm) per element	580°C (liq. 26.6%)		610°C (liq. 25.5%)		660°C (liq. 23%)	
	Au	In	Au	In	Au	In
25	79.8	19.5				
35	80.2	19.5				
40	80.4	19.4				
60	79.8	19.6	78.1	20.9	80.4	19.3
100	71.3	28.2	71.0	28.3	77.2	22.5

The values are in atm%. The standard deviation was ~2 atm%. Trace amount of As (<0.5 atm%) was also detected in the nanowire tips (reprinted from [13], Copyright 2006, with permission from Elsevier)

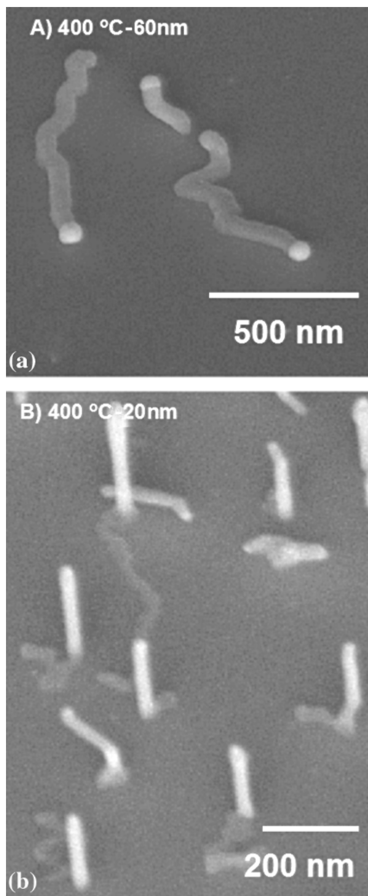

Fig. 1.4 InAs nanowires grown at 400°C for (**a**) 60 nm and (**b**) 20 nm sized Au nanoparticles (reprinted from [21], Copyright 2006, with permission from Elsevier)

where T_m is the bulk melting temperature, γ is the free surface energy, Ω is the molar volume, and ΔS is the molar entropy change for melting. Assuming ΔS to be approximately independent of temperature, then $\Delta S = L/T_\mathrm{m}$, where L is the molar latent heat of melting, so that $(T_\mathrm{r} - T_\mathrm{m})/T_\mathrm{m} \approx 2\gamma\Omega/rL$. Using the values for Au ($\gamma = 1.4\,\mathrm{J\,m^{-2}}$, $\Omega = 10.2\,\mathrm{cm^3\,mol^{-1}}$, $L = 12.55\,\mathrm{kJ\,mol^{-1}}$) and a radius of 40 nm gives a melting temperature reduction of 6%. This would also apply to a single-component sphere sitting on a "noninteracting" substrate. For the case of Au on the InAs substrate, however, it is a two-component alloy on an "interacting" substrate. Nevertheless, since the expressions for Gibbs–Thomson effects in multicomponent systems have the same dependence on the size of the crystal and similar dependences on the surface thermodynamic parameters [26], it is expected that a finite size Au–In alloy would display a similar order of magnitude reduction for the liquidus temperature. Also, since the free surface area of the crystal is larger than the

crystal–substrate interfacial area, the contribution from the crystal–substrate interface is not expected to significantly change the order of magnitude of the effect.

Thus, strictly based on the Gibbs–Thompson effect, one can predict the melting point depression ΔC to be about 65 for the case of the 25–40-nm nanowire tips. This suggests that for the 610 and 660°C growths, the tips will be almost fully in the liquid state at 20% In composition. However, for nanostructures on the order of 60 nm, one can expect a much smaller melting temperature reduction from this theory, which will not shift the liquidus line sufficiently. This means that the nanowire tips with sizes of 60 nm shown in Table 1.1 will remain in a partially solid state during growth and those grown below the eutectic would not exhibit any liquid state at all. However, several published experimental results reported much larger melting point suppression in nanostructures [27–29] than predicted by pure theory, and thus it is useful to consider these. These studies include the vaporization of Au particles on graphite [27], melting of thin In film on an amorphous silicon nitride membranes $(\mathrm{a}-\mathrm{SiN}_x)$ [28], and melting of Ge nanowires [29]. For the studies on surfaces, the substrate materials were carefully chosen so that they had a very low affinity to the nanostructure being studied, since the melting behavior of nanostructures is known to be strongly influenced by the surrounding environment [30, 31].

From the above published works, the melting point reduction results reported by Wu and Yang [29] on 30-nm diameter Ge nanowires may be of interest, since similar nanostructure sizes were studied as in our experiments. In the case of the Ge nanowires, a 25% melting point reduction was reported during heating of the nanowires in a TEM. This is a much more significant effect than would be predicted from pure theory. For example, for a similar diameter Ge nanowire, the Gibbs–Thomson expression for the melting point depression is $(T_\mathrm{r} - T_\mathrm{m})/T_\mathrm{m} \approx \gamma\Omega/rL$. Using the values for Ge ($\gamma = 1.4\,\mathrm{J\,m^{-2}}$, $\Omega = 13.6\,\mathrm{cm^3\,mol^{-1}}$, $L = 36.94\,\mathrm{kJ\,mol^{-1}}$) and a radius of 30 nm gives a melting temperature reduction of only 2%, yet this is an order of magnitude smaller than the experimental value reported. Thus, although Ge is a different material, these experimental results indicate that far larger melting temperature reductions can occur than would be predicted by the Gibbs–Thompson effect.

If we now examine our experimental results, it is possible to estimate the extent of melting point depression, assuming a uniform drop of the liquidus, as suggested by Vallee et al. [32] (of course in this respect, the correct description would be termed a *liquidus depression*, and not melting point depression). For the nanowires grown at 400°C, we can estimate ΔC, the amount of melting point reduction, to be about 250, which is about four times that of the value predicted from the Gibbs–Thompson effect for Au, as calculated above. Although it is true that the calculation was performed on pure Au and not on Au–In alloy for which no data exist, it is still clear that the melting point reduction estimated from our experiment far surpasses what the theory would predict. This is a similar magnitude as the large melting point reduction reported in the case of the 30 nm Ge wires, in which the Gibbs–Thompson theory only predicts a 2% drop. The reason for this large size-dependent melting reduction is not clear at this point, but these results suggest that additional factors must be considered in the theory in the case where the sizes are at or below 60 nm.

Taking into account the size-dependent liquidus depression factor in a binary system, the results of Kamins et al. [24] and Persson et al. [11] (as well as those of Dick et al. [12]) should be revisited and reinterpreted. In the case of Ti-catalyzed Si nanowires reported by Kamins et al., the nanowire growth temperature is so below the Ti–Si eutectic temperature that the liquidus depression factor does not seem applicable at all in this particular case. It is very unclear what process may be occurring, but it appears to be the only nanowire growth with a solid metal alloy tip during the nanowire growth. For the Persson et al. (and Dick et al.) results in the derivation of VSS growth mechanism, however, the liquidus depression factor seems to contradict the claim of a solid metal alloy tip. The authors reported a low Ga(In) content in the Au–Ga(Au–In) binary system required for the eutectic melt measured at the nanowire growth temperature near the Au–Ga eutectic (Au–In), but if the liquidus depression factor is taken into consideration, the Au–Ga(Au–In) was most likely in liquid state, and not solid, during the nanowire growth. This result then implies that the nanowires grew according to the VLS and not VSS growth mechanism.

One further consideration needs to be emphasized: The Au nanoparticles resting on an InAs substrate (forming Au–In alloy) present quite a reactive system, a fact which was not considered by Persson et al. (and Dick et al.). Earlier in the derivation of the VSS growth mechanism, Persson et al. stated that the size-dependent melting point depression factor was not considered due to the larger size of the Au–Ga alloy seed particle (20–70 nm) examined in their growth, compared with the size of the Au nanoparticle (2–5 nm) examined in the work of Buffat et al. (a work which they had referenced), where the size-dependent melting point depression was observed [27]. It is important, however, to point out that many of the previous size-dependent melting point depression studies were done on the substrate materials that had a very low affinity to the nanostructure being studied, since the melting behavior of nanostructures is known to be strongly influenced by the surrounding environment [30,31]. In the work of Buffat et al., for example, the size-dependent melting point depression of Au nanoparticles has been examined on an amorphous carbon surface which has a minimal interaction with Au. This description of minimal nanostructure–substrate surface interaction cannot be applied for a system of Au on the GaAs and InAs substrates, where Au forms an intermetallic phase even at low temperature with Ga and In.

Although there seems to be differing (and contradictory) results with the newly proposed VSS growth mechanism, one thing that should be mentioned is that the growth systems (MOCVD, MBE, etc.) are all different, and thus more research is needed to clarify the VLS and VSS growth mechanisms with the decrease in the dimension of the metal alloy particles.

1.3 Si-Assisted Growth Mechanism

To investigate the effect of SiO_x on the growth of InAs nanowires, we performed growths [21] on two types of substrates, InAs(111)B and Si(111), with 1.3 nm of SiO_x (no Au catalyst). We first examined the growth in the absence of any

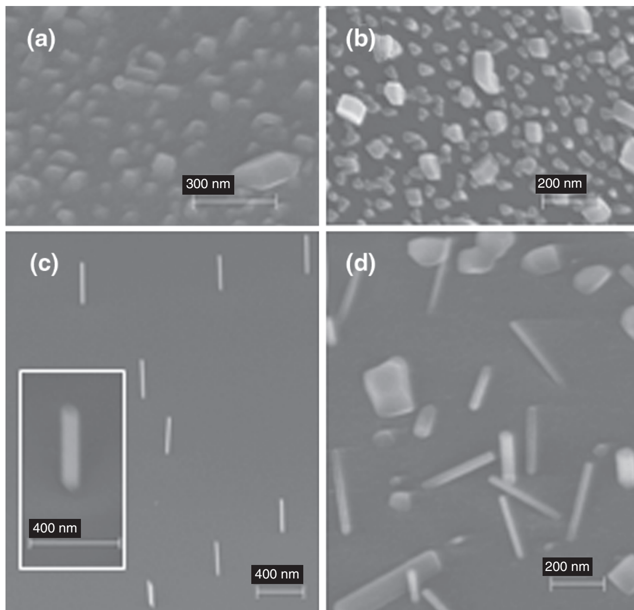

Fig. 1.5 InAs deposits on (**a**) InAs(111)B (scale bar 300 nm) and (**b**) Si(111) (scale bar 200 nm) substrates *without* any SiO_x and native oxides. InAs nanowires on (**c**) InAs(111)B (scale bar 400 nm) and (**d**) Si(111) (scale bar 200 nm) substrates *with* 1.3 nm of SiO_x. *Insert* in (**c**) is the close view of the InAs nanowire (reprinted with permission from [21], Copyright 2006, American Institute of Physics)

SiO_x (including native oxides), and the results of growth on bare InAs(111)B and Si(111) substrates are shown in Fig. 1.5a and b, respectively. The images show variously shaped InAs islands, with the structures on the Si(111) substrate revealing more crystalline features. We next used 1.3 nm of SiO_x and the growth results on InAs(111)B and Si(111) substrates are shown in Fig. 1.5c and d, respectively. Interestingly, the typical diameter of the nanowires was about 20–30 nm on both substrates, and the resulting lengths were quite similar. However, while the growth direction of the nanowires on the InAs(111)B was along the $\langle 111 \rangle$ direction, the growth direction on the Si(111) was random, as shown in Fig. 1.5d. In Fig. 1.6a and b, the TEM images of the VLS and SiO_x-grown InAs nanowires are shown, respectively, at the point of their growth termination. As can be seen, the terminating surface of the SiO_x-grown nanowire is flat and absent of any catalyst particle, unlike the typical VLS- (and VSS)-grown nanowires. Inset in Fig. 1.6b shows the opposite end of the nanowire (typically fractured), identifying it as the base of the nanowires where it had broken off from the substrate during TEM sample preparation. The electron diffraction pattern also revealed SiO_x-grown nanowires to be single crystal.

Growth was also attempted with only the native oxides of InAs (In–O_x and As–O_x), where no Au catalyst was used. The HCl-etched InAs substrate was left

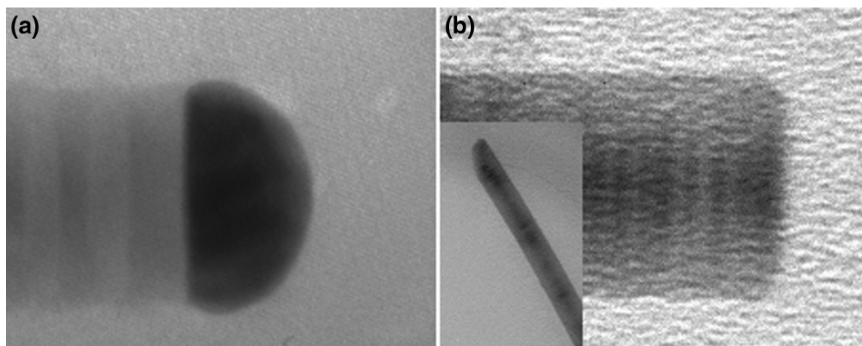

Fig. 1.6 Growth terminating points for the (**a**) VLS and (**b**) Si-assisted grown nanowires. *Insert* shows the wire end broken off the substrate (reprinted with permission from [21], Copyright 2006, American Institute of Physics)

out in the air and allowed to oxidize at room temperature for 3 days prior to growth (no Au catalyst was used). The expected native oxide thickness for an HCl-etched InAs substrate, oxidized at room temperature for 3 days, will be approximately 10 Å [33]. After a growth time 30 min in the furnace, the substrate was examined under SEM, but unlike in the SiO_x case, no growth was noted in this case.

Finally, to examine the VLS and the SiO_x growth simultaneously, Au nanoparticles were deposited on existing 1.3-nm SiO_x on the InAs(111)B substrate. In this case, catalyst-free nanowires still grew (as evidenced by the uniform 20-nm diameters and random growth directions), but no Au-mediated nanowires were noted in the 30 min growths. However, some were found to grow after longer growth times.

Now, let us consider the effect of an oxide layer on the growth of these nanowires. As discussed earlier, no nanowire growth occurred when the substrate contained a thin In- or As-based suboxide. This would suggest the deleterious nature of oxygen on the resultant nanowire growth. However, the results were quite different when a silicon suboxide layer was present, where InAs nanowires of characteristic 20–30 nm diameters grew. This suggests that the type of oxide, and not the presence of oxygen alone, may be the determining factor.

In the case of a silicon suboxide, the stoichiometry of evaporated SiO_x films is strongly dependent on various evaporation parameters, such as temperature, pressure, and rate of evaporation [34]. Since our deposition conditions were very similar to those used in the previous study [35], we expect $x \approx 1$ for our SiO_x film. It is well known that SiO undergoes a phase separation reaction $(2SiO \rightarrow Si + SiO_2)$ [34] at higher temperatures $(T > 400^\circ C)$, yielding nanometer-sized Si clusters [36, 37]. We would thus expect this phase separation to occur at our growth temperature of 580°C. Since Zhang et al. [38] have reported that Si clusters in the silicon suboxide are energetically very reactive, while SiO_2 is quite stable, one would expect that these nanometer-sized Si clusters could enhance the In attachment rate at the cluster surface sites. Since the silicon clusters are in solid state at 580°C, the growth

of the nanowires has to occur via In diffusion through the solid cluster or surface diffusion around the cluster to the growing interface. This suggests a Si-assisted growth mechanism with Si in solid state. The growth mechanism may seem similar to VSS (or Ti-catalyzed growth of Si nanowires), but unlike VSS (or even VLS), not only the mediating catalyst in Si-assisted growth is nonmetallic, but also the catalyst particle is noticeably absent at the point the nanowire growth terminates. Also, in comparison to the OA growth mechanism, Si-assisted growth does not have any oxygen involved in the growth process.

In our case, an additional factor which enhances our nanowire growth involves the presence of stable SiO_2 surrounding the Si clusters after the phase separation. One can look at this as analogous to growth of nanowires using SiO_2-masked regions and openings in the mask, where wires nucleate. In this case, enhanced wire growth has been reported as a result of surface diffusion of the growth species from the masked oxide regions to the growing nanowires in the openings [39]. In the growth of InAs quantum dots on Si substrate, the success in the selective deposition of InAs on Si using SiO_2 mask was similarly attributed to the combination of larger In diffusion coefficient and surface energy of SiO_2 ($7 \times 10^{-9}\,cm^2\,s^{-1}$, 3.83 eV) in comparison to Si ($10^{-20}\,cm^2\,s^{-1}$, 0.483 eV) [40]. Thus, a significant amount of material is provided by diffusion from the surrounding stable oxide and not just from the vapor phase, allowing a faster NW growth.

It should be mentioned that In and Si form a eutectic at $\sim$157°C [41], and thus it is possible for a Si–In liquid phase to form, which could act as a liquid metal catalyst for the nanowire growth by the VLS. However, the at.% of In at the eutectic temperature is $\sim$99.98, which is extremely unlikely to form in this growth process. Furthermore, no metal alloy tip has been seen in these nanowires, ruling out the VLS mechanism.

1.4 Concluding Remarks

In this chapter, we have examined several of our recent results that have implications to the VLS growth mechanism as well as the newly proposed Si-assisted growth mechanism. In summary, the study on the effect of oxygen showed the presence of oxygen clearly inhibiting the VLS growth mechanism during the nanowire growth. The results on the observation of size-dependent liquidus depression, more importantly, do not seem applicable on the results of Ti-catalyzed grown Si nanowires, but bring into the question the validity of the VSS growth mechanism in the Au-catalyzed grown GaAs and InAs nanowires. In the newly proposed growth mechanism, namely the Si assisted using SiO_x, a growth model is proposed based on the phase separation of SiO at higher temperature which forms a stable SiO_2 and reactive, nanometer-sized Si clusters. It is suggested that these clusters consequently serve as the nucleating/catalyst sites for the growth of InAs nanowires with the growth mechanism different from VLS, VSS, and OA.

References

1. Zhang YF, Tang YH, Wang N, Lee CS, Bello I, Lee ST (2000) Germanium nanowires sheathed with an oxide layer. Phys Rev B 61:4518
2. Tang YH, Wang N, Zhang YF, Lee CS, Bello I, Lee ST (1999) Synthesis and characterization of amorphous carbon nanowires. Appl Phys Lett 75:2921
3. Peng HY, Zhou XT, Wang N, Zheng YF, Liao LS, Shi WS, Lee CS, Lee ST (2000) Bulk-quantity GaN nanowires synthesized from hot filament chemical vapor deposition. Chem Phys Lett 327:263
4. Lee ST, Wang N, Zhang YF, Tang YH (1999) Oxide-assisted semiconductor nanowire growth. MRS Bull 24:36
5. Westwater J, Gosain DP, Tomiya S, Usui S, Ruda H (1997) Growth of silicon nanowires via gold/silane vapor–liquid–solid reaction. J Vac Sci Technol B 15:554
6. Bootsma GA, Gassen HJ (1971) A quantitative study on the growth of silicon whiskers from silane and germanium whiskers from germane. J Cryst Growth 10:223
7. Gu G, Burghard M, Kim GT, Dusberg GS, Chiu PW, Krstic V, Roth S, Han WQ (2001) Growth and electrical transport of germanium nanowires. J Appl Phys 90:5747
8. Duan X, Lieber CM (2000) General synthesis of compound semiconductor nanowires. Adv Mater 12:298
9. Hiruma K, Yazawa M, Katsuyama T, Ogawa K, Haraguchi K, Koguchi M, Kakibayashi H (1995) Growth and optical properties of nanometer-scale GaAs and InAs whiskers. J Appl Phys 77:447
10. Park HD, Prokes SM, Cammarata RC (2005) Growth of epitaxial InAs nanowires in a simple closed system. Appl Phys Lett 87:063110
11. Persson AI, Larsson MW, Stenstrom S, Ohlsson BJ, Sameulson L, Wallenberg LR (2004) Solid-phase diffusion mechanism for GaAs nanowire growth. Nat Mater 3:677
12. Dick KA, Deppert K, Martensson T, Mandl B, Samuelson L, Seifert W (2005) Failure of the vapor–liquid–solid mechanism in Au-assisted MOVPE growth of InAs nanowires. Nano Lett 5:761
13. Park HD, Gaillot A-C, Prokes SM, Cammarata RC (2006) Observation of size dependent liquidus depression in the growth of InAs nanowires. J Cryst Growth 296(2):159
14. Kolb FM, Hofmeister H, Scholz R, Zacharias M, Gosele U, Ma DD, Lee ST (2004) Analysis of silicon nanowires grown by combining SiO evaporation with the VLS mechanism. J Electrochem Soc 151:G472
15. Wagner RS, Ellis WC (1964) Appl Phys Lett 4:89
16. Wagner RS (1970) *Whiskers Technology*, Levitt AP (ed), Wiley, New York, pp 47–119
17. Givargizov EI (1978) Growth of whiskers by the vapor–liquid–solid mechanism. In: Kaldis E (ed) *Current Topics in Materials Science*, vol. 1, North-Holland, Amsterdam
18. Morales AM, Lieber CM (1998) A laser ablation method for the synthesis of crystalline semiconductor nanowires. Science 279:208
19. Park HD, Hogan TP (2004) Growth of Si wires on a Si(111) under ultrahigh vacuum condition. J Vac Sci Technol B 22:237
20. Hiruma K, Yazawa M, Haraguchi K, Ogawa K, Katsuyama T, Koguchi M, Kakibayashi H (1993) GaAs free-standing quantum-size wires. J Appl Phys 74:3162
21. Park HD, Prokes SM, Twigg ME, Cammarata RC, Gaillot A-C (2006) Si-assisted growth of InAs nanowires. Appl Phys Lett 89:223125
22. Simic V, Marinkovic Z (1977) Thin film interdiffusion of Au and In at room temperature. Thin Solid Films 41:57
23. Pasquevich AF, Hoffmann A, Vianden R, Wrede U (1985) Oxidation of indium in gold–indium alloys. J Appl Phys 58:3200
24. Kamins TI, Williams RS, Basille DP, Hesjedal T, Harris JS (2001) Ti-catalyzed Si nanowires by chemical vapor deposition: Microscopy and growth mechanisms. J Appl Phys 89:1008
25. Harmand JC, Patriarche G, Pere-Laperne N, Merat-Combes M-N (2005) Analysis of vapor–liquid–solid mechanism in Au-assisted GaAs nanowire growth. Appl Phys Lett 87:203101

26. Cahn JW (1980) Surface stress and the chemical equilibrium of small crystals. Acta Metall 28:1333
27. Buffat P, Borel JP (1976) Size effect on the melting temperature of gold particles. Phys Rev A 13:2287
28. Zhang M, Efremov MY, Schiettekatte F, Olson EA, Kwan AT, Lai SL, Wisleder T, Greene JE, Allen LH (2000) Size-dependent melting point depression of nanostructures: Nanocalorimetric measurements. Phys Rev B 62:10548
29. Wu Y, Yang P (2000) Germanium/carbon core-sheath nanostructures. Appl Phys Lett 77:43
30. Sheng HW, Liu K, Ma E (1998) Melting and freezing behavior of embedded nanoparticles in ball-milled Al-10 wt% M (M = In, Sn, Bi, Cd, Pb) mixtures. Acta Mater 46:5195
31. Jin ZH, Sheng HW, Lu K (1999) Melting of Pb clusters without free surfaces. Phys Rev B 60:141
32. Vallee R, Wautelet M, Dauchot JP, Hecq M (2001) Size and segregation effects on the phase diagrams of nanoparticles of binary systems. Nanotechnology 12:68
33. Petrovykh DY, Yang MJ, Whitman LJ (2003) Chemical and electronic properties of sulfur-passivated InAs surfaces. Surf Sci 523:231
34. Pliskin WA, Lehman HS (1965) Structural evaluation of silicon oxide films. J Electrochem Soc 112:1013
35. Fogarassy E, Slaoui E, Fuchs AC, Regolini JL (1987) Rapid thermal oxidation of silicon monoxide. Appl Phys Lett 51:337
36. Rinnert H, Vergnat M, Matchal G, Burneau A (1999) Strong visible photoluminescence in amorphous SiO_x and SiO_x: H thin films prepared by thermal evaporation of SiO powder. J Lumin 80:445
37. Nesheva D, Raptis C, Perakis A, Bineva I, Aneva Z, Levi Z, Alexandrova S, Hofmeister H (2002) Raman scattering and photoluminescence from Si nanoparticles in annealed SiO_x thin films. J Appl Phys 92:4678
38. Zhang RQ, Chu TS, Cheung HF, Wang N, Lee ST (2001) Mechanism of oxide-assisted nucleation and growth of silicon nanostructures. Mater Sci Eng C 16:31
39. Noborisaka J, Motohisa J, Fukui T (2005) Catalyst-free growth of GaAs nanowires by selective-area MOVPE. Appl Phys Lett 86:213102
40. Choi BH, Park CM, Song SH, Son MH, Wang SW, Ahn D, Kim EK (2005) Selective growth of InAs self-assembled quantum dots on nanopatterned SiO_2/Si substrate. Appl Phys Lett 78:10
41. Thurmond CD, Kowalchik M (1960) Bell Syst Tech J 39:169

Chapter 2
One-Dimensional SiC Nanostructures: Synthesis and Properties

Weimin Zhou, Yafei Zhang, Xiaoming Niu, and Guoquan Min

Abstract SiC with unique properties, such as wide band gap, excellent thermal conductivity, chemical inertness, high electron mobility, and biocompatibility, promises well for applications in microelectronics and optoelectronics, as well as nanocomposites. The chapter reviews the recent progress on one-dimensional SiC nanostructures in both experimental and theoretical level, including synthesis methods and some properties (field emission, optical, electronic transport, mechanical, photocatalyst, and hydrogen storage) of SiC nanowires. Importantly, some novel results on SiC nanowires were elucidated clearly in our laboratory. Personal remarks end with some views on development and application of one-dimensional SiC nanostructures.

2.1 Introduction

Recently, one-dimensional (1D) semiconductor nanostructures (wires, rods, belts, and tubes) have become the focus of intensive research, owing to their unique application in the fabrication of electronic, optoelectronic, and sensor devices on a nanometer scale. They possess novel properties intrinsically associated with low dimensionality and size confinement, which make "bottom-up" construction of nanodevices possible [1–7]. Because of their potential applications in nanodevices, 1D semiconductor nanomaterials were selected as one of the top 10 technologies by the MIT Technical review in 2003 [8]. So far, many kinds of 1D semiconductor nanomaterials, including single element [9–14] and compound semiconductors [15–21], have been successfully synthesized by a rich variety of methods, and the detailed research information on these 1D nanostructures can be readily seen in the pertinent literature [22–44]. Among these semiconductor nanowires, SiC has very unique properties, such as wide bandgap, excellent thermal conductivity, chemical inertness, high electron mobility, and biocompatibility, which promise well for applications in microelectronics and optoelectronics, and has thus attracted much interest from the materials and devices communities [45–47]. In particular, SiC nanowires

are used for the reinforcement of various nanocomposite materials or as nanocontacts in harsh environments, mainly due to their superior mechanical properties and high electrical conductance. Hence, research on 1D SiC nanowires is highlighted, both from the fundamental research standpoint and for potential application in nanodevices and nanocomposites.

In this chapter, research on 1D SiC nanostructure (nanowires/nanotubes, nanowire heterostructures, and nanowire arrays) is highlighted in a comprehensive review and some important results of pioneering work conducted in our laboratory on SiC nanowires are reported. The review is divided into three main parts. The first part introduces crystallographic structures of SiC; the second part focuses on the synthesis of SiC nanowires and the third part on some special nanostructures of orient SiC nanowire arrays, SiC nanotubes, and SiC nanowire heterostructures. Some properties of SiC nanowires are described later. The review ends with a summary, which is our personal opinion on future research in 1D SiC nanowires.

2.2 Crystallographic Structures of SiC

SiC is a IV–IV compound semiconductor and occurs in many different crystal structures (polytypes). The crystalline structure of SiC can be considered to consist of the close-packed stacking of double layers of Si and C atoms. Each C or Si atom is surrounded by four Si or C atoms in strong tetrahedral SP^3 bonds. The distance between neighboring Si and C atoms is approximately 3.08 Å for all polytypes [48,49]. There are more than 200 polytypes in existence. The polytypes can be defined by the number of stacking layers in a unit cell. The atom arrangements of popular polytypes are 3C, 4H, and 6H. The 3C-SiC polytype is the only cubic polytype and it has a stacking sequence ABCABC. 4H-SiC consists of an equal number of cubic and hexagonal bonds with stacking sequences of ABCB. Two-thirds of 6H-SiC is composed of cubic bonds and one-third of hexagonal bonds, with stacking sequences of ABCACB. Only 3C-SiC is referred to as β-SiC; other 4H- and 6H-SiC are called α-SiC. Figure 2.1 shows the schematic diagram illustrating the stacking layer of

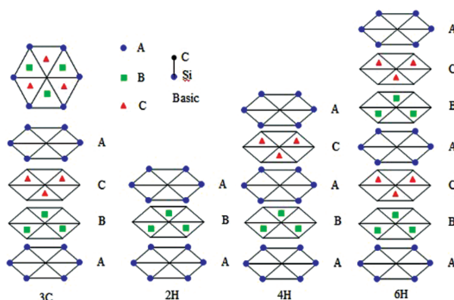

Fig. 2.1 The stacking sequence of 3C-, 2H-, 4H-, and 6H-SiC

Table 2.1 Typical properties of SiC and other semiconductors [49]

	Si	GaAs	3C-SiC	4H-SiC	6H-SiC	Diamond
Lattice *a* (Å)	5.43	5.65	4.36	3.08	3.08	3.567
Lattice *a* (Å)	5.43	5.65	4.36	15.12	10.05	3.567
Bond length (Å)	2.35	2.45	1.89	1.89	1.89	1.54
TEC (10^{-6} K)	2.6	5.73	3.0	–	4.5	0.8
Density (g cm^{-3})	2.3	5.3	3.2	3.2	3.2	3.5
Thermal conductivity (W cm^{-1} K^{-1})	1.5	0.5	5	5	5	2
Melting point (°C)	1,420	1,240	2,830	2,830	2,830	4,000
Mohs hardness			9	9	9	10
E_g (eV)	1.1	1.43	2.3	3.3	3.0	5.4

the common 3C-, 2H-, 4H-, and 6H-SiC. In general, β-SiC, which often appears at low temperature, is easy to nucleate and grow. However, 4H-SiC and 6H-SiC are known as high-temperature stable polytypes, which need relatively high temperatures to grow. Typical properties of SiC and other semiconductors are summarized in Table 2.1.

SiC materials are extremely hard, very inert, and have high thermal conductivity. Properties such as the breakdown electric field strength, the saturated drift velocity, and the impurity ionization energies are unique for the different polytypes. β-SiC possesses the smallest bandgap (∼2.4 eV) and has the highest electron carrier mobility compared with α-SiC, which makes it an important SiC material in the microelectronics industry [50]. Because of these excellent properties, SiC is a perfect material in the electronics industry, with a wide application in the areas of high-temperature device, high-power device, high-frequency device, and optoelectronic device, including rectifiers, power switches, RF, and microwave power devices [51, 52]. Besides, SiC, known for its high-temperature structure and reinforced composite material, can be also find application in the aerospace, car, machine, and petrochemical industries [52–57].

2.3 Synthesis of One-Dimensional SiC Nanostructures

Since the discovery of the carbon nanotube (CNT) [58, 59], 1D SiC nanostructures have attracted many scientists because of their unique electronic, optical, and mechanical properties. A significant progress in synthesis methods in SiC nanowire/nanotube was achieved by various technologies, such as carbon template, arc discharge, chemical vapor deposition (CVD) via silicon precursor, carbothermal reduction of silica xerogels, etc. In this section, some recent progress in the fabrication of 1D SiC nanostructures is addressed.

2.3.1 Carbon Nanotube-Confined Reaction

In 1994, Prof. Zhou at the University of Arizona reported for the first time a method to produce SiC whiskers without the presence of metal catalysts by reacting carbon nanotubes with SiO at 1,700°C under a flow of Ar [60]. The length and diameter of the as-synthesized SiC nanowire are one order greater in magnitude than that of the carbon nanotube precursor. The dark carbon nanotubes with hollow cores are converted to solid greenish SiC nanowires. The carbon nanotube acts as a template and defines the diameter and length of SiC nanowires. The reaction is as follows:

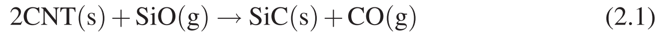

$$2\mathrm{CNT(s)} + \mathrm{SiO(g)} \rightarrow \mathrm{SiC(s)} + \mathrm{CO(g)} \tag{2.1}$$

In 1995, Lieber's group [61] at Harvard University reported in *Nature* that carbon nanotubes can be converted to carbide rods by reaction with SiO or Si–I_2. The SiC nanorods (NRs) are in high yield with typical diameters similar to or much smaller than the diameters of the carbon nanotube, of between 2 and 30 nm and lengths of up to 20 μm.

A two-step reaction process has been developed to synthesize SiC nanorods at 1,400°C [62]. SiO vapor was generated via the silicon reduction of silica, and reacted with the carbon nanotube to form SiC nanorods. In the two-step reaction process, the reaction equations are

$$\mathrm{SiO_2(s)} + \mathrm{Si(s)} \rightarrow 2\mathrm{SiO(v)} \tag{2.2}$$

$$\mathrm{SiO(v)} + 2\mathrm{C(s)} \rightarrow \mathrm{SiC(s)} + \mathrm{CO(v)} \tag{2.3}$$

The nanorods are single-crystalline β-SiC with the diameters between 3 and 40 nm. The thinner SiC nanorods, namely 3 nm in diameter, show a high density of defect planes on the (111) basal planes. In this experiment, the diameter of the SiC nanowire differed from the precursor carbon nanotube. It may be explained as follows.

The generated CO vapor in (3) can react with SiO vapor on the generated SiC nanorod surface by the following reaction:

$$\mathrm{SiO(v)} + \mathrm{CO(v)} \rightarrow \mathrm{SiC(s)} + 2\mathrm{CO_2(v)} \tag{2.4}$$

In this reaction, the diameter of the synthesized SiC nanorods is larger than that of the starting carbon nanotubes. On the contrary, the thinner diameters of SiC nanorods can be explained by the following reaction.

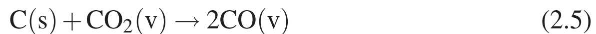

$$\mathrm{C(s)} + \mathrm{CO_2(v)} \rightarrow 2\mathrm{CO(v)} \tag{2.5}$$

The surface of the carbon nanotubes is consumed by the CO_2 and the residual carbon nanotube reaction with SiO leads to thinner SiC nanorods.

The diameter and shape of the produced SiC nanorods can be controlled by the local partial pressure of CO gas and the reaction temperature, respectively. Tang

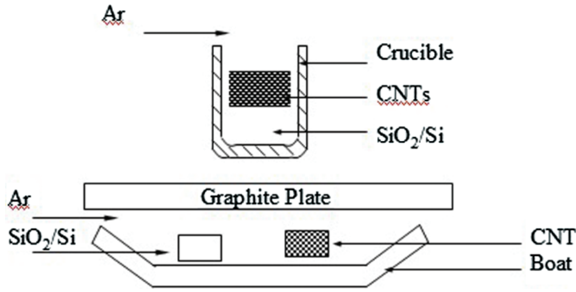

Fig. 2.2 Geometry of the reactor. (**a**) Reactants of SiO_2/Si source covered with carbon nanotubes were put in a crucible. (**b**) SiO_2/Si source and carbon nanotubes were put in a boat and the latter kept clear of the former along the downstream direction of gas flowing

et al. [63] developed a new way as shown in Fig. 2.2. The generated CO byproduct from (3) can be effectively carried away from the reaction area, thus preventing reactions (4) and (5). The size of the diameter of SiC nanowires is consistent with the starting carbon nanotubes. The growth mechanism of SiC nanorods is basically a shape memory synthesis, where the product keeps the shape of the starting nanotubes to form nanorods. The shape memory synthesis has the advantages of the shape of the generated nanorods adjusted by the initial carbon nanotubes, the CO-generated concentration, and reaction temperature.

The unexpected synthesis of SiC nanorods with thermally annealing single-walled carbon nanotube sheets (SWNTs) formed by a filtration process using surfactant-dispersed nanotubes, at a significantly lower temperature of 1,000°C between two silicon wafers [64]. In the experiment, the exterior layers of the carbon nanotube sheets were converted into a network of SiC nanorods, while the carbon nanotubes interior to the sheet remained unchanged. The SEM images are shown in Fig. 2.3.

2.3.2 Arc Discharge

Since carbon nanotubes were synthesized by arc discharge, scientists attempted to fabricate SiC nanowires with the arc-discharge process, considering the simple setup, ease of operation and high production. Seeger et al. [65] reported for the first time the synthesis of nanometer-sized SiC whiskers using the arc-discharge process. The samples were synthesized using an arc discharge between two graphite electrodes, the anode of which was filled with a mixture SiO_2 and C powder in the atomic ratio 1:1. The arc discharge was ignited by 40 A at 22 V under a 53 kPa helium atmosphere. The graphite cathode of 10 mm diameter was placed horizontally, facing the composite anode of 6.15 mm diameter, which had a 3.2 mm diameter hole drilled, with 25 mm filled with a mixture of graphite and Si powder. β-SiC whiskers of 10 nm in diameter were synthesized directly.

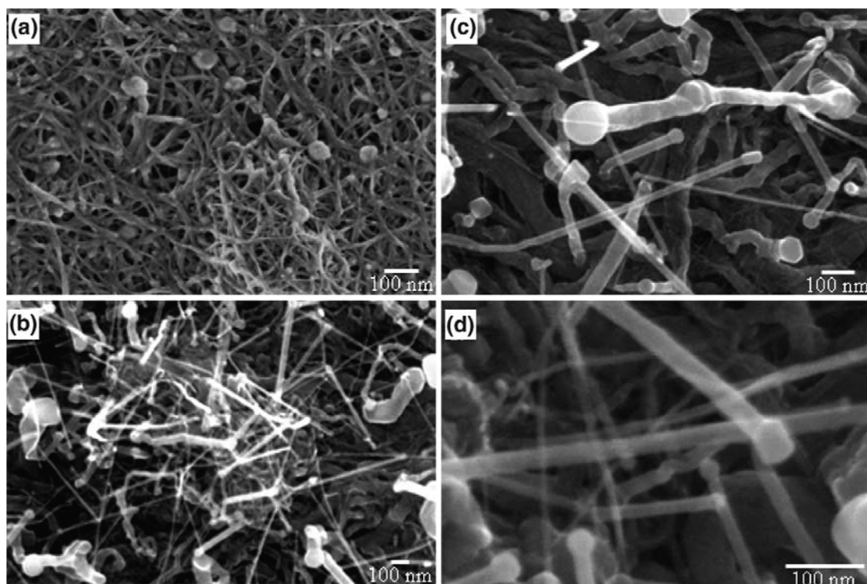

Fig. 2.3 SEM micrographs of a carbon nanotube sheet before (**a**) and SiC nanorods: after (**b**)–(**d**) thermal annealing this sheet at 1,000°C between two parallel silicon wafers. The large quasi-spherical particles in (**a**), with a diameter of typically above 30 nm, contain iron [Ref. 3]

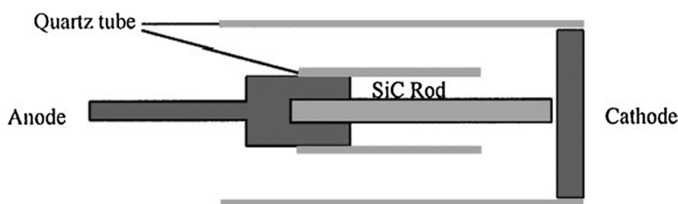

Fig. 2.4 Arc-discharge setup

Later, Xie's group [66] devised a new route, using a SiC rod as the anode in an arc-discharge process, developed to fabricate SiC nanorods on a large scale as shown Fig. 2.4. A graphite rod (15 mm in diameter) had a hole drilled (7.5 mm in diameter and 10 mm in depth) at one end and its other end was thinned to 6 mm in diameter. A SiC rod (about 7.5 mm in diameter and 8 cm in length) was inserted into the hole and acted as the anode, and a graphite plate (with a diameter of 30 mm) was used as the cathode. The characterization indicated that the prepared nanorods possess a β-SiC crystal core with a uniform diameter of 5–20 nm and an amorphous SiO_2 wrapping layer tens of nanometers in thickness, and their lengths ranging from hundreds of nanometers to several micrometers (Fig. 2.5). A possible growth mechanism could be explained as follows: during discharging, SiC at the tip of the anode decomposes into silicon and carbon due to the high temperature of the arc-zone.

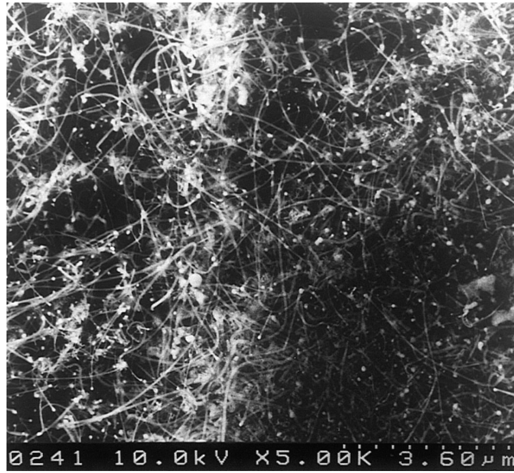

Fig. 2.5 SEM image of the powder by arc discharge [Ref. 51]

$$SiC(s) \rightarrow Si(g) + C(g) \quad (2.6)$$

The silicon gas may react with the quartz (SiO_2) to form SiO gas.

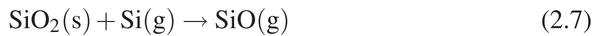

$$SiO_2(s) + Si(g) \rightarrow SiO(g) \quad (2.7)$$

Hence, the Si, C, and SiO gas were absorbed and dissolved in the liquid-iron droplets to form a liquid Fe–Si–C–O alloy. When cooled, the liquid droplets were supersaturated and the β-SiC core together with the SiO_2 sheath was nucleated.

2.3.3 Laser Ablation

Laser ablation has been widely synthesized for carbon nanotubes [67, 68] and Si nanowires [69, 70], because the method can produce free-standing nanoscale material in high-purity yields at a low working temperature for high-melting and multicomponent materials. Shi et al. [71] used the laser-ablation technique (Fig. 2.6) to synthesise SiC nanowires from a target of SiC target $(25 \times 25 \times 5\,mm)$. The KrF excimer pulsed laser beam (wavelength 248 nm, energy 400 mJ per pulse, and frequency 10 Hz) was focused on the SiC target and the ablation lasted for 2 h. Large quantities of straight, curved, and randomly oriented nanowires were formed on the graphite substrate in the system. The lengths of the nanowires were up to tens of micrometers (Fig. 2.7). There were also some spherical nanoparticles at the tips of the nanowires (as seen in Fig. 2.7). The SiC nanowire consists of a crystal SiC core with numerous stacking faults and an amorphous silicon oxide shell. The transmission electron microscopy (TEM) observation showed that the diameters of the crystalline cores varied from 20 to 70 nm and the mean value was $\sim$55 nm. The thickness of the amorphous outer layers varied from 11 to 30 nm and the mean value was $\sim$17 nm.

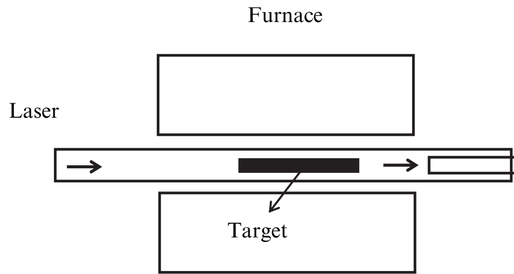

Fig. 2.6 Laser-ablation scheme

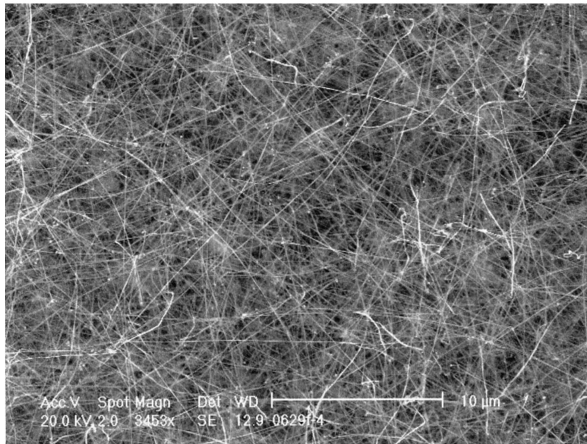

Fig. 2.7 Typical SEM image of SiC nanowires [Ref. 71]

2.3.4 Sol-Gel and Carbothermal Reduction

Meng et al. [72, 73] have successfully developed a novel method to synthesize bulk quantities of β-SiC nanowires from silica xerogels containing carbon nanoparticles. Nanowires were fabricated by carbothermal reduction at 1,650°C for 1.5 h, followed by annealing to 1,800°C and holding for 30 min in flowing Ar atmosphere. TEM, SAED, and EDX showed that the nanowires consist of 10–25 nm diameter crystalline β-SiC cores surrounded by amorphous SiO_2 sheathes with outer diameters between 20 and 70 nm. The nanowires formed by carbothermal reduction at 1,650°C for 2.5 h in flowing argon atmosphere are bare SiC nanowires with diameters in the range of 15–30 nm.

Silicon carbide nanorods were synthesized by sol-gel and carbothermal reduction processing with TEOS (tetraethoxysilane) and PVP (polyvinyl pyrrolidone) as starting materials and $Fe(NO_3)_3$ as catalyst [74]. Results show that the morphologies of

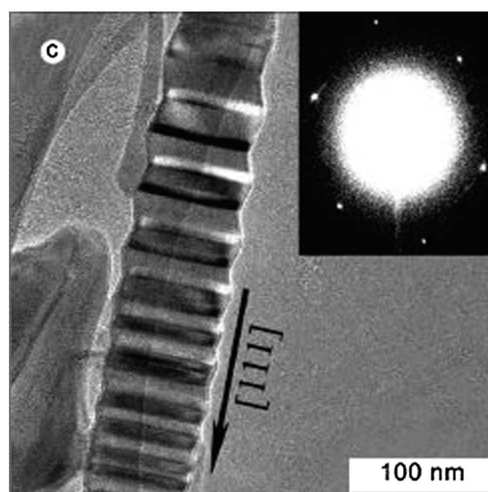

Fig. 2.8 TEM images of resulting SiC sample catalyzed by Fe [Ref. 74]

the resulting sample are tower-like β-SiC nanorods which typically have a tower base width between 80 and 100 nm, a step layer thickness of about 10 nm between two layers and a height from 0.4 to 1.0 μm (Fig. 2.8).

2.3.5 Chemical Vapor Deposition

In this process, a mixture of silicon (carbon) precursor of $SiH_4(SiCl_4, Si(CH_3)Cl$, $CH_3SiCl_3, CH_4)$ is introduced into the reaction chamber [75–77]. During the reaction, SiC nanowires are formed on the substrate by the reaction of carbon and silicon. Although this is at the cost of lower yield, the catalyst can be deposited on the desired location of substrate, which allows for the formation of novel nanostructures by predefined position of catalyst [78].

Zhang et al. [79] used microwave plasma CVD to synthesize bulk quantity singe-crystalline β-SiC nanowires on a Si substrate. The process is divided into two steps: first, smooth Si(100) substrates of $10 \times 20 \times 0.6$ mm were ultrasonically cleaned in ethanol and etched with 3% HF acid in water for 3 min. An Fe film of a different thickness (9–105 nm) was deposited on the Si(100) substrate by the sputtering method. Then the Si substrate was placed in the CVD system. A 100 sccm hydrogen (H_2) and a $\sim$0.05 sccm methane (CH_4) were introduced into the chamber. The Si substrate temperature is from 800 to 1,000°C. Figure 2.9 shows the TEM images of the as-synthesized SiC nanowires by the CVD method. The SiC nanowires are smooth and straight. Many nanowires are cylinder shaped with a circular cross section, while some of the nanowires have cross-sectional shapes of squares, rectangles, triangles, and hexagons. Moreover, no Fe catalyst has been found on the nanowires.

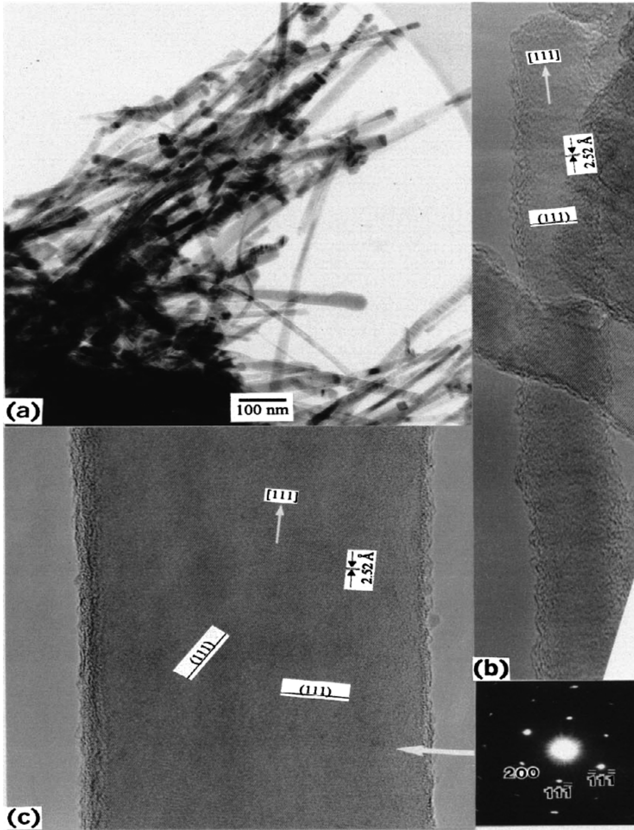

Fig. 2.9 (**a**) TEM image of the nanowhiskers obtained by scratching the nanowhiskers from the Si substrate. The whiskers with circular, square, rectangle, triangle, and hexagon cross-sectional shapes. (**b**) High-resolution TEM image of a thin 3C-SiC nanowhisker with an approximate axial orientation of [111]. (**c**) A thick 3C-SiC nanowhisker with its selected area electron diffraction pattern taken by the electron beam parallel to the [011] zone axis

The most commonly occurring diameter of the nanowire sample fabricated at different temperatures and different Fe film thickness is shown in Fig. 2.10.

The relation between PL peak energy and SiC nanowire diameter is shown in Fig. 2.11. A blueshift of the PL with decreasing nanowire diameters can easily be seen for quantum confinement effects. The experimental date was made to coincide with the PL peak energy formula: $E_{\text{peak}} = 2.16 + 32d_{\text{mo}}^{-2}$, where d_{mo} is the most commonly occurring diameter of the β-SiC nanowires in the sample.

Zhou et al. [80] synthesized SiC nanorods on silicon substrate by hot filament CVD. The carbon and silicon powders in a molar ratio of 1:1 were mixed and pressed into a solid disk and loaded into a HFCVD chamber. Hydrogen fed into the chamber etched the Si/C solid disk and brought Si/C-containing reactive species to the substrate surface. After 2 h, nanowires of SiC with a 10–30 nm diameter core–shell structure were found deposited directly on the substrate surface.

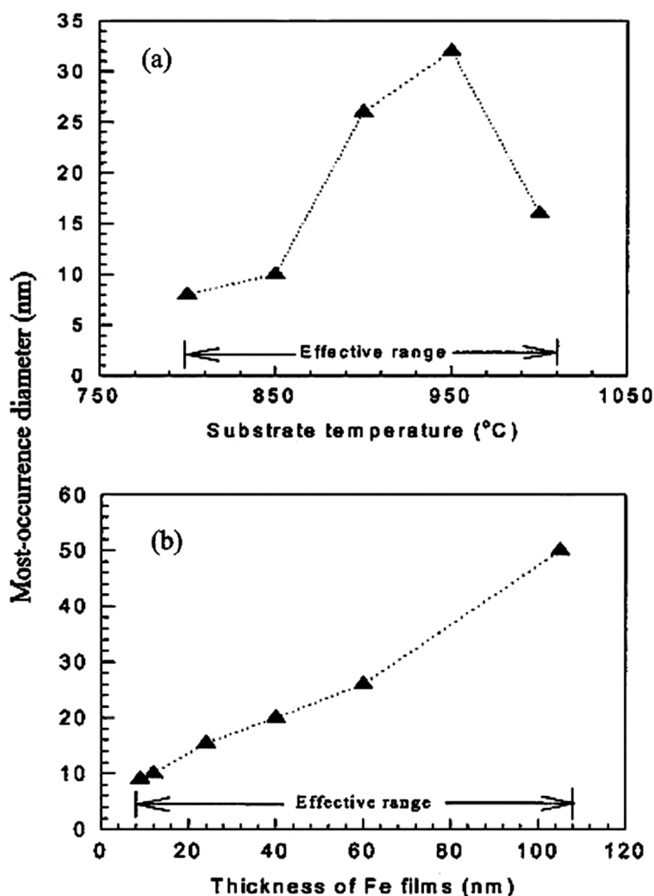

Fig. 2.10 The dependence of the most commonly occurring diameter of the nanowhisker samples synthesized on (**a**) different temperatures and (**b**) different Fe film thickness

SiC nanowires with diameters of <50 nm and lengths of several micrometers have been fabricated on Si substrates coated with a thickness of 2 nm Ni film by direct current magnetron sputtering methods [81]. Methyltrichlorosilane (MTS, CH_3SiCl_3) was used as a source precursor because it has an equivalent ratio of Si to C and decomposes at a low temperature. H_2 was used both as the carrier gas, which transfers the source precursor through a bubbler to the quartz reactor, and as a diluent gas, which regulates the concentration of the mixture containing MTS vapor and carrier gas. The XRD, TEM, and HRTEM observations confirm that the nanowires are single-crystalline cubic zinc-blend structures with a $\langle 111 \rangle$ direction and SiC nanowire growth via the VLS mechanism. Figure 2.12 shows that the SiC nanowires grow under a reactor pressure of ca. 5 Torr for 2 h. The nanowires have diameters from several tens to hundreds of nanometers and are vertically well aligned without templates such as anodic alumina templates. Interestingly, Al-doped SiC

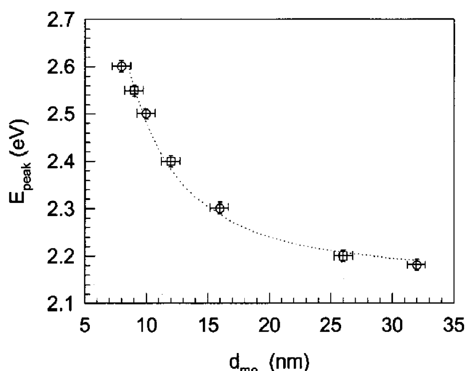

Fig. 2.11 The dependence of the photoluminescence peak energy (E_{peak}) on the most commonly occurring diameter (d_{mo}) of the 3C-SiC nanowhisker samples. The *dotted line* corresponds to $E_{\mathrm{peak}} = 2.16 + 32d_{\mathrm{mo}}^{-2}$. The photoluminescence spectra were measured by using a Renishaw 2000 micro-Raman spectrometer with a 350 nm cutoff filter. The wavelength-dependent sensitivity of the optical system was calibrated by a standard lamp. The 325 nm emission line from a He–Cd laser was used to excite the luminescence

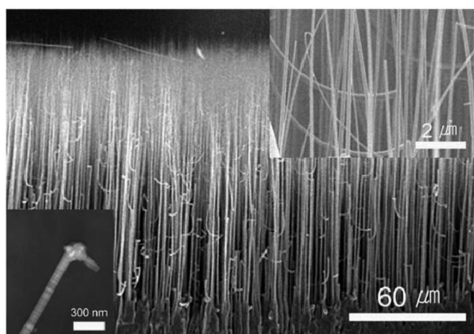

Fig. 2.12 SEM images of vertically aligned SiCNWs grown on a Si substrate at 1,100°C for 2 h under total reactor pressure of 5 Torr. The total hydrogen flow rate including carrier and dilute gas was maintained at 775 cm^3 min^{-1}. *Left lower inset* is a TEM image of SiCNWs [Ref. 81]

nanowires were fabricated for the first time by simply placing the $AlCl_3$ precursor located upstream in the distance of 5 cm from the substrate. So, the n-type β-SiC nanowires can be adjusted to p-β-SiC by doping. Figure 2.13 shows the SEM and EDS images of Al-doped SiC nanowires. An energy dispersion spectroscopy (EDS) analysis of individual SiC nanowires indicated the existence of Al in the nanowires.

SiC nanostructures in the shape of crystalline nanowire flowers have been synthesized by CVD [82]. The silicon substrate and GaN powder are placed in an alumina boat in a tube furnace. A steady flow of 300–400 sccm methane gas was introduced at 1,100°C. Flower-like structures of diameter 1–2 μm and length 3–5 μm are shown in Fig. 2.14a, b. A typical flower (Fig. 2.14c, d) is composed of an intertwined/weaved stem, a bulbous head consisting of a tight bundle of nanowires of

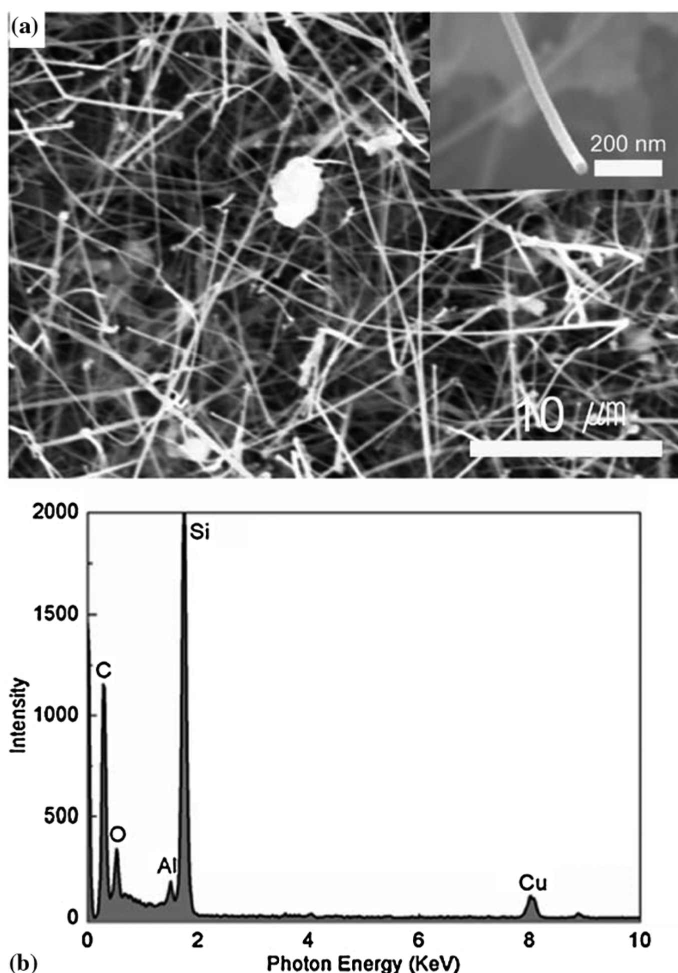

Fig. 2.13 (**a**) SEM image of the NWs grown at 950°C for 5 min by using $AlCl_3$ powders as doping precursor in MTS–H_2 system under atmospheric pressure. *Inset* is TEM image of individual NW. (**b**) EDS data recorded from individual NW indicate the existence of Al in the NW [Ref. 81]

diameter ~100–200 nm, and a single catalyst particle attached at the top end of the nanowire flowers. The cross section of the broken base (Fig. 2.14c, inset) reveals a hollow stem of ~400–800 nm in diameter. The flowers are composed of β-SiC and the formation mechanism is the VLS process.

Novel 2D semiconductor SiC nanonetworks have been synthesized at relatively low temperature (1,250°C) via CVD [83]. The mixture of Si and SiO_2 powders and C_3H_6 were used as precursor materials. The straight or curved SiC networks that the nanowires are connected to were formed on carbon cloth. The nanowires with diameter of about 20–70 nm are single-crystalline β-SiC and the growth direction is along [111].

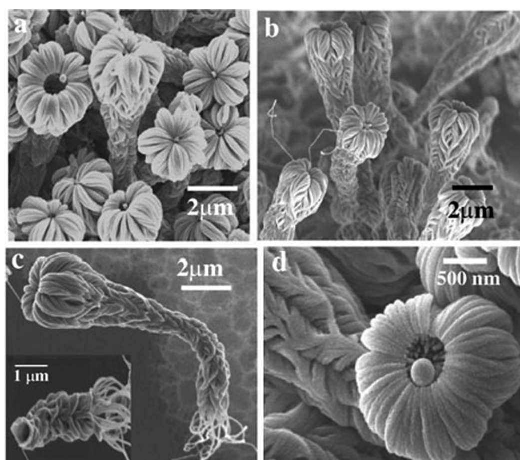

Fig. 2.14 (**a**) SEM images of, and (**b**) an overview of, nanowire flowers grown on the silicon substrate; (**c**) a detached flower showing its base made up of bundles of nanowires (*inset*: cross-sectional view of a broken SiC nanowire flower); (**d**) a typical flower with a catalyst particle attached to the tip [Ref. 82]

SiC nanorods have been synthesized by floating catalyst methods. Iron particle catalyst was decomposed from ferrocene vapor while being carried into the chamber by the flowing gases. In the $SiCl_4$–C_6H_6–H_2–Ar system, $SiCl_4$ and C_6H_6 reacted with each other, catalyzed by the Fe cluster [84].

2.3.6 High-Frequency Induction Heating

Zhou [85] invented a novel method to fabricate β-SiC nanowires without catalyst introduction in high yields on the surface of the activated carbon fibers (ACFs). The experiments were performed in a vertically set high-frequency induction-heating furnace as schematically outlined in Fig. 2.15, which consisted of a quartz tube and an inductive heat cylinder of graphite coated by a layer of ACFs. First, 2 g of commercial SiO powder (purity more than 99.9%) was put into a graphite crucible. Before heating, the chamber was flushed with high-purity 100 sccm Ar to eliminate O_2 by means of rotary vacuum pump for three times. Afterwards, the furnace was rapidly heated from room temperature to around 1,450°C within 2 min and maintained for reaction for 15 min under a total pressure of 50–100 Torr. After the furnace was cooled to room temperature in the flowing Ar, the ACF surface was deposited with a thick layer of light-blue fluff-like products having a thickness of several millimeters as shown in the inset of Fig. 2.16. Many mushroom-like lumps grew perpendicularly and separately from the surface of the ACF and joined each other at their tip.

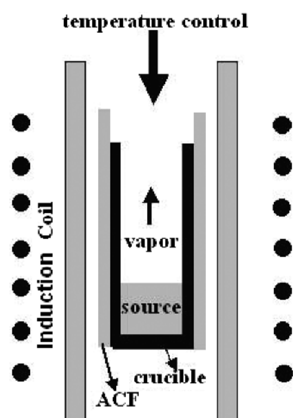

Fig. 2.15 High-frequency induction-heating furnace

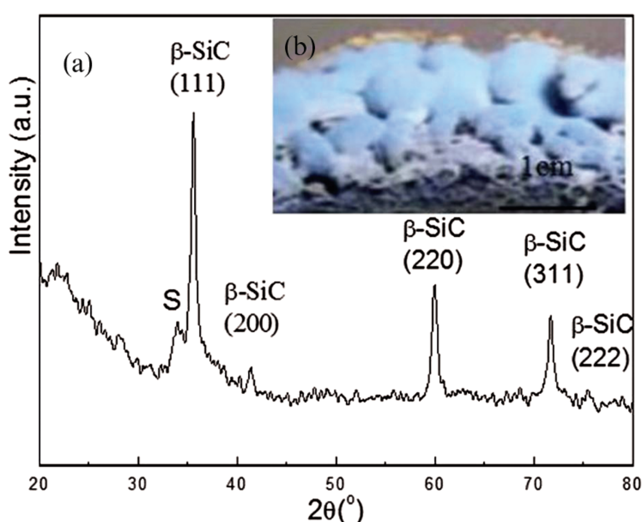

Fig. 2.16 (**a**) XRD pattern of the as-synthesized products. *Inset* (**b**): the digital camera photo of the products

The X-ray diffraction (XRD) pattern (Fig. 2.16) suggests that the as-synthesized product consists of the crystalline zinc-blend (cubic) form of β-SiC with the unit constant of $a = 4.358 \mathring{A}$, close to the standard value for β-SiC (4.359 Å, JCPDS card no. 29-1129). A broad peak at $2\theta = \sim 20^{\circ}$–$30^{\circ}$ may be attributed to some amorphous materials with the product. Besides, there is a low-intensity peak (marked with S) at a lower diffraction angle than that of the strong (111) peak, which usually ascribes to the stacking faults in the (111) plane. The low-magnification SEM image shown in Fig. 2.17a reveals that the product consists of numerous wire-like nanostructures (a large amount of straight, curved, randomly oriented, and free-standing nanowires) with a length of up to tens of micron. Figure 2.17b shows the chemical composition of the nanowires characterized by EDS. It is found that the nanowires are mainly

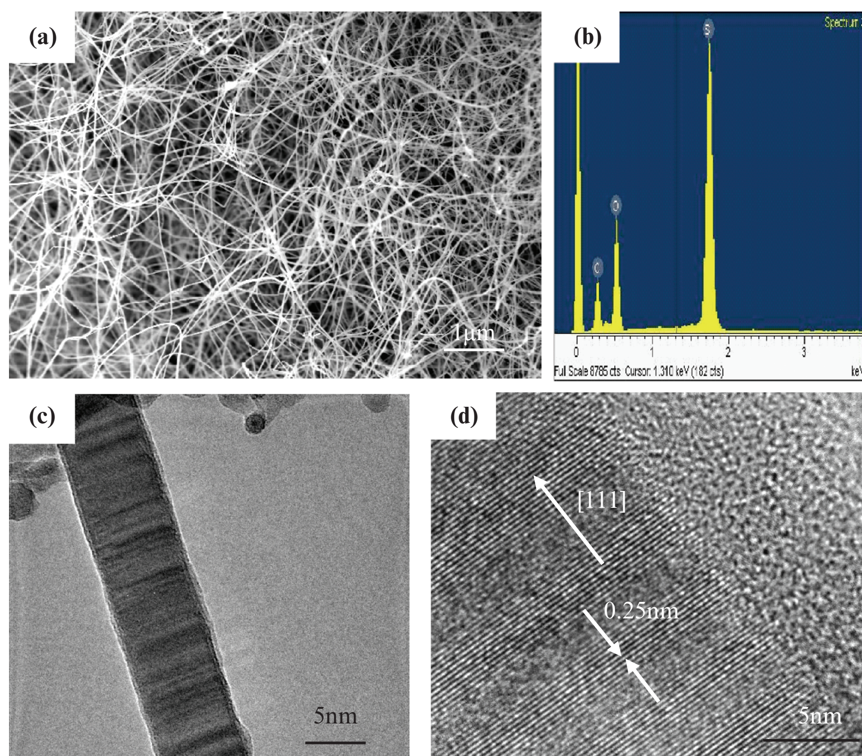

Fig. 2.17 (**a**) SEM image of as-prepared samples grown at 1,450°C for 20 min by SiO powder and carbon fiber, (**b**) EDS spectrum of the nanowires, (**c**) TEM image of SiC nanowire, and (**d**) HRTEM image of the individual SiC nanowire

composed of Si, C, and O. The large resolution TEM image shows that a d-spacing of 0.25 nm corresponds to the (111) plane spacing, indicating that SiC nanowire grows along [111] direction.

In addition, the SiC/SiO_2 nanosprings, as shown in Fig. 2.18, were synthesized by the method [86]. The diameter of the nanospring is $\sim$25 nm and with the nanospring pitch of 10 nm, this amounts to a diameter/pitch ratio of 2.5. The total nanostructures consist of three segments: two end of the nanostructure is SiC/SiO_2 nanocables, but SiC/SiO_2 nanospring is clearly seen in the midst of the whole nanostructure. TEM dark images (Fig. 2.18b) indicate that the nanospring is composed of a crystalline core and an amorphous coating. In the previous chapter, the important role of the catalyst in the formation of SiC/SiO_2 nanosprings was elucidated by Zhang et al. [87], which is different from our experiment without a catalyst. The helical spring structure is the most fundamental structural configuration for DNA and many biological proteins, which is due to van der Waals force and hydrogen bonding [88]. These shapes of nanostructures will be found to be a great potential application in electronic circuits and light-emitting devices such as nanospring-based transducers and actuators, and tunable functional components

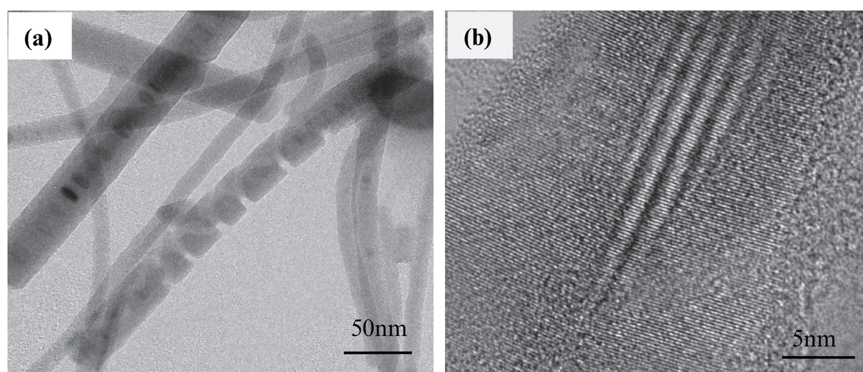

Fig. 2.18 (**a**) Typical TEM images for SiC/SiO_2 nanosprings and (**b**) HRTEM image nanostructures

for MEMS and NEMS. Moreover, the nanosprings are preferable to 1D and 0D nanostructures when acting as reinforcements in advanced materials because of their better-combined interface between SiC nanosprings and the matrix in the same condition.

Similarly, Shen et al. [89] used high-frequency induction heating to synthesize bamboo-like β-SiC nanowires by thermal evaporation of SiO + C + GaN powders in an Ar atmosphere at 1,350°C for 1h. Later, they adjusted the mixture ratio of SiO + C + GaN powders. Hierarchical single-crystalline β-SiC nanowires have been successfully synthesized. Studies found that the central nanowires have diameters of ∼10–20 nm and the branched nanoplatelets have thicknesses of 5–10 nm [90].

2.3.7 Comparison of Methods of SiC Nanowire Synthesis

The aforementioned methods to synthesize SiC nanowire – namely carbon nanotube template, arc discharge, CVD via silicon and carbon precursor – and the high-frequency heating method invited by us, have been often reported during the last several years. To show the difference clearly, Table 2.2 provides the comparison of several methods of synthesizing SiC nanowire. In most cases the product is available at the cost of either high-purity or expensive CNT or the hazardous and easily explosive silicon (carbon) precursor of SiH_4 or $SiCl_4(CH_4)$. In addition, the synthesized materials were low in yield and purity and the methods time-consuming. Hence, the preparation of pure SiC on a large scale is still a challenge. Fortunately, we have developed a method for low-cost, large-scale production of β-SiC nanowires by high-frequency heating of SiO powders and ACF layers. The synthesized, high yield, SiC nanowires were directly deposited on ACF without metal catalyst introduction. Most importantly, the ACF and SiO powders are readily available because they are mass-produced in the industry and the technology of SiC nanowire synthesis invented by us can easily be scaled up to industrial levels.

Table 2.2 The comparison of several synthetic methods of SiC nanowire

Synthesized methods	Efficiency	Cost	Temperature (°C)	Diameter (nm)	Catalyst
Carbon nanotube-confined reaction	Low	Higher	1,400	20–25	No
Arc discharge	Higher	Low	3,000	20–60	Yes
Laser ablation	High	High		20–70	Yes
Sol-gel and carbothermal reduction	Higher	Lower	900	40–80	No
Chemical vapor deposition method	Higher	Higher	1,100	10–100	Yes
High-frequency induction heating	Higher	Lower	1,450	5–20	No

2.4 Orient SiC Nanowire Arrays

With the development of electronic and photonic devices such as light-emitting diodes and laser diodes, field-emission display, high density and well-aligned nanowire arrays would be necessary. The unique structure and features of the anodic alumina membranes (AAM) make it an ideal template for the synthesis of aligned nanostructures. Li et al. [91] reported for the first time the synthesis of large–area, highly oriented, SiC nanowire arrays in an ordered nanoporous AAO temperature through a chemical vapor reaction method. The 1.2:1 molar mixture of ball-milled Si and SiO_2 and AAO template were placed in a graphite cell. The C_3H_6 flow of 8–10 sccm was introduced from the bottom of the graphite cell and maintained for 3–5 min at 1,230°C under a total gas pressure of 540–650 Torr. The results show that the SiC nanowires are single crystalline with diameters of ∼30–60 nm and lengths of ∼8 μm, which are parallel to each other, uniformly distributed, highly aligned, and in agreement with the nanopore diameter of the AAO template. The fabricated SiC nanowires grow along the [111] direction and possess a high density of planar defect.

Aligned SiC nanowires have also been synthesized by reaction-aligned carbon nanotubes with SiO [92]. High-magnification SEM observations (Fig. 2.19) show that the products consist of highly oriented nanowires that are similar in appearance to the originally aligned carbon nanotubes. The SiC nanowires within the arrays have diameters (10–40 nm), spacing (∼100 nm), and length (up to 2 mm) similar to those of the aligned carbon nanotubes. The SiC nanowire is a solid rod and does not have a hollow core structure (Fig. 2.20). The periphery of the SiC nanowire is very clean, without any coating of amorphous material, and possesses a high density of planar defects or stacking faults, which are perpendicular to the wire axes. The selected area electron diffraction (SAED) pattern (inset of Fig. 2.20a) demonstrates that the SiC nanowire has a single-crystalline phase.

Highly aligned β-SiC nanowires with a mean diameter of 40 nm and length of 500 μm on a large area Si substrate were synthesized by a novel catalytic reaction

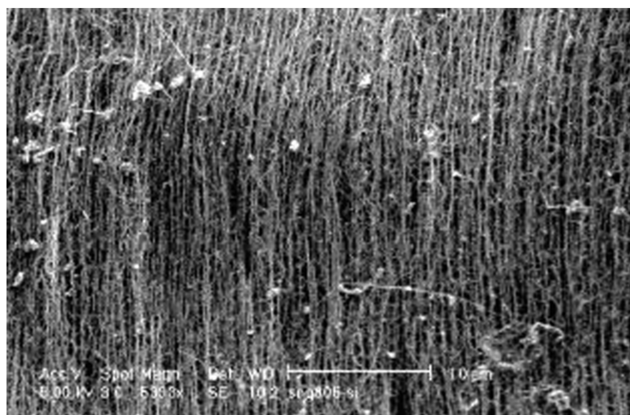

Fig. 2.19 High-magnification SEM image of a SiC nanowire array, showing that the wires are highly aligned and have uniform external diameters and spacing between wires. The particles present on the array surface are silicon-containing particles formed and deposited during reaction [Ref. 92]

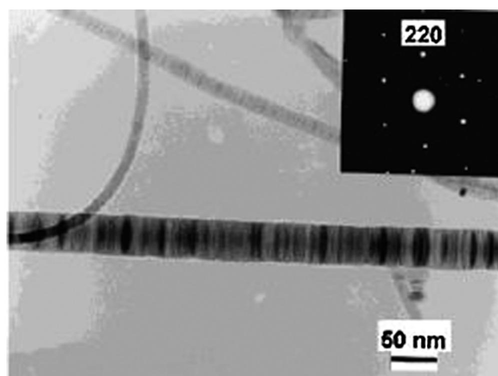

Fig. 2.20 TEM image of β-SiC nanowires. The SiC nanowires exhibit a high density of stacking faults perpendicular to the wire axes. The *inset* shows a selected area electron diffraction pattern of the β-SiC nanowires [Ref. 20]

1,100°C [93]. The Si substrate and CH_4 were used as the Si and C source, respectively. The Si substrate was coated with Ga metal, GaN powder, and Fe nanoparticle catalyst.

2.5 SiC Nanotubes

Sun et al. [94] used the equipment (Fig. 2.21) to synthesise SiC nanotubes (SiCNTs). SiO powders were placed at position A, the middle of the high-temperature zone of the furnace. Four pieces of Si substrate on which multiwalled carbon nanotube

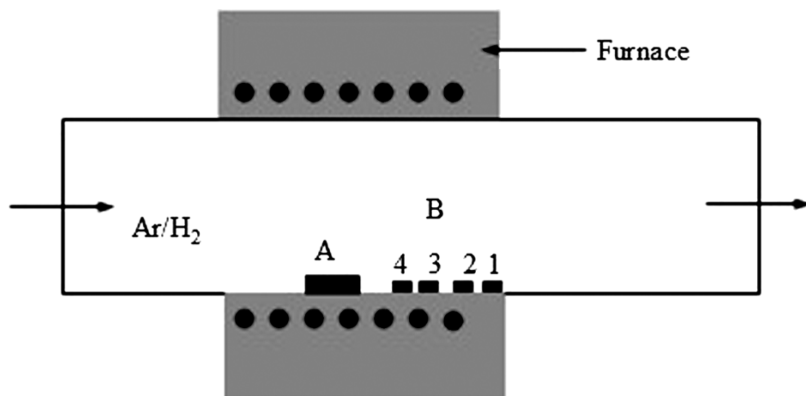

Fig. 2.21 Synthesis apparatus

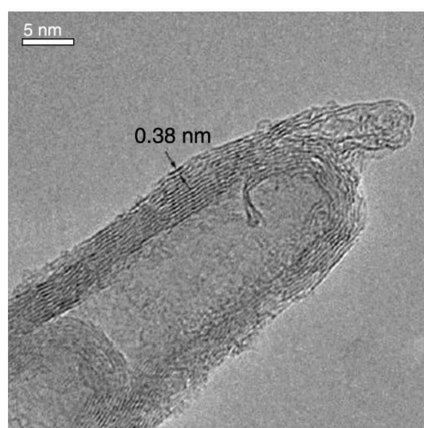

Fig. 2.22 HRTEM image of a SiC nanotube structure with 3.8 Å spacing [Ref. 94]

had been grown were placed at positions marked B_1–B_4. The temperature of the system was set to 1,250°C for 40 min and B_4–B_1 position temperatures were found to decrease from 980 to 850°C. Si nanowires were found in all B_4–B_1 positions, but the quantities of Si nanowires decreased from B_4 to B_1. However, at position B_3, ~935°C, besides Si nanowires, multiwalled SiC nanotubes were also obtained. A typical image of the fabricated SiC nanotubes is shown in Fig. 2.22. The interlayer spacing of the SiC nanotubes ranges from 3.5 to 4.5 Å.

The SiC nanotubes are carbon-filled and open-ended, and use a high-temperature substitution reaction between multiwalled carbon nanotubes and Si powder. The mean diameter and diameter distribution (45–70 nm) are smaller than previously reported for SiC nanotubes [95].

Single-phase silicon carbide nanotubes were successfully synthesized by the reaction of carbon nanotubes with silicon powder at 1,200°C for 100 h [96]. TEM

observations revealed the formation of both single-phase SiC nanotubes and C–SiC coaxial nanotubes, which are carbon nanotubes sheathed with a SiC layer.

2.6 SiC Nanowire Heterostructures

1D nanowire heterostructures are important for their potential applications in nanodevices. There are three basic structures: axial heterostructures, in which the heterointerface is perpendicular to the wire axis, radial heterostructures, in which the heterointerface is parallel to the wire axis, and branched nanowire structures, in which the structures have branched and tree-like nanowire structures. Detailed information as to semiconductor nanowire heterostructures can be found in [97, 98].

Multielement nanotubes comprising multiple phases, with diameters of a few tens of nanometers and lengths up to 50 μm, were successfully synthesized by means of reactive laser ablation in NEC Corporation [99]. A mixed and compressed powder of BN, C, SiO, and Li_3N acted as starting material. The synthesized structure consists of β-SiC–SiO_2–BN/C nanocables, as shown in Fig. 2.23. They have high aspect ratios with lengths of several tens of micrometers and diameters of a few tens of nanometers, which is relatively homogeneous for each wire. The structure resembles a coaxial nanocable with a semiconductor–insulator–metal (semiconductor–insulator–semiconductor) geometry and suggests applications in nanoscale electronic devices that take advantage of this self-organization mechanism for multielement nanotube formation. Later, heterostructures of single-walled SiC nanotubes and nanorods were fabricated by solid–solid reaction between single-walled carbon nanotubes (SWCNTs) and Si/Ti [100].

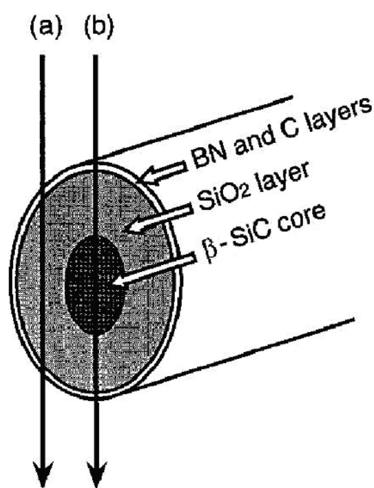

Fig. 2.23 Multiphase nanocable. *Solid arrows* indicate the probe positions in the electron energy loss fine structure analysis (not shown) [Ref. 99]

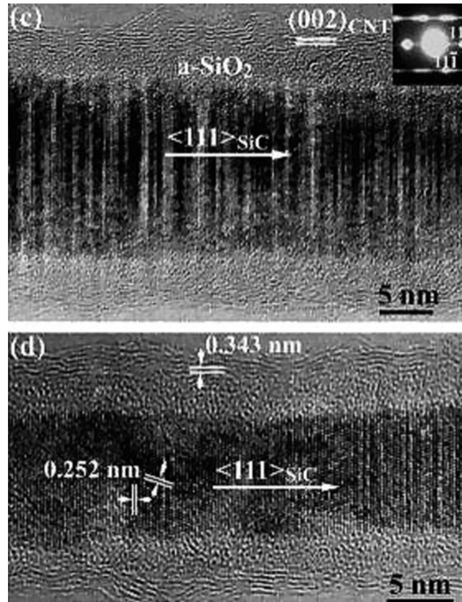

Fig. 2.24 High-resolution TEM images of coaxial nanocables, displaying single-crystalline β-SiC cores, amorphous SiO_2 intermediate layers (**c**), and outer graphitic C sheaths (**d**). The *inset* in (**c**) represents the corresponding ED pattern [Ref. 101]

Li et al. [101] reported a simple thermal evaporation route for the mass production of SiC–SiO_2–CNT coaxial nanocables (Fig. 2.24). Most importantly, they found that these nanocables may be further transformed into nanochains of SiC–CNT junctions during high-temperature annealing at 1,600°C in a high vacuum of 1.5×10^{-3} Pa (Fig. 2.25).

An insulating tubular boron nitride (BN)-sheathed SiC semiconductor nanowire was synthesized [102–107]. The BN nanotube may serve as a naturally insulating and/or protective shield for any nanowire encapsulating within because of its advantages. Hexagonal BN, a covalently bonded compound, displays stable insulating properties (∼5.5 eV bandgap) independent of its morphology. Moreover, graphitic-like BN is chemically inert and remarkably thermally stable [108].

The BN-sheathed SiC nanowires can be synthesized by heating a mixture of B and SiO_2 with molar ratio of 1:1 [102]. The inside SiC nanowires exhibit a wide diameter distribution from several nanometers to 80 nm. The sheathed BN layer has a uniform coating thickness from 2 to 4 nm, which is independent of the diameter of the SiC nanowires. B_2O_2 and SiO vapors were generated by heating the mixture of B and SiO_2 powders at the high temperature of 1,500°C by the following solid-state reaction:

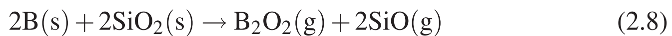

$$2B(s) + 2SiO_2(s) \rightarrow B_2O_2(g) + 2SiO(g) \quad (2.8)$$

The simultaneously formed vapors (B_2O_2 and SiO) were transported to a deposition area, where highly oriented pyrolitic graphite (HOPG) covered with fine nickel

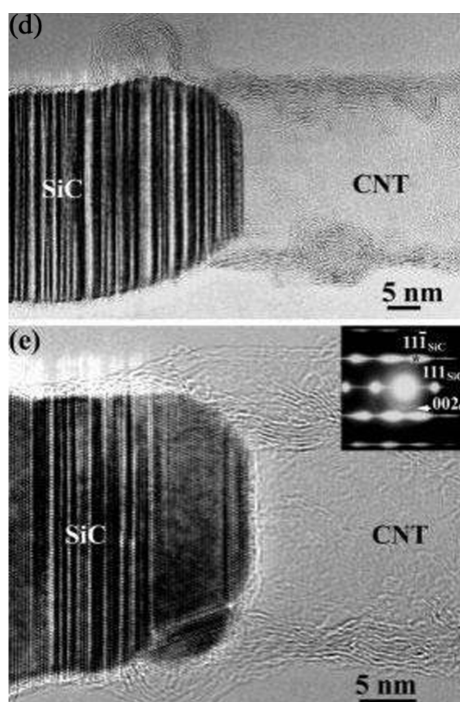

Fig. 2.25 (**d**) and (**e**) selected high-resolution TEM images of SiC–CNT junctions after annealing [Ref. 101]

catalyst grains was placed. SiC and BN can be formed on the surface of HOPG in the presence of nitrogen by further reactions at about 1,400°C.

$$SiO(g) + 2C(s) \rightarrow 2SiC(s) + CO(g) \quad (2.9)$$

$$B_2O_2(g) + 2C(s) + N_2(g) \rightarrow 2BN(s) + 2CO(g) \quad (2.10)$$

The ZnS/SiC nanocables and SiC-shelled ZnS nanoribbons were synthesized using ZnS nanowires and nanoribbons as templates via a controllable two-stage thermal process. First, ZnS nanowires were formed by heating SiO and ZnS powders. Then, the decomposition of CH_4 and disproportion of SiO resulted in the synthesis of SiC nanowires on the ZnS-based template surface [109].

A two-step process was used to synthesize a direct heterojunction of ZnO nanorods on SiC nanowires [110]. First, a nanowire substrate was synthesized by heating NiO-catalyzed Si wafer at 1,050°C. Then, diethylzine was used as a metal-organic gas source to fabricate ZnO nanorods on SiC nanowires at 450°C. An atomically abrupt interface without interfacial layers was detected. ZrO_2 and metal coating on SiC nanowire were also synthesized by CVD [111–113].

The synthesis of SiC/ZnO shell–core nanostructures involved two steps [114]. First, ZnO nanostructures (nanobelt, nanocombs, nanojunctions, and nanohelices) were fabricated using a vapor–solid growth. Then, a SiC layer was deposited on

the surface of ZnO nanostructures via plasma-enhanced chemical vapor deposition (PECVD). The source materials for SiC were CH_4 and SiH_4 gases. Subsequent dissolution of ZnO (by HCl solution) left a SiC shell that preserved the same shape at the original ZnO nanostructure. This is one of the most effective methods for producing hollow nanostructures. The SiC shell nanostructures could have potential application in space-confined nanoreactors, catalysts, nanofluid channel, and drug delivery.

2.7 Properties of SiC Nanowires

2.7.1 Field Emission

Because of the small curvature of the tip radius, high ratio, chemical inertness, and electrical conductivity, SiC wide-bandgap semiconductors are considered to be promising for the next generation of large-area filed-emission flat panel displays (FEDs) [115–119]. A series of experiments have been carried out to investigate the field-emission characteristics of the 1D SiC nanostructures, which indicate that the SiC nanowires are characteristic of excellent emitting behavior for application in field-emission technology.

The field-emission measurements were carried out in a vacuum chamber at a pressure of 3×10^{-5} Pa at room temperature. Figure 2.26 shows the schematic diagram of the field-emission experimental setup. A platinum film coated on glass substrate with SiC nanowires was used as a cathode and a stainless steel plate with a diameter of 6 mm was used as an anode. Before testing the field emission, a 0.008 g SiC sample (HF-etched SiC fabricated by the high-frequency heating invented by

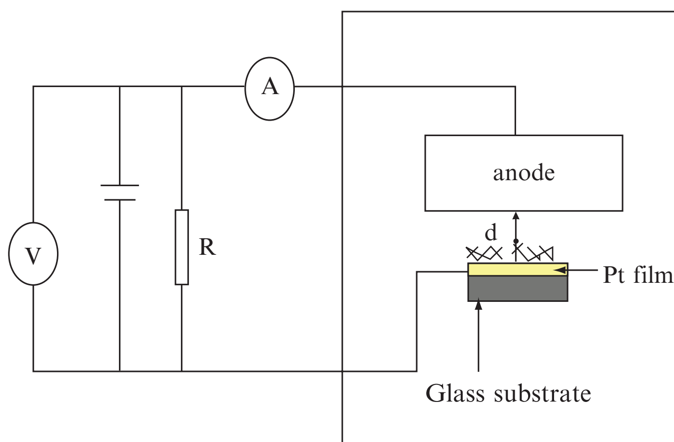

Fig. 2.26 Experiment setup used for the field-emission measurement

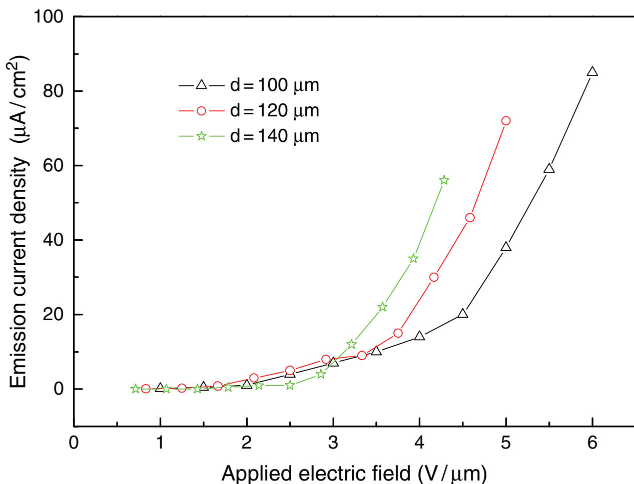

Fig. 2.27 The dependence of the field-emission current density J on the applied electric field strength E of the samples at three anode-sample distances of 100, 120, and 140 μm

us) was sonicated into a suspension in deionized water (DE) for 20 min and 20 drops of DE solution of SiC were dropped on the platinum film and dried at 50°C. The distance (d) between the emitting surface and the plate was determined by first lowering the plate to the product until electric contact was observed, then lifting the plate to a certain value [120]. Figure 2.27 shows the field-emission current density (J) of the SiC nanowires as a function of the applied electric field (E) at three anode-sample separation: 100, 120, and 140 μm. Here, we define the turn-on field as the electric field required to produce a current density of 10 μA cm^{-2}. It can be seen that the turn-on field is dependent on the anode-sample distance, its value increase as the anode-sample distances decrease, and measured to be 3.5, 3.4, and 3.1 V μm^{-1}, respectively, which indicates the strong electron emission property of the SiC nanowires because of the high aspect ratio.

The field-emission property was also analyzed by applying the first-order approximation of Fowler–Nordheim (FN) theory to understand the emission characteristics, using the following equation [121]

$$J = 1.56 \times 10^{-6} E^2/\Phi \exp(-6.83 \times 10^7 \Phi^{3/2}/E), \tag{2.11}$$

where J is the field-emission current density (A cm^{-2}), Φ is the work function of the emission tip (eV), and E is the microscopic local electric field at the emission sites (V cm^{-1}). The actual value of E could not be measured directly and is related to the applied voltage V by setting $E = \beta V/d$, where d is the anode-sample separation and β is the field enhancement factor. The FN emission behavior can be examined from the linearity of curves plotting $\ln(J/E^2)$ vs. $1/E$ as shown in Fig. 2.28. It is found that they yield straight lines for the three different anode-sample distances in agreement with the Fowler–Nordheim equation, confirming that the current is indeed the

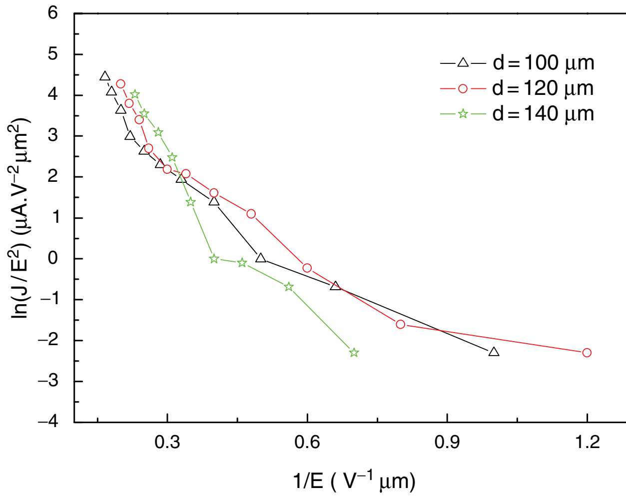

Fig. 2.28 Fowler–Nordheim relationship of $\ln(J/E^2) - 1/E$ plot at three anode-sample distances of 100, 120, and 140 μm

result of field emission. In other words, the field emission from SiC nanowires is a barrier tunneling, quantum mechanical process. Besides, the straight lines also show that the field emission is independent of the anode-sample separation, and only a function of the applied voltage. In addition, a stability and durability test was carried out on the SiC nanowires at anode-sample 100 μm separation. The results show that field-emission current density of 60 μA cm^{-2} was recorded for 15 min at the same applied voltage of 550 V. The current fluctuation was as low as ±15% and the average current did not decrease over this period.

The BN coatings reducing effectively the turn-on field of SiC nanowires were investigated by Tang [122]. It was found that BN–SiC 1D nanocomposite is a promising emitting material for applications in flat display. The low turn-on field is due to a decrease of the effective potential barrier height, which is considered to result from the existence of a defect-induced positive space charge. Figure 2.29 shows the field-emission plots for single-crystal β-SiC nanowires, BN nanotubes, and BN-coated SiC nanowires. The single-crystal SiC nanowires showed a high turn-on field at 13 V μm^{-1}. The turn-on field of pure BN nanotubes is also larger than 14 V μm^{-1}. But the pattern of field emission of BN–SiC nanowires clearly showed a low turn-on field at 6 and ~20 V μm^{-1} of threshold field providing 10 mA cm^{-2} of current density, which is typically required for effectively exciting a phosphor pixel in flat display.

Core–shell SiC/SiO_2 nanowires were fabricated by directly heating Si substrate with Ni film under reductive environments using the carbothermal reduction of WO_3 by C [123]. The thickness of SiO_2 layer can be controlled by HF-etching duration. Figure 2.30 shows the field-emission currents from the bare SiC and the SiC/SiO_2 samples for various shell thickness. The turn-on field of the samples was 4.0 V μm^{-1}

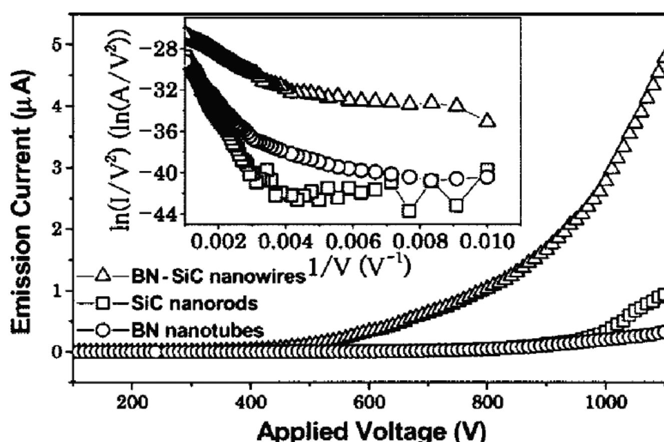

Fig. 2.29 Field-emission plots for single-crystal SiC nanowires, BN nanotubes, and BN-coated SiC nanowires. The *insets* show the corresponding FN plots [Ref. 122]

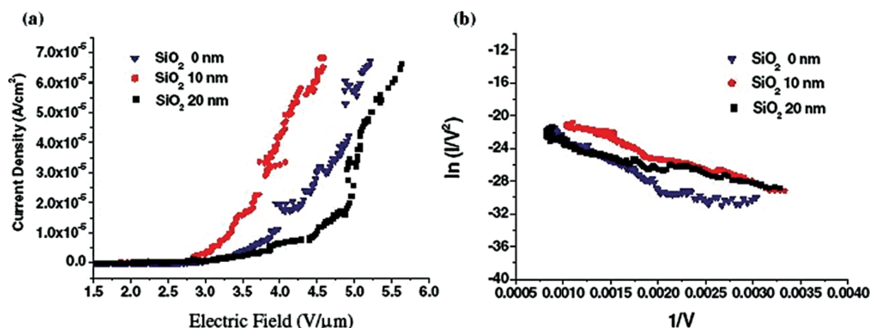

Fig. 2.30 (**a**) Current density $(\mathrm{A\,cm^{-2}})$–electric field $(\mathrm{V\,\mu m^{-1}})$ characteristics of core–shell SiC–SiO_2 and bare SiC nanowire emitters. (**b**) The Fowler–Nordheim plots of nanowires [Ref. 123]

(bare SiC nanowires), $3.3\,\mathrm{V\,\mu m^{-1}}$ (10 nm SiO_2-coated SiC), and $4.5\,\mathrm{V\,\mu m^{-1}}$ (20 nm SiO_2-coated SiC nanowires). It can be seen that SiC nanowires coated with an optimum SiO_2 thickness (10 nm) have a higher field-emission current than bare SiC nanowires. It is because the wide-bandgap SiO_2 shell layer has small electron affinity (0.6–0.8 eV) and can hence field emission properties of SiC nanowires. However, a very thick shell layer could induce charge buildup at the shell layer–SiC emitter due to limited electron supply through a thick insulating layer. The emission mechanism follows with Fowler–Nordheim equation.

The turn-on field of carbon-coated SiC nanowires at the emission current density of $10\,\mathrm{mA\,cm^{-2}}$ was about $4.2\,\mathrm{V\,\mu m^{-1}}$ [124]. The aligned SiC nanowires have a very low field $(2.5\text{–}3.5\,\mathrm{V\,\mu m^{-1}})$ to be excellent field emitter material.

2.7.2 Optical Properties

There have been some reports on the optical properties of SiC nanowires. Experiments showed that SiC nanowires have a significant redshift owing to the size confinement effect. Figure 2.31 shows the typical Raman spectra of SiC nanowires and SiC bulk ceramic target [71]. The SiC nanowires have the typical Raman features at ~784 and 938 cm^{-1} and both peaks have a marked redshift of 12 and 34 cm^{-1} compared to the TO and LO phonon modes of bulk SiC.

SiC/SiO_2 nanocables were synthesized by the low-cost arc-discharge method in deionized water [125]. The SiC with 10 nm core diameter possesses two broad PL peaks at 317 and 368 nm (Fig. 2.32a). But two emission peaks of the SiC nanowires with 20 nm diameter are located at 312 and 393 nm. It is believed that the second peak results from the central β-SiC nanowire and the blueshift may be the result of the quantum size effects. The thinner the central SiC nanorod is, the higher the correspondent PL peak energy is.

The PL spectra of the SiC with core diameter of 20 nm are shown in Fig. 2.32b. It can be seen that the positions of the PL peaks change little while the strength changed significantly. It can also be noted that high-temperature annealing would release the local stress formed during the growth of the nanocables and decrease the amount of defects; then the PL peak's intensity and position would change.

The β-SiC nanowires with different diameters, synthesized by our high-frequency heating method, were investigated by Fourier transition infrared (FT-IR) spectroscopy. In the FT-IR spectrum, each curve has strong adsorption peaks (Fig. 2.33). The values of 781 and 1,045 cm^{-1}, 788 and 1,082 cm^{-1}, and 800 and

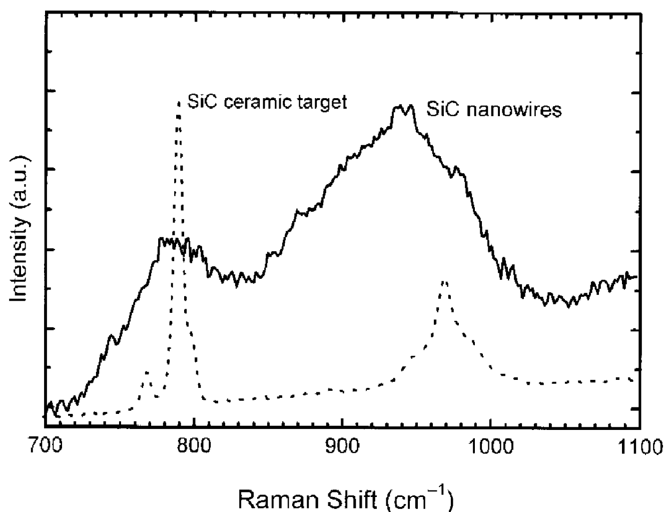

Fig. 2.31 Raman spectrum of SiC nanowires by laser ablation

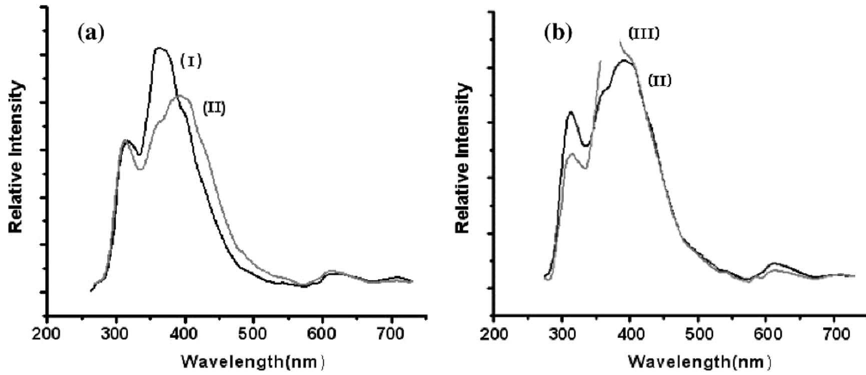

Fig. 2.32 (**a**) PL spectra of the as-prepared SiC nanocables with core diameters of 10 nm (I) and 20 nm (II), respectively. (**b**) The PL spectra of the SiC nanocables with core diameter of 20 nm before (II) and after (III) annealing

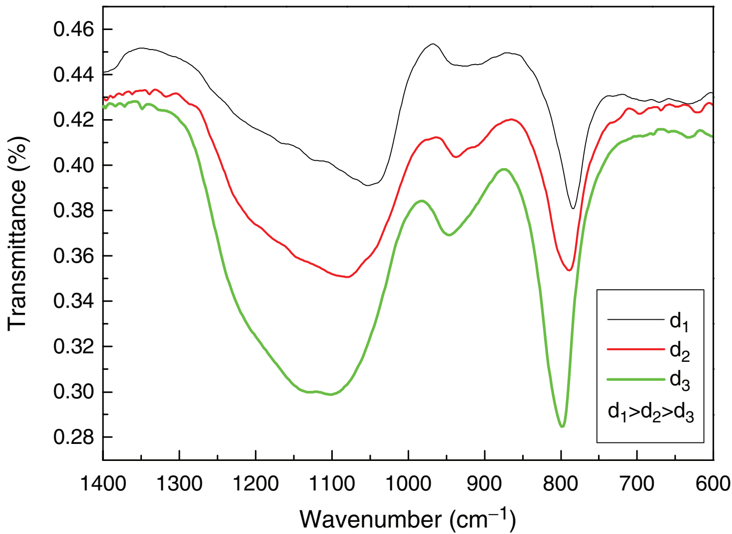

Fig. 2.33 IR spectrum of β-SiC nanowires with different diameters. d_i is the diameter of SiC

$1,100\,cm^{-1}$ are for SiC nanowires with different mean diameters, namely 36.9, 24.8, and 15.5 nm, respectively. The first value of each curve is the characteristic peak of SiC, and the second value is attributed to SiO_2. Compared with $760\,cm^{-1}$ of bulk SiC and $1{,}040\,cm^{-1}$ of SiO_2, the different SiC nanowires have a significant bulk-shift, and the bulk-shift value number increased with the decreased diameter of SiC nanowires.

2.7.3 Electron Transport Properties

2.7.3.1 Electrical Transport in Individual SiC

Li [126] synthesized SiC nanowires with BN sheaths by high-temperature evaporation of a mixture of Si and In_2O_3 powders in a small BN crucible at 1,600°C for 1 h. The electrical transport of the individual SiC/BN nanowires was measured by AFM. It showed that the BN nanotube sheath is a good insulation layer between the SiC nanowire core and Au electrode (contacting points 1 and 2). Point 3 coated by gold and the *I–V* curve confirm good conductivity. The bare SiC nanowire had a high semiconductor behavior (Fig. 2.34). Hence, the construction of complex 3D networks made from the present nanostructures becomes possible with the independent electrical performance of each 1D nanostructure.

2.7.3.2 SiC Nanowire Field-Effect Transistors

The SiC nanowire field-effect transistor was investigated systematically by Zhou et al. [127]. The electronic measurement configuration for a bottom-contacted nanowire device following drop deposition of a single nanowire onto prepatterned

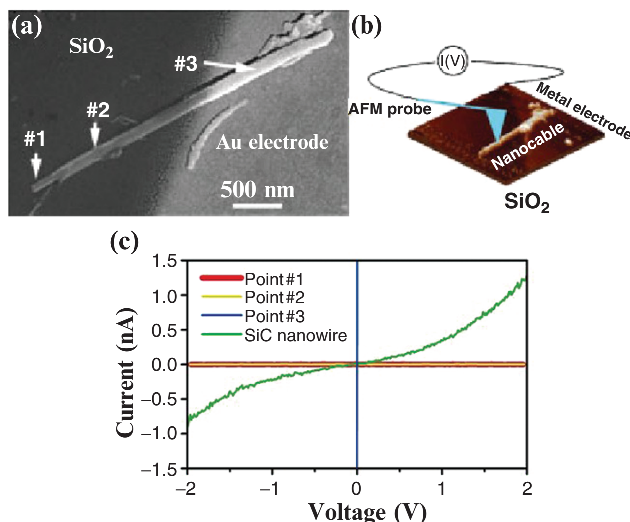

Fig. 2.34 (**a**) SEM image of a BN–SiC nanocable partially covered on the right by a metal electrode. The left tip end of its SiC core protrudes from the BN sheath whereas the right tip is encapsulated in it. The three designated points were used for electrical contacting with an AFM tip. (**b**) 3D AFM image of the nanocable and schematic of the two-probe measurement with the AFM tip. (**c**) *I–V* curves taken at contacting points 1–3, and on a bare SiC nanowire. No current was detected for the SiC–BN nanocable within the sensitivity of the experimental setup ($\sim$2 pA), whereas SiC nanowires without any coating exhibited semiconducting behavior [Ref. 126]

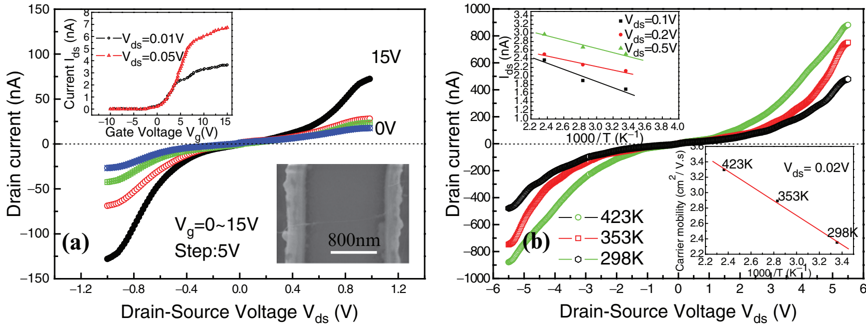

Fig. 2.35 (**a**) Current (I_{ds}) vs. voltage (V_{ds}) curves recorded for different gate voltages at room temperature. *Low-right inset*: the SiC nanowire bridges the two electrodes. *Left inset*: typical I_{ds} vs. V_g curves measured at a drain voltage of 0.01 and 0.05 V, respectively. (**b**) $I_{ds} - V_{ds}$ curves obtained at the different temperatures at $V_g = 5\,V$. *Low-right inset*: Arrhenius plots of mobility of SiC FET for various temperature. *Left inset*: temperature dependence of I_{ds} of the SiC nanowire FET with Au contact electrodes at $V_g = 5\,V$

gold microelectrodes on oxidized Si chip substrates (Fig. 2.35a (low-right inset)) shows a SEM image of a typical device, where a nanowire can be seen bridging two gold electrodes. A typical I_{ds}–V_{ds} characteristic of SiC FETs is shown in Fig. 2.35a. It is very clear that the conductance increased monotonically with the increase of the gate voltage V_g, which corrresponds to n-type properties of the SiC nanowire channel.

From Fig. 2.35a (left inset) and the formula [128]

$$\mu_e = g_m L^2 / C V_{ds}, \tag{2.12}$$

where transconductance (g_m) is expressed as $g_m = dI_{ds}/dV_g$ and C is the gate capacitance estimated by

$$C = 2\pi\varepsilon\varepsilon_0 L / \ln(2h/r), \tag{2.13}$$

where ε, h, and r are the dielectric constant, the thickness of silicon dioxide, and the radius of the SiC nanowire, respectively. It can be obtained as $\mu_e = 15.9$ and $6.4\,cm^2\ V^{-1}\ s^{-1}$ from the formula for $V_{ds} = 0.01$ and $0.05\,V$, respectively. The transconductance (g_m) that is obtained from the linear portion of the curve has the value of 10×10^{-10} and $5 \times 10^{-10}\,A\ V^{-1}$ at $V_{ds} = 0.05$ and $0.01\,V$, respectively (Fig. 2.35a, left inset). The normalized transconductance of 5×10^{-10} and $2.5 \times 10^{-10}\,A\ V^{-1}\ m^{-1}$, respectively. In addition, the transistor has an on–off ratio of nearly 10^3. The carrier concentration of SiC FET is approximately 0.82×10^7 and $1.76 \times 10^7\,cm^{-1}$ at $V_{ds} = 0.01$ and $0.05\,V$, respectively. Compared with the theoretical value of the bulk β-SiC ($\sim 1{,}000\,cm^2\,V^{-1}\ s^{-1}$), the results are very low for 1D nanoscale confinement and scattering from the lattice defects and electron–electron interaction.

Figure 2.35b shows the temperature dependence of the drain current of the n-type SiC nanowire FET at $V_g = 5\,V$. It can be seen that the drain current increased

by one order of magnitude at high temperature from that at room temperature. It is commonly believed that the role of the V_g is to change the value of R_{SiC} through Fermi level (EF) modulation, thus changing the slope. Figure 2.35b (low-right inset) shows the carrier mobility in log scale as a function of 1,000/T at $V_{ds} = 0.02$ V. The liner relation, as observed in the figure, suggests an Arrhenius function

$$\mu_e = \mu_0 \exp(-E_a/kT), \tag{2.14}$$

where E_a is the activation energy, μ_0 is the preexponential factor, and k is the Boltzmann constant. The carrier mobility increased with the increasing temperature and has an activated energy of 82 meV.

The dependence of the I_{ds} in log scale on 1,000/T at $V_g = 5$ V and $V_{ds} = 0.1, 0.2$, and 0.5 V is shown in the left inset of Fig. 2.35b. The results tally with the thermionic emission of carriers, in which the current $I \propto \exp(-\Phi_b/kT)[\exp(qV_{ds}/kT)^{-1}]$, the barrier heights between the Au electrodes and SiC nanowire were extracted from the slope as $\Phi_b = 58.5$, 39.3, and 39.6 meV for $V_{ds} = 0.1$, 0.2, and 0.5 V, respectively.

2.7.4 Mechanical Properties

1D nanostructures are supposed to be significantly stronger than their counterparts. Wong [129] used atomic force microscopy to determine the mechanical properties of individual, structurally isolated SiC NRs that were pinned at one end to molybdenum disulfide surfaces. The bending force was measured against displacement along the unpinned lengths. The strengths of the SiC nanorods were substantially greater (610–660 GPa) than those found previously for larger SiC structures, and they approach theoretical values. These results are in good agreement with the 600 GPa value predicted theoretically for [111] oriented SiC, the average values obtained previously for micrometer diameter whiskers.

Wang et al. [130, 131] used another method called the resonance vibration for measuring the mechanical properties of the SiC nanowire. The experimental results are in agreement with theoretically expected values. Some measured and theoretical values are shown in Tables 2.3 and 2.4.

Table 2.3 Measured Young's modulus for core–shell SiC/SiO_2 nanowire

D_s (nm) ($\pm$2 nm)	D_c (nm) ($\pm$1 nm)	L (µm) ($\pm$0.2 µm)	f_0 (MHz)	E_{eff} (GPa) Exp.	E_{eff} (GPa) Theor.
51	12.5	6.8	0.693	46 ± 9.0	73
74	26	7.3	0.953	56 ± 9.2	78
83	33	7.2	1.044	52 ± 8.2	82
132	48	13.5	0.588	78 ± 7.0	79
190	105	19.0	0.419	81 ± 5.1	109

D_s and D_c are the outer and inner of the SiO_x sheath, respectively. L the nanowire length, f_0 the fundamental resonance frequency

Table 2.4 Measured Young's modulus of biaxially structured SiC–SiO_x nanowires

D_{wire} (nm) (± 2 nm)	D_{SiC} (nm) (± 1 nm)	L (μm) (± 0.2 μm)	f_0 (MHz)	E_{eff} (GPa) Exp.
58	24	4.3	1.833	54 ± 24.1
70	36	7.9	0.629	53 ± 8.4
83	41	4.3	2.707	61 ± 13.8
92	47	5.7	1.750	64 ± 14.3

D_{wire} and D_{SiC} are the widths across the entire nanowire and across the SiC subnanowire, respectively

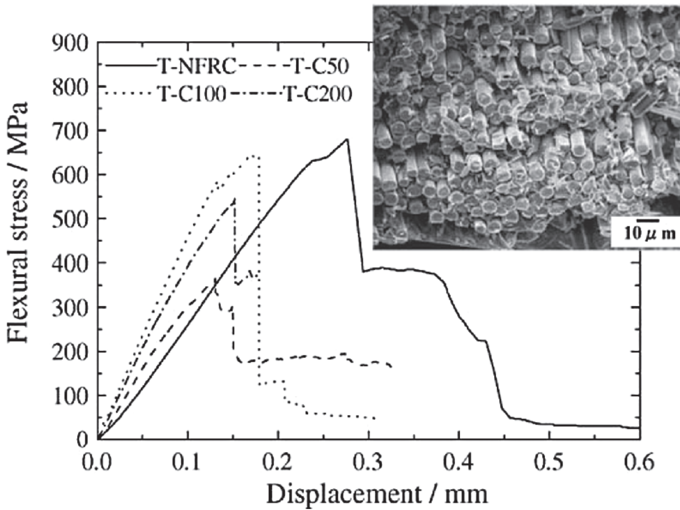

Fig. 2.36 Typical flexural stress–displacement curves and fiber pullout fracture surface (T-NFRC) [Ref. 133]

The measured values of SiC nanowires suggest that SiC nanowires can be used as reinforcement materials for ceramic matrix composites to improve their strength and toughness. Fabrication and flexural properties (measured by three-point bending) of a SiC nanowire/Tyranno-SA fiber-reinforced SiC/SiC composite made by the chemical vapor infiltration (CVI) process have been reported [132–134]. A representative flexural stress–displacement curve is shown in Fig. 2.36. The composite T-NFRC (T stands for Tyranno-SA fiber and NFRC stands for SiC nanowire/fiber-reinforced composites) possesses common features with conventional Tyranno-SA/SiC composites upon flexural fracture. However, the SiC nanowire-reinforced Tyranno-SA/SiC composites show marked improvements on the flexural strength and work of fracture compared with a series of conventional Tyranno-SA/SiC composites (T-C50, T-C100, and T-C200). The flexural properties, such as flexural modulus (E_f), proportional limit stress (PLS), ultimate flexural strength (σ_u), and the fracture energies (W_f), are give in Table 2.5.

Table 2.5 Density, interlayer, and flexural properties of composite with SiC nanowires and conventional composites

Composite ID	Density $(\mathrm{mg\ m^{-3}})$	Pyc layer (nm)	E_f (GPa)	PLS (MPa)	σ_u	W_f
T-NFRC	2.62 ± 0.03	60	120 ± 17	570 ± 120	660 ± 77	6.1 ± 0.7
T-C50	2.41 ± 0.03	50	140 ± 13	260 ± 5	410 ± 92	1.8 ± 0.5
T-C100	2.63 ± 0.04	100	160 ± 11	430 ± 32	610 ± 28	3.2 ± 0.4
T-C200	2.61 ± 0.03	200	140 ± 10	340 ± 18	550 ± 58	2.3 ± 0.3

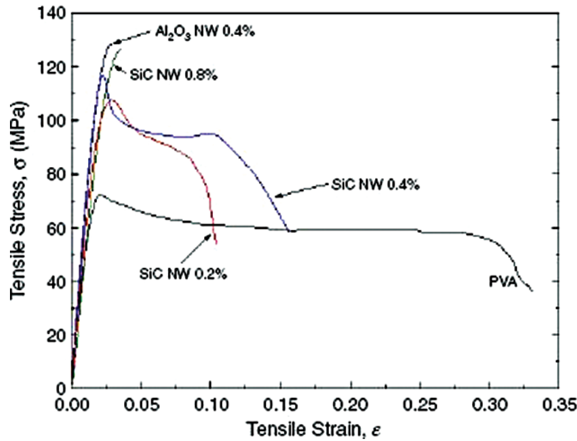

Fig. 2.37 Tensile stress–strain curves of PVA and NW composites, showing an increase in the ultimate tensile strength and reduction in ductility with increasing NW volume fraction [Ref. 135]

Rao et al. [135] have investigated the mechanical properties of composites of SiC nanowire-reinforced polymer–matrix (PVA) composites. Experimental results show that enhancements of these mechanical properties occur even with a small vol% addition of SiCNWs. A representative curve of tensile stress vs. strain is shown in Fig. 2.37. With increasing SiC nanowire volume fraction (V_f), a significant increase in the yield strength takes place. PVA without SiC nanowire reinforcement behaves like an elastic, perfectly plastic solid. The 0.8 vol% SiCNW composites show near-zero ductility, fracturing immediately after yielding. The composites exhibit higher strength; a significant strain softening is seen immediately after the peak in the load. Figure 2.38 shows tensile strength as a function of nanowire volume fraction. As for the SiC nanowire-reinforced composite, the strength of the composites increases markedly initially and reaches a plateau. The initial hardening rate is commensurate with the strength of the SiCNWs. The measured result is compatible with the least-square fit of the equation.

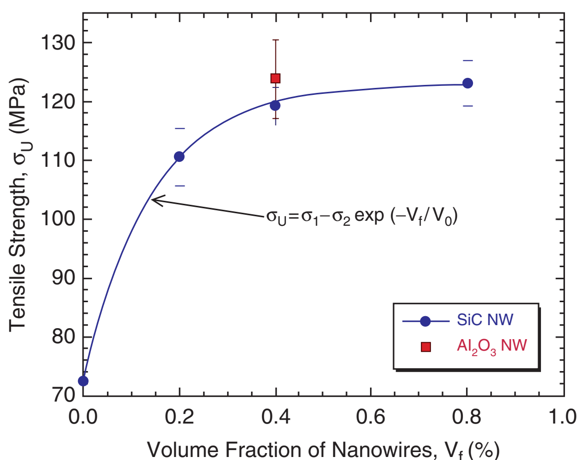

Fig. 2.38 Variation of tensile strength as function of nanowire volume fraction. The *solid line* represents the least-square fit to the equation given in the figure [Ref. 135]

2.7.5 Photocatalyst Properties

The photocatalytic activity of the SiC nanowires was evaluated by measuring the photodegradation rates of CH_3CHO for SiC in a quartz vessel as a function of UV irradiation time under UV light $(1.5\,\mathrm{mW\,cm^{-2}})$ [136]. It was found from Fig. 2.39a that the increase of the initial gaseous acetaldehyde concentration leads to a strengthened conversion of gaseous acetaldehyde. This is attributed to the larger amount of gaseous acetaldehyde molecules attached to the surface of the SiC nanowire powders. After 6 h, the photodegradation of SiC to the initial 100 ppm of gaseous acetaldehyde is 54.99%, increased by 12% for the initial 50 ppm of gaseous acetaldehyde. These results, shown in Fig. 2.39b, are also corroborated by the concentration variation of produced CO_2, evolved as result of photodecomposition of acetaldehyde, as a function of irradiation time. The CO_2 concentration increases with the photodegradation rate of gaseous acetaldehyde. That is to say, the acetaldehyde is converted into CO_2. Besides, the synthesized SiC nanowires coated with SiO_2 layers have higher photocatalytic activity than the HF-treated (bare) SiC nanowires. Semiconducting SiC nanowires offer an alternative to titanium and other metal oxides for use in smart nanoelectronics for environmental control and monitoring, which is highlighted by *Nature Nanotechnology* [137].

2.7.6 Hydrogen Storage Properties

Since the time it was proved that carbon nanotubes (CNTs) can store hydrogen [59], several experimental and theoretical attempts have been performed to investigate

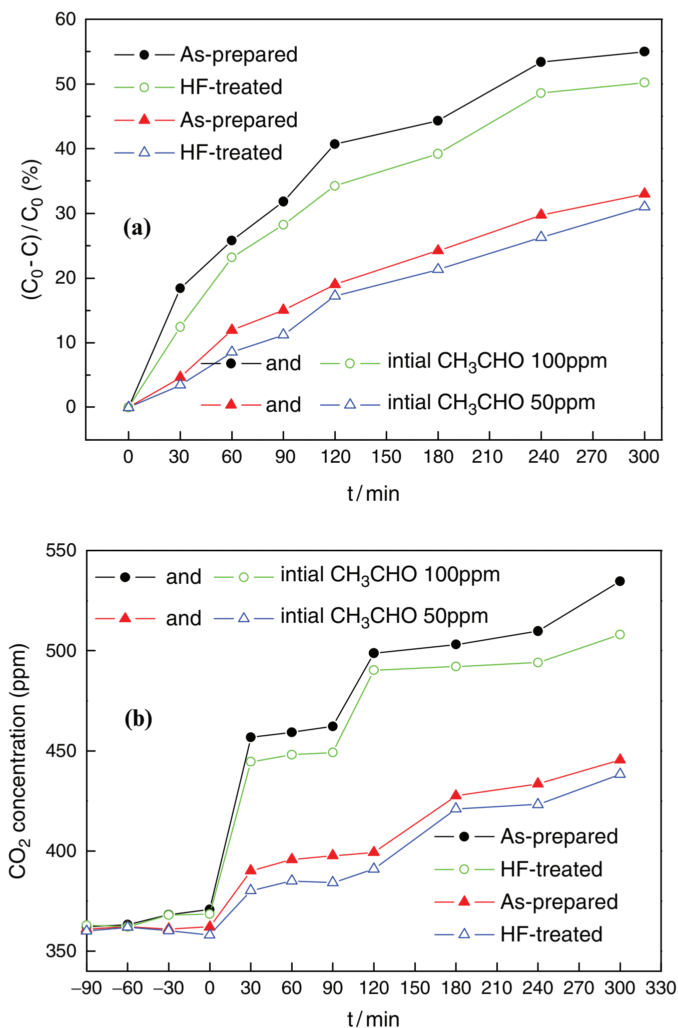

Fig. 2.39 (**a**) SiC photodegradation rates as a function of irradiation time during the photodegradation of acetaldehyde gas under UV irradiation and (**b**) CO_2 evolution as a function of irradiation time (light on at zero) during the photodegradation of acetaldehyde gas under UV irradiation

hydrogen adsorption in CNTs. A detailed review of inorganic nanotubes can be found [138–140]. In the case of SiC nanotubes that store hydrogen, no record of the experiment is available. However, theoretical work is underway. Recently, Mpourmpakis and Froudakis [141] reported hydrogen storage in SiCNTs by a multiscale theoretical approach. First, ab initio calculations at the density functional level of theory (DFT) showed an increase of 20% in the binding energy of H_2 in SiCNTs compared with pure CNTs. Second, classical Monte Carlo simulation of nan-

otube bundles showed an even larger increase of the storage capacity in SiCNTs, especially in low-temperature and high-pressure conditions. Both the results indicate that SiCNTs seem to be more suitable materials for hydrogen storage than pure CNTs.

2.8 Concluding Remarks

This chapter has reviewed the synthesis of SiC 1D nanostructures (nanowire/nanotube) and their applications. The unique properties of SiC nanowires and nanotubes make them good candidates for nanodevices and nanocomposites. From the published literature on 1D SiC nanostructures, it can easily be seen that research on 1D SiC nanostructures mainly focuses on synthesis methods. Optical properties (PL and Raman spectra, etc.) are also reported. However, theoretical research on the mechanical properties, electronic properties, and quantum confinement effect of β-SiC is scarcely reported [142–146]. Hence, intensive work would be attempted to investigate various properties of 1D SiC nanowires on the experimental and theoretical levels. An understanding of the mechanical, electronic, transport, thermal, and other properties would be gained, as well as the fundamental physical phenomenon of 1D SiC nanostructures differing from bulk SiC.

In the next stage, some issues should be highlighted. (1) SiC nanostructure materials fabricated previously were in the shape of hollow nanosphere, nanosprings, nanoflower, and nanotubes. However, some novel synthesized methods of SiC nanostructures are still being developed. Various kinds of 1D SiC nanostructures would be fabricated in high yields at low cost, for example, SiC with other semiconductors in the form of core–shell and hybrid heteronanostructures. The diameter, position, and length, of nanostructures can easily be controlled. Besides, the growth kinetics and thermodynamics of 1D SiC nanostructures are complex, and fully understanding them will help to device/modulate the desired rich morphologies of 1D SiC nanowires. (2) The doping for semiconductor materials applicable to 1D SiC nanostructure materials is a hot topic, because the optical, magnetic, electrical, and electrochemical properties of as-doped SiC can be modified on a nanometer scale. (3) SiC nanowires/nanotubes could be promising candidates to act as connections at nanoscale because they have exceptional mechanical, electronic, and optical properties. Most importantly, self-assembling nanocircuits made from SiC nanowire/nanotube building blocks may play an important role in future nanodevices for next-generation electronic devices. (4) It may be possible to develop a novel SiC nanowire synthesized process compatible with the state-of-the-art Si semiconductor technology. (5) The SiC-reinforced matrix composites are expected to find an application in aerospace and the flexible electronic field. (6) SiC nanowires are ideally suited as interfaces capable of efficiently bridging biological systems and nanoelectronic devices because of their biocompatibility [143]. The explorations of the fundamental properties of SiC have foundthat it can enrich applications in nanodevices (sensor, detector, and actuator) nanocomposites and biological systems.

Acknowledgements This work is jointly supported by Shanghai Municipal Commission for Science and Technology (Grant No. 03DZ14025), Developing Foundation of Shanghai Science and Technology Grant No. 0452nm056 and National Basic Research Program of China No 2006CB300406 and 2007CB935400, China Postdoctoral Scientific Foundation founded project (20070420105). The authors are grateful to all the other authors of related papers and some cited Figures.

References

1. Liu W, Lieber CM (2006) Semiconductor nanowires. J. Phys. D: Appl. Phys. 39:R387–R406
2. Thelander C, Agarwal P (2006) Nanowire-based one-dimensional electronics. Mater. Today 9:28–35
3. Rao CNR, Deepak FL, Gundiah G, Govindaraj A (2003) Inorganic nanowires. Progr. Solid State Chem. 31:5–147
4. Wang ZL (2003) *Nanowires and Nanobelts*. Kluwer, New York
5. Li Y, Qian F, Xiang J, Lieber CM (2006) Nanowire electronic and optoelectronic devices. Mater. Today 9:18–27
6. Zhang DH, Wang YY (2006) Synthesis and applications of one-dimensional nano-structured polyaniline: An overview. Mater. Sci. Eng. B 134:9–19
7. Samuelson L, Thelander C, Björk MT, Borgström, M (2004) Semiconductor nanowires for 0D and 1D physics and applications. Physica E 25:313–318
8. http://www.lib.demokritos.gr/InTheNews/emerging0204.htm
9. Buttner CC, Zacharias M (2006) Retarded oxidation of Si nanowires. Appl. Phys. Lett. 89:263106.1–263106.3
10. Wang N, Tang YH, Zhang YF, Lee CS, Lee ST (1998) Nucleation and growth of Si nanowires from silicon oxide. Phys. Rev. B 58:R16024–R16026
11. Hasunuma R, Komeda T, Mukaida H, Tokumoto H (1997) Formation of Si nanowire by atomic manipulation with a high temperature scanning tunneling microscope. J. Vac. Sci. Technol. B 15:1437–1441
12. Rougemaille N, Schmid AK (2006) Self-organization and magnetic domain microstructure of Fe nanowire arrays. J. Appl. Phys. 99:08S502–08S504
13. Oon CH, Khong SH, Boothroyd CB, Thong JT (2006) Characteristics of single metallic nanowire growth via a field-emission induced process. J. Appl. Phys. 99:064309–064320
14. Wu Y, Xiang J, Yang C, Lu W, Lieber CM (2004) Single-crystal metallic nanowires and metal/semiconductor nanowire heterostructures. Nature 430:61–65
15. Cha SN, Jang JE, Choi Y (2006) High performance ZnO nanowire field effect transistor using self-aligned nanogap gate electrodes. Appl. Phys. Lett. 89:63102–63104
16. Sanghyun J, Kangho L, Janes DB (2005) Low operating voltage single ZnO nanowire field-effect transistors enabled by self-assembled organic gate nanodielectrics. Nano Lett. 5:2281–2286
17. Wang X, Sun XY (2006) Fabrication of GaN nanowire arrays by confined epitaxy. Appl. Phys. Lett. 89:233115–233117
18. Motayed A, He MQ (2006) Realization of reliable GaN nanowire transistors utilizing dielectrophoretic alignment technique. J. Appl. Phys. 100:114310–114318
19. Yin LW, Bando Y, Zhu YC (2004) Synthesis of InN/InP core/sheath nanowires. Appl. Phys. Lett. 84:1546–1548
20. Heo YW, Norton DP, Tien LC, Kwon Y, Kang BS, Ren F, Pearton SJ, LaRoche JR (2004) ZnO nanowire growth and devices. Mater. Sci. Eng.: R Rep. 47:1–47
21. Ren S, Bai YF, Chen J (2007) Catalyst-free synthesis of ZnO nanowire arrays on zinc substrate by low temperature thermal oxidation. Mater. Lett. 61:666–670
22. Liang C, Towe E, Kuball M (2006) Opto-electronic simulation of GaN nanowire lasers GaN, AlN, InN and related materials. Mater. Res. Soc. Symp. Proc. 892:225–230

23. Magdas DA, Cremades A (2006) Three dimensional nanowire networks and complex nanostructures of indium oxide. J. Appl. Phys. 100:094320–094324
24. Vaddiraju S, Mohite A, Chin A (2005) Mechanisms of 1D crystal growth in reactive vapor transport: Indium nitride nanowires. Nano Lett. 5:1625–1631
25. Tao T, Song H, Wu J (2004) Synthesis and characterization of single-crystal indium nitride nanowires. J. Mater. Res. 19:423–426
26. Chang CY, Chi GC, Wang WM (2006) Electrical transport properties of single GaN and InN nanowires. J. Electron. Mater. 35:738–743
27. Yang J, Liu TW, Hsu CW (2006) Controlled growth of aluminium nitride nanorod arrays via chemical vapour deposition. Nanotechnology 17:S321–S326
28. Li ZJ, Shen ZQ, Wang Fu (2006) Arc-discharge synthesis and microstructure characterization of AlN nanowires. J. Mater. Sci. Technol. 22:113–116
29. Mingo N (2003) Calculation of Si nanowire thermal conductivity using complete phonon dispersion relations. Phys. Rev. B 68:113308–113310
30. Wang N, Zhang YF, Tang YH, Lee CS, Lee ST (1998) SiO_2-enhanced synthesis of Si nanowires by laser ablation. Appl. Phys. Lett. 73:3902–3904
31. Wang ZY, Hu J, Yu MF (2006) One-dimensional ferroelectric monodomain formation in single crystalline $BaTiO_3$ nanowire. Appl. Phys. Lett. 89:263119–263121
32. Park JM, Kim SJ, Kim PG, Yoon DJ, Hansen G, DeVries KL (2007) Self-sensing and actuation of CNF and Ni nanowire/polymer composites using electro-micromechanical test. Proc. SPIE 6463:64630–64634
33. Salfi J, Philipose U, deSousa CF, Aouba S, Ruda HE (2006) Electrical properties of Ohmic contacts to ZnSe nanowires and their application to nanowire-based photodetection. Appl. Phys. Lett. 89:261112–261114
34. Tutuc E, Chu JO, Ott JA, Guha S (2006) Doping of germanium nanowires grown in presence of PH3. Appl. Phys. Lett. 89:263101–263103
35. Chen YJ, Chen XD, Li BJ, Yu DS, He ZQ, Li GJ, Zhang MQ (2006) Optical properties of synthesized organic nanowires. Appl. Phys. Lett. 89:241121–241123
36. Feng P, Zhang JY, Li QH, Wang TH (2006) Individual-Ga_2O_3 nanowires as solar-blind photodetectors. Appl. Phys. Lett. 88:153107–153109
37. He MQ, Mohammad SN (2006) Novel chemical-vapor deposition technique for the synthesis of high-quality single-crystal nanowires and nanotubes. J. Chem. Phys. 124:064714–064720
38. Xiang J, Lu W, Hu YJ, Wu Y, Yan H, Lieber CM (2006) Ge/Si nanowire heterostructures as high-performance field-effect transistors. Nature 441:489–493
39. Zhong ZH, Wang DL, Cui Y, Bockrath MW, Lieber CM (2003) Nanowire Crossbar arrays as address decoders for integrated nanosystems. Science 302:1377–1379
40. Cui Y, Wei QQ, Park HK, Lieber CM (2001) Nanowire nanosensors for highly sensitive and selective detection of biological and chemical species. Science 293:1289–1292
41. Huber CA, Huber TE, Sadoqi M, Lubin JA, Manalis S, Prater CB (1994) Nanowire array composites. Science 263:800–802
42. Huang MH, Mao S, Feick H, Yan HQ, Wu YY, Kind H, Weber E, Russo R, Yang PD (2001) Room-temperature ultraviolet nanowire nanolasers. Science 292:1897–1899
43. Hong BH, Bae SC, Lee CW, Jeong SM, Kim KS (2001) Ultrathin single-crystalline silver nanowire arrays formed in an ambient solution phase. Science 294:348–351
44. Wang ZL, Song JH (2006) Piezoelectric nanogenerators based on zinc oxide nanowire arrays. Science 312:242–246
45. Ruff M, Mitlehner H, Helbig R (1994) SiC devices: Physics and numerical simulation. IEEE Trans. Electron. Devices 41:1040–1054
46. Morkoc H, Strite S, Gao GB, Lin ME, Sverdlov B, Burns M (1994) Large-band-gap SiC, III–V nitride, and II–VI ZnSe-based semiconductor device technologies. J. Appl. Phys. 76:1363–1398
47. Cicero G, Catellani A, Galli G (2004) Atomic control of water interaction with biocompatible surfaces: The case of SiC(001). Phys. Rev. Lett. 93:016102–016105
48. Harris GL (1995) *Properties of Silicon Carbide*. INSPEC, the Institution of Electrical Engineers, London

49. Zetterling CM (2002) *Process Technology for Silicon Carbide Devices*. EMIS Processing Series, no. 2. INSPEC, IEE, UK
50. Casady JB, Johnson RW (1996) States of silicon carbide (SiC) as a wide-bandgap semiconductor for high-temperature applications: A review. Solid State Electron. 39:1409–1422
51. Baliga BJ (1996) *Power Semiconductor Devices*. PWS-Kent, Boston, MA
52. Treu M, Rupp R, Blaschitz P (2006) Commercial SiC device processing: Status and requirements with respect to SiC based power devices. Superlattice Microstruct. 40:380–387
53. Sha JJ, Park JS, Hinoki T, Kohyama A (2007) Bend stress relaxation of advanced SiC-based fibers and its prediction to tensile creep. Mech. Mater. 39:175–182
54. Mehregany M, Zorman CA (1999) SiC MEMS: Opportunities and challenges for applications in harsh environments. Thin Solid Films 355–356:518–524
55. Djenkal D, Goeuriot D, Thevenot F (2000) SiC-reinforcement of an Al_2O_3–γ AlON composite. J. Eur. Ceram. Soc. 20:2585–2590
56. Müller G, Krötz G, Niemann E (1994) SiC for sensors and high-temperature electronics. Sens. Actuators A: Phys. 43:259–268
57. Dimitrijev S, Jamet P (2003) Advances in SiC power MOSFET technology. Microelectron. Reliab. 43:225–233
58. Iijima S (1993) Helical microtubules of graphitic carbon. Nature 354:56–58
59. Iijima S, Ichihashi T (1993) Single-shell carbon nanotubes of 1-nm diameter. Nature 363:603–605
60. Zhou D, Seraphin S (1994) Production of silicon carbide whiskers from carbon nanoclusters. Chem. Phys. Lett. 222:233–238
61. Dai HJ, Wong EW, Lu YZ, Fan SS, Lieber CM (1995) Synthesis and characterization of carbide nanorods. Nature 375:769–772
62. Han WQ, Fan SS, Li QQ, Liang WJ, Gu BL, Yu DP (1997) Continuous synthesis and characterization of silicon carbide nanorods. Chem. Phys. Lett. 265:374–378
63. Tang CC, Fan SS, Dang HY, Zhao JH, Zhang C, Li P, Gu A (2000) Growth of SiC nanorods prepared by carbon nanotubes-confined reaction. J. Cryst. Growth 210:595–599
64. Muñoz E, Dalton AB, Collins S, Zakhidov AA (2002) Synthesis of SiC nanorods from sheets of single-walled carbon nanotubes. Chem. Phys. Lett. 395:397–402
65. Seeger T, Redlich PK, Rühle M (2000) Synthesis of nanometer-sized SiC whiskers in the arc-discharge. Adv. Mater. 12:279–282
66. Li YB, Xie SS, Zou XP, Tang DS, Liu ZQ, Zhou WY, Wang G (2001) Large-scale synthesis of β-SiC nanorods in the arc-discharge. J. Cryst. Growth 223:125–128
67. Thess A, Lee R, Nikolaev P, Dai H, Petit P (1996) Crystalline ropes of metallic carbon nanotubes. Science 273:483–487
68. Liu J, Rinzler AG, Dai H, Hafner JH, Bradley PK, Boul PJ, Lu A (1998) Fullerene pipes. Science 280:1253–1255
69. Zhang YF, Tang YH, Wang N, Yu DP, Lee CS, Belllo I, Lee ST (1998) Silicon nanowires prepared by laser ablation at high temperature. Appl. Phys. Lett. 72:1835–1837
70. Tang YH, Zhang YF, Peng HY, Wang N, Lee CS, Lee ST (1999) Si nanowires synthesized by laser ablation of mixed SiC and SiO_2 powders. Chem. Phys. Lett. 314:16–20
71. Shi WS, Zheng YF, Peng HY, Wang N, Lee CS, Lee ST (2000) Laser Ablation synthesis and optical characterization of silicon carbide nanowires. J. Am. Ceram. Soc. 83:3228–3230
72. Meng GW, Cui Z, Zhang LD, Phillipp F (2000) Growth and characterization of nanostructured β-SiC via carbothermal reduction of SiO_2 xerogels containing carbon nanoparticles. J. Cryst. Growth 209:801–806
73. Liang CH, Meng GW, Zhang LD, Wu YC, Cui Z (2000) Large-scale synthesis of β-SiC nanowires by using mesoporous silica embedded with Fe nanoparticles. Chem. Phys. Lett. 329:323–328
74. Xu WJ, Xu Y, Sun XY, Liu YQ, Wu D, Sun YH (2006) Fabrication of tower like β-like by sol-gel and carbothermal reduction processing. New Carbon Mater. 21:167–170
75. Yang W, Araki H, Thaveethavorn S, Suzuki H, Nada T (2005) In situ synthesis and characterization of pure SiC nanowires on silicon wafer. Appl. Surf. Sci. 241:236–240

76. Yang W, Araki H, Hu QL, Ishikawa N, Suzuki S, Noda T (2004) In situ growth of SiC nanowires on RS-SiC substrates. J. Cryst. Growth 264:278–283
77. Ying YC, Gu Y, Li ZF, Gu HZ, Cheng LY, Qia YT (2004) A simple route to nanocrystalline silicon carbide. J. Solid State Chem. 177:4163–4166
78. Mamails AG, Vogtlander LOG, Markopoulos A (2004) Nanotechnology and nanostructured materials: Trends in carbon nanotubes. Precis. Eng. 28:16–30
79. Zhang YF, Gamo MN, Xiao CY, Ando T (2002) Synthesis of 3C-SiC nanowhiskers and emission of visible photoluminescence. J. Appl. Phys. 91:6066–6070
80. Zhou XT, Wang N, Lai HL, Peng Y, Bello I, Lee ST (1999) β-SiC nanorods synthesized by hot filament chemical vapor deposition. Appl. Phys. Lett. 74:3942–3944
81. Chio HJ, Seong HK, Lee JC, Sung YM (2004) Growth and modulation of silicon carbide nanowires. J. Cryst. Growth 269:472–478
82. Ho GW, Wong SW, Kang DJ, Welland ME (2004) Three-dimensional crystalline SiC nanowire flowers. Nanotechnology 15:996–999
83. Li HJ, Li ZJ, Meng AL, Li KZ, Zhang XN, Xu YP (2003) SiC nanowire networks. J. Alloys Compd. 352:279–282
84. Zhang YJ, Wang NL, He RR, Chen XH, Zhu J (2001) Synthesis of SiC nanorods using floating catalyst. Solid State Commun. 118:595–598
85. Zhou WM, Yang B, Yang ZX, Zhu F, Yan LJ, Zhang YF (2006) Large-scale synthesis and characterization of SiC nanowires by high-frequency induction heating. Appl. Surf. Sci. 252:5143–5148
86. Zhou WM, Yang ZX, Zhu F, Zhang YF (2006) SiC/SiO_2 nanocables and nanosprings synthesized by catalyst-free method. Physica E 31:9–12
87. Zhang HF, Wang CM, Wang SL (2002) Helical crystalline SiC/SiO_2 core–shell nanowires. Nano Lett. 2:941–944
88. Kong XY, Wang ZL (2003) Spontaneous polarization-induced nanohelixes, nanosprings, and nanorings of piezoelectric nanobelts. Nano Lett. 3:1625–1631
89. Shen GZ, Bando YS, Ye CH, Liu BD, Golberg D (2006) Synthesis, characterization and field-emission properties of bamboo-like β-SiC nanowires. Nanotechnology 17:3468–3472
90. Shen GZ, Bando YS, Golberg D (2006) Self-assembled hierarchical single-crystalline β-SiC nanoarchitectures. Crystal growth & design 7:35–38
91. Li ZJ, Zhang JL, Meng A, Guo JZ (2006) Large-area highly oriented SiC nanowires: Synthesis, Raman, and photoluminescence properties. J. Phys. Chem. B 110:22382–22386
92. Pan ZW, Lai HL, Au CK, Duan XF, Zhou WY, Shi WS, Wang N, Lee CS, Wong NB, Lee ST, Xie SS (2000) Oriented silicon carbide nanowires: Synthesis and emission properties. Adv. Mater. 12:1186–1190
93. Kim HY, Park J, Yang H (2003) Direct synthesis and aligned silicon carbide nanowires from the silicon substrates. Chem. Commun. 37:256–257
94. Sun XH, Li CP, Wong WK, Wong NB, Lee CS, Lee ST, Teo BK (2002) Formation of silicon carbide nanotubes and nanowires via reaction of silicon (from disproportionation of silicon monoxide) with carbon nanotubes. J. Am. Chem. Soc. 124:14464–14472
95. Palen EB, Ruemmeli MH, Gemming T, Knupfer M, Biedermann K, Leonhardt A, Pichler T (2005) Bulk synthesis of carbon-filled silicon carbide nanotubes with a narrow diameter distribution. J. Appl. Phys. 97:056102–056104
96. Taguchi T, Igawa N, Yamamoto H (2004) Synthesis of silicon carbide nanotubes. J. Am. Ceram. Soc. 88:459–461
97. Lauhon LJ, Gudiksen MS, Lieber CM (2004) Semiconductor nanowire heterostructures. Philos. Trans. R. Soc. Lond. A 362:1247–1260
98. Lu W, Lieber CM (2006) Semiconductor nanowires. J. Phys. D: Appl. Phys. 39:R387–R406
99. Zhang Y, Suenage K, Colliex C, Iijima S (1998) Coaxial nanocable: Silicon carbide and silicon oxide sheathed with boron nitride and carbon. Science 281:973–975
100. Zhang Y, Ichihashi T, Landree E, Nihey F, Iijima S (1999) Heterostructures of single-walled carbon nanotubes and carbide nanorods. Science 285:1719–1722
101. Li YB, Bando YS, Golberg D (2004) $SiC–SiO_2–C$ coaxial nanocables and chains of carbon nanotube–SiC heterojunctions. Adv. Mater. 16:93–96

102. Tang CC, Bando YS, Sato TD, Kurashima KJ (2002) Uniform boron nitride coatings on silicon carbide nanowires. Adv. Mater. 14:1406–1409
103. Han WQ, Redlich P, Ernst F, Ruhle M (1999) Synthesizing boron nitride nanotubes filled with SiC nanowires by using carbon nanotubes as templates. J. Appl. Lett. 75:1875–1877
104. Tang CC, Bando YS, Sato TD, Kurashima KJ (2002) SiC and its bicrystalline nanowires with uniform BN coatings. Appl. Phys. Lett. 80:4641–4643
105. Wenger KS, Cornu D, Chassagneux F, Ferro G, Epicier T, Miele P (2002) Direct synthesis of β-SiC and h-BN coated β-SiC nanowires. Solid State Commun. 124:157–161
106. Tang CC, Bando YS, Sato TD, Kurashima KJ (2002) Comparative studies on BN-coating on SiC and Si_3N_4 nanowires. J. Mater. Chem. 12:1910–1913
107. Pokropivny V, Pokropivny A, Lohmus A, Lohmus R, Kovrygin S, Sylenko P, Partch R, Prilutskii E (2006) Extremely high-frequency piezoelectroacoustic transducer based on BN-tube/SiC-whiskers rope. Physica E 37:283–286
108. Zhu YC, Bando YS, Xue DF, Xu FF, Golberg D (2003) Insulating tubular BN sheathing on semiconducting nanowires. J. Am. Chem. Soc. 125:14226–14227
109. Hu JQ, Bando Y, Zhan JH, Golberg D (2004) Fabrication of ZnS/SiC nanocables, SiC-shelled ZnS nanoribbons (and sheets), and SiC nanotubes (and tubes). Appl. Phys. Lett. 85:2932–2934
110. Tak YJ, Ryu YH, Yong KJ (2005) Atomically abrupt heteronanojunction of ZnO nanorods on SiC nanowires prepared by a two-step. Nanotechnology 16:1712–1716
111. Tak YG, Yong KJ (2005) ZrO_2-coated SiC nanowires prepared by plasma-enhanced atomic layer chemical vapor deposition. Surf. Rev. Lett. 12:215–219
112. Lalonde AD, Norton MG, McIlroy DN, Zhang DQ (2005) Metal coatings on SiC nanowires by plasma-enhanced chemical vapor deposition. J. Mater. Res. 20:549–553
113. Min BD, Lee JS, Cho KG, Hwang JW, Kim H, Sung MY, Kim S, Park J, Seo HW, Bae SY, Lee MS, Park SO, Moon JT (2003) Semiconductor nanowires surrounded by cylindrical Al_2O_3 shells. J. Electron. Mater. 32:1344–1348
114. Zhou J, Liu J, Yang R, Lao CS, Gao PX, Tummala R, Xu NS, Wang ZL (2006) SiC-shell nanostructures fabricated by replicating ZnO nano-objects: A technique for producing hollow nanostructures of desired shape. Small 2:1344–1347
115. Wu ZS, Deng SZ, Xu NS, Chen J, Zhou J, Chen J (2002) Needle-shaped silicon carbide nanowires: Synthesis and filed electron emission properties. 80:3829–3831
116. Wong KW, Zhou XT, Au CK, Lai HL, Lee CS, Lee ST (1999) Filed-emission characteristics of SiC nanowires prepared by chemical-vapor deposition. Appl. Phys. Lett. 75:2918–2920
117. Lo HC, Hwang JS, Chen KH, Hsu CH, Chen CF, Chen LC (2003) SiC-capped nanotip arrays for field emission with ultralow turn-on filed. Appl. Phys. Lett. 83:1420–1422
118. Feng DH, Jia TQ, Li XX, Xu ZZ, Chen J, Deng SZ (2003) Catalytic synthesis and photoluminescence of needle-shaped 3C-SiC nanowires. Solid State Commun. 128:295–297
119. Deng SZ, Li ZB, Wang WL, Xu NS, Zhou J, Zheng XG, Xu HT, Chen J, She JC (2006) Field emission study of SiC nanowires/nanorods directly grown on SiC ceramic surface. Appl. Phys. Lett. 89:023118–023200
120. Zhou WM, Wu YJ, Kong ESW, Zhu F, Hou ZY, Zhang YF (2006) Field emission from nonaligned SiC nanowires. Appl. Surf. Sci. 253:2056–2058
121. Fowler RH, Nordheim LW (1928) Electron beams formed by photoelectric field emission. Proc. R. Soc. Lond. A 119:173–181
122. Tang CC, Bando Y (2003) Effect of BN coatings on oxidation resistance and field emission of SiC nanowires. Appl. Phys. Lett. 83:659–661
123. Ryu YW, Tak YJ, Yong KJ (2005) Direct growth of core–shell SiC–SiO_2 nanowires and field emission characteristics. Nanotechnology 16:S370–S374
124. Ryu YH, Park BT, Song YH, Yong K (2004) Carbon-coated SiC nanowires: Direct synthesis from Si and filed emission characteristics. J. Cryst. Growth 271:99–104
125. Liu XM, Yao KF (2005) Large-scale synthesis and photoluminescence properties of SiC/SiO_x nanocables. Nanotechnology 16:2932–2935
126. Li YB, Dorozhkin PS, Bando YS, Golberg D (2005) Controllable modification of SiC nanowires encapsulated in BN nanotubes. Adv. Mater. 17:545–549

127. Zhou WM, Fang F, Hou ZY, Yan LJ, Zhang YF (2006) Field-effect transistor based on β-SiC nanowire. IEEE Electron. Device Lett. 27:463–465
128. Avouris P, Martel R, Derycke V, Appenzeller J (2002) Carbon nanotube transistors and logic circuits. Phys. B 323:6–14
129. Wong EW, Sheehan PE, Lieber CM (1997) Nanobeam mechanics: Elasticity, strength, and toughness of nanorods and nanotubes. Nature 277:1971–1975
130. Wang ZL, Dai ZR, Gao RP, Bai ZG, Gole JL (2000) Side-by-side silicon carbide–silica biaxial nanowires: Synthesis, structure, and mechanical properties. Appl. Phys. Lett. 77: 3349–3351
131. Wang ZL, Dai ZR, Gao RP, Bai ZG, Gole JL (2002) Measuring the Young's modulus of solid nanowires by in situ TEM. J. Electron. Microsc. 51(Suppl.):S79–S85
132. Yang W, Araki H, Kohyama A, Katoh Y, Hu Q, Suzuki H, Noda T (2004) Tyranno-SA/SiC composite with SiC nanowires in the matrix by CVI process. J. Nucl. Mater. 329–333: 539–543
133. Yang W, Araki H, Kohyama A, Thaveethavorn S, Suzuki H, Noda T (2004) Fabrication in-situ SiC nanowires/SiC matrix composite by chemical vapour infiltration process. Mater. Lett. 58:3145–3148
134. Yang W, Araki H, Tang CC, Thaveethavorn S, Kohyama A, Suzuki H, Noda T (2005) Single-crystal SiC nanowires with a thin carbon coating for stronger and tougher ceramic composites. Adv. Mater. 17:1519–1523
135. Vivekchand SRC, Ramamurty U, Rao CNR (2006) Mechanical properties of inorganic nanowire reinforced polymer–matrix composites. Nanotechnology 17:S344–S350
136. Zhou WM, Yan LJ, Wang Y, Zhang YF (2006) SiC nanowires: A photocatalytic nanomaterial. Appl. Phys. Lett. 89:013105–013107
137. http://www.nature.com/nnano/reshigh/2006/0706/full/nnano.2006.21.html
138. Remškar M (2004) Inorganic nanotubes. Adv. Mater. 16:1497–1504
139. Tenne R, Rao CNR (2004) Inorganic nanotubes. Philos. Trans. R. Soc. Lond. A 362:2099–2125
140. Ma RZ, Golberg D, Bando YS, Sasaki T (2004) Philos. Trans. R. Soc. Lond. A 362:2161–2186
141. Mpourmpakis G, Froudakis GE (2006) SiC nanotubes: A novel material for hydrogen storage. Nano Lett. 6:1851–1853
142. Yan BH, Zhou G, Duan WH, Wu J, Gu BL (2006) Uniaxial-stress effects on electronic properties of silicon carbide nanowires. Appl. Phys. Lett. 89:023104–023106
143. Rurali R (2005) Electronic and structural properties of silicon carbide nanowire. Phys. Rev. Lett. 71:205405.1–205405.7
144. Kim TY, Han SS, Lee HM (2004) Nanomechanical behavior of β-SiC nanowire in tension: Molecular dynamic simulations. Mater. Trans. 45:1442–1449
145. Moon WH, Ham JK, Hwang HJ (2003) Mechanical properties of SiC nanotubes. *Technical Proceedings of the 2003 Nanotechnology Conference and Trade Show*, vol. 3, pp 158–161
146. Cicero G, Catellani A, Galli G (2004) Atomic control of water interaction with biocompatible surfaces: The case of SiC(001). Phys. Rev. Lett. 93:016102.1–016102.4

Chapter 3
Self-Organized Nanowire Formation of Si-Based Materials

Hideo Kohno

Abstract I summarize our results of the nanowire fabrication of various Si-based materials on substrate surfaces. By heating source materials in an evacuated silica tube, we have grown various types of wire-like one-dimensional structures such as Si nanochains, SiGe core/shell needles, and SiC fractal nanowires. Furthermore, Cu silicide nanochains and Fe silicide/Si heterostructured nanowires have also been fabricated using nanowire templates. We discuss their structure, formation mechanism, and properties based on transmission electron microscopy (TEM) observations and related analytical methods.

3.1 Introduction

Inorganic materials such as silicon are often found in one-dimensional forms, which are called whiskers, needles, ribbons, rods, or wires. In 1960s and 1970s, growth of whiskers of single crystalline Si or Ge was studied actively [1–6]. They are typically submicrometer to several micrometers in diameter and hundreds of micrometers in length. A typical growth mode of such one-dimensional structures is the vapor–liquid–solid (VLS) mechanism [3, 5, 6] (see Fig. 3.1), in which source materials such as silane are supplied as supersaturated vapor and captured by a molten alloy droplet of eutectic Au–Si system at the vapor–liquid interface. Eventually Si in the droplet becomes supersaturated and crystallizes at the interface to the substrate, namely the liquid–solid (LS) interface. Successive deposition of crystalline Si at the liquid-solid interface results in the formation of a rod- or wire-shaped crystalline Si. The diameter of the rod/wire is defined by that of the liquid-solid interface. Thus, a gradual decrease in the diameter of the liquid-solid interface for some reasons results in the whisker/needle formation. In addition, direct deposition of source materials on the sidewall of a needle, namely the vapor-solid (VS) growth, can also form tapered shape.

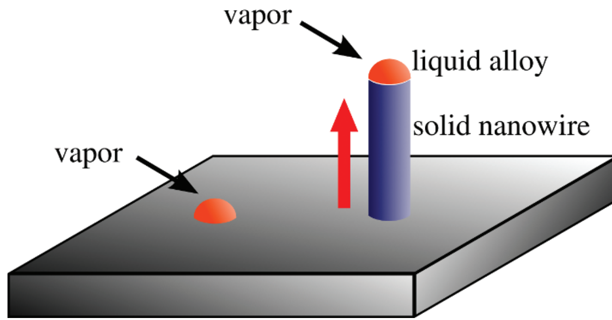

Fig. 3.1 VLS growth of a nanowire

In the early 1990s, Hiruma et al. reported the growth of InAs [7] and GaAs [8] nanowhiskers as thin as 10–20 nm using organometallic vapor phase epitaxy. Stimulated by these works, in the late 1990s, effort to fabricate nanometer-scale Si whiskers via the VLS process was also made by several groups. In 1997, Westwater et al. [9] reported the chemical vapor deposition (CVD) growth of Si nanowires as thin as 40–100 nm using silane and Au catalyst. In 1998, Ozaki et al. [10] reported the CVD fabrication of Si nanowires with the minimum Si core diameter of 3 nm on a hydrogen-terminated Si surface using silane and Au catalyst. In addition to the CVD method, Si nanowires have also been fabricated by laser ablation [11, 12].

In addition to simple homogeneous one-dimensional structures, heterostructured [13–26] or branched [27–29] nanowires are also the focus of recent interest in expectation of fascinating functions, for example, light emission and nonlinear charge transfer.

In this chapter, I describe our recent results on the fabrication and characterization of several kinds of one-dimensional nanostructures of Si-based materials, such as Si nanochains, SiGe core-shell nanoneedles, Fe-silicide nanowires, and SiC fractal nanowires. These nanowires are heterostructured or have a fascinating shape. It should be also addressed that these nanowires can be fabricated via simple processes.

3.2 Si Nanochains

3.2.1 Discovery of Si Nanochains

Si nanochains were first reported by Kohno and Takeda [30, 31]. Typical transmission electron microscopy (TEM) micrographs are shown in Fig. 3.2. Crystalline-Si nanoparticles are covered with and connected by amorphous Si oxide, forming a chain-like structure. They are typically 10–30 nm in diameter and several micrometers in length. Kohno and Takeda discovered this material by serendipity when they observed a Si specimen which underwent Au deposition and annealing by TEM.

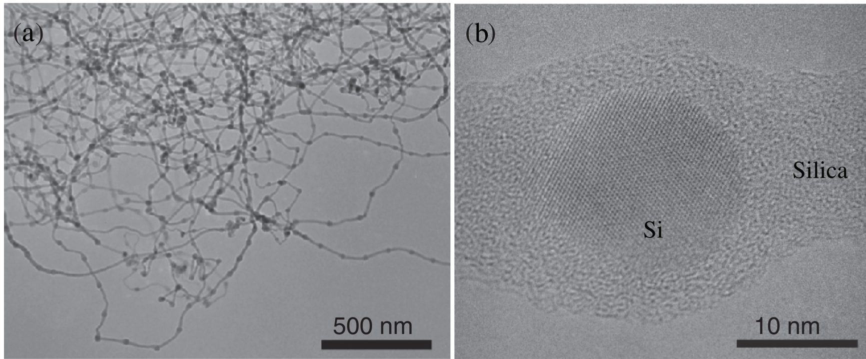

Fig. 3.2 TEM micrographs of Si nanochains, (**a**) low-magnified image showing numerous Si nanochains and (**b**) high-resolution image of a nanochain (after [31])

These one-dimensional periodic arrangements of semiconductor (Si) and insulator (silica) are formed via a fully self-organized process in a closed silica reaction tube without any artificial modulation of growth conditions such as temperature or the pressure of source gas.

3.2.2 Fabrication Procedure and Growth Mechanism

Fabrication of Si nanochains does not require any special equipment. Only a vacuum evaporator and a furnace are used. A Si substrate is first coated by a Au thin film several nanometers thick (see Fig. 3.3). Second, the Si substrate is sealed in a silica tube with a small piece of additive metal such as Pb in a vacuum of 10^{-5} Torr, and then heated to several hundred degrees centigrade to make the catalyst active for the VLS growth of Si nanochains. Without this first annealing process, the yield of nanochain growth is very low [32]. Although the amount of Pb in the Au catalyst particles is below the detection limit of energy dispersive X-ray spectroscopy (EDX) in TEM, the effect of additive metal is significant. Third, the Si substrate is taken out of the tube, and then sealed in an evacuated silica tube for the second annealing at around 1200°C. During this annealing, the silica tube is filled with Si vapor, which works as a source gas. Finally, the silica tube is taken out of the furnace to be cooled slowly to room temperature. The supersaturation of the Si vapor during the cooling is the driving force of the chain growth.

While the simple VLS mechanism explains the one-dimensional growth of Si nanochains as well as Si nanowires, the origin of their morphology and internal structure is not straightforward to reveal. We have proposed a formation mechanism of Si nanochains: periodic instability in diameter of Si nanowires and the surface oxidation of the Si nanowires with modulated diameter, which results in the fragmentation of Si cores at their necks.

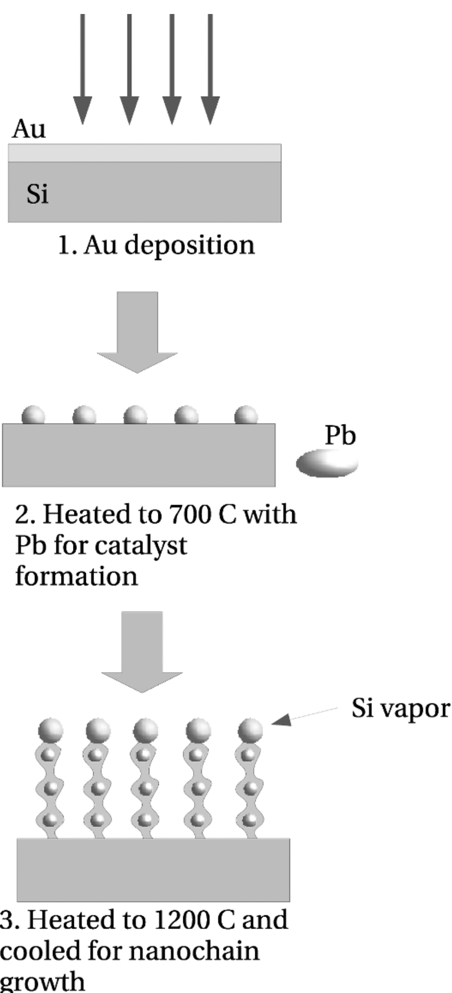

Fig. 3.3 Procedure for the Si nanochain fabrication

3.2.2.1 Periodic Diameter Modulation

Givargizov [33] reported periodic instability in the growth of Si whiskers. The diameter of his whiskers is modulated nearly periodically. The whiskers are as thick as several hundred nanometers and grow epitaxially to a Si substrate, thus their Si core may not be fragmented. A basic idea on the mechanism of the periodic instability, namely the diameter modulation, was given by Givargizov and modified by Kohno and Takeda [34]. The model is as follows. Since a molten alloy droplet has large curvature, the equilibrium vapor pressure of Si of the eutectic Au–Si droplet is higher than that for a flat surface, and the equilibrium vapor pressure depends on the curvature because of the Gibbs–Thomson effect. Assuming that the volume of the droplet

is constant, small diameter corresponds to a large wetting angle and large curvature. Accordingly, the net amount of Si captured by the droplet at the vapor–liquid (VL) interface decreases with decrease in diameter. As a result, for a thin nanowire, the degree of supersaturation of Si in the droplet becomes lower. Supersaturated Si atoms in the droplet crystallize at the liquid–solid (LS) interface, forming the Si nanowire. When the degree of supersaturation is small, the LS interface can become flat via a thermal process because deposited Si atoms have enough time to diffuse around and are captured by holes, kinks, or steps before being captured by other impinging Si atoms. On the other hand, the interface becomes roughened when the degree of supersaturation is high; this phenomenon is called kinetic roughening. Since the wetting property is largely affected by the interface roughness, the diameter of the wire also changes when the roughness of the LS interface changes. Thus, the process constructs a complex feedback. Numerical simulations confirmed that the feedback model can exhibit periodic diameter modulation [34]. The simulated instability is sensitive to parameters, such as temperature, diameter, and interface tensions, used in the simulations. This gives a clue to understanding the effect of the additive metals such as Pb. We speculate that the additive metals work as surfactants, which change interface tensions, and as a result, the instability is induced.

3.2.2.2 Surface Oxidation

Although the periodic instability results in the periodic modulation of diameter, the Si core of a nanowire still remains running through the wire without another mechanism. We consider that the Si core is fragmented to a chain of Si nanoparticles by surface oxidation [35]. A piece of evidence is obtained by energy-filtered TEM (see Fig. 3.4). The energy-filtered TEM image shows tails of Si nanoparticles. In addition, a Si nanowire with modulated diameter without fragmentation is also observed. The morphology of these kinds can be naturally explained by our surface oxidation model.

We speculate that the surface oxidation is self-limited [36–39]. When Si is oxidized, its volume increases. As a result, compressive stress works on the inner Si core, and suppresses further oxidation because an extra work has to be done against the compressive stress to create a room for newly formed oxide. At the necks of a diameter modulated Si nanowire, the surface has a saddle-like shape, therefore the compressive stress can be readily relaxed. On the other hand, the compressive stress works effectively at knots because the shape is roughly spherical. Accordingly, the oxidation can reach the core at necks, resulting in the fragmentation of the core, whereas the oxidation is strongly suppressed at knots. The value of the compressive stress was determined to be 10^8–10^9 Pa by Raman scattering spectroscopy [40] (see Fig. 3.5). It is known that a Raman peak of a nanomaterial red-shifts and the peak becomes asymmetric and broad owing to phonon confinement [41, 42]. As shown in Fig. 3.5, the phonon confinement model can explain the shape of the peak very well; however, it does not explain the peak position. When we also assume compressive

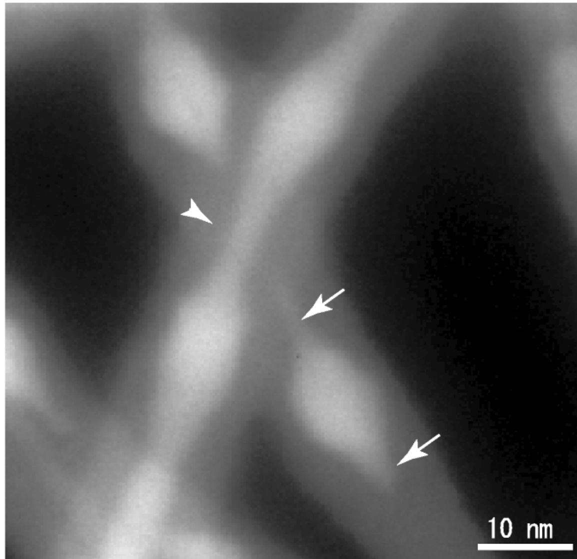

Fig. 3.4 Si plasmon-loss image of Si nanochains, where electrons each of which exited a Si volume plasmon were used to form the image. The arrows indicate tails of Si nanoparticles and the arrowhead indicates a neck of a Si core (after [31])

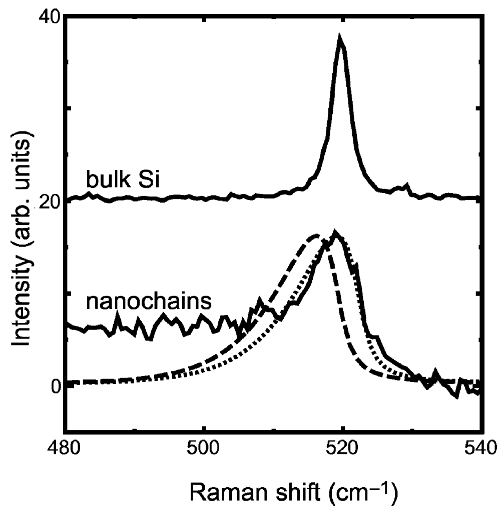

Fig. 3.5 Raman spectra of bulk Si and Si nanochains (solid curves) with calculated curves (dashed curve: phonon confinement model, dotted curve: phonon confinement + compressive stress) (after [31,40])

stress, the calculated curve reproduces the experimental result very well. The estimated value is consistent with the reported critical stress of $\sim 10^9$ Pa at which the oxidation stops [39].

3.2.3 Si Nanochains as Templates: Fabrication of Cu-Silicide/Si/Oxide Nanochains

Si nanochains can be used as templates for fabricating derivative nanostructures. When Si nanochains are heated with Cu in a closed silica ampule that is evacuated, Cu infuses into the nanochains through the surface oxide and forms Cu-silicide. It is interesting that the silicidation is partial under the annealing condition of 700°C for 10 min as shown in Fig. 3.6. Hemispherical halves of Si nanoparticles in the nanochains are converted to Cu silicide. As a result, more complex nanostructures, namely Cu-silicide/Si/oxide nanochains, can be formed using Si nanochains as templates. It is expected that the degree of silicidation can be controlled by temperature and time of the annealing. Furthermore, other kinds of nanochains will be fabricated using this simple method.

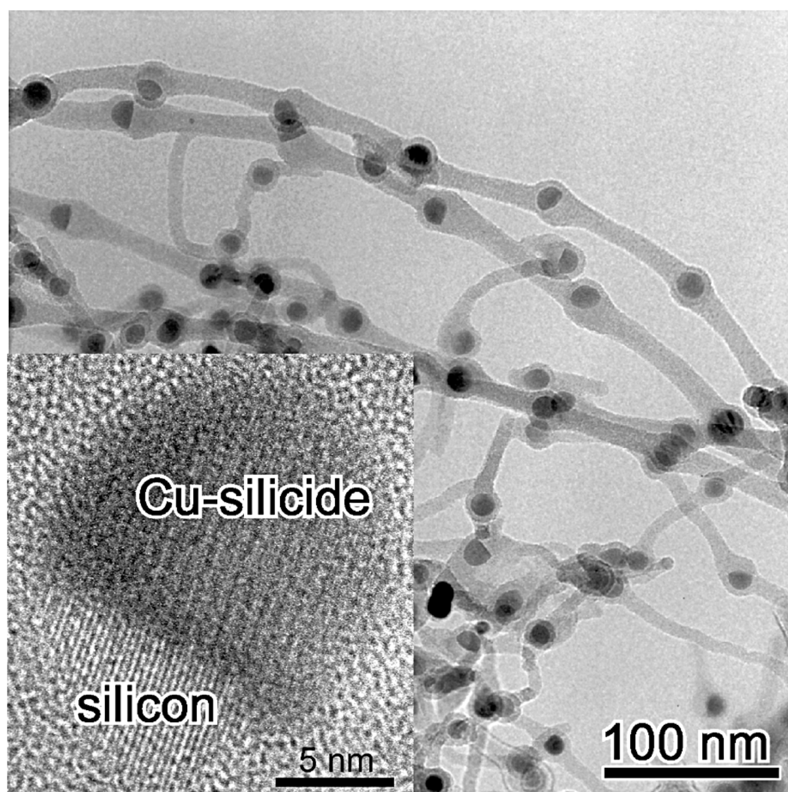

Fig. 3.6 TEM image of Cu-silicide/Si/oxide nanochains. *Inset*: high-resolution image. Si nanochains were heated with Cu at 700°C for 10 min for silicidation (after [31, 43])

3.3 SiGe Core-Shell Nanoneedles

3.3.1 Sulfur-Assisted Growth of Si Core-Shell Needles

In the case of the previous Si nanochain fabrication, the Si source gas is considered to be supplied by simple thermal evaporation of Si atoms from the Si substrate and silica tube. In addition to such simple Si evaporation, we found that S can be used for Si vapor formation. When a Si substrate on which a Au thin film is deposited is annealed with a small piece of S and then cooled slowly to room temperature, numerous Si needles are formed on the Si substrate [44]. During annealing, S makes vapor of Si sulfides and the vapor fills in the silica tube. When the sample is taken out of a furnace for cooling, the vapor of Si sulfides becomes supersaturated. Then Si vapor is captured by Au–Si molten droplets and the VLS growth occurs.

In addition to the VLS growth at the tips of nanoneedles, direct crystallization of the Si vapor also occurs at the sidewalls of the needles. This is the VS process (see Fig. 3.7). Owing to the VS growth on the sidewall of a needle, the shape of the needle becomes tapered, since the VS growth duration is longer at its bottom. In the following, we show that the similar growth mode is available for the formation of SiGe core-shell needles.

3.3.2 Sulfur-Assisted Growth of SiGe Core-Shell Needles

SiGe core-shell needles can be fabricated by heating a Si substrate that is coated with Au, with Ge and S at 1200°C followed by slow cooling to room temperature [45]. A typical scanning electron microscopy (SEM) image of SiGe needles on a Si substrate is shown in Fig. 3.8. The growth direction is $\langle 111 \rangle$. Microsampling by focused ion beam (FIB) technique is very useful to reveal the inner structure, namely the core-shell structure, of the needles (see Fig. 3.9). High-angle annular dark field (HAADF) scanning transmission electron microscopy (STEM) images (z-contrast images) of the cross-sections clearly show that the core is Ge rich. The core-shell structure

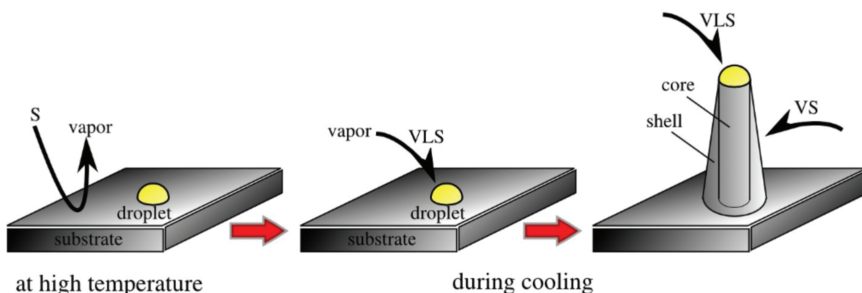

Fig. 3.7 Sulfur-assisted growth of a core-shell needle

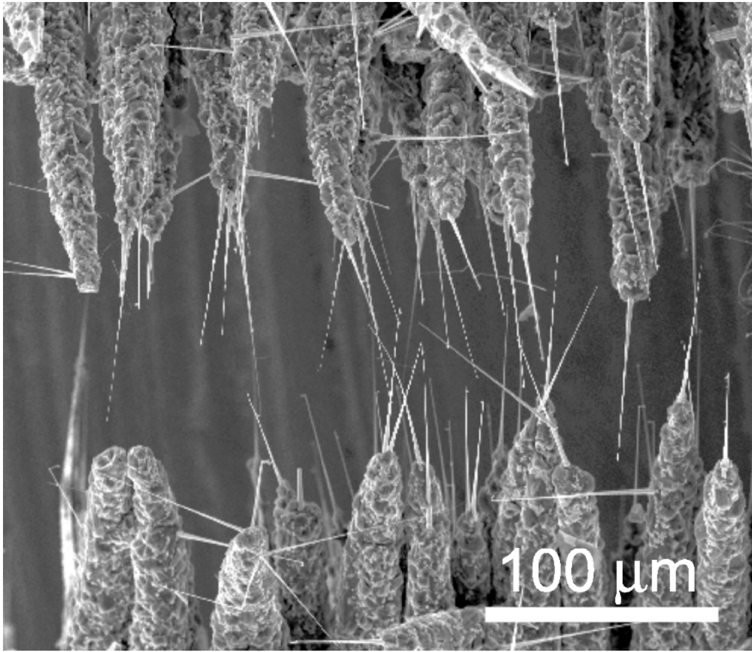

Fig. 3.8 SEM image of core-shell SiGe needles (after [45])

and the tapering evidence that the core and shell are formed via different process as mentioned earlier: the VLS and VS for the core and shell, respectively. The diameter of the core is nearly constant (about 300 nm for this sample). This is consistent with the VLS growth of the core, since the VLS growth usually does not show change in the diameter during the growth when the volume of the metal catalyst is conserved.

It is also shown that both the core and shell have composition gradient along the axial direction of the needle: Ge is richer at the tip (Fig. 3.10). Since the needles grow during the cooling process, the growth temperature is higher at the beginning of the growth than at the end. Thus we speculate that the composition gradient along the axial direction is due to the change in the growth temperature. This result indicates that the Ge/Si ratio becomes larger at lower growth temperature for both the VLS and VS growth.

Our method provides a simple way to fabricate core-shell nanoneedles although the dimensions of the SiGe needles are rather large at present. Effort to reduce their dimensions is underway. We consider that this approach can be useful to fabricate core-shell p-n junctions utilizing possible difference in the doping levels in the core and shell, since the growth mechanism of the core is different from that of the shell.

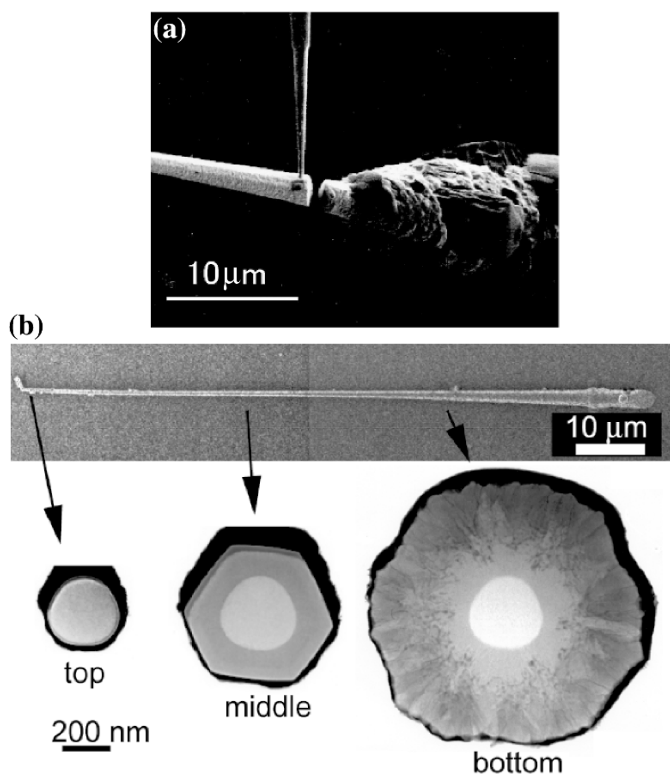

Fig. 3.9 (**a**) Microsampling of a SiGe needle using FIB and (**b**) SEM image of the needle and HAADF-STEM images of its cross-sections (after [45])

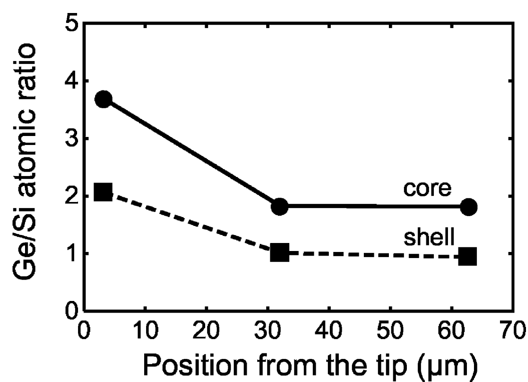

Fig. 3.10 Values of Ge/Si atomic ratio of the core and shell vs. the position from the tip of the needle (after [45])

3.4 Fe-Silicide Nanowires

β-$FeSi_2$ is a promising material for thermoelectric and optoelectronic device applications. In addition, it consists of only Fe and Si, which are abundant and harmless. Therefore, much effort has been made on the investigation of this material. In this section, we show that heterostructured nanowires of α-$FeSi_2$, ε-FeSi, and β-$FeSi_2$ can be fabricated [46]. Our approach is to use templates similar to the Cu-silicide nanochains. Fe-silicide nanowires are fabricated using Si nanowires: Fe infuses into Si nanowires and silicidation occurs. Especially, when Si/Au heterostructured nanowire templates are used, β-$FeSi_2$ nanowires can be formed.

3.4.1 Fabrication of α-$FeSi_2$ and ε-FeSi Nanowires

Si nanowire templates are fabricated using the sulfur-assisted VLS process, in which Fe is used as a catalyst. After heating the Si nanowire templates with Fe at 850°C for 30 min, we find that α-$FeSi_2$ or ε-FeSi are formed in the Si templates. As shown in Fig. 3.11, Si cores are fragmented and partially converted to silicide. Bright regions in the HAADF images are silicide, and the other parts of the cores are Si. The cores are covered with oxide shell. The formation of these Fe-silicide nanowires is considered to be due to a simple infusion of Fe into Si nanowire templates and successive silicidation. TEM observations give a piece of evidence of the Fe infusion. Figure 3.12 shows Fe nanoparticles infusing into a Si nanowire through a surface oxide layer. The Si nanowire has already been converted to silicide partially.

3.4.2 Fabrication of β-$FeSi_2$ Nanowires

We also found that β-$FeSi_2$ can be formed in nanowire templates. In this case, templates were fabricated via another process: Au was used as catalyst and the Au catalyst was heated with Cu to prevent the formation of Si nanochains [32]. The

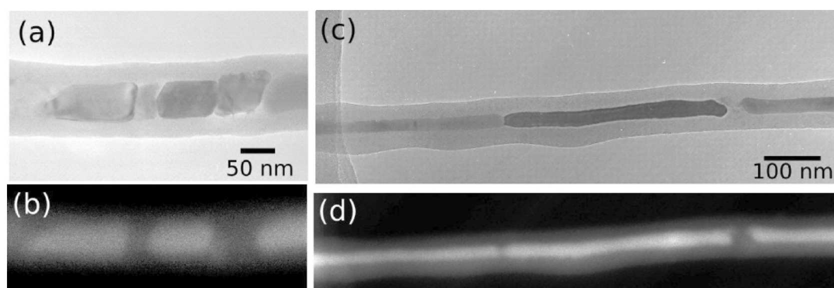

Fig. 3.11 (Left) α-$FeSi_2$ nanowire and (right) ε-FeSi nanowire. Top and bottom images are bright-field TEM and HAADF-STEM images, respectively. Bright regions in the HAADF images are silicide. Structures were confirmed by electron diffraction and EDX (after [46])

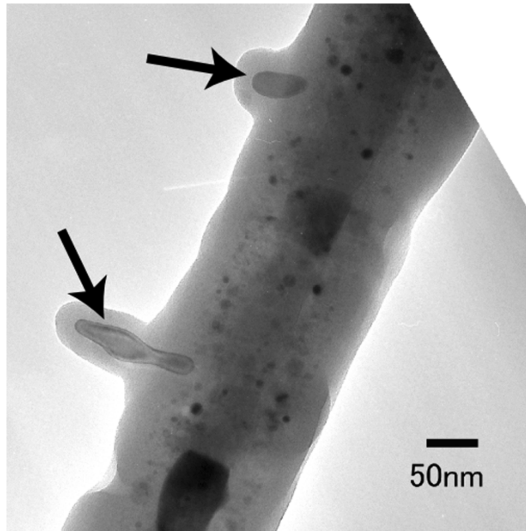

Fig. 3.12 Snapshot of silicidation. Fe is infusing into a Si nanowires (indicated by arrows) which has already been converted to silicide partially (after [46])

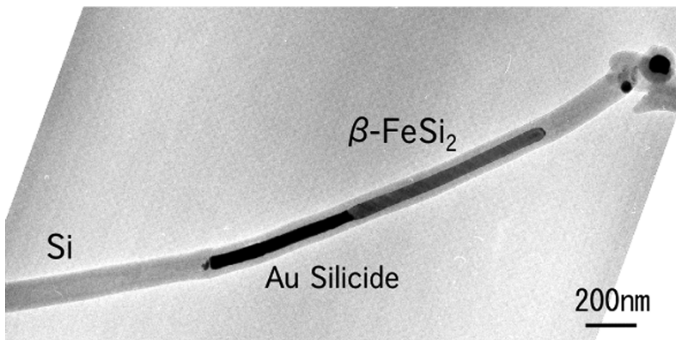

Fig. 3.13 β-$FeSi_2$/Au silicide/Si nanowire (after [46])

sample was heated to 1200°C and then cooled to room temperature for the nanowire growth. Then the templates were annealed with Fe at 900°C for 30 min for the silicide formation. Fig. 3.13 shows a TEM image of a β-$FeSi_2$ nanowire. In fact, the nanowire has a heterostructure: it consists of β-$FeSi_2$, Au silicide, and Si. We speculate that this nanowire is formed from a template of a special kind, namely a Au/Si nanowire. As shown in Fig. 3.14, a few templates are Au/Si nanowires while most of the templates are simple Si nanowires. Electron microdiffraction revealed that the Au nanowire is polycrystalline. The formation mechanism of the β-$FeSi_2$/Au silicide/Si nanowire is speculated as follows. First, Fe infuses into a Au/Si template during the annealing with Fe at 900°C, forming molten Fe/Au/Si alloy in a shell

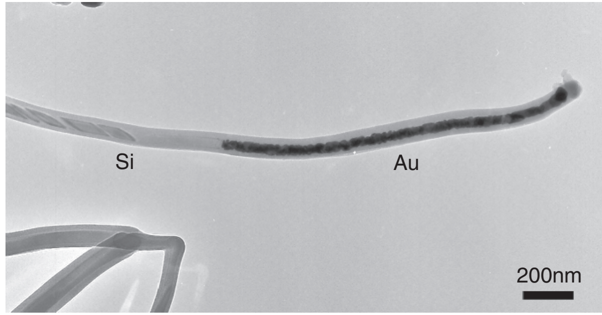

Fig. 3.14 Au/Si nanowire template (after [46])

of surface oxide. Second, while the cooling process, phase separation into β-$FeSi_2$ and Au silicide occurs in the oxide shell. At this moment, the formation mechanism of the Au/Si templates is unknown. In addition, since the yield of Au/Si template formation is very low, the yield of β-$FeSi_2$ nanowire formation is also low. For the high-yield formation of β-$FeSi_2$ nanowires, it is very important to reveal the formation mechanism of the Au/Si templates. Our method provides a simple route to the selective fabrication of β-$FeSi_2$ nanowires. Optical and electrical properties of such β-$FeSi_2$ nanowires are of great interest and further investigation is necessary.

3.5 SiC Fractal Nanowires

Fascinating properties can also be found in the shape of nanowires. In this section, I describe our study on the shape of SiC nanowires. We found complex diameter fluctuations in the growth of SiC nanowires. The diameter fluctuations are investigated in terms of fractal and random walk [47–49].

3.5.1 Diameter Fluctuations as Fractal

3.5.1.1 Brief Introduction to Mono- and Multiaffinity

Self-affine patterns are anisotropic fractal, and can be found in various system such as Brownian motion, interface roughening [50], and mountain topography [51, 52]. A self-affine function $F(t)$ satisfies the following scaling relation:

$$F(t) \sim \lambda^{-\alpha} F(\lambda t),$$

where α is the Hurst or roughness exponent. The correlation function $C(t)$ of the self-affine function $F(x)$ is calculated using the scaling relation as follows

$$C(t) = \langle |F(t+t') - F(t')| \rangle \sim t^{\alpha},$$

where angular brackets denote averaging over t'. We can also calculate the qth-order correlation function:

$$C_q(t) = \left\langle \left| F(t+t') - F(t') \right|^q \right\rangle \sim t^{q\alpha}.$$

The qth-order correlation function of a self-affine function can be characterized by a single parameter, namely the Hurst or roughness exponent, α. Therefore, curves of this type is called mono-affine. On the other hand, it is known that the exponent α is not constant for some curves: α depends on q. A curve of this type is called multi-affine. The qth-order correlation function of a multi-affine curve is given by

$$C_q(t) = \left\langle \left| F(t+t') - F(t') \right|^q \right\rangle \sim t^{q\alpha_q}.$$

To our knowledge, experimental observations of multiaffinity is very limited while many theoretical works have been reported [53–56]: Myllys et al. [57] found spacial and temporal multiscaling in kinetic roughening of slow combustion fronts in paper, and Luhman and Hallock [58,59] also observed multifractality in thermally evaporated rough CaF_2 film surfaces.

3.5.1.2 Fractality of the Diameter Fluctuations

SiC nanowires were fabricated via the VLS process using metal catalyst particles [47, 48]. While most nanowires have a simple cylindrical shape, some exhibit complex diameter fluctuations as shown in Fig. 3.15. We examined two types of diameter fluctuations. To reveal their selfaffinity, qth-order correlation functions were calculated (see Fig. 3.16). The values of α_q is almost constant for the nanowire of Fig. 3.15(a) showing mono-affinity. On the other hand, α_q decreases with increasing q for the nanowire of Fig. 3.15(b) showing clear multiaffinity. It is very interesting that such very complex shapes appear in nanometer scale. At this moment, the origin of these types of diameter fluctuations is unknown. To reveal the mechanism of the diameter fluctuations, in situ observations of the growth will be necessary.

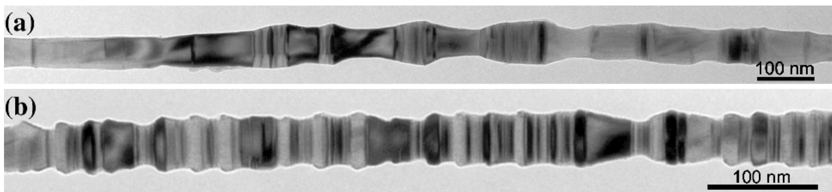

Fig. 3.15 SiC nanowires with complex diameter fluctuation: (**a**) mono-affine and (**b**) multi-affine (after [48])

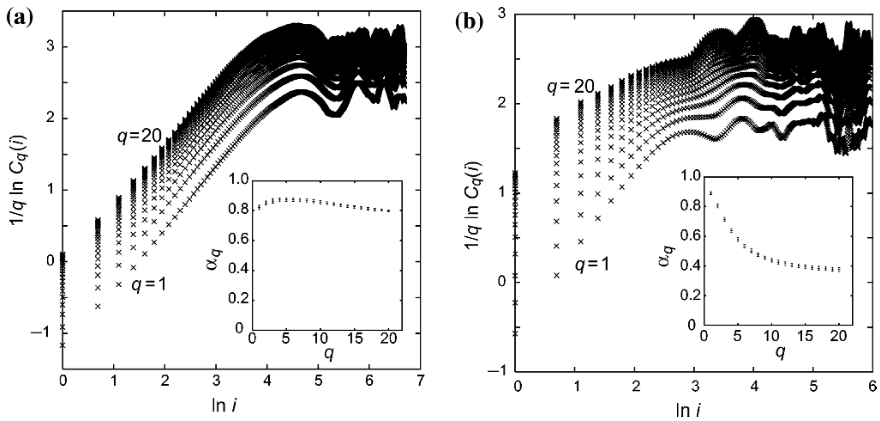

Fig. 3.16 Plots of qth-order correlation functions (*inset*: the values of α_q as a function of q) for (**a**) mono-affine and (**b**) multi-affine nanowires (after [48])

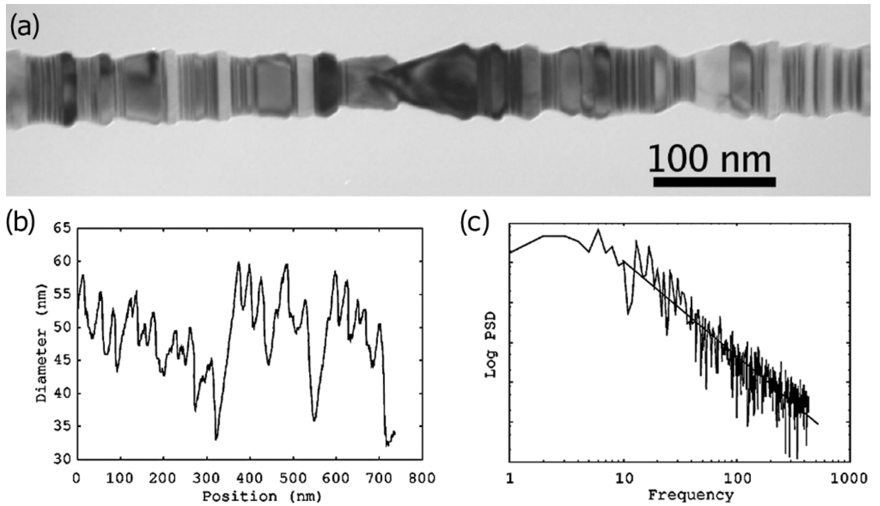

Fig. 3.17 (**a**) TEM image of a SiC multi-affine nanowire, (**b**) plot of the diameter, and (**c**) its power spectrum (after [47])

3.5.2 Diameter Fluctuations as Random Walk

The position on a nanowire along the axial growth direction has one-to-one relation to time. In the simplest case, the growth rate is constant. Next, we investigate the diameter fluctuations in terms of random walk. A multi-affine type SiC nanowire shown in Fig. 3.17a is studied in detail. The power spectrum of the digitized diameter fluctuation data is colored and shows $1/f^{\mu}$ dependency with $\mu = 2.5$. We note that $\mu = 2$ for ordinary Brownian motions. This analysis reveals that the

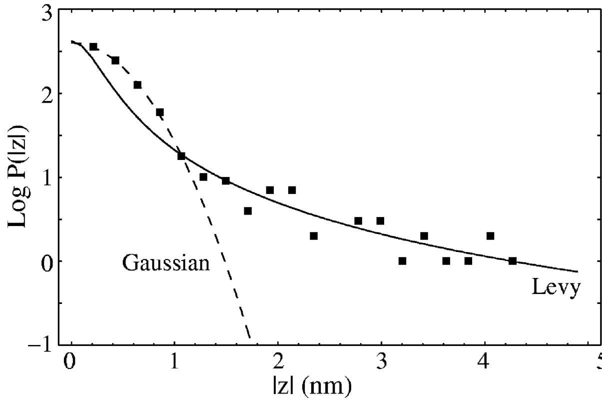

Fig. 3.18 Probability distribution function of displacements of the diameter fluctuation (after [47])

diameter fluctuation is not a simple Brownian motion. To reveal the property of this fluctuation, the probability distribution function of the displacements of the fluctuation is plotted in Fig. 3.18. Small displacements obey a Gaussian function; however, large displacements obey a Lévy distribution,

$$L_\alpha(z,\Delta t) = \frac{1}{\pi}\int_0^\infty \exp(-\gamma\Delta t q^\alpha)\cos(qz)dq.$$

This special type of random walk has a fat power-law tail in its distribution function, and can be found in various systems such as the motion of a particle in a two-dimensional rotating flow [60] and an economic index [61].

3.6 Summary

I have reviewed our results on the fabrication of nanowires of Si-based materials. Si is still the most important material for device fabrication and therefore such nanowires of Si-based materials are of great importance. Our studies have concentrated on a fundamental aspect of nanowire growth. Further study is necessary to utilize such nanowires for device applications. It is also necessary to develop methods of device fabrication using the nanowires that are compatible with conventional device processes.

Acknowledgments The author is grateful to S. Takeda, T. Akita, K. Tanaka, S. Ichikawa, H. Yoshida, K. Shoda, and all the other coauthors of related papers.

References

1. E.S. Greiner, J.A. Gutowski, and W.C. Ellis: J. Appl. Phys. 32 (1961) 2489
2. R.S. Wagner and R.G. Treuting: J. Appl. Phys. 32 (1961) 2490
3. R.S. Wagner and W.C. Ellis: Appl. Phys. Lett. 4 (1964) 89
4. R.S. Wagner: In *Whisker Technology* (A.P. Levitt Ed.) Wiley, New York, 1970, pp. 47–119
5. G.A. Bootsma and H.J. Gassen: J. Cryst. Growth 10 (1971) 223
6. E.I. Givargizov: J. Cryst. Growth 31 (1975) 20
7. M. Yazawa, M. Koguchi, and K. Hiruma: Appl. Phys. Lett. 58 (1991) 1080
8. K. Hiruma, T. Katsuyama, K. Ogawa, M. Koguchi, H. Kakibayashi, and G.P. Morgan: Appl. Phys. Lett. 59 (1991) 431
9. J. Westwater, D.P. Gosain, S. Tomiya, S. Usui, and H. Ruda: J. Vac. Sci. Technol. 15 (1997) 554
10. N. Ozaki, Y. Ohno, and S. Takeda: Appl. Phys. Lett. 73 (1998) 3700
11. A.M. Morales and C.M. Lieber: Science 279 (1998) 208
12. Y.F. Zhang, Y.H. Tang, N. Wang, D.P. Yu, C.S. Lee, I. Bello, and S.T. Lee: Appl. Phys. Lett. 72 (1998) 1835
13. M.S. Gudiksen, L.J. Lauhon, J. Wang, D.C. Smith, and C.M. Lieber: Nature 415 (2002) 617
14. Y. Wu, R. Fan, and P. Yang: Nano Lett. 2 (2002) 83
15. D. Li, Y. Wu, P. Kim, L. Shi, N. Mingo, Y. Liu, P. Yang, and A. Majumdar: Appl. Phys. Lett. 83 (2003) 3186
16. Y. Wu, J. Xiang, C. Yang, W. Lu, and C.M. Lieber: Nature 430 (2004) 61
17. F. Qian, Y. Li, S. Gradecak, D. Wang, C.J. Barrelet, and C.M. Lieber: Nano Lett. 4 (2004) 1975
18. W. Lu, J. Xiang, B.P. Timko, Y. Wu, and C.M. Lieber: Proc. Natl. Acad. Sci. USA 102 (2005) 10046
19. J.X. Wang, H.Y. Chen, Y. Gao, D.F. Liu, L. Song, Z.X. Zhang, X.W. Zhao, X.Y. Dou, S.D. Luo, W.Y. Zhou, G. Wang, and S.S. Xie: J. Cryst. Growth 284 (2005) 73
20. Y. Li, J. Xiang, F. Qian, S. Gradecak, Y. Wu, H. Yan, D.A. Blom, and C.M. Lieber: Nano Lett. 6 (2006) 1468
21. J. Xiang, W. Lu, Y. Hu, Y. Wu, H. Yan, and C.M. Lieberi: Nature 441 (2006) 489
22. M. Law, L.E. Greene, A. Radenovic, T. Kuykendall, J. Liphardt, and P. Yang: J. Phys. Chem. B 110 (2006) 22652
23. N. Skold, J.B. Wagner, G. Karlsson, T. Herman, W. Seifert, M.E. Pistol, and L. Samuelson: Nano Lett. 6 (2006) 2743
24. H. Yoshida, T. Uchiyama, J. Kikkawa, and S. Takeda: Solid State Commun. 141 (2007) 632
25. A. Fuhrer, L.E. Froberg, J.N. Pedersen, M.W. Larsson, A. Wacker, M.E. Pistol, and L. Samuelson: Nano Lett. 7 (2007) 243
26. M.W. Larsson, J.B. Wagner, M. Wallin, P. Hakkansson, L.E. Froberg, L. Samuelson, and L.R. Wallenberg: Nanotechnology 18 (2007) 015504
27. K.A. Dick, K. Deppert, M.W. Larsson, T. Mårtensson, W. Seifert, L.R. Wallenberg, and L. Samuelson: Nature Mater. 3 (2004) 380
28. J. Su, G. Cui, M. Gherasimova, H. Tsukamoto, J. Han, D. Ciuparu, S. Lim, L. Nurmikko, C. Broadbridge, and A. Lehman: Appl. Phys. Lett. 86 (2005) 013105
29. S.J. May, J.-G. Zheng, B.W. Wessels, and L.J. Lauhon: Adv. Mater. 17 (2005) 598
30. H. Kohno and S. Takeda: Appl. Phys. Lett. 73 (1998) 3144
31. H. Kohno and S. Takeda: e-J. Surf. Sci. Nanotech. 3 (2005) 131
32. H. Kohno and S. Takeda: Solid State Commun. 116 (2000) 591
33. E.I. Givargizov: J. Cryst. Growth 20 (1973) 217
34. H. Kohno and S. Takeda: J. Cryst. Growth 216 (2000) 185
35. H. Kohno, S. Takeda, and K. Tanaka: J. Electron Microsc. 49 (2000) 275
36. R. Okada and S. Iijima: Appl. Phys. Lett. 58 (1991) 1662
37. H.I. Liu, D.K. Biegelsen, F.A. Ponce, N.M. Johnson, and P.F.W. Peace: Appl. Phys. Lett. 64 (1994) 1383

38. J.L. Liu, Y. Shi, F. Wang, Y. Lu, S.L. Gu, R. Zhang, and Y.D. Zheng: Appl. Phys. Lett. 69 (1996) 1761
39. H. Heidemeyer, C. Single, F. Zhou, F.E. Prins, D.P. Kern, and E. Plies: J. Appl. Phys. 87 (2000) 4580
40. H. Kohno, T. Iwasaki, Y. Mita, and S. Takeda: J. Appl. Phys. 91 (2002) 3232
41. H. Richter, Z.P. Wang, and L. Ley: Solid State Commun. 39 (1981) 625
42. I.H. Campbell and P.M. Fauchet: Solid State Commun. 58 (1986) 739
43. H. Kohno and S. Takeda: Appl. Phys. Lett. 83 (2003) 1202
44. H. Kohno and S. Takeda: Jpn. J. Appl. Phys. 41 (Part 1) (2002) 577
45. K. Mori, K. Shoda, and H. Kohno: Appl. Phys. Lett. 87 (2005) 083111
46. K. Yamamoto, H. Kohno, S. Takeda, and S. Ichikawa: Appl. Phys. Lett. 89 (2006) 083107
47. H. Kohno and H. Yoshida: Solid State Commun. 132 (2004) 59
48. H. Kohno and H. Yoshida: Phys. Rev. E 70 (2004) 062601
49. H. Kohno, H. Yoshida, and T. Akita: e-J. Surf. Sci. Nanotechnol. 4 (2006) 330
50. S.V. Buldyrev, A.-L. Barabási, F. Caserta, S. Havlin, H.E. Stanley, and T. Vicsek: Phys. Rev. A 45 (1992) R8313
51. M. Matsushita and S. Ouchi: J. Phys. Soc. Jpn. 58 (1989) 1489
52. A. Czirók, E. Somfai, and T. Vicsek: Phys. Rev. Lett. 71 (1993) 2154
53. A.-L. Barabási, R. Bourbonnais, M. Jensen, J. Kertész, T. Vicsek, and Y.-C. Zhang: Phys. Rev. A 45 (1992) R6951
54. S. Das Sarma, C.J. Lanczycki, R. Kotlyar, and S.V. Ghaisas: Phys. Rev. E 53 (1996) 359
55. H. Katsuragi and H. Honjo: Phys. Rev. E 59 (1999) 254
56. H. Katsuragi and H. Honjo: Phys. Rev. E 67 (2003) 011601
57. M. Myllys, J. Maunuksela, M.J. Alava, T. Ala-Nisshila, and J. Timonen: Phys. Rev. Lett. 84 (2000) 1946
58. D.R. Luhman and R.B. Hallock: Phys. Rev. E 70 (2004) 051606
59. D.R. Luhman and R.B. Hallock: Phys. Rev. Lett. 92 (2004) 051606
60. T.H. Solomon, E.R. Weeks, and H.L. Swinney: Phys. Rev. Lett. 71 (1993) 3975
61. R.N. Mantegna and H.E. Stanley: Nature 376 (1995) 46

Chapter 4
Controlled Formation of Individually Addressable Si Nanowire Arrays for Device Integration

Ying-Lan Chang and Sung Soo Yi

Abstract The formation of large-scale arrays of individually seeded, electrically addressable Si nanowires with controlled dimension, placement, and orientation is demonstrated. E-beam evaporated gold nanoparticles were used for nanowire synthesis by the vapor–liquid–solid growth mechanism. By controlling the lithography and metal deposition conditions, nanowire arrays with narrow size distributions have been achieved. Low-energy postgrowth ion-beam treatment has been utilized to control the orientation of Si nanowires. This process also leads to the attachment of nanowires on the substrate surface. Fabrication of planar devices with robust metal contact formation becomes feasible. Our method, combining bottom-up and top-down approaches, can enable efficient and economical integration of nanowires into device architectures for various applications.

Low-dimensional nanomaterials are a new class of advanced materials that have been receiving a lot of research interest in the last decade because of their superior physical and chemical properties. Nanowires (NWs) have been demonstrated to exhibit superior electrical [1], optical [2, 3], mechanical [4], piezoelectric [5], and field emission [6] properties, and can be used as fundamental building blocks for nanoscale science and technology, ranging from chemical and biological sensors, field effect transistors to logic circuits.

Field effect transistors (FETs) based on NWs have been demonstrated as good candidates for ultrasensitive, miniaturized molecule sensors [7, 8]. Because of the high surface-to-volume ratio of these one dimensional nanostructures, their electronic characteristics may be sensitive enough to a very small amount of charge transfer such that single molecule detection becomes possible [7]. Nanosensors based on Si nanowires (SiNWs) are a promising candidate for label-free, direct, real-time electrical detection of the event of biomolecule binding, because of their several appealing properties including the following: (i) The electrical properties and sensitivity of SiNWs can be tuned by controlling NW diameter and the dopant type and concentration. (ii) The modification of silicon oxide surface, required for the preparation of interfaces selective for binding various analytes of interest, is well established.

The vapor–liquid–solid (VLS) growth mechanism, studied in detail in the 1960s and 1970s by Wagner et al. [9], is an ideal growth technique in the gas phase to produce NWs with high crystalline quality, required for sensing applications. Superior performance based on individual SiNW devices has been demonstrated [7, 10]. However, most of the existing studies based on nanostructures assembled using a bottom-up approach are limited by complex integration. Devices have been constructed around single, or several dispersed SiNWs. For practical applications, efficient and precise manipulation and placement of NWs at desired locations needs to be established to allow the integration with microfluidics and CMOS circuits. Methods that can enable reliable contact formation are essential in order for the intrinsic properties of the nanostructures to be realized.

We begin this chapter with an overview of prior methods that have been used for nanostructure assembly and device fabrication, including top-down (Sect. 4.1.1) and bottom-up (Sect. 4.1.2) approaches. The advantage and disadvantage of various approaches are discussed.

A pathway to fabricating large-scale arrays of individually seeded, electrically addressable SiNWs with controlled dimension, placement, and orientation is described (Sect. 4.2). SiNWs with controlled dimensions and specific placement were produced by the conventional chemical vapor deposition via the VLS process. By controlling the lithography and metal deposition conditions, NW arrays with narrow size distributions have been achieved (Sect. 4.2.2). Low-energy postgrowth ion-beam treatment has been utilized to control the orientation of SiNWs (Sect. 4.2.3). This process also leads to the attachment of NWs on the substrate surface. Fabrication of planar devices with robust metal contact formation becomes feasible. Electrical and structural characterizations were used to assess the quality of NWs after device fabrications (Sect. 4.2.4). Our method, which combines bottom-up and top-down approaches, can enable efficient and economical integration of NWs into device architectures for various applications.

4.1 Overview of Prior Approach

In this section, the various approaches that have been applied for the fabrication of NW devices are discussed.

4.1.1 Top-Down Approach

The nanoscale features of the SiNWs fabricated by top-down semiconductor processing make it possible to fabricate sensor arrays with extremely high density and direct integration with Si-based signal processing and communication circuits.

Li and coauthors combined standard semiconductor processing and silicon on insulator (SOI) wafers to fabricate Si-based nanoscale sensors [11]. The doping level in the Si layer was controlled by ion implantation. The top Si layer was then patterned by electron beam lithography (EBL) (for NWs) and optical lithography (for micron-scale electric leads.) A set of SiNWs with width of 50 nm was formed on the top of the SiO_2 insulating layers by reactive ion etching.

Instead of using lithography, a method of producing ultrahigh-density arrays of aligned metal and semiconductor NWs and NW circuits was demonstrated by Melosh and others [12]. The technique is based on translating thin film growth thickness control into planar wire arrays. Aligned metal NWs can be fabricated through a one-step deposition process without subsequent etching or lift-off. The metal NWs can be used as etch masks to transfer the NW pattern to an underlying semiconductor substrate, such as SOI wafers.

In both cases, the SiNWs are defined by etching of Si top layer on SOI wafers. The electronic properties of the NWs can be affected by the reactive ion etching process, used to define the nanostructures. Subsequent surface treatments need to be employed to remove process-induced damage and improve surface characteristics. The quality of SiO_2/Si interface, depending on the manufacturing process of SOI wafers, can also affect the device characteristics. The extent of the interface sets a fundamental limitation of the channel width one can produce with such approach.

4.1.2 Bottom-Up Approach

The VLS growth mechanism, studied in detail by many groups [9, 13], is an ideal growth technique in the gas phase to produce NWs with high crystalline quality, required for various applications. Superior performance based on individual SiNW devices has been demonstrated. Diameters as small as several nanometers with controlled hole and electron doping levels have been achieved [7, 10]. Comparison of scaled SiNW FET transport parameters with those for state-of-the-art planar MOSFETs shows that SiNWs have the potential to exceed substantially the performance of conventional devices, and NWs formed by VLS mechanisms could be ideal building blocks for future nanoelectronics and sensors [10].

The density, diameters, and length of the NWs can be controlled to some degree by the catalysts and the growth parameters. The relative ease of handling the catalyst particles on substrates and the chemical reactions have given rise to extensive research employing the VLS method as a basis for NW growth. Anodic alumina and mesoporous materials are frequently employed as templates for fabricating NWs [14]. NWs can be easily produced in high volume. However, the control of placement of catalyst particles with the precision required to form large-scale arrays remains a challenge. As a result, various approaches for nanostructure assembly, either postgrowth or during growth, have been proposed.

4.1.2.1 Postgrowth Assembly

An electric-field assisted assembly technique has been used to position individual NWs suspended in a dielectric medium between two electrodes defined lithographically on a SiO_2 substrate. During the assembly process, the forces that induce alignment arise as a result of NW polarization in the applied alternating electric field. This alignment approach has facilitated rapid electrical characterization of NWs. However, such approaches may not be suitable for NWs with small diameters [15].

Other approach has been proposed to aid assembly. For example, the work done by Filas and coworkers deals with the alignment of NWs magnetically [16]. The NWs are coated with a magnetic material. The coated NWs are then dispersed in a low-adhesive liquid medium by mixing and stirring. The NWs can be magnetically aligned. Array structures with a specific spacing may be formed as a result of repulsion induced by neighboring magnetic dipoles. The liquid medium is then evaporated while maintaining the magnetic field. The final step involved removing the matrix from a back side by use of acid, ion milling, laser beam, evaporation, or other techniques. For practical considerations, e.g., sensor applications, the removal of magnetic coating may be required.

4.1.2.2 Alignment during Growth

Many groups have demonstrated that semiconductor NWs often grow nearly normal to the surface of a (111)-oriented Si substrate and make good mechanical connection to the substrate [17]. Controlled growth of SiNWs in predetermined configurations has been demonstrated using (111)-oriented Si substrates. Patterned depositions of the gold seeds led to confinement of the vertically oriented NW growth to selected regions. However, formation of metal contact remains challenging for such device configuration [18].

If (111) surface can be oriented vertically, NWs should grow laterally. Anisotropic KOH wet chemical etching of a masked (110)-oriented Si wafer has been used to create vertical (111) planes. The nucleating metal catalyst was deposited by electron-beam evaporation onto the vertical (111) surfaces of the etched grooves. Lateral growth of NWs from one sidewall towards the opposing sidewall of the trench has been demonstrated [19]. However, since the catalyst is deposited by angle deposition, it is difficult to control the location and sizes. Diameters of the NWs formed were typically in the range of 180 nm. Although the NW carries a molten droplet of Au-Si alloy at its tip, formation of robust electrical connection remains a challenge. More work is needed to establish the sensitivity to gravity, mechanical vibration, and liquid and gas flow, etc.

Electric-field assisted growth and self-assembly of intrinsic SiNWs, in situ, has been demonstrated [20]. The NWs are seen to respond to the presence of a localized DC electric field set up between adjacent micro-electromechanical system (MEMS) structures. The response is expressed in the form of improved NW order, alignment,

and organization while transcending a gap. This process provides a method for enhanced control over intrinsic one-dimensional nanostructure placement and handling. However, it does add complexity to the fabrication process.

4.1.2.3 Postgrowth Alignment

A method of aligning NWs on a substrate has been proposed by Kamins and Chang [21]. In their study, titanium-containing islands were first formed by chemical vapor deposition on Si(001) and Si(111) substrates. Nucleation of SiNWs on titanium islands occurs upon exposure to Si-containing gas. Most NWs grown by titanium catalysts were randomly oriented. When the NWs were exposed to a flux of energetic ions, e.g., argon at ion energy of 5 KV and an integrated flux density of about 6×10^{15} ions/cm^2, the NWs became parallel to each other. The flux of energetic ions may also be used to align the NWs parallel to the substrate surface. Compared with other approaches, this method is less complex and easier to be implemented. However, the effects of ion beam process on the quality of NWs remained to be established.

4.2 Proposed Method for the Formation of Aligned Nanowire Array

4.2.1 Process Flow for Proposed Method (Fig. 4.1)

In this report, a pathway to fabricating large scale, high-density NW arrays by combining bottom-up and top-down approaches is proposed. Metal catalysts are formed by EBL and electron-beam evaporation (step (a) and step (b)). SiNWs with controlled dimensions and specific placement were produced by the conventional chemical vapor deposition via the VLS process (step (c)). Postgrowth ion-beam alignment process was employed to control the orientation of NWs (step (d)). Subsequent lithography and metallization steps can be used for metal contact formation (step (e)). This process provides a simple yet reliable method for enhanced control over the placement and handling of one-dimensional nanostructures. As a result, integration of NWs with various device architectures can be realized.

4.2.2 Growth of SiNWs

One of convenient methods of preparing catalyst nanoparticles suitable for SiNW growth is depositing a thin film of metal by evaporation and breaking up the thin film at high temperature into nanoparticles [17]. Figure 4.2 is a secondary electron

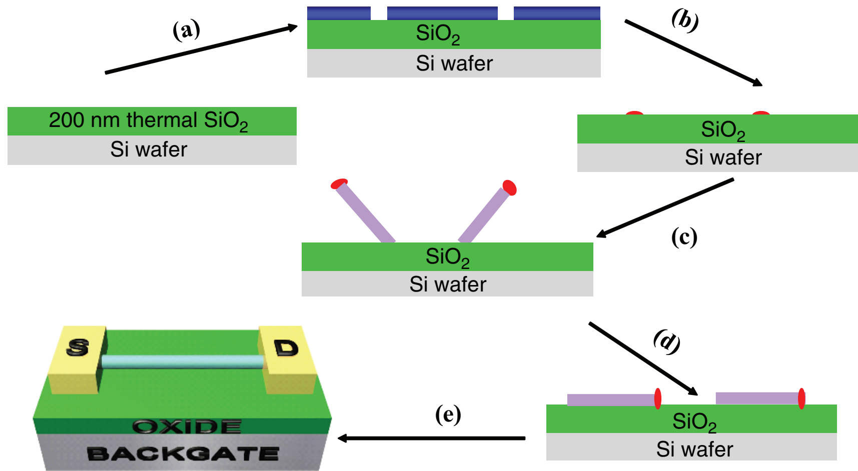

Fig. 4.1 Process flow of proposed method: (**a**) electron-beam lithography, (**b**) electron-beam evaporation, (**c**) Si nanowire growth, (**d**) ion-beam alignment, and (**e**) metal contact formation

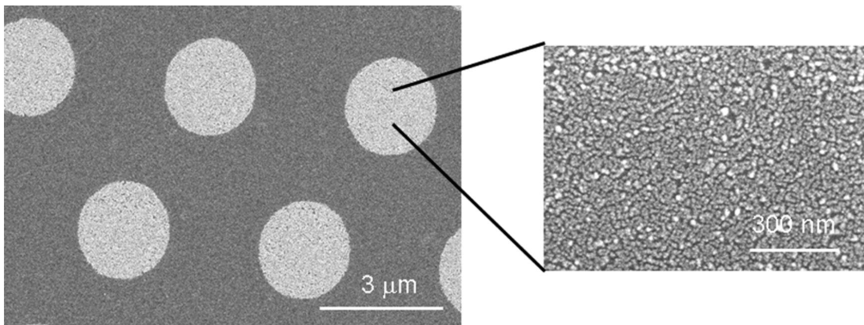

Fig. 4.2 SEM image of an optical lithography-patterned substrate with islands of Au nanoparticles

microscopy (SEM) image of an optical lithography-patterned substrate with islands of Au nanoparticles. The nominal thickness of electron-beam evaporated Au film is less than 1 nm.

Figure 4.3a and b shows plan-view and cross-sectional SEM images of high-density, randomly oriented SiNWs grown on Au islands on the patterned substrate. The distribution of resulting SiNW diameters is quite large, ranging from ∼20 to 120 nm because of randomness of thin film break-up and subsequent nanoparticle formation. In addition, the density of SiNWs varies from island to island.

For the growth of arrays of position- and diameter-controlled SiNWs, the fabrication process begins with a doped Si wafer with a 160 nm-thick thermal oxide layer. EBL was utilized to define the location of catalyst. A layer of 100 nm PMMA was first spin-coated onto the Si wafer, and was subsequently exposed in a direct-write EBL system at 50 keV. After exposure, the resist was developed in MIBK: IPA (1:2)

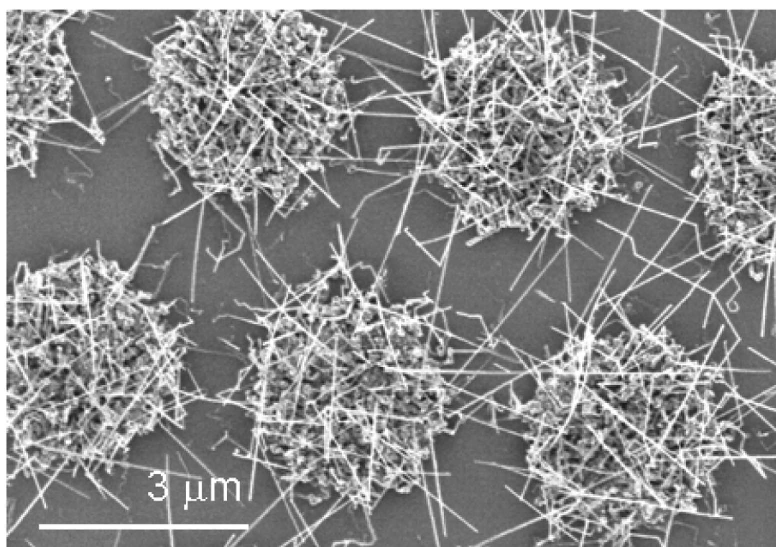

(a)

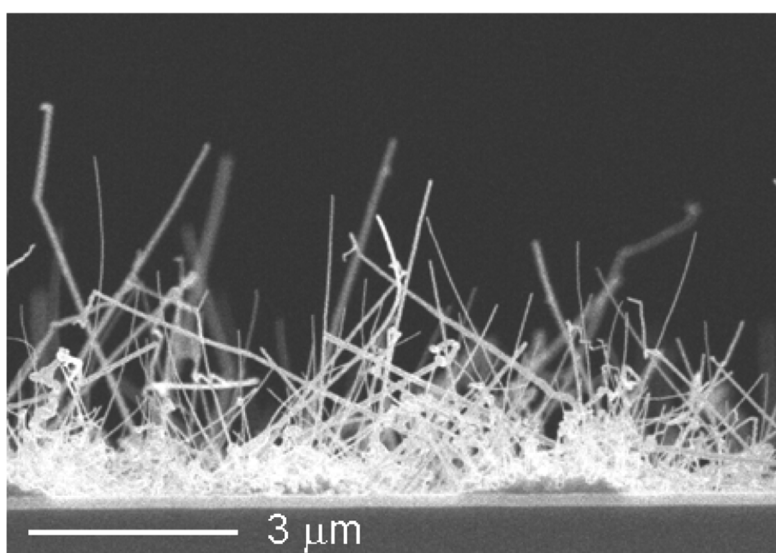

(b)

Fig. 4.3 (**a**) Plan view and (**b**) cross-sectional SEM images of high density, randomly oriented SiNWs grown on Au islands on the patterned substrate

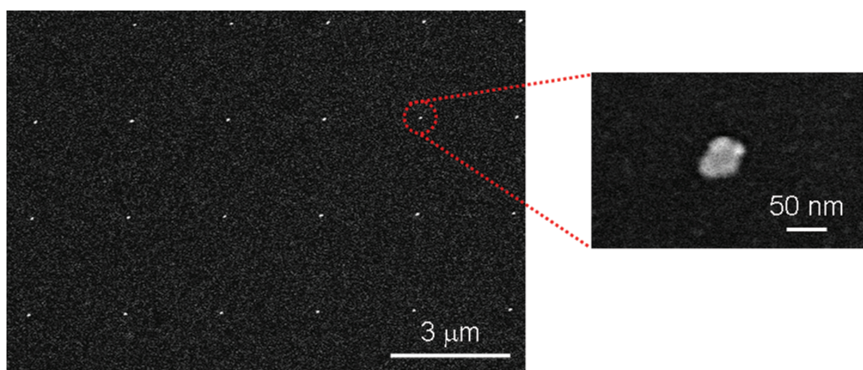

Fig. 4.4 SEM images of an array of Au nanoparticles on SiO_2 surface prepared by e-beam lithography followed by e-beam evaporation of gold and lift-off

mixture, resulting in an array of holes with diameter$\sim$40 nm in PMMA. A layer of 10 nm-thick gold was then deposited by electron-beam evaporation and followed by lift-off in acetone. After lift-off, an array of Au nanodisks with diameter $\sim$40 nm and thickness $\sim$10 nm was formed as shown in Fig. 4.4.

EBL and metal lift-off typically produce disk-shaped particles. Typically, a thin Au disk tends to break up at high temperature and forms multiple particles and the growth of NWs using such thin disks results in the formation of multiple NWs from an individual catalyst site. Therefore, it is necessary to control a thickness-to-diameter ratio to obtain a single NW from each lithographically defined catalyst site. In the Au-catalyzed growth of SiNWs, the size of Au nanodisks, which determines the diameter of SiNWs, can be tailored by EBL and Au deposition steps. It is notable that the edge of Au nanodisks is not well-defined. This is most likely related to imperfection in EBL/Au deposition/lift-off processes.

The growth of SiNWs was carried out in a vertical metal-organic chemical vapor deposition reactor equipped with a close-coupled showerhead. 2% disilane (Si_2H_6) in H_2 was used as a Si precursor and H_2 was used a carrier gas. The reactor was typically operated at 76 Torr with total H_2 flow of $\sim$10 slm (standard liter per minute). Typical growth rate of SiNWs was $\sim 0.2\,\mu m/min$. Dopants were not introduced during the growth and SiNWs grown were unintentionally doped. Figure 4.5 shows an array of SiNWs grown on a 3-inch, electron-beam patterned substrate. A single SiNW was grown from each catalytically defined catalyst site, as shown in Fig. 4.5. The diameter of SiNWs grown from Au nanodisks with diameter of $\sim$40 nm was in the range of 40–50 nm as determined by SEM, indicating that SiNWs were grown with narrow size distribution closely matching the size of seed catalyst nanoparticles.

We were able to control EBL and metal deposition processes to produce SiNWs with diameter as small as $\sim$20 nm. With a growth rate of $\sim 0.2\,\mu m/min$, 1- to 5-μm-long SiNWs can be grown by controlling growth time. Our result shows that with optimum catalyst preparation process and growth conditions, the diameter,

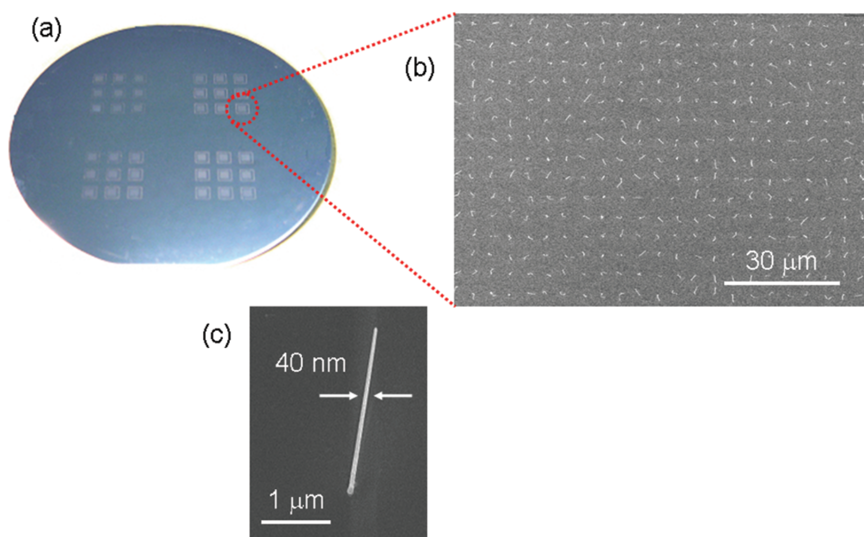

Fig. 4.5 (**a**) Large-scale arrays of Si nanowires grown on a 3-inch e-beam patterned substrate. (**b**) SEM image of an array of Si nanowires grown over large area. (**c**) SEM image of a typical, single Si nanowire grown from lithographically defined catalyst site

position, and density of SiNWs can be controlled to create desired arrays of SiNWs in large scale. This is in sharp contrast with a conventional approach based on thin film deposition and break-up, where good control over diameter, density, and exact location of SiNWs cannot be achieved.

To verify the crystalline quality of SiNWs grown from lithographically defined Au nanoparticles, we investigated the SiNWs using high-resolution transmission electron microscopy (TEM). Figure 4.6 is a high-resolution TEM image of a SiNW showing an Au nanoparticle at the tip, indicating that SiNWs were grown via the VLS growth process. Clear [111] lattice fringes shown in Fig. 4.6 indicates the high crystalline quality of the SiNW.

Although most of SiNWs grown were straight, as shown in Fig. 4.5, some SiNWs exhibited kinking. Kinking of SiNWs has been reported in the literature and has been attributed to growth defects and high growth rate. Figure 4.7 shows a high-resolution TEM image of a kinked SiNW observed in this work. Kinking at a sharp angle is seen with a change in growth direction from $<-111>$ to $<111>$ or vice versa. Contrary to previous reports in the literature [22, 23], the kinked SiNW does not exhibit any noticeable defects and shows high crystalline quality. Kinking is most likely related to the instability of liquid–solid interface between molten Au-Si alloy and a solid SiNW during the growth.

Figure 4.8 is high-resolution SEM images showing the bases of SiNWs. Most of SiNWs grown straight out of each catalyst site had bases similar to a tree trunk as shown in Fig. 4.8a. However, some SiNWs grew zigzagged before they grew straight out of SiO_2 surface as shown in Fig. 4.8b. We found that SiNWs having a zigzag segment near the root of NWs were less responsive to a NW alignment process utilizing ion beam irradiation.

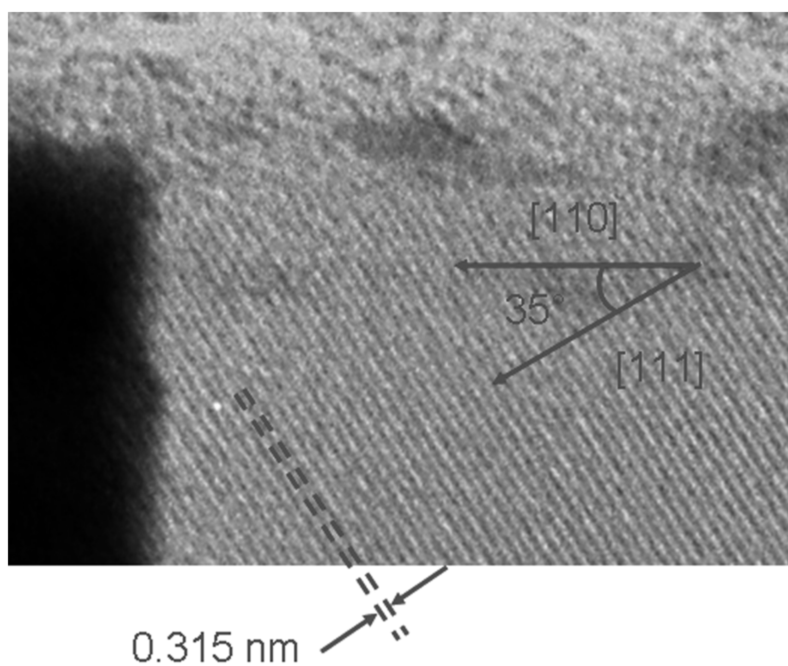

Fig. 4.6 High-resolution TEM image of a Si nanowire showing [111] lattice fringes and <110> growth direction

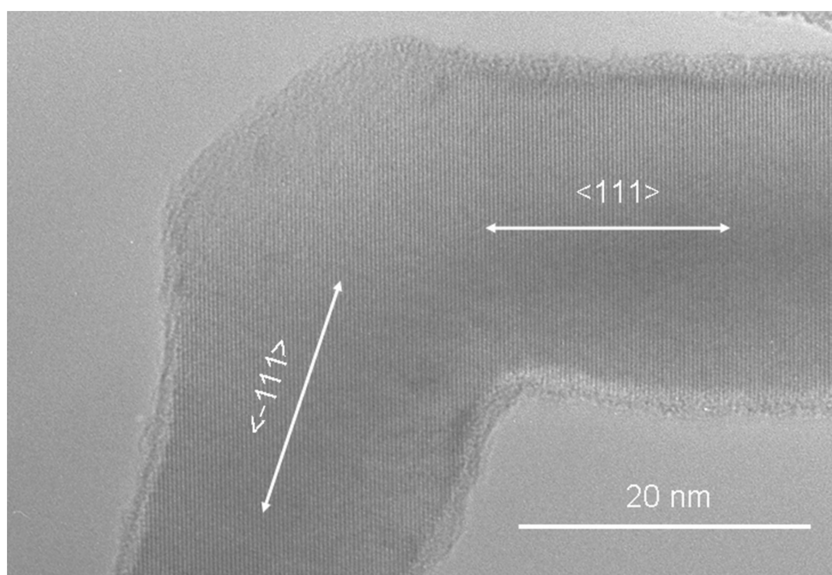

Fig. 4.7 High-resolution TEM image of a kinked SiNW

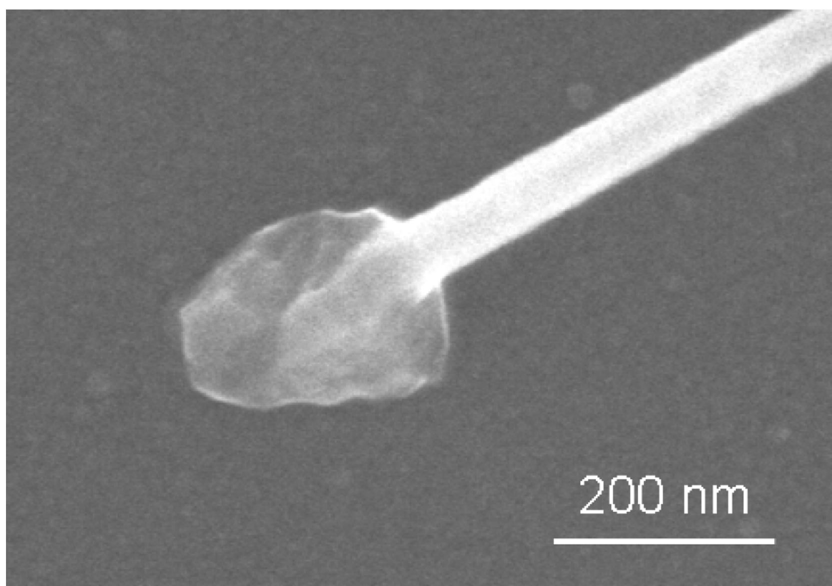

(a)

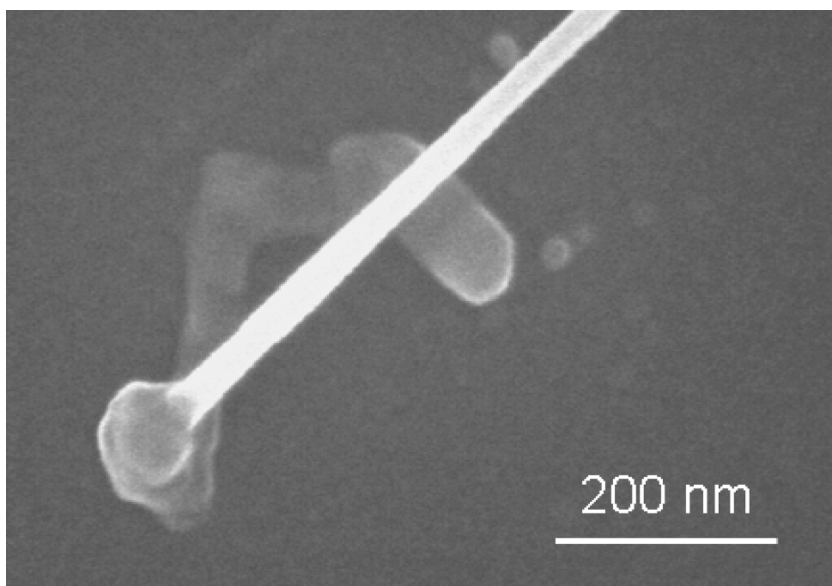

(b)

Fig. 4.8 High-resolution SEM images showing the bases of SiNWs

Although further investigation is necessary to elucidate this behavior, the fact that Au–Si molten alloy can be mobile on bare SiO_2 surface at the beginning of SiNW growth may be related to the zigzagging behavior. To immobilize molten Au–Si alloy nanoparticles at the beginning of SiNW growth, the following steps were added to the catalyst preparation process. First, a patterned substrate was exposed to 5% HF solution briefly before Au evaporation to form shallow holes on SiO_2 surface that can contain molten Au–Si alloy nanoparticles. Second, thin (less than $\sim$5 nm) Ti was evaporated onto SiO_2 before Au deposition to enhance the adhesion of Au on the surface.

We have also observed the presence of a thin amorphous layer on the substrate surface when growth was carried out in nonoptimized conditions. The presence of amorphous layer is due to uncatalyzed decomposition of Si precursors on SiO_2 surface during the growth of SiNWs. In some nonoptimized growth conditions, the thickness of amorphous layer containing Si was $\sim$10 nm, which was determined by X-ray photoemission spectroscopy measurement. The presence of this amorphous layer is detrimental and can lead to an increase in leakage current. Therefore, growth parameters such as H_2 carrier gas flow rate and growth temperature was optimized to minimize uncatalyzed decomposition of Si precursors on SiO_2 surface.

4.2.3 Postgrowth Alignment

When the critical supersaturation concentration is reached in Au–Si molten nanoparticle alloy, Si begins precipitating on the SiO_2 surface. The NWs are attached to the substrate on one end. Unlike SiNWs grown epitaxially on Si (111) substrate, due to lack of crystalline characteristics of the SiO_2 surface, the NWs grown on SiO_2 surface are randomly oriented after growth, as shown in Fig. 4.5. For many applications, having the NWs parallel to each other and possibly parallel to the substrate surface would aid fabrication. Accordingly, an ion beam irradiation process was employed to align the SiNWs in a desired manner. It was found that by exposing the NWs to a flux of energetic ions, such as argon ions, the NWs become aligned parallel to each other and may be parallel to the surface of the substrate.

At the present case, typical argon ion energy within the range of about 1–4 KeV, with a flux density of $\sim 6 \times 10^{15}$ ions/cm^2 was applied. The treatment was performed at some angle to the substrate surface, typically within the range of about 5° to 45°. A minimum angle of about 5° is required to allow beam positioning. Above the maximum of 45°, the lateral component of the bombardment decreases, and hence a shallower angle, such as 15°, is preferred. Effectiveness of alignment with different process parameters was investigated by SEM, as shown in Fig. 4.9.

It was experimentally demonstrated that effective alignment of NWs with diameters ranging from 20 to 50 nm can be readily achieved with $<$30 s treatment. The attachment of NWs to substrate surface after ion beam irradiation and the subsequent device fabrication process is verified by atomic force microscope (AFM) measurement. When similar conditions were used for sputter etching of thermally grown

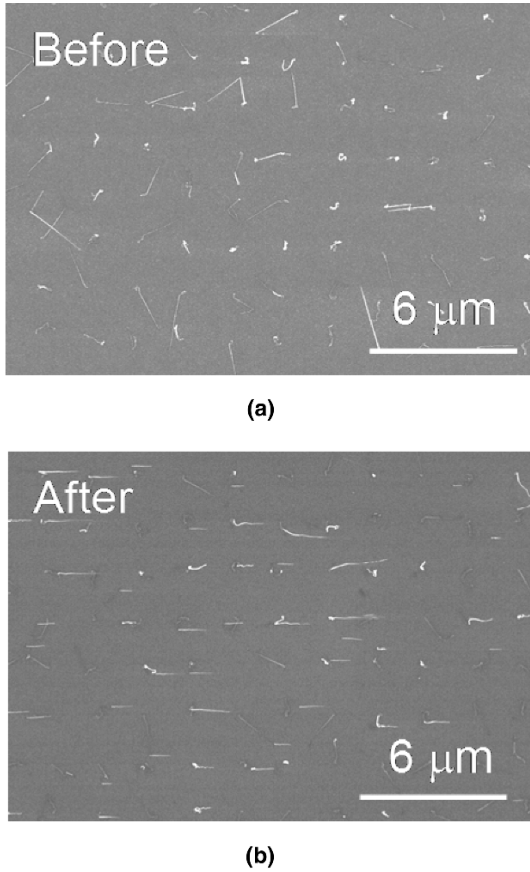

Fig. 4.9 SEM of Si nanowire array before (**a**) and after (**b**) ion beam alignment

SiO_2, the thickness of SiO_2 sputter-etched during a similar exposure to the ion beam was less than ∼2 nm. Therefore, the alignment process using an ion beam should not significantly change the properties of the NWs. Although the kink formation during the growth does not affect the crystalline quality, as indicated in Fig. 4.7, it does affect the process yield of alignment. Further growth optimization to minimize kink formation should lead to further improvement of process yield.

4.2.4 Contact Formation and Electrical Characterization

Lastly, electrical contacts to the ends of SiNWs were made by defining pairs of electrodes using EBL and subsequent evaporation of contact metal and lift-off. As discussed earlier, the attachment of NWs to substrate surface after the ion beam

irradiation was strong and the placement of NWs did not change through the subsequent lithography process. Arrays of high density SiNWs with controlled orientation have been successfully obtained. The SEM and AFM images of a finished device are shown in Fig. 4.10.

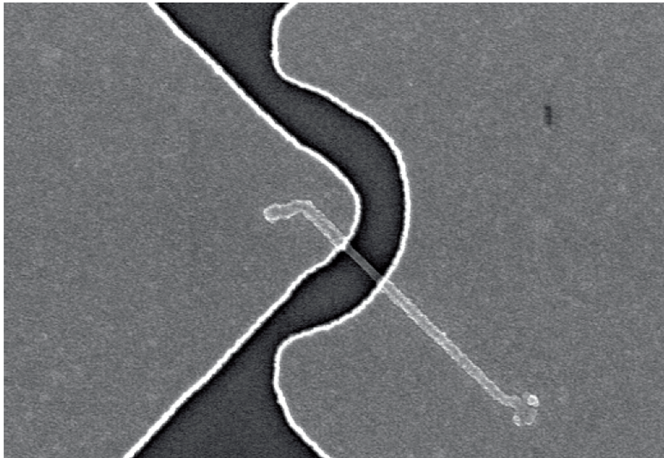

(a)

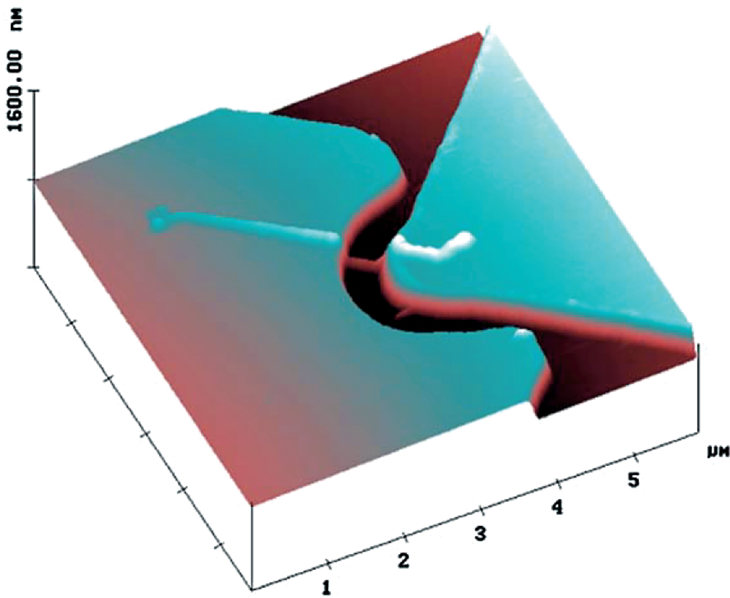

(b)

Fig. 4.10 (**a**) SEM picture and (**b**) AFM picture of finished devices

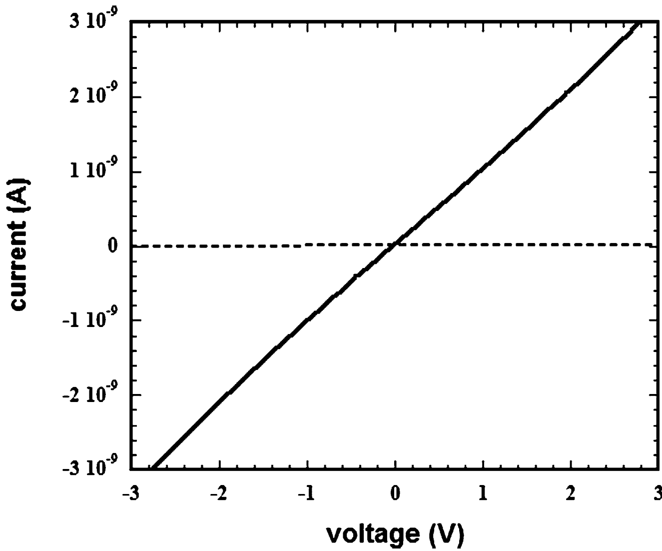

Fig. 4.11 *I–V* measurement of an electrically connected Si nanowire. Solid line: with a nanowire, dotted line: without a nanowire

Compared with a prior approach employing formation of vertically aligned SiNWs relative to substrates, this method provides a route to the fabrication of planer devices with robust metal contact formation. A typical *I–V* characteristic of finished devices is shown in Fig. 4.11. The *I–V* characterization from devices without a connected wire indicate that the leakage current is negligible (less than pA) after the growth and processing steps. The *I–V* characterization from devices with connected NWs with diameter of 35–40 nm exhibit linear characteristics with resistivity in the range of 100 Ωcm, which is fairly consistent with the value for the nonintentionally doped Si.

These experimental observations indicate that the negative effects of postgrowth process such as ion-beam alignment and metal contact formation on the crystalline quality of NW is minimal. We have also found that the presence of thin amorphous layer on substrate surface, due to nonoptimized growth conditions, can lead to increase of leakage current. Therefore, process parameters should be optimized to minimize noncatalytic deposition.

4.3 Discussions and Future Work

In this work, a method of fabricating arrays of SiNWs with control over NW location, density, diameter, and orientation has been demonstrated. Since Au has been widely used as catalyst for NW growth, it is therefore expected that the method described herein can be generally applied to NWs made of other materials.

The postgrowth alignment using an ion beam has been found to be effective for SiNWs formed on both SiO_2 and Si substrates [21, 24]. For Si, the native oxide naturally formed on the Si surface act as a sacrificial layer for ion bombardment required for the alignment process. For other material system, the effects of ion flux on material quality need to be investigated, and process parameters need to be optimized to minimize negative effects. As an example, the native oxide formed on Ge surface is more complex and may affect the etching rate upon exposure to the ion flux. For compound semiconductor NWs, including GaAs and InP, preferential sputtering of group V material, e.g., As and P, may occur upon exposure to energetic ion beam [25]. The change of surface stoichiometry may lead to defect formation on the surface and degrade the electronic properties.

Core shell heterostructures formed by the growth of crystalline overlayers on nanocrystals have been widely investigate for different material system, and have been found to offer enhanced electronic properties of nanostructure. The growth of doped silicon shells on intrinsic silicon and silicon–silicon oxide core-shell nanowires indicates that homoepitaxy can be achieved at relatively low temperature on clean silicon. The possibility of heteroepitaxial growth of crystalline germanium-silicon core shell structures has also been demonstrated [26]. GaAs/AlGaAs core-shell NWs have been reported using selective-area metalorganic vapor phase epitaxy [27]. In this case, the AlGaAs was grown on the sidewalls of the GaAs NWs, forming GaAs/AlGaAs core-shell structures. Microphotoluminescence measurements of GaAs and GaAs/AlGaAs core-shell NWs reveal an enhancement of photoluminescence intensity in GaAs/AlGaAs core-shell structures. With proper choice of structure parameters, including the alloy composition and thickness of the crystalline overlayers, one should be able to minimize the effects of ion beam process on the intrinsic properties of nanostructure.

In summary, a method of fabricating arrays of SiNWs with control over NW location, density, diameter, and orientation has been demonstrated. The method described herein, utilizing standard semiconductor fabrication processes, may serve as a basis for forming high density nanoscale sensors that can be integrated with microfluidics and CMOS driver circuits.

Specifically, the implementation of postgrowth ion-beam alignment makes this process ideal for fabricating array of planar devices with robust metal contact formation. The alignment can be performed by exposing an area of interest to the ion beam for a short period of time (<30 s). Results indicate that with optimized process parameters, the process-induced damage can be minimized. Depending on the equipment capabilities available, this method can potentially offer high throughput for the fabrication of devices in large scale. Density of ion flux and impact energy of ionic species can be precisely controlled, which leads to a reproducible process.

Acknowledgments The authors acknowledge the technical assistance and valuable discussions from Edmond Chow, Grant Girolami, Yim Young, Maozi Liu, Jörg Albuschies, Jun Amano, D. Yang, L. Mirkarimi, and T. Kopley. The authors also thank the management support from D. Chamberlin, R. Jaeger, A. Grot, and J. Hollenhorst.

References

1. Huang Y, Duan X, Wei Q, Lieber CM (2001) Directed assembly of one-dimensional nanostructures into functional networks. Science 291: 630–633
2. Wang J, Gudiksen MS, Duan X, Cui Y, Lieber CM (2001) Highly polarized photoluminescence and photodetection from single Indium Phosphide nanowires. Science 293: 1455–1457
3. Huang M, Mao S, Feick H, Yan H, Wu Y, Kind H, Weber E, Russo R, Yang P (2001) Room-temperature ultraviolet nanowire nanolasers. Science 292: 1897–1899
4. Wong EW, Sheehan PE, Lieber CM (1997) Nanobeam mechanics: elasticity, strength and toughness of nanorods and nanotubes. Science 277: 1971–1975
5. Wang ZL, Song JH (2006) Piezoelectric nanogenerators based on Zinc Oxide nanowire arrays. Science 312: 242–246
6. Li Z, Chen Y, Li X, Kamins T, Nauka K, Williams RS (2004) Sequence-specific label-free DNA sensors based on silicon nanowires. Nano Lett 4: 245–247
7. Patolsky F, Zheng G, Hayden O, Lakadamyali M, Zhuang X, Lieber CM (2004) Electrical detection of single viruses. Proc Natl Acad Sci 101: 14017–14022
8. Hahm J, Lieber CM (2004) Direct ultrasensitive electrical detection of DNA and DNA sequence variations using nanowire nanosensors. Nano Lett 4: 51–54
9. Levitt AP (1971) VLS growth mechanism of crystal growth in whisker technology. Wiley-Interscience: New York.
10. Cui Y, Zhong Z, Wang D, Wang WU, Lieber CM (2003) High performance silicon nanowire field effect transistors. Nano Lett 3: 149–152
11. Li YB, Bando Y, Golberg D (2004) ZnO nanoneedles with tip surface perturbations: Excellent field emitters. Appl Phys Lett 84: 3603–3605
12. Melosh NA, Boukai A, Diana F, Gerardot B, Badolato A, Petroff P, Heath JR (2003) Ultra-high-density nanowire lattices and circuits. Science 300: 112–115
13. Wu Y, Yang P (2001) Direct observation of vapor–liquid–solid nanowire growth. J Am Chem Soc 123: 3165–3166
14. Itaya K, Sugawara S, Arai K, Saito S (1984) Properties of porous anodic aluminum oxide films as membranes. J Chem Eng Jpn 17: 514–520
15. Smith PA, Nordquist CD, Jackson TN, Mayer TS, Martin BR, Mbindyo J, Mallouk TE (2000) Electric-field assisted assembly and alignment of metallic nanowires. Appl Phys Lett 77: 1399–1401
16. Filas WR, Jin S, Kochanski GP, Zhu W (2004) Article comprising aligned nanowires. United States Patent 6741019
17. Wu Y, Yan H, Huang M, Messer B, Song JH, Yang P (2002) Inorganic semiconductor nanowires: Rational growth, assemblies and novel properties. J Chem Eur 8: 1260–1263
18. Hochbaum AI, He R, Fan R, Yang P (2005) Controlled growth of Si nanowire arrays for device integration. Nano Lett 5: 457–460
19. Islam MS, Sharma S, Kamins TI, Williams RS (2004) Ultrahigh-density silicon nano-bridges formed between two vertical silicon surfaces. Nanotechnology 15: L5–L8
20. Englander O, Christensen D, Kim J, Lin L, Morris SJS (2005) Electric-field assisted growth and self-assembly of intrinsic silicon nanowires. Nano Lett 5: 705–708
21. Kamins T, Chang YL (2001) Method of aligning nanowires. United States Patent 6248674
22. Westwater J, Gosain DP, Tomiya S, Usui S, Ruda H (1997) Growth of silicon nanowires via gold/silane vapor–liquid–solid reaction. J Vac Sci Technol B 15: 554–557
23. Wagner RS, Doherty CJ (1968) Mechanism of branching and kinking during VLS crystal growth. J Electroanal Chem 115: 93–99
24. Chang YL, Yi SS, Chow E, Girolami G, Young Y, Liu M, Albuschies J, Amano J (2006) Controlled formation of individually seeded, electrically addressable silicon nanowire arrays for device integration. Appl Phys Lett 89: 223123–223125
25. Valeri S, Lolli M (1990) AES, EELS and XPS study of ion-induced GaAs and InP(110) surface and subsurface modifications. Surf Interface Anal 16: 59–64

26. Lauhon LJ, Gudlksen MS, Wang D, Lieber CM (2002) Epitaxial core-shell and core-multi-shell nanowire heterostructures. Nature 420: 57–61
27. Noborisaka J, Motohisa J, Hara S, Fukui T (2005) Fabrication and characterization of free-standing GaAs/AlGaAs core-shell nanowires and AlGaAs nanotubes by using selective-area metalorganic vapor phase epitaxy. Appl Phys Lett 87: 093109–093111

Chapter 5
Physical Properties of GaN Nanotubes as Revealed by Computer Simulation

Zhiguo Wang, Fei Gao, Xiaotao Zu, and William J. Weber

Abstract Single-crystalline wurtzite GaN nanotubes have been synthesized recently with proposed applications in nanoscale electronics, optoelectronics, and the biochemical sensing field. In this work, molecular dynamics methods with a Stillinger-Weber potential have been used to investigate the melting behavior, thermal conductivity, and mechanical properties of wurtzite-type single-crystalline GaN nanotubes. (1) The simulations show that the melting temperature of the GaN nanotubes increases with the thickness of the nanotubes to a saturation value, which is close to the melting temperature of a bulk GaN. The results reveal that the nanotubes begin to melt at the surface, and then the melting rapidly extends to the interior of the nanotubes as the temperature increases. (2) The thermal conductivity of nanotubes is smaller than that of the bulk GaN single crystal. The thermal conductivity is also found to decrease with temperature and increase with increasing wall thickness of the nanotubes. The change of phonon spectrum and surface inelastic scattering may account for the reduction of thermal conductivity in the nanotubes, while thermal softening and high-frequency phonon interactions at high temperatures may provide an explanation for its decrease with increasing temperature. (3) The simulation results show that at low temperatures, the nanotubes show brittle properties, whereas at high temperatures, they behave as ductile materials. The brittle to ductile transition temperature generally increases with increasing thickness of the nanotubes and strain rate. (4) The simulation temperature, tube length, and strain rate all can affect the buckling behavior of GaN nanotubes. The critical stress decreases with the increase of simulation temperature and tube length. The tube length dependence of buckling is compared with those from the analysis of equivalent continuum structures using Euler buckling theory.

5.1 Introduction

Nanotubes have been a focus of increasing research interest during recent years because of their unique and fascinating properties, as well as their potential for a wide range of applications. Since the discovery of carbon nanotubes [1], other

nanometer-scale tubular forms of various solids have been reported [2–5]. Among them, the binary materials composed of Group III nitrides are viewed as ideal analogs of carbon because of their isoelectrons in a hexagonal network, and they can potentially be used in a light emitting device [6–9].

Gallium nitride is a wide-bandgap semiconductor and a prime candidate for use in future high-performance, high-power optoelectronic devices because of its high melting point, carrier mobility, and electrical breakdown field [10, 11]. Goldberger and coworkers [12] have successfully synthesized single crystalline GaN nanotubes with an "epitaxial casting" approach. The inner diameters of the tubes are 30–200 nm, and the wall thicknesses and lengths are 5–50 nm and 2–5 µm, respectively. The cross section of the nanotubes is hexagonal. The axial direction of the nanotubes is along the [001] direction, while the normal of lateral facets is along the [110] direction. Recently, single-crystalline wurtzite GaN nanotubes have also been synthesized by Au-catalyzed metalorganic chemical vapor deposition without a template [13]. Although several theoretical studies related to GaN nanotubes have been reported in the literature [14–17], all of the calculations to-date were based on hypothetical single-walled GaN nanotubes and do not accurately model realistic single-crystalline nanotubes. Xu and his coworkers [18] have proposed an effective "cutting" method to construct realistic models of single-crystalline GaN nanotubes, and they have studied Young's modulus of these model GaN nanotubes. A better understanding and fundamental knowledge of the physical properties of a new material configuration, such as a nanotube, are critical to develop future practical applications. In this work the melting behavior, thermal conductivity, and mechanical properties of wurtzite-type single crystalline GaN nanotubes have been reviewed.

5.2 Construction of GaN Nanotubes

A simple structural model of a GaN nanotube can be constructed in the same way as that for carbon nanotubes. A rectangular thin slab is cut out from wurtzite GaN, and then the slab is rolled up into a seamless cylinder. In this case, the atoms in different coaxial layers have different radii, and this leads to the different packing fractions in different coaxial GaN layers. With the increase in the thickness of GaN nanotubes, the outer atomic layers are significantly stretched and the inner atomic layers are contracted. The heavily strained atomic layers lead to the entire system becoming very unstable. Figure 5.1a shows the simulation results for crystalline GaN nanotubes with different thicknesses as a function of simulation time. It has been observed that GaN nanotubes constructed in the manner break into many fragments within a few picoseconds, and the time for the GaN nanotubes to collapse generally decreases with increase in wall thickness. The results clearly demonstrate that the strained tubes result in poor stabilities for the GaN nanotubes constructed using the wrapping method described above. To reduce the constraints, we have adjusted the number of atoms in some coaxial atomic layers, which forms a GaN slab with a stepwise shape, as shown on the bottom of Fig. 5.1b. In this case, there is no

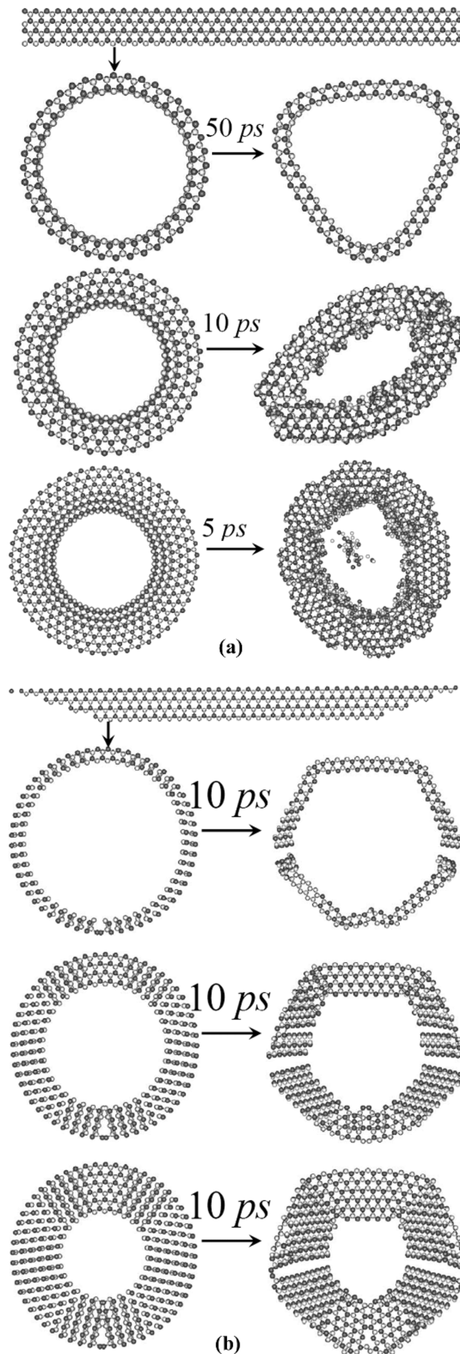

Fig. 5.1 Schematic of generating GaN nanotubes by rolling up (**a**) a rectangular thin slab of wurtzite GaN and (**b**) a slab with a stepwise shape MD simulation results show that the generated nanotubes are unstable

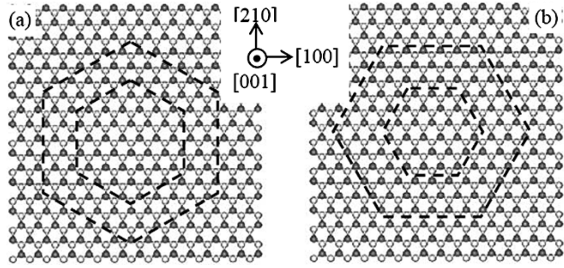

Fig. 5.2 Schematic of generating a GaN nanotube by cutting method. The (**a**) [110]- and (**b**) [100]-oriented lateral facet GaN nanotubes are generated by cutting the outside part of the big hexagon and the inside part of the small one

stretching or contraction generated in the atomic layers. However, there are topological defects such as dangling bond defects and dislocations introduced into the GaN nanotubes. Several nanotubes are constructed in this manner and relaxed using MD methods. The atomic plots shown in Fig. 5.1b clearly indicate that these defected GaN nanotubes are also unstable and collapse into hexagonal shapes, with a number of defects. Although the wrapping method has been successfully used to generate layered nanotubes such as BN and carbon nanotubes, the aforementioned results suggest that it is not valid for creating single-crystal GaN nanotubes. It should be noted that there is a stable phase with layered structures of sp^2 hybridization in both C and BN. However, the sp^2 hybridization is more unstable in GaN, which leads to instabilities when rolling a GaN slab into single-crystal nanotube.

Experimental results have shown that single-crystalline GaN nanotubes have hexagonal cross sections, and the axial orientations of the tubes are in the [001] direction with the lateral facets oriented along the [110] direction. Also, theoretical investigations have shown that the hexagonal structure in GaN is the most stable structure [19]. Consequently, a method of cutting tubes directly from bulk GaN, which is an effective approach to construct models of Pd [20], Ni [21], and GaN [22] single-crystal nanowires, is employed to form model GaN nanotubes. As shown in Fig. 5.2, a hexagonal GaN nanotube can be formed by cutting away the outside and inside sections of a GaN model crystal. Using this approach, a number of nanotubes with different radii have been formed from a large wurtzite single crystal of GaN, and these are used as the initial states for the simulations. In the radial directions, the GaN nanotubes have a finite number of unit cells, while in the axial direction a periodic boundary condition has been applied.

5.3 Potentials

The interaction potential employed is a Stillinger–Weber (SW) form [23], which is the most suitable potential for tetrahedral semiconductors like Si and it is composed of both two- and three-atom contributions:

$$v_2\left(r_{ij}\right) = \varepsilon \mathrm{A}\left[\mathrm{B}\left(\tfrac{r_{ij}}{\sigma}\right)^{-4} - 1\right] \exp\left\{\left[\left(\tfrac{r_{ij}}{\sigma}\right) - \alpha\right]^{-1}\right\}, \quad \tfrac{r_{ij}}{\sigma} < \alpha \tag{5.1}$$

$$v_3\left(r_{ij}, r_{ik}, \theta_{jik}\right) = \varepsilon\lambda \exp\left[\gamma(r_{ij} - \alpha)^{-1} + \gamma(r_{ik} - \alpha)^{-1}\right]\left(\cos\theta_{jik} + \tfrac{1}{3}\right)^2, \tag{5.2}$$

where ε and σ are the cohesive energy and length units, respectively; α represents the cut-off distance; and θ_{ijk} is the angle formed by *ji* and *jk* bonds. The original SW potential for GaN, which was developed by Aïchoune and coworkers [24], takes into account the specificity of the different bonds, namely, Ga–N, Ga–Ga, and N–N bonds. The potential has been fitted to the lattice parameters, the experimental elastic constants, and the results of the ab initio calculations for an inversion domain boundary. Béré and Serra [25] modified the potential to stabilize an inversion domain boundary structure in GaN and to allow all interactions to smoothly decrease to zero just before the second-neighbor distance. Kioseoglou et al. [26] modified the potential further to achieve a realistic description of the microscopic structure and the energetics of different planar defects as well as their interactions in the wurtzite GaN. Although the potentials were calibrated to reproduce bulk structures and mechanical properties, they have been successfully employed to evaluate the Young's modulus of defect-free and defected single-crystal GaN nanotubes [18, 27]. These calculations have demonstrated that the empirical SW potentials for GaN can be employed to study the mechanical properties of defected single-crystal GaN nanotubes. In addition, the potentials can handle dangling bonds, wrong bonds, and excess bonds in bulk GaN very well. Therefore, these potentials should be reliable to study the thermal and mechanical behavior of GaN nanotubes.

5.4 Simulation Results

5.4.1 Melting of GaN Nanotubes

The reliability of many devices will depend critically on the thermal stability of these nanotubes; thus, studies of the thermal stability of GaN nanotubes are of great interest for both fundamental understanding of their physical properties and technological applications. The melting behavior of metal nanostructures has been demonstrated to be dramatically different from the bulk. Theoretical studies [28] predict that the decrease in the melting temperature of a metal cluster is proportional to the inverse of the cluster diameter. This relationship has been validated experimentally [29–31] and by computer simulations [20, 32, 33].

The melting processes of bulk GaN were simulated to compare the melting behavior of GaN nanotubes with that of bulk materials. The bulk GaN consists of a cubic box containing 360 unit cells with 2,880 atoms, and periodic boundary conditions were imposed on the boundaries along three directions, with zero pressure control. The initial configuration was equilibrated at 300 K by 200,000 time steps (100 ps), and then, several successive equilibration calculations were carried out by increasing the temperature at an interval of 200 K. However, the step-size was decreased to 50 K when the temperature approached the melting temperature. Figure 5.3 shows the potential energy per atom as a function of simulation temperature. Several atomic plots at different temperatures illustrate the melting process, where

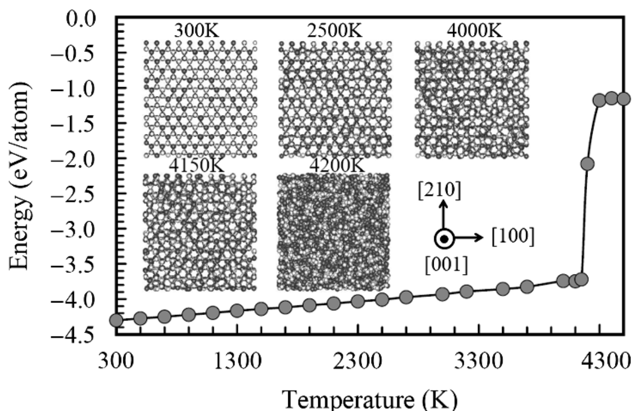

Fig. 5.3 Variation of potential energy of the bulk system during the heating process. The inset shows the snapshots of the bulk at 300, 2,500, 4,000, 4,150, and 4,200 K. Red and blue circles denote the Ga and N atoms, respectively. The melting temperature is estimated to be 4,200 K

red and blue circles denote the Ga and N atoms, respectively. The curve shows a linear increase in energy with increase in temperature till 4,150 K, above which a sharp increase in the energy is clearly shown. This sharp increase corresponds to the onset of melting in bulk GaN. It is also clear from the insert configurations that the crystal structure has both long-range and short-range order at a temperature of 4,150 K, similar to those in a perfect GaN. At 4,200 K, the long-range order disappeared, and all of the atom positions were abruptly randomized, resulting in a liquid-like structure. From these results, the melting point was estimated for the present simulation to be approximately 4,200 K. Experiments in a high-pressure anvil cell indicated that GaN does not melt at temperature up to 2,573 K under 68 kbar of pressure [34]. There have been a few reports on theoretical investigations of the melting point of bulk GaN crystals. Van Vechten [35] estimated a melting temperature of 2,791 K based on a semiempirical theory of electronegativity, whereas Nord et al. [36] used molecular dynamics (MD) simulations to determine the melting point to be $3{,}500 \pm 500$ K at 20 kbar. Using a single phase or a two-phase MD calculation, Harafuji et al. [37] showed that the melting point of GaN is about 3,200 and 2,550 K at 10^{-4} GPa, respectively. The melting temperature $T_m = 4{,}200$ K is higher than the temperatures reported in the literature for other simulations. The melting temperature calculated by a single phase simulation for bulk GaN is too high, and this may be due to the fact that in a periodic cell without defects and grain boundaries/surfaces, significant overheating usually required to melt GaN. Therefore, a two-phase system with coexisting solid and liquid was used to determine the melting temperature of the bulk GaN. The bulk GaN consists of a cubic box containing 720 unit cells with 5,760 atoms, and periodic boundary conditions were imposed on the boundaries along three directions. The initial configuration was created by fixing the atoms in one half of the box, and melting the other half at a temperature of 4,500 K. Then the system was quenched to 0 K. Three cases with solid/liquid interfaces along <001>,

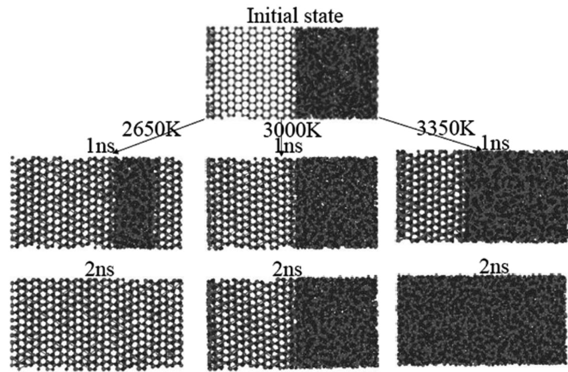

Fig. 5.4 MD simulations of liquid/solid phases along <001> direction as a function of time at different temperatures. The observed crystallization or melting depends on the simulation temperatures

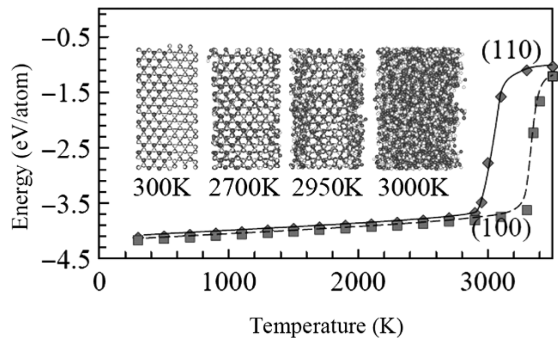

Fig. 5.5 Variation of potential energy of the slabs after the heating process, where the inset shows the snapshots of the (110)-slab at 300, 2,700, 2,950, and 3,000 K. The melting temperatures are 3,000 and 3,350 K for the (110)- and (100)-slabs, respectively

<100>, and <110> directions are considered. After the system was rescaled to a selected temperature, the fixed atoms were released, and the system was equilibrated for 1 ns to study the growth of liquid and solid phases. Figure 5.4 shows the solid and liquid phases, where the interfaces are along the <001> directions. At 2,650 K, the simulations clearly show the growth of solid phase, but at 3,350 K, growth of the liquid phase occurs. The position of the solid/liquid interface is almost the same as that of the initial configuration at 3,000 K, indicating no movement of the interface. On the basis of these results, the melting temperature is estimated to be 3,000 K at 0 GPa, which is close to the values reported in the literature. The melting temperature of bulk GaN using the same method are 3,000 and 2,950 K with solid/liquid interfaces along <100> and <110> interface, respectively. These results demonstrate that the melting temperature slightly depends on the crystalline direction.

To understand surface effects, we also studied the melting behavior of two different slabs, one with a (110) surface and the other with a (100) surface. Periodic boundary conditions were applied to the boundaries along the directions perpendicular to the surfaces. The thickness of the slabs with the (110) and (100) surfaces was ∼1.9 and 2.1 nm, respectively. Figure 5.5 shows the potential energy per atom as a function of simulation temperature, together with several atomic plots (side view) at different temperatures for the slab with a (110) surface. In this case, the atomic identification is the same as that in Fig. 5.3. A linear increase in potential energy

with increasing temperature can be clearly seen, which is similar to the melting behavior of a bulk GaN. However, a sharp increase in potential energy represented an initial onset of the melting process, and the corresponding temperatures are 2,900 and 3,300 K for slabs with the (110) and (100) surfaces, respectively. The atomic configurations show that the long-range order disappeared at 3,000 K, and all of the atom positions were randomized, resulting in a liquid-like structure. The melting temperatures are determined to be 3,000 and 3,350 K for the slabs with the (110) and (100) surfaces, respectively. One interesting result is that the melting starts from the surface, as demonstrated by the atomic configurations inserted. The detailed analysis shows that surface atoms have three nearest neighbors, as compared with four atoms as the nearest neighbors in a bulk GaN. The smaller nearest neighbors of the surface atoms suggest that these atoms are weakly bound and less constrained, and thus, the surface atoms can be easily disordered with increasing temperature. This provides a low energy pathway for the surface atoms to be melted and decreases the corresponding melting temperature.

Figure 5.6 shows the variation in the potential energy, E_a, of the GaN nanotubes as a function of simulation temperature for all the nanotube configurations. A supercell length of 20.4 Å for all the nanotubes is considered. Figure 5.6a shows the potential energy per atom for the nanotubes with [110] lateral faces, and Fig. 5.6b shows the value for nanotubes with [100] lateral faces. The energy profiles in Fig. 5.6 reveal that the potential energy per atom in the nanotubes is higher than that in a bulk system (Fig. 5.3), but approaches that of the slabs (Fig. 5.5). The energy generally increases with decreasing thickness of the nanotubes at a given temperature. For example, in the case of nanotube 4 (1.44 nm) considered in Fig. 5.6a,

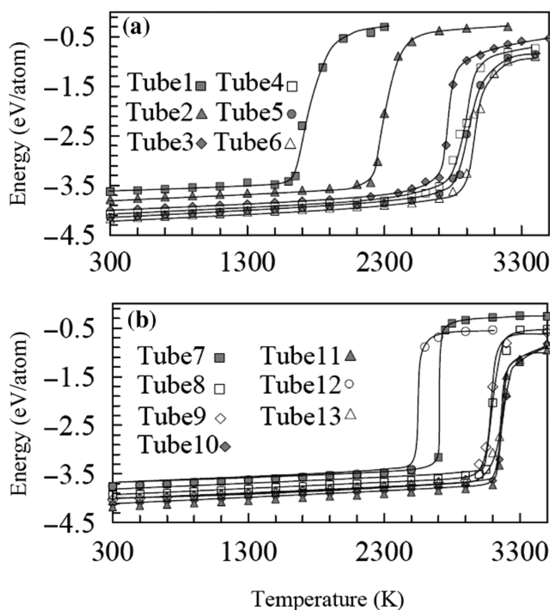

Fig. 5.6 Variation of potential energy of the GaN nanotubes with (**a**) [110]- and (**b**) [100]-oriented lateral facets during the heating process

the difference in potential energy at 300 K is 0.21 eV per atom relative to the bulk material, but this difference in potential energy decreases to 0.13 eV in nanotube 6 (2.39 nm). This observation indicates that the nanotubes possess an additional surface energy that increases with decreasing thickness. The potential energy increases linearly with increasing temperature at the initial stage, but deviates from linear behavior at higher temperatures. However, the changes in potential energy during this early stage are very small because most of the atoms in the nanotubes, including those in the central part and on the surface, do not have large amplitude motion, but merely vibrate around their original lattice positions. The nanotubes exhibit a solid state nature at these temperatures. The melt transition is clearly identified by the rapid increase in energy, but this increase is much broader than that in a bulk system, which indicates that surface melting is occurring. Surface melting is observed frequently in nanostructure materials. Surface atoms melt first at temperatures just below the melting temperature, and then the quasi-liquid skin grows continuously as the temperature increases. The inner regions maintain a solid-like structure until the transition temperature is attained. From Fig. 5.6, it can be seen that the melting temperatures of the nanotubes with small thickness wall are lower than in the bulk GaN, which is consistent with the fact that the melting behavior of nanostructure materials is strongly dependent on size. The effect of size on the melting of metallic nanoparticles and nanowires has been previously explored, both experimentally and theoretically [20, 30, 32, 38–40]. The results of these studies have shown that a decrease in metal cluster melting temperature is inversely proportional to the cluster diameter.

Figure 5.7 shows snapshots of atom positions projected onto the plane in a nanotube with a thickness of 1.91 nm (perpendicular to the axis of the nanotubes). It is clear that an increase in surface disorder exists with increasing temperature, and this provides direct evidence for surface melting of the nanotubes. It should also be noted that at 2,700 K, which is 200 K below the melting point, atoms in the central part of the cluster are still in the crystalline configurations, similar to those in the wurtzite GaN. However, when the temperature increases to 2,850 K, many atoms in the nanotube are in a liquid-like phase, and several atoms evaporate from the surface.

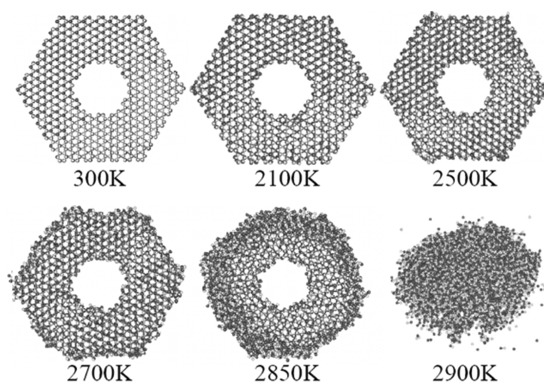

Fig. 5.7 Snapshots of the GaN nanotube (tube 5) at 300, 2,100, 2,500, 2,700, 2,850 and 2,900 K. The surface begins to melt at 2,700 K

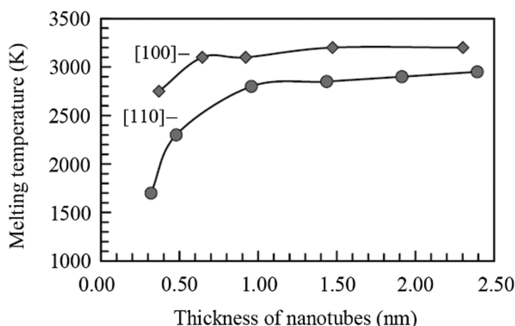

Fig. 5.8 Melting temperatures of GaN nanotubes as a function of thickness

At 2,900 K, none of the atoms exhibit lattice configurations and their positions are randomized. The nanotube collapses into a nanoparticle, forming a liquid-like structure that suggests the melting of the nanotube.

Figure 5.8 illustrates dependence of the melting temperature on the thickness of nanotubes. The melting temperatures of the GaN nanotubes increase initially and reach the saturated values of 3,200 and 2,950 K at thicknesses of about 0.6 and 1.0 nm for [100]- and [110]-oriented lateral facets, respectively. The saturated values of melting temperatures for all the nanotubes considered are close to that in the slabs, as demonstrated above. This should be attributed to the free surface that existed on the nanotubes and slabs. However, the saturated values are slightly higher than in the bulk GaN, this should be attributed to the different methods used. From the results in Fig. 5.8, it is clear that the melting temperatures of the single-crystalline GaN nanotubes with [100]-oriented lateral facets are higher than those with [110]-oriented lateral facets, which suggests that the GaN nanotubes with (100) facets are more stable than those with (110) facets. These results are consistent with previous results, indicating that the surface energy of a GaN (100) surface is $\sim$5 meVÅ^{-2} lower than that of a GaN (110) surface [41], and that GaN single-crystal nanotubes with (100) facets are more energetically favorable. This is also consistent with the experimental observations in that all the side facets of hexagonal GaN nanotubes, which are fabricated with a chemical thermal evaporation process [42], consist of [100] planes rather than [110] planes.

5.4.2 Thermal Conductivity of GaN Nanotubes

As the sizes of electronic, optical, and mechanical devices are being decreased to the nanometer level, and the speed of their operation is being steadily increased, the thermal transport of the low-dimensional system is becoming an important issue, since it plays an important role in controlling the performance and stability of these nanodevices. Although one-dimensional nanostructures show unique properties unattainable in bulk due to high surface-to-volume ratios at the nanoscale, some drawbacks of these nanostructures are inevitable. One of the challenges is that the

thermal conductivity of nanostructures is greatly deduced, as compared with that in the bulk [43–46]. Quantitative understanding of the size dependence of thermal conductivity could provide design and fabrication criteria for nanoscale devices.

The thermal conductivity $\overleftrightarrow{\lambda}$ is related to the heat flux and the applied temperature gradient by Fourier's law: $\overrightarrow{J}_{\mathrm{q}} = -\overleftrightarrow{\lambda} \cdot \overrightarrow{\nabla} T$. The energy flux expression is derived from the energy balance equation: $\frac{1}{V}\frac{\partial E(\overrightarrow{r},t)}{\partial t} + \overrightarrow{\nabla} \cdot \overrightarrow{J}_{\mathrm{q}}(\overrightarrow{r},t) = 0$. In a classical approach, the heat flux can be given by following expression in a solid [47,48]:

$$\overrightarrow{J}_{\mathrm{q}}(t) = \frac{1}{V}\frac{\mathrm{d}}{\mathrm{d}t}\sum_{i}^{N} r_i E_i = \frac{1}{V}\left(\sum_{i}^{N}\overrightarrow{v}_i E_i + \frac{1}{2}\sum_{i,j\neq i}^{N}(\overrightarrow{F}_{ij}\cdot\overrightarrow{v}_i)\overrightarrow{r}_{ij}\right). \tag{5.3}$$

Thermal conductivity can be obtained from molecular dynamics using either equilibrium simulations [49–51], based on Green–Kubo equations; steady-state nonequilibrium simulations [52,53]; or Nonequilibrium molecular dynamics (NEMD) simulations. The Green–Kubo approach is an equilibrium MD method that uses current fluctuations to compute the thermal conductivity via the fluctuation–dissipation theorem. However, very long simulation times are needed to sufficiently converge the current autocorrelation function with the Green–Kubo approach. In addition, it has been established that finite-size effects do play a role in applying this method [54]. The steady-state NEMD method relies on imposing a temperature gradient across the simulation cell and is therefore analogous to the experimental conditions. This method requires large simulation boxes in order to partition the system into a number of slabs where equilibrium can take place. In addition, instabilities may appear in the neighborhood of hot and cool slabs [55]. These drawbacks may be overcome with another nonequilibrium molecular dynamics method, the homogeneous field method [56–60]. In this method a "heat field" $\overrightarrow{f}^{\mathrm{ext}}$ is introduced in the Newton's equations so as to produce a desired heat flow: $m\overrightarrow{a}_i = \overrightarrow{F}_i + \overleftrightarrow{D}_i \cdot \overrightarrow{f}^{\mathrm{ext}}(t)$, where $\overleftrightarrow{D}_i$ is defined as

$$\overleftrightarrow{D}_i^{ab} = \left(\frac{\overrightarrow{p}_i^{\,2}}{2m_i} + \phi_i\right)\delta_{ab} - \frac{1}{2}\sum_{j=1}^{N} r_{ij}^a f_{ij}^b + \frac{1}{2N}\sum_{k=1}^{N}\sum_{j=1}^{N} r_{kj}^a f_{kj}^b, \tag{5.4}$$

which represents the coupling between the perturbation and the system. The N particle system is coupled to the "heat field" $\overrightarrow{f}^{\mathrm{ext}}$. The coupling is defined in such a way that the energy dissipation is proportional to $\overrightarrow{J}_{\mathrm{q}}\overrightarrow{f}^{\mathrm{ext}}$. The thermal conductivity can then be obtained from extrapolation to zero field amplitude:

$$\lambda = \lim_{\overrightarrow{f}^{\mathrm{ext}} \to 0}\left(\lim_{t\to\infty}\frac{\langle J_{\mathrm{q}}(t)\rangle}{VT\overrightarrow{f}^{\mathrm{ext}}}\right). \tag{5.5}$$

As pointed out in the literature [60], the method works only for $\vec{f}^{\,ext}$ not too large and not too small. If the $\vec{f}^{\,ext}$ is too large, a solitary wave will travel in the direction of heat flow, and heat is transported in the form of highly localized energy pulse carried by a soliton. In which case, the average value of the heat flux is nearly independent of $\vec{f}^{\,ext}$. However, when the heat field is too small, the noise–signal ratio would become too large and the accuracy of this method would be reduced drastically.

In all the MD simulations, 0.5 fs time step is used. The fictitious force was set along the tube length direction, and the force f^{ext} was set to 5–8 $\times$ $10^6\,\mathrm{m}^{-1}$. The averaging of the heat flux in (5.3) was calculated over the last 10 ps of a 50 ps simulation. To maintain a constant temperature within the box, the following scaling method is adopted [61]: $v_i^{new} = v_i\sqrt{\frac{T_D}{T_R}}$. v_i^{new} is the velocity of particle i after correction, and T_D and T_R are the desired and actual temperatures of the system, respectively. Nanotubes with [100] and [110] lateral-oriented facets are simulated, with lengths varying from 2.08 to 10.4 nm. The inner radius of the nanotube with [100] lateral-oriented facets is 0.92 nm, and the outer radius ranges from 1.29 to 2.67 nm, i.e., the thickness of the nanotubes changes from 0.37 to 1.75 nm and the corresponding number of atoms changes from 3,840 to 2,1840 for the nanotubes with length of 10.4 nm. The inner radius of the nanotube with [110] lateral-oriented facets is 0.92–1.12 nm with thickness changes from 0.48 to 2.39 nm.

For comparison, the thermal conductivity of bulk GaN was initially calculated. The force f^{ext} was set along the [001] direction. In performing this calculation, we have carefully checked the size effect on the thermal conductivity by varying the dimension of the MD cell, and the numbers of atoms used in the present calculations are 768, 1,600, 2,880, 4,704, 9,720, and 12,800. The calculated thermal conductivity of bulk GaN at 600 K as a function of the number of atoms in the cell is shown in Fig. 5.9a. The results suggest that the thermal conductivity initially increases with increase in the number of atoms, and saturates at a value of 152 W mK^{-1} when the number of atoms is greater than 2,880. Consequently, 2,880 atoms in a MD cell were used for the calculations of thermal conductivity of bulk GaN over the temperature range from 300 to 2,300 K, and the results are shown Fig. 5.9b. It can be seen that the thermal conductivity of bulk GaN is 215 W mK^{-1} at 300 K, which is consistent with experimental values. Jezowski et al. [62] reported that the thermal conductivity of bulk GaN is 220 W mK^{-1} at 300 K, while Florescu et al. [63] obtained the thermal conductivities of fully and partially coalesced lateral epitaxial overgrowth GaN/sapphire to be 186–205 and 200–210 W mK^{-1}, respectively. In general, the thermal conductivity decreases with increasing temperature, as seen in Fig. 5.9b. Following the initial rapid reduction of thermal conductivity, it saturates at a value of 30 W mK^{-1} at temperatures higher than 1,800 K.

In the case of GaN nanotubes, one main concern of using MD to calculate the thermal conductivity is the size effect of the simulation box due to periodic boundary conditions. To verify that the tube length does not affect the MD results, the sensitivity of the thermal conductivity to the simulation tube length has been carefully examined. Figure 5.10 shows the dependence of thermal conductivity on the

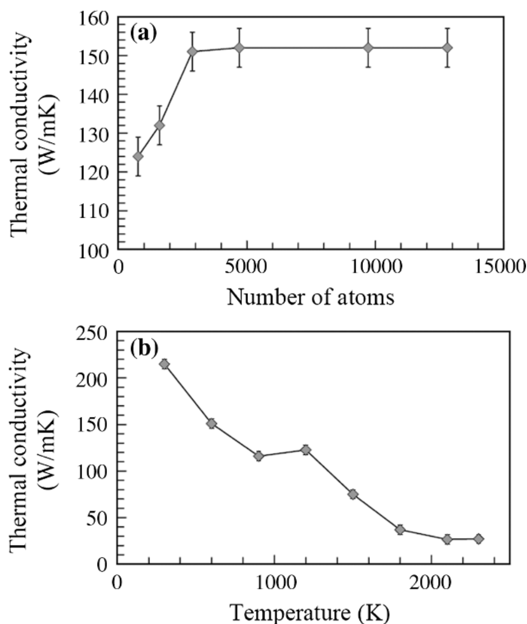

Fig. 5.9 (**a**) Thermal conductivity of bulk GaN at 600 K as a function of number of atoms; and (**b**) temperature dependence of thermal conductivity of bulk GaN, where the number of atoms are 2,880

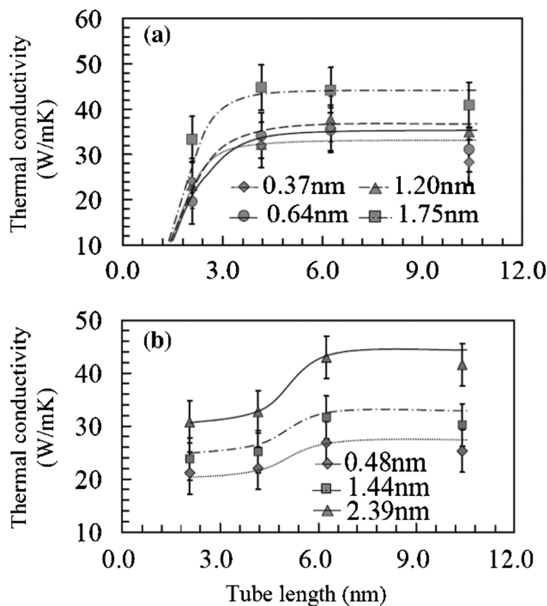

Fig. 5.10 Dependence of thermal conductivity on the tube length of GaN nanotubes with different thicknesses at a simulation temperature of 600 K. (**a**) [100]- and (**b**) [110]-oriented

length of the GaN nanotubes with different thicknesses at a simulation temperature of 600 K. The error bars shown in the figure correspond to $\pm 5\,\text{W mK}^{-1}$. In small simulation systems, the calculated thermal conductivity is between 19 and $34\,\text{W mK}^{-1}$, which depends on the thickness of the nanotubes. Because of the overestimation of phonon scattering in a small cell, these values may not be accurate. As seen in Fig. 5.10, the thermal conductivity increases with increasing length of the nanotube, and converges to a constant when the nanotube length is larger than 6.0 nm. To eliminate possible phonon scattering, a tube length of 10.4 nm is used in the following simulations.

As described earlier, the fictitious force must be carefully set to obtain accurate results. In the present calculations, we have tested the fictitious force and found that the force f^{ext} in the range of $5\text{–}8 \times 10^6\,\text{m}^{-1}$ provides reliable results. The relationship between the thermal conductivity and f^{ext} obtained by the nonequilibrium molecular dynamics calculation is shown in Fig. 5.11. The thermal conductivity of the nanotubes can then be obtained from the extrapolation to zero field amplitude and they are 28, 31, 35, and $41\,\text{W mK}^{-1}$ for nanotubes with wall thicknesses of 0.37, 0.64, 1.20, and 1.75 nm, respectively, at 600 K. A similar approach has been applied to calculate the thermal conductivity of various GaN nanotubes at other temperatures considered in the present study.

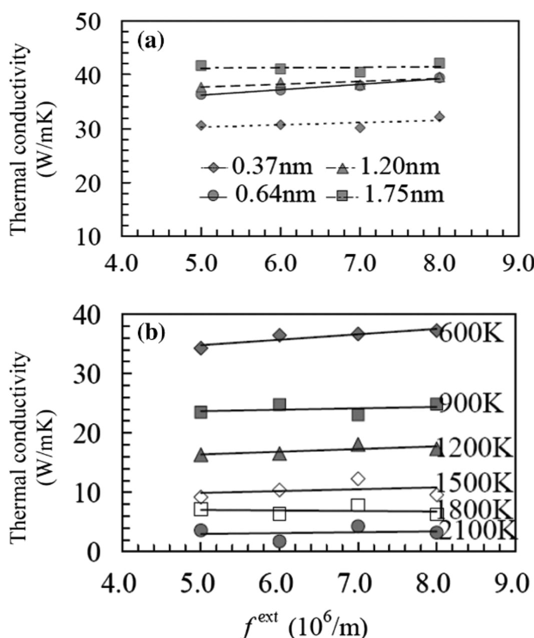

Fig. 5.11 Dependence of thermal conductivity on the applied force f^{ext} (**a**) at a simulation temperature of 600 K for the GaN nanotubes with [100]-lateral oriented facets with different thickness, and (**b**) at simulation temperature between 600 and 2,100 K for the one with [110]-lateral oriented facets with thickness of 1.44 nm at a given length of 10.4 nm

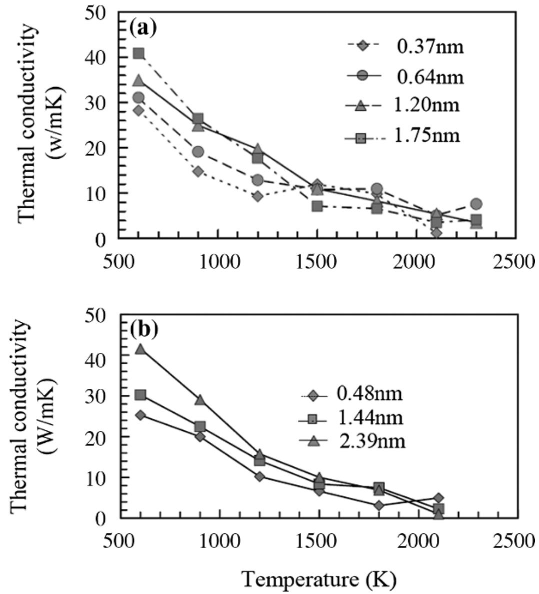

Fig. 5.12 Temperature dependence of thermal conductivity for GaN nanotubes with (**a**) [100]- and (**b**) [110]-oriented lateral facets with different thickness at a given length of 10.4 nm

Figure 5.12 shows the temperature dependence of thermal conductivity for GaN nanotubes. It is clearly seen that the thermal conductivities decrease with increasing temperature for all the nanotubes considered. However, the thermal conductivities increase with increase in the wall thickness of the nanotubes, but the difference between them is very small at high temperatures. As compared with that of bulk GaN, the thermal conductivities of the nanotubes are generally smaller than the corresponding data for bulk material. The thermal conductivity of a nanotube can be written as [64] $\lambda(T) = \frac{1}{3}\sum Cvl$ over all phonon states, where C, v, and l are the specific heat, group velocity, and phonon mean-free-path, respectively. The reduction of the nanotube thermal conductivity should be attributed to (5.1) the change of phonon spectrum in one-dimensional structures, which modifies the phonon group velocity and the scattering mechanisms [65, 66], and (5.2) the boundary inelastic scattering, which increases diffuse reflections on the surfaces. As the thickness of nanotubes increases, so does the thermal conductivity, mainly because the boundary scattering rate decreases [67]. The phonon–phonon interaction increases with size reduction due to the confinement, which causes the increase of thermal resistance and the decrease of heat conduction [68]. The decrease of thermal conductivity with increasing temperature should be associated with thermal softening and higher frequency phonon interactions at high temperatures. The lower lattice stiffness at high temperatures results in low average phonon group velocities. Also at high temperatures, high frequency acoustic and optical phonon interactions become appreciable, lowering the mean free path [45].

5.4.3 Tensile Behavior of GaN Nanotubes

The application of these GaN nanotubes will depend on not only the optoelectronic characteristics but also their mechanical properties. Strain–stress simulations have been performed using the following procedure: the three atomic layers at the top and bottom of nanotubes are fixed during simulations, forming two rigid borders. The wall thickness of nanotubes with [110]-oriented lateral facets are 3.19, 4.79, and 9.57 Å, which are denoted as tube 1, tube 2, and tube 3, and the corresponding numbers of atoms are 2,304, 3,312, and 6,768, respectively. And the wall thicknesses of nanotubes with [110]-oriented lateral facets are 3.68, 6.45, and 9.21 Å, which are denoted as tube 4, tube 5, and tube 6, and the corresponding numbers of atoms are 2,880, 4,752, and 6,912, respectively. A periodic boundary condition has been applied along the axial direction, with a supercell length (L) of 61.2 Å for all the nanotubes considered. The initial structures of the nanotubes were equilibrated for 100 ps at a given temperature, which allows the nanotubes to have stable configurations. The strain was then applied along the tube direction to study the mechanical properties of the nanotubes, with a displacement of Δz. The atoms in the rigid borders were displaced by $\Delta z/2$, and the coordinates of remaining atoms were scaled by a factor $(L+\Delta z)/L$ along the z direction. This deformed tube was relaxed for 10 ps, and then the relaxed tube was used as an initial configuration for the next MD simulation. The procedure was repeated until the tube failed (ruptured). The strain rate was calculated using the expression

$$\dot{\varepsilon} = \frac{\varepsilon_z}{s\Delta t}, \tag{5.6}$$

where s is the number of relaxation steps after each strain increment and Δt is the simulation time step, which was fixed to be 0.5 fs. The strain increment was varied, with $\varepsilon_z = 0.003$, 0.002, 0.0015, 0.001, and 0.0005, which leads to simulation strain rates of 0.03, 0.02, 0.015, 0.01, and $0.005\%\,\text{ps}^{-1}$, respectively. The stress during each strain increment was computed by averaging over the final 2,000 relaxation steps. Figure 5.13 shows the relationships between tensile stress and strain for the tube 2 and tube 4 with a strain rate of $0.005\%\,\text{ps}^{-1}$ at various temperatures. The stress–strain curves show different behavior at low and high temperatures. For example, for the tube 2 at 300 K, the stress increases with increasing strain up to 50 GPa (at strain 16.95%), but the further increase in strain leads to stress abruptly dropping to 3.0 GPa. At 1,500 K, the stress–strain relation displays a zigzag behavior after a critical stress level of 19.9 GPa (at strain 7.05%). These results demonstrate that the tube fails in a brittle manner at low temperatures, but in a ductile manner at higher temperatures. It is of interest to note that the critical stress at low temperatures is larger than that at high temperatures. As the temperature increases, a large number of atoms gain sufficient energy to overcome the activation energy barrier, and hence plastic deformation occurs. This result suggests that a thermally activated process plays a predominant role in the elongation of the GaN NTs.

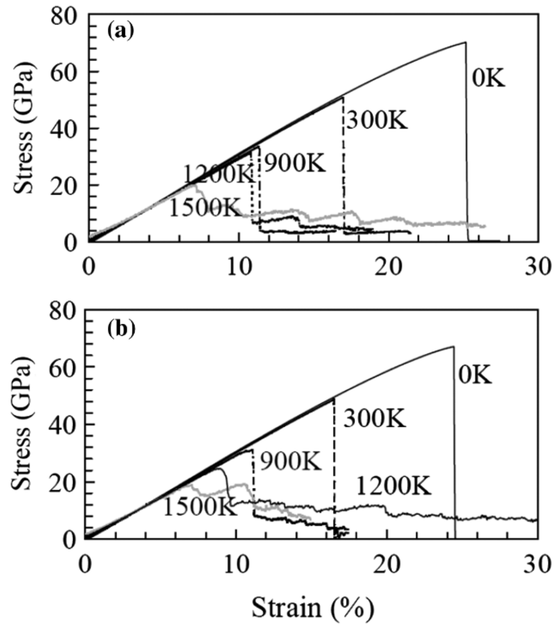

Fig. 5.13 Tensile stress–strain curves for the (**a**) tube 2 and (**b**) tube 4 with a strain rate of 0.005% ps^{-1} at various temperatures

Figure 5.14a and b shows the top and side views of the atomic configurations at several stages of stretching tube 2 with a strain rate of 0.005% ps^{-1} at the simulation temperatures of 600 and 1,500 K, respectively. Red and blue atoms indicate Ga and N atoms, respectively. At 600 K and up to a strain of 27%, the Ga–N bond lengths increase uniformly and no structural defects appear in the NTs. Upon reaching the critical strain of 27.95%, the crystal structure experiences an abrupt dislocation, and the NTs rupture with a clean cut without any observed necking. Obviously, at 600 K the tube shows brittle properties. At 1,500 K, the extension of the nanotubes also begins with an elastic deformation from its initial state to the critical strain of 13.9%, after which necking can be clearly seen in Fig. 5.14b, and several atomic chains occur to link two separated GaN crystals before rupture. The atomic structures near the "tips" appear much highly disordered, and the NTs show the ductile behavior. Figure 5.15a and b shows the top and side views of the atomic configuration at various stages of the stretching of tube 4 at simulation temperatures 300 and 1,200 K, respectively, which also shows the nanotubes fracture with a brittle manner at 300 K and a dutile one at 1,200 K.

Figure 5.16 shows the variation of critical stress τ_c with temperature T. The results show that the critical stress (and the corresponding tensile strain) decreases with increasing temperature for all the NTs considered. A break appears at a critical temperature, T_c, in the $\tau_c(T)$ curves. Similar phenomenon have been found in GaAs [69], InSe [70], and SiC [71, 72] experimentally, with breaks in their $\tau_c(T)$ curves at T_c, which is close to the brittle to ductile transition (BDT) temperature. One way to represent the variations of the yield stress of a semiconductor with respect to

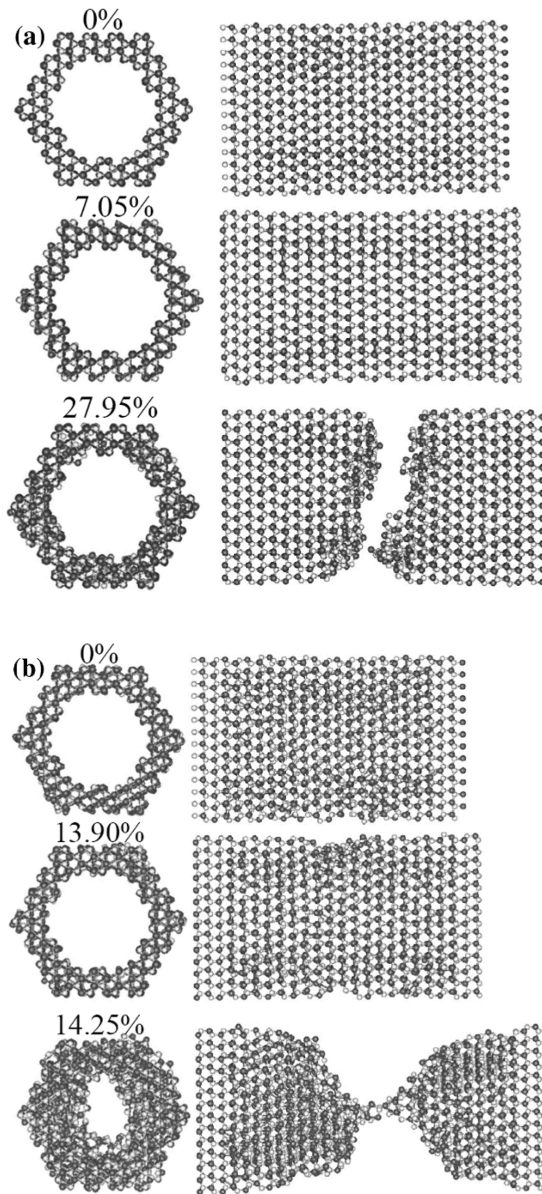

Fig. 5.14 Atomic configurations in selected stages for the tube 2 at the temperatures of (**a**) 600 K and (**b**) 1,500 K

temperature is to plot $\ln(\tau_c)$ vs. $1/T$, as suggested by the kink-diffusion model [73]. In this model, the plastic strain rate can be described by Orowan's equation, which is proportional to the stress-independent activation enthalpy, H, for the glide of the dislocations corresponding to crystal deformation. Specifically,

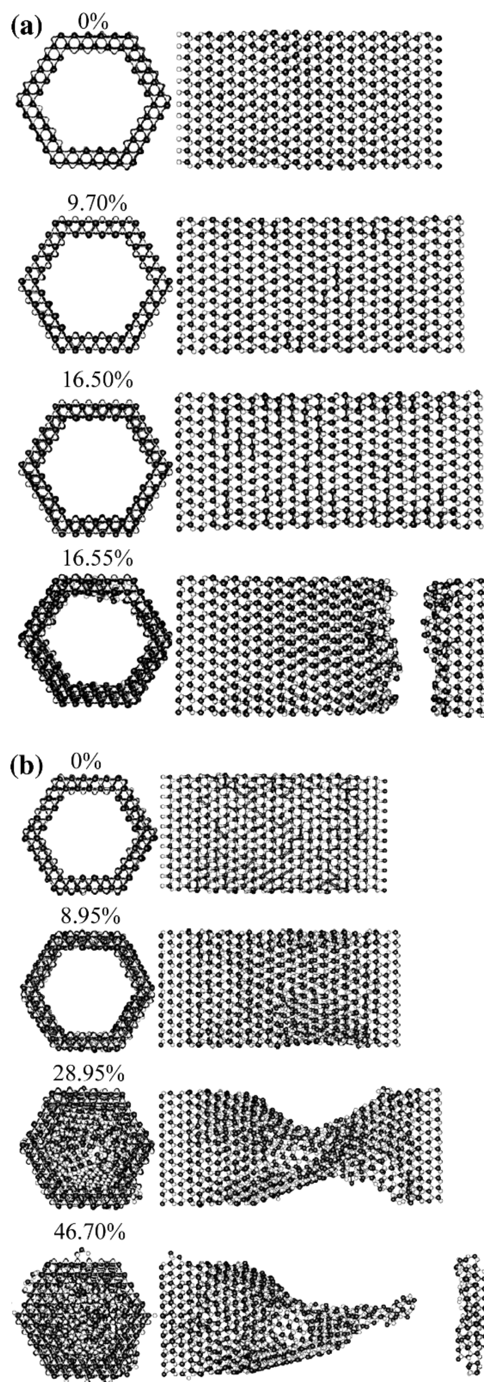

Fig. 5.15 Atomic configurations in selected stages for the tube 4 at the temperatures of (**a**) 300 K and (**b**) 1,200 K

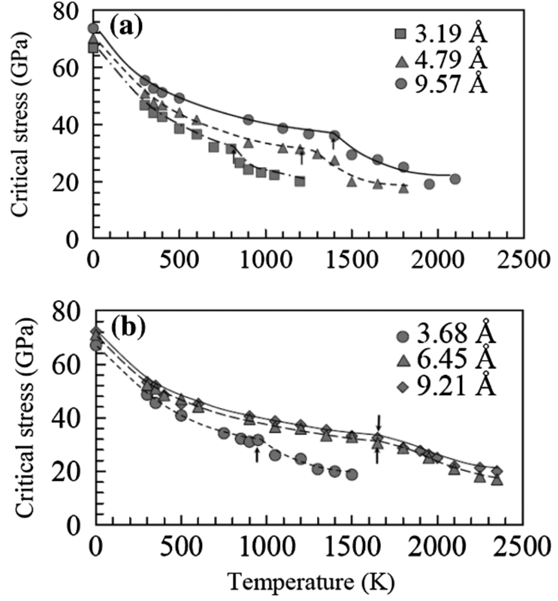

Fig. 5.16 Temperature dependence of the critical stress of GaN nanotubes with (**a**) [110]- and (**b**) [100]-oriented lateral facets

$$\tau_c = A\dot{\varepsilon}^{1/n} \exp\left(\frac{\Delta H_\tau}{k_B T}\right), \tag{5.7}$$

where A and n are constants, k_B is the Boltzmann constant, and ΔH_τ is an energy parameter, such that $n\Delta H_\tau$ is approximately the activation enthalpy H [74]. The changes of $\ln(\tau_c)$ as a function of $1/T$ are shown in Fig. 5.17. In general, $\ln(\tau_c)$ increases with increasing reciprocal temperature, but its slope changes abruptly at T_c. The different slopes in the $\ln(\tau_c)$ curve characterize the transition, and thus correspond to two different activation enthalpies, H_t and H_l, for dislocation glide in high-temperature $(T > T_c)$ and low-temperature $(T < T_c)$ regimes, respectively. These features are qualitatively very similar to the experimental observations in InP [75], GaAs [76], and SiC [71, 72]. The BDT temperatures deduced from Fig. 5.16a are 770, 1,200, and 1,400 K for the tube 1, tube 2, and tube 3, respectively, and 900, 1,450, and 1,450 K for the tube 4, tube 5, and tube 6, respectively, which is consistent with the present observations of changes from nanotubes ruptured with a clean cut at low temperatures to ruptured with necking at higher temperatures under tensile loading. This demonstrates that the BDT temperature increases with increasing wall thickness of nanotubes, which may be associated with large surface to volume ratio of the nanotubes. The ratio of the number of surface atoms to the total number of atoms generally increases with decrease in the wall thickness of nanotubes. The cohesive energy of surface atoms is smaller than that of core atoms, and thus, less energy is demanded for the surface atoms to overcome the activation energy barrier. This suggests that plastic deformation is more favorable in thin nanotubes, and thus, lowers the BDT temperature.

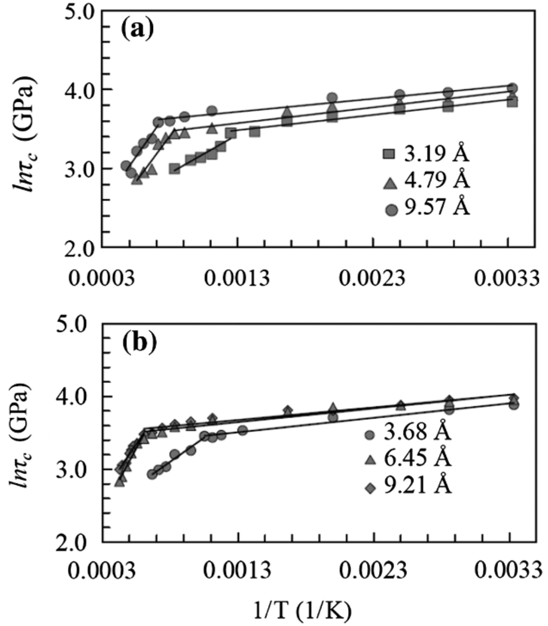

Fig. 5.17 Evolution of $\ln(\tau_c)$ as a function of reciprocal temperature of nanotubes with (**a**) [110]- and (**b**) [100]-oriented lateral facets. The temperature at which an abrupt change in the slope of $\ln(\tau_c)$ corresponds to the BDT temperature that increases with increase in the thickness of the nanotubes

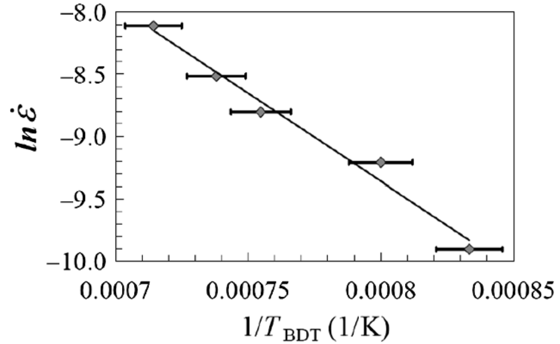

Fig. 5.18 Variation of $\ln\dot{\varepsilon}$ versus $1/T_{BDT}$ for tube 2 with different strain rates of 0.03%, 0.02%, 0.015%, 0.01%, and 0.005% ps^{-1}. As the rate of applied loading increases, the BDT temperatures shift to high temperatures. $\ln\dot{\varepsilon}$ changes with $1/T_{BDT}$ linearly

Since the bond energy does not vary with temperature significantly, bond rupture and consequent fracture stress are expected to have much weaker temperature dependence than the yield stress [77]. The BDT temperature can be written as

$$T_{BDT} = \frac{\Delta H_{\tau}}{k_B In(\frac{S\sigma_F}{A\dot{\varepsilon}^{1/n}})}, \tag{5.8}$$

where σ_F is a temperature-independent fracture stress and S a geometrical factor. $\ln\dot{\varepsilon}$ will change with $1/T_{BDT}$ linearly. Figure 5.18 shows $\ln\dot{\varepsilon}$ as a function of $1/T_{BDT}$ for tube 2 with different strain rates of 0.03, 0.02, 0.015, 0.01, and 0.005% ps^{-1}. As the rate of applied loading increases, the BDT temperatures shift to high temperatures. It can be seen that $\ln\dot{\varepsilon}$ changes with $1/T_{BDT}$ linearly, which is consistent with the

prediction given in (5.3). The BDT temperature is a phenomenological quantity, below which the material is brittle but above which the material undergoes plastic deformation. Also, these behaviors depend on the test conditions, such as the strain rate and environmental effects. It should be noticed that the simulated strain rates in the present work are several orders of magnitude higher than those encountered in experiments. If a strain rate of $5.0 \times 10^{-4}\,\mathrm{s}^{-1}$ is applied to tube 2 in experimental conditions, the BDT temperature is expected to be about 380 K using the linear relationship between $\ln \dot{\varepsilon}$ and $1/T_{\mathrm{BDT}}$. The BDT temperature of cubic GaN is about 800 K, as predicted by Kamimura et al. [78]. Our results show that the BDT temperature of NTs is smaller than that given by Kaminura et al, which indicates that the BDT temperature will decrease with decrease in the dimension of GaN. These results are consistent with our results, and the BDT temperature decreases with decrease in the thickness of nanotubes.

5.4.4 Buckling Behavior of GaN Nanostructures

Figures 5.19a and 5.20a show the stress–strain relationship of the [110] lateral-oriented faceted nanotubes with tube length of 12.5 nm and the [100] lateral-oriented faceted nanotubes with the tube length of 16.6 nm, respectively, simulated at 300 K

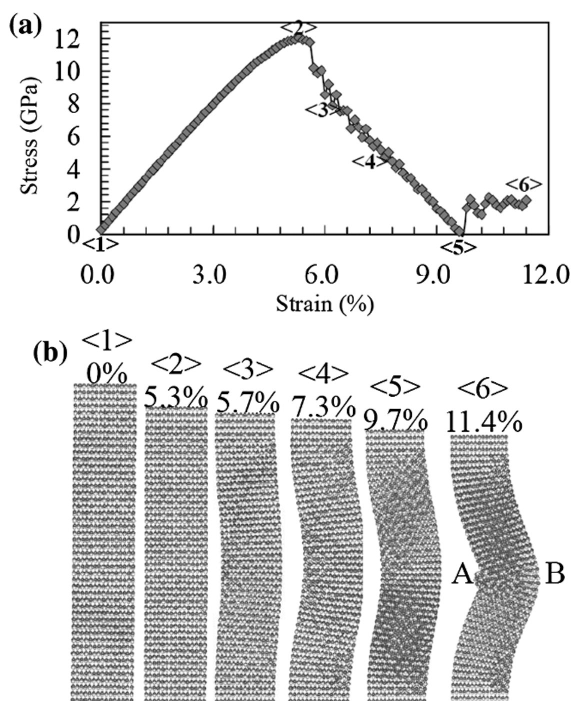

Fig. 5.19 (**a**) Stress–strain curves of GaN nanotube with [110]-lateral oriented facets with the tube length of 12.5 nm at temperature 300 K and strain rate of $0.001\%\,\mathrm{ps}^{-1}$. (**b**) Snapshots of atomic configurations at various strains

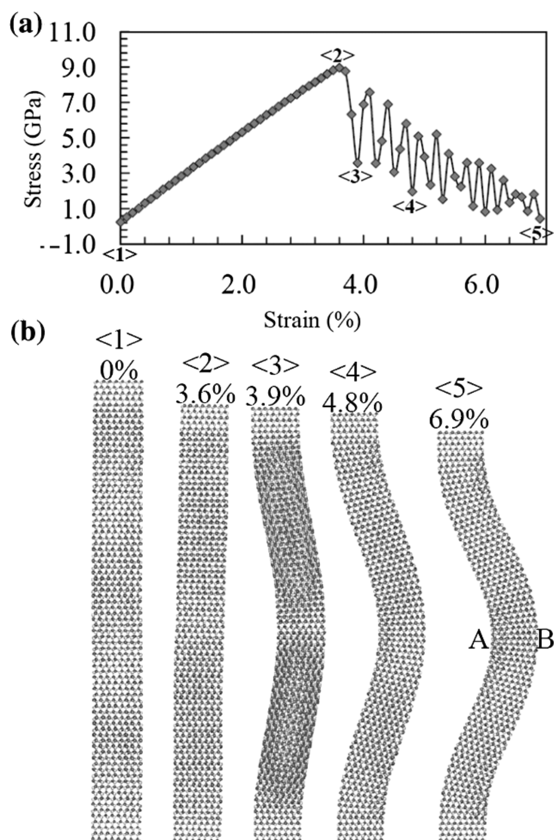

Fig. 5.20 (**a**) Stress–strain curves of GaN nanotube with the [100]-lateral oriented facets with tube length of 20.8 nm at temperature 300 K and strain rate of 0.001% ps^{-1}. (**b**) Snapshots of atomic configurations at various strains

with a strain rate of 0.001% ps^{-1}. Points where changes take place on the nanotubes' crystal structure and stress–strain response are marked on the plot, indicated by numerical notations with angular brackets $\langle\rangle$. Its corresponding atom configurations are shown in Figures 5.19b and 5.20b, respectively. The nanotubes remain in cylindrical symmetry until the critical strain is reached at which they will buckle. The stress increases with the increase in strain and falls down when the structures of nanotubes buckle. We can see that near the critical buckling strain, the nanotubes undergo considerable structure rearrangements of the atoms near the central region of the nanotubes. The region near point "A" is under highly compressive strain, and significant rearrangement and even randomization of the atoms occur to release the built up strain in this region. In the region near point "B", the atomic lattice is under tensile strain.

Figure 5.21 shows the effects of temperature, strain rate, and tube length on the buckling behavior. Figure 5.21a and a$'$ shows the stress–strain curves of [100] and [110] lateral-oriented faceted nanotubes with a tube length of 16.6 and 12.5 nm, respectively, which are simulated at 300–1,200 K with a strain rate of 0.001% ps^{-1}. The stress increases with increasing strain initially and then reaches a maxi-

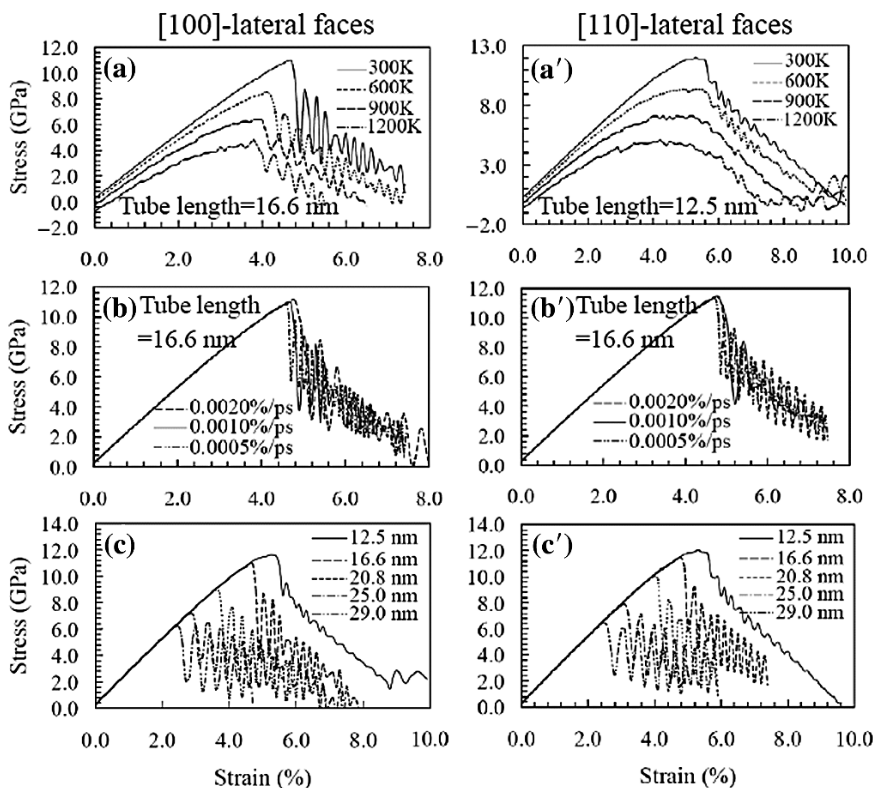

Fig. 5.21 Stress–strain curves for the GaN nanotubes upon compression. Effects of (**a**) and (**a**′) temperature, (**b**) and (**b**′) strain rate, (**c**) and (**c**′) tube length on the compression behavior of GaN nanotubes

mum value. After passing the maximum stress, the nanotubes cannot keep the microstructure in good order to accommodate the further strain increments, and the stress decreases. The critical stress of the [100] and [110] lateral-oriented faceted nanotubes decreases from 10.9 to 4.8 GPa and from 12 to 5 GPa as temperature increases from 300 to 1,200 K, respectively, and the corresponding critical strain also decreases with the increase of temperature. At higher temperature, the atomic structure has high entropy and its constituent atoms vibrate about their equilibrium position at much larger amplitude, as compared to the low temperature, and hence plastic deformation occurs easily at high temperature. Figures 5.21b and b′ show the stress–strain curves of [100] and [110] lateral-oriented faceted nanotubes with tube length of 16.6, respectively, which are simulated at 300 K with strain rate varying from 0.0005 to 0.002% ps^{-1}. There is little change of the critical stress with the change of strain rate. The critical stress decreases from 11.0 to 10.8 GPa and from 11.4 to 11.2 GPa. Figures 5.21c and c′ show the stress–strain curves of [100] and [110] lateral-oriented faceted nanotubes with tube length varying from 12.5 and 29.0 nm, respectively, which are simulated at 300 K with a strain rate of

$0.001\%\,\mathrm{ps}^{-1}$. The buckling load decreases as the length of the nanotube increases. The [100] lateral-oriented faceted nanotube with tube length 12.5 nm buckles at 5.3% and it has the highest buckling load of 11.6 GPa, while the nanotube with length of 29.0 nm buckles at 2.5% with 6.2 GPa. Hence, the shorter a nanotube is, the higher the buckling load required.

There are two approaches to obtain the Young's modulus, i.e., the force approach and the energy approach [79]. The Young's modulus, for the force approach, is directly obtained from the ratio of the stress to the strain, whereas the energy approach calculates the Young's modulus from the second derivative of the strain energy with respect to strain per unit volume. In this article, the force approach is adopted to evaluate Young's modulus of the nanotubes. The Young's modulus can be determined from the results of the compressed tests for the strain $<2\%$ using linear regression. The Young's modulus are about 260 and 250 GPa for the nanotubes with [110] and [100] lateral-oriented facets at 300 K, respectively. The values agree well with the experimental result of 223.4 GPa of GaN nanotube [80], and 227–305 GPa of GaN nanowires [81]. The Young's modulus shows no dependence on the tube length and decreases with the increase of temperature. The decrease of Young's modulus with increasing temperature is due to the significantly weakened bond forces and the large atom vibration at the higher temperature, which results in a less stiffness of nanotube.

In general, under compression two kinds of deformation behaviors are found for those nanotubes, depending on the strength of external loading. Within a critical compressive force or yield stress, the length of nanotube decreases, and the nanotubes retain their original atomic structures with small amplitude modifications of the interatomic distances. Such behavior can be viewed as elastic deformation. On the other hand, under the external loading beyond the elastic limit, the nanotubes no longer retain their tube structure. For a long tube, the critical buckling load is [82].

$$P_{\mathrm{cr}} = \frac{\pi^2 EI}{L_{\mathrm{e}}^2}, \tag{5.9}$$

where E is the Young's modulus; L_{e} is the effective length of the tube, as both ends of the tubes are fixed against rotation, $L_{\mathrm{e}} = L/2$ [80]; L is the length of the tube; and I is the moment of inertia, $I = \frac{\pi(R^4 - r^4)}{4}$. R and r are the outer and inner radii of a circular tube. So the critical load is inversely proportion to the square of the length. Using the linear relationship between stress and strain we can predict an upper bound of the critical strain. The critical buckling load P_{cr} for each GaN nanotube in compression can be expressed by the equation [80] $P_{\mathrm{cr}} = AE\varepsilon_{\mathrm{cr}}$, where A is the cross-section area under force. A is approximately $\pi(R^2 - r^2)$ in this work. The critical stress and strain at buckling vs. the tube length is shown in Fig. 5.22. We find in the simulations that the longer the GaN nanotubes, the smaller the critical stress (and corresponding critical strain) for buckling. The trend is in agreement with the Euler theory. For the tube length greater than 20 nm, the MD results are very close to the value predicted by Euler theory.

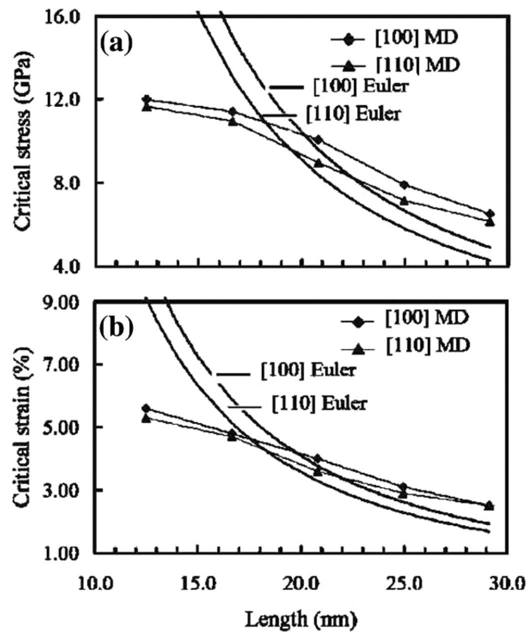

Fig. 5.22 The nanotube length dependence of (**a**) critical stress and (**b**) critical strain of GaN buckling

5.5 Summary

In conclusion, MD simulations of the melting behavior, thermal conductivity, tensile and compressive behavior of GaN nanotubes were carried out using an empirical potential. The GaN nanotubes generated by a cutting method formed stable configurations, while those created using the wrapping method previously proposed collapse.

1. The melting temperature increases with increasing thickness of the nanotubes and saturates when the radius increases to 0.6 and 1.0 nm for the nanotubes with [100]- and [110]-oriented lateral facets, respectively. The large surface-to-volume ratio of the nanotubes may account for the decreased melting temperature observed in the present simulations.
2. The thermal conductivity of GaN nanotubes is smaller than the value of 150 W mK^{-1} in bulk GaN at the same temperature. The thermal conductivity decreases with increase in temperature and increases with increase in the wall thickness of the nanotubes. The change of phonon spectrum, surface inelastic scattering, thermal softening, and higher frequency phonon interactions at high temperatures may account for the observed phenomena.
3. The nanotubes show brittle properties at low temperatures, whereas they behave as ductile materials at higher temperatures. The BDT greatly depends on the thickness of the nanotubes and strain rate.
4. The GaN nanotubes buckle with Euler behavior, the critical stress decreases with the increase of wire length, which is in agreement with the Euler theory. Buckling

strain (and corresponding stress) decreases as temperature is increased, which indicates that a thermal activated process plays an activating role in the buckling of GaN nanotubes.

Acknowledgments Z.G.W. and X.T.Z. are grateful for the National Natural Science Foundation of China (10704014) and the Young Scientists Foundation of UESTC (JX0731). F. Gao and W.J. Weber are supported by the Division of Materials Sciences and Engineering, Office of Basic Energy Sciences, US Department of Energy under Contract DE-AC05-76RL01830. The authors also thank the Molecular Science Computing Facility in the Environmental Molecular Sciences Laboratory at the Pacific Northwest National Laboratory for a grant of computer time.

References

1. Iijima S (1991) Helical microtubules of graphitic carbon. Nature (London) 354:56–58
2. Durgun E, Tongay S, Ciraci S (2005) Silicon and III–V compound nanotubes: Structural and electronic properties. Phys. Rev. B 72:075420
3. Rapoport L, Bilik Y, Feldman Y, Homyonfer M, Cohen SR, Tenne R (1997) Hollow nanoparticles of WS2 as potential solid-state lubricants. Nature (London) 387:791–793
4. Tenne R, Margulis L, Genut M, Hodes G (1992) Polyhedral and cylindrical structures of tungsten disulfide. Nature (London) 360:444–446
5. Feldman Y, Wasserman E, Srolovitz DJ, Tenne R (1995) High-rate, gas-phase growth of mos2 nested inorganic fullerenes and nanotubes. Science 267:222–225
6. Tondare VN, Balasubramanian C, Shende S, Joag DS, Godbale VP, Bhoraskar SV (2002) Field emission from open ended aluminum nitride nanotubes. Appl. Phys. Lett. 80:4813–4815
7. Loiseau A, Willaime F, Demoncy N, Hug G, Pascard H (1996) Boron nitride nanotubes with reduced numbers of layers synthesized by arc discharge. Phys. Rev. Lett. 76:4737
8. Liliental-Weber Z, Chen Y, Ruvimov S, Washburn J (1997) Formation mechanism of nanotubes in GaN. Phys. Rev. Lett. 79:2835–2838
9. Lauret JS, Arenal R, Ducastelle F, Loiseau A, Cau M, Attal-Tretout B, Rosencher E, Goux-Capes L (2005) Optical transitions in single-wall boron nitride nanotubes. Phys. Rev. Lett. 94:037405
10. Johnson JC, Choi HJ, Knutsen KP, Schaller RD, Yang PD, Saykally RJ (2002) Single gallium nitride nanowire lasers. Nature Mater. 1:106–110
11. Morkoc H, Strite S, Gao GB, Lin ME, Sverdlov B, Burns M (1994) Large-band-gap SiC, III–V nitride, and II–VI ZnSe-based semiconductor-device technologies. J. Appl. Phys. 76: 1363–1398
12. Goldberger J, He RR, Zhang YF, Lee S, Yan HQ, Choi HJ, Yang PD (2003) Single-crystal gallium nitride nanotubes. Nature (London) 422:599–602
13. Lu MC, Chueh YL, Chen LJ, Chou LJ, Hsiao HL, Yang AB (2005) Synthesis and formation mechanism of gallium nitride nanotubular structure. Electrochem Solid State Lett. 8: G153–G155
14. Lee SM, Lee YH, Huang YG, Elsner J, Porezag D, Frauenheim T (1999) Stability and electronic structure of GaN nanotubes from density-functional calculations. Phys. Rev. B 60:7788–7791
15. Jeng YR, Tsai PC, Fang TH (2004) Molecular dynamics investigation of the mechanical properties of gallium nitride nanotubes under tension and fatigue. Nanotechnology 15:1737–1744
16. Kang JW, Hwang HJ (2004a) Atomistic study of III-nitride nanotubes. Comput. Mater. Sci. 31:237–246
17. Kang JW, Huang HJ (2004b) Molecular dynamics simulations of single-wall GaN nanotubes. Mol. Simulat. 30:29–35

18. Xu B, Lu AJ, Pan BC, Yu QX (2005) Atomic structures and mechanical properties of single-crystal GaN nanotubes. Phys. Rev. B 71:125434
19. Zhang M, Su ZM, Yan LK, Qiu YQ, Chen GH, Wang RS (2005) Theoretical interpretation of different nanotube morphologies among Group III (B, Al, Ga) nitrides. Chem. Phys. Lett. 408:145–149
20. Miao L, Bhethanabotla VR, Joseph B (2005) Melting of Pd clusters and nanowires: A comparison study using molecular dynamics simulation. Phys. Rev. B 72:134109
21. Wen YH, Zhu ZZ, Zhu RZ, Shao GF (2004) Size effects on the melting of nickel nanowires: A molecular dynamics study. Phys. E 25:47–54
22. Wang Q, Sun Q, Jena P (2005) Ferromagnetism in Mn-doped GaN nanowires. Phys. Rev. Lett. 95:167202
23. Stillinger FH, Weber TA (1985) Computer-simulation of local order in condensed phases of silicon. Phys. Rev. B 31:5262–5271
24. Aïchoune N, Potin V, Ruterana P, Hairie A, Nouet G, Paumier E (2000) An empirical potential for the calculation of the atomic structure of extended defects in wurtzite GaN. Comput. Mater. Sci. 17:380–383
25. Béré A, Serra A (2001) Atomic structure of dislocation cores in GaN. Phys. Rev. B 65:205323
26. Kioseoglou J, Polatoglou HM, Lymperakis L, Nouet G, Komninou Ph (2003) A modified empirical potential for energetic calculations of planar defects in GaN. Comput. Mater. Sci. 27:43–49
27. Xu B, Pan BC (2006) The effect of atomic vacancies and grain boundaries on the mechanical properties of single-crystal GaN nanotubes. J. Appl. Phys. 99:104314
28. Reiss H, Mirabel P, Whetten RL (1988) Capillarity theory for the coexistence of liquid and solid clusters. J. Phys. Chem. 92:7241–7246
29. Peters KF, Cohen JB, Chung YW (1998) Melting of Pb nanocrystals. Phys. Rev. B 57: 13430–13438
30. Lai SL, Guo JY, Petrova V, Ramanath G, Allen LH (1996) Size-dependent melting properties of small tin particles: Nanocalorimetric measurements. Phys. Rev. Lett. 77:99–102
31. Dippel M, Maier A, Gimple V, Wider H, Evenson WE, Rasera RL, Schatz G (2001) Size-dependent melting of self-assembled indium nanostructures. Phys. Rev. Lett. 87:095505
32. Huang KC, Wang T, Joannopoulos JD (2005) Nanoscale properties of melting at the surface of semiconductors. Phys. Rev. B 72:195314
33. Li H, Wang BL, Wang JL, Wang GH (2004) Melting behavior of one-dimensional zirconium nanowire. J. Chem. Phys. 120:3431–3438
34. Karpinski J, Jun J, Porowski S (1984) Equilibrium pressure of n-2 over GaN and high-pressure solution growth of GaN. J. Cryst. Growth 66:1–10
35. Van Vechten JA (1973) Quantum dielectric theory of electronegativity in covalent systems. III. pressure–temperature phase diagrams, heats of mixing, and distribution coefficients. Phys. Rev. B 7:1479–1507
36. Nord J, Albe K, Erthart P, Nordlund K (2003) Modelling of compound semiconductors: Analytical bond-order potential for gallium, nitrogen, and gallium nitride. J. Phys. Condens. Matter 15:5649–5662
37. Harafuji K, Tsuchiya T, Kawamura K (2004) Molecular dynamics simulation for evaluating melting point of wurtzite-type GaN crystal. J. Appl. Phys. 96:2501–2512
38. Fang KC, Weng CI (2005) An investigation into the melting of silicon nanoclusters using molecular dynamics simulations. Nanotechnology 16:250–256
39. Cleveland CL, Luedtke WD, Landman U (1999) Melting of gold clusters. Phys. Rev. B 60:5065–5077
40. Delogu F (2005) Structural and energetic properties of unsupported Cu nanoparticles from room temperature to the melting point: Molecular dynamics simulations. Phys. Rev. B 72:205418
41. Northrup JE, Neugebauer J (1996) Theory of GaN(10(1)over-bar-0) and (11(2)over-bar-0) surfaces. Phys. Rev. B 53:10477–10480
42. Liu BD, Bando Y, Tang CC, Shen GZ, Golberg D, Xu FF (2006) Wurtzite-type faceted single-crystalline GaN nanotubes. Appl. Phys. Lett. 88:093120

43. Lü X, Shen WZ, Chu JH (2002) Size effect on the thermal conductivity of nanowires. J. Appl. Phys. 91:1542–1552
44. Volz SG, Chen G (1999) Molecular dynamics simulation of thermal conductivity of silicon nanowires. Appl. Phys. Lett. 75:2056–2058
45. Kulkarni AJ, Zhou M (2006) Size-dependent thermal conductivity of zinc oxide nanobelts. Appl. Phys. Lett. 88:141921
46. Shi L, Hao Q, Yu C, Mingo NY, Kong X, Wang ZL (2004) Thermal conductivities of individual tin dioxide nanobelts. Appl. Phys. Lett. 84:2638
47. Allen PB, Feldman JL (1993) Thermal-conductivity of disordered harmonic solids. Phys. Rev. B 48:12581–12588
48. Hardy RJ (1963) Energy-flux operator for a lattice. Phys. Rev. 132:168–177
49. Volz SG, Chen G (2000) Molecular-dynamics simulation of thermal conductivity of silicon crystals. Phys. Rev. B 61:2651–2656
50. Hirosaki N, Ogata S, Kocer C, Kitagawa H, Nakamura Y (2002) Molecular dynamics calculation of the ideal thermal conductivity of single-crystal alpha- and beta-Si3N4. Phys. Rev. B 65:134110
51. Tretiakov KV, Scandolo S (2004) Thermal conductivity of solid argon from molecular dynamics simulations. J. Chem. Phys. 120:3765–3769
52. Daly BC, Maris HJ, Imamura K, Tamura S (2002) Molecular dynamics calculation of the thermal conductivity of superlattices. Phys. Rev. B 66:024301
53. Konashi K, Ikeshoji T, Kawazoe Y, Matsui H (2003) A molecular dynamics study of thermal conductivity of zirconium hydride. J. Alloys Comp. 356–357:279–282
54. Che J, Cagin T, Deng W, Goddard WA (2000) Thermal conductivity of diamond and related materials from molecular dynamics simulations. J. Chem. Phys. 113:6888–6900
55. Fevre M, Finel A, Caudrom R, Mevrel R (2005) Local order and thermal conductivity in yttria-stabilized zirconia. II. Numerical and experimental investigations of thermal conductivity. Phys. Rev. B 72:104118
56. Evans D, Morris G (1990) Statistical Mechanics of Non-Equilibrium Liquids, Academic Press, London
57. Maeda A, Munakata T (1995) Lattice thermal-conductivity via homogeneous nonequilibrium molecular-dynamics. Phys. Rev. E 52:234–239
58. Motoyama S, Ichikawa Y, Hiwatari Y, Oe A (1999) Thermal conductivity of uranium dioxide by nonequilibrium molecular dynamics simulation. Phys. Rev. B 60:292–298
59. Berber S, Kwon YK, Tamanek D (2000) Unusually high thermal conductivity of carbon nanotubes. Phys. Rev. Lett. 84:4613–4616
60. Zhang F, Isbister DJ, Evans DJ (2000) Nonequilibrium molecular dynamics simulations of heat flow in one-dimensional lattices. Phys. Rev. E 61:3541–3546
61. Haile JM (1992) Molecular Dynamics Simulation, Wiley, New York
62. Jeżowski A, Danilchenko BA, Boćkowski M, Grzegory I, Krukowski S, Suski T, Paszkievicz T (2003) Thermal conductivity of GaN crystals in 4.2–300 K range. Solid State Commun. 128:69–73
63. Florescu DI, Asnin VM, Pollak FH (2000) Thermal conductivity of fully and partially coalesced lateral epitaxial overgrown GaN/sapphire (0001) by scanning thermal microscopy. Appl. Phys. Lett. 77:1464–1466
64. Zimann JM (1960) Electrons and phonons, Clarendon Press, Oxford
65. Stroscio MA, Sirenko YM, Yu S, Kim KW (1996) Acoustic phonon quantization in buried waveguides and resonators. J. Phys. Condens. Matter 8:2143–2151
66. Balandin A, Wang KL (1998) Significant decrease of the lattice thermal conductivity due to phonon confinement in a free-standing semiconductor quantum well. Phys. Rev. B 58: 1544–1549
67. Huang MJ, Chong WY, Chang TM (2006) The lattice thermal conductivity of a semiconductor nanowire. J. Appl. Phys. 99:113318
68. Liang LH, Li BW (2006) Size-dependent thermal conductivity of nanoscale semiconducting systems. Phys. Rev. B 73:153303

69. Suzuki T, Yasutomi T, Tokuoka T, Yonenaga I (1999a) Plastic deformation of GaAs at low temperatures. Phil. Mag. A 79:2637–2654
70. Suzuki T, Yasutomi T, Tokuoka T, Yonenaga I (1999b) Plasticity of III–V compounds at low temperatures. Phys. Status Solidi A 171:47–52
71. Pirouz P, Samant AV, Hong MH, Moulin A, Kubin LP (1999) On temperature dependence of deformation mechanism and the brittle-ductile transition in semiconductors. J. Mater. Res. 14:2783–2793
72. Zhang M, Hobgood HM, Demenet JL, Pirouz P (2003) Transition from brittle fracture to ductile behavior in 4H-SiC. J. Mater. Res. 18:1087–1095
73. Hirth JP, Lothe J (1982) Theory of Dislocations, 2nd ed., Wiley, New York
74. Rabier J, George A (1987) Dislocations and plasticity in semiconductors. II. The relation between dislocation dynamics and plastic-deformation. Rev. Phys. Appl. 22:1327–1351
75. Suzuki T, Nishisako T, Taru T, Yasutomi T (1998) Plastic deformation of InP at temperatures between 77 and 500 K. Phil. Mag. Lett. 77:173–180
76. Boivin P, Rabier J, Garem H (1990) Plastic-deformation of GaAs single-crystals as a function of electronic doping. I. Medium temperatures (150–650°C). Phil. Mag. A 61:619–645
77. Pirouz P, Zhang M, Demenet JL, Hobgood HM (2003) Yield and fracture properties of the wide band-gap semiconductor 4H-SiC. J. Appl. Phys. 93:3279–3290
78. Kamimura Y, Kirchner HOK, Suzuki T (1999) Yield strength and brittle-to-ductile transition of boron-nitride and gallium-nitride. Scr. Mater. 41:583–587
79. Rafii-Tabar H (2004) Computational modelling of thermo-mechanical and transport properties of carbon nanotubes. Phys. Rep. 390:235–452
80. Hung SC, Su YK, Fang TH, Chang SJ, Ji LW (2005) Buckling instabilities in GaN nanotubes under uniaxial compression. Nanotechnology 16:2203–2208
81. Nam CY, Jaroenapibal P, Tham D, Luzzi DE, Evoy S, Fisher JE (2006) Diameter-dependent electromechanical properties of GaN nanowires. Nano Lett. 6:153–158
82. Timoshenko SP, Gere JM (1961) Theory of Elastic Stability, 2nd ed., McGraw-Hill, New York, p. 541

Chapter 6
Optical Anisotropy of Semiconductor Nanowires

Jaime Gómez Rivas, Otto L. Muskens, Magnus T. Borgström, Silke L. Diedenhofen, and Erik P.A.M. Bakkers

Abstract Semiconductor nanowires are novel nanostructures full of promise for optical applications. Nanowires have subwavelength diameters and large aspect ratios, which combined with the high permittivity of semiconductors lead to a strong optical anisotropy. We review in this chapter this optical anisotropy, focusing on the polarization anisotropy of the photoluminescence of individual nanowires and the propagation of light through birefringent ensembles of aligned nanowires.

Recent developments in bottom-up nanofabrication techniques allow the growth of free-standing semiconductor nanowires with controlled composition, lateral dimensions of typically 10–100 nm, and lengths of several micrometers (see Fig. 6.1). The small lateral dimensions of nanowires enables to grow them heteroepitaxially onto different substrates [1–3] or even to design heterostructures with segments, shells, and/or quantum dots of different semiconductors in a single nanowire [4–8]. Nanowires are full of promise for monolithic integration of high-performance semiconductors with new functionality [8–11] into existing silicon technology [2, 3, 12]. These nanostructures will offer new possibilities as next generation of optical and optoelectronical components. Junctions in semiconductor nanowires and light emitting devices have been demonstrated [4, 13–17]. Although the quantum efficiency of these nano-LEDs is still low, fast progress is being made on the passivation of the nanowire surface and the increase of their efficiency [18, 19]. Also, optically and electrically driven nanowire lasing have been reported [9, 20, 21]. Nanowires have been proposed as polarization sensitive photodetectors [22, 23] and as a source for single photons [8, 24].

The encouraging perspectives for novel applications has lead to improved control over nanowire synthesis and materials composition [4, 5, 25–27]. However, little is known about how light is emitted by individual nanowires or how light is scattered by ensembles of these nanostructures. The large geometrical anisotropy of nanowires and the high refractive index of semiconductors give rise to a huge optical anisotropy, which has been reported as a strongly polarized photoluminescence of individual nanowires along their long axis [22, 28]. In this chapter we review

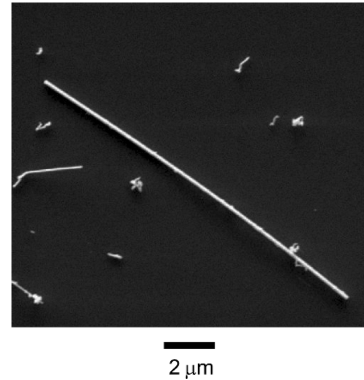

Fig. 6.1 Scanning electron microscope image of an indium phosphide nanowire

the polarization anisotropy in the photoluminescence of individual nanowires. We also describe the propagation of light through ensembles of nanowires oriented perpendicularly to the surface of a substrate. The controlled growth and alignment of the nanowires leads to a medium with giant birefringence [29], i.e., a medium with a large difference in refractive indexes for different polarizations. The giant birefringence in ensembles of nanowires can be easily tuned by changing the semiconductor filling fraction and is not restricted to narrow frequency bands as in periodic structures [30]. Broadband and giant birefringence constitutes an elegant example of the extreme optical anisotropy of nanowires, which may lead to nanoscale polarization controlling media [31], the efficient generation of nonlinear signals [32], and the observation of novel surface electromagnetic modes on birefringent materials [33].

6.1 Growth of Semiconductor Nanowires

Nanowires of semiconductor materials as group III–V (InP, GaAs, GaN), II–VI (ZnSe, ZnO), IV (Si, Ge) and ternaries thereof have been demonstrated using a vapor–liquid–solid (VLS) bottom-up approach by chemical vapor deposition, molecular beam epitaxy, laser ablation, and chemical beam epitaxy. The method was developed in the 1960s for the growth of microwires (whiskers) [34]. In the case of VLS growth, a small metal particle is located on a heated substrate forming a liquid/solid interface, thus forming a local liquid phase epitaxy system. So far gold has been predominantly used as catalyzing metal particle for the growth of Si or III–V whiskers, even though a number of other metals can be employed [35]. The schematics of VLS growth is represented in Fig. 6.2. Material supplied from the vapor enters the liquid metal particle. When the alloy becomes supersaturated, a semiconductor precipitates underneath the particle and a wire grows. In the 1990s

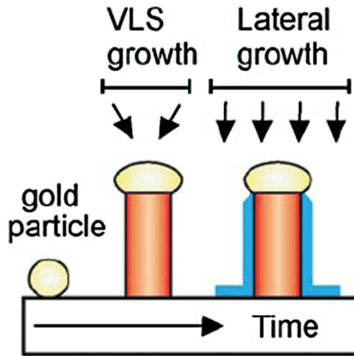

Fig. 6.2 Schematics of VLS and shell nanowire growth. Material supplied from the vapor enters the gold particle. When the gold alloy becomes supersaturated, material precipitates underneath the particle and a nanowire grows. By a temperature increase the kinetic barrier for lateral growth can be overcome, which enables the synthesis of core/shell structures

Hiruma et al. [36] made pioneering work on nanowire growth in a metal-organic-vapor-phase epitaxy (MOVPE) system. These authors evaporated thin films of gold on substrates and, upon annealing the samples at an appropriate temperature, nano-scale gold particles of different sizes were formed. These particles catalyzed the growth of nanowires. Hiruma and co-workers found that the preferential direction for the growth of nanowires is $\langle 111 \rangle$ and pioneered electrical and optical measurements in these nanostructures [1, 37–39].

We focus here on a particular optical property, namely the polarization anisotropy in the photoluminescence and scattering by nanowires. The anisotropy in the absorption and emission of light by nanowires (Sect. 6.2) can be investigated with individual nanowires of a direct bandgap semiconductor. For this purpose, InP nanowires were synthesized on $\langle 111 \rangle$ InP substrates by the use of spin coated 20 nm colloidal gold particles as catalyst. The samples were heated up to a temperature of 420°C under a PH_3 molar fraction of $\chi_{PH_3} = 8.3 \times 10^{-3}$ in a total flow of 6 l/min at 50 mbar using H_2 as carrier gas. After reaching the growth temperature (420°C), and in order to induce the nanowire growth, trimethylindium (TMI) was added to the flow with a molar fraction of $\chi_{TMI} = 2.98 \times 10^{-5}$. To tune the optical properties of nanowires, full control over the length to diameter ratio is necessary. This control can be achieved by adjusting the growth time, which determines the nanowire length, and catalyst particle size, which determines the nanowire diameter. The InP nanowires used in the photoluminescence description of the next section were grown for 20 min, after which the TMI flow was stopped and the MOVPE reactor cooled down. The nanowires were then broken off the surface and dispersed on a silica wafer in such a way that individual nanowires could be studied with an optical microscope.

To investigate the scattering and propagation of light through ensembles of nanowires (Sect. 6.3), layers of aligned GaP nanowires were prepared. We used GaP $\langle 111 \rangle$ as substrate with both sides mechanically and chemically polished to

optical quality. A thin film of gold with a thickness of approximately 0.2 nm was evaporated, from which the metal catalyst droplets were formed at the nanowire growth temperature. Although this method limits the precise control over nanowire diameter, we found that higher wire densities were obtained than when using spin-coated colloidal gold particles. In addition, the aspect ratio of the nanowires can be tuned by varying the growth temperature over two growth mode regimes to make core/shell structures (see Fig. 6.2). The lateral growth of the nanowires enables to increase the GaP filling fraction while keeping constant their density. In this way, optical materials exhibiting birefringence were synthetized by growing a core at 420°C, after which the temperature was ramped up to 630°C in order to grow a shell of a certain thickness. Phosphine and trimethylgallium (TMG) molar fractions were $\chi_{PH_3} = 15.0 \times 10^{-3}$ and $\chi_{TMI_3} = 9.16 \times 10^{-5}$, respectively, for the growth of the shell. Figure 6.3 displays three scanning electron microscope images of layers of GaP nanowires with different diameters grown without a shell (a), with a shell grown during 350 s (b), and with a shell grown during 500 s (c).

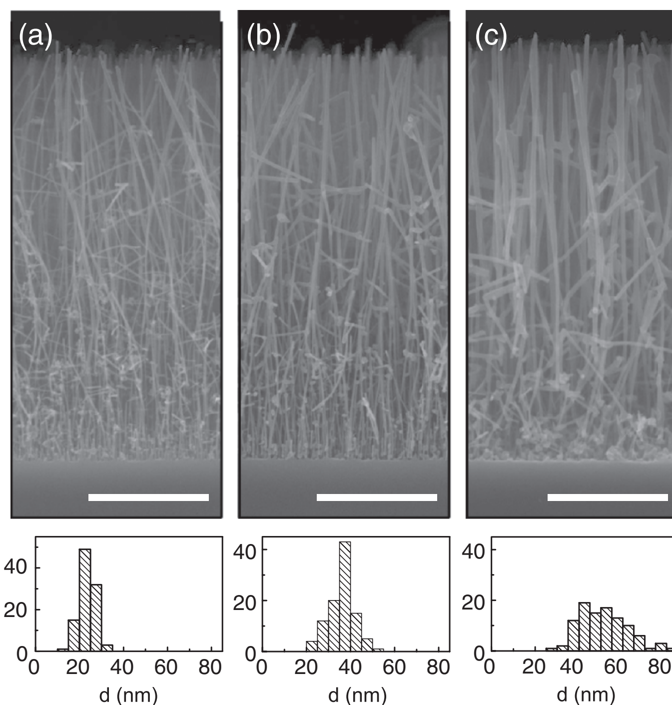

Fig. 6.3 (**a–c**) Cross-sectional SEM images of epitaxially grown ensembles of GaP nanowires with lateral growth times of 0 s (**a**), 350 s (**b**), and 500 s (**c**). Scale bars denote 1 μm. Histograms of the distributions of nanowire diameters are shown below the images

6.2 Polarization Anisotropy of the Photoluminescence of Individual Nanowires

Semiconductor nanowires are nanostructures with a large geometrical anisotropy, which leads to anisotropic light scattering, absorption, and emission. In this section, we review the polarization anisotropy of the absorption and the emission of light by individual nanowires in the quasistatic limit, i.e., when the diameter of the nanowire is much smaller than the wavelength of the incident and emitted light.

6.2.1 Polarization Anisotropy of the Absorption

Let us consider a plane electromagnetic wave incident onto an infinitely long nanowire. The polarization of the wave can be set parallel or perpendicular to the long axis of the nanowire, as it is schematically represented in Fig. 6.4a, b, respectively. The wavelength of the incident wave is much longer than the diameter of the nanowire. In this limit the field amplitude inside the wire is spatially constant. The electric field of the incident wave is parallel to all the interfaces of the nanowire only when its polarization is parallel to the nanowire axis. In this situation, the continuity of the tangential component of the electric field at the interface, imposed by the electromagnetic boundary conditions [40], leads to a field inside the nanowire $E_{\text{in}||}$ that equals the incident field $E_{\text{out}||}$.

$$E_{\text{in}||} = E_{\text{out}||} \; . \tag{6.1}$$

When the incident wave is polarized perpendicular to the nanowire axis, the incident electric field has a component normal to the interface of the nanowire. The boundary conditions impose the continuity of the normal component of the electric displacement $\mathbf{D}$ across the interface, $\mathbf{D} = \varepsilon_0\mathbf{E} + \mathbf{P}$, where ε_0 is the vacuum

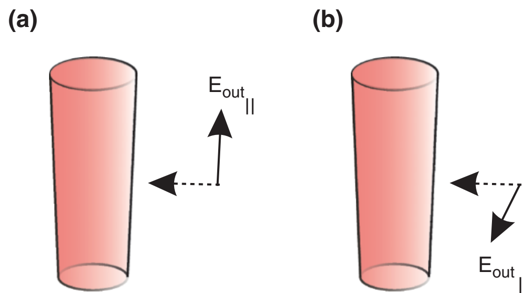

Fig. 6.4 Incident wave onto a nanowire polarized parallel (**a**) and perpendicular (**b**) to the long axis of the nanowire. The vector represented by the *dotted line* is the **k**-vector of the incident wave, while the *solid line* vector displays the polarization

permittivity, $\mathbf{E}$ is the electric field, and $\mathbf{P}$ is the electric polarization. Therefore, there is a depolarization or reduction of the electric field inside the nanowire given by $\boldsymbol{E}_{\text{in}\perp} = \boldsymbol{E}_{\text{out}\perp} - \mathbf{P}/\varepsilon_0$ when the incident wave is polarized perpendicular to the nanowire axis. In the quasistatic limit, the field amplitude inside a cylindrical nanowire is given by [41]

$$E_{\text{in}\perp} = \frac{2}{1+\varepsilon(\omega)} E_{\text{out}\perp} \;, \tag{6.2}$$

where $\varepsilon(\omega)$ is the permittivity contrast between the nanowire and the surrounding medium at frequency ω and $2/(1+\varepsilon(\omega))$ is the depolarization factor.

The fraction of absorbed energy from a beam illuminating a nanowire below the saturation limit is proportional to the intensity (square of the field) inside the nanowire. In the linear regime, the photoluminescence intensity is proportional to the fraction of absorbed energy. Therefore, the photoluminescence intensity from a nanowire is expected to be larger when it is illuminated with a wave polarized parallel to its long axis by a factor that defines the polarization contrast of the absorption

$$\rho_{\text{abs}} = \frac{|E_{\text{in}\parallel}|^2}{|E_{\text{in}\perp}|^2} = \frac{|1+\varepsilon(\omega)|^2}{4} \;. \tag{6.3}$$

The large polarization anisotropy in nanowires, which has been quoted as giant [22], is caused by the large dielectric contrast between self-standing semiconductor nanowires and air. It should be noted that ρ_{abs} depends on the permittivity of the nanowire and its surroundings at the excitation frequency ω. The polarization anisotropy can thus be modified by changing the excitation wavelength. A different way of presenting the polarization anisotropy is the factor $(|E_{\text{in}\parallel}|^2 - |E_{\text{in}\perp}|^2)/(|E_{\text{in}\parallel}|^2 + |E_{\text{in}\perp}|^2)$. However, this parameter converges rapidly to 1 and the representation of the polarization anisotropy in terms of the contrast (Eq.(6.3)) is preferred for the anisotropies typically found in nanowires ($\rho_{\text{abs}} > 10$).

The absorption anisotropy of a single nanowire is illustrated in Fig. 6.5a, where the photoluminescence spectra from an InP nanowire with a diameter of $\simeq$30 nm and a length of a couple of micrometers is displayed. The nanowire was illuminated with a laser beam ($\lambda = 458$ nm) polarized parallel (solid curve) and perpendicular (dashed curve) to its long axis. The polarization contrast was obtained by integrating the photoluminescence intensity in the range 700–950 nm for both polarizations, reaching the very large value of 20 for this particular nanowire.

6.2.2 Polarization Anisotropy of the Emission

We have discussed in the previous section the anisotropy in the photoluminescence when a nanowire is excited with a beam polarized parallel and perpendicular to its long axis, i.e., the anisotropy in the absorption. A similar but somewhat different situation is the anisotropy in the emission, namely the anisotropy of the light emitted

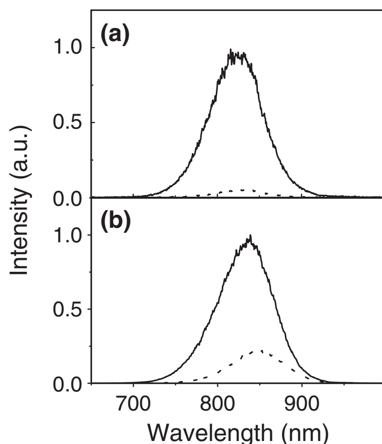

Fig. 6.5 (**a**) Photoluminescence spectra of an InP nanowire excited with beam polarized parallel (*solid curve*) and perpendicular (*dashed curve*) to its long axis. (**b**) Photoluminescence spectra of the same nanowire excited with a polarization parallel to its long axis and detected with a polarization parallel (*solid curve*) and perpendicular (*dashed curve*) to this axis

by a nanowire with a polarization parallel and perpendicular to its axis. This situation has been described theoretically by Ruda and Shik [42]. They considered an array of dipoles randomly oriented in a dielectric cylinder and calculated the Poynting vector outside the cylinder resulting from the incoherent dipole emission. The random orientation of the emitting dipoles, even when the excitation beam is polarized, assumes that the polarization information of the excitation is lost during the inelastic relaxation of the photoexcited electrons before they recombine radiatively. Ruda and Shik found that under this assumption the anisotropy contrast of the emission ρ_{em} is given by

$$\rho_{\mathrm{em}} = \frac{I_{\mathrm{em}_{\parallel}}}{I_{\mathrm{em}\perp}} = \frac{2+|\varepsilon(\omega)+1|^2}{6}\,, \tag{6.4}$$

where $I_{\mathrm{em}_{\parallel}}$ and $I_{\mathrm{em}\perp}$ are the intensities emitted with a polarization parallel and perpendicular to the long axis of the nanowire, and $\varepsilon(\omega)$ is the permittivity contrast between the nanowire and its surrounding at the frequency of the emission.

The anisotropy in the emission of the same nanowire of Fig. 6.5a is represented in Fig. 6.5b, where the photoluminescence spectra measured for a polarization parallel and perpendicular to the nanowire axis are displayed by the solid and dashed curves, respectively. This pholuminescence was excited by illuminating the nanowire with a laser beam ($\lambda = 458\,\mathrm{nm}$) polarized parallel to its long axis. The anisotropy in the emission reaches a value of 4.6 for this nanowire, being roughly a factor 4 lower than the anisotropy in the absorption. The difference between the measured absorption and the emission anisotropies are in qualitative agreement with (6.3) and (6.4), which predict a larger anisotropy in the absorption. It should be pointed

out that these equations are derived for a nanowire in a homogeneous medium. The nanowires of Fig. 6.5 were laying on top of a silica substrate, which has an influence on the optical anisotropy. Another point of attention is the validity of the quasistatic approximation on which (6.3) and (6.4) are based. This approximation is only valid in the limit of very thin nanowires with a diameter smaller than $\approx 10\,\text{nm}$. A more accurate description of the polarization anisotropy of nanowires is provided by Mie scattering theory [43], which is beyond the scope of this chapter.

6.3 Coherent propagation of Light Through Ensembles of Nanowires: Birefringence

In the previous section we described the absorption and emission of light by individual nanowires. We will now discuss the coherent propagation of light through ensembles of nanowires aligned along a certain direction. Scanning electron microscope images of the type of samples that are discussed in this section were given in Fig. 6.3. By coherent propagation we refer to the elastically scattered radiation on the forward direction. This terminology is adopted from the multiple scattering community, where incoherent radiation refers to the scattered light into other directions than the incident one, i.e., the diffusely scattered light [44, 45].

Generally, the coherent propagation of light through ensembles of scatterers is described by the propagation in an effective medium that is considered homogeneous. The basic idea of any effective medium theory of a disordered system of scatterers is to focus on a particular scatterer and replace the rest by a homogeneous medium which is self-consistently determined imposing the condition that any other scatterer could have been chosen. The optical response of a linear and homogeneous medium is described by its relative permittivity ε and its relative permeability μ, which are defined by the constitutive relations

$$\mathbf{D} = \varepsilon\varepsilon_0\mathbf{E}, \;\; \mathbf{B} = \mu\mu_0\mathbf{H}\,, \tag{6.5}$$

where $\mathbf{D}, \mathbf{E}, \mathbf{B}$, and $\mathbf{H}$ are the displacement field, electric field, magnetic induction, and magnetic field, respectively, and ε_0 and μ_0 are the vacuum permittivity and permeability. In the following we will consider nonmagnetic materials with $\mu = 1$. If the medium is isotropic, its permittivity is a scalar. A plane wave propagating in this medium will have a phase velocity given by

$$v = \frac{c_0}{(\varepsilon)^{1/2}} = \frac{c_0}{n}\,, \tag{6.6}$$

with c_0 the speed of light in vacuum and n the refractive index.

If the medium is formed by anisotropic scatterers and these scatterers are aligned along certain directions, the homogenization performed by any effective medium model leads to the permittivity tensor

$$\tilde{\varepsilon} = \begin{pmatrix} \varepsilon_1 & 0 & 0 \\ 0 & \varepsilon_2 & 0 \\ 0 & 0 & \varepsilon_3 \end{pmatrix}, \tag{6.7}$$

with ε_1, ε_2, and ε_3 the effective medium permittivities along the three principal axes. A medium with this characteristic is called birefringent, as light propagating through it experiences different refractive indexes or has different phase velocities depending on its polarization state. If $\varepsilon_1 \neq \varepsilon_2 \neq \varepsilon_3$ the medium is called biaxial, whereas if $\varepsilon_1 = \varepsilon_2 \neq \varepsilon_3$ we have an uniaxial medium. In uniaxial media ε_1 and ε_2 are usually referred to as the ordinary permittivity and ε_3 is called the extraordinary permittivity.

Birefringence induced by macroscopic scatterers is usually referred to as form birefringence to differentiate it from the natural birefringence of some crystals such as quartz and calcite. Natural birefringence is due to the anisotropy in the microscopic structure, which leads to the aforementioned polarization dependent phase velocity [46].

Semiconductor nanowires are anisotropic scatterers. As we have seen in the previous section, the absorption and emission of light by nanowires depends strongly on polarization. One should also expect that the scattering cross-section for light polarized parallel to the long axis of the nanowire is larger than for light polarized perpendicular to this axis. Moreover, nanowires can be grown epitaxially on crystalline substrates along well-defined crystallographic directions. If this direction of growth is unique, layers of aligned nanowires form an uniaxial birefringent material with an effective permittivity given by the tensor

$$\tilde{\varepsilon} = \begin{pmatrix} \varepsilon_\perp & 0 & 0 \\ 0 & \varepsilon_\perp & 0 \\ 0 & 0 & \varepsilon_\parallel \end{pmatrix}, \tag{6.8}$$

where $\varepsilon_\perp$ represents the effective ordinary permittivity or the permittivity that light polarized perpendicular to the long axis of the nanowires experiences, and $\varepsilon_\parallel$ refers to the effective extraordinary permittivity or the permittivity for light polarized parallel to the nanowire axis.

If the **E**-field of the wave propagating in the medium is parallel to all the interfaces of the nanowires, as it is the case for a polarization parallel to their long axis, the effective permittivity is equal to the weighted average of the permittivity of the constituents [47]. The effective extraordinary permittivity $\varepsilon_\parallel$ is thus given by

$$\varepsilon_\parallel = \varepsilon_1 f + \varepsilon_2 (1 - f) , \tag{6.9}$$

where ε_1 represents the permittivity of the material forming the nanowires, f is the nanowire volume fraction, and ε_2 is the permittivity of the dielectric matrix in which the nanowires are embedded.

In the long-wavelength limit, i.e., when the wavelength of the light propagating in the medium is much larger than the diameter of the nanowires and the mean distance between nanowires, and for nanowire filling fractions smaller than $\simeq$50% the ordinary permittivity $\varepsilon_\perp$ approaches the Maxwell–Garnett effective permittivity [48]

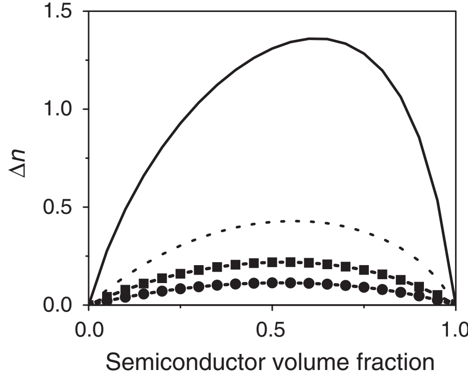

Fig. 6.6 Birefringence parameter calculated with the Maxwell–Garnett effective medium approximation for four different anisotropic media formed by a semiconductor and air as a function of the semiconductor volume filling fraction. The *solid curve* and the *squares* represent the birefringence for semiconductor nanowires in air with a permittivity of 16 and 4, respectively. The *dashed curve* and the *circles* correspond to the birefringence in samples of pores in a semiconductor matrix for the same values of the permittivity

$$\varepsilon_{\perp} \simeq \varepsilon_2 \left(1 + \frac{2f\alpha}{1 - f\alpha}\right) , \tag{6.10}$$

where α is a depolarization factor given by $\alpha = (\varepsilon_1 - \varepsilon_2)/(\varepsilon_1 + \varepsilon_2)$.

Contrary to other effective medium models such as the Bruggeman approximation, the Maxwell–Garnett approximation is not symmetric to the interchange of the permittivity between the scatterers and the surrounding medium. In other words, the effective Maxwell–Garnett permittivity of semiconductor nanowires in air is not the same as that of air pores in a semiconductor matrix. To illustrate this asymmetry we have plotted in Fig. 6.6 the birefringence parameter defined as

$$\Delta n = n_{\parallel} - n_{\perp} = \sqrt{\varepsilon_{\parallel}} - \sqrt{\varepsilon_{\perp}} , \tag{6.11}$$

where $n_{\parallel}$ and $n_{\perp}$ are the refractive indexes for polarizations parallel and perpendicular to the nanowire axis, as a function of the semiconductor filling fraction for direct (nanowires in air) and inverse (air pores in a semiconductor matrix) structures. The squares and circles in Fig. 6.6 correspond to a direct and inverse medium, respectively, containing a semiconductor of permittivity $\varepsilon = 4$ and air. The solid and dashed curves represent the birefringence of similar direct and inverse media with a semiconductor of permittivity $\varepsilon = 16$ and air. In general, the birefringence increases as the permittivity of the semiconductor gets larger and an ensemble of nanowires has a larger birefringence than a similar medium of nanopores. To date, form birefringence has been mainly investigated in porous systems made by top-down techniques [49–51]. In the next section we show that giant birefringence can be easily obtained in films of semiconductor nanowires.

6.4 Experimental Determination of the Birefringence

Angular-dependent polarization interferometry can be used to determine the refractive indexes of nanowire layers. A schematic representation of an angular dependent reflection and transmission experiment is shown in Fig. 6.7. In this experiment the polarization state of the input beam (a laser beam or a white light source) is set by a $\lambda/2$ wave plate and/or a polarizer, while the transmitted and reflected beams are sent through an analyzing polarization filter before being detected by a photodetector or by a spectrometer.

For the quantitative determination of optical birefringence, the polarization vector of the input beam is set to 45° with respect to the plane of incidence, defined by the **k** vector of the incident wave and the normal to the sample surface, in order to have equal contributions of in-plane (p-polarized) and out-of-plane (s-polarized) polarizations. The polarization state of the light either transmitted or reflected from the sample is determined by measuring the intensity of the polarization components at 45° (parallel to the incident beam) and −45° (perpendicular to the incident beam). For normal incidence onto a sample of vertically aligned nanowires ($\theta_{\text{in}} = 0°$), the polarization is always perpendicular to the nanowire axis. As the angle of incidence onto the sample is varied between 0° and 90° with respect to the normal of the surface, the effective refractive index for the p-polarization increases due to the larger projection of the electric field along the nanowire axis. The s-polarization remains perpendicular to the long axis of the nanowire for all angles of incidence. The dependence of n_{s} and n_{p} with the angle of incidence θ_{in} is given by [52]

$$n_{\text{s}}(\theta_{\text{in}}) = n_{\perp}\,, \quad n_{\text{p}}(\theta_{\text{in}}) = \left(n_{\perp}^2 + \frac{n_{\parallel}^2 - n_{\perp}^2}{n_{\parallel}^2} \sin^2 \theta_{\text{in}} \right)^{1/2} . \tag{6.12}$$

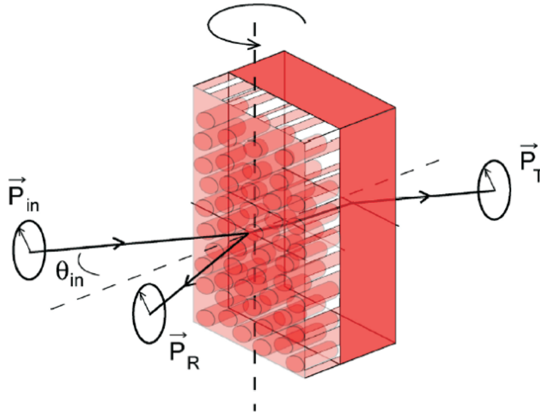

Fig. 6.7 Schematic representation of the experimental setup used for the determination of the birefringence parameter in ensembles of aligned nanowires. The polarization state of the incident beam $\mathbf{P}_{\text{in}}$ is set at an angle of 45° with respect to the plane of incidence. The reflected and transmitted intensities $\mathbf{P}_{\text{R}}$, $\mathbf{P}_{\text{T}}$ with a polarization parallel (as represented in the figure) and perpendicular to the incident polarization are detected. The ratio of these intensities define the reflection and transmission contrast, which can be fitted to obtain the ordinary and extraordinary refractive indexes

The total phase for the s- and p-polarizations $\phi_{s,p}$ accumulated after a single transmission through the birefringent layer can be expressed as

$$\phi_{s,p} = \frac{2\pi}{\lambda} n_{s,p} L \cos\theta_{s,p} , \tag{6.13}$$

where L denotes the thickness of the nanowire layer, λ the optical wavelength in vacuum, and $\theta_{s,p}$ the angles between the normal to the surface of the sample and the wave vector in the medium.

The increase of the refractive index with θ_{in} for the p-polarization component and the increase of the phase for this polarization gives rise to a retardation and the rotation of the polarization vector. This retardation is measured as an increase of the intensity detected with crossed polarizers I_{perp} and a concomitant decrease of intensity obtained with parallel polarizers I_{par}.[1] The polarization contrast I_{perp}/I_{par} in transmission or reflection represents the extinction of the original polarization state and is thus a measure for the quality of the birefringent material.

In Fig. 6.8, the polarization contrast in transmission ρ_T (a) and in reflection ρ_R (b) of a sample of GaP nanowires are displayed. This sample consists of nanowires

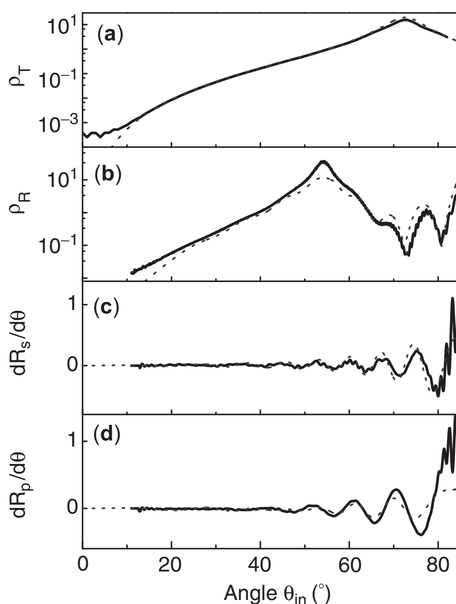

Fig. 6.8 Transmission and reflection measurements at $\lambda = 633$ nm as a function of the angle of incidence on a sample of vertically aligned GaP nanowires with an average thickness of 5 μm and average nanowire diameter of 25 nm. (**a**) Transmission contrast, (**b**) reflection contrast, (**c**) derivative of the s-polarized reflection, and (**d**) derivative of the p-polarized reflection. The *dotted curves* correspond to fits using the transfer matrix method

[1] We use the subindexes perp and par to differentiate the intensities measured with parallel and perpendicular polarizers from the luminescence intensity parallel $I_{\parallel}$ and perpendicular $I_{\perp}$ to the nanowire axis that were defined in the previous section.

with an average length of 5 μm and diameter of 25 nm. The retardation measured in reflection is larger than that in transmission as it is apparent from the smaller angle at which the maximum reflection contrast is obtained. This difference in retardation between transmission and reflection is due to the two times larger optical path inside the nanowire layer when measuring the reflection.

Additional measurements to the polarization contrast are the angle dependent reflectivity for s- and p-polarizations. These curves contain multiple reflection fringes that can be used to derive independently the values of the refractive indexes of the nanowire layers. Figure 6.8c,d shows the angle-dependent reflectivity measurements, where we have plotted $\mathrm{d}R/\mathrm{d}\theta$ to better visualize the thin-film Fabry–Pérot fringes.

The set of experimental data, consisting of the contrast factors ρ_T and ρ_R and the Fabry–Pérot fringes in $\mathrm{d}R_{\mathrm{s,p}}/\mathrm{d}\theta$ can be fitted consistently using the transfer matrix method [53]. The result of the fits are represented in Fig. 6.8 by the dotted curves, from which we obtain for this particular sample $n_{\perp} = 1.045 \pm 0.003$, $n_{\parallel} = 1.100 \pm 0.003$, and $\Delta n = 0.055 \pm 0.006$.

6.4.1 Long Nanowires

According to (6.9) and (6.10), the birefringence in a layer of aligned semiconductor nanowires can be tuned by varying the filling fraction of the semiconductor. This tunability can be achieved by increasing the density of nanowires or by increasing their diameter. The last option is preferred because, as we have seen in Sect. 6.1, the VLS method allows to grow shells around nanowires in a very controllable manner. However, it should be pointed out that increasing the nanowire diameter leads also to an increase of multiple scattering and reduction of the coherent beam intensity. Multiple scattering by ensembles of nanowires is beyond the scope of this chapter and it will be obviated in the following discussion.

The polarization contrast ρ_{T} measured in three layers of nanowires at $\lambda = 633$ nm is shown in Fig. 6.9a–c as a function of the angle of incidence. These measurements correspond to light transmitted through the sample consisting of a bare GaP substrate (dashed curve in Fig. 6.9a) and a GaP substrate covered with 5 μm long nanowires with an average wire diameter of 22, 35, and 43 nm (solid curves in Fig. 6.9a–c, respectively). In the absence of a nanowire layer, i.e., transmission through a bare GaP substrate, the cross-polarized intensity remains low at all angles of incidence. For the samples containing nanowires, a clear maximum in the contrast is observed. With increasing nanowire diameter, this maximum shifts from 76° to 54°, while the maximum extinction ratio increases from 14.7 to 115.

The reflected-light traces for the same materials (solid curves in Fig. 6.9d–f) follow the same behavior as for the transmission. The contrast function of the bare GaP substrate (dashed curve in Fig. 6.9d) can be explained by the behavior of the p-polarized reflectivity. Again, for all layers of nanowires a clear first-order

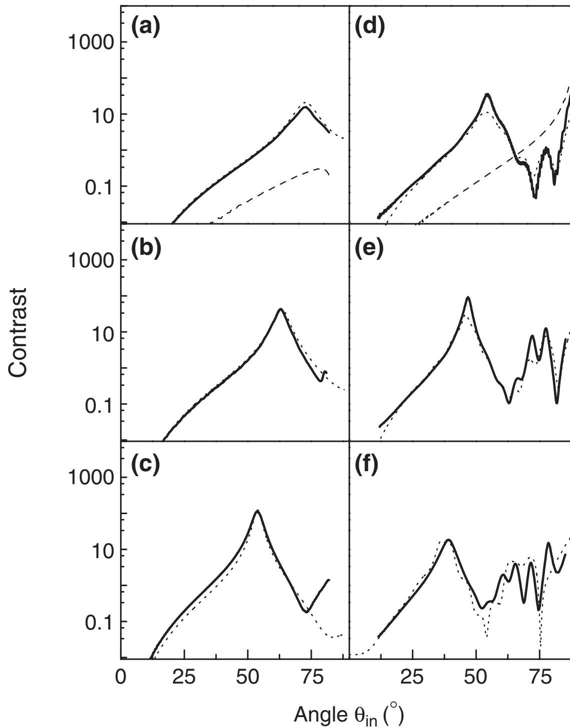

Fig. 6.9 Transmission (**a–c**) and reflection (**d–f**) contrast for three layers of GaP nanowires with an average length of 5 μm and a average diameter of 22 (**a, d**), 35 (**b, e**), and 43 nm (**c, f**). The *dotted curves* are fits to the measurements using the transfer matrix model. The *dashed curves* in (**a**) and (**d**) correspond to the transmission and reflection contrast of a bare GaP substrate

maximum is observed at a smaller angle than in transmission due to the double passage of the reflected light through the birefringent layer.

Figure 6.10a shows the values of the ordinary (squares) and extraordinary (triangles) refractive indexes as a function of the nanowire filling fraction, while b represents the birefringence parameter $\Delta n = n_{\|} - n_{\perp}$. These values were obtained from the fits to the measurements shown as dashed curves in Fig. 6.9. The nanowire volume filling fraction can be controlled by the shell growth technique and can be estimated from gravimetric measurements. With the increase of the nanowire filling fraction, $n_{\perp}$ and $n_{\|}$ rise from 1.05 to 1.2 and from 1.1 to 1.35, respectively, while the birefringence Δn has an initial value of 0.05 increasing to 0.15 for the thicker wires. The lines in Fig. 6.10a, b correspond to the expected values of $n_{\perp}$, $n_{\|}$, and Δn for a medium of perfectly aligned nanowires (see Sect. 6.3). The measured birefringence parameter is significantly lower than the expected values, and this discrepancy gets more pronounced as the nanowire filling fraction increases. The disagreement can be partially attributed to the misalignment of long nanowires as they bend at the top due to their weight, which leads to a reduction of the birefringence with respect

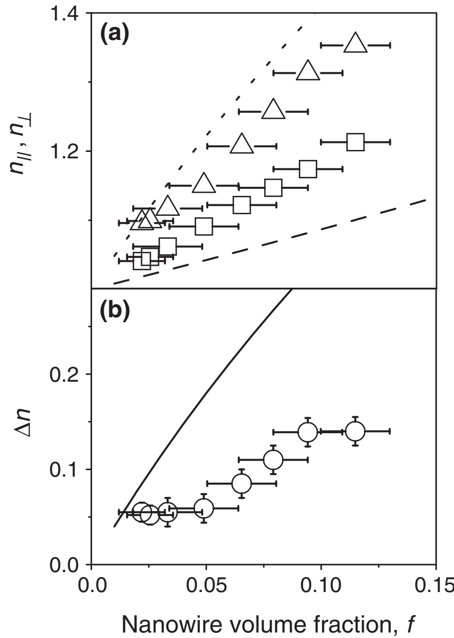

Fig. 6.10 (**a**) Ordinary (*squares*) and extraordinary (*triangles*) refractive indexes of ensembles of epitaxially grown GaP nanowires with increasing diameter as a function of the nanowire filling fraction. The *dashed* and *dotted lines* correspond to the calculated ordinary and extraordinary effective refractive indexes for a medium of perfectly aligned nanowires. (**b**) Birefringence parameter $\Delta n = n_{\|} - n_{\perp}$ for the same samples of panel (**a**). The *solid curve* is the calculated birefringence

to the case of samples of perfectly aligned cylinders. To confirm this hypothesis we have measured samples with nanowires of different length. The values of the birefringence parameter for three of these samples of GaP nanowires with an average nanowire diameter of $\simeq$21.5 nm and average length of 15, 5, and 1.5 µm are displayed in Fig. 6.11 as a function of the nanowire length. As the nanowires get longer, their misalignment due to bending becomes more relevant and the reduction of Δn is more pronounced.

6.4.2 Short Nanowires: Giant Birefringence

As we have seen in the previous section, to obtain the maximum possible birefringence the nanowire layers should be formed by short nanowires that are aligned vertically. Layers of short nanowires ($\simeq$1.5 µm) with different diameters are shown in Fig. 6.12. These layers were grown as described in Sect. 6.1 without a radial growth (a) and with 950 s of lateral growth (b), leading to an average nanowire diameter of 21.5 and 90 nm, respectively.

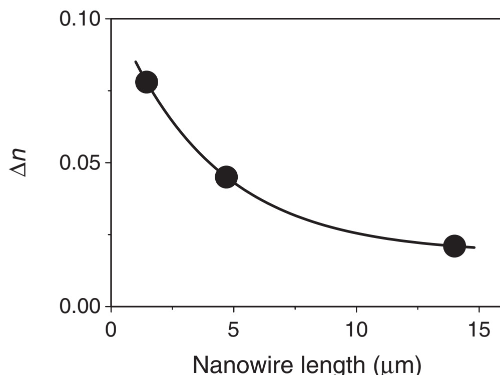

Fig. 6.11 Birefringence parameter of layers of GaP nanowires with equal average diameter ($\simeq$21.5 nm) and different lengths. The *solid curve* is a guide to the eye (reproduced from [29])

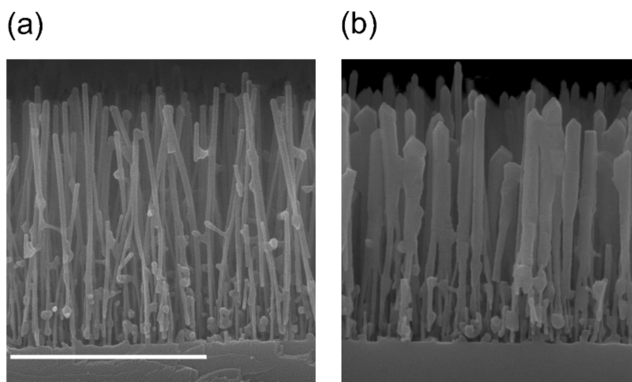

Fig. 6.12 Cross-sectional SEM images of GaP nanowire layers with radial growth times of 0 s (**a**) and 950 s (**b**). The nanowires have an average diameter of 21.5 and 90 nm, respectively. Scale bar denotes 1 μm (reproduced from [29])

Reflection and transmission measurements have been performed, as described in Sect. 6.4, in these and other samples with intermediate nanowire diameters. The resulting values of the birefringence parameter obtained from fits to these measurements are represented in Fig. 6.13a as a function of the nanowire filling fraction. As in the case of long nanowires, the birefringence increases with the volume fraction, but now we obtain values of Δn as high as 0.80 ± 0.07 for a filling fraction of 40%. The solid curve in Fig. 6.13a represents the effective birefringence coefficient calculated using Eqs. 6.9–6.11. The small discrepancy between measurements and calculation can be attributed to the aforementioned bending of the nanowires, which yields a lower Δn than that predicted by the theoretical model of perfectly aligned nanowires. The calculated birefringence coefficient for an inverted structure consisting of air pores in a matrix of high dielectric material is also plotted in Fig. 6.13a (dashed curve). As discussed in Sect. 6.3, high density ensembles of nanowires exhibit a much larger birefringence than inverted materials.

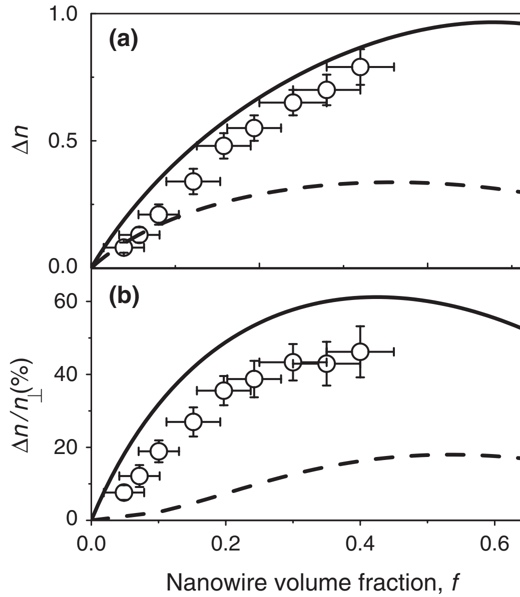

Fig. 6.13 (a) Birefringence parameter Δn as a function of the nanowire volume fraction for GaP samples with an average nanowire length of 1.5 µm, and different nanowire volume fraction. The *solid* and *dashed curves* are the Maxwell–Garnett calculations of Δn for the direct (GaP nanowires in air) and inverse medium (pores in GaP). (**b**) Relative birefringence $\Delta n/n_\perp$ versus the nanowire volume fraction. *Solid* and *dashed curves* are the calculations for a direct and inverse medium (reproduced from [29])

A parameter of considerable interest is the birefringence normalized to the ordinary refractive index $n_\perp$, describing the relative difference of the phase velocity of light of different polarizations. The relative birefringence, plotted as a function of the semiconductor filling fraction in Fig. 6.13b, reaches values up to 43% at high filling fractions. The large relative birefringence again is specific for the nanowire material, and it is very different from porous materials (dashed curve in Fig. 6.13b).

6.5 Summary and Conclusions

In this chapter, we have reviewed the extreme optical anisotropy of individual nanowires and of ensembles of nanowires. The photoluminesce intensity of these nanostructures is polarized along their long axis and depends strongly on the polarization state of the excitation. Light is scattered anisotropically in ensembles of aligned nanowires giving rise to birefringence. Layers of short nanowires, in which the vertical alignment of the nanowires is the best, exhibit giant birefringence approaching the maximum birefringence expected for a system of perfectly aligned cylinders in the long-wave limit.

Acknowledgements The authors thank G. Immink, E. Evens, F. Holthuysen, and P. Breijmer for technical assistance, and L. Feiner and M. van Weert for discussion. This work was supported by the Netherlands Foundation "Fundamenteel Onderzoek der Materie (FOM)" and the "Nederlandse Organisatie voor Wetenschappelijk Onderzoek (NWO)," and is part of an industrial partnership program between Philips and FOM.

References

1. M. Yazawa, M. Koguchi, K. Hiruma: Appl. Phys. Lett. **58**, 1080 (1991).
2. T. Martensson, et al: Nano Lett. **4**, 1987 (2004).
3. E.P. Bakkers, et al: Nat. Mater. **3**, 769 (2004).
4. M.S. Gudiksen, L.J. Lauhon, J. Wang, D.C. Smith, C.M. Lieber: Nature **415**, 617 (2002).
5. M.T. Bjork, et al: Nano Lett. **2**, 87 (2002).
6. D.Y. Li, Y. Wu, R. Fan, P.D. Yang, A. Majumdar: Appl. Phys. Lett. **83**, 3186 (2003).
7. L.J. Lauhon, M.S. Gudiksen, C.L. Wang, C.M. Lieber: Nature **420**, 57 (2002).
8. M.T. Borgström, V. Zwiller, E. Müller, A. Imamoglu: Nano Lett. **5**, 1439 (2005).
9. J.C. Johnson, et al: Nature Mat. **1**, 106 (2002).
10. G.F. Zheng, F. Patolsky, Y. Cui, W.U. Wang, C.M. Lieber: Nature Biotechnology **23**, 1294–1301 (2005).
11. J.A. van Dam, Y.V. Nazarov, E.P.A.M. Bakkers, S. De Franceschi, L.P. Kouwenhoven: Nature **442**, 667 (2006).
12. T.I. Kamins, X. Li, R.S. Williams: Nano Lett. **4**, 503 (2004).
13. K. Haraguchi, T. Katsuyama, K. Hiruma, K. Ogawa: Appl. Phys. Lett. **60**, 745 (1992).
14. H.M. Kim, et al: Nano Lett. **4**, 1059 (2004).
15. J.M. Bao, M.A. Zimmler, F. Capasso, X.W. Wang, Z.F. Ren: Nano Lett. **6**, 1719 (2006).
16. F. Qian, S. Gradecak, Y. Li, C.Y. Wen, C.M. Lieber: Nano Lett. **5**, 2287 (2005).
17. E.D. Minot, et al: Nano Lett. **7**, 367 (2007).
18. L.K. van Vugt, S.J. Veen, E.P.A.M. Bakkers, A.L. Roest, D. Vanmaekelbergh: J. Am. Chem. Soc. **127**, 12357 (2005).
19. M. Mattila, T. Hakkarainen, H. Lipsanen, H. Jiang, E.I. Kauppinen: Appl. Phys. Lett. **90**, 033101 (2007).
20. M.H. Huang, et al: Science **292**, 1897 (2001).
21. X. Duan, Y. Huang, R. Agarwal, C.M. Lieber: Nature **421**, 241 (2003).
22. J. Wang, M.S. Gudiksen, X. Duan, Y. Cui, C.M. Lieber: Science **293**, 1455 (2001).
23. H. Kind, H.Q. Yan, B. Messer, M. Law, P.D. Yang: Adv. Mat. **14**, 158 (2002).
24. N. Panev, A.I. Persson, N. Skold, L. Samuelson: Appl. Phys. Lett. **83**, 2238 (2003).
25. Y.Y. Wu, R. Fan, P.D. Yang: Nano Lett. **2**, 83 (2002).
26. J. Goldberger, A.I. Hochbaum, R. Fan, P.D. Yang: Nano Lett. **6**, 973 (2006).
27. M.T. Borgström, M.A. Verheijen, G. Immink, T. de Smet, E.P.A.M. Bakkers: Nanotechnol. **17**, 4010 (2006).
28. J. Qi, A.M. Belcher, J.M. White: Appl. Phys. Lett. **82**, 2616 (2003).
29. O.L. Muskens, M.T. Borgström, E.P.A.M. Bakkers, J. Gómez Rivas: Appl. Phys. Lett. **89**, 233117 (2006).
30. R.-C. Tyan, et al: J. Opt. Soc. Am. A **14**, 1627 (1997).
31. M. Kotlyar, L. Bolla, M. Midrio, L. O'Faolain, T. Krauss: Opt. Express **13**, 5040 (2005).
32. M.J.A. de Dood, W.T.M. Irvine, D. Bouwmeester: Phys. Rev. Lett. **93**, 040504 (2005).
33. D. Artigas, L. Torner: Phys. Rev. Lett. **94**, 013901 (2005).
34. R.S. Wagner, W.C. Ellis: Appl. Phys. Lett. **4**, 89 (1964).
35. E.I. Givargizov: J. Crystal Growth **31**, 20 (1975).
36. K. Hiruma, H. Murakoshi, M. Yazawa, T. Katsuyama: J. Crystal Growth **163**, 226 (1996).
37. K. Hiruma, et al: J. Appl. Phys. 77, 447–462 (1995).

38. K. Haraguchi, K. Hiruma, K. Hosomi, M. Shirai, T. Katsuyama: J. Vac. Sci. Technol. B **15**, 1685 (1997).
39. A.K. Viswanath, K. Hiruma, M. Yazawa, K. Ogawa, T. Katsuyama: Microwave and Opt. Technol. Lett. **7**, 94 (1994).
40. Born, Wolf: *Principles of Optics* (Cambridge University Press, Cambridge 1997) pp 4–7.
41. L.D. Landau, E.M. Lifshitz, L.P. Pitaevskii: *Electrodynamics of Continuous Media* (Elsevier Butterworth Heinemann, Amsterdam 2004) pp 39–40.
42. H.E. Ruda, S. Shik: Phys. Rev. B **72**, 115308 (2005).
43. C.F. Bohren, D.R. Huffman: *Absorption and Scattering of Light by Small Particles* (Wiley-VCH Verlag GmbH, Weinheim 2004).
44. A. Ishimaru: *Wave Propagation and Scattering in Random Media* (Academic Press, New York 1978).
45. P. Sheng: *Introduction to Wave Scattering, Localization and Mesoscopic Phenomena* (Academic Press, New York 1995).
46. Hecht: *Optics* (Addison Wesley, San Francisco 2002) pp 336–344.
47. D.J. Bergman, D. Stroud: Solid State Phys. **46**, 197 (1992).
48. A. Kirchner, K. Busch, C.M. Soukoulis: Phys. Rev. B **57**, 277 (1998).
49. F. Genereux, S.W. Leonard, H.M. van Driel, A. Birner, U. Gösele: Phys. Rev. B **63**, R161101 (2001).
50. N. Künzner, et al: Opt. Lett. **26**, 1265 (2001).
51. L. Markham, et al: Appl. Phys. Lett. **86**, 011912 (2005).
52. C.J. Oton et al: Appl. Phys. Lett. **81**, 4919 (2002).
53. S.L. Diedenhofen, O.L Muskens, M.T. Borgström, E.P.A.M. Bakkers. J. Gómez Rivas: Unpublished.

Chapter 7
FDTD Spectroscopic Study of Metallic Nanostructures: On the Pertinent Employment of Tabulated Permittivities

Thierry Laroche and Alexandre Vial

Abstract We investigate the plasmonic properties of silver nanowires. By comparing our computations with previously published experimental results, we propose a way to correct tabulated permittivities to obtain a better description of the dispersive properties of this kind of structure.

7.1 Introduction

Development of plasmonic structures has become an important topic today. Nanowires especially arouse interest for nanoscience applications. However, the actual spatial distribution of the field and the role of surface plasmon modes in single elongated nanoparticles are not fully understood. Some indications were experimentally gathered recently [1–3]. Some theoretical approaches have completed these results [4, 5]. Nevertheless, some disagreements between experiments and theory show the way for the upcoming works [6].

In a larger framework, many numerical methods have been used for plasmonic structures' design and optimization. One of these method is the Finite-Difference Time-Domain (FDTD) method. This purely numerical scheme was successfully applied to different nano-optic problems [7–9]. This method is particularly well suited for spectroscopic studies, but can also be used for field cartography. An important requirement of this method for the study of dispersive media is the need of an analytical law of dispersion. Tabulated data for many materials can be found in several references, and can be fitted over the range of wavelengths of interest.

The use of these tabulated data for the study of nanostructures is questionable, as they were most of the times obtained for a bulk thin layer of amorphous materials, which crystalline properties may then strongly differ from the ones of the nanostructures.

In this work, we first give the theoretical background of the FDTD method for the description of dispersive media. We then investigate the plasmonic properties

of silver nanowires. By comparing our computations with previously published experimental results, we propose a way to correct tabulated permittivities in order to obtain a better description of the dispersive properties of this kind of structure.

7.2 FDTD Method for Dispersive Materials

The FDTD method is widely used for the modeling of many elecromagnetic phenomena, from radar back-scattering from an aircraft to visible light diffraction by sub-wavelength structures. Although the derivation of the discrete version of Maxwell's equations, as first published by Yee [10], can be easily obtained, taking care of the dispersive properties of materials is not obvious.

7.2.1 Nondispersive Case

The FDTD method is based on the discretization of Maxwell's curl equations,

$$\nabla \times \mathbf{H} = \frac{\partial \mathbf{D}}{\partial t} + \sigma \mathbf{E}, \tag{7.1}$$

$$\nabla \times \mathbf{E} = -\frac{\partial \mathbf{B}}{\partial t}, \tag{7.2}$$

with a choice of the spatial and temporal grids insuring that the two equations

$$\nabla . \mathbf{D} = 0, \tag{7.3}$$

$$\nabla . \mathbf{B} = 0 \tag{7.4}$$

are satisfied. To link **D** and **B** to **E** and **H** we use the constitutive equations,

$$\mathbf{D} = \epsilon_0 \hat{\varepsilon} \mathbf{E}, \tag{7.5}$$

$$\mathbf{B} = \mu_0 \hat{\mu} \mathbf{H}, \tag{7.6}$$

where $\hat{\varepsilon}$ and $\hat{\mu}$ are the relative permittivity and permerability tensor respectively, ϵ_0 and μ_0 the permittivity and permeability of free space. We will only consider isotropic, linear and nonmagnetic media, thus $\hat{\varepsilon}$ and $\hat{\mu}$ are actually scalar and $\hat{\mu} = 1$. Moreover, for nondispersive media, ε is a constant.

The conductivity σ is explicitely written in Eq. 7.1, but can be implicitely taken into account. Starting from Eqs. 7.1 and 7.5 and assuming a temporal dependence of the fields in $e^{-i\omega t}$ we get

$$\begin{aligned}\nabla \times \mathbf{H} &= \frac{\partial \mathbf{D}}{\partial t} + \sigma \mathbf{E} \\ &= \left(\epsilon_0 \varepsilon \frac{\partial}{\partial t} + \sigma\right) \mathbf{E} \\ &= (-\mathrm{i}\omega\epsilon_0\varepsilon + \sigma)\,\mathbf{E} \\ &= -\mathrm{i}\omega\epsilon_0 \left(\varepsilon - \frac{\sigma}{\mathrm{i}\omega\epsilon_0}\right) \mathbf{E}.\end{aligned} \tag{7.7}$$

Introducing the new complex permittivity

$$\tilde{\varepsilon} = \varepsilon + \mathrm{i}\frac{\sigma}{\omega\epsilon_0}, \tag{7.8}$$

we finally obtain

$$\nabla \times \mathbf{H} = \epsilon_0 \tilde{\varepsilon} \frac{\partial \mathbf{E}}{\partial t}. \tag{7.9}$$

For a one-dimensional propagation along the x-axis, with a spatial discretization Δx and a temporal discretization Δt, we represent the value of any field U at position $x = i\Delta x$ and for the instant $t = n\Delta t$ by $U\,|_i^n$, and the standard FDTD recursion equations in a nondispersive and nonmagnetic medium for the electric and magnetic fields are [11]:

$$H_y\,|_{i+1/2}^{n+1/2} = H_y\,|_{i+1/2}^{n-1/2} + \frac{\Delta t}{\mu_0 \Delta x}\left(E_z\,|_{i+1}^{n} - E_z\,|_{i}^{n}\right), \tag{7.10}$$

$$E_z\,|_{i}^{n+1} = E_z\,|_{i}^{n} + \frac{\Delta t}{\epsilon_0 \epsilon_i \Delta x}\left(H_y\,|_{i+1/2}^{n+1/2} - H_y\,|_{i-1/2}^{n+1/2}\right), \tag{7.11}$$

with ϵ_i the relative permittivity at position $x = i\Delta x$.

Let us now consider the scalar wave equation,

$$\frac{\partial^2 u(x,t)}{\partial x^2} - \frac{\varepsilon}{c^2}\frac{\partial^2 u(x,t)}{\partial t^2} = 0. \tag{7.12}$$

If $\Re(\varepsilon) > 0$, this is an hyperbolic partial differential equation, and it can be shown that its numerical solution, using an explicit finite difference scheme, is conditionally stable. On the other hand, if $\Re(\varepsilon) < 0$, Eq. 7.12 is an elliptic partial differential equation, and its numerical solution cannot be stable using an explicit finite difference scheme.

From a more pragmatic point of view, standard FDTD recursion equations 7.10 and 7.11 for nondispersive materials are obtained using Eq. 7.5, which actually means

$$\mathbf{D}(\omega) = \epsilon_0 \epsilon(\omega) \mathbf{E}(\omega) = \epsilon_0(\epsilon_\infty + \chi(\omega))\mathbf{E}(\omega), \tag{7.13}$$

but we work in the time domain, thus the equation we should use is

$$\mathbf{D}(t) = \epsilon_0(\epsilon_\infty \delta_t + \chi(t)) \otimes \mathbf{E}(t), \tag{7.14}$$

where $\chi(t)$ is the Fourier transform of the susceptibility $\chi(\omega)$, and ϵ_∞ is the value of the permittivity when $\omega \to \infty$. In the nondispersive case, $\chi(t)$ is zero, and the use of Eq. 7.5 is equivalent to Eq. 7.14. On the other hand, if $\chi(t)$ is different from zero, FDTD recursion equations must be rewritten.

Specific methods were developed to deal with this difficulty: the recursive convolution method [12], the auxiliary differential equation method [11], and the Z-transform method [13]. All these methods require the use of analytical laws of dispersion (Debye, Drude, Lorentz) or any linear combination of them [14–16]. Examples of studies made using such combinations with these methods have been published recently for gold [17–19] (Drude and Lorentz), silver [6, 20, 21] (Drude plus one or two Lorentz poles) or aluminum [16] (two Drude terms).

In the following, we will briefly present the two first methods, and a special emphasis will be placed on the recursive convolution method, which we believe to be the more flexible when combinations of dispersion models are to be used.

7.2.2 The Auxiliary Differential Equation Method

From Eq. 7.2 and assuming $\mu = 1$, we obtain Eq. 7.10, noted as

$$H\,|^{n+1/2} = f(H\,|^{n-1/2}, E\,|^{n}). \tag{7.15}$$

From Eq. 7.1 we obtain

$$D\,|^{n+1} = f(D\,|^{n}, H\,|^{n+1/2}). \tag{7.16}$$

To link Eqs. 7.15 and 7.16 (and obtain Eq. 7.11 in the nondispersive case), we need the relation between **E** and **D** as given by Eq. 7.13. Let us consider that the dispersion may be described by the Drude model,

$$\varepsilon(\omega) = 1 - \frac{\omega_{\mathrm{p}}^2}{\omega(\omega + \mathrm{i}\gamma)}, \tag{7.17}$$

with ω_{p} the plasma frequency and γ the damping frequency, we can then rewrite Eq. 7.13 as

$$(-\omega^2 - \mathrm{i}\omega\gamma)\mathbf{D}(\omega) = \epsilon_0(-\omega^2 - \mathrm{i}\omega\gamma + \omega_{\mathrm{p}}^2)\mathbf{E}(\omega). \tag{7.18}$$

After Fourier transforming, integrating and discretizing Eq. 7.18 we finally get

$$E\,|^{n+1} = \frac{-2 + \gamma\Delta t - \omega_{\mathrm{p}}^2\Delta t^2}{2 + \gamma\Delta t + \omega_{\mathrm{p}}^2\Delta t^2} E\,|^{n-1} \tag{7.19}$$

$$+ \frac{4\epsilon_0 E\,|^{n} + (2 + \gamma\Delta t)D\,|^{n+1} - 4D\,|^{n} + (2 - \gamma\Delta t)D\,|^{n-1}}{\epsilon_0(2 + \gamma\Delta t + \omega_{\mathrm{p}}^2\Delta t^2)} \tag{7.20}$$

The computation precedure thus becomes

- $H|^{n+1/2} = f(H|^{n-1/2}, E|^{n})$,
- $D|^{n+1} = f(D|^{n}, H|^{n+1/2})$,
- $E|^{n+1} = f(E|^{n}, E|^{n-1}, D|^{n+1}, D|^{n}, D|^{n-1})$.

To update E, we need to store its values for the two previous time steps, as well as the values of D for the three previous time steps.

An example of application of this method in the case of the creation and diffraction of surface plasmons and the propagation of a light pulse through a metal-coated tip can be found in [22].

7.2.3 The Z-Transform Method

As indicated by its name, this method is based on the properties of the Z-transform. Without entering too deeply in the details of the calculation, if we once again consider that the dispersion can be described using the Drude model as given in Eq. 7.17, transforming Eq. 7.13 into the Z domain leads to [13]

$$D(z) = \epsilon_0 E(z) + z^{-1} S(z), \tag{7.21}$$

where

$$S(z) = \epsilon_0 \frac{\omega_p^2 \Delta t}{\gamma} \left[\frac{1 - e^{-\gamma \Delta t}}{1 - z^{-1}(1 + e^{-\gamma \Delta t}) + z^{-2} e^{-\gamma \Delta t}} \right] E(z). \tag{7.22}$$

We can then deduce that

$$E(z) = \frac{1}{\epsilon_0} (D(z) - z^{-1} S(z)), \tag{7.23}$$

and using the finite difference scheme,

$$E|^{n+1} = \frac{1}{\epsilon_0} (D|^{n+1} - S|^{n}) \tag{7.24}$$

with

$$S|^{n} = (1 + e^{-\gamma \Delta t}) S^{n-1} - e^{-\gamma \Delta t} S \Big|^{n-2} + \epsilon_0 \frac{\omega_p^2 \Delta t}{\gamma} (1 - e^{-\gamma \Delta t}) E \Big|^{n} \tag{7.25}$$

Consequently, the numerical computation flow is now

- $H|^{n+1/2} = f(H|^{n-1/2}, E|^{n})$,
- $D|^{n+1} = f(D|^{n}, H|^{n+1/2})$,
- $S|^{n} = f(S^{n-1}, S|^{n-2}, E|^{n})$,
- $E|^{n+1} = f(D|^{n+1}, S|^{n})$.

To update E, only $D|^{n+1}$ and $S|^n$ are required, but the update of S itself requires the storage of its two previous values.

Recent works using this method include the modeling of gold films properties at infrared frequency [23] and surface plasmon polaritons [24].

7.2.4 The Recursive Convolution Method

The third and final method we will describe in this work was first proposed by Luebbers et al. [12], and is based on the evaluation of the convolution product seen in Eq. 7.14. As a first step, we rewrite this equation as

$$\mathbf{D}(t) = \epsilon_0\epsilon_\infty\mathbf{E}(t) + \epsilon_0\int_{\tau=0}^{t}\mathbf{E}(t-\tau)\chi(\tau)\,\mathrm{d}\tau. \tag{7.26}$$

For $t = n\Delta t$, we can write Eq. 7.26 as

$$\mathbf{D}|^n = \epsilon_0\epsilon_\infty\mathbf{E}|^n + \epsilon_0\int_{\tau=0}^{t}E(n\Delta t-\tau)\chi(\tau)\,\mathrm{d}\tau \tag{7.27}$$

$$= \epsilon_0\epsilon_\infty E|^n + \epsilon_0\sum_{m=0}^{n-1}\int_{m\Delta t}^{(m+1)\Delta t}E(n\Delta t-\tau)\chi(\tau)\,\mathrm{d}\tau. \tag{7.28}$$

If we consider $\mathbf{E}(t)$ as constant on the interval $[m\Delta t,(m+1)\Delta t]$, we can simplify Eq. 7.28 as

$$\mathbf{D}|^n = \epsilon_0\epsilon_\infty\mathbf{E}|^n + \epsilon_0\sum_{m=0}^{n-1}\left(E((n-m)\Delta t)\int_{m\Delta t}^{(m+1)\Delta t}\chi(\tau)\,\mathrm{d}\tau\right). \tag{7.29}$$

By setting

$$\chi^m = \int_{m\Delta t}^{(m+1)\Delta t}\chi(\tau)\,\mathrm{d}\tau, \tag{7.30}$$

we finally get

$$\mathbf{D}|^n = \epsilon_0\epsilon_\infty\mathbf{E}|^n + \epsilon_0\sum_{m=0}^{n-1}\mathbf{E}|^{n-m}\chi^m. \tag{7.31}$$

The discrete form of Eq. 7.1 can then be written

$$\begin{aligned}\nabla\times\mathbf{H}|^{n+1/2} &= \frac{\mathbf{D}|^{n+1}-\mathbf{D}|^n}{\Delta t} + \sigma\mathbf{E}|^{n+1} \\ &= \frac{\epsilon_0}{\Delta t}\left[\left(\epsilon_\infty + \chi^0 + \frac{\sigma\Delta t}{\epsilon_0}\right)\mathbf{E}|^{n+1}\right. \\ &\qquad \left. - \epsilon_\infty\mathbf{E}|^n + \sum_{m=0}^{n-1}\mathbf{E}|^{n-m}.(\chi^{m+1}-\chi^m)\right].\end{aligned} \tag{7.32}$$

After introducing $\Delta\chi^m = \chi^m - \chi^{m+1}$ we finally achieve

$$\mathbf{E}\,|^{n+1} = \frac{\epsilon_\infty}{\epsilon_\infty + \chi^0 + (\sigma\Delta t)/\epsilon_0}\mathbf{E}\,|^{n} + \frac{\Delta t}{\epsilon_0(\epsilon_\infty + \chi^0 + (\sigma\Delta t)/\epsilon_0)}\nabla\times\mathbf{H}\,|^{n+1/2} + \frac{1}{\epsilon_\infty + \chi^0 + (\sigma\Delta t)/\epsilon_0}\sum_{m=0}^{n-1}\mathbf{E}\,|^{n-m}\,\Delta\chi^m. \tag{7.33}$$

We now define $\mathbf{\Psi}$ as

$$\mathbf{\Psi}\,|^{n} = \sum_{m=0}^{n-1} E\,|^{n-m}\,\Delta\chi^m. \tag{7.34}$$

To compute $\mathbf{\Psi}\,|^{n}$, we would need to store all of the previous values of $\mathbf{E}$, which is not realistic. But it can be shown that for materials which dispersion can be described by Debye, Drude, or Lorentz models, $\mathbf{\Psi}$ can be efficiently evaluated through the use of an *recursive accumulator*, which can be written

$$\mathbf{\Psi}\,|^{n} = \Delta\chi^0\mathbf{E}\,|^{n} + C_{\text{rec}}\mathbf{\Psi}\,|^{n-1}, \tag{7.35}$$

with coefficient C_{rec} to be explicited later.

The numerical implementation of the recursive convolution method thus requires the introduction of a new vectorial quantity Ψ, which needs to be computed at the same position as $\mathbf{E}$ in the FDTD grid. In the one-dimensional case, Eq. 7.11 for the computation of the electrical field has then to be replaced by Eqs. 7.35 and 7.33

$$\Psi_z\,|_i^n = C_{\text{rec}}\Psi_z\,|_i^{n-1} + \Delta\chi^0 E_z\,|_i^n, \tag{7.36}$$

$$E_z\,|_i^{n+1} = C_1 E_z\,|_i^n + C_2\left(H_y\,|_{i+1/2}^{n+1/2} - H_y\,|_{i-1/2}^{n+1/2}\right) + C_3\Psi_z\,|_i^n, \tag{7.37}$$

where coefficients C_1, C_2 and C_3 are given by

$$C_1 = \frac{\epsilon_\infty}{\epsilon_\infty + \chi_0 + (\sigma\Delta t)/\epsilon_0}, \tag{7.38}$$

$$C_2 = \frac{\Delta t}{\Delta x\epsilon_0(\epsilon_\infty + \chi^0 + (\sigma\Delta t)/\epsilon_0)}, \tag{7.39}$$

$$C_3 = \frac{1}{\epsilon_\infty + \chi_0 + (\sigma\Delta t)/\epsilon_0}. \tag{7.40}$$

The computation precedure is then summarized as

- $H\,|^{n+1/2} = f(H\,|^{n-1/2}, E\,|^{n})$,
- $\Psi\,|^{n} = f(\Psi\,|^{n-1}, E\,|^{n})$,
- $E\,|^{n+1} = f(E\,|^{n}, H\,|^{n+1/2}, \Psi\,|^{n})$.

Coefficients χ^0, $\Delta\chi^0$, and C_{rec} depend on the model of dispersion. In the following, we will precise these coefficients for the Debye, the Drude, the Lorentz and the Critical Points models.

7.2.4.1 Debye Model

The first model we study is the Debye model,

$$\chi(\omega) = \tilde{\varepsilon}(\omega) - \epsilon_\infty = \frac{\epsilon_s - \epsilon_\infty}{1 - i\tau_0\omega}. \tag{7.41}$$

Its Fourier transform is given by

$$\chi(t) = \frac{\epsilon_s - \epsilon_\infty}{\tau_0} e^{-t/\tau_0} U(t), \tag{7.42}$$

where $U(t)$ is the unit step, and

$$\chi^0 = (\epsilon_s - \epsilon_\infty)(1 - e^{-\Delta t/\tau_0}), \tag{7.43}$$

$$\Delta\chi^0 = (\epsilon_s - \epsilon_\infty)(1 - e^{-\Delta t/\tau_0})^2, \tag{7.44}$$

$$C_{rec} = e^{-\Delta t/\tau_0}. \tag{7.45}$$

Moreover, since the conductivity is equal to zero at $\omega = 0$, we also find that $\sigma = 0$, which simplify coefficients 7.38–7.40.

7.2.4.2 Drude Model

The case of the Drude model can be deduced from the previous case [12]. Indeed, looking at expression 7.17, we can write it as

$$\chi(\omega) = \epsilon(\omega) - \epsilon_\infty = -\frac{\omega_p^2/\gamma}{\gamma - i\omega} - \frac{\omega_p^2/\gamma}{i\omega} = -\frac{\omega_p^2/\gamma^2}{1 - i\omega/\gamma} + i\frac{\omega_p^2/\gamma}{\omega}, \tag{7.46}$$

and by analogy with Eqs. 7.41 and 7.8, we can deduce

$$\epsilon_s - \epsilon_\infty = -\frac{\omega_p^2}{\gamma^2}, \tag{7.47}$$

$$\tau_0 = \frac{1}{\gamma}, \tag{7.48}$$

$$\sigma = \epsilon_0 \frac{\omega_p^2}{\gamma}. \tag{7.49}$$

Consequently,

$$\chi_D^0 = -\frac{\omega_p^2}{\gamma^2}(1 - e^{-\gamma\Delta t}), \tag{7.50}$$

$$\Delta\chi_D^0 = -\frac{\omega_p^2}{\gamma^2}(1 - e^{-\gamma\Delta t})^2, \tag{7.51}$$

$$C_{rec} = e^{-\gamma\Delta t}. \tag{7.52}$$

7.2.4.3 Lorentz Model

For this model,

$$\chi(\omega) = \tilde{\varepsilon}(\omega) - \epsilon_\infty = -\frac{\Delta\epsilon\Omega^2}{\omega^2 - \Omega^2 + \mathrm{i}\Gamma\omega}. \tag{7.53}$$

After introducing $\alpha = \Gamma/2$, $\beta = \sqrt{\Omega^2 - \alpha^2}$, and $\eta = \Delta\epsilon.\Omega^2/\beta$, we can then write

$$\chi(t) = \eta \mathrm{e}^{-\alpha t}\sin(\beta t)U(t). \tag{7.54}$$

As defined by Eq. 7.54, $\chi(t)$ does not have the right properties to be used in the recursive accumulator method, hence we need to define a new quantity $\hat{\chi}(t)$ with the required properties [11, 12],

$$\hat{\chi}(t) = -\mathrm{i}\eta\, \mathrm{e}^{(-\alpha+\mathrm{i}\beta)t}U(t). \tag{7.55}$$

It can be verified that $\chi(t) = \Re(\hat{\chi}(t))$. We finally get

$$\hat{\chi}^0 = -\mathrm{i}\frac{\eta}{\alpha - \mathrm{i}\beta}(1 - \mathrm{e}^{(-\alpha+\mathrm{i}\beta)\Delta t}), \tag{7.56}$$

$$\Delta\hat{\chi}^0 = -\mathrm{i}\frac{\eta}{\alpha - \mathrm{i}\beta}(1 - \mathrm{e}^{(-\alpha+\mathrm{i}\beta)\Delta t})^2. \tag{7.57}$$

Eq. 7.35 is then replaced by

$$\hat{\Psi}\,|^n = \Delta\hat{\chi}^0 E\,|^n + \hat{\Psi}\,|^{n-1}\, \mathrm{e}^{(-\alpha+\mathrm{i}\beta)\Delta t}, \tag{7.58}$$

$\chi^0 = \Re(\hat{\chi}^0)$ is used in Eqs. 7.38–7.40, and $\mathbf{\Psi}\,|^n = \Re(\hat{\mathbf{\Psi}}\,|^n)$ is used in Eq. 7.37. For the reason explained in the Debye case, we also have $\sigma = 0$.

7.2.4.4 Critical Points Model

The critical points model was recently used in conjunction with the Drude model for the description of the gold permittivity [25], and is defined by

$$\chi(\omega) = A\Omega\left(\frac{\mathrm{e}^{\mathrm{i}\phi}}{\Omega - \omega - \mathrm{i}\Gamma} + \frac{\mathrm{e}^{-\mathrm{i}\phi}}{\Omega + \omega + \mathrm{i}\Gamma}\right). \tag{7.59}$$

After rewriting $\chi(\omega)$ as

$$\chi(\omega) = 2A\Omega\left(\cos\phi\frac{\Omega}{\Omega^2 + (-\mathrm{i}\omega + \Gamma)^2}\right. \tag{7.60}$$

$$\left.-\sin\phi\frac{-\mathrm{i}\omega + \Gamma}{\Omega^2 + (-\mathrm{i}\omega + \Gamma)^2}\right), \tag{7.61}$$

we can find its Fourier transform

$$\begin{aligned}\chi(t) &= 2A\Omega\left(\cos\phi\,\mathrm{e}^{-\Gamma t}\sin(\Omega t) - \sin\phi\,\mathrm{e}^{-\Gamma t}\cos(\Omega t)\right)U(t)\\ &= 2A\Omega\,\mathrm{e}^{-\Gamma t}\sin(\Omega t - \phi)U(t).\end{aligned} \tag{7.62}$$

It has a form close to the Fourier transform of a Lorentz term, thus the procedure detailed in the previous section can be applied.

7.2.4.5 Limit Case of Nondispersive Media

It should be noted that Eqs. 7.36 and 7.37 can be used to describe nondispersive media. Starting from the Debye model, we have in this case $\epsilon_s = \epsilon_\infty$, and this implies

$$\chi^0 = 0, \tag{7.63}$$

$$\Delta\chi^0 = 0, \tag{7.64}$$

we can thus deduce the simplified Luebbers coefficients

$$C_1 = 1, \tag{7.65}$$

$$C_2 = \frac{\Delta t}{\Delta x \epsilon_0 \epsilon}, \tag{7.66}$$

$$C_3 = \frac{1}{\epsilon}, \tag{7.67}$$

and $\Psi\,|^n = 0$, thus Eq. 7.37 is equivalent to Eq. 7.11.

7.2.5 Combination of Models

As indicated in the beginning of this section, the models previously described may be used in combination with each others. For example, if we use a combination of Drude and Lorentz models, the permittivity is defined as

$$\epsilon_{\mathrm{DL}}(\omega) = \epsilon_\infty - \frac{\omega_p^2}{\omega^2 + i\gamma\omega} - \sum_i \Delta\epsilon_i \frac{\Omega_i^2}{\omega^2 - \Omega_i^2 + i\Gamma_i\omega}. \tag{7.68}$$

In much the same way, we can combine the Drude and Critical Points models

$$\epsilon_{\mathrm{DCP}}(\omega) = \epsilon_\infty - \frac{\omega_p^2}{\omega^2 + i\gamma\omega} + \sum_i A_i\Omega_i\left(\frac{\mathrm{e}^{i\phi_i}}{\Omega_i - \omega - i\Gamma_i} + \frac{\mathrm{e}^{-i\phi_i}}{\Omega_i + \omega + i\Gamma_i}\right). \tag{7.69}$$

For each term of Eqs. 7.68 or 7.69, a new Ψ has to be defined and updated through Eq. 7.35 or 7.58. After defining

$$\chi^0 = \chi_D^0 + \Re\left(\sum_i \hat{\chi}_i^0\right), \tag{7.70}$$

we can finally write the update equation for E as

$$\begin{aligned}\mathbf{E}\,|^{n+1} &= \frac{\epsilon_\infty}{\epsilon_\infty + \chi^0 + (\sigma\Delta t)/\epsilon_0}\mathbf{E}\,|^n + \frac{\Delta t}{\Delta x \epsilon_0(\epsilon_\infty + \chi^0 + (\sigma\Delta t)/\epsilon_0)}\nabla\times\mathbf{H}\,|^{n+1/2} \\ &+ \frac{1}{\epsilon_\infty + \chi^0 + (\sigma\Delta t)/\epsilon_0}\left(\Psi_D\,|^n + \Re\sum_i \hat{\Psi}_i\,|^n\right).\end{aligned} \tag{7.71}$$

The choice of the model and the number of terms to use are strongly dependent on the material to study, but also on the range of wavelengths of interest. Large intervals may require many additional term to the Drude one [26], thus rapidly increasing the memory requirement of the computation.

7.2.6 Examples of Permittivities Description

We present here some examples of model choice. The parameters of the different models were optimized through the minimization of a fitness function Φ [17] defined as

$$\Phi = \sum_\omega |\epsilon_\mathrm{T}(\omega) - \epsilon_\mathrm{model}(\omega)|^2, \tag{7.72}$$

with ϵ_T the values tabulated in [27]. For our first example, we study silver for wavelengths between 400 and 800 nm. Silver is often described using a single Drude model, and the result of the optimization is depicted on Fig. 7.1a. The agreement seems good. Nevertheless, looking on the relative errors for both the real and imaginary parts, on Fig. 7.1b, we see that the imaginary part of the permittivity is actually not accurately described. To improve the description, we add a lorentzian term, and results presented in Fig. 7.2a and b show that the accuracy has been improved. Parameters for the models are given in Table 7.1, as well as the value of the fitness function Φ. Using the Drude–Lorentz model, Φ is divided by 3.

Our second example deals with the description of the permittivity of aluminum for wavelengths between 500 and 1000 nm. Starting directly with the Drude–Lorentz, results presented in Fig. 7.3a and b show that the agreement is not as good as expected. On the other hand, using the Drude-Critical point model, the agreement is fairly good, as it can be seen on Fig. 7.4a and b. The improvement of the description is once again suported by Table 7.1, where we can see that the value of Φ has been divided by 10.

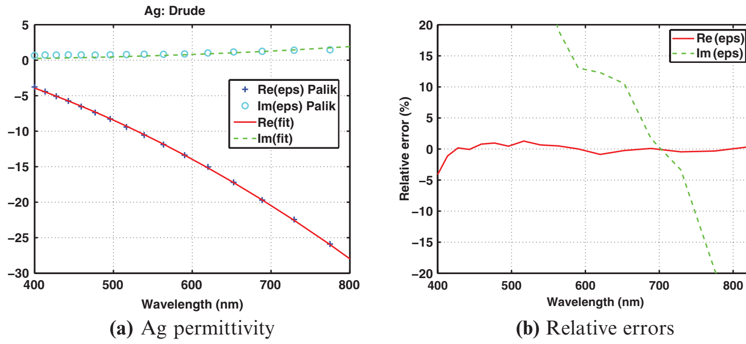

(a) Ag permittivity **(b)** Relative errors

Fig. 7.1 Silver permittivity and relative error on both real and imaginary part using the Drude model. (**a**) Crosses and circles respectively depict the real and imaginary part of the permittivity tabulated in [27]. The dashed and solid lines respectively show the imaginary and real part of the fitted permittivity. (**b**) The solid and dashed line respectively depict the relative error on the real and imaginary part of the fitted permittivity

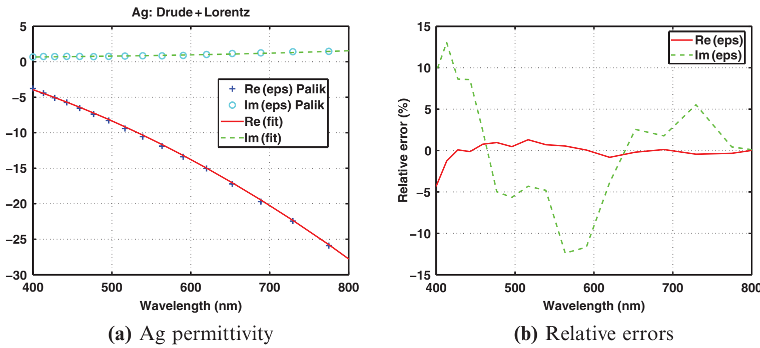

(a) Ag permittivity **(b)** Relative errors

Fig. 7.2 Silver permittivity and relative error on both real and imaginary part using the Drude–Lorentz model. (**a**) Crosses and circles respectively depict the real and imaginary part of the permittivity tabulated in [27]. The dashed and solid lines respectively show the imaginary and real part of the fitted permittivity. (**b**) The solid and dashed line respectively depict the relative error on the real and imaginary part of the fitted permittivity

Table 7.1 Optimized parameters of the Drude, Drude–Lorentz and Drude-Critical Points models for silver and aluminum

	Silver (400–800 nm)		Aluminum (500–1000 nm)	
	Drude	Drude+Lorentz	Drude+Lorentz	Drude+CP
ϵ_∞	4.1028	3.91	8.5116	1.0000
ω_p (THz)	13362	13420	20876	20951
γ (THz)	140.67	84	0.039	219.06
$A_1 - \Delta\epsilon_1$	–	0.76	20.2856	6.8011
Ω_1 (THz)	–	6870	2443.8	2270.9
Γ_1 (THz)	–	12340	1130.0	376.66
ϕ_1 (rad)	–	–	–	−0.4780
Φ	1.7695	0.5349	375.8	38.4

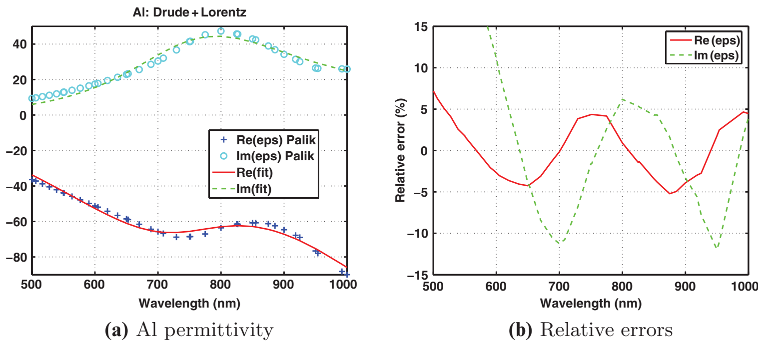

(a) Al permittivity **(b)** Relative errors

Fig. 7.3 Aluminum permittivity and relative error on both real and imaginary part using the Drude–Lorentz model. (**a**) Crosses and circles respectively depict the real and imaginary part of the permittivity tabulated in [27]. The dashed and solid lines respectively show the imaginary and real part of the fitted permittivity. (**b**) The solid and dashed line respectively depict the relative error on the real and imaginary part of the fitted permittivity

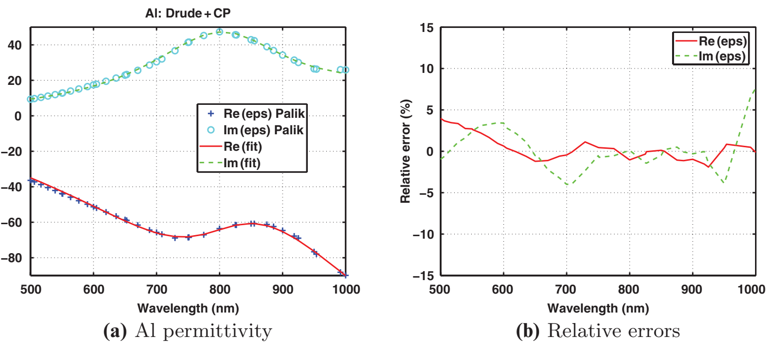

(a) Al permittivity **(b)** Relative errors

Fig. 7.4 Aluminum permittivity and relative error on both real and imaginary part using the Drude–CP model. (**a**) Crosses and circles respectively depict the real and imaginary part of the permittivity tabulated in [27]. The dashed and solid lines respectively show the imaginary and real part of the fitted permittivity. (**b**) The solid and dashed line respectively depict the relative error on the real and imaginary part of the fitted permittivity

7.2.7 Conclusion

In this section, we have presented the main steps required for the description and the modeling of dispersive media in the framework of the FDTD method. The recursive convolution method is a versatile tool that can easily take into account the combinations of dispersion models. The efficieny of the description of the permittivity strongly depends on the models used and on the wavelength range, and the number of dispersive terms has to be carefully chosen, as it has a direct influence on the memory requirements of the computation. The accuracy of the computation is then strongly dependant on the quality of the fit of the permittivity.

7.3 Near-Field Optical Properties of Single Plasmonic Nanowires

The problem of the electromagnetic energy transport through metallic nano-wires has been recently treated in several experimental and theoretical works [2, 3, 6, 28]. The authors have shown that the employment of such nanostructures could allow to achieve nanoscale propagators of the optical information or surface plasmon resonators.

In this part, we numerically demonstrate the role of the surface plasmons in metallic nanowires deposited on a dielectric substrate. The nanowires are silver metallic elongated cylinders of diameter smaller than the incident wavelength. We determine the propagation conditions of a local excitation along the nanowires by computing the near-field distribution above the nanowire when one end is locally illuminated by a focused gaussian beam. The studied geometry is depicted in Fig. 7.5. To treat this complex problem, we achieve numerical simulations from a FDTD method. We take care of the dispersive properties of the metal by using the recursive convolution method described in Sect. 7.2.4 with the optimized Drude–Lorentz

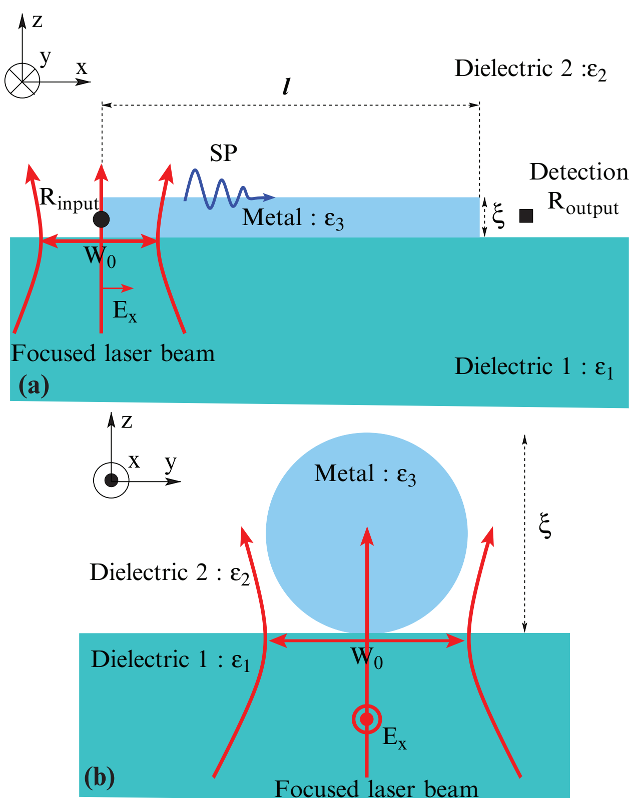

Fig. 7.5 Side view (**a**) and cross-section (**b**) of the local illumination of a cylindrical nanowire by a focused gaussian beam

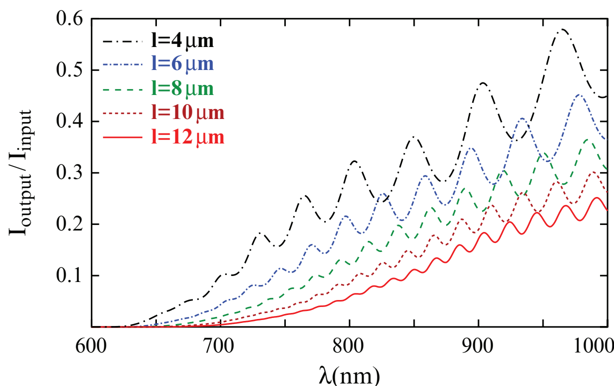

Fig. 7.6 Normalized transmittance spectra computed for five different lengths of silver nanowires. The length increases from $l = 4\,\mu$m to $l = 12\,\mu$m. The wire diameter has been fixed to 120 nm and the polarization of the incident electric field is parallel to the main axis of the nanowire (longitudinal mode)

coefficients in Table 7.1 for only one Lorentz pole, and Eq. 7.68 becomes

$$\epsilon_{\mathrm{DL}}(\omega) = \epsilon_\infty - \frac{\omega_{\mathrm{D}}^2}{\omega(\omega + \mathrm{i}\gamma_{\mathrm{D}})} - \frac{\Delta\varepsilon\Omega_{\mathrm{L}}^2}{(\omega^2 - \Omega_{\mathrm{L}}^2) + \mathrm{i}\Gamma_{\mathrm{L}}\omega}, \tag{7.73}$$

where Ω_{L} and Γ_{L} represent the frequency and the spectral width of the Lorentz oscillator. The parameters ω_{D} and γ_{D} are the usual constants of the Drude model, and $\Delta\varepsilon$ characterizes the strength of the Lorentz oscillator.

7.3.1 The Near-Field Transmission Coefficient of a Single Silver Nanowire

To visualize the guiding efficiency of a single silver nanowire, we present in Fig. 7.6 a study of the near-field optical transmittance versus the incident wavelength λ of the excitation beam. The spectra have been plotted for five increasing wire lengths from $l = 4\,\mu$m to $l = 12\,\mu$m. The diameter is fixed at $\xi = 120$ nm. The wire lies on a glass substrate ($\varepsilon_1 = 2.25$) and is surrounded by air ($\varepsilon_2 = 1$). The illumination light is a gaussian laser beam focused at its input end. The beam waist is set to $w_O = 1.5\,\mu$m and the electric field polarization is aligned along the main axis of the nanowire. Thus, the near-field optical transmittance can be defined by the dimensionless quantity

$$T(\lambda) = \frac{\mathrm{I}_{\mathrm{output}}}{\mathrm{I}_{\mathrm{input}}} = \frac{|\mathbf{E}(\mathbf{R}_{\mathrm{output}}, \lambda)|^2}{|\mathbf{E}(\mathbf{R}_{\mathrm{input}}, \lambda)|^2}, \tag{7.74}$$

where $\mathbf{E}(\mathbf{R}_{\text{output}},\lambda)$ represents the electric field computed at the nanowire exit ($\mathbf{R}_{\text{output}}$) and $\mathbf{E}(\mathbf{R}_{\text{input}},\lambda)$ the incident electric field computed at $\mathbf{R}_{\text{input}}$ in the absence of the nanowire. The position of the vector $\mathbf{R}_{\text{input}}$ has been placed at the center of the enter side of the nanowire while the output observation point $\mathbf{R}_{\text{output}}$ has been shifted of 100 nm from its exit side. Let us note that the influence of integrating or not the optical near-field over the complete area of the side exit of the nanowire does not lead to a significant change of the signature of the near-field optical transmittance.

In fairly good agreement with experimental data reported in [28], we observe that the excitation of the structure gives rise to large band spectra superimposed by a weak modulation. The spectra of nanowires reveal a longitudinal mode structure characterized by regular increasings of the signal. Indeed, it has been shown that silver nanowire can be considered as a plasmonic Fabry–Perot cavity [28].

7.3.2 Comparison with a Discontinuous Nanostructure

To highlight the difference between the previous geometry (continuous case) and a discontinuous one, we now study a chain of metallic nanoparticles (see Fig. 7.7). The chain consists in fifteen gold dots with a square base ($l \times l = 100 \times 100\,\text{nm}^2$) and 40 nm high.

The previous results (Fig. 7.6) showed a weakly modulated large band in the transmittance spectra of the silver nanowire. On the contrary, the transmittance spectrum of discontinuous nanostructures (Fig. 7.8) reveals a narrow band [29]. Indeed, two different phenomena leads to the optical information transport along continuous and discontinuous nanostructures. For the continuous case, the surface plasmon propagation allows this transfer whereas it is achieved by the coupling of all the localized surface plasmon in the discontinuous nanostructures [30].

The behavior of the transmittance spectrum of a chain against its length has been demonstrated in a previously published work [31], where the length of the chain was changed by controlling the number of metallic dots and letting the others parameters unchanged. Thus, Girard et al. have shown that the position and the shape of the narrow band in the spectrum do not depend on the length of the chain. Only the mean value of the transmittance is modified with the varying of the chain's length.

In contrast to that work, we control the length of the chain by varying the spacing between the nanodots from $e = 50\,\text{nm}$ to $e = 100\,\text{nm}$ for the geometry depicted in Fig. 7.7. This method also allows to study the effect of the coupling between the metallic dots on the transmittance spectrum for such a nanostructure.

The study of the spacing between the dots of the chain leads to the same comment than in [31]. In Fig. 7.8, we also demonstrate that the efficiency of the transmittance decreases when the spacing increases. In fact, the coupling between the surface plasmon localized on each dot is weaker when the spacing increases.

To conclude this brief comparison, it clearly appears that the physical phenomena leading to the optical information's transfer are drastically different for continuous and discontinuous nanostructures.

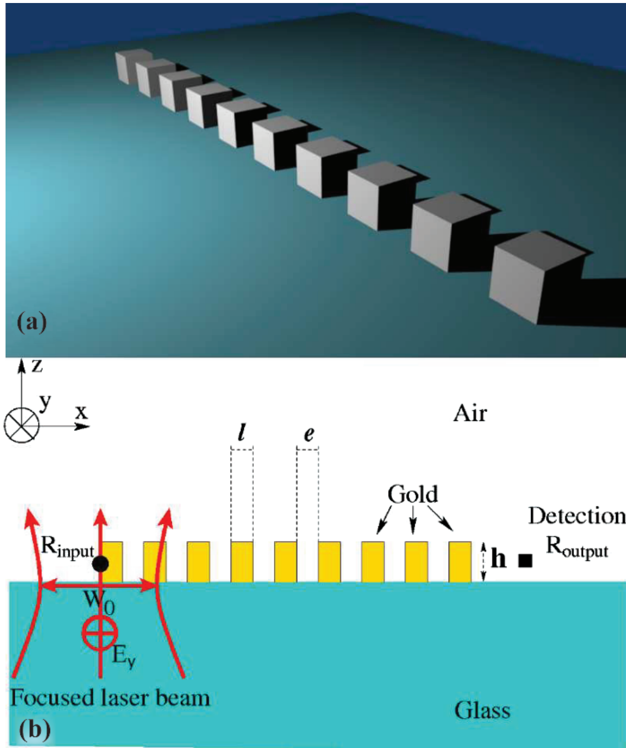

Fig. 7.7 Perspective view (**a**) and cross-section (**b**) of a discontinuous metallic nanostructure illuminated by a focused gaussian beam. This nanostructure is a chain of 15 gold nanodots ($h = 40$ nm and $l \times l = 100 \times 100\,\text{nm}^2$). The spacing between the dots vary from $e = 50$ nm to $e = 100$ nm

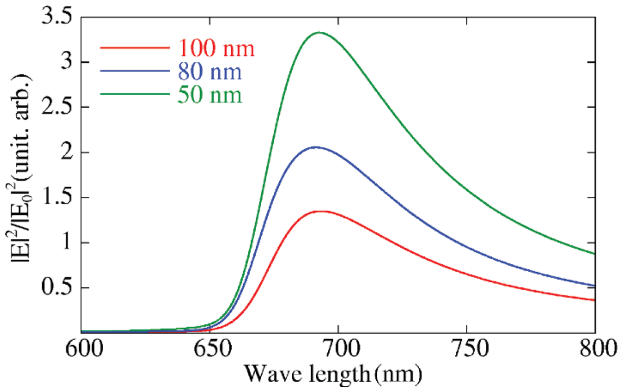

Fig. 7.8 Normalized transmittance spectra computed for three different spacing between gold dots of chain. The spacing increases from $e = 50$ nm to $l = 100$ nm. The polarization of the incident electric field is perpendicular to the main axis of the chain

7.3.3 The Origin of the Guiding in a Single Silver Nanowire

In the continuous nanostructure described in Fig. 7.5, an interaction arises between the incident and reflected surface plasmons on both extremities of the wire. This leads to an interference pattern located along the nanowire as depicted in Fig. 7.9. This figure presents a map of the optical near-field intensity. For computing this electric field intensity map, we have stored the three electromagnetic field components in a plane located at 200 nm from the top of the silver nanowire. For this study, both wire length and diameter are fixed respectively to $l = 12\,\mu\text{m}$ and $\xi = 120\,\text{nm}$. We have also tuned the incident wavelength to $\lambda = 785\,\text{nm}$ and kept the others parameters unchanged. In Fig. 7.9, we observe the neat interference pattern due to the incident and reflected plasmon coupling above the nanowire ($x < 12\,\mu\text{m}$).

To calculate the plasmon effective wavelength for that nanowire, we have drawn a cross-section at $y = 0$ of the normalized intensity depicted in Fig. 7.9 for x varying from $x = 7.5\,\mu\text{m}$ to $x = 10.5\,\mu\text{m}$. This cross-section is shown in Fig. 7.10. We extract from these data the interfringe spacing and deduce the surface plasmon effective wavelength in Eq. 7.75,

$$\lambda_{sp} = 2\Lambda, \tag{7.75}$$

where Λ is the interfringe spacing and λ_{sp} is the effective surface plasmon wavelength. From the interfringe spacing in Fig. 7.10, we have found a surface plasmon effective wavelength equal to 430 nm. Although higher than the experimental effective wavelength $\lambda_{sp-exp} = 414\,\text{nm}$ found in [28], the theoretical value remains significantly shorter than the excitation wavelength ($\lambda = 785\,\text{nm}$). Thus, it is straightforward that the surface plasmon is not a single mode neither in air (index equal to 1) nor in the glass substrate (index equal to 1.5 that is to say $\lambda_{sp} = 523\,\text{nm}$).

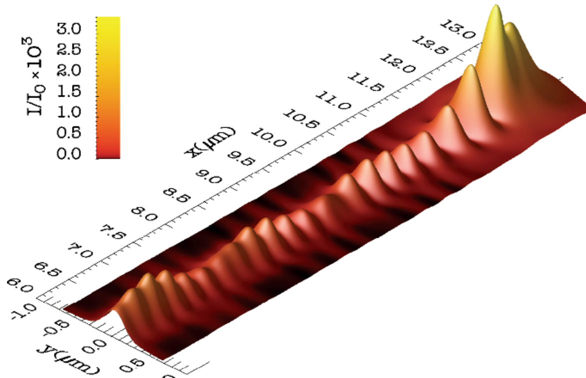

Fig. 7.9 Normalized intensity ($|E^2|$) above the end of a 12 µm length and 120 nm diameter silver wire. The observation plane is located at 200 nm from the wire's top. We have chosen the origin of the x-axis at the input end of the wire and the y-axis one at the wire center. The excitation light is a gaussian beam focused around the input face of the silver wire. The incident fiel has a wavelength equal to 785 nm and is polarized along x-axis

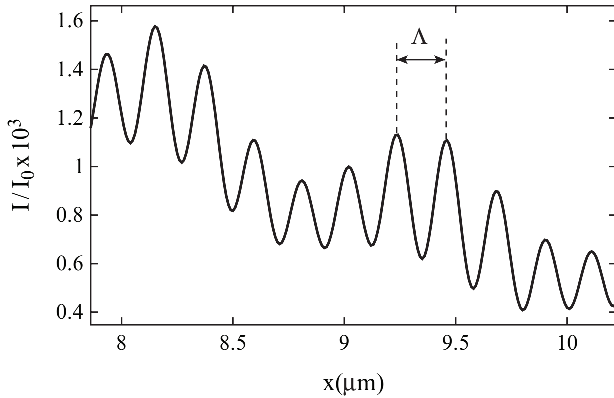

Fig. 7.10 Cross-section at $y = 0$ of the normalized intensity ($|E^2|$) depicted in Fig. 7.9 for x increases from $x = 7.5\,\mu$m to $x = 10.5\,\mu$m. the origin of the x-axis at the input end of the wire. Λ is the interfringe spacing

Indeed the effective index of the surface plasmon is 1.82. So this mode cannot be directly generated by the far field excitation and only occur by dint of the diffraction of the source at the input face of the nanowire.

In the field map of Fig. 7.9, we can observe an enhanced field intensity located at the output extremity of the wire ($x > 12\,\mu$m). This enhancement reveals the surface plasmon diffraction at the output side of the silver nanowire. This scattered field could provide a versatile mean to control a localized source in coplanar geometry.

In such a plasmonic cavity, the excitation of allowed surface plasmon modes depends on both the nanowire length (l) and the incident wavelength (λ). This behavior has been observed in Fig. 7.6. As expected intuitively, the number of available modes increases with the nanowire length with a simultaneous damping owing to ohmic losses. We observed also in Fig. 7.6 that the modulation depth ΔI (see also Fig. 7.11) increases with the wavelength. The relative modulation depth defined by $\Delta I/I_{\min}$ can be fairly well fitted by a simple Fabry–Perot cavity law expressed as a function of the propagation loss parameter $A = \exp(-l/L)$ (where L is the propagation length of the surface plasmon mode and R represents the reflectivity) in Eq. 7.76

$$\frac{\Delta I}{I_{\min}} = \frac{4RA}{(1-RA)^2}. \tag{7.76}$$

The two parameters L and R can be calculated by studying the five transmittance spectra of Fig. 7.6. The relative modulation depth is obtained from these spectra and then reported in Fig. 7.11, in which the inset indicates the procedure we used to define ΔI and $I/I_{\min}$ (once again, the wavelength has been fixed at $\lambda = 785$ nm). In Fig. 7.11, where these values are schematized by black crosses, we have also represented (with a solid line) the Fabry–Perot law of Eq. 7.76 by fitting the couple of parameters L and R. This method yields the values of $R = 0.21$ and $L = 3.16\,\mu$m.

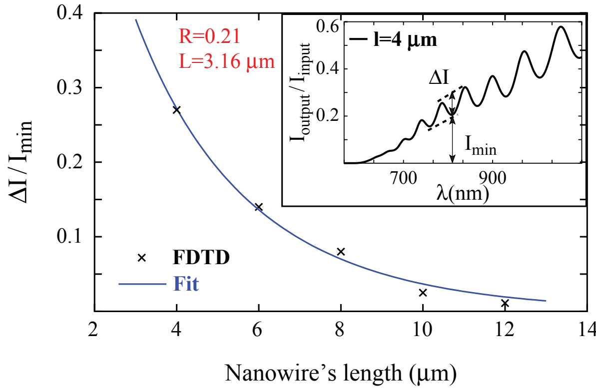

Fig. 7.11 Spectral relative modulation depth ($\Delta I/I_{\text{min}}$) at a wavelength equal to 785 nm versus nanowire length. The crosses give the theoretical values obtained by FDTD computation for five different lengths of nanowire with diameter equal to 120 nm. The solid line is the fit of the Fabry–Perot cavity model. The inset (normalized transmittance spectra computed for 4 µm long nanowire) shows the measure of ΔI and I_{min}

Although the numerical propagation length (computed here with Palik's silver data) is three times weaker than the experimental value measured in [28], our results confirm that silver nanowires behave as efficient optical resonators.

7.3.4 Conclusion

In this part, we have simulated the electromagnetic field transfer along a metallic nanowire deposited on a dielectric substrate. Our FDTD study confirm the experimental results about the similarity between metallic nanowires and Fabry–Perot cavities. We have also compared the behavior of such a nanostructure with a discontinuous one. Unlike what happens with chains of nanoparticles which open a narrow band [31], the spectra of nanowires reveal the longitudinal mode structure. As expected, by using the bulk permittivity of silver, we have found an effective surface plasmon wavelength and a propagation length of the surface plasmon mode which differ from the experimental ones for a single silver nanowire. In fact, by introducing bulk dielectric data in our FDTD code, the metal is treated as an amorphous medium so they do not completely match the monocrystalline features of silver wire used in [28]. Since the dielectric constant in visible range of such photonic elements is not well known in the literature, the numerical scheme described in this part could be used to fit parameters able to provide the permittivity of monocrystalline metallic nanostructures. For example, this might be realized by varying the mean free path of the electrons in the Drude–Lorentz model (through γ_{D}, Γ_{L}) used in this study. This is the topic of our next section.

7.4 Further Improvements of the Dispersion Models in Order to Take into Account the Fabrication Process of the Nanoscale Structures

The usual tabulated data of the permittivity [27, 32–34] are defined for bulk thin layer but always for amorphous materials. Although this values are commonly employed in most of the simulations about optical dispersive phenomena in nanostructures, they should not be used for all cases. Indeed, we have seen in Sect. 7.3 that they do not lead to the experimental value of propagation length of the surface plasmon for a single monocrystalline silver nanowire. So, we have to take into account the fabrication process in the nano-optic simulation. In fact, each process provide a peculiar crystalline structure, which leads to a specific optical dispersive behavior.

In this part, we demonstrate a efficient mean to obtain theoretical results in better agreement with experimental ones for a monocrystalline nanostructure. Further, this method enables us to determine the real permittivity of the nano-structured material.

7.4.1 A Mean to Adapt the Tabulated Permittivities to a Specific Nanostructure

A large part of the nano-optic community agrees that the permittivity of nanostructured objects dissent from the bulk values. In metallic nanostructures, the mean free path of the electrons is modified when the size of the structure decreases. This phenomena should increase the damping inside the nanostructure and thus change the permittivity [35].

In our case, the silver nanowire depicted in Fig. 7.5 is a monocrystalline nanostructure. So, the previous argument does not work here. Indeed, the mean free path increases because of the absence of the crystalline domains walls. However, the approach is fairly similar to the one used for the damping phenomena [35]. Instead of modify the damping of the Drude and Lorentz models to decrease the mean free path of the electrons, we increase it.

To achieve this for the silver nanowire, we multiply the previous Drude–Lorentz constants γ_D ans γ_L in Table 7.1 by a constant κ and Eq. 7.73 becomes

$$\epsilon_{DL}(\omega) = \epsilon_\infty - \frac{\omega_D^2}{\omega(\omega + i\kappa\gamma_D)} - \frac{\Delta\epsilon\Omega_L^2}{(\omega^2 - \Omega_L^2) + i\kappa\Gamma_L\omega}. \tag{7.77}$$

In order to verify that only the imaginary part of the permittivity is significantly modified, we plot the real and imaginary parts of the permittivity against the excitation wavelength for three values of κ (see Fig. 7.12).

In Fig. 7.12a, the real part of the silver's permittivity is fairly the same whatever be the κ coefficient. On the contrary, we show in Fig. 7.12b that the mean of the imaginary part decrease with the value of κ all along the wavelength range.

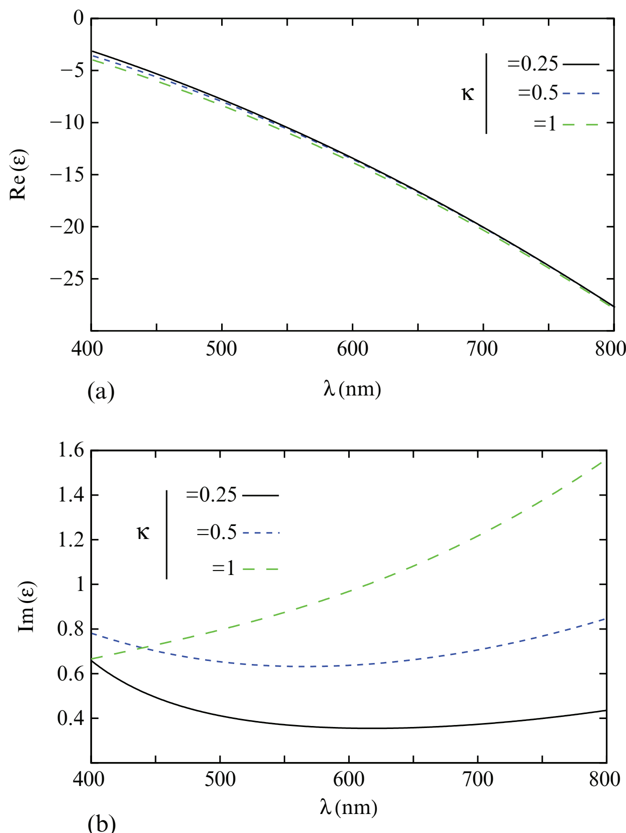

Fig. 7.12 Fit of the silver's permittivity. The mean free path correction is taken into account with the parameter κ. There is no correction when $\kappa = 1$. (**a**) Fit of the real part of the permittivity ans (**b**) for the imaginary one

However, even if this method allows us to theoretically control the mean free path of the electron in silver, we are not yet able to find the value of κ, which match the permittivity of single monocrystalline silver nanowire. To this end, we have to employ an empiric method. Otherwise said, we try to match experimental results by varying the κ coefficient in our numerical computation.

7.4.2 Influence of the Mean Free Path on the Guiding Efficiency for a Single Silver Nanowire

Once again, we numerically study the transmittance spectra of the single silver nanowire depicted in Fig. 7.5 but we now care about the influence of the mean free path of the electrons on the surface plasmon guiding efficiency. Indeed, we

demonstrated that the theoretical and experimental propagation lengths differ when the tabulated permittivity are used to simulate the dispersive aspect of silver (see Sect. 7.3.3). Here, we increase the mean free path to take into account the monocrystalline behavior of the nanowire. For each values of κ ($\kappa = \{0.25, 0.5, 1\}$), we apply the same procedure as in Sect. 7.3.3 in order to compute the spectral modulation depth versus the nanowire's length. We show these results in Fig. 7.13 for a wavelength equal to 785 nm.

The previous result obtained for $\kappa = 1$ in Fig. 7.11 is plotted in Fig. 7.13 with stars for FDTD results and with double dotted dashed line for the Fabry–Perot fit. We also plot the fit of the experimental results found in [28] with solid line. It may be seen in Fig. 7.13 that the mean value of the spectral relative modulation depth increases when the value of κ decreases. Moreover, the calculation of the different fits shows that the reflectivity and the propagation length of the surface plasmon increase too. In Table 7.2, we summarize the coefficient of the fit for each value of κ as well as the experimental results of [28].

It may be seen that the reflectivity and the propagation length are in good agreement with the experimental ones when $\kappa = 0.25$. This result allows to define a new

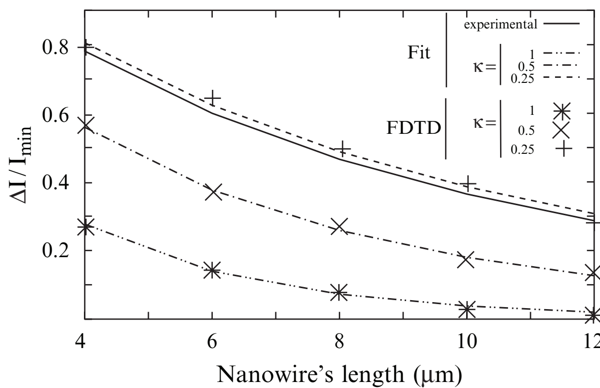

Fig. 7.13 Spectral relative modulation depth at a wavelength equal to 785 nm versus nanowire length for several values of the κ coefficient. The different crosses give the theoretical values obtained by FDTD computation for each value of κ. The different lines are the fits of the Fabry–Perot cavity model for each value of κ. The solid line is the fit of the experimental values obtained in [28]

Table 7.2 Reflection coefficient and propagation length of surface plasmon in a single silver nanowire for several values of κ

κ	R	L (μm)
1	0.21	3.16
0.5	0.213	6.1
0.25	0.217	10.2
Experimental	0.216	10.1

The experimental line of this table summarize the values found in [28]

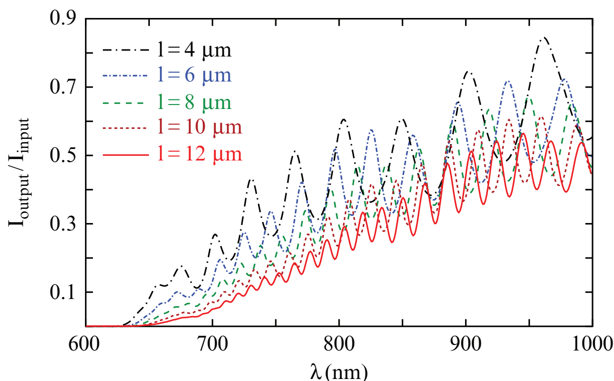

Fig. 7.14 Normalized transmittance spectra computed for five different lengths of silver nanowires. The configuration is the same as in Fig. 7.6. The dispersive aspect is taken into account with $\kappa = 0.25$

permittivity for the single monocrystalline silver nanowire, which is given by the solid line in Fig. 7.12a for the real part and in Fig. 7.12b for the imaginary part. We have also computed the transmittance spectra for five different lengths of silver nanowire, results are displayed in Fig. 7.14. For all lengths, the modulation depth is greater than the one found with $\kappa = 1$ in Fig. 7.6. Moreover, the mean value of the transmittance is higher whatever be the length of the nanowire.

7.4.3 Conclusion

In this part, we have adapted the common tabulated permittivity to simulate a specific experimentation. We demonstrated a numerical method leading to a better correlation between experimental and theoretical results and we are now able to describe the propagation of surface plasmons on a monocrystalline metallic nanowire, in good agreement with experiments.

Our method is still in its early stage of development, as we used the same empirical parameter to modify both the Drude and the Lorentz parts of the permittivity. In further studies, different parameters could be employed for each term of the permittivity. The optimization of these parameters would require the use of specific methods like evolutionary algorithms, already successfully applied to the recovering of different kind of nanostructures properties [36].

7.5 Concluding Remarks

An FDTD approach has been presented for the study of the dispersive properties of metallic nanostructures with particular interest in monocrystalline silver nanowires.

In Sect. 7.2, we described several numerical methods to take into account the dispersion of the permittivity in FDTD calculations. These methods are mainly based on the common dispersive models (e.g., Drude or Lorentz model) as well as the recently introduced critical points model. We also discussed the validity of these models for silver and aluminium.

In Sect. 7.3, we applied the previous dispersive numerical method (the recursive convolution method associated to Drude–Lorentz model) to study the dispersive properties of a silver nanowire. We showed that the physical phenomena yielding an optical information transfer along metallic nanostructures are drastically different in continuous and discontinuous configurations. In fact, this transfer is achieved by surface plasmon propagation in continuous nanostructures whereas it is the coupling between the surface plasmon on each particle in the discontinuous case. The silver nanowire can be compared to a Fabry–Perot cavity, and numerical results are qualitatively in fairly good agreement with the experiment. However, the experimental parameters fitting the behavior of the nanowire significantly dissent from the numerical ones. Indeed, the simulated experiment takes into account a monocrystalline nanowire whereas we use the bulk permittivity commonly tabulated for our numerical simulations.

In Sect. 7.4, we demonstrated a method to simulate the monocrystalline property of the nanowire. We showed that we are able to describe this property starting from the bulk permittivities by modifying the damping in dispersive models. By decreasing the damping, we obtained numerical results in better agreement with the experimental ones. This emphasize the fact that the permittivity of a nanostructure may be different from the corresponding bulk, and the numerical method outlined in Sect. 7.4 provides a first approach to the estimation of the effective permittivity of the
nanostructure.

We have highlighted the paramount character of the crystalline property in the understanding of nanostructures behavior. In several fabrication process, properties of nanostructures drastically differ from those of the bulk counterparts. Therefore, we do not afford to simulate all nanostructures by using tabulated permittivity and we have to take an interest in the crystalline properties of the nanostructures.

References

1. K. Imura, T. Nagahara, and H. Okamoto. Plasmon mode imaging of single gold nanorods. *J. Am. Chem. Soc.*, 126:12730–12731, 2004.
2. K. Imura, T. Nagahara, and H. Okamoto. Near-field optical imaging of plasmon modes in gold nanorods. *J. Chem. Phys.*, 122:154701, 2005.

3. R.M. Dickson and L.A. Lyon. Unidirectional plasmon propagation in metallic nanowires. *J. Phys. Chem. B*, 104:6095–6098, 2000.
4. J.C. Weeber, A. Dereux, C. Girard, J.R. Krenn, and J.-P. Goudonnet. Plasmon polaritons of metallic nanowires for controlling submicron propagation of light. *Phys. Rev. B*, 60: 9061–9067, 1999.
5. C. Girard. Near fields in nanostructures. *Rep. Prog. Phys.*, 68:1883–1933, 2005.
6. T. Laroche and C. Girard. Near-field optical properties of single plasmonic nanowires. *Appl. Phys. Lett.*, 89:233119, 2006.
7. F.I. Baida and D. Van Labeke. Three-dimensional structures for enhanced transmission through a metallic film: annular aperture arrays. *Phys. Rev. B*, 67:155314, 2003.
8. T. Laroche, F.I. Baida, and D. Van Labeke. Three-dimensional finite-difference time domain study of enhanced second-harmonic generation at the end of a apertureless scanning near-field optical microscope metal tip. *J. Opt. Soc. Am. B*, 22:1045–1051, 2005.
9. A.-S. Grimault, A. Vial, and M. Lamy de la Chapelle. Modeling of regular gold nanostructures arrays for SERS applications using a 3D FDTD method. *Appl. Phys. B* 84(1–2):111–115, 2006.
10. K.S. Yee. Numerical solution of initial boundary value problems involving Maxwell's equations in isotroptic media. *IEEE T. Antenn. Propag.*, 14:302–307, 1966.
11. A. Taflove and S.C. Hagness. *Computational Electrodynamics: The Finite-Difference Time Domain Method*, 2nd ed. Artech House, Boston, 2000.
12. K.S. Kunz and R.J. Luebbers. *The Finite-Difference Time-Domain Method for Electromagnetics*. CRC Press, New York, 1993.
13. D.M. Sullivan. *Electromagnetic Simulation Using the FDTD Method*. Wiley-IEEE Press, 2000.
14. M.C. Beard and C.A. Schmuttenmaer. Using the finite-difference time-domain pulse propagation method to simulate time-resolved THz experiments. *J. Chem. Phys.*, 114(7):2903–2909, 2001.
15. M. Moskovits, I. Srnová-Sloufová, and B. Vlcková. Bimetallic ag-au nanoparticles: extracting meaningful optical constants from the surface-plasmon extinction spectrum. *J. Chem. Phys.*, 116(23):10435–10446, 2002.
16. N.G. Skinner and D.M. Byrne. Finite-difference time-domain analysis of frequency-selective surfaces in the mid-infrared. *Appl. Opt.*, 45(9):1943–1950, 2006.
17. A. Vial, A.-S. Grimault, D. Macías, D. Barchiesi, and M. Lamy de la Chapelle. Improved analytical fit of gold dispersion: application to the modelling of extinction spectra with the FDTD method. *Phys. Rev. B*, 71(8):085416–085422, 2005.
18. T. Grosges, A. Vial, and D. Barchiesi. Models of near-field spectroscopic studies: comparison between finite-element and finite-difference methods. *Opt. Express*, 13(21):8483–8497, 2005.
19. A. Hohenau, J.R. Krenn, J. Beermann, S.I. Bozhevolnyi, S.G. Rodrigo, L. Martin-Moreno, and F. Garcia-Vidal. Spectroscopy and nonlinear microscopy of au nanoparticle arrays: experiment and theory. *Phys. Rev. B*, 73(15):155404, 2006.
20. T.-W. Lee and S.K. Gray. Subwavelength light bending by metal slit structures. *Opt. Express*, 13(24):9652–9659, 2005.
21. H. Ibn El Ahrach, R. Bachelot, A. Vial, G. Lérondel, J. Plain, P. Royer, and O. Soppera. Spectral degeneracy breaking of the plasmon resonance of single metal nanoparticles by nanoscale near-field photopolymerization. *Phys. Rev. Lett.*, 98(10):107402, 2007.
22. G. Parent, D. Van Labeke, and F.I. Baida. Theoretical study of transient phenomena in near-field optics. *J. Microsc.*, 202(2):296–306, 2001.
23. R. Qiang, R.L. Chen, and J. Chen. Modeling electrical properties of gold films at infrared frequency using fdtd method. *Int. J. Infrared Millimeter Waves*, 25(8):1263–1270, 2004.
24. A. Mohammadi and Mario Agio. Dispersive contour-path finite-difference time-domain algorithm for modelling surface plasmon polaritons at flat interfaces. *Opt. Express*, 14(23): 11330–11338, 2006.
25. P.G. Etchegoin, E.C. Le Ru, and M. Meyer. An analytic model for the optical properties of gold. *J. Chem. Phys.*, 125:164705, 2006.

26. C.F. Bohren and D.R. Huffman. *Absorption and Scattering of Light by Small Particles*. Wiley, 1983.
27. E.D. Palik, editor. *Handbook of Optical Constants of Solids*. Academic Press, 1985.
28. H. Ditlbacher, A. Hohenau, D. wagner, U. Kreibig, M. Rogers, F. Hofer, F.R. Aussenegg, and J.R. Krenn. Silver nanowires as surface plasmon resonators. *Phys. Rev. Lett.*, 95:257403, 2005.
29. P. Ghenuche, R. Quidant, and G. Badenes. Cumulative plasmon field enhancement in finite metal particle chains. *Opt. Lett.*, 30:1882–1884, 2005.
30. C. Girard and E. Dujardin. Near-field optical properties of top-down and bottom-up nanostructures. *J. Opt. A* 8:s73–s86, 2005.
31. C. Girard and R. Quidant. Near-field optical transmittance of metal paticle chain waveguides. *Opt. Express*, 12:6141–6146, 2004.
32. E.D. Palik (Ed). *Handbook of Optical Constants of Solids*, Vol. II, Academic Press, 1991.
33. P.B. Johnson and R.W. Christy. Optical constants of the noble metals. *Phys. Rev. B*, 6: 4370–4379, 1972.
34. M.J. Weber. *Handbook of Optical Materials*. CRC Press, 2003.
35. S. Kawata, editor. *Near-field optics and surface plasmon polaritons*, Springer, chapter 5, pp 97–122, 2001.
36. D. Macías, A. Vial, and D. Barchiesi. Application of evolution strategies for the solution of an inverse problem in near-field optics. *J. Opt. Soc. Am. A*, 21:1465–1471, 2004.

Chapter 8
Electromagnetic Nanowire Resonances for Field-Enhanced Spectroscopy

Annemarie Pucci, Frank Neubrech, Javier Aizpurua, Thomas Cornelius, and Marc Lamy de la Chapelle

Abstract Electromagnetic resonances of metal nanowires lead to strong enhancement of the near field of the particle. Antenna-like resonances that give the biggest enhancement are explained theoretically. The preparation of high-quality wires is introduced. Spectroscopic results for resonance curves are shown and discussed with respect to field enhancement. Surface-enhanced Raman scattering and surface-enhanced infrared absorption are introduced focusing on nanowire-assisted configurations, and examples of these enhanced spectroscopies for molecules on resonant nanowires are shown.

8.1 Introduction

Nanosized metal objects exhibit interesting optical properties with numerous applications in technology and life science [1–4]. They may be used as effective hosts for spectroscopy and light emission [5–8, 118]. The optical properties of such metal nanoobjects are dominated by electromagnetic resonances that are related to considerable electromagnetic field enhancement in the proximity of a nanoparticle [9]. If such resonances are due to free-charge carrier (plasmon-like) excitations, this field enhancement can be particularly strong, which is related to the large negative real part of the dielectric function in a metal (for energies below the plasma edge), much larger than characteristic values of other excitations, like for example optical phonons in a halide or oxide. The fields are strongly enhanced in the range of few nanometers from sharpened metal points, if the radius of curvature is much smaller than the incident illumination wavelength. Therefore rod-like metallic particles may give higher nearfield strength than spherical ones, as we will show below. The dimensions of the particle are of multifold importance for resonance positions and the related field enhancement. For example, in case of a prolate ellipsoid, two fundamental dipole-like resonances exist. The excitation with electric field along the long axis is shifted towards lower frequencies as the ellipsoid aspect ratio increases. When the wavelength is comparable to the length of the particle, retardation

is triggered and the limited velocity of light has to be considered in the calculations of resonance effects. Such particle excitations are known as antenna resonances. On the other hand, resonances of spherical nanoparticles are known as Mie resonances [10] and can be calculated in the electrostatic limit. An ideal metal antenna with a length several orders of magnitude larger than the diameter and with negligible penetration depth (skin depth) of the electromagnetic field into the antenna compared with the diameter has its fundamental antenna resonance wavelength at about two-times the length. This relationship is a rough estimate also for nanoantennas (with a deviation up to about 30% from the exact resonance position). It means that resonances in the infrared need lengths of a few to several microns. Such antennas can be fabricated as wires with diameters down to a few ten nanometers, i.e. considerably smaller than the wavelength, which enables high field enhancement at the wire ends. To get resonances in the visible range, one can use shorter wires or higher order antenna excitations. In both cases field enhancement is smaller than in the infrared.

The resonant nearfield enhancement can be increased by the interaction with another resonant particle in proximity. For example, an extremely high optical nearfield enhancement localized in nanoslits between gold nanorods is possible to obtain [11]. This example indicates that the surface plasmon resonances of metal nanoparticles can be exploited to confine electromagnetic radiation to a volume of subwavelength dimensions [12]. This volume can also be a nanohole in a continuous metal film and the plasmon resonances of that structure give rise to the phenomenon of enhanced transmittance through apertures smaller than the incident wavelength [13].

In periodic metallic structures the electromagnetic coupling to neighbor particles or holes, respectively, influences the resonance conditions. These photonic (plasmonic) effects and the enhanced transmittance have motivated a renewed interest in particle scattering studies, with the aim of understanding the nearfield coupling of closely spaced metallic particles much smaller than the optical wavelength [14]. Because of that coupling, the lattice structure and the lattice constants determine the conditions for wavevector and frequency of transmittance and of reflectance maxima, i.e. a band structure for photons arises [15].

The spectral properties of such photonic structures are influenced by the real dynamic conductivity of the metal that may be different to the textbook value if a lot of defects from preparation may shorten the mean free path of free charge carriers. In case of dimensions of only several nanometers surface scattering of free charge carriers limits that mean free path [16]. From the mid-infrared to the visible range the shortened mean free path of free charge carriers affects only very weakly the skin depth, but the real part of the conductivity is changed.

The substrate of a metal nanostructure is of relevance for three reasons: It may chemically interact with the metal modifying the surface properties at the interface, charge carriers may penetrate through the interface, and the electromagnetic field is changed because of the polarizabilty of the substrate. Thus, the substrate surface structure and chemical surface composition are crucial.

A metal-island film can be considered as a more or less random array of metal nanoparticles with distribution of sizes, shapes, and orientations. Optical spectra for

electric field parallel to the layer show a broad resonance that further broadens toward lower frequency with decreasing particle distances. At the percolation threshold, where at least one conductive cluster has formed because of coalescence of particles, the optical spectra (transmittance, reflectance, absorbance) are nearly frequency independent [17]. On a local scale, strong field enhancement is predicted for such films, especially at certain "hot spots" for random (fractal-structured) metal-island film; an effect that is used to explain extraordinary strong surface enhanced Raman scattering (SERS), different to ordered metal structures [18–20]. The basic idea is that the local field enhancement obtained by metal nanostructures at resonance produces increased local response of an excitation at the resonance frequency. This excitation can be of vibrational nature (SEIRA = surface enhanced infrared absorption), of electronic nature (second harmonic generation A. Bouhelier, M. Beversluis, A. Hartschuh, and L. Novotny (2003) Near-Field Second-Harmonic Generation Induced by Local Field Enhancement. Phys Rev Lett 90: 013903-1), and a combination of both (SERS, fluorescence [5, 119]).

Microscopy techniques based on IR absorption and Raman scattering would be ideally suited for label-free imaging of molecular complexes in life sciences (DNA, proteins, etc.). Because of the sharp and well-defined spectral signatures of the molecules, in fact, no sample's labeling would be needed. These two techniques are already well known as powerful tools to characterize organic materials since the vibrational modes are actual fingerprints of the studied species (information on the molecule conformation, on chemical groups, and bonding etc.). The two vibration spectroscopies are complementary with respect to their application possibilities and to the excitation cross-sections of molecular vibrations. Moreover, the Raman spectrum may be difficult to observe and even hidden because of strong fluorescence emission especially for biological species; however, the spatial resolution achieved can be less than 1 μm and can then allow a very precise characterization. Concerning IR spectroscopy, there is no fluorescence, but the spatial resolution is much larger (around 10 μm). Unfortunately, IR absorption and Raman scattering cross-sections are far too low (10^{-20}–$10^{-30}\,\mathrm{cm}^2$) for fast imaging applications and suffer from their poor spatial resolution.

But SERS and SEIRA have indicated the pathway towards the extreme amplification of the electromagnetic field on the local scale, required to accomplish nanoscale resolved imaging, and single-molecule sensitivity. They have the power to get nanoscale information on specific molecular groups and on their response behavior to external disturbances without artificial labeling. Sufficiently high and predictable nearfield enhancement can be achieved with antenna-like plasmon resonances of rod-like metal particles (here they are called "wires"). Until now, surface enhanced scattering studies that approached single-molecule sensitivity have used randomly distributed metal particles, which yields only qualitative information. It is a great challenge to produce well-defined antenna structures according to precise theoretical predictions for maximum field enhancement over the whole frequency range of the molecular excitations of interest.

In this chapter on electromagnetic nanowire resonances only metal particles are considered. First, the resonances are explained theoretically as ideal antennas and

within full electrodynamics. It follows two examples on wire fabrication including physical characterization; however there are other means to obtain metallic nanowires. In the later sections, examples for optical spectroscopy of wires in different spectral regions are introduced. The last two sections are devoted to examples from surface enhanced spectroscopy.

8.2 Theory of Nanowire Resonances and Simulation of Spectra

In this section we review some of the main factors governing the optical response of metallic nanowires: directionality, surrounding medium, and coupling. The theoretical input of their optical response is a key element for understanding, producing, engineering, and obtaining appropriate hosts for optimal response in field-enhanced spectroscopies.

8.2.1 Basics of Nanowire Resonances: Surface Plasmons and Ideal Antennas

If metal structures are exposed to electromagnetic radiation, modes of collective charge carrier motion, called plasmons, can be excited. Many properties of such plasmons can be qualitatively understood in the semiclassical model as follows.

In the range of the skin depth the incident electric field shifts the free electrons collectively with respect to the positive charge of the fixed lattice ions. A charge carrier separation is built up. The attraction between the separated charges produces a restoring force that mainly depends on the dynamic polarizability of the metal in the intraband region, like plasma frequency and relaxation rate [21].

This force gives rise to collective electronic oscillations at the surface of the metal, known as surface plasmon [22]. The surface plasmons can propagate along a distance of several tens of micrometers on the surface of a film and the plasmon resonance condition is achieved for one specific wavevector and one specific excitation wavelength. In the case of one nanoparticle, the surface plasmon is confined to the three dimensions of the nanostructure and it is then called localized surface plasmon (LSP) [22,23]. In this situation, the LSP resonance depends on the metallic nature (effect of the metal permittivity) and on the geometry (effect of the confinement of the electron cloud) of the nanostructure. The strength of the oscillation is influenced from radiative (scattering) and nonradiative (absorption) damping. Excitations with resonance frequencies in the visible or near ultraviolet spectral range are investigated experimentally [2] and theoretically by solving Maxwell's equations within the quasistatic limit [10] if particle dimension are much smaller than the wavelength (Mie resonances).

It has been shown through the quasistatic approximation that the LSP resonance, for a nanoparticle in air, is achieved when the excitation wavelength corresponds to the one determined by the following condition: $\mathrm{Re}(\varepsilon) = 1 - 1/Q_{\mathrm{eff}}$ where ε is the

metal dielectric function and Q_{eff} is the effective depolarization factor described in [23]. This factor takes into account the shape of the particle. However, Q_{eff} can also include some first order corrections to the quasistatic model such as the dynamic depolarization or the radiation damping.

For a sphere, $Q_{\text{eff}} = 1/3$, and thus the resonance condition will be $\text{Re}(\varepsilon) = -2$, which is fulfilled at 484 nm for gold, at 354 nm for silver, and at 367 nm for copper [24]. The experimental values are different not only because of the effect of interband transitions on the plasmon resonance but also because of deviations from the spherical shape. For a nanoparticle with different shape, Q_{eff} is lower than 1/3 and can be very small. In this case, the LSP resonance position is redshifted. The value of Q_{eff} is closely related to the detailed shape of the nanoparticle. Going from spherical particles to elongated ones, the plasmon resonance has split into different branches according to the electric field direction and the geometry dependence becomes increasingly important, in particular for the LSP resonance [2]. The low-energy LSP resonance can be detected even in the mid-IR for an adequate length of the nanoparticle [25]. The larger is the aspect ratio (long axis L/small axis D) of the particle the lower the frequency of this mode (for constant D). If the wire length approaches the range of the exciting wavelength, the effects of retardation dominate the resonance condition and the limited speed of light results in a direct dependence of the resonance frequency on the absolute dimensions of the particle. This is well known from purely classical theory of scattering of electromagnetic waves by metal objects [26]. If the smallest dimension of the particle is much larger than the skin depth of the electromagnetic radiation in the metal, also real metal wires can be estimated as perfect conductors. For ideal metal objects it is assumed that the light does not penetrate into the particle. This means an infinitely large negative dielectric function. Then, antenna-like resonances occur if the length L of an infinitely thin wire matches with multiples of the wavelength λ, i.e.

$$L = \frac{\lambda}{2n} \cdot l, \tag{8.1}$$

where l is a natural number and n is the refractive index of the surrounding medium. The fundamental mode of the resonance corresponds to $l = 1$, higher dipole-like excitations correspond to odd l. These higher orders of resonance can be observed as new bands on the extinction spectra at wavelengths lower than the dipolar resonance.

Electromagnetic scattering of perfect conducting antennas with D smaller than the wavelength and L in the range of the wavelength is discussed in classical antenna scattering theory. These scattering calculations point out an influence of a nonnegligible diameter D in comparison with the wavelength on the resonance frequency and line shape [27]. Considering nanowires with the same length L, but different diameters D, one finds out that the smaller the aspect ratio L/D, the more broadened the resonance and the lower the resonance wavelength.

It is a frequently used approximation to consider a metal nanowire as an ideal antenna. This approach has been proposed also for the modeling of nanowires in the visible spectral range, as described for example by Martin et al. [28]. The authors of this work assume the nanowire as a perfect conductor, show the existence of antenna modes by means of the finite difference element in time domain (FDTD), and

demonstrate that the field is enhanced at the tip of the nanowire when the excitation wavelength corresponds to an antenna mode.

The assumption of having a perfect conductor means that – Re(ε) is either infinite or at least very large. This is not valid in the visible range. That approximation is applicable for very large wavelengths only, i.e. from the far infrared up to radio frequencies. From the mid-IR and to UV range, the details of the dielectric function of the nanowire-material (including surface induced effects) should be taken into account because they determine the excitations of the free electron gas in the wire.

In addition to the mentioned effects, the polarizability of the surrounding media affects the optical properties of metal nanoparticles. Regarding the effect of the substrate (with the refractive index $n_s = \sqrt{\varepsilon_s}$) on which the nanowires are placed and the surrounding medium (air, refractive index of 1), an effective medium completely embedding the wires is a reasonable assumption. Its effective dielectric constant is given by the following equation [27]:

$$\varepsilon_{\mathrm{eff}} = \frac{1}{2}(1 + \varepsilon_s) \tag{8.2}$$

Using the relation $n = n_{\mathrm{eff}} = \sqrt{\varepsilon_{\mathrm{eff}}}$ the influence of the substrate on optical spectra can be described well [29].

8.2.2 Factors Governing Nanowire Plasmon Modes

Electromagnetic resonances of nanowires in the optical and near infrared are a result of several effects. On the one hand, as pointed out in the previous section, the structure of a finite one-dimensional conductor supports efficient antenna behavior for certain wire lengths. On the other hand, the end of the nanowires in a relatively sharp and abrupt surface is a perfect candidate to host a lighting rod effect. Finally, the valence electrons in metals oscillating freely and coherently on the wires surface as a response to radiation produces certain resonant modes, known as surface plasmons, that determine the optical and near infrared response of these structures. The solution of Maxwell's equations for metallic nanorods with the consideration of the exact length and width of the wire and the use of a local dielectric response to characterize the optical response of the metal is able to account for all those effects. One of the main features in the optical response of metallic nanorods is connected with the strong directionality of the plasmon response. The presence of one dimension much longer than the other two generates a long wavelength resonance (the low-energy LSP), also called longitudinal plasmon, which presents a much lower energy than the low wavelength resonances also called transversal plasmon [30]. In Fig. 8.1a we show the calculated optical extinction spectra of a 500 nm long gold nanorod with two different diameters, 80 and 200 nm, respectively. The excitations for two different polarizations (parallel and perpendicular to the long wire axis) of the incoming light are completely different not only in resonance wavelength but also in extinction at resonance. The long wavelength peak is associated with the

dipolar-like polarization of the long axis, whereas the short wavelength peak is associated with transversal polarizations at the nanorod. The strength of the latter is noticeably smaller as the induced charge at the surfaces is scattered along the rod walls. For the longitudinal excitation, the induced charge is piled up at the rod ends, driving a considerable strength of the induced dipole. In Fig. 8.1a an extinction spectrum for the thinner wire as an ideal antenna ($L/D \gg 1$, perfect conducting metal, calculation according to [26]) is shown for comparison.

In optical and infrared spectroscopy usually only the antenna-like surface modes are identified, but higher order modes are also solutions supported by the geometry and identified for different applications as in SERS [31]. For a given external excitation, the total surface induced charge σ can be expressed as a weighted summation of the surface modes: $\sigma = \Sigma_{lm} A_{lm} \sigma_m^l e^{im\varphi}$, where σ_m^l is the induced surface charge density of the l mode, projected over the azimuthal index m, and A_{lm} is the weight of the σ_m^l mode, which depends on the characteristics of the incoming radiation (polarization, intensity, angle of incidence, etc.) on the geometry, and on the material. In Fig. 8.1b we show the polarization patterns for the first $m = 0$ and $m = 1$ modes. The set of surface modes σ_m^l spread out as antisymmetric A (net dipole) and symmetric S solutions (no net dipole), all over the spectrum, from the lowest energy mode $\left(\sigma_0^0\right)$ up to modes with energies close to the planar surface plasma frequency $\omega_\mathrm{s} = \omega_\mathrm{p}/\sqrt{2}$ for free charge carriers with the bulk plasma frequency ω_p. The first antisymmetric mode $\left(\sigma_0^1\right)$ is the lowest energy physical mode and shows total net dipole. This mode is effectively excited by light linearly polarized along the rod axis, giving rise to the longitudinal plasmon. Higher order modes are also present in the spectrum for higher energies, and although they are usually masked in optical spectra because of pile up, homogeneous broadening, and lower excitation weight, they have been identified for example in photoluminescence [32–34] and SERS [31]. On the other hand, the first mode with $m = 1$ $\left(\sigma_1^1\right)$ is usually associated with the transverse peak of extinction. This mode presents cosine dependence around the azimuthal angle of the rod, therefore is effectively excited by light linearly polarized perpendicular to the rod axis.

A similar behavior can be found for metallic wires larger than several hundred nanometers. The increasing size of the nanoantennas makes the resonances to appear at wavelengths that present larger negative values of the dielectric function, i.e. for wavelengths well in the mid infrared portion of the spectrum in the case of micron-sized wires. It is actually this extension of the resonant behavior to micron-sized antennas what makes these structures optimal candidates for surface enhanced Raman spectroscopy (SERS) and surface-enhanced infrared absorption spectroscopy (SEIRA).

Tuning of the optical response can be achieved via changing the length and adjusting the width of the nanorod. Several detailed geometries have been used to calculate the scattering effects of nanorods and nanowires. One of the most commonly used has been the ellipsoidal geometry since it presents analytical solutions for the polarizabilities in an electrostatic approximation [35, 36]. As the nanorods become larger in size, the shape of the wires departs from an ellipsoid, therefore a geometry with straight walls and hemispherical ends seems to be reasonable to

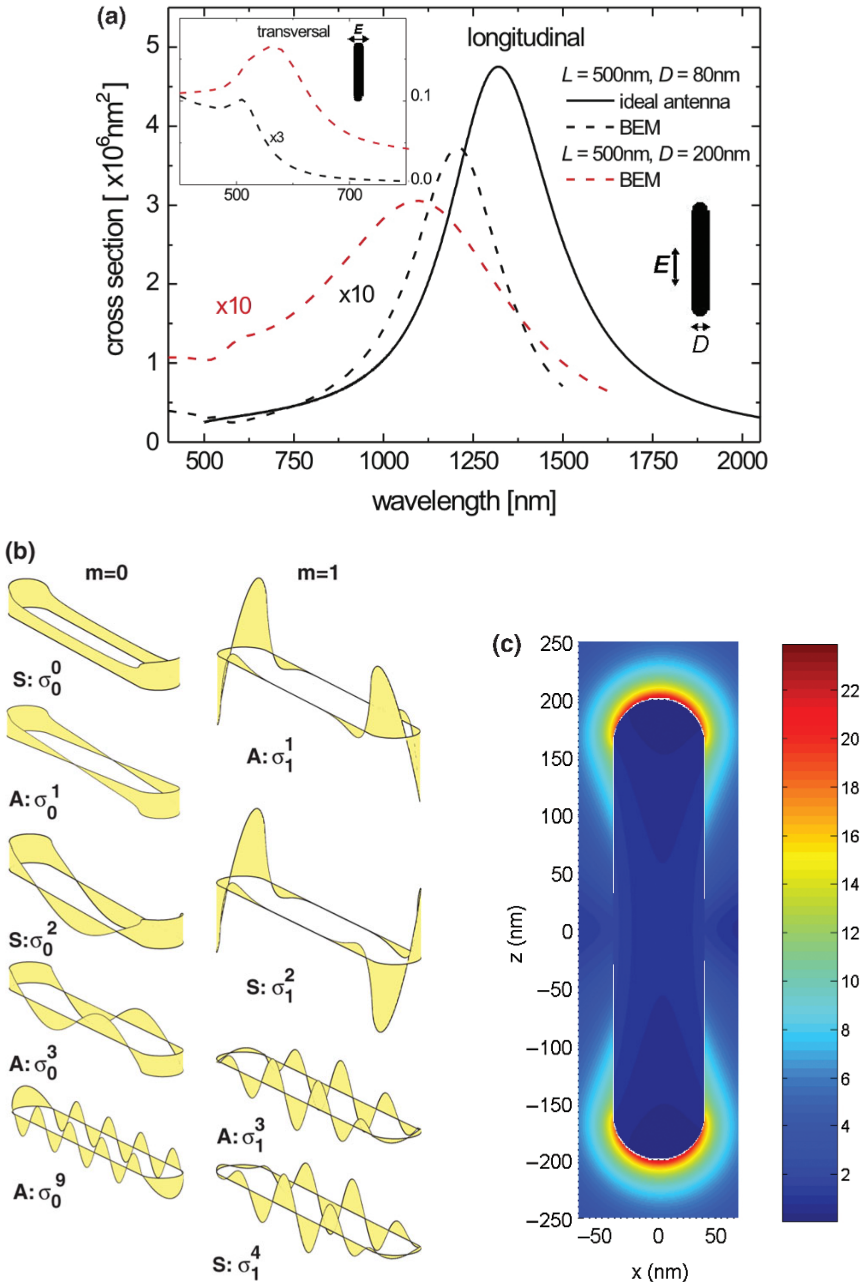

Fig. 8.1 **(a)** Extinction cross-section (in the farfield) of 500 nm long gold nanorods for different polarizations of the incoming light calculated with BEM and with classical theory for ideal antennas. Longitudinal and transverse (inset) plasmon excitations can be observed. **(b)** Surface charge oscillation patterns σ_m^l of modes in a nanorod. First order modes for $m = 0$ and $m = 1$ symmetry as calculated from solving Laplace's equation. **(c)** Distribution of nearfield enhancement for the fundamental antenna resonance (at 1255 nm) of a gold nanorod with $L = 400$ nm and $D = 80$ nm at (BEM result, field-enhancement factor according to the different colours as defined on the right)

describe the wires. Moreover, effects of retardation have a strong influence, reducing the energy of the plasmon resonances. Especially for the case of micron-sized antennas, where the interactions along the edges and the walls can be comparable to the incoming wavelength, full electrodynamical calculations are needed to account for the position of the resonances. Several techniques have been developed to solve Maxwell's equations in inhomogeneous media. All of them present advantages in certain aspects and disadvantages in others. For example, the dipole discrete dipole approximation (DDA) [37], finite difference methods in time domain (FDTD) [38], multiple multipole expansion (MMP) techniques [39], transfer matrix methods [40], or finite element methods in frequency domain, are among some of the most commonly used techniques to solve Maxwell's equations. Here we explain and apply the boundary element method (BEM) [41,42], where the surfaces separating two different media are discretized, and Maxwell's equations are expressed in integral form, in terms of the scalar potential ϕ and the vector potential $\boldsymbol{A}$, involving the surface charge densities σ_j and the currents $\boldsymbol{h}_j$ at the boundaries separating two different media:

$$\phi(\boldsymbol{r}) = \phi^e(\boldsymbol{r}) + \int_{S_j} \mathrm{d}\boldsymbol{s}\, G_j(|\boldsymbol{r}-\boldsymbol{s}|)\,\sigma_j(\boldsymbol{s}) \tag{8.3}$$

and

$$\boldsymbol{A}(\boldsymbol{r}) = \boldsymbol{A}^e(\boldsymbol{r}) + \int_{S_j} \mathrm{d}\boldsymbol{s}\, G_j(|\boldsymbol{r}-\boldsymbol{s}|)\,\boldsymbol{h}_j(\boldsymbol{s}) \tag{8.4}$$

with

$$G_j(|\boldsymbol{r}-\boldsymbol{s}|) = \frac{e^{\mathrm{i}k_j|\boldsymbol{r}-\boldsymbol{s}|}}{|\boldsymbol{r}-\boldsymbol{s}|} \tag{8.5}$$

the scalar-wave Green's function propagator in medium j, and $\boldsymbol{k}_j(k_j = (\omega/\mathrm{c})\sqrt{\varepsilon_j})$ is the wave vector of light in medium j. $\phi^e(\boldsymbol{r})$ and $\boldsymbol{A}^e(\boldsymbol{r})$ are the potentials created by the external source. Each medium is characterized by its local dielectric function $\varepsilon(\omega)$, which represents the local bulk dielectric response. Solving the integral equations in (8.3) and (8.4), involving the self-consistent induced charges and currents, allows for obtaining the near field and far field distribution from any scattering object [11,43]. We will describe the geometry of the rods as a cylindrical wire of total length L, with hemispherical ends of radius R that relate to the width of the rod D as $D = 2R$. This geometry seems to account very accurately for all the experimental features in the optical scattering of nanorods [11]. Figure 8.1c shows the nearfield enhancement for such nanorod at the fundamental antenna resonance.

In Fig. 8.2a we present the extinction cross-sections of different gold nanoantennas and microantennas for incoming light polarized along the long axis. The extinction peaks spread all over from the optical to the mid-infrared range of the spectrum as a function of rod length. As the rod becomes longer, the spectral peak is red shifted. As we show in Fig. 8.2b, the evolution of the resonances (extinction peaks) presents a quasilinear behavior that is described by the relationship $L \approx \lambda/2.5$ for such relatively wide wires. This behavior departs from the standard $L = \lambda/2$ for ideal antennas. As the length of the rods exceeds 5 μm, the slope of the resonances

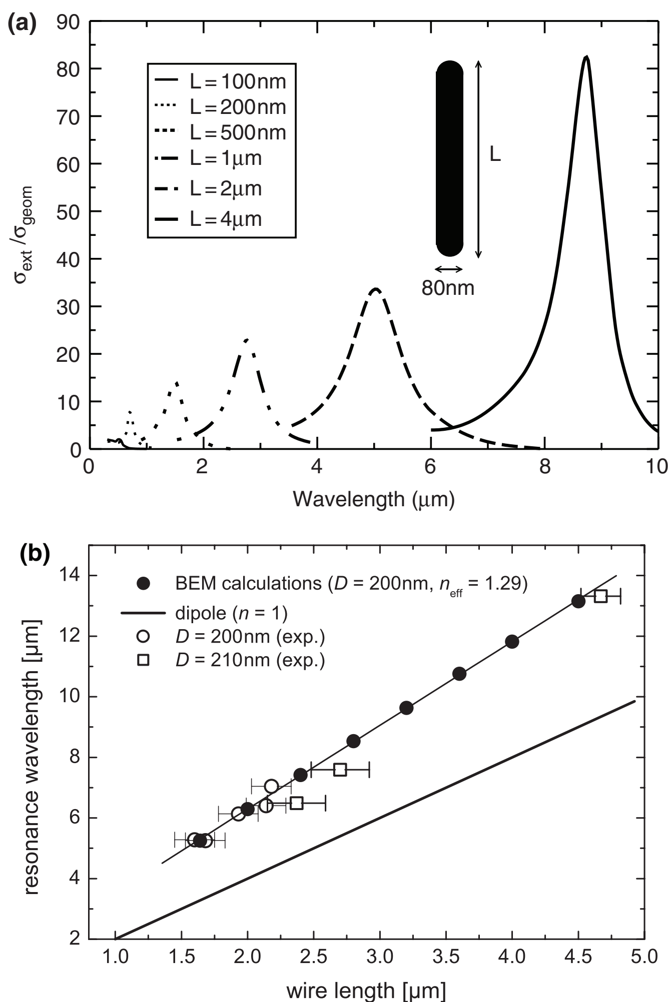

Fig. 8.2 **(a)** Total extinction cross-section of 80 nm wide gold nanowires for different lengths L in the farfield. **(b)** Linear behavior of resonances with wire length for different diameters. A deviation from antenna theory is observed in the resonances position, see curves for dipole (ideal antenna). The polarizability of the substrate is considered with the effective refractive index n_{eff}. The substrate for the experiments was KBr

is reduced to $L \approx \lambda/2.2$, therefore approaching slowly to the behavior of a perfect conductor. When the skin depth to diameter ratio is very large, the denominator is enhanced up to even 10.

As shown in Fig. 8.2a, the extinction cross-section of an elongated wire normalized to its geometrical surface is at least one order of magnitude larger than the corresponding normalized extinction in a spherical particle. The finite conductivity (finite negative dielectric function) of the metals in this range of the spectrum is responsible for the modification of the slope. It is commonly assumed in the

literature that this linear behavior follows a scaling law for the aspect ratio in different rods. Even though that is the case in a nonretarded solution of electrical fields, this is not the case when the full electromagnetic solution to the scattering problem is considered. Because of retardation, a set of rods with a certain width follows a linear behavior that is different to the linear behavior of another rod with a different width [44]. This effect is more evident for very thin wires.

Surface plasmon modes are mainly given by the plasma frequency of the electron gas that adapts to the geometrical boundaries of the system, generating the surface plasmons. Both gold and silver are commonly used for nanoparticle plasmonics because of the relatively easy production and manipulation. Their optical responses do not correspond exactly to that of a free electron gas, due to the role of *d* electrons, but a modified Drude-like function describes well their responses in a wide range of the spectrum. For optical frequencies, gold and silver show distinctively different surface plasmon resonances. However, in the near and mid infrared portions of the spectrum, both materials adopt large negative values of the permittivity, giving rise to similar positions and weight of the antenna resonances. Another metal that behaves as a free electron gas and is well described by a Drude response function is aluminum. Plasmon resonances in this material fall into the ultraviolet ($\lambda_s = 110\,\text{nm}$), but its nanorod resonances can fall in the optical portion of the spectrum because of the induced redshift. Another set of interesting materials for resonant response in the infrared are polar materials such as SiC [45]. In this case, the phonon-polaritons rather than electrons are responsible for the electromagnetic resonances. Finally, nanorods of semiconductor materials [46] are also another set of materials that can produce electromagnetic resonances in the low frequency region because of the reduced electronic density [47]. We focus in this chapter on pure metallic nanowire resonances.

Earlier we have pointed out shortly how the effect of the surrounding medium needs to be considered for the exact position of the antenna resonance. The medium surrounding a metal nanostructure determines, through its polarizability, how intensely the surface charge density can be induced, and ultimately, which energy the resonance falls into. During the last years, a renewed interest to study the influence of the environment in surface plasmons has occurred because of the capacity of the surface plasmon resonance for sensing the local refractive-index change by monitoring the wavelength shift [48–50]. When dealing with nanowire resonances, and due to the different substrates and media surrounding the wires, it is relevant to establish how strongly the environment affects the optical and near infrared response of the nanorods. As pointed out earlier, an effective medium surrounding the nanowire can account for the main features of the substrate effect. In Fig. 8.3, we show the extinction cross-section of a nanorod when it is surrounded by media with different dielectric constant value. As we increase the permitivity of the surrounding material, the plasmon resonances red-shift. This shifts can be as large as 2000 nm in wavelength for changes of $\varepsilon = 1$ to $\varepsilon = 3$. An accurate estimation of the effect of the surrounding medium is therefore crucial for the exact description of the resonances position. We typically consider an effective medium given by eq. 8.2, which turns to describe very accurately the substrate effect [29].

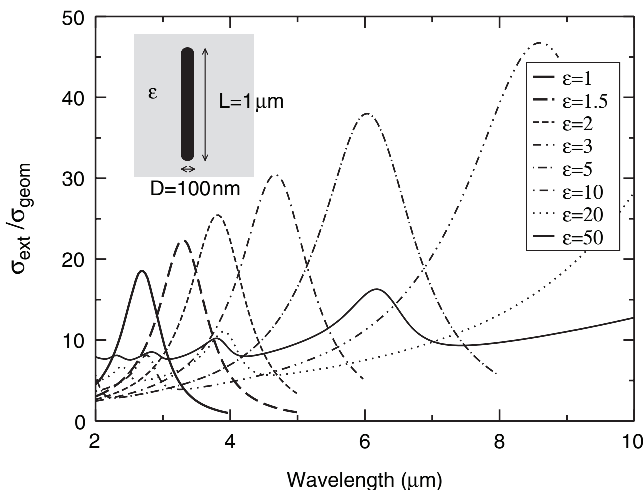

Fig. 8.3 Extinction cross-section (in the farfield) of a 1 μm long and 100 nm wide gold nanorod in different surrounding media characterized by a dielectric constant ε. Large values of ε red-shift the longitudinal excitation response towards the infrared

Standard theory of nanorod resonances, on the basis of an electrostatic approach, predicts a scaling law with the rods aspect ratio for the resonances position [30]. It has been mentioned here (in Fig. 8.2b) that this scaling is not fulfilled when an exact full electrodynamical description of the scattering is considered. The width and the length of the rods account separately for the resonances positions, and even though a linear behavior with length is observed and corrected with respect to classical antenna theory, the actual proportionality of the wire length and resonances position is different for different widths.

Coupled metallic systems are known to produce red shifts and plasmon hybridization [51, 52]. The lowest energy resonance usually generates a strong local field in the vicinity of the coupling area. Situations where the coupling produces large field enhancement have been proven to be the key to obtain single molecule sensitivity in SERS [53, 54]. The use of cavities or other effective configurations that produce this large field enhancement has allowed for pushing the limits of this spectroscopy [55], even though certain limits (10^{11}) are inherent to the electromagnetic contribution of the SERS enhancement [20]. Several situations creating large field enhancement and singular optical response have been studied in dimers [56], bowtie antennas [57], and sets of metal nanoparticles [58]. Coupled nanorods have also been treated recently as convenient field-enhancers at the cavity between rods [12, 59, 60].

In an attempt to search for an optimal field-enhancing structure, we present here the results for the optical response when two nanorods are coupled together. A computational study of such a situation has been reported previously [11], and similar effects as those reported in the coupling of dimers have been found. As a general trend, field enhancement increases as the rods are located closer together.

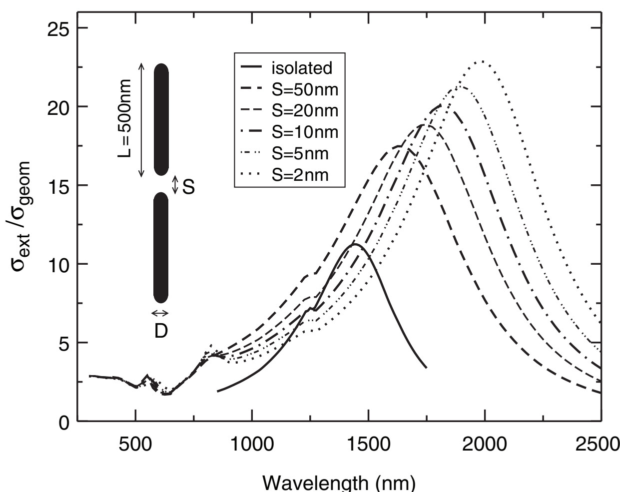

Fig. 8.4 Extinction cross-section of a pair of 500 nm long nanorods for different inter-rod separation distance S, farfield result

The geometry of the rod, with one privileged dimension, is the main effect to consider in the coupling of nanorods. In Fig. 8.4 we plot the extinction cross-section normalized to the geometrical surface for a pair of nanorods with different separation distances. Even though the main effect is obtained in the near field at the cavity, also in the far field, the effects of the coupling are relevant with large shifts into the near IR and larger excitation of the cavity modes for small separation. These effects might increase even more the efficiency of the antennas used for SEIRA, when the samples under study are located at the cavity.

8.3 Nanowire Fabrication

There are many different approaches for metal–nanowire fabrication. Here we introduce only two methods: wire growth in ion tracks of membranes, which is rather exotic, but produces nearly ideally cylindrical wires, and electron-beam lithography, which is a common method today, but the obtained structures do not show cylindrical symmetry. Instead they have a certain height and their two-dimensional shape is fixed by writing with the electron beam.

8.3.1 Wire Growth in Ion Tracks of Membranes

Metal (Au, Cu) [61–65] and semimetal (Bi) [66,67] nanowires were prepared by the template method being schematically depicted in Fig. 8.5. For this purpose, poly-

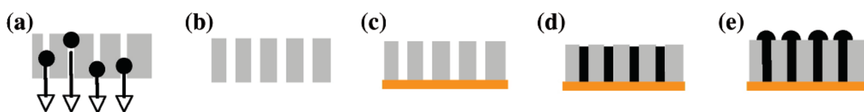

Fig. 8.5 Schema of the template method: **(a)** A polymer foil is irradiated with swift heavy ions and **(b)** subsequently etched in aqueous NaOH leading to a nanoporous template. **(c)** One side is coated with a conductive layer. **(d)** Metal is deposited electrochemically into the pores. **(e)** As soon as the metal reaches the opposite side of the membrane, caps start to form on top of the wires

carbonate membranes of thickness 30 μm were irradiated with swift heavy ions that were accelerated to a specific kinetic energy of 11.4 MeV per nucleon at the UNILAC linear accelerator of GSI (Fig. 8.5a). The applied fluence was varied from a single ion per foil to 10^9 ions per cm^2. The ions modify the polymer along their trajectories so that cylindrical volumes—so-called latent tracks—are created, which behave chemically different than the nonirradiated polymer. Therefore, the tracks can be selectively dissolved, leading to nanoporous templates (Fig. 8.5b). Prior to chemical etching in 6 M aqueous sodium hydroxide at 50°C, the foils were exposed to UV light in order to sensitize them for the etchant. The pore diameter is directly proportional to the etching time, i.e., the resulting wire diameter was controlled via the etching process. After rinsing the templates, a thin gold layer was sputtered on one side of the membrane and reinforced by an electrochemically deposited copper layer (Fig. 8.5c). This conductive layer served as cathode during the subsequent electrochemical deposition of the metal in the nanopores (Fig. 8.5d). The electrodepositions were performed in a two-compartment electrochemical cell. When the metal reaches the opposite side of the membrane, caps start to grow on top of the wires (Fig. 8.5e). To fabricate wires of a certain length, the deposition process was interrupted as soon as the wire height reached the desired value, calculated from the charge deposited using Faraday's law.

The depositions were accomplished in a two-compartment electrolytical cell schematically depicted in Fig. 8.6a. For the fabrication of copper and gold nanowires, a simple-salt electrolyte containing 238 g/l $CuSO_4 \cdot 5H_2O$ and 21 g/l sulfuric acid and an alkaline cyanide solution, namely potassium dicyanoaurate (I) Puramet 402 bath (Doduco, gold content = 10 g/l) was employed, respectively [61, 62, 64, 65]. As anodes a copper and a gold rod were used during the fabrication process. In Fig. 8.6b, the current versus deposition time is displayed for the fabrication of Cu nanowires with diameter $d = 50$ nm at 50°C and -120 mV. The deposition curve is dividable in four different sections: (i) The peak in the beginning is due to the electrical double layer which discharges with increasing time. (ii) During the deposition of the metal inside the pores a constant current is recorded. (iii) As soon as the wires reach the upper side of the membrane and caps start to form, the current increases because of the increasing deposition area. (iv) The current saturates when the caps coalesce to a homogeneous layer and the area does not grow any further.

While the nanowires remained embedded in the template, their crystallinity was studied by means of X-ray diffraction (XRD) using a STOE four-circle diffrac-

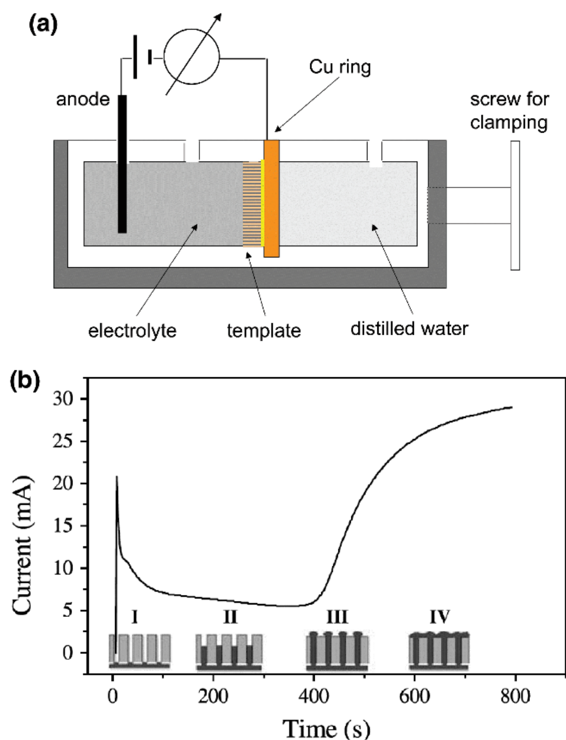

Fig. 8.6 **(a)** Schematic of the two-compartment electrolytical cell. **(b)** Deposition current versus time for copper nanowires with diameter 50 nm fabricated at 50°C and −120 mV

tometer with graphite monochromatized Co-K_α radiation ($\lambda = 1.7902$ Å). X-ray diffractograms of gold nanowires deposited potentiostatically at 65°C and different potentials are displayed in Fig. 8.7a. The dashed lines indicate the position and intensity of diffraction signals for a standard gold powder. The wires exhibit a <220> texture that becomes more pronounced for lower overpotentials during the fabrication process. For wires created at 65°C and −1.2 V more than 90% of the crystals are oriented along the <220> direction. A similar behavior was observed for Cu and Bi nanowires.

The morphology of both nanowires and caps was examined by scanning electron microscopy (SEM) (Philips XL30). SEM images of caps grown on top of the wires that were deposited at 65°C and different overpotentials are depicted in Fig. 8.7b and c. The mean grain size increases with decreasing overpotential and distinct facets are developed. Hence, the cap morphology is a strong indication for the wire crystallinity. The development of texture is based on the different growth rates of various crystal faces. During the deposition process, ad-atoms are attached on the surface of an already existing crystal. Depending on their mobility, they may move to vacant positions of the crystal and build it up further or may act as starting nuclei for a new crystal. Higher mobilities of the ad-atoms lead to a more pronounced tex-

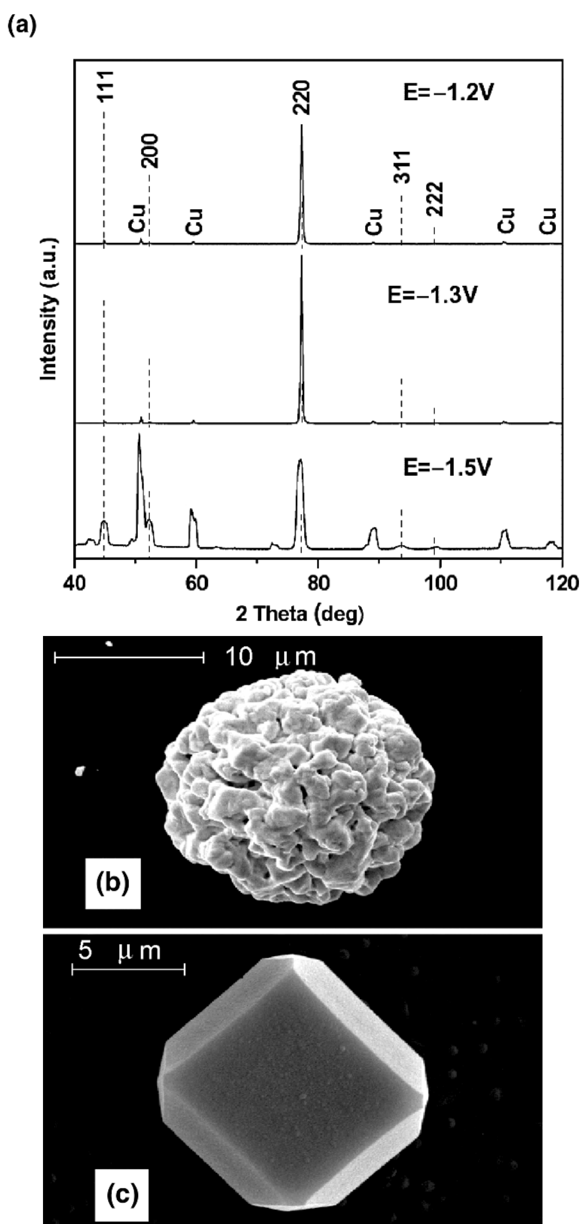

Fig. 8.7 **(a)** X-ray diffractograms gold nanowires deposited at 65°C and different potentials. SEM micrographs of caps grown on top of Au nanowires deposited at 65°C applying **(b)** −1.5 V and **(c)** −1.2 V

ture. The higher the number of ad-atoms per time on a given surface area, i.e., higher current densities j, the smaller is their mobility because of interaction between them. Larger overpotentials involve larger j. Hence, increased U leads to nucleation and thus to polycrystalline wires.

The crystallinity and crystallographic orientation of the nanowires were also studied by transmission electron microscopy (TEM) (Philips CM20), including selected-area electron diffraction (SAED). For this purpose, the polymer membrane was dissolved in dichloromethane (CH_2Cl_2) and the wires were detached from the back electrode by sonication. Then, few drops of the suspension of the volatile solvent containing clean nanowires were put on a carbon covered TEM grid or, for subsequent IR spectroscopy, on infrared transparent substrates, respectively.

A TEM image and a SAED pattern of a Cu nanowire with diameter 60 nm deposited at 50°C and -45 mV are presented in Fig. 8.8a and b, respectively. The nanowire possesses a smooth contour and a well-defined diameter. The SAED pattern shows regular reflections confirming the single-crystallinity of the wire.

In summary, single crystalline <110> textured gold and copper nanowires were electrochemically deposited in etched ion-track polycarbonate membranes.

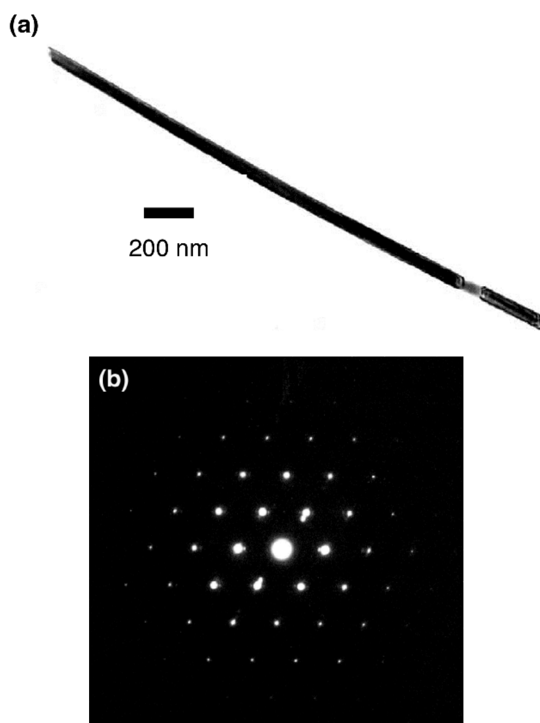

Fig. 8.8 (a) Transmission electron-microscopy image and (b) selected-area electron-diffraction pattern of a copper nanowire with diameter 60 nm

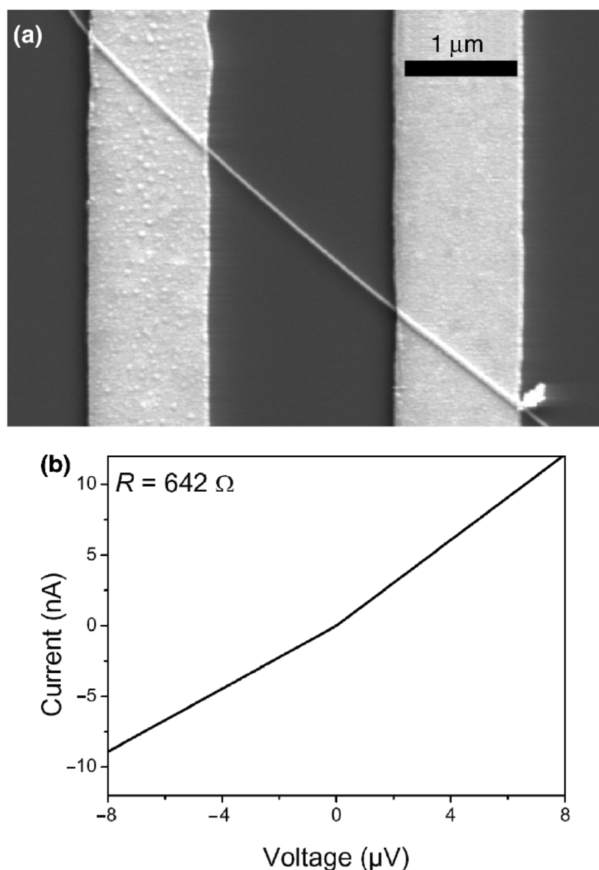

Fig. 8.9 **(a)** SEM image of a lithographically contacted copper nanowire and **(b)** the corresponding *I–V* curve

Electrical transport properties of copper nanowires produced with the same method were studied [68]. The wires were removed from the template, placed on a Si wafer, and contacted lithographically (Fig. 8.9a). The wire resistance showed a linear *I–V* curve, i.e., it was Ohmic (Fig. 8.9b). The resistance increased with increasing time of exposure to air and, finally, the *I–V* curve became nonlinear. This behavior was observed at 4.2 as well as at 300 K. The copper wire oxidized to Cu_2O, which behaves like a p-semiconductor. Hence, two Schottky diodes placed back-to-back in series were created at the lithographic contacts, leading to the observed nonOhmic behavior.

To investigate the thermal stability, wires of different diameters were prepared and subsequently annealed at elevated temperatures for a predetermined time period. Cu and Au wires become instable and fragment at temperatures of few hundred degrees Celsius being far below the bulk melting temperature of 1083 and 1064°C, respectively [61, 62, 69]. An as-prepared gold wire with diameter 25 nm is

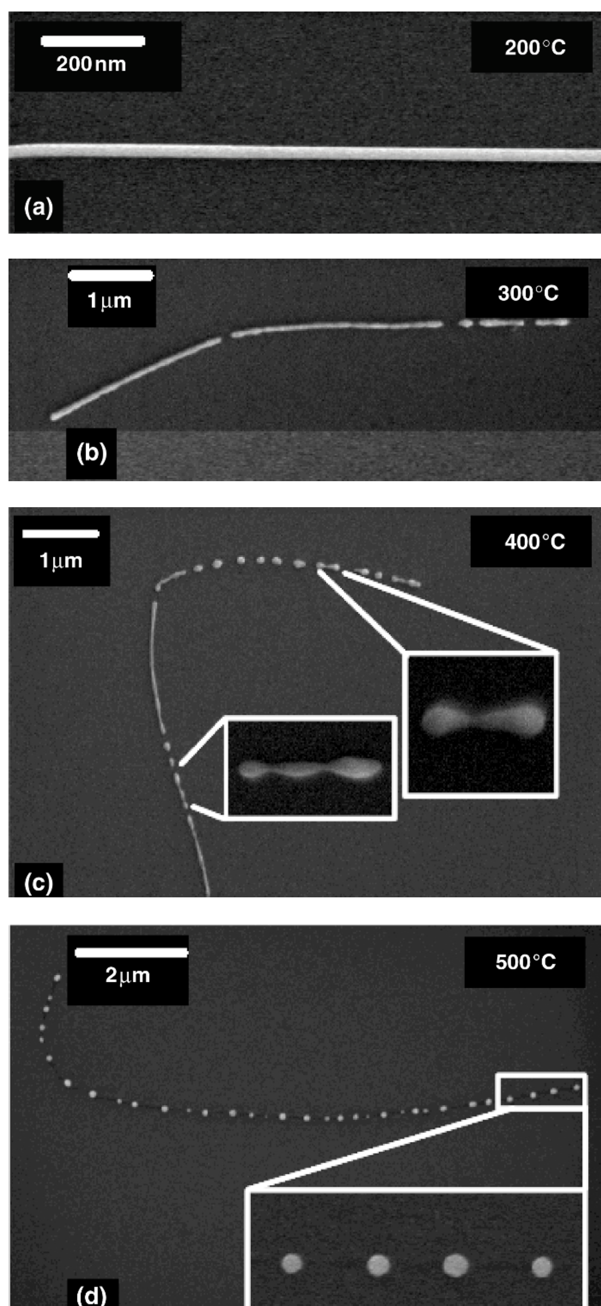

Fig. 8.10 SEM micrographs of **(a)** an as-prepared wire with diameter 25 nm and **(b)**–**(d)** wires after annealing for 30 min at different temperatures

depicted in Fig. 8.10a. Fig. 8.10b–d display SEM images of Au wires after annealing for 30 min at different temperatures. The micrographs reveal different states of the fragmentation process. At 300°C the wires fragment, at 400°C the fragments become oval, and at 500°C the wires are completely transformed into a chain of nanospheres. The driving force of the fragmentation is the so-called Rayleigh instability, i.e., the minimization of the surface energy of the initial cylinder [70]. More than a century ago, Lord Rayleigh described this process for liquid jets. Nichols and Mullins extended the model to solid cylinders by [71]. For the nanowires grown in ion tracks, the distance of adjacent spheres for different wire diameters was found to be larger than predicted by the Nichols and Mullins model. The deviation between experiment and theory originates from the fact that the model assumes an initial cylinder with an isotropic surface energy while solids in general possess crystalline facets and, thus, have an anisotropic surface energy.

8.3.2 Electron-Beam Lithography

Electron-beam lithography (EBL) makes possible the fabrication of nanostructures of desired shape, size, and arrangement.

As shown in Fig. 8.11, to achieve EBL it is necessary to follow different stages.

1: The first consists in depositing, by spin-coating, on a glass substrate carefully cleaned the polymer, polymethyl methacrylate (PMMA), whose chains will be broken during the exposure. The thickness of deposited PMMA is about 150 nm. The choice of the PMMA thickness depends on the height of the structures which one wants to design. A ratio 3:1 is generally respected between the thickness of the layer of polymer and the height of the deposited metal.

2: The purpose of the second stage is to remove the solvent used, methylisobutylketon (MIBK), from the PMMA film while placing the glass substrate covered with polymer in a drying oven (160°C) during at least 2 h. If the substrate used is glass or another insulator material, it will accumulate the electrons received during the

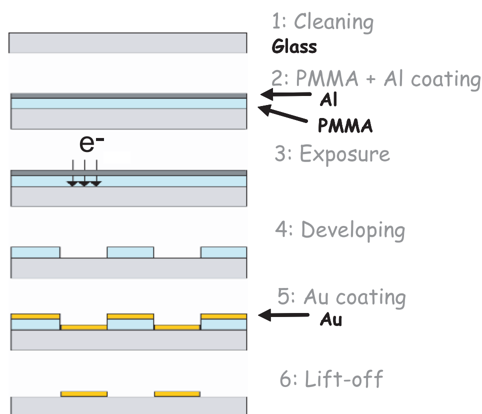

Fig. 8.11 Main stages of the design of a sample by EBL and lift-off techniques

exposure in the scanning electron microscope (SEM). That generates an electric field on the surface of the sample, which disturbs the incident electron beam. To avoid this problem, an aluminum film of 10 nm could be evaporated on the layer of PMMA, thus allowing the dissipation of the charges. That requires an additional stage compared to the use of a conducting substrate like silicon or indium titanium oxide (ITO).

3: For exposure with the SEM, it is necessary to use a system of control of the electron beam such as Nanometer Pattern Generation System (NPGS). The designed nanostructures reproduced on the substrate are drawn using a software package as DesignCad LT 2000 and the NPGS system transforms the created nanostructures into a dot matrix. It is then possible to choose the distance between the points to be exposed as well as the distance between lines of points in a very precise way. The coordinates of the points to expose are then transmitted to the system of deflection of the electron beam and to a beam blanker. The exposed zones have typical size from approximately 100 μm.

4: For processing, it is necessary to dissolve the layer of aluminum using a solution of potassium hydroxide, KOH. The development can then be carried out. This stage consists of a selective dissolution of the PMMA. Only the exposed zones, having a lower molecular mass, must be dissolved. One usually uses a mixture of 1:3 MIBK and isopropanol (IPA).

5: After processing, the metal is evaporated and deposited with the desired thickness on the surface.

6: The purpose of the last stage is to dissolve the PMMA remaining on the sample using acetone: the lift-off stage.

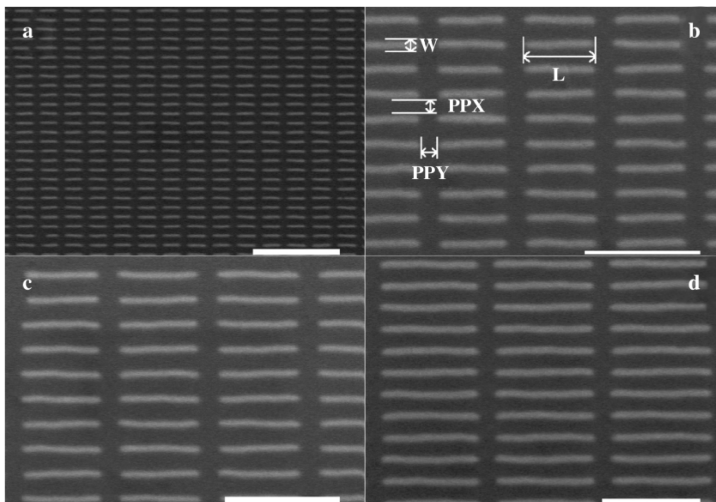

Fig. 8.12 SEM images of arrays of gold nanowires with variable length L (**a**: $L = 420$ nm, **b**: $L = 620$ nm, **c**: $L = 720$ nm, **d**: $L = 1$ μm), 50 nm height, 60 nm width (W). The gap between nanowires is constant for all arrays and is fixed to 150 nm (PPX and PPY). Scale bars: 2 μm for **a** and 1 μm for **b–d**

This technique provides homogenous arrays of gold or silver nanowires as it can be seen in Fig. 8.12. The limitation of such technique is given by the SEM resolution. It then is not possible to get nanostructures with a size lower than the diameter of the electron beam. Typically, the lowest resolution achieved is few tens of nanometer.

8.4 Spectroscopy of Nanowire Resonances

8.4.1 Infrared Spectroscopy

This subsection reports on the experimental farfield spectroscopy of nanowire resonances of individual metal nanowires prepared by growth in ion tracks, see Sect. 8.3.1, supported by a dielectric substrate in the infrared. Different to studies on ensembles of nanowires [25], one can exclude the influence of wire–wire interaction and averaging over locally varying parameters. Therefore, the experimental results can be compared with existing theories and simulations for individual metal nanowires (see Sect. 8.2.2).

Spectroscopy was performed on metal nanowires prepared by electrochemical deposition in etched ion-track polycarbonate membranes (see Sect. 8.3.1). After fabrication the polymer foil was dissolved in dichloromethane and the clean nanowires were deposited on an infrared transparent substrate, e.g. KBr, ZnS, or CaF_2.

Spectroscopic IR microscopy of single metal nanowires was performed with synchrotron radiation with a higher brilliance compared with conventional IR light sources, e.g. globar. The higher brilliance allows mapping spectral properties of nanowires. Before IR spectroscopy the individual nanowire on the IR-transparent substrate was located by optical microscopy with visible light and its length is determined from those images. Estimating the wire length in this way, a rather big error up to 8% has to be assumed. Operating in the infrared mode of the microscope a circular area of the IR-beam with a diameter of 8.3 μm in the focal plane (sample position) was selected by inserting a circular aperture in the optical path behind the sample. After the IR-beam had been centered on the selected nanowire, IR-transmittance spectra (sample spectra) were recorded. Subsequently, to eliminate effects from beam profile and from substrate inhomogeneities, reference spectra were taken at least 10 μm away from any nanowire and the ratio of sample and reference measurement, called relative transmittance spectrum, is calculated. To determine the lateral position of maximum response of the single nanowire, a grid with a lateral step size of 1 μm is defined and relative transmittance spectra were taken at each grid point. The spectroscopic measurements were done with a Fourier-transform infrared (FT-IR) spectrometer and a LN_2-cooled mercury-cadmium telluride (MCT) detector, which collects light normally transmitted through the sample area. A small fraction of the light scattered away from the normal direction could also be detected because of the collection lens (Schwarzschild objective, numerical aperture: 0.52). This can be neglected in further data analysis because most of the intensity scattered

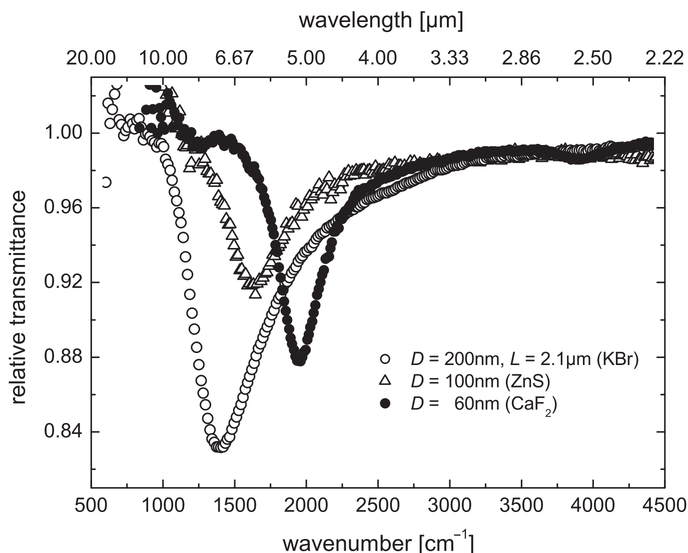

Fig. 8.13 Typical relative transmittance spectra (parallel polarization) of different single gold nanowires with different lengths and diameters (down to 60 nm) placed on different substrates. The fundamental mode of the antennas can be seen clearly

by the nanowire is directed outside the cone of collected light. For both sample and reference measurement IR spectra were recorded by acquisition of at least 10 scans in the spectral range from 600 to $7000\,\mathrm{cm}^{-1}$. A resolution of at least $16\,\mathrm{cm}^{-1}$ was sufficient for fundamental nanowire studies because of the spectrally broad response. An even higher resolution of $2\,\mathrm{cm}^{-1}$ was used for the SEIRA measurements (see Sect. 6.1). For further analysis of the transmitted light a polarizer was inserted in the optical path before the sample.

The relative transmittance spectra T_{rel} of nanowires (Au, Cu) with a length of a few microns reveal fundamental antenna resonances (see Fig. 8.13). Apart from the fundamental mode much weaker structures of resonant excitation are detected at higher wavenumbers. These modes can be attributed to higher order resonances. Even dipole inactive excitations are observed, which may be due to an electric field component oblique to the long wire axis [72, 73] or bent nanowires. Since the detailed study of higher order resonances of individual wires was hampered by their low signal strength when compared with disturbing effects (beam instability, substrate inhomogenities), only the fundamental mode of the antenna resonance ($l = 1$ in eq. 8.1) is discussed in the following. The main resonance was only observed for electric field parallel to the long axis of the wire (parallel polarization). For an electric field perpendicular with respect to the long wire axis (perpendicular polarization) the IR-signal was below the noise level, no plasmon was excited.

In Fig. 8.13 the resonance positions (position of minimum transmission) of the different wires depend on length, diameter, and the used substrate. To separate the influence of the length on the resonance frequency, wires with comparable diameters

of about 200 nm placed on KBr are considered (Fig. 8.2b). Assuming the ideal dipole relation as given in eq. 8.1 for a wire completely embedded in vacuum ($n = 1$), a shift of the measured data towards higher resonant wavelengths is obvious. Using the value of the refractive index of KBr in eq. 8.1 the calculated curve seems to fit the measured data. But the used assumption does not fit to the real configuration. The wires are not completely embedded in the substrate, rather they are supported and less than the half of the environment is truly KBr. To get deeper insight, BEM calculations for diameter $D = 200$ nm and variable lengths (L from 1.5 to 4.5 μm) were performed. But, also these calculations do not fit to the data if vacuum around the wire is assumed. Only the BEM calculations for wires embedded in an effective medium with refractive index n_{eff} according to eq. 8.2 yield reasonable agreement to the measured data.

This clearly indicates the influence of the substrate on the resonance position. The polarizibility of a cover medium gives further effect. To demonstrate this, individual gold nanowires on different substrates were covered with a thin dielectric layer, e.g. paraffin wax, and IR spectra were taken before and after evaporation. Because of the coverage the resonance wavelength is shifted towards higher wavelengths, which can be estimated with an effective dielectric constant using $\varepsilon_{\text{eff}} = \frac{1}{2}(\varepsilon_{\text{c}} + \varepsilon_{\text{s}})$ with ε_{c} as the dielectric constant of the cover medium. Together with eq. 8.2 this gives calculated ratios $n_{\text{eff}}^{\text{air}}/n_{\text{eff}}^{\text{paraffin}} = 0.875$ for the KBr substrate (with $\varepsilon_{\text{s}} = 2.34$ and $\varepsilon_{\text{c}} = 2.02$ for paraffin) and 0.923 for the ZnS substrate (with $\varepsilon_{\text{s}} = 4.84$), respectively. These ratios are consistent with the measured data obtained from the spectral shift before and after deposition of paraffin [29].

Comparing experimental nanowire data for Au and Cu, it becomes obvious that the resonance width is proportional to the resonance frequency. This behavior corresponds to that of perfectly conducting cylinders in vacuum [26]. It means that the width of the fundamental resonance in the IR is dominated by the geometry of the nanowire (length L and diameter D), not by its material properties. In the IR the dielectric functions of the metals gold and copper show only marginal quantitative differences and the wire diameters are relatively large compared with the skin depth and to the typical dimensions (a few 10 nm) for the onset of size effects in the conductivity. Deviation could arise if wires are of worse crystalline quality.

From relative transmittance spectra (in Fig. 8.13) the ratio of the extinction cross-section of a single nanowire related to its geometric cross-section was estimated. Assuming $1 - T_{\text{rel}} \approx 2(\sigma_{\text{ext}}/A_0)/(n_{\text{s}} + 1)$, where the influence of the substrate on the signal strength is taken into account in analogy to the transmittance change by the substrate of a thin film [74] in comparison with a freestanding film [75], the ratio

$$\frac{\sigma_{\text{ext}}}{\sigma_{\text{geo}}} \approx A_0(1 - T_{\text{rel}}) \cdot (n_s + 1) \cdot \frac{1}{2LD} \tag{8.6}$$

was obtained. Inserting the spot size A_0, the transmittance change in the spectrum $(1 - T_{\text{rel}})$, the refractive index of substrate n_{s}, L from microscopy in the visible spectral range, and D (known from wire growth process) leads to a $\sigma_{\text{ext}}/\sigma_{\text{geo}}$ shown in Fig. 8.14 for a wire with $L \approx 2.37$ μm and $D = 210$ nm placed on KBr. Any result

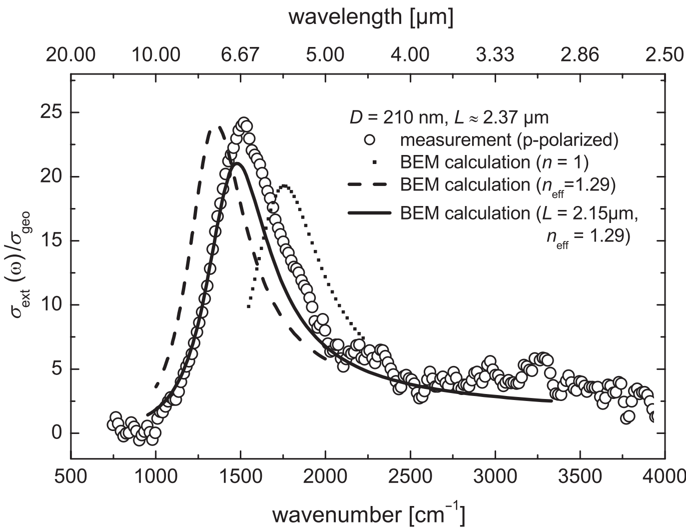

Fig. 8.14 Extinction cross-section related to the geometric cross-section of a gold nanowire with length $L = 2.37\,\mu\mathrm{m}$ and diameter $D = 210\,\mathrm{nm}$: experimental data (open circles) and BEM calculations assuming different refractive indices

above 1 means an extinction of intensity above geometric shadowing, which is a clear indication of the nanowires ability to confine light and therefore an indication for an enhanced local field in the vicinity of the nanowire. Since the measurements are performed in the farfield, only a spatially averaged field enhancement factor $\sqrt{\sigma_{\mathrm{ext}}/\sigma_{\mathrm{geo}}}$ can be calculated. For the representative spectrum in Fig. 8.14 a farfield enhancement factor of about 5 can be estimated for the resonance position.

The calculated resonance curves of single gold nanowires in Fig. 8.14 are obtained using the boundary element method BEM (see Sect. 8.2.2). Here, the gold nanowire is modeled as a rod with hemispherical tip ends completely embedded in a medium. As discussed in Sect. 8.2, the calculated data for a nanowire in vacuum deviate from the experimental ones because of the polarizibility of the substrate. Considering an effective refractive index $n_{\mathrm{eff}} = 1.29$ (according to eq. 8.2) in order to describe the influence of the substrate approximately, an even better agreement in strength and shape of the resonance curve with the experimental data is obtained. Only the position of the resonance maximum differs slightly. But, a BEM calculation with a length changed within its error fits the measured spectrum data. The same does a calculation (not shown) with an unchanged length but a slightly different n_{eff} of 1.20. At this point the wire-length uncertainty for this sample type limited a more precise conclusion.

The important role of the substrate polarizability was also discussed by Fumeaux [76] who studied the resonance length of gold nanoantennas for two fixed IR wavelengths and one in the visible range with a special microbolometer setup.

8.4.2 Antenna Resonances in the Visible Range

In the visible to ultraviolet range, below the optical plasma edge of the respective metal, several types of plasmon resonances of metal nanowires can be observed. These are the resonances for electric field along the short axis of nanowires, antenna resonances (LSP) of accordingly short nanowires, and higher orders of antenna resonances from wires with micron length.

The LSP resonance position is strongly dependent on the detailed particle shape. For fixed length that resonance is red-shifted with diameter, and, as shown in Fig. 8.15, this shift could be of several tens of nanometers and even more when the size of the nanoparticle increases [2,35,77]. For an ellipsoidal particle the redshift is faster than for a cylindrical particle as shown in Fig. 8.15. For an increase of 10 nm in size, the shift of the LSP for an ellipse (e-beam lithographically written structure with certain height) is of 30 nm whereas it is only of 10 nm for a cylinder-like structure [2].

The plasmon resonances were measured by extinction (all the losses due to scattering and absorption) spectroscopy in transmission. The e-beam lithographically prepared samples (Sect. 8.3.2) were illuminated at normal incidence with collimated white light polarized along the nanowires length. To take into account the optical transfer function of the experimental set-up (different optical transmission for each wavelength due to the mirrors, the array or the CCD), it was necessary, in a first stage, to record the intensity of the light transmission without the nanowires (I_0). In a second stage, the intensity of the light transmission is measured considering the presence of the nanowires (I_t). The nanowire spectrum corresponding to

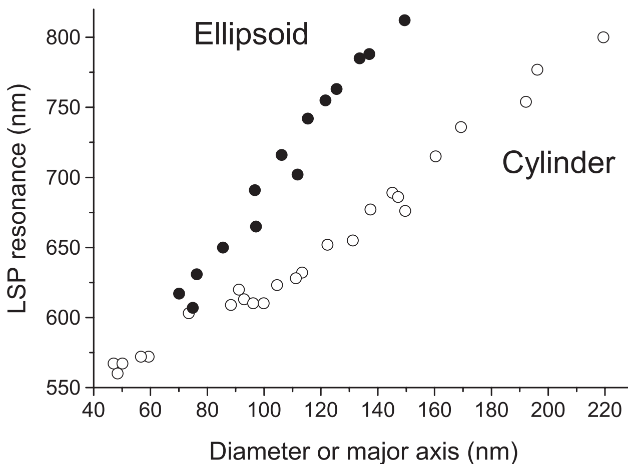

Fig. 8.15 Variation of the LSP resonance wavelength with diameter of cylinder-like structures (open circle) or with length of ellipse-like structures (full circle), respectively. The minor axis of the ellipsoids is 50 nm and the height of the two kinds of nanoparticles is 50 nm. The gap between two nanoparticles is kept constant at 200 nm. The particles were made by electron-beam lithography on glass

the plasmon resonance was obtained by simply dividing I_0 by I_t, i.e. it is shown as $(T_{rel})^{-1}$. Since the experiments were done in transmission configuration, it implies that the nanowires had been deposited on a transparent substrate such as glass or ITO.

Extinction spectra were recorded on a Jobin–Yvon micro-Raman spectrophotometer (Labram) [78]. Each extinction spectrum was recorded, by removing the notch filter, over an area of $80 \times 80\,\mu m^2$ in diameter selected by the confocal hole. A 10-fold magnification objective (NA $= 0.28$) was used. It was important to use an objective with a small numerical aperture (NA) since only the transmitted light should be collected and not the light diffusely scattered by the nanowire. The use of nanoparticle arrays was necessary to get enough signal strength since the extinction signal of isolated nanoparticles was too low with such experimental set up. (It has to be noticed that the antenna resonances in the visible range are much weaker than in the infrared.) With scanning nearfield optical microscopy individual nanoantennas can be studied, however, still with less energy resolution than in farfield spectroscopy.

Higher orders of resonance of longer nanowires can be observed as new bands in extinction spectra at wavelengths considerably lower than the dipolar LSP resonance, as shown in Fig. 8.16. Thus, on the spectra, when one resonance band is

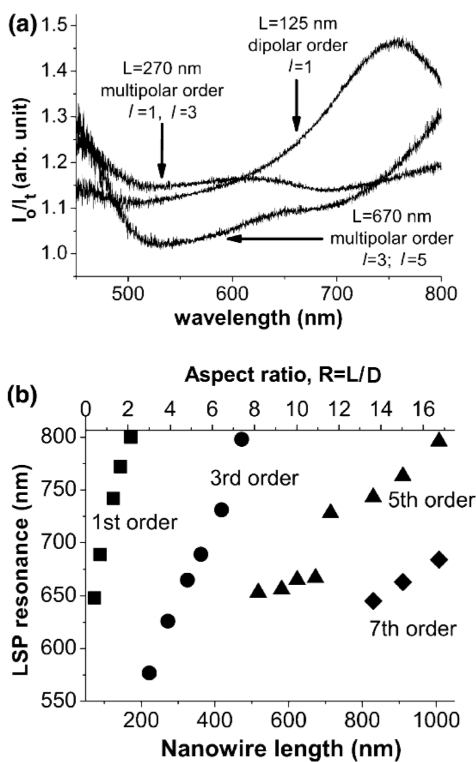

Fig. 8.16 **(a)** Extinction spectra I_o/I_t of electron-beam lithographically made gold nanowires arrays of different lengths L on glass. The value of l represents the LSP order. **(b)** Development of the LSP resonance with nanowires length L and respective aspect ratio (in the array plane) of the nanowire (ratio R between L and the width of the nanowires): 1st order (square), 3rd order (circle), 5th order (triangle), 7th order (diamond). The width and height of the nanowire, and the gap between two nanowires were kept constant at 60, 50, and 150 nm, respectively

red-shifted because of an increasing length, another one appears in the low wavelength range and is also red-shifted when the length of the nanowire further increases [79]. Schider et al. have assigned these multiorder resonances to odd orders l ((1)) because the resonance should keep the same symmetry than the nanowire [4]. With nanowires up to 1 µm long, we can observe up to the 7th order, as shown in Fig. 8.16. In the case of multiorder resonances, it should be noticed that the red shift is not identical for each order, but the variation the LSP resonance position is lower for higher order [4, 31, 72, 73, 79].

For nanowires longer than 1 µm, Félidj et al. were able to observe some multiorder resonances and the associated local maxima by Raman imaging [80]. They have then measured a LSP beat wavelength of 379 nm. Moreover, Ditlbacher et al. have proposed to consider the nanowires as LSP resonators [81]. In the case of nanowires longer than 10 µm, they have been able to determine a propagation length of about 10 µm and a nanowire end face reflectivity of 25%. They assume that the nanowire can be applied as efficient LSP Fabry–Perrot resonator.

Another application takes advantage of the fact that the position of the LSP resonance is both, different for each of the three nonidentical dimension of the nanowire along their respective directions and strongly dependent on the polarization of the exciting field. It is the design of a spectral selective polarizing nanowire device for the visible range proposed by Schider et al. The authors of this work optimized the extinction ratio between TE and TM polarization through the use of a nanowire grating and the selection of the appropriate grating parameters and nanowire width [82]. In the IR similar metal-grating polarizers are in practical use since many years.

8.5 Application to Surface Enhanced Raman Scattering

The surface enhanced Raman scattering (SERS) is a powerful tool that has made possible the observation of small numbers of molecules. Moreover, it has allowed the observation of individual molecules because of a Raman signal enhancement estimated to 10^{14} [54, 83].

This important intensification of the Raman signal is achieved by using some metallic nanostructures such as nanoparticles, rough thin films, colloidal solutions, etc. The origin of the Raman scattering enhancement can be interpreted in terms of two different processes: the first one of electromagnetic nature [23, 84] and the second process with chemical origin [85, 86].

The electromagnetic process is based on the nearfield interaction between a metallic "particle" (Au, Ag, Cu...) and a molecule. During the illumination of the SERS surface at the excitation wavelength λ_0, the particle interacts with light and creates a significant local enhancement of the electromagnetic field that can be achieved under specific conditions: plasmon resonance, lightning rod effect, or confinement effect. Therefore, a molecule in the vicinity of the resonant particle is excited because of a huge field. Since the Raman process is proportional to the excitation field, the molecule scatters a large Raman signal at a shifted wavelength

λ_R. The Raman wavelength can also interact with the particle (re-radiation process) and be enhanced. Thus, the enhancement factor can be written as [23]:

$$\left|\frac{E_{\text{local}}(\lambda_0)}{E_0(\lambda_0)}\right|^2 \left|\frac{E_{\text{local}}(\lambda_R)}{E_0(\lambda_R)}\right|^2 = f(\lambda_0)f(\lambda_R) \tag{8.7}$$

The first term, at λ_0, stems from the particle nearfield enhancement at the incident wavelength. The second one, at λ_R, arises from the re-radiation of the molecule Raman nearfield by the particle. As a rough approximation it is assumed that the Raman enhancement is proportional to the fourth power of the nearfield local enhancement around the particles. Then a field enhancement factor of 10^3 induces a Raman enhancement of 10^{12}. That simple approximation is not completely valid since the spectral shift between the incident and Raman wavelength can be important (several tens of nanometers). Then the position of the Raman wavelength has an influence on the signal enhancement [2, 87].

The chemical enhancement is less understood. However, it is often explained in terms of the electronic interactions between metal surface and molecules adsorbed to certain defect sites. Some models proposed a dynamic charge transfer (Otto 1983 [86, 88–90]). Unified treatments for Raman and fluorescence have also been developed to account for the quantum-mechanical process in a metallic electrodynamical environment [91,92]. The contribution of such process to SERS enhancement has been estimated to two orders of magnitude. That means that the chemical process does not contribute significantly to the Raman signal enhancement. Therefore and since it is observed only in case of special atomic defects on the metal surface, we will focus on the electromagnetic enhancement here. In contrast to the control of the chemical effect [93], it is much better known how the electromagnetic field enhancement can be manipulated in a controlled manner, which is still under investigation for the first layer effect [93].

The precise determination of the SERS efficiency of a nanostructured substrate and its relation to the optical properties of the substrate requires the control of size and shape of the nanostructures. For this, several groups have used lithographic techniques such as e-beam lithography (see Sect. 8.3.2) or nanosphere lithography to design some nanoparticle arrays [1,2,87,94–96]. Chemical self-assembly has also been used to produce such arrays [97]. In these cases, one can control precisely the position of the plasmon resonance of the nanoparticle. It is then possible to estimate the role of the plasmon resonance on the Raman signal enhancement.

Since there are two different enhancement factors at the incident and Raman wavelengths, λ_0 and λ_R, one would intuitively assume that the best Raman signal is obtained for a position of the plasmon resonance located between the two wavelengths λ_0 and λ_R. Indeed, this has been observed for cylindrical (Fig. 8.17) or triangular nanoparticles with a maximum of enhancement achieved for a plasmon resonance close to $(\lambda_0 + \lambda_R)/2$ [2, 87, 94, 96].

For the results shown here, SERS-active substrates were obtained by immersion in a 10^{-3} M solution of the probe molecule, *trans*-1,2-*bis*(4-pyridyl)ethylen (BPE), during 1 h and drying with nitrogen. Raman spectra are recorded on a Jobin–Yvon

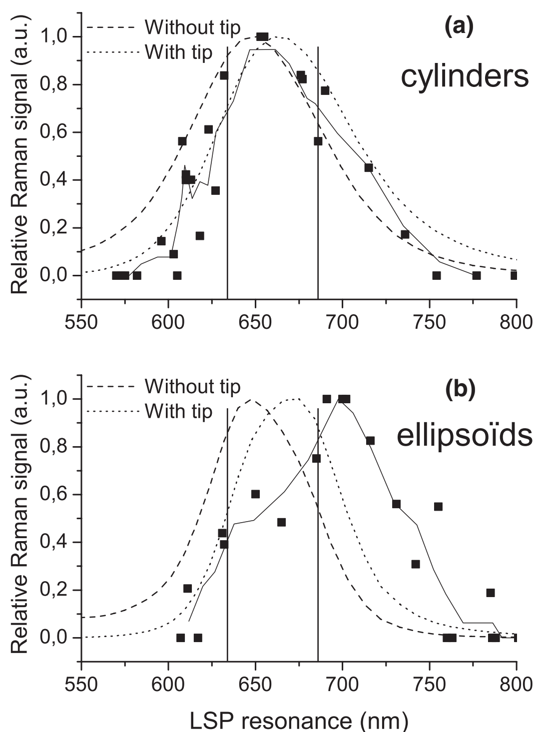

Fig. 8.17 Raman signal enhancement versus LSP resonance: **(a)** for cylinder-like structures, **(b)** for ellipse-like structures, both as in Fig. 8.15. The enhancement has been estimated from the intensity of the $1200\,\mathrm{cm}^{-1}$ line of the *trans*-1,2-*bis*(4-pyridyl)ethylene used as molecular probe and the LSP resonances correspond to the ones observed in Fig. 8.15. Solid lines are the binned average values of the LSP resonance and the Raman intensity. The dashed and dotted lines are the Raman signal enhancement calculated in the quasistatic approximation without the lightning rod effect of the tip (dashed line) and with that effect (dotted line), respectively. The minor axis of the ellipsoids is 50 nm and the height of the two kinds of nanoparticle is 50 nm. The gap between two nanoparticles is kept constant at 200 nm. The excitation wavelength was the 632.8 nm line of an He–Ne laser. The excitation wavelength and the Raman wavelength are marked with vertical lines

micro-Raman spectrophotometer (Labram). For Raman spectroscopy a $100\times$ magnification objective $(\mathrm{NA} = 0.90)$ in back scattering geometry was used. Raman measurements were carried out with the 632.8 nm line of an He–Ne laser. To actually determine the effect of the nanowire length on the Raman enhancement, the laser polarization was fixed for all experiments relatively to the long axis of the nanowires. Even if the chosen microscope objective has a large numerical aperture $(\mathrm{NA} = 0.90)$, the laser beam depolarization was small and not significant [98, 99]. Thus, only a small amount (a few percent) of the total energy of the excitation light was depolarized. Moreover, this depolarized light was not located on the central focus spot but laterally [98, 99]. It was easily eliminated with an appropriate confocal hole. The intensity of the signal was estimated by calculating the area of a Lorentzian fitted band of *trans*-1,2-*bis*(4-pyridyl)ethylene located at $1200\,\mathrm{cm}^{-1}$

(this mode has significant ethylene C = C stretch character, see [100] for details). To see the role of the nanowire characteristics (length, plasmon resonance, etc.) on the SERS signal, only the relative Raman intensity is considered. Accordingly, for each figure of this section, the collected Raman signal was normalized to the best Raman signal obtained with nanowires.

Different to the cylinders, in the case of ellipsoidal nanoparticles Fig. 8.17 shows the best enhancement for the plasmon resonance close to the Raman wavelength λ_R [2]. This result can be explained with a simple quasistatic model, which allows the determination of the position of the plasmon resonance and the Raman signal enhancement [2]. The authors of this work have shown that depending on whether the lightning rod effect due to the wire tip is taken account or not, the LSP resonance required to achieve the best Raman signal enhancement will be shifted or not shifted, respectively. That is, this LSP resonance is red-shifted and close to the Raman wavelength when this tip effect is introduced in the model whereas it is still located between the two wavelengths λ_0 and λ_R if this tip effect is not considered, as shown in Fig. 8.17 [2]. In this case, one can assume that the process of Raman re-radiation seems to be more favored because of the lightning rod effect and, therefore, for elongated particles that play the role of a nanoantenna [2].

To determine the effect of nanoparticles with high aspect ratio on the Raman enhancement, several research groups have studied gold nanowires and their SERS efficiency [11, 31, 72, 73]. Laurent et al. have shown that nanowires with lengths from 200 nm to 650 nm are also active as SERS substrates and that such structures are also relevant to make SERS experiments [72, 73]. It means that the higher (multi)-order LSP observed with long nanowires are also efficient for SERS as could be dipolar modes. The effect of the multiorder LSP modes was demonstrated by Billot et al. [31]. In this reference, it is shown how the Raman signal enhancement is strongly dependent on the length of the nanowire. As depicted on Fig. 8.18 the Raman signal shows a strong variation with the length of the nanowire. Three maxima can be observed on such curve between 100 and 200 nm and about 650 and 900 nm. The size and shape of the nanowire seem to be of real importance to determine the best Raman signal enhancement.

The SERS gains were calculated with the three-dimensional finite-difference time-domain (FDTD) method using the Drude–Lorentz dispersion model. The Raman signal enhancement is determined at the surface of the nanoparticles and molecules are considered as polarizable point dipoles homogeneously distributed at the particle surface (for more details on the model, see [101, 102]).

The FDTD method gives a good agreement with the experimental data as shown in Fig. 8.18. From the enhancement mapping around the nanowire, these calculations make obvious that the Raman enhancement is highly located at the tip end of the nanowire and that the main contribution to the Raman signal enhancement comes from the two extremities of the nanowire [31].

To confirm this observation, the results can be compared qualitatively to some other numerical calculations done by Calander et al. [103]. Indeed, Calander et al. [103] have calculated the field enhancement at the tip of silver ellipses with length up to 1.6 μm and aspect ratio up to 25. They observed some maxima of field enhancement for specific lengths and aspect ratios. There are especially three zones

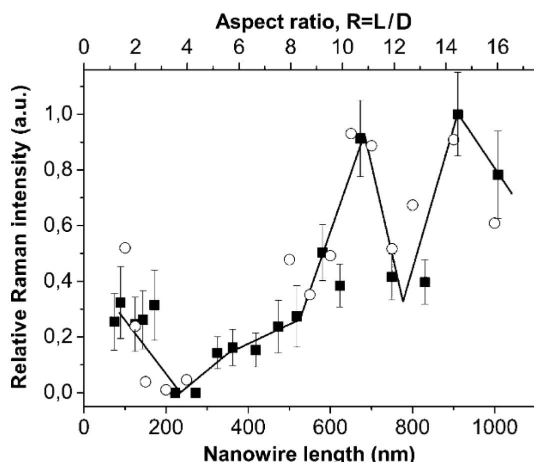

Fig. 8.18 Evolution of the Raman signal enhancement versus the nanowire aspect ratio *R* and the nanowire length for experimental data (plain square) and for FDTD calculations (open circle). The enhancement has been estimated from the intensity of the 1200 cm^{-1} line of the *trans*-1,2-*bis*(4-pyridyl)ethylene used as molecular probe. The plain line is just a guide for the eyes. The width and height of the nanowire and gap between two nanowires are kept constant at 60, 50, and 150 nm, respectively. The excitation wavelength was the 632.8 nm line of an He–Ne laser

of maxima for lengths about 50, 500, and 1000 nm and respective aspect ratios 5, 10, and 14. Although the authors of these references do not use the same materials (gold [31] and silver [103]), one could suppose that the results obtained for these two different metals should be close since their dielectric functions are rather similar at the excitation wavelength of 633 nm used in both papers. The importance of these results lies on the fact that they point out the crucial role of the size and the shape of the nanowire in the determination and optimization of their SERS efficiency.

To go further and to determine the plasmon resonance contribution, the Raman signal enhancement can also be plotted versus the plasmon resonance position (Fig. 8.19). This has been done for each plasmon order since multiorder LSP modes are observable for nanowires with length above 200 nm (see Sect. 8.4.2 and notice that the nanowires used for SERS experiments presented in Fig. 8.19 are the same for which the LSP resonance has been shown in Fig. 8.16). To choose the plasmon resonance order, the plasmon resonance used was the closest to the excitation wavelength (633 nm). In this case, the best enhancement is achieved for the 5th and the 7th order, which means that in specific conditions the higher order LSP modes can give better enhancement than dipolar order [31]. Moreover, another interesting result is that for almost each order, the best enhancement is obtained for a plasmon resonance close to the Raman wavelength [31]. This means that even for higher-order LSP modes, the best SERS efficiency is achieved for a LSP resonance close to the Raman wavelength. This latter observation seems to be a general rule that can be applied to either dipolar or multiorder LSP modes. Regarding the interpretation given for small ellipses and for the dipolar modes, the nanowire can be considered, independently of its length, as an optical nanoantenna.

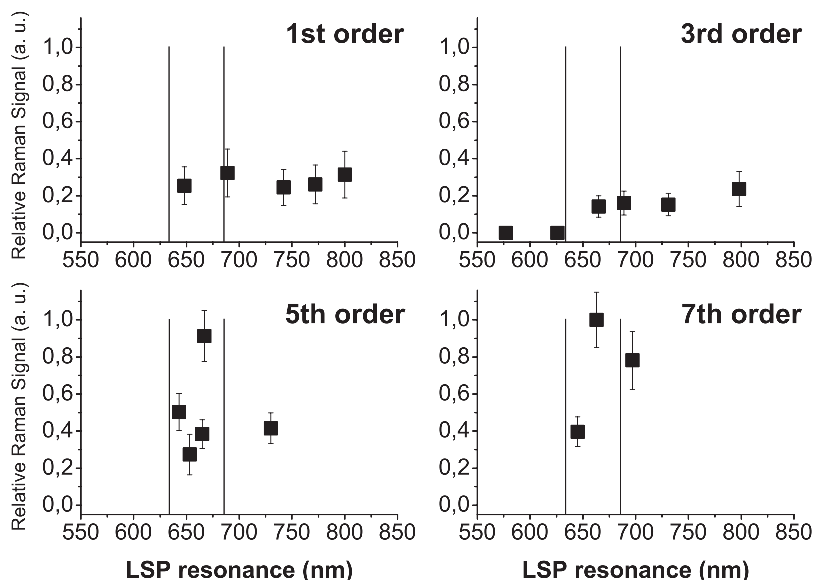

Fig. 8.19 Evolution of the Raman signal enhancement versus the LSP resonance for each order observed in Fig. 8.16. The enhancement has been estimated from the intensity of the 1200 cm^{-1} line of the *trans*-1,2-*bis*(4-pyridyl)ethylene used as molecular probe. The excitation wavelength and the Raman wavelength are marked with vertical lines

8.6 Application to Surface Enhanced Infrared Spectroscopy

In 1980, Hartstein et al. [104] found that the IR absorption of molecules can be enhanced. The enhancement factor can reach the order of 1000, if the molecules are adsorbed on Au or Ag island films. [105–107 and references therein].

This effect was called surface enhanced infrared absorption (SEIRA). As explained earlier for antennas, the strength of the enhancement depends on the metal type according to the specific dielectric function in the infrared and, because of the relation to the excitation spectrum of surface plasmons in the IR range, on the metal-film morphology. Also to SEIRA may contribute a first-layer effect [108], which is not considered here. For metal-island films, maximum enhancement is found at the percolation threshold [109]. Model calculations based on effective dielectric functions are able to describe the experimental results from IR transmittance spectroscopy of extended film areas well. However, it is important to note that the real film morphology must fit to the assumptions of the model [110]. Such model calculations revealed enhanced adsorbate-vibration signals but also a change in the adsorbate lineshape with metal-filling factor of the film [109]. The lineshape may be strongly asymmetric [111]. The strongest asymmetry occurs at the percolation threshold at which the enhancement reaches the maximum [109]. Looking at the individual metal islands this maximum enhancement can be understood well, since at percolation the number of adsorbate sites in the smallest possible grooves between

neighbor islands becomes maximum. In these grooves the local field enhancement $|E_{\text{local}}(\lambda_{\text{IR}})/E_0(\lambda_{\text{IR}})|$ is expected to be particularly strong. For random film morphologies certain hot spots with huge field enhancement are mentioned in the SERS literature, for example [112]. There is no reason why they should not exist in the IR range.

The local adsorbate-vibration signal enhancement can be estimated as $|E_{\text{local}}(\lambda_{\text{IR}})/E_0(\lambda_{\text{IR}})|^2$, the detailed lineshape change was not considered. The signal enhancement (or the enhancement factor, respectively) depends on the electromagnetic resonance spectrum in the nearfield. Since the islands usually are rather flat and broad and since they have a strong electromagnetic coupling to neighbor islands such resonance curves in the IR are extremely broadened. The oscillator strength of these broad resonances depends on size, shape, and the kind of array on the one hand, and, on the other hand, on the metallic properties of the particles; for example, on the relaxation rate of the free charge carriers and on their plasma frequency. The enhancement therefore depends strongly on the metal properties [113]. In reality this means also, that too small particles give less enhancement because of the strong effect of surface scattering of free charge carriers.

SEIRA studies of extended areas of metal–nanoparticle films always give only information on the average enhancement [113]. The best average enhancement factors are only three orders of magnitude [106], since higher local enhancement is balanced with lower ones at adsorption sites in wider grooves or at smaller islands.

In the following we will show one attempt to get an information on the possible local enhancement factor for molecules on an individual object; here a nanowire.

The enhanced farfield cross-section of a single nanowire at resonance mentioned in Sect. 8.4.1 already indicates the enhanced nearfield in the vicinity of the nanowire tips. Moreover, theoretical calculations (with use of BEM) reveal the enhanced nearfield for a nanowire oscillating in resonance (e.g. for a wire with $L \approx 2.37\,\mu\text{m}$ and $D = 210\,\text{nm}$ in vacuum) to be $|E_{\text{local}}/E_0| \approx 30$ at a distance of 5 nm from the tip end of the wire. Even higher enhancement should be achieved for closer distances to the tip. To detect the enhanced nearfield experimentally, an absorbate molecule is used as probe. The well-known molecule octadecanethiol (ODT), which is an organic compound containing one thiol (SH) group as a functional group, is adsorbed. Concerning SEIRA, the usage of the long-chained ODT ($C_{18}H_{37}SH$) provides three advantages: (i) it easily adsorbs on noble metals because of the particular affinity of sulfur, which ensures a well-defined sample preparation (e.g., ODT only adsorbs on gold surfaces, like films or wires, and not on the surface of the substrate). This fact is well known from preparation of self-assembled monolayers (SAM) [114]. (ii) The surface of an ODT monolayer is very inert preventing multilayer absorption; a well-defined thickness (2.4 nm [115]) of the ODT monolayer is feasible. (iii) ODT features several infrared active absorption modes. The IR spectrum of ODT reveals absorption bands because of the vibration of methyl (CH_3) and methylene (CH_2) groups. For the investigations in the following the strongest absorption modes of these groups (symmetric ($2919\,\text{cm}^{-1}$) and asymmetric ($2850\,\text{cm}^{-1}$) CH_2 stretching vibrations [116]) are considered.

The sample preparation is rather common. Single gold nanowires are deposited on an infrared-transparent substrate (CaF_2) and exposed to a 1 mM solution of ODT in ethanol for at least 8 h. After such long deposition time one can be sure that one monolayer of ODT is adsorbed on the gold nanowires. To obtain an absorption band of ODT close to the fundamental resonance of the nanowire, a nanowire with an appropriate length has to be chosen. After localizing such a wire by microscopy with visible light, normal IR transmittance measurements under the same conditions as described in Sect. 8.4.1 are performed. Sample spectra are recorded at the position of the selected gold nanowire covered with ODT, reference spectra are taken at a position beside the nanowire without ODT (see Fig. 8.20). The relative transmittance of the selected single nanowire (diameter 100 nm) reveals the fundamental antenna resonance. In addition absorption bands at 2850 and 2919 cm^{-1}, which can be identified as symmetric and asymmetric CH_2 stretching vibrations of ODT (see Fig. 8.21, black line), are detected in the infrared spectrum. In the case of gold wires

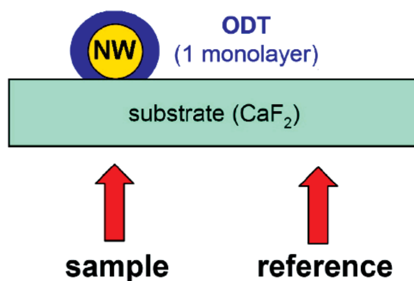

Fig. 8.20 Sketch of the applied measurement principle

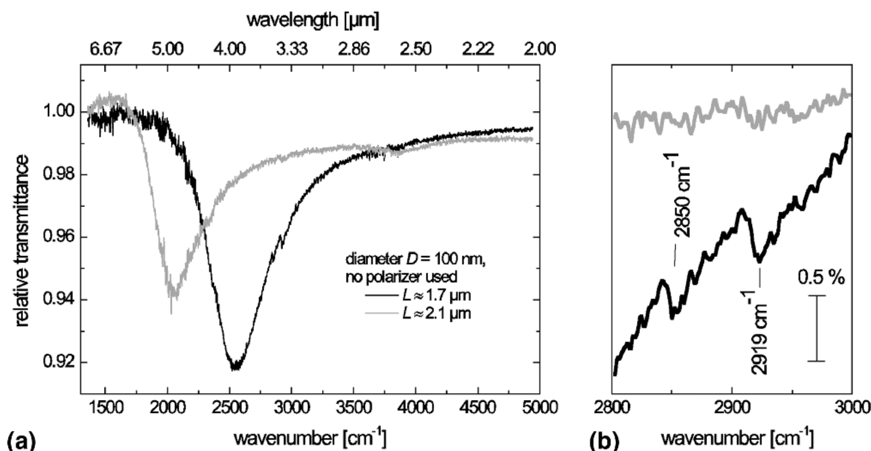

Fig. 8.21 **(a)** Relative transmittance spectra of two different single gold nanowires covered with one monolayer ODT. **(b)** Magnification: The absorption bands can be assigned to the stretching vibrations of CH_2 for the wire with resonance frequency in the range of these vibrations (black line). For the wire with resonance frequency at lower wavenumbers no absorption bands are detected (grey line)

with antenna resonances at much lower resonance frequency than the CH_2 stretching modes of ODT these vibrations could not be observed (grey line). The appearance of the absorption bands of one monolayer ODT on a single nanowire is an indication of local field enhancement due to the antenna resonance. As it follows from the spatial distribution of the local field enhancement around a nanowire at resonance, the detected signal should mainly originate from the molecules adsorbed on the wire tips. Also, the contributions to the signal from ODT molecules adsorbed elsewhere are suppressed by mirror charges at the nanowires surface or the absorption modes cannot be excited because of the orientation of their dynamic dipole perpendicular to the exciting field. The nearfield enhancement can be estimated by comparing the antenna-enhanced symmetric CH_2 absorption band to the nonenhanced symmetric CH_2 absorption band achieved from infrared reflection-absorption spectroscopy (IRRAS) measurements of ODT on smooth gold films [117]. Taking into account the areas that really contribute to the signal (the hole sample area in IRRAS, for the SEIRA spectrum the tip ends from the individual nanowire as a small part of the focal area), the SEIRA-factor was estimated to reach 100,000 for the spectrum in Fig. 8.21. Even higher enhancement is achieved if the resonance wavelength is exactly at the molecular vibration [117].

Acknowledgments F.N. and A.P. gratefully acknowledge technical support by M. Süpfle, helpful discussions with A. Otto, B. Gasharova, and Y.-L. Mathis. J.A. acknowledges software access from F.J. García de Abajo, discussions with G.W. Bryant, and financial support from Gipuzkoa Foru Aldundia (Gipuzkoa Fellows program) and the Government of the Basque Country (NANOTRON project).

References

1. Félidj N, Aubard J, Lévi G, Krenn JR, Salerno M, Schider G, Lamprecht B, Leitner A, Aussenegg FR (2002) Controlling the optical response of regular arrays of gold particles for surface-enhanced Raman scattering. Phys Rev B 65:075419
2. Grand J, Lamy de la Chapelle M, Bijeon JL, Adam PM, Vial A, and Royer P (2005) Role of localized surface plasmons in surface-enhanced Raman scattering of shape-controlled metallic particles in regular arrays. Phys Rev B 72:033407
3. Link S, El-Sayed MA (1999a) Spectral properties and relaxation dynamics of surface plasmon electronic oscillations in gold and silver nano-dots and nano-rods. J Phys Chem B 103:8410
4. Schider G, Krenn JR, Hohenau A, Ditlbacher H, Leitner A, Aussenegg FR, Schaich WL, Puscasu I, Monacelli B, and Boreman G (2003) Plasmon dispersion relation of Au and Ag nanowires. Phys Rev B 68:155427
5. Anger P, Bharadwaj P, Novotny L (2007) Spectral dependence of single molecule fluorescence enhancement. Nanotechnology 18:044017
6. Farahani JN, Pohl DW, Eisler HJ, Hecht B (2005) Single quantum dot coupled to a scanning optical antenna: A tunable superemitter. Phys Rev Lett 95:017402
7. Frey HG,Witt S, Felderer K, Guckenberger R (2004) High resolution imaging of single fluorescent molecules with the optical near-field of a metal tip. Phys Rev Lett 93:200801
8. Mertens H, Biteen JS, Atwater HA, Polman A (2006) Polarization-selective plasmon-enhanced silicon quantum-dot luminescence. Nano Lett 6:2622

9. Girard G (2005) Near fields in nanostructures. Rep Prog Phys 68:1883
10. Mie G (1908) Beiträge zur Optik trüber Medien, speziell kolloidaler Metallösungen. Ann Phys, Lpz 25, 377
11. Aizpurua J, Bryant GW, Richter LJ, García de Abajo FJ, Kelley BK, Mallouk T (2005) Optical properties of coupled metallic nanorods for field-enhanced spectroscopy. Phys Rev B 71:235420
12. Cubukcu E, Kort EA, Crozier KB, Capasso F (2006) Plasmonic laser antenna. Appl Phys Lett 89:093120
13. Ebbesen TW, Lezec HJ, Ghaemi HF, Thio T, Wolff PA (1998) Extraordinary optical transmission through sub-wavelength hole arrays. Nature 391:667
14. Bozhevolnyi SI, Volkov VS, Devaux E, Laluet JY, Ebbesen TW (2006) Channel plasmon subwavelength waveguide components including interferometers and ring resonators. Nature 440:508
15. Fan S, Joannopoulos JD (2002) Analysis of guided resonances in photonic crystal slabs. Phys Rev B 65:235112
16. Steinhögl W, Schindler G, Steinlesberger G, and Engelhardt M (2002) Size-dependent resistivity of metallic wires in the mesoscopic range. Phys Rev B 66:075414
17. Berthier S, Peiro J (1997) Infrared absorption of nanocermets close to the percolation threshold. J Phys III (France) 7:537
18. Jackson JB, Halas NJ (2004) Surface-enhanced Raman scattering on tunable plasmonic nanoparticle substrates. Proc Natl Acad Sci USA 101:17930
19. Shubin VA, Sarychev AK, Clerc JP, and Shalaev VM (2000) Local electric and magnetic fields in semicontinuous metal films: Beyond the quasistatic approximation. Phys Rev B 62:11230
20. Xu H, Aizpurua J, Apell SP, Käll M (2000) Electromagnetic contributions to single-molecule sensitivity in Surface-enhanced Raman scattering. Phys Rev E 62:4318
21. Dvoynenko MM, Goncharenko AV, Romaniuk VR, Venger EF (2001) Effects of dimension on optical transmittance of semicontinuous gold. Physica B 299:88
22. Raether H (1988) Surface Plasmons on Smooth and Rough Surfaces and on Gratings (Springer Tracts in Modern Physics, Vol. 111), Springer-Verlag, Berlin
23. Wokaun AW (1984) Surface enhanced electromagnetic processes. Solid State Phys 38:223
24. Lynch DW, Hunter WR (1985) In: Palik ED (Ed) Handbook of Optical Constants of Solids. Academic Press, San Diego, pp 275
25. Crozier KB, Sundaramurthy A, Kino GS, Quate CF (2003) Optical antennas: Resonators for local field enhancement. J Appl Phys 94:4632
26. Ruck TG (1970) Radar Cross Section Handbook. Plenum press, New York
27. Kreibig U and Vollmer M (1995) Optical Properties of Metal Clusters. Springer, Berlin/Heidelberg
28. Martin YC, Hamann HF, Wickramasinghe HK (2001) Strength of the electric field in apertureless near-field optical microscopy. J Appl Phys 89:5774
29. Neubrech F, Kolb T, Lovrincic R, Fahsold G, Aizpurua J, Toimil-Molares ME, Karim S, Cornelius TW, Neumann R, and Pucci A (2006) Resonances of individual metal nanowires in the infrared. Appl Phys Lett 89:253104
30. Link S, Mohamed MB, El-Sayed MA (1999b) Simulation of the optical absorption spectra of gold nanorods as a function of their aspect ratio and the effect of the medium dielectric constant. J Phys Chem B 103:3073
31. Billot L, Lamy de la Chapelle A, Grimault AS, Vial A, Barchiesi D, Bijeon JL, Adam PM, Royer P (2006) Surface enhanced raman scattering on gold nanowire arrays: evidence of strong multipolar surface plasmon resonance enhancement. Chem Phys Lett 422:303
32. Imura K, Nagahara T, Okamoto H (2004) Coacervate formation from natural glycolipid: One acetyl group on the headgroup triggers coacervate-to-vesicle transition. J Am Chem Soc 126:12730
33. Imura K, Nagahara T, Okamoto H (2005a) Near-field two-photon-induced photoluminescence from single gold nanorods and imaging of plasmon modes. J Phys Chem B 109:13214

34. Imura K, Nagahara T, Okamoto H (2005b) Near-field optical imaging of plasmon modes in gold nanorods. J Chem Phys 122:154701
35. Grand J, Adam PM, Grimault AS, Vial A, Lamy de la Chapelle M, Bijeon JL, Kostcheev S, Royer P (2006) Optical extinction spectroscopy of oblate, prolate, and ellipsoid shaped gold nanoparticles: Experiments and theory. Plasmonics 1:135
36. Little JW, Callcott TA, Ferrell TL, Arakawa ET (1984) Surface-plasmon radiation from ellipsoidal silver spheroids. Phys Rev B 29:1606
37. Purcell EM and Pennypacker CR (1973) Scattering and absorption of light by non-spherical dielectric grains. Astrophys J 186:705
38. Miller EK (1994) Time domain modelling in electromagnetics. J Electromagn Waves Appl 8:1125–72
39. Hafner Ch, Ballist R (1983) The multiple multipole method (MMP). Int J Comput Electr Electron Eng 2:1
40. Pendry JB and MacKinnon A (1992) Calculation of photon dispersion relations. Phys Rev Lett 69:2772
41. García de Abajo FJ, Howie A (1998) Relativistic electron energy loss and electron induced photon emission in inhomogeneous dielectrics. Phys Rev Lett 80: 5180
42. García de Abajo FJ, Howie A (2002) Retarded field calculation of electron energy loss in inhomogeneous dielectrics. Phys Rev B 75:115418
43. Aizpurua J, Hanarp P, Sutherland D, Bryant GW, Garcia de Abajo FJ, Kall M (2003) Optical properties of nanorings. Phys Rev Lett 90:057401
44. Bryant GW, García de Abajo FJ, and Aizpurua J (2008) Mapping the plasmon resonances of metallic nanoantennas. Nano Lett 8: 631
45. Hillenbrand R, Taubner, Keilman F (2002) Phonon-enhanced light–matter interaction at the nanometer scale. Nature 418:159
46. Hu J, Li L, Yang W, Manna L, Wang L, Alivisatos AP (2001) Linearly polarized Emission from colloidal semiconductor quantum rods. Science 292:2060
47. Gómez Rivas J, Kuttge M, Kurz H, Haring Bolivar P, Sánchez-Gil JA (2006) Low-frequency active surface plasmon optics on semiconductors. Appl Phys Lett 88:082106, 1
48. Englebienne P (1998) Use of colloidal gold surface plasmon resonance peak shift to infer affinity constants from the interactions between protein antigens and antibodies specific for single of multiple epitopes. Analyst 123:1599
49. McFarland AD, Van Duyne RP (2003) Single silver nanoparticles as real-time optical sensors with zeptomole sensitivity. Nano Lett 3:1057
50. Raschke G, Kowarik S, Franzl T, Soennichsen C, Klar TA, et al. (2003). Biomolecular recognition based on single gold nanoparticle light scattering. Nano Lett 3:935
51. Liebsch A and Persson BNJ (1983) Optical properties of small metallic particles in a continuous dielectric medium. J Phys C 16:5375
52. Prodan E, Radloff C, Halas NJ, Nordlander P (2003) A hybridization model for the plasmon response of complex nanostructures. Science 302:419
53. Emory SR, Nie S (1997) Probing single molecules and single nanoparticles by surface-enhanced Raman scattering. Science 275:1102
54. Kneipp K, Wang Y, Kneipp H, Perelman LT, Itzkan I, et al. (1997) Single molecule detection using surface-enhanced Raman scattering (SERS). Phys Rev Lett 78:1667
55. Xu H, Bjerneld EJ, Käll M, Börjesson L (1999) Spectroscopy of single hemoglobin molecules by surface enhanced Raman scattering. Phys Rev Lett 83:4357
56. Romero I, Aizpurua J, Bryant GW, García de Abajo FJ (2006) Plasmons in nearly touching metallic nanoparticles: Singular response in the limit of touching dimmers. Optics Express 14:9988
57. Fromm DP, Sundaramurthy A, Schuck J, Kino G, Moerner WE (2004) Gap-dependent optical coupling of single "bowtie" nanoantennas resonant in the visible. Nano Lett 4:957
58. Li K, Stockman MI, Bergman DJ (2003) Self-similar chain of metal nanospheres as an efficient nanolens. Phys Rev Lett 91, 227402
59. Hao E, Schatz G (2004) Electromagnetic fields around silver nanoparticles and dimers. J Chem Phys 120:357

60. Mühlschlegel P, Eisler HJ, Martin OJF, Hecht B, Pohl DW (2005) Resonant optical antennas. Science 308:1607
61. Karim S, Toimil-Molares ME, Maurer F, Miehe G, Ensinger W, Liu J, Cornelius TW, Neumann R (2006a) Synthesis of gold nanowires with controlled crystallographic characteristics. Appl Phys A 84:403
62. Karim S, Toimil-Molares ME, Balogh AG, Ensinger W, Cornelius TW, Khan EU, and Neumann R (2006b) Morphological evolution of Au nanowires controlled by Rayleigh instability. Nanotechnology 17:5954
63. Liu J, Duan JL, Toimil-Molares ME, Karim S, Cornelius TW, Dobrev D, Yao HJ, Sun YM, Hou MD, Mo D, Wang ZG, and Neumann R (2006) Electrochemical fabrication of single crystalline and polycrystalline Au nanowires: the influence of deposition parameters. Nanotechnology 17:1922
64. Toimil Molares EM, Brötz J, Buschmann, Dobrev D, Neumann R, Scholz R, Schuchert IU, Trautmann C, and Vetter J (2001a) Etched heavy ion tracks in polycarbonate as templates for copper nanowires. Nucl Instr Meth B 185:192
65. Toimil Molares ME, Buschmann V, Dobrev D, Neumann R, Scholz R, Schuchert IU, and Vetter J (2001b) Single-crystalline copper nanowires produced by electrochemical deposition in polymeric ion track membranes. Adv Mat 13:62
66. Cornelius TW, Brötz J, Chtanko N, Dobrev D, Miehe G, Neumann R, Toimil Molares ME (2005) Controlled fabrication of poly- and single-crystalline bismuth nanowires. Nanotechnology 16:246
67. Cornelius TW, Toimil-Molares ME, Neumann R, Karim S (2006) Finite-size effects in the electrical transport properties of single bismuth nanowires. J Appl Phys 100:114307
68. Toimil Molares ME, Höhberger EM, Schaeflein C, Blick RH, Neumann R, and Trautmann C (2003) Electrical characterization of electrochemically grown single copper nanowires. Appl Phys Lett 8:2139
69. Toimil-Molares ME, Balogh AG, Cornelius TW, Trautmann C, and Neumann R (2004) Fragmentation of nanowires driven by Rayleigh instability. Appl Phys Lett 85:5337
70. Rayleigh L (1878) On the instability of jets. Proc Lond Math Soc 10:4
71. Nichols FA, and Mullins WW (1965) Surface- (Interface-) and Volume-diffusion contributions to morphological changes driven by capillarity. Trans Metal Soc AIME 233:1840
72. Laurent G, Félidj N, Aubard J, Lévi G, Krenn JR, Hohenau A, Schider G, Leitner A, and Aussenegg FR (2005a) Evidence of multipolar excitations in surface enhanced Raman scattering. Phys Rev B 71:045430
73. Laurent G, Félidj N, Aubard J, Lévi G, Krenn JR, Hohenau A, Schider G, Leitner A, Aussenegg FR (2005b) Surface enhanced Raman scattering arising from multipolar plasmon excitation. J Chem Phys 122: 011102
74. Teschner U and Huebner K (1990) IR-spectroscopic data of thin insulating films on semiconductors. New methods of interpretation and analysis. Phys Status Solidi B 159:917
75. Berreman DW (1963) Infrared absorption at longitudinal optic frequency. Cubic Cryst Films Phys Rev 130:2193
76. Fumeaux C, Gritz MA, Codreanu I, Schaich WL, Gonzalez FJ, Boreman GD 2000 Measurement of the resonant lengths of infrared dipole antennas. Infrared PhysTecn 41:271
77. Ueno K, Mizeikis V, Juodkazis S, Sasaki K, Misawa H (2005) Optical properties of nanoengineered gold block. Opt Lett 30:2158
78. Royer P, Bijeon JL, Goudonnet JP, Inagaki T, and Arakawa ET (1989) Optical absorbance of silver oblate particles substrate and shape effects. Surface Science 217:384
79. Krenn JR, Schider G, Rechberger W, Lamprecht B, Leitner A, and Aussenegg FR (2000) Design of multipolar plasmon excitations in silver nanoparticles. Appl Phys Lett 77:3379
80. Félidj N, Laurent G, Grand J, Aubard J, Lévi G, Hohenau A, Aussenegg FR, Krenn JR (2006) Far-field Raman imaging of short-wavelength particle plasmons on gold nanorods. Plasmonics 1:39
81. Ditlbacher H, Hohenau A, Wagner D, Kreibig U, Rogers M, Hofer F, Aussenegg FR, Krenn JR (2005) Silver Nanowires as Surface Plasmon Resonators. Phys Rev Lett 95:257403

82. Schider G, Krenn JR, Gotschy W, Lamprecht B, Ditlbacher H, Leitner A, and Aussenegg FR (2001) Optical properties of Ag and Au nanowire gratings. J Appl Phys 90:3825
83. Nie S, Emory SR (1997) Probing single molecules and single nanoparticles by surface-enhanced Raman scattering. Science 275:1102
84. Jeanmarie DL, Duyne RPV (1977) Surface Raman spectroelectrochemistry. J Electroanal Chem 84:1
85. Moskovits M (1985) Surface-enhanced spectroscopy. Rev Mod Phys 57:783
86. Otto A (2005) The chemical (electronic) contribution to surface-enhanced Raman scattering. J Raman Spectrosc 36:497
87. Haynes CL, Duyne RPV. (2003) Plasmon-sampled surface-enhanced Raman excitation spectroscopy. J Phys Chem B 107:7426
88. Otto A (1983) On the first layer enhancement in Raman scattering of pyrioline on silver. J. de Physique C 10:37
89. Hein M, Dumas P, Sinther M, Priebe A, Lilie P, Bruckbauer A, Pucci A, Otto A (2006) Relation between surface resistance, infrared-, surface enhanced infrared- and surface enhanced Raman-spectroscopy's of C"2H"4 and CO on copper. Surface Science 600:1017
90. Lombardi JR, Birke RL, Sanchez LA, Bernard I, and Sun SC (1984) The effect of molecular structure on voltage induced shifts of charge transfer excitation in surface enhanced Raman scattering. Chem Phys Lett 104:240
91. Johansson P, Xu H, Käll M (2005) Surface-enhanced Raman scattering and fluorescence near metal particles. Phys Rev B 72:035427
92. Xu H, Wang X, Persson MP, Xu HQ, Käll M, Johansson P (2004) Unified treatment of fluorescence and Raman scattering processes near metal surfaces. Phys Rev Lett 93:243002
93. Skibbe O, Binder M, Pucci A, Otto A, Electronic contributions to infrared spectra of absorbate molecules on metal surfaces: ethylene on Cu(111). Submitted to The Journal of Chemical Physics
94. Félidj N, Aubard J, Lévi G, Krenn JR, Hohenau A, Schider G, Leitner A, Aussenegg FR (2003) Optimized surface-enhanced Raman scattering on gold nanoparticle arrays. Appl Phys Lett 82:3095
95. Grand J, Kostcheev S, Bijeon JL, Lamy de la Chapelle M, Adam PM, Rumuantseva A, Le'rondel G, Royer P (2003) Optimization of SERS-active substrates for near-field Raman spectroscopy. Synth Met 139:621
96. McFarland AD, Young MA, Dieringer JA, and Van Duyne RP (2005) Wavelength-scanned surface-enhanced Raman excitation spectroscopy. J Phys Chem B 109:11279
97. Wang H, Levin CS, Halas NJ (2005) Nanosphere arrays with controlled sub-10 nm gap as surface-enhanced Raman spectroscopy substrates. J Am Chem Soc 127:14992
98. Débarre A, Jaffiol R, Julien C, Nutarelli D, Richard A, Tchénio P, Chaput F, Boilot JP (2004) Quantitative determination of the 3D dipole orientation of single molecules. Eur Phys J D 28: 67
99. Novotny L, Sanchez EJ, Xie XS (1998) Near-field optical imaging using metal tips illuminated by higher-order Hermite–Gaussian beams. Ultramicroscopy 71:21
100. Yang W, Hulteen J, Schatz GC, and Duyne RV (1996) A surface-enhanced hyper-Raman and surface-enhanced Raman scattering study of trans-1,2-bis(4-pyridyl)ethylene adsorbed onto silver film over nanosphere electrodes. Vibrational assignments: Experiment and theory. J Chem Phys 104 4313
101. Grimault AS, Vial A, Lamy de la Chapelle M (2006) Modeling of regular gold nanostructures arrays for SERS applications using a 3D FDTD method. Appl Phys B 84:115
102. Vial A, Grimault AS, Macias D, Barchiesi D, Lamy de la Chapelle M (2005) Improved analytical fit of gold dispersion: Application to the modeling of extinction spectra with a finite-difference time-domain method. Phys Rev B 71:085416
103. Calander N, Willander M (2002) Theory of surface-plasmon resonance optical field enhancement at prolate spheroids. J Appl Phys 92: 4878
104. Hartstein A, Kirtley JR, Tsang JC. (1980) Enhancement of the Infrared absorption from molecular monolayers with thin metal overlayers. Phys Rev Lett 45:201

105. Aroca RF, Ross DJ, Domingo C (2004) Surface-Enhanced Infrared Spectroscopy. Appl Spectrosc 58: 324A
106. Enders D, Pucci A (2006) Surface enhanced infrared absorption of octadecanethiol on wet chemically prepared Au nanoparticle films. Appl Phys Lett 88:184104
107. Osawa M (2001) Near-Field Optics and Surface Plasmon Polaritons. in: Topics in Applied Physics, Vol. 81, Springer, Berlin/Heidelberg, p 163
108. Priebe A, Pucci A, and Otto A (2006) Infrared reflection-absorption spectra of C_2H_4 and C_2H_6 on Cu: Effect of surface roughness. J Phys Chem B 110:1673
109. Priebe A, Sinther M, Fahsold G, and Pucci A (2003) The correlation between film thickness and adsorbate line shape in surface enhanced infrared absorption. J Chem Phys 119:4887
110. Priebe A, Fahsold G, and Pucci A (2004) Strong pyramidal growth of metal films studied with IR transmittance and SEIRA of CO. J Phys Chem B 108:18174
111. Bjerke AE, Griffiths PR, Theiss W (1999) Surface-enhanced infrared absorption of CO on platinized platinum. Anal Chem 71:1967
112. Ducourtieux S, Podolskiy VA, Grésillon S, Buil S, Berini B, Gadenne P, Boccara AC, Rivoal JC, Bragg WD, Banerjee K, Safonov VP, Drachev VP, Ying ZC, Sarychev AK, Shalaev VM (2001) Near-Field Optical Studies of Semicontinuous Metal Films. Phys Rev B 64:165403
113. Pucci A (2005) IR spectroscopy of adsorbates on ultrathin metal films: Advanced optical diagnostics of surfaces, nanostructures, and ultrathin films. Physica Status Solidi (b) 242:2704
114. Schreiber F (2000) Structure and growth of self-assembling monolayers. Prog Surf Sci 65:151
115. Seo EK et al. (2004) Atomic layer deposition of titanium oxide on self-assembled-monolayer coated gold. Chem Mater 16:1878
116. Lin-Vien D, Colthup NB, Fateley WG, and Grasselli JG (1991) The Handbook of Infrared and Raman Characteristic Frequencies of Organic Molecules. Academic Press, San Diego, pp. 9
117. Neubrech F, Pucci A, Cornelius TW, Karim S, García-Etxarri A, and Aizpurua J (2008) Resonant plasmonic and vibrational coupling in a taylored nanoantenna for infrared detection. Submitted to Phys Rev Lett
118. Bouhelier A, Bachelot R, Lerondel G, Kostcheev S, Royer S, Wiederrecht G (2005) Surface plasmon characteristics of tunable photoluminescence in single gold nanorods. Phys Rev Lett. 95:267405
119. Taminiau TH, Moerland RJ, Segerink FB, Kuipers L, van NF (2007) $\lambda/4$ Resonance of an optical monopole antenna probed by single molecule fluorescence. Nano Lett 7:28

Chapter 9
Designing the Carbon Nanotube Field Effect Transistor Through Contact Barrier Engineering

Byoung-Kye Kim, Hyo-Suk Kim, Hye-Mi So, Noejung Park, Suklyun Hong, Ju-Jin Kim, and Jeong-O Lee

Abstract Through recent publications, as reviewed in this article, we have determined the effects of contact barrier change on the electrical transport properties of carbon nanotube field-effect transistors. To analyze the Fermi level alignment and the Schottky barrier at the contact, we used the first-principles electronic structure calculations of different types of metal electrodes with various bonding configurations. In parallel, we have used various experimental techniques to engineer the contact barrier: decorations of metal nanoparticles, the self-assembled monolayers of molecules, and protein nanoparticles. We investigated the changes in the electron transport properties of the nanotube transistors in relation to the adjustment of the contact barrier. Overall reviews of these studies are presented here, and a few potential applications are also suggested.

9.1 Introduction

A carbon nanotube (CNT) is a long cylinder-shaped material consisting of sp^2-bonded carbon atoms [19]. In most synthetic Processes the CNTs are very sharp and needle-shaped with diameters of a few nanometers and lengths of several micrometers or even centimeters. When a few or many concentrically rolled-up graphene planes constitute the wall of the cylinder, the nanotube is called a multiwalled carbon nanotube (MWNT) [27b.]. Nanotubes with a cylinder wall consisting of only one sp^2-bonded carbon layer are known as single-walled nanotubes (SWNTs), and have also often been synthesized [20]. Of the various types of nanotubes, SWNTs are considered the most intriguing. An elementary investigation of the π electronic structures of SWNTs has been carried out using the tight-binding approximation, which found that SWNTs can be either metallic or semiconducting, depending on the wrapping angle [44, 45]. Scanning tunneling microscopy (STM) images have confirmed this theoretically predicted relation between the wrapping angle and the SWNT electronic structure [39, 51]. Such a fundamental change in electronic

structure due to a subtle variation in the atomic geometry has rarely been observed and has attracted significant interest.

Further, measurements of the electronic properties of CNTs have found features characteristic of coherent one-dimensional electronic states. The Coulomb blockade phenomena and quantum interference patterns observed for CNTs between metal electrodes have been attributed to standing wave states that range across the whole CNT [6, 32, 50]. At low temperature, the one-dimensional confinement of the CNT has led to the Luttinger liquid behavior [5]. Ballistic electron transport with two units of quantum conductance has also been demonstrated, and is attributed to the two conducting channels at the Fermi level of metallic CNTs [27c., 32]. Besides, the maximum current in a single SWNT has also been a subject of great interest. It has been shown that the current saturates at high fields, with a maximum current of about $25\,\mu A(\approx 10^9\,A/cm^2)$ per tube [14, 17, 22, 56]. Under high bias conditions, the emission pertube optical phonons by high energy electrons is believed to be the main reason for current saturation.

Diverse nanoscale electronic devices utilizing carbon nanotubes have been suggested [43]. Field effect transistors in which semiconducting carbon nanotubes are employed as electron channels are among the most widely investigated nanodevice structures [35, 52]. Single-walled carbon nanotube field effect transistors (SWNT-FETs) usually exhibit *p*-type operations only. Such a characteristic *p*-type behavior of SWNT-FETs has long been an important issue [2,15,16]. Hole doping by environmental oxygen molecules was thought to be the main origin of the *p*-type behavior of SWNT-FETs [9, 49]. This applies to the cases when the semiconducting channel of the SWNT-FETs consists of a network of CNTs or a very long single CNT. However, it is now thought that the fundamental cause is the low-lying Schottky barrier to hole transport at the metal–CNT contact interface [3, 34]. Particularly, when the channel consists of a clean isolated SWNT with a length of less than a few hundred nanometers, the Fermi level positioning at the interface between the metal electrode and the CNT channel is likely to be the key influence on transport characteristics. The fabrication of *n*-type SWNT-FETs is a challenge that has been taken up by many research groups: some have tried a low work function metal such as K and Ca as the electrode of the SWNT-FETs [23, 38], while others have tested nitrogen doping with the aim of increasing the number of electron carriers in the channel region. However, it has been shown in CVD experiments that nitrogen dopants are likely to have a pyridine-like structure, and so cannot act as electron donors to a CNT. The fabrication of electrodes with low-work-function metals is also not very practical, since they are very active and not stable under ambient conditions. In this regard, a practical method for achieving air-stable *n*-type transistors is technically important and remains to be found.

In recent years we have investigated the transport properties of SWNT-FETs. Our main concern in this field is learning how to control the Schottky barrier at the metal–nanotube contact, in order to achieve low-resistance contact and adjust the conduction pattern. The goals of our research are the practical synthesis of *n*-type transistors and the fabrication of low-cost CNT-based gas sensors. We have found that the adsorption of biomolecules on the contact significantly affects the transport

properties of SWNT-FETs. Modification of the contact barrier by promoting the adsorption of various molecules after the fabrication of SWNT-FETs has been successfully performed. For example, we have fabricated diode-like devices after selective postprocessing of either the source or drain electrodes. In this review, we present the studies of SWNT-FETs that we have published in recent years. First, we discuss our theoretical results for the electronic structure of metal–CNT interfaces. Next, our fabrication of SWNT-FETs, and contact barrier engineering through posttreatments with various forms of biomolecules are presented. In the later sections of this article, some new results that have not been published elsewhere are included.

9.2 Theoretical Study of the Metal–Carbon Nanotube Contact

In this section we discuss our theoretical results for the electronic structure at metal–nanotube contacts. We principally investigated the effect of the metal work function, the detailed bonding configuration, and oxygen adsorption on the Fermi level alignment between the metal electrode and the carbon nanotube. We used the density-functional theory (DFT) method with the Vienna ab initio simulation package (VASP) [28, 29]. For exchange and correlation, a PBE-type functional was used in the generalized gradient approximation (GGA) [42]. Electron–ion interactions were described with the projector augmented wave PAW method [30], and a plane-wave basis with a kinetic energy cutoff of 400 eV was employed to describe the Kohn–Sham single-electron equations. A Gaussian broadening with a width of 0.05 eV was used to accelerate the convergence in the *k*-point sum. The atoms were relaxed with a residual force smaller than 0.02 eV/Å.

9.2.1 Carbon Nanotubes in Contact with Metal Surfaces and the Effects of Metal Oxidation

We now investigate the effect of varying the metal work function on the Fermi level alignment between a metal surface and an adsorbed carbon nanotube [41a.]. We used gold (Au) and aluminum (Al) as typical examples of high and low work function metals, respectively. To investigate the Schottky barrier at the metal–nanotube contact we simulated the semiconducting (10,0) nanotubes adsorbed on the metal surfaces. In this study, we assumed that the metal surfaces are well defined. Here metal layers with (111) surfaces were chosen as a model. Three layers of Al (Au) were excised from the bulk fcc structures to form a two-dimensional slab geometry, as shown in Fig. 9.1a and b. The unit cell along the axial direction of the nanotube is twice the minimal unit cell of the (10,0) nanotube ($\approx$8.49 Å). The mismatch of the lattice along the CNT axis causes a 2% compression in the gold layer, whereas the mismatch with the aluminum layer is negligible. Along the direction

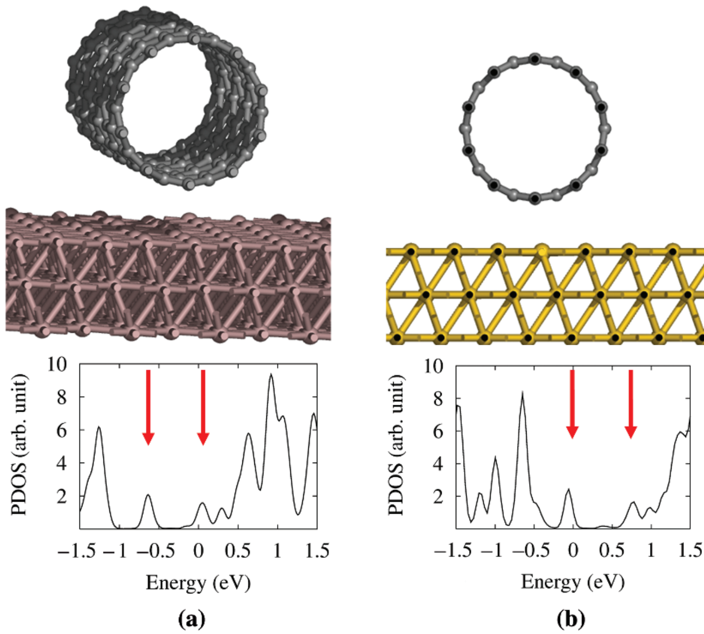

Fig. 9.1 Optimized geometries for the (10,0) carbon nanotube in contact with three layers of **(a)** aluminum and **(b)** gold. The metal surfaces in both cases are (111). The lower panels of **(a)** and **(b)** are the projected densities of states for the carbon nanotubes. The downward arrows in **(a)** and **(b)** indicate the valence band and conduction band edges of the nanotubes, respectively

(z) perpendicular to the two-dimensional slab, the nanotube and metal layer system is separated from its replica by a large vacuum region (10 Å). The geometry of the (10,0) carbon nanotube on the metal (111) surfaces and the partial density of states for the carbon nanotubes are shown in the upper and lower panels of Fig. 9.1a and b, respectively. Note that the Fermi level of the aluminum (gold) surface sits at the conduction (valence) band edge of the semiconducting (10,0) nanotube. For this simple weak contact, the development of metal-induced-gap states should be minimal, and the Fermi level alignment at the metal–nanotube contact should mostly be governed by the metal work function. The work function of gold is larger that that of aluminum by about 1 eV [36]. Despite this large difference, the alignment of the Fermi level from the conduction band edge to the valence band edge of the semiconducting carbon nanotube is different by only about 0.5 eV, as shown in Fig. 9.1a and b.

This difference in the Fermi level alignment results from the interplay between the differences in the work functions of the metal surfaces and the small dipole fields developed at the interfaces. The charge density difference is defined as $\Delta\rho = \rho[\mathrm{CNT/M}] - \rho[\mathrm{CNT}] - \rho[\mathrm{M}]$, where M is the gold or aluminum slab, and is averaged in the xy plane and plotted along the direction (z) perpendicular to the surface in Fig. 9.2. Note the small charge depletion and accumulation in the

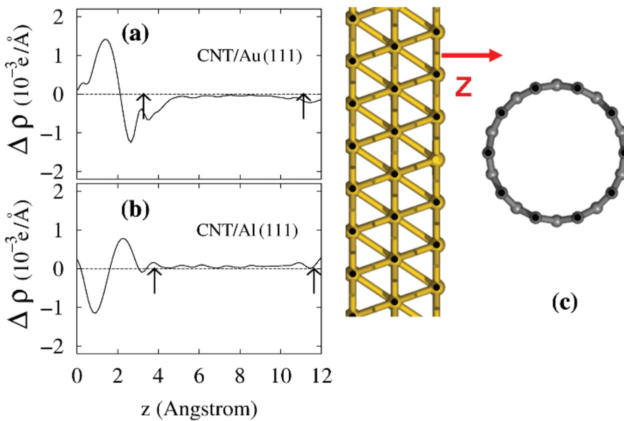

Fig. 9.2 The charge density differences $\Delta\rho = \rho$ [CNT/M] $- \rho$ [CNT] $- \rho$ [M], where M denotes the **(a)** gold and **(b)** aluminum slabs, are averaged over the *xy* plane and plotted along the direction perpendicular to the metal surface (z). z is the distance from the topmost metal layer, as depicted in panel **(c)**. The two upward arrows in **(a)** and **(b)** indicate the positions of the carbon nanotube edges. Reprinted figures with permission from [43]. Copyright (2005) by the American Physical Society

overall nanotube region when the CNT is in contact with Au(111) and Al(111), respectively. However, a more significant feature is the charge rearrangement at the interface. Electron charge can be seen to have accumulated on the metal side in Fig. 9.2a, whereas it has accumulated on the CNT side in Fig. 9.2b. Thus the dipole field is directed from the Au surface to the CNT in the case of Fig. 9.2a, whereas it points towards the Al surface in Fig. 9.2b. This dipole field compensates for the work function difference between the metal surfaces, and fixes the Fermi level at the valence band or conduction band edge.

Aluminum is, like other low-work-function metals, very vulnerable to oxidation under ambient conditions. We calculated the Fermi level alignment between the oxidized aluminum surface and the (10,0) carbon nanotube, as shown in Fig. 9.3. To construct a model geometry for the oxidized surface, we assumed that all the fcc hollow sites are occupied by oxygen atoms. The oxidation of aluminum has previously been discussed [18, 46] and adsorption on fcc sites is known to be the most stable [21]. The Fermi level of the oxided Al layers is located at the valence band edge of the carbon nanotube in marked contrast to the case of the clean Al surface, as shown in Fig. 9.3a and b. This result suggests that an oxidized Al surface has a work function similar to that of a clean gold surface. The work function of gold surfaces is known to be larger than that of aluminum surfaces by about 0.8 eV [36].

For confirmation, we independently calculated the work function of the Al(111) surface and its variation with oxygen adsorption, as shown in Fig. 9.4. A symmetric slab composed of six metal layers was positioned in a supercell with a large vacuum region (10 Å). The single electron potential, without nonlocal terms, is then averaged over the *xy* plane and plotted along the z direction, where the energy reference is the Fermi level and z is the distance from the topmost aluminum layer (see Fig. 9.4).

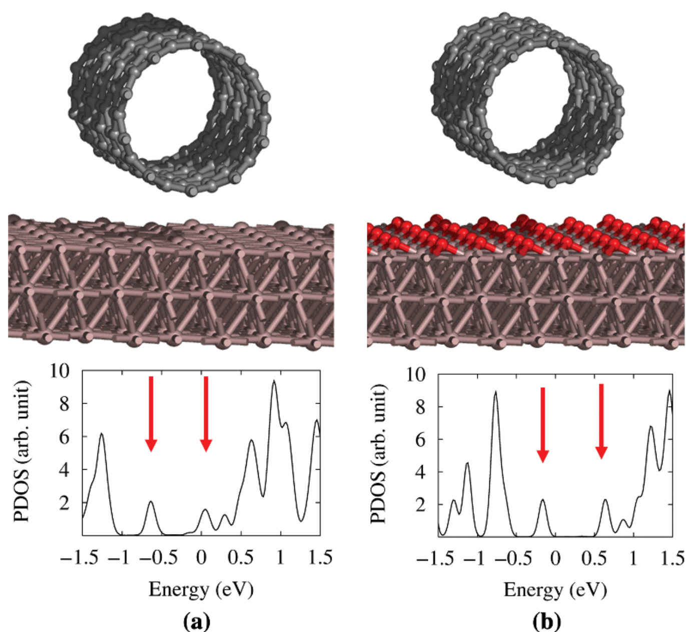

Fig. 9.3 Optimized geometries for the (10,0) carbon nanotube in contact with **(a)** a bare aluminum (111) surface and **(b)** an oxidized aluminum surface. Here the part **(a)**, the same as Fig. 9.1a, is reproduced for better comparison with **(b)**. The lower panels of **(a)** and **(b)** are the projected densities of states for the carbon nanotubes. The downward arrows in **(a)** and **(b)** indicate the valence band and conduction band edges of the nanotubes, respectively. Darker spheres on the surface in panel **(b)** represent the oxygen adatoms

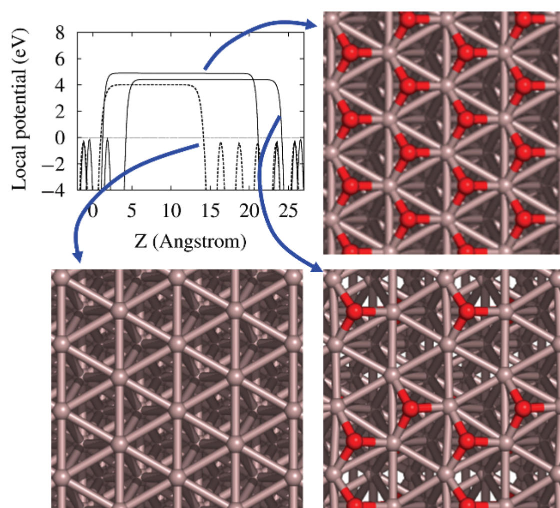

Fig. 9.4 The electrostatic potentials (eV) of the clean and oxidized Al(111) surfaces were averaged over the *xy* plane and plotted along the direction (*z*) perpendicular to the metal surface. Symmetric slabs consisting of six aluminum layers with or without oxygen adatoms on the outmost layers were used in these calculations

The work function of the clean Al(111) surface was found to be 4.12 eV. The work function for the Au(111) surface was found with the same approach to be 5.28 eV. These results are consistent with the literature values [13, 36]. When the oxygen adatoms occupy all of the fcc hollow sites, as shown in the upper right panel, the oxidation-induced increment of the work function of the Al(111) surface was found to be about 0.8 eV. Thus the oxidized Al surface is likely to have a similar work function to the Au(111) surface. Indeed, the increment in the work function depends on the coverage of the oxygen adsorbates. When the oxygen coverage was reduced by half, as shown in the lower right panel, the work function increment was found to be approximately half of the earlier-mentioned value. The Fermi level alignment and its change upon oxygen adsorption are consistent with out transport measurement. In Sect. 9.3.2, we discuss our experimental results showing that aluminum-decorated CNFETs with n-type operation develop p-type operation as oxidation proceeds.

In our calculations we used the periodic boundary condition, and thus the model geometries shown in Fig. 9.1 assume an infinitely long interface between the metal and the nanotube. In a realistic device structure, however, only parts of the nanotube are in contact with the metal, and the remaining part of the CNT forms a channel connecting the source and drain electrodes. If the metal-induced gap state (MIGS) is strong at the interface in the contact region, the Schottky barrier height that the tunneling electron experiences as it passes from the metal into the CNT body in the channel region may not be due solely to the Fermi level alignment. However, it has been shown that when the nanotube is separated from the metal surface by a van der Waals distance, the MIGS decays sufficiently in the vacuum region between the metal and nanotube [55]. The Schottky barrier height for such a contact can be obtained directly from the Fermi level alignment in the model geometry, as presented earlier.

So far we have investigated the effect of the metal work function and the adsorption of oxygen on the Schottky barrier at the metal–nanotube contact, assuming that the nanotube is adsorbed on a well-defined metal surface. These considerations provide only a partial characterization of experimental situations. In recent fabrications of SWNT-FETs, CNTs have been embedded under the metal layers of the electrode. In these systems it is possible that the metal atoms bind chemically to the carbon atoms, and that the CNT is under substantial pressure. In the next section, we examine the electronic structure of the metal–CNT interface under such conditions.

9.2.2 The Effects of Pressure and Interfacial Contact on a Carbon Nanotube Embedded under Metal Layers

In this section, we first discuss our investigation of CNTs embedded under metal layers without chemical bonds between the CNT and the metal [41b.]. We only consider noble metal surfaces, since low work function metals are likely to bind chemically or to be oxidized, and examine a semiconducting (10,0) nanotube placed onto or beneath the Au(111) surface. The model geometries and the corresponding projected

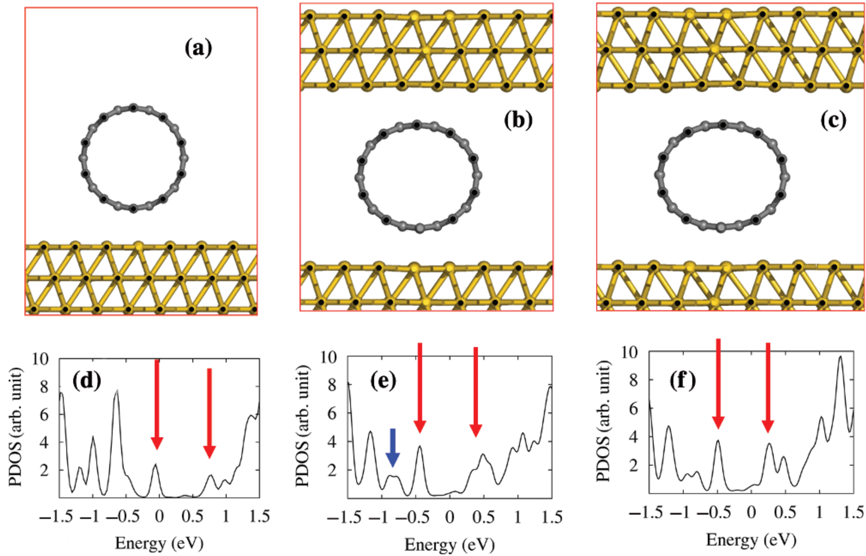

Fig. 9.5 Optimized geometries for the (10,0) carbon nanotube **(a)** on the Au(111) surface, and between two gold slabs with **(b)** small and **(c)** large pressures. Panels **(d)**, **(e)**, and **(f)** show the projected densities of states for the (10,0) carbon nanotubes for the cases of **(a)**, **(b)**, and **(c)**, respectively. Two long downward arrows in **(d)**, **(e)**, and **(f)** indicate the valence and conduction band edges, respectively. The short downward arrow in **(e)** indicates the second valence band state; the orbital characteristics of this state are depicted in Fig. 9.6

density of states (PDOS) for the nanotube are shown in Fig. 9.5. In Fig. 9.5a, only one side of the nanotube is in contact with the gold surface. The equilibrium distance of 3.01 Å indicates that the nanotube is physisorbed on the surface. Since gold has a larger work function, the Fermi level is aligned at the valence band edge of the carbon nanotube.

To simulate the compressing metal layers, we reduced the unit cell length of the supercell along the z-direction, as shown in Fig. 9.5b and c. The most striking feature of Fig. 9.5b and c is that as the nanotube–metal distance is reduced, the Fermi level shifts up, and thus becomes aligned closer to the conduction band edge of the nanotube, as shown in Fig. 9.5f. The calculated quantum-mechanical stresses along the z-direction are 0.61 and 6.03 kbar for Fig. 9.5b and c, respectively. The nonzero density of states in the band gap region is due to the metal-induced gap states. It is also noticeable that the peaks corresponding to the second van Hove singularity are suppressed significantly when the nanotube is compressed by the gold slabs, as indicated by the short downward arrow in Fig. 9.5e.

To understand these changes in the PDOS, we calculated the electronic structure of an isolated squeezed (10,0) nanotube with the same atomic geometry as in Fig. 9.5c without the metal layers. Note that the energy gap and band dispersion of the squeezed nanotube are almost the same as those of the pristine nanotube, as shown in Fig. 9.6a. The isosurfaces of the three doubly-degenerate valence band states at Γ are plotted in Fig. 9.6b, c, and d. The phase changes of the Kohn–Sham

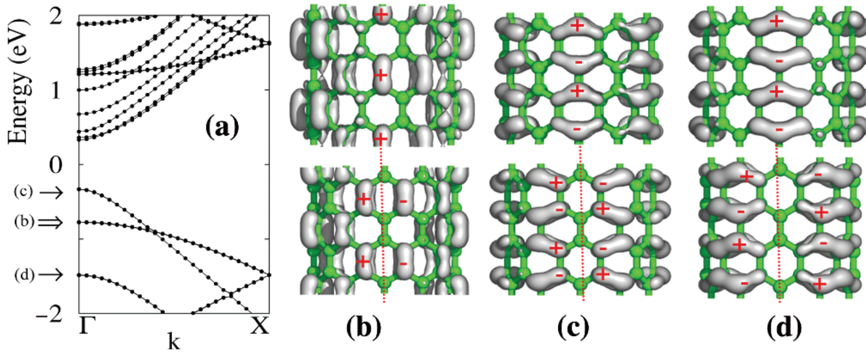

Fig. 9.6 The band structure of the isolated squeezed nanotube with the same geometry as Fig. 9.5b without the compressing metal layers. Panels **(b)**, **(c)**, and **(d)** are contour plots of the charge density of the three doubly degenerate states at the Γ point, as indicated by the three rightward arrows in panel **(a)**. The +/− signs in **(b)**, **(c)**, and **(d)** indicate the phase of the wave function. The vertical dotted lines in **(b)**, **(c)**, and **(d)** represent the mirror reflection plane. Reused with permission from Noejung Park, Donghoon Kang, and Suklyun Hong, Applied Physics Letters, 87, 013112 (2005). Copyright 2005, American Institute of Physics

wave function, indicated by +/− signs, show that the second valence state changes most slowly along the nanotube–metal contact (dotted lines). Therefore, the hybridization of this state with the Au 6s bands is easier than other valence states. This explains why the second van Hove singularity is strongly affected, as shown in Fig. 9.5e, by the shortening of the nanotube–metal distance. As a result, the occupation of the Au 6s bands increases, which means that the amount of charge transfer from the CNT to the gold layer is also increased. Thus the Fermi level up-shift shown in Fig. 9.5e and f is a consequence of the lowered local potential, which is in turn due to the increased electron depletion in the CNT region.

The variation in the charge transfer with the pressure can be seen explicitly in the charge density differences, $\Delta\rho = \rho[\mathrm{CNT/M}] - \rho[\mathrm{CNT}] - \rho[\mathrm{M}]$, where M is a metal layer. $\Delta\rho$ was plotted along the z-direction after averaging over the xy plane. z is the distance from the topmost gold layer, and the arrows in Fig. 9.7c and d indicate the edges of the CNT. Figure 9.7c shows that electronic charge accumulates on the side of the gold surface, which indicates that the electronegativity of gold is larger than that of the CNT. The comparison of Fig. 9.7c and d shows that electron accumulation just above the gold surface increases when the contact is under pressure. This result is consistent with the increased Au-C hybridization, as discussed earlier. The charge transfer induced by the hybridization largely compensates the difference between the local work functions of gold and the CNT, pushing the Fermi level toward the conduction edge of the CNT. We also performed a similar calculation with other faces of gold and found similar results.

Now we turn to the case in which strong chemical bonds have formed at the metal–CNT interface [40, 59]. In Fig. 9.8, we show that the Fermi levels of both the gold and aluminum layers are located at the midgap of the carbon nanotube when the metal layers and the carbon nanotube are chemically bonded. This suggests that the Fermi level of the metal is strongly pinned at the midgap of the CNT, irrespective

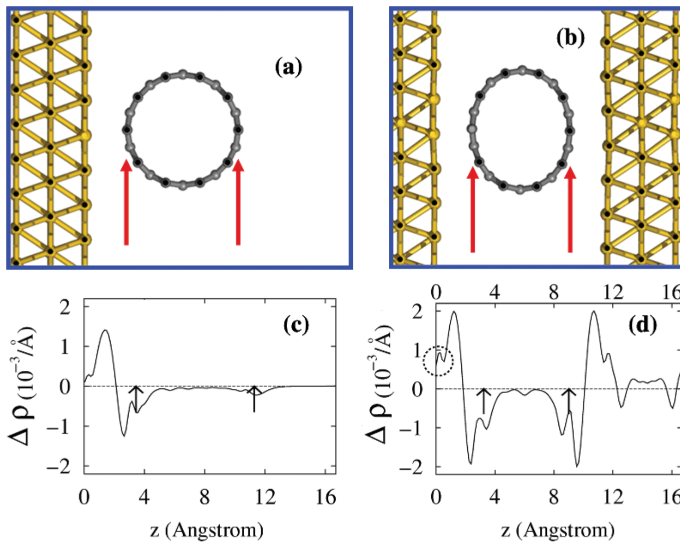

Fig. 9.7 Optimized geometries for the (10,0) carbon nanotube **(a)** on the Au(111) surface and **(b)** between two gold slabs. The charge density differences, as defined in Fig. 9.2, for the configurations **(a)** and **(b)** are plotted along the direction perpendicular to the metal surface in **(c)** and **(d)**, respectively. Two upward arrows in **(a)**–**(d)** indicate the edges of the nanotubes. Reused with permission from Noejung Park, Donghoon Kang, and Suklyun Hong, Applied Physics Letters, 87, 013112 (2005). Copyright 2005, American Institute of Physics

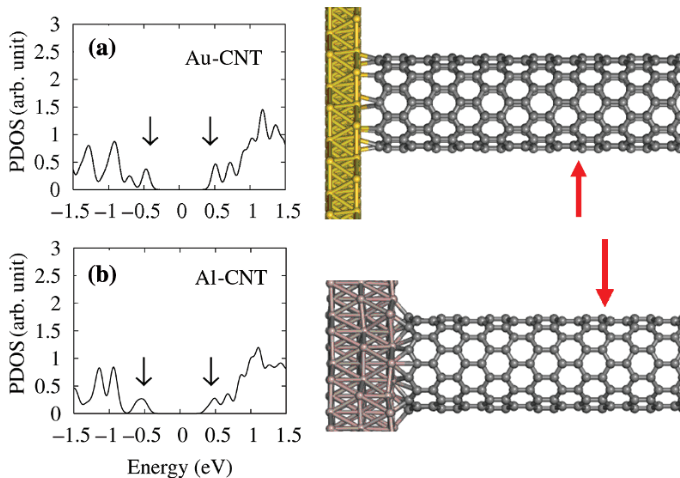

Fig. 9.8 Electronic structures and bonding configurations of **(a)** Au layers and **(b)** Al layers in end-contact with a semiconducting (10,0) CNT. Partial densities of states (PDOS) for 20 carbon atoms of the CNT, which is the 9th zigzag chain from the metal surface, indicated by the red arrows in the atomic geometries, are shown with respect to the Fermi level of each configuration. The two downward arrows in the PDOS indicate the valence and conduction band edges. In these calculations, the 10 nm long CNT is connected to the metal at both ends, but only one end part is shown. Reused with permission from Sunkyoung Moon, Sun-Gul Lee, Woon Song, Joon Sung Lee, Nam Kim, Jinhee Kim, and Noejung Park, Applied Physics Letters, 90, 092113 (2007). Copyright 2007, American Institute of Physics

of the metal work function. On the basis of these results, we suggest that the microscopic differences between the metal–CNT interfaces are very important influences on the Schottky barrier. The adsorption states and bonding configurations at the metal–CNT interface are also likely to substantially affect the transport behavior of SWNT-FETs. This also means that engineering of the metal–CNT interface could be exploitable to achieve SWNT-FETs with desired conduction patterns.

9.3 Metal–Carbon Nanotube Contact Engineering

In this section, we describe various experimental techniques for controlling the height of the Schottky barrier at metal–nanotube contacts, and their effects on the electronic transfer properties of SWNT-FETs. By controlling the Schottky barrier height, it is possible to fabricate electronic devices such as diodes and *n*-type transistors that are necessary for logic circuits, and the delicate modulation of the Schottky barrier can be used to develop highly sensitive SWNT-FET based sensors.

9.3.1 Fabrication of Carbon Nanotube Diodes with Contact Engineering

In this section, we focus on the fabrication of a SWNT device that operates as a rectifying diode. Several research groups have fabricated SWNT-based diodes, either by using conventional approaches such as selective doping of part of the nanotube, or by adopting local split gates to control the carrier concentration in the nanotube [1, 15, 31, 60]. However, by exploiting the well-known characteristics of the Schottky barriers of SWNT-FETs, it may be possible to construct a SWNT-based diode simply by adjusting the Fermi-level lineup at the nanotube–metal contact.

We tested this suggestion by fabricating symmetric *p*-type SWNT-FETs with high work function metals, and then converted these devices into Schottky diodes by modifying one of the contact barriers with a self assembled monolayer (SAM) of molecules containing a thiol group.

The SWNT-FETs used in this study were fabricated with the patterned growth method [27b.] and conventional photolithography followed by lift-off. The sample fabrication procedure was as follows. First, catalyst patterns were created on a heavily doped *p*-type Si wafer with 500 nm thermal oxide by using a deep-UV mask-aligner, and the samples were allowed to react with Fe/Mo catalyst in methanol for $10 \sim 30$ s. The samples were lifted off in boiling acetone, and washed three times with fresh acetone and isopropanol. The samples with patterned catalyst were then transferred to a furnace, where nanotube growth was carried out in a CH_4 and H_2 atmosphere at 900°C. The electrode patterns were fabricated with photolithography, and 5 nm titanium and 20 nm Au were evaporated successively using thermal evaporation. Figure 9.9a shows an AFM image of the bare device used in our

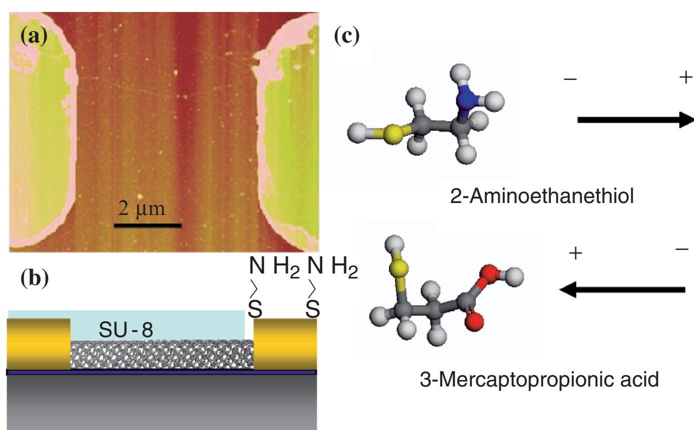

Fig. 9.9 **(a)** AFM image of the device used in these experiments. **(b)** Schematic drawing of a SWNT-FET with a SAM on one contact. **(c)** Molecular structures of the two self-assembling molecules used in this study. Reused with permission from Byoung-Kye Kim, Ju-Jin Kim, Hye-Mi So, Ki-Jeong Kong, Hyunju Chang, Jeong-O Lee, and Noejung Park, Applied Physics Letters, 89, 243115 (2006). Copyright 2006, American Institute of Physics

experiments (i.e., before SAM treatment). Patterns were created on this bare device with an SU-8 negative photoresist to expose one of the contacts for chemical treatment, as depicted in Fig. 9.9b. Two self-assembling molecules, 2-aminoethanethiol ($HSCH_2CH_2NH$; Mw 77.15), and 3-mercaptopropionic acid ($HSCH_2CH_2CO_2H$; Mw 106.14) were purchased from Sigma-Aldrich, and used without further treatment. These molecules were selected because they each contain a thiol group, which is well known to favor the formation of highly ordered monolayers on Au surfaces [54a.]. Figure 9.9c shows the molecular structures of 2-aminoethanethiol and 3-mercaptopropionic acid, and the predicted directions of the dipole moments of the pristine molecules.

The electrical transport characteristics of the devices were recorded prior to molecular treatment, and then the devices were reacted with a 10 mM solution of self assembling molecules in ethanol. Figure 9.10 shows the *I–V* characteristics of the SWNT-FET before (black curve) and after treatment of the exposed contact with 2-aminoethanethiol (gray curve; reaction time of 10 min). The upper left inset shows an optical microscopy image of the device, and the lower right inset shows the band diagram after the 2-aminoethanethiol treatment. As shown in Fig. 9.10a, a symmetric *I–V* curve was observed before introduction of the SAM. After the 2-aminoethanethiol treatment, in contrast, the device exhibits highly asymmetric, diode-like *I–V* characteristics.

For comparison, we fabricated a device in which both contact electrodes were covered with SU-8, exposing only the nanotube body region. After treatment of these SU-8-covered electrodes with 2-aminoethanethiol, the device was found to exhibit symmetric *I–V* characteristics with decreased conductance (Fig. 9.10b). This result is consistent with those of Kong et al., who attributed this conductance decrease to the electron doping nature of the amine groups [26]. When we used a 3-mercaptopropionic acid SAM in similar experiments, no significant changes in the transport characteristics were observed (data not shown).

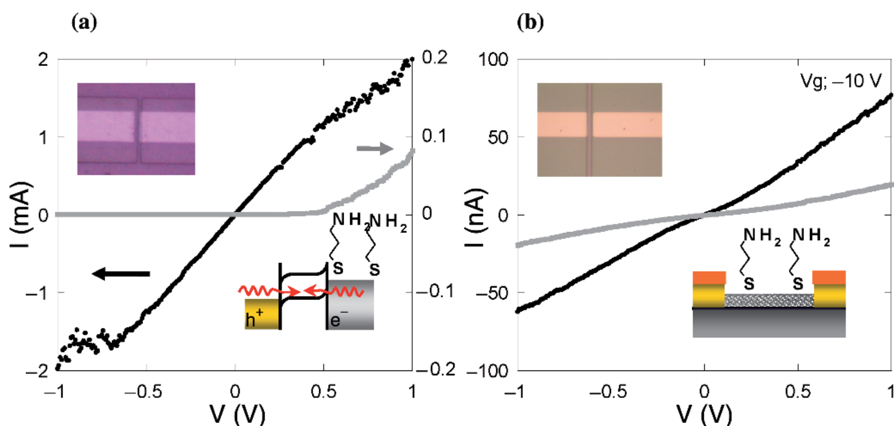

Fig. 9.10 **(a)** I–V curves measured before (black, at $V_g = 0$) and after treatment of the surface with 2-aminoethanethiol (gray curve). Upper inset: optical microscopy image of the single-contact open device. Lower inset: schematic band diagram of the device. **(b)** I–V curves before (black) and after (gray) 2-aminoethanethiol treatment of the contact-passivated device. Reused with permission from Byoung-Kye Kim, Ju-Jin Kim, Hye-Mi So, Ki-Jeong Kong, Hyunju Chang, Jeong-O Lee, and Noejung Park, Applied Physics Letters, 89, 243115 (2006). Copyright 2006, American Institute of Physics

The diode-like operation of the SWNT-FET with a 2-aminoethanethiol SAM can be explained by the formation of asymmetric contacts after the molecular treatment of the cathode surface, as depicted in the inset in Fig. 9.10a. To fabricate the Schottky diode, we used a self assembly technique to adjust the Fermi-level lineup of the predefined nanotube transistor. A similar self assembly approach has been used to control the Schottky barrier height in organic electronic devices. [7, 10] For comparison, we used two molecules, 2-aminoethanethiol and 3-mercaptopropionic acid, which were expected to have different dipole directions (see Fig. 9.9c). We found that only treatment with 2-aminoethanethiol resulted in diode-like operation.

We investigated the different effects of adding the 2-aminoethanethiol and 3-mercaptopropionic acid molecules to a bare Au surface by carrying out ab initio electronic structure calculations. We used the calculation method described in our previous study [41a.]. Here we adopted a slab geometry with six gold layers, in which the two layers in the center were fixed during the geometry optimization calculation. Plotting the local potential with respect to the Fermi level, we obtained the work function of the bare Au surface and of the Au surfaces with adsorbed 2-aminoethanethiol and 3-mercaptopropionic acid, as shown in Figs. 9.11a, as well as 11b, and c, respectively. The calculated work function of the bare Au surface ($\approx$5.2 eV) is very close to the previously reported value [36]. The work functions of the Au surfaces with adsorbed 2-aminoethanethiol and 3-mercaptopropionic acid (Fig. 9.11b and c) are significantly different. Specifically, the adsorption of 2-aminoethanethiol molecules substantially decreases the work function ($\approx$3.9 eV), whereas the adsorption of 3-mercaptopropionic acid has little effect ($\approx$4.7 eV). This difference confirms that the asymmetric I–V pattern observed after treatment of one

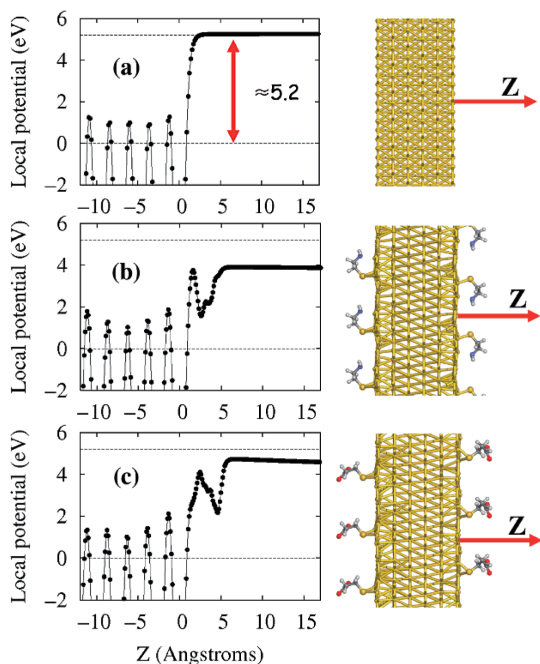

Fig. 9.11 Plots of the local potentials with respect to the Fermi level of **(a)** the bare 6 layers of Au, **(b)** the 6 layers of Au with adsorbed 2-aminoethanethiol molecules, and **(c)** the 6 Au layers with adsorbed 3-mercaptopropionic acid molecules. Reused with permission from Byoung-Kye Kim, Ju-Jin Kim, Hye-Mi So, Ki-Jeong Kong, Hyunju Chang, Jeong-O Lee, and Noejung Park, Applied Physics Letters, 89, 243115 (2006). Copyright 2006, American Institute of Physics

electrode of the SWNT-FET with 2-aminoethanethiol was due to a change in the Schottky barrier at the treated contact.

To investigate the effect on the transfer characteristics of treatment with 2-aminoethanethiol, we measured the evolution of the I–V_g characteristics of the SWNT-FETs, as shown in Fig. 9.12a. Before the reaction with 2-aminoethanethiol, the device exhibits typical p-type transistor behavior (black circles). After treatment with 2-aminoethanethiol for 10 min (empty squares) and 5 h (gray symbols), however, the p-channel conduction decreases and n-type conduction becomes dominant, as indicated by the solid arrows in Fig. 9.12a. The effect of adding the 2-aminoethanethiol SAM seems to saturate after a reaction time of about 5 h, with the I–V_g characteristics remaining almost unchanged upon further treatment. As a result, the SWNT-FET with a 2-aminoethanethiol SAM on one contact exhibits ambipolar transfer characteristics.

The ambipolar transfer characteristics can be explained by considering the band diagram for a device with asymmetric contacts, as generated by SAM treatment of one contact. Before the SAM treatment (Fig. 9.12b), the Fermi levels of the electrodes are aligned with the valence band of the carbon nanotube, leading to p-type behavior. After the formation of the 2-aminoethanethiol SAM (Fig. 9.12c), however, the Fermi level of the cathode is aligned with the conduction band edge. For

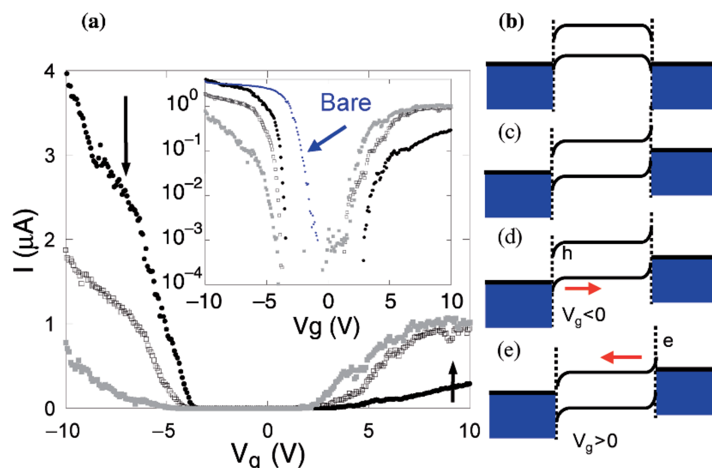

Fig. 9.12 **(a)** The evolution of the electrical transfer characteristics with the formation of a 2-aminoethanethiol SAM: before reaction (black circles); after 10 minutes of reaction (empty squares); and after 5 h of reaction (gray squares). The inset shows a log-scale plot. The band diagram of the SWNT-FET **(b)** before and **(c)** after SAM treatment. The band diagram of the SWNT-FET with one contact modified for **(d)** $V_g < 0$ and **(e)** $V_g > 0$. Reused with permission from Byoung-Kye Kim, Ju-Jin Kim, Hye-Mi So, Ki-Jeong Kong, Hyunju Chang, Jeong-O Lee, and Noejung Park, Applied Physics Letters, 89, 243115 (2006). Copyright 2006, American Institute of Physics

a SWNT-FET with a SAM-modified electrode, the hole current would still dominate when $V_g < 0$, as shown in Fig. 9.12d. However, significant electron conduction will occur in the SAM-modified device when $V_g > 0$, as shown in Fig. 9.12e. As a result, the device exhibits ambipolar transfer characteristics.

It is also noteworthy that the threshold voltage of the device does not change significantly after the SAM treatment of one of the contact electrodes, as shown in Fig. 9.12a. It is well known that shifts in the threshold voltage are largely due to variations in the doping level in the semiconductor channel region, whereas changes in the slope of I–V_g curves are due to variations in the Schottky barrier at the contact [12]. As shown in Fig. 9.12a, the 2-aminoethanethiol treatment induces slope changes in the I–V_g curve, eventually resulting in ambipolar behavior, with no prominent shifts in the threshold voltage. These findings confirm that the introduction of the 2-aminoethanethiol SAM modifies the Schottky barrier at the engineered contact.

In summary, we have fabricated a *p*-type SWNT-FETs and then converted it into a diode by tuning the Schottky barrier height using a SAM technique. Highly asymmetric, diode-like I–V curves were observed when one of the contacts was functionalized with a 2-aminoethanethiol SAM. Ab initio electronic structure calculations confirmed that the adsorption of 2-aminoethanethiol onto an Au surface induces a strong decrease in the work function, whereas the adsorption of 3-mercaptopropionic acid has little effect. These results indicate that tuning the Schottky barrier by introducing a SAM of a selected molecular species could be a practical method to control the conduction patterns of nanotube-based electronic devices.

9.3.2 *Fabrication of n-Type Single-Walled Carbon Nanotube Transistors with Al Decoration*

In this section, we discuss the fabrication of *n*-type SWNT-FETs using a controlled in situ Al decoration technique. By using the Al decoration technique, Schottky barrier control and channel doping are possible at the same time, and it is possible to compare the effects of channel doping with those of contact-barrier control.

The same sample fabrication process as described in the previous section was used. Bare SWNT-FETs (open devices) were prepared, and contact-decorated SWNT-FETs or channel-decorated SWNT-FETs were prepared by using an SU8-2002 negative photoresist or a PMMA mask.

For the in situ electrical measurements, the samples were wired to a chip connected to electrical feedthrough in an evaporation chamber. For Al decoration, the vacuum chamber was pumped down to 2×10^{-6} torr, and the Al source was slowly evaporated by using an electron beam while monitoring the conductance of the SWNT-FETs. Figure 9.13 shows the variation of the electronic transfer characteristics of the SWNT-FETs with controlled Al deposition. Upon Al deposition, the electronic transfer curves shift toward more negative gate voltages. The curves were obtained by carrying out measurements every 10 s: it can be seen that *p*-type conduction disappears completely after about 30 s. The deposition rate was carefully kept below 0.1 Å/s. After about 2–4 min deposition, the *p*-type SWNT-FETs were converted into *n*-type SWNT-FETs. Figure 9.14 shows the changes in the electronic transfer characteristics and AFM images of an open SWNT-FET. For this sample, about 30 Å thick Al was deposited while monitoring the conductance. As shown in Fig. 9.14a, the sample exhibits enhanced *n*-type conduction following the Al deposition. The doping level of the Al-decorated *n*-type SWNT-FET

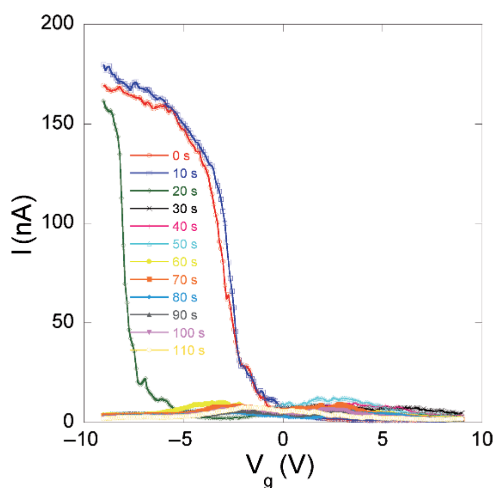

Fig. 9.13 The changes in the electronic transfer properties of an open SWNT-FET resulting from in situ Al decoration

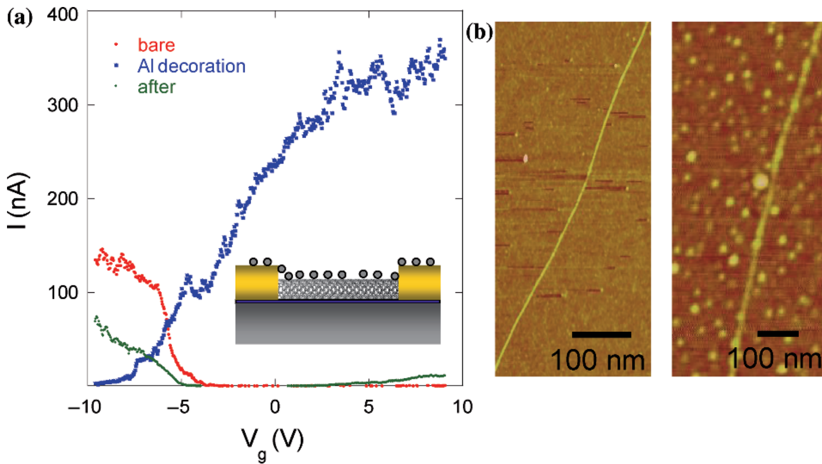

Fig. 9.14 **(a)** The changes in the electronic transfer properties of the device resulting from Al decoration. **(b)** AFM images of the device. Reused with permission from Hyo-Suk Kim, Byoung-Kye Kim, Ju-Jin Kim, Jeong-O Lee, and Noejung Park, Applied Physics Letters, 91, 153113 (2007). Copyright 2007, American Institute of Physics

can be controlled by varying the Al deposition time. In this particular device, the on/off ratio of the *n* transistor is about 10^3, and channel pinch off does not occur until $V_g = -10\,V$. Upon adsorption of Al onto the carbon nanotube, electrons will be transferred from Al to the carbon nanotube, since Al has a lower work function (4.1 eV) than the nanotube (4.8 eV). Further, the presence of Al clusters in the contact region can lower the height of the Schottky barrier to electron transport. However, the device gradually became a *p*-type SWNT-FET again when exposed to air. Such phenomena are attributed to the oxidation of Al and the subsequent work function increase, as indicated by electronic structure calculations in Sect. 9.2.1.

Similar behavior was observed for the contact-decorated and channel-decorated devices; the devices become *n*-type transistors after decoration, and are gradually converted back to *p*-transistors in air. Channel-decorated devices exhibit decreased conductance after Al decoration, whereas improved transistor performance was observed in the contact-decorated devices. The controlled deposition of metallic nanoparticles can thus be an effective method for the fabrication of complementary SWNT-FETs and highly sensitive sensor devices, though care must be taken not to introduce oxygen into the system.

9.3.3 The Effects of Metal Clusters on Carbon Nanotube Sensors

In the previous section, we showed that it is possible to fabricate *n*-type nanotube transistors by decorating low work function metals onto nanotubes. In this section, we discuss the effects of the decorated metal particles on the sensing characteristics of SWNT-FET based chemical sensors and how the change in work function affects them.

SWNT-based sensors bearing the appropriate functional groups have been investigated as potential sites for chemical or biological analyte recognition [27a., 4]. Pd nanoparticles [25], polyethyleneimine (PEI)-starch functionalization [47], and nafion [48] have been suggested as suitable surfaces for H_2 and CO_2 sensors, as well as for humidity and NH_3 sensors, respectively. In addition, SWNT-FETs functionalized with antibodies or receptor molecules have been shown to exhibit strong propensities for the selective detection of biological molecules such as proteins and other small molecules [8].

In this section, we investigate the effect of metal cluster decoration on the electrical transport properties and sensing characteristics of SWNT-FETs. It has been demonstrated that the use of metal cluster coatings on nanoscale structures can deplete or populate carriers locally, thereby making the device either sensitized or ineffective with respect to molecular adsorption [24, 59]. Here, we apply this concept to *p*-type SWNT-FETs, and investigate the effects of different metal clusters on the electrical transport and chemical sensing properties of carbon nanotubes.

First, the electrical transfer characteristics of the bare SWNT-FETs were measured, and then Al nanoparticle layers (approx. 5 Å in thickness) were thermally evaporated onto the devices at high vacuum. The gas sensing experiments were conducted in a vacuum chamber, with Ar, NO_2, NH_3, and H_2 gases supplied with precise flow control.

Figure 9.15 shows the current–gate voltage characteristics (I–V_g) of the SWNT-FETs before (black) and after (gray) metal cluster decoration. As shown in Fig. 9.15a, the device exhibited clear *p*-type semiconducting behavior, with complete depletion of the current around $V_{th} = 1\,V$. However, the SWNT-FET was

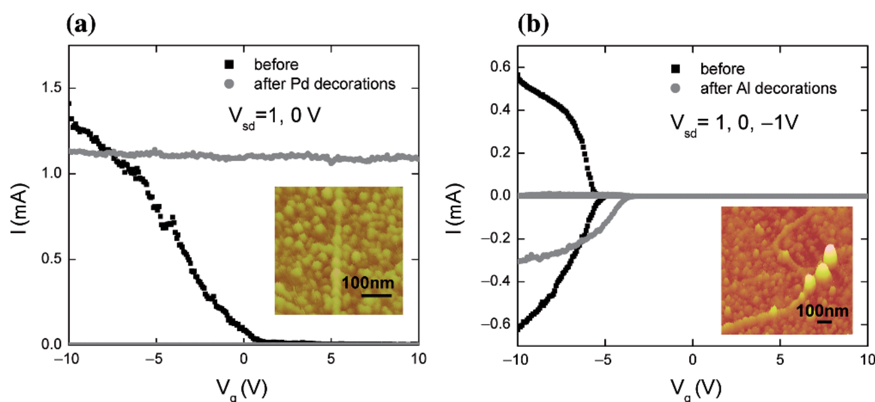

Fig. 9.15 The transfer characteristics (I–V_g) of SWNT-FETs before (black) and after (gray) metal cluster decoration with **(a)** Pd and **(b)** Al nanoparticles. The current was measured at $V_{sd} = 1$, 0, and $-1\,V$. In panel **(a)**, the current was symmetric with respect to V_{sd} before and after decoration with the Pd nanoparticles, so we only show the current measured at positive bias. In panel **(b)**, the current became highly asymmetric with respect to V_{sd} after the SWNT-FET was coated with Al nanoparticles. The insets in **(a)** and **(b)** show AFM images of the metal-decorated carbon nanotubes. Reused with permission from Byoung-Kye Kim, Noejung Park, Pil Sun Na, Hye-Mi So, Ju-Jin Kim, Hyojin Kim, Ki-Jeong Kong, Hyunju Chang, Beyong-Hwan Ryu, Youngmin Choi and Jeong-O Lee, Nanotechnology 17, 496 (2006), Copyright 2006, Institute of Physics Publishing

found to lose much of its gate dependency after the nanotube was coated with Pd nanoparticles. It is believed that the electrical conduction occurs through the nanotube, rather than through the Pd film. Indeed, if the Pd film did provide continuous paths for electron conduction, then the magnitude of the current should be much larger than that of the on-state *p*-channel current through the nanotube. Note that the current shown in the gray curve in Fig. 9.15a is approximately 1.1 μA irrespective of the gate voltage. The AFM image in the inset in Fig. 9.15a also shows that the Pd particles are unlikely to form continuous paths between the source and drain electrodes. Instead, the loss of gate-dependency is ascribed to screening induced by the Pd nanoparticles. By carrying out electrostatic calculations, we determined that the metal nanoparticle monolayers (typically 5 nm in diameter, with a 3 nm interparticle separation) are effective at screening the gate field. Thus, Pd-decorated SWNTs can be described as *p*-type degenerate semiconductors, and contain carriers that are present even at positive gate voltages as a result of screening by the metal particles. Note that Pd is a high work function metal, and thus the adsorption of Pd particles onto the carbon nanotubes is expected to induce the formation of hole carriers. Figure 9.15b shows the evolution of the electrical transfer characteristics of an SWNT-FET coated with Al nanoparticles. Unlike the case in which Pd nanoparticle coatings were used, a gate effect is observed for the Al-decorated SWNT-FETs. The decreased conductance after Al decoration is consistent with the results discussed in the previous section. The marked difference between this behavior and that of the Pd-decorated SWNT-FETs may be either due to the difference between the adhesion properties of Al and Pd, or to the difference between the work functions of Pd and Al particles. As shown in the inset images in Fig. 9.15, Al deposited on the nanotube tends to form large discrete particles, whereas the Pd nanoparticles form much finer particles with smaller interparticle spacings [57, 58]. Therefore, the gate field screening is likely to be greater following Pd decoration. Although the Pd-coated devices exhibit ohmic transport behavior before and after nanoparticle decoration, Al decoration results in the formation of a Schottky barrier, as discussed later.

The sensitivity of the metal cluster-decorated SWNT-FETs to gas exposure was also investigated.

Figure 9.16 shows the electrical transfer characteristics and gas sensing properties of the Al-decorated nanotubes. As shown in Fig. 9.16a, there is a significant decrease in the current immediately after Al decoration of the SWNT-FET (black empty squares), which eventually partially recovers (gray filled circles and empty dots). We also note that rightward shifts in the threshold voltage accompany the recovery in the current. Moreover, the observed decrease in the I_{ds}–V_g slope can be explained as a decrease in the work function of the electrode, whereas the shift in the threshold voltage is due to an increase in carrier density [8]. Note that as oxidation proceeds, the work function of the Al surface increases to levels normally associated with gold particles [41a.]. Thus, the partial recovery of the I_{ds}–V_g slope and the rightward shift in the threshold voltage (as shown in Fig. 9.18a) are largely due to oxidation of the Al nanoparticle surfaces. Remarkably, many SWNT-FETs exhibit diode-like, highly asymmetric behavior following Al decoration, as shown

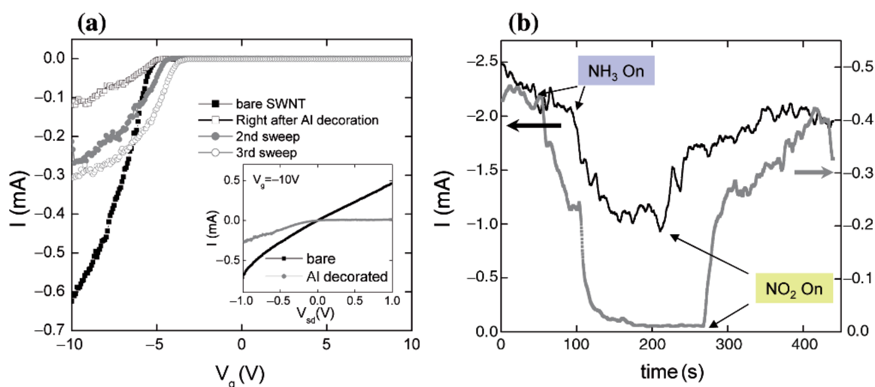

Fig. 9.16 **(a)** I–V_g characteristics of an Al-decorated SWNT-FET in ambient air conditions. Bias voltage $V_{sd} = 1\,V$. The image inset shows the I–V_{sd} results for the bare (black) and Al-decorated (gray) devices. **(b)** Gas sensing with bare (black) and Al-decorated (gray) SWNT-FETs. The back gate voltage V_g was maintained at $-10\,V$, whereas the source to drain bias was fixed at 1 V. Reused with permission from Byoung-Kye Kim, Noejung Park, Pil Sun Na, Hye-Mi So, Ju-Jin Kim, Hyojin Kim, Ki-Jeong Kong, Hyunju Chang, Beyong-Hwan Ryu, Youngmin Choi and Jeong-O Lee, Nanotechnology 17, 496 (2006), Copyright 2006, Institute of Physics Publishing

in the inset in Fig. 9.16a. Such asymmetric I_{ds}–V_{sd} curves and the observed decrease in the I_{ds} value are thought to be due to modifications of the contact barrier by the Al nanoparticles in the metal–SWNT contact regions. It is likely that the adsorbed Al particles increase the Schottky barrier in either the source or drain electrode, thus inducing asymmetric I_{ds}–V_{sd} patterns. A few devices exhibited symmetric I–V_{sd} curves, which may result from the formation of Al particle layers on both electrodes.

Upon gas exposure, most of the Al-decorated SWNT-FETs were found to exhibit greatly enhanced sensitivities in the range of 300–1,000%. Figure 9.16b shows the gas sensitivity of the bare (black) and Al-decorated (gray) SWNT-FETs. Before Al-decoration, the sensitivity of the SWNT-FET is around 50%. However, this value is significantly enhanced (>1,000%) by Al decoration. This enhancement in sensitivity can be explained with one of two possible mechanisms. First, nanoscale Schottky barriers are formed by the Al nanoparticle decorations at either the metal–SWNT contact regions or on the nanotube itself. The formation of nano-Schottky barriers will modulate the width of the conduction channel, such that the nano-Schottky barrier itself will be modulated by molecular adsorption. The adsorption of NH_3 (or NO_2) decreases (increases) the work function of the metal surface [27(a)], resulting in a concomitant increase (decrease) in the Schottky barrier to hole transport. It was observed that when the devices contained metallic nanotubes, the sensitivity improvement was not appreciable after decoration with Al nanoparticles. We note that in these metallic devices the work function change as a result of metal electrode or metal particle decoration is not expected to lead to modification of the Schottky barrier. Second, we cannot completely rule out the effects of modulation of the carrier density in the nanotube body. Aluminum nanoparticles in the vicinity of the carbon nanotube may increase the chemical reactivity toward the gas molecules [24, 59].

To clarify the origin of the sensitivity enhancement, we performed the following experiment. First, we patterned nanotube devices so that only their source and drain electrodes are exposed for metal cluster deposition. In the second type of device, the AZ5214 photoresist and image reverse technique was used to deposit clusters only on nanotubes. The electrical properties and sensor characteristics of both types of devices were measured after careful lift-off. Figure 9.17a and b show the sensing characteristics of the contact-decorated and channel-decorated SWNT-FETs, respectively. In both cases, a decrease in the conductance was observed after Al cluster decoration. Figure 9.17a shows the sensing characteristics of the SWNT-FET with contact electrodes that were decorated with Al clusters. The inset in Fig. 9.17a shows an optical microscopy image of the device with its channel covered with AZ5214. As shown in this figure, the sensitivity of the device, which was around 10% before contact decoration (the original device contained metallic nanotubes, so the on/off ratio of the transistor was only 2), has improved to about 50%. In the case of the channel-decorated SWNT-FET, almost no change or inferior sensitivity was observed following Al decoration, as shown in Fig. 9.17b. Therefore, we conclude that the observed sensitivity enhancement is mostly due to the modulation of the contact barrier by the Al cluster decoration. This conclusion is confirmed by the observation that the largest sensitivity enhancement was achieved with the SWNT-FET that exhibited highly asymmetric *I–V* characteristics after Al decoration.

In summary, we investigated the effect of metal nanoparticle decoration on the gas sensing capabilities of nanotube-based sensors. After coating the carbon nanotube with Al nanoparticles, the device was found to exhibit Schottky behavior, i.e., the current passing through the nanotube was found to decrease. However, the sensitivity to both NO_2 and NH_3 was found to be greatly enhanced by the Al nanoparticle decoration. We suggest that metal-particle decoration could be used to

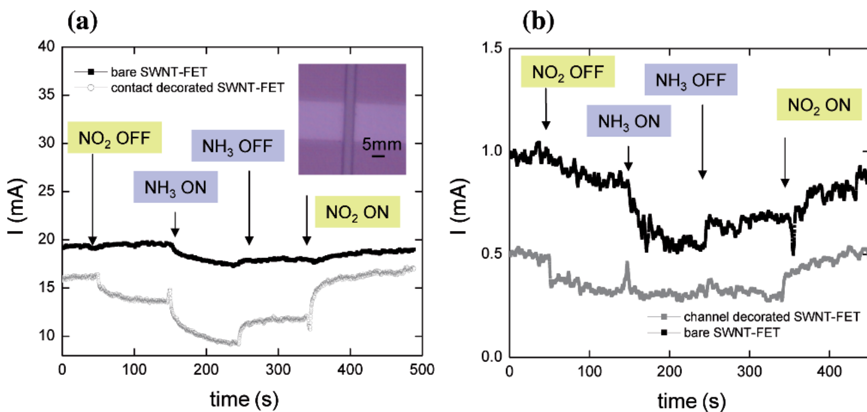

Fig. 9.17 **(a)** Gas sensing with bare (black) and contact-decorated (gray) SWNT-FETs. Bias voltage $V_{sd} = 1\,V$. The inset shows an optical microscopy image of the device with its contact electrodes open for Al decoration. **(b)** Gas sensing with bare (black) and channel-decorated (gray) SWNT-FETs. Reused with permission from Byoung-Kye Kim, Noejung Park, Pil Sun Na, Hye-Mi So, Ju-Jin Kim, Hyojin Kim, Ki-Jeong Kong, Hyunju Chang, Beyong-Hwan Ryu, Youngmin Choi and Jeong-O Lee, Nanotechnology 17, 496 (2006), Copyright 2006, Institute of Physics Publishing

tailor the transfer characteristics of nanoscale devices or to tune the sensitivity of nanotube-based chemical and biological nanosensors.

9.3.4 Contact Engineering with Protein Nanoparticles

In this section we show that by modifying the contact barrier, metallic or semiconducting carbon nanotubes can be transformed into field effect transistors. By placing protein-coated nanoparticles in the metal–nanotube contact area, we achieved p-type transport behavior in the device irrespective of whether the nanotube was metallic or semiconducting.

Laser ablation grown tubes were spun over prefabricated alignment markers from dichloroethane solution, and atomic force microscopy (AFM) was used to locate individual SWNTs. Electrical leads consisting of 5 nm Ti/30 nm Au were patterned on top of the individual nanotubes by using e-beam lithography, and the electrical characteristics of these devices were recorded as a reference. The devices were then allowed to react overnight with a diluted solution of streptavidin-coated polystyrene nanoparticles ($\sim$120 nm diameter) or a solution of streptavidin-coated 10 nm diameter Au particles. Deionized water (pH 5.0) or 10 mM PBS (phosphate buffered saline, pH 7.4) was used to dilute the protein-coated nanoparticles. After the reactions with the protein-coated nanoparticles solution, the samples were washed with clean buffer or DI water, and blown dry with dry N_2 gas. The electrical transport properties of the samples reacted with the protein-coated nanoparticles were measured, and the sample morphologies were characterized with AFM.

Figure 9.18a shows the typical I–V_g characteristics of the nanotube devices before (black) and after (red) the adsorption of the protein-coated nanoparticles. Before the reaction with the protein-coated nanoparticles, the devices exhibited p-type gate effects with a mobility of $\mu = 263\,\mathrm{cm^2/Vs}$, where it was assumed that the gate capacitance is given by $C \approx 2\pi\varepsilon\varepsilon_0 L/\ln(h/r) \sim 6.08 \times 10^{-17}\,\mathrm{F}$, where L equals the tube length (2 µm for this sample), r is the radius of the nanotube, and h is the dielectric layer thickness. The tube diameter was measured with AFM and found to be around 1 nm, and the dielectric SiO_2 layer thickness was 200 nm. As shown in Fig. 9.18a, this device has a rather poor on/off ratio ($\sim$6) and a large subthreshold swing (>5 V/decade) before the adsorption of the protein-coated nanoparticles. Here, the subthreshold swing S is defined as $S = (\mathrm{d}\log I/\mathrm{d}V_g)^{-1}$. After reaction with the streptavidin-coated nanoparticles, the device exhibits a highly enhanced p-type gate response. It is noteworthy that the channel closes completely at around $V_g = 0.5\,\mathrm{V}$, whereas there was substantial current up to $V_g = 5\,\mathrm{V}$ before the reaction with the streptavidin-coated nanoparticles. The on/off ratio was increased to 10^4 and S (subthreshold swing) was decreased to 0.15 V/decade by the reaction with the protein-coated nanoparticles. Considering that S is usually near 2 V/decade for this thickness of SiO_2 gate dielectric layer ($\sim$200 nm), this value for S is remarkably small. If we assume that the self capacitance of each single tube does not change, the enhancement of the mobility due to the reaction is $\sim 1900\,\mathrm{cm^2/Vs}$.

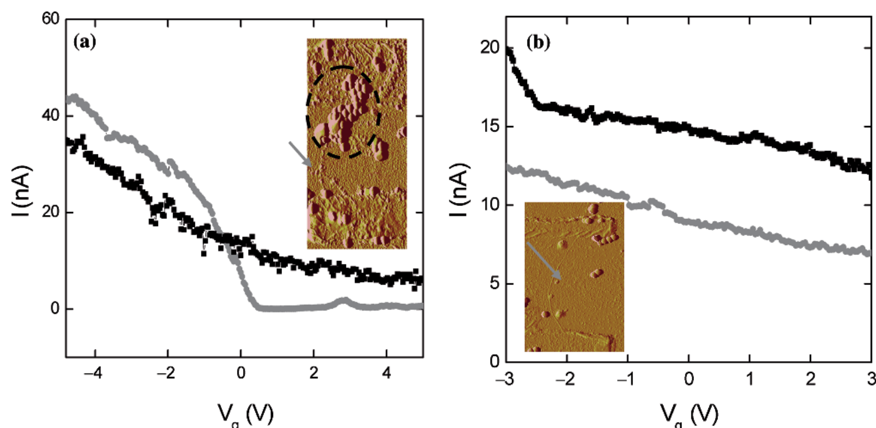

Fig. 9.18 Transport characteristics of semiconducting nanotube FETs with streptavidin-coated polystyrene nanoparticles adsorbed **(a)** in the metal nanotube contact area, and **(b)** near the nanotube body far from the contact. The black lines in panels **(a)** and **(b)** are the I–V_g curves before protein adsorption, and the gray lines are those after protein adsorption. The insets in **(a)** and **(b)** show AFM images of the devices after reaction with streptavidin-coated nanoparticles. Reused with permission from Pil Sun Na, Noejung Park, Jinhee Kim, Hyojin Kim, Ki-Jeong Kong, Hyunju Chang and Jeong-O Lee, A Field Effect Transistor Fabricated with Metallic Single-Walled Carbon Nanotubes, Fullerenes, Nanotubes and Carbon Nanostructures 14, 141 (2006), Copyright 2006, Taylor & Francis Ltd.

The inset in Fig. 9.20a shows an AFM image of the device after the reaction with the streptavidin-coated nanoparticles. As indicated by the circle, large clusters of streptavidin-coated polystyrene nanoparticles were adsorbed only at the contact area between the metal electrodes and the SWNT. When the protein-coated nanoparticles were situated on the nanotube body in areas far from the contact region, there was no apparent change in the conductance (Fig. 9.18b).

For metallic tubes, a more marked change occurs after the reaction with the streptavidin-coated nanoparticles. Figure 9.19a shows the changes in the gate dependent conductance after the sample had reacted with streptavidin-coated 10 nm Au nanoparticles. Before the reaction, the sample exhibited typical metallic behavior (black curve), i.e., the conductance does not vary with variation of the gate voltage from -5 to 5 V. After the sample had reacted with the streptavidin-coated 10 nm Au particles, the conductance increases for $V_g < 1$ V, and decreases abruptly to zero for $V_g > 1$ V, i.e. there is a FET-like gate response from the metallic nanotube. The on/off ratio, mobility, and S of the device become 10^3, 215 $\mathrm{cm^2/Vs}$, and 0.8 V/decade, respectively. It is also noteworthy that the conductance of this device saturates immediately after the p-channel current turns on, unlike the behavior of Si-MOSFETs and typical SWNT-FETs. We believe this result confirms that the nanotube in our device is indeed metallic. The inset in Fig. 9.19a shows the AFM images of the device before (left) and after (right) the reaction with the streptavidin-coated 10 nm Au particles. A large cluster of streptavidin-coated Au particles is marked with a black dotted circle in the inset on the right.

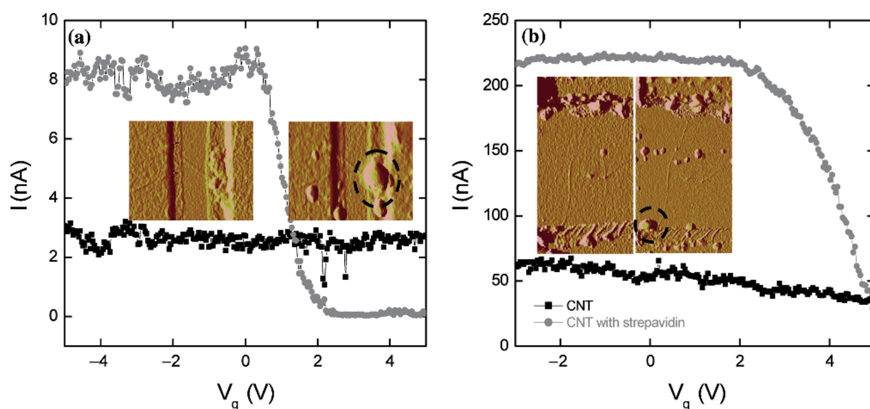

Fig. 9.19 **(a, b)** Transport characteristics of the two metallic nanotube devices decorated with streptavidin-coated 10 nm Au particles. The black and gray curves in panels **(a)** and **(b)** are the I–V_g curves before and after protein adsorption, respectively. In panels **(a)** and **(b)**, the left and right insets show AFM images of the device before and after protein adsorption, respectively. Reused with permission from Pil Sun Na, Noejung Park, Jinhee Kim, Hyojin Kim, Ki-Jeong Kong, Hyunju Chang and Jeong-O Lee, A Field Effect Transistor Fabricated with Metallic Single-Walled Carbon Nanotubes, Fullerenes, Nanotubes and Carbon Nanostructures 14, 141 (2006), Copyright 2006, Taylor & Francis Ltd.

Figure 9.19b shows the measurements for another SWNT device with its contact area loaded with streptavidin-coated 10 nm Au particles. As is shown in the inset, a few streptavidin-coated Au particles are observed nearby the nanotube body. However, most of them are present in the metal–SWNT contact region (dotted black circle). A sharp transition from almost metallic behavior to *p*-type semiconducting behavior is also observed in this device. If we assume a tube length of 2.8 μm and a diameter of 1.5 nm, the estimated mobility of this device is $\sim$3300 $\mathrm{cm}^2/\mathrm{Vs}$. Again, the conductance saturates after the *p*-channel current commences. The devices decorated with streptavidin-coated polystyrene nanoparticles exhibited similar transitions (data not shown) to those with streptavidin-Au particles.

In previous studies, changes in the Schottky barrier at the metal–nanotube contact have been discussed in relation to the conversions between *p*-type and *n*-type behaviors and between ambipolar and unipolar behaviors [12, 33]. Adsorbed proteins are known to affect the work functions of metal electrodes [8]. However, all previous observations should be attributed to the Schottky barrier between the semiconducting nanotube and the metal electrodes. The conversion observed in this study from metallic behavior to semiconducting behavior and the sharp increase in the gate response have not previously been reported. Since streptavidin is known to have different charge states depending on the pH of the solution [54b.], its charge state is expected to depend on the gate bias in our device structure. When streptavidin-coated nanoparticles were used in this experiment, about 5,000 protein molecules were immobilized on each polystyrene nanoparticle, and the proteins are likely to adsorb in close vicinity to the metal–nanotube contact. Figure 9.20 shows a schematic diagram

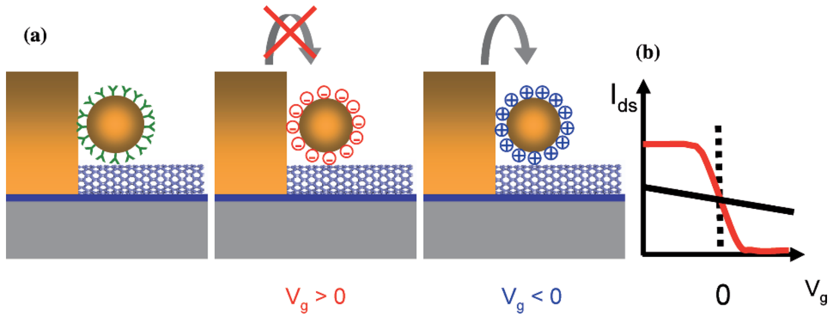

Fig. 9.20 Schematic illustrations of **(a)** the dependence of the charge states of the protein-coated nanoparticles on the gate bias, and **(b)** the resulting changes in the I–V_g curves. In panel **(b)**, the dark and gray lines are the I–V_g curves before and after protein adsorption, respectively. Reused with permission from Pil Sun Na, Noejung Park, Jinhee Kim, Hyojin Kim, Ki-Jeong Kong, Hyunju Chang and Jeong-O Lee, A Field Effect Transistor Fabricated with Metallic Single-Walled Carbon Nanotubes, Fullerenes, Nanotubes and Carbon Nanostructures 14, 141 (2006), Copyright 2006, Taylor & Francis Ltd.

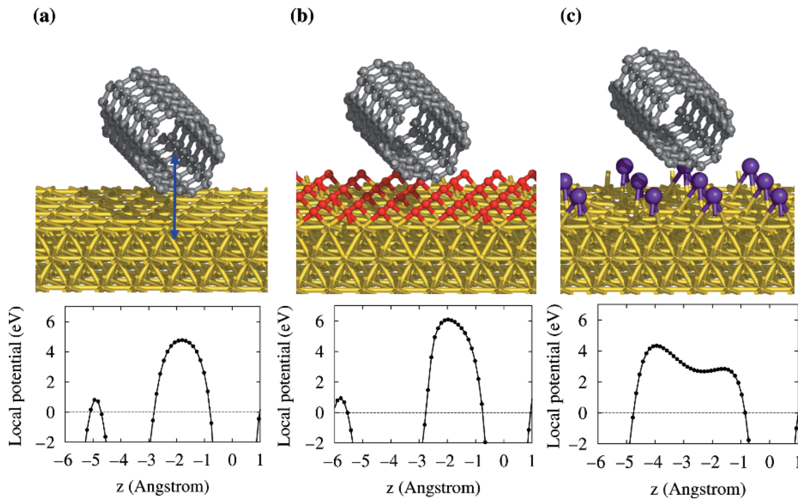

Fig. 9.21 Atomic geometries optimized in ab initio calculations for (5,5) nanotubes in contact with **(a)** the bare Au (111) surface and **(b)** oxygen and **(c)** rubidium adsorbates on the metal surface. In the lower panels, the local potentials across the contact with respect to the Fermi level are shown, as indicated by the arrow in panel **(a)**. Reused with permission from Pil Sun Na, Noejung Park, Jinhee Kim, Hyojin Kim, Ki-Jeong Kong, Hyunju Chang and Jeong-O Lee, A Field Effect Transistor Fabricated with Metallic Single-Walled Carbon Nanotubes, Fullerenes, Nanotubes and Carbon Nanostructures 14, 141 (2006), Copyright 2006, Taylor & Francis Ltd.

of the effects of the gate voltage on the electron transport and charge states of the proteins.

The common observation of a large contact resistance has been attributed to the presence of a tunneling barrier between the metal and the nanotube [11, 53]. We suspect that after the reaction with protein-coated nanoparticles the metal–nanotube

contact might be contaminated with the terminal groups of the protein. Depending on the gate bias, the protein could be charged either negatively or positively, which affects the tunneling barrier at the metal–nanotube contact because of the contaminating terminal groups. We now show with ab initio electronic structure calculations [28, 29] that the tunneling barrier at the metal–nanotube contact is sensitive to the presence of charged species near the metal–nanotube contact. Figure 9.21a shows the optimized atomic geometry of a metallic (5,5) nanotube in contact with a bare gold (111) surface. In Figs. 9.21b and c, there are oxygen and rubidium atoms respectively adsorbed within the contact region. Owing to the electron transfer between the adsorbates and the metal surface, the oxygen adsorbates form a negatively charged layer, whereas the rubidium atoms form a positively charged layer after donating electrons to the metal. In the lower panels of Fig. 9.21, the local potentials in the Kohn–Sham equation are plotted across the contact, as indicated by the arrow in Fig. 9.21a, with respect to the Fermi level. Note that oxygen adsorption, and consequently, the presence of negatively charged particles, increases the tunneling barrier, whereas the presence of rubidium adsorbates reduces the potential barrier. Because of the large Au–Rb bond length ($\sim$3.4 Å), the distance from the Au (111) surface to the carbon nanotube is increased, and thus the vacuum barrier becomes thicker. However, we postulate that in our experiment the charge states of the contaminating terminal groups at the metal–nanotube contact vary depending on the gate bias, with only negligible changes in their chemical structures.

In conclusion, we fabricated carbon nanotube field effect transistors and decorated the metal–nanotube contact region with protein-coated nanoparticles. Remarkably, the gate response was found to be sensitive to protein adsorption even for metallic carbon nanotubes. Upon the adsorption of protein-coated nanoparticles at the metal–nanotube contact, the devices fabricated with metallic SWNTs exhibit *p*-type transport behavior. In the case of semiconducting SWNT devices, the adsorption of protein-coated nanoparticles makes the gating more effective, resulting in greatly enhanced device performance, such as higher on/off ratios and decreased S. This enhancement is due to the sensitivity of the contact barrier to the charge states of the proteins, which can be controlled by varying the gate bias. This switching mechanism could be generalized in the nanoelectronics, relieving a significant effort to separate semiconducting nanotubes from the aggregate.

9.4 Conclusion

We have investigated the importance of the contact in SWNT-FETs to their electrical transfer properties by using electronic structure calculations and experimental electrical transfer measurements. By varying the work function of the metal electrode in contact with the nanotube, it is possible to fabricate *n*-type transistors and Schottky diodes with single-walled carbon nanotubes. Metal decoration and SAM techniques were used to vary the Schottky barrier height. Contact decoration with Al was shown to be an effective method of increasing the sensitivity of nanotube-based

sensors. It was found that variation of the polarity of the SAM molecule can significantly affect the Schottky barrier height. Thus care must be taken with sensors that use Schottky barrier height change as the transducing mechanism. Although the effects of the contact are significant for carbon nanotubes, the effects of channel doping by oxygen and other species are also non-negligible.

Finally, we have shown that by substituting materials that can be charged by the gate bias voltage at the metal–nanotube contact, it is possible to create transistors even with metallic nanotubes. The charge state of the substituted particle can change the height of the metal–nanotube tunneling barrier, resulting in a switch that can be turned on and off by varying the gate voltage.

In summary, we have shown that nanotube devices with desirable properties can be fabricated by using delicate control of the properties of the contact barrier. However, if large scale production of such designed nanotube devices is to be achieved, methods with more precise control are required.

Acknowledgments This work was supported by MOST and grants from the KOSEF through the Center for Nanotubes and Nanostructured Composites (CNNC), and KRISS-University Program and Core Technology Development Project by ITEP, Korea

References

1. Antonov RD, Johnson AT (1999) Subband population in a single-wall carbon nanotube diode. Phys Rev Lett 83:3274–3276
2. Appenzeller J, Knoch J, Derycke V, Martel R, Wind S, Avouris Ph (2002) Field-modulated carrier transport in carbon nanotube transistors. Phys Rev Lett 89:126801–126804
3. Bachtold A, Hadley P, Nakanishi T, Dekker C (2001) Logic circuits with carbon nanotube transistors. Science 294:1317–1320
4. (a)Besteman K, Lee J, Wiertz FGM, Heering HA, Dekker C (2003) Enzyme-coated carbon nanotubes as single-molecule biosensor. Nano lett 3:727–730; (b) Star A, Gabriel J-CP, Bradley K, Grüner G (2003) Electronic detection of specific protein binding using nanotube fet devices. Nano Lett 3:459–463
5. Bockrath M, Cobden DH, Lu J, Rinzler AG, Smalley RE, Balents L, McEuen PL (1999) Luttinger-liquid behaviour in carbon nanotubes. Nature 397:598–601
6. Bockrath M, Cobden DH, McEuen PL, Chopra NG, Zettl A, Thess A, Smalley RE (1997) Single-electron transport in ropes of carbon nanotubes. Science 275:1922–1925
7. Campbell IH, Rubin S, Zawodzinski TA, Kress JD, Martin RL, Smith DL, Barashkov NN, Ferraris JP (1996) Controlling Schottky energy barriers in organic electronic devices using self-assembled monolayers. Phys Rev B 54:R14321–R14324
8. Chen RJ, Choi HC, Bangsaruntip S, Yenilmez E, Tang X, Wang Q, Chang YL, Dai H (2004) An investigation of the mechanisms of electronic sensing of protein adsorption on carbon nanotube devices. J Am Chem Soc 126:1563–1568
9. Collins PG, Bradley K, Ishigami M, Zettl A (2000) Extreme oxygen sensitivity of electronic properties of carbon nanotubes. Science 287:1801–1804
10. de Boer B, Hadipour A, Mandoc MM, van Woudenbergh T, Blom PWM (2005) Tuning of metal work functions with self-assembled monolayers. Adv Mater 17:621–625
11. Delaney P, Ventra MD (1999) Comment on "Contact resistance of carbon nanotubes". Appl Phys Lett 75:4028–4029

12. Derycke V, Martel R, Appenzeller J, Avouris Ph (2002) Controlling doping and carrier injection in carbon nanotube transistors. Appl Phys Lett 80:2773–2775
13. Fall CJ, Binggeli N, Baldereschi A (1998) Anomaly in the anisotropy of the aluminum work function. Phys Rev B 58:R7544–R7547
14. Frank S, Poncharal P, Wang ZL, de Heer WA (1998) Carbon nanotube quantum resistors. Science 280:1744–1746
15. Freitag M, Radosavljevic M, Zhou Y, Johnson AT (2001) Controlled creation of a carbon nanotube diode by a scanned gate. Appl Phys Lett 79:3326–3328
16. Heinze S, Tersoff J, Avouris Ph (2003) Electrostatic engineering of nanotube transistors for improved performance. Appl Phys Lett 83:5038–5040
17. Hertel T, Avouris Ph, Martel R, Shea HR, Schmidt T, Walkup RE (1998) Carbon nanotubes: Nanomechanics, manipulation, and electronic devices. Appl Surf Sci 141:201–209
18. Honkala K, Laasonen K (2000) Oxygen molecule dissociation on the Al(111) Surface. Phys Rev Lett 84:705–708
19. Iijima S (1991) Helical microtubules of graphitic carbon. Nature 354:56–58
20. Iijima S, Ichihashi T (1993) Single-shell carbon nanotubes of 1-nm diameter. Nature 363:603–605
21. Jacobsen J, Hammer B, Jacobsen KW, Norskøv JK (1995) Electronic structure, total energies, and STM images of clean and oxygen-covered Al(111). Phys Rev B 52:14954–14962
22. Javey A, Guo J, Wang O, Lundstrom M, Dai H (2003) Ballistic carbon nanotube field-effect transistors. Nature 424:654–657
23. Javey A, Tu R, Farmer DB, Guo J, Gordon RG, Dai H (2005) High performance n-type carbon nanotube field-effect transistors with chemically doped contacts. Nano Lett 5:345–348
24. Kolmakov A, Klenov DO, Lilach Y, Stemmer S, Moskovits M (2005) Enhanced gas sensing by individual SnO_2 nanowires and nanobelts functionalized with Pd catalyst particles. Nano Lett 5:667–673
25. Kong J, Chapline MG, Dai H (2001) Functionalized carbon nanotubes for molecular hydrogen sensors. Adv Mater 13:1384–1386
26. Kong J, Dai H (2001) Full and modulated chemical gating of individual carbon nanotubes by organic amine compounds. J Phys Chem B 105:2890–2893

27a. Kong J, Franklin NR, Zhou C, Chapline MG, Peng S, Cho K, Dai H (2000) Nanotube molecular wires as chemical sensors. Science 287:622–625

27b. Someya T, Small J, Kim P, Nuckolls C, Yardley JT (2003) Alcohol vapor sensors based on single-walled carbon nanotube field effect transistors. Nano Lett 3:877–381

27c. Someya T, Small J, Kim P, Nuckolls C, Yardley JT (2003) Nerve agent detection using networks of single-walled carbon nanotubes. Appl Phys Lett 83:4026–4028

28. Kong J, Soh HT, Cassell AM, Quate CF, Dai H (1998) Synthesis of individual single-walled carbon nanotubes on patterned silicon wafers. Nature 395:878–881
29. Kong J, Yenilmez E, Tombler TW, Kim W, Dai H, Laughlin RB, Liu L, Jayanthi CS, Wu SY (2001) Quantum interference and ballistic transmission in nanotube electron waveguides. Phys Rev Lett 87:106801–106804
30. Kresse G, Furthmüller J (1996) Efficiency of ab-initio total energy calculations using a plane-wave basis set. Comput Mater Sci 6:15–50
31. Kresse G, Hafner J (1993) *Ab initio* molecular dynamics for liquid metals. Phys Rev B 47:558–561
32. Kresse G, Joubert D (1999) From ultrasoft pseudopotentials to the projector augmented-wave method. Phys Rev B 59:1758–1775
33. Lee JU (2005) Photovoltaic effect in ideal carbon nanotube diodes. Appl Phys Lett 87:073101–073103
34. Liang W, Bockrath M, Bozovic D, Hafner JH, Tinkham M, Park HK (2001) Fabry–Perot interference in a nanotube electron waveguide. Nature 411:665–669
35. Lin YM, Appenzeller J, Avouris Ph (2004) Ambipolar-to-unipolar conversion of carbon nanotube transistors by gate structure engineering. Nano Lett 4:947–950

36. Martel R, Derycke V, Lavoie C, Appenzeller J, Chan KK, Tersoff J, Avouris Ph (2001) Ambipolar electrical transport in semiconducting single-wall carbon nanotubes. Phys Rev Lett 87:256805–256808
37. Martel R, Schmidt T, Shea HR, Hertel T, Avouris Ph (1998) Single- and multi-wall carbon nanotube field-effect transistors. Appl Phys Lett 73:2447–2449
38. Michaelson HB (1977) The work function of the elements and its periodicity. J Appl Phys 48:4729–4733
39. Moon S, Lee S-G, Song W, Lee JS, Nam K, Kim J, Park N (2007) Appl Phys Lett:90:092113
40. Nosho Y, Ohno Y, Kishimoto S, Mizutani T (2005) n-Type carbon nanotube field-effect transistors fabricated by using Ca contact electrodes. Appl Phys Lett 86:073105–073107
41a. Odom TW, Huang JL, Kim P, Lieber CM (1998) Atomic structure and electronic properties of single-walled carbon nanotubes. Nature 391:62–64
41b. Wong SS, Joselevich E, Woolley AT, Cheung CL, Lieber CM (1998) Covalently functionalized nanotubes as nanometre-sized probes in chemistry and biology. Nature 394:52–55
42. Oh H, Kim JJ, Song W, Moon S, Kim N, Kim J, Park N (2006) Fabrication of *n*-type carbon nanotube field-effect transistors by Al doping. Appl Phys Lett 88:103503–103505
43. Park N, Hong S (2005) Electronic structure calculations of metal–nanotube contacts with or without oxygen adsorption. Phys Rev B 72:045408–045412
44. Park N, Kang D, Hong S, Han S (2005) Pressure-dependent Schottky barrier at the metal–nanotube contact. Appl Phys Lett 87:013112–013114
45. Perdew JP, Burke K, Ernzerhof M (1996) Generalized gradient approximation made simple. Phys Rev Lett 77:3865–3868
46. Rueckes T, Kim K, Joselevich E, Tseng GY, Cheung CL, Lieber CM (2000) Carbon nanotube-based nonvolatile random access memory for molecular computing. Science 289:94–97
47. Saito R, Dresselhaus G, Dresselhaus MS (1993) Electronic structure of double-layer graphene tubules. J Appl Phys 73:494–500
48. Saito R, Fujita M, Dresselhaus G, Dresselhaus MS (1992) Electronic structure of graphene tubules based on C_{60}. Phys Rev B 46:1804–1811
49. Sasaki T, Ohno T (1999) Calculations of the potential-energy surface for dissociation process of O_2 on the Al(111) surface. Phys Rev B 60:7824–7827
50. Star A, Han T-R, Joshi V, Gabriel J-C P, Grüner G (2004) Nanoelectronic carbon dioxide sensors. Adv Mater 16:2049–2052
51. Star A, Han T-R, Joshi V, Stetter JR (2004) Electroanalysis 16:108–112
52. Sumanasekera GU, Adu CKW, Fang S, Eklund PC (2000) Effects of gas adsorption and collisions on electrical transport in single-walled carbon nanotubes. Phys Rev Lett 85:1096–1099
53. Tans SJ, Devoret MH, Dai H, Thess A, Smalley RE, Geerligs LJ, Dekker C (1997) Individual single-wall carbon nanotubes as quantum wires. Nature 386:474–477
54a. Tans SJ, Devoret MH, Groeneveld RJA, Dekker C (1998) Electron-electron correlations in carbon nanotubes. Nature 394:761–764
54b. Wilder JWG, Venema LC, Rinzler AG, Smalley RE, Dekker C (1998) Electronic structure of atomically resolved carbon nanotubes. Nature 391:59–62
55. Tans SJ, Verschueren ARM, Dekker C (1998) Room-temperature transistor based on a single carbon nanotube. Nature 393:49–52
56. Tersoff J (1999) Contact resistance of carbon nanotubes. Appl Phys Lett 74:2122–2124
57. Ulman A (1991) An introduction to ultrathin organic films; from Langmuir-Blodgett to self assembly. Academic Press, San Diego, CA
58. van Oss CJ, Giese RF, Bronson PM, Docoslis A, Edwards P, Ruyechan WT (2003) Macroscopic-scale surface properties of streptavidin and their influence on a specific interactions between streptavidin and dissolved biopolymers. Colloids Surf B 30:25–36
59. Xue Y, Datta S (1999) Fermi-level alignment at metal–carbon nanotube interfaces: Application to scanning tunneling spectroscopy. Phys Rev Lett 83:4844–4847
60. Yao Z, Kane CL, Dekker C (2000) High-field electrical transport in single-wall carbon nanotubes. Phys Rev Lett 84:2941–2944

61. Zhang Y, Dai H (2000) Formation of metal nanowires on suspended single-walled carbon nanotubes. Phys Lett 77:3015–3017
62. Zhang Y, Franklin NW, Chen RJ, Dai H (2000) Metal coating on suspended carbon nanotubes and its implication to metal–tube interaction. Chem Phys Lett 331:35–41
63. Zhao Q, Buongiorno Nardelli M, Lu W, Bernholc J (2005) Carbon nanotube-metal cluster composites: A new road to chemical sensors? Nano Lett 5:847–851
64. Zhou C, Kong J, Yenilmez F, Dai H (2000) Modulated chemical doping of individual carbon nanotubes. Science 290:1552–1555

Chapter 10
Low Dimensional Nanomaterials for Spintronics

Jinlong Yang and Hongjun Xiang

Abstract Moore's Law in microelectronic technology will break down as the size of individual bits approaches the dimension of atoms; this has been called the end of the silicon road map. For this reason and also for enhancing the multifunctionality of devices, the spin degree of freedom of electron is being investigated for magneto-electronics applications, i.e., spintronics. Spin-based devices are closely connected with the development of nanotechnology. In this chapter, recent developments of the low-dimensional nanomaterials for spintronics are reviewed. In the first section, the main concepts of spintronics including nanospintronics are briefly discussed. Experimental studies on transition-metal-doped nanowires and nanotubes are summarized in the second section. Extensive theoretical works in this field are reviewed in the third section. Finally, an outlook is given in the last section.

10.1 Spintronics

Spintronics (a neologism for "spin-based electronics") [1, 2], also known as magnetoelectronics, is an emergent technology that exploits the quantum propensity of electrons to spin as well as make use of their charge state. The spin itself is manifested as a detectable weak magnetic energy state characterized as "spin up" and "spin down". Spintronics started attracting massive interest with the discovery of giant magnetoresistance (GMR) in the 1980s, which has already been adopted as the norm in the hard disk drive (HDD) manufacturing industry. Indeed, the impact of spintronics in the HDD industry is a mere indication of things to come.

Spintronics has a number of potentially groundbreaking applications that are set to drive next-generation electronics. Although GMR can arguably be considered the driving force for spintronics at present, the biggest potential of spin-based devices is in embedded memories. Magnetoresistive random access memory (MRAM) is expected to revolutionize the memory market and contribute to the development of advanced and versatile computing and personal devices. Advances in instantly

bootable computers and MRAM could be the next big thing in sprintronics. Magnetic sensors have already found a wide market application, thereby establishing the commercial viability of spin-based devices. Each spin could carry a bit of information—in effect, a single-spin transistor—which could lead to faster computers that consume less electricity, alleviating the problem of heat dissipation. Quantum computation is perhaps one of the most exciting potential applications of spintronics. However, harnessing the power of the quantum states to enable information processing and storage is not easy. The evolution of MRAMs and various spin-based technologies could be critically important in facilitating the development of the first quantum computer.

To make a spintronic device, the primary requirement is to have a system that can generate a current of spin polarized electrons, and a system that is sensitive to the spin polarization of the electrons. Most devices also have a unit in between that changes the current of electrons depending on the spin states. The simplest method of generating a spin polarized current is to inject the current through a ferromagnetic material. In particular, half metallic (HM) [3] ferromagnetic materials are ideal for such applications since in these systems conduction electrons are 100% spin polarized because of a gap at the Fermi level (E_f) in one spin channel, and a finite density of states (DOS) for the other spin channel.

10.1.1 Nano-Spintronics

Spin-based devices are closely connected with the development of nanotechnology. The manipulation of spin calls for working at very small dimensions and this has led to a high degree of miniaturization in these devices. Small is the way to go in technology and miniaturization could potentially take spintronic devices to the next level. The miniaturization of electronic devices represents an ongoing trend for both industrial manufacture and academic research. Spintronics requires the fabrication of ferromagnetic nanostructures that, at room temperature, can transport spin-polarized carriers, and that can be assembled into addressable hierarchies on a macroscopic chip. Dimensionality and size are known to play a significant role in determining various properties of the systems.

Among many other possibilities, nanotubes (NTs) and nanowires are now being actively explored as the possible building blocks for electronic devices with features smaller than 100 nm. The controlled fabrication and fundamental understanding of low-dimensional ferromagnetic semiconductor nanostructures is thus crucial to the development of semiconductor-based spintronic devices and spin-based quantum-computation schemes. Meanwhile, one-dimensional diluted magnetic semiconductor (DMS) nanowires are advantageous to the integration of DMSs toward a three-dimensional architecture of nanoscale spintronics chips for several reasons. First, nanowires themselves are attractive building blocks for nanometer-scale electronic and optoelectronic devices; second, magnetic nanowires could act as spin filters to supply spin-polarized carrier currents and could also have large

magnetic anisotropy energies; third, carriers could be confined in the radial direction of nanowires and, therefore, high carrier concentrations and efficient injection of spin-polarized carriers could be potentially achieved; finally, the single-crystalline nanowires could be used as a model DMS system for exploring the origin of ferromagnetism in these semiconductors by excluding extrinsic effects such as secondary phases. It is reasonable that the combination of low dimensionality and room temperature ferromagnetism in diluted magnetic oxides would generate new functional nanomaterials useful for future miniaturized devices because of the strong confinement effect and the shape anisotropy. The availability of diluted magnetic semiconductor nanowires with Curie temperatures above room temperature may also open up new opportunities to realize nanometer-scale spintronic and optoelectronic devices such as spin-LEDs, transistors, and ultradense nonvolatile semiconductor memory, optical devices such as diodes and displays which can be operated by a magnetic field as well as spin-injection devices, e.g., amplifiers, frequency multipliers and square-law detectors based on 1D heterostructures.

10.2 Brief Overview of Experimental Works

With the advancement of experimental techniques, it has recently been possible to synthesize low-dimensional nanostructures including nanowires and NTs. Recently, several groups have succeeded in synthesizing single-crystalline Mn-doped GaN nanowires free of defects with diameters ranging from 10–100 nm and of lengths up to tens of micrometers [4–6]. More importantly, Mn-doped GaN nanowires have been found to be ferromagnetic up to 300 K and exhibit negative magnetoresistance. Ham and Myoung found that the room-temperature ferromagnetism depends on (Ga, Mn)N nanowires, which were converted from n-type to p-type with increasing Mn concentration [7]. Cui et al. [8] used an electrochemical process to grow Co-doped ZnO nanowire arrays at low temperature. The Co dopant introduces room-temperature ferromagnetism in ZnO nanowires and affects their optical properties. FeCo-codoped ZnO nanowires were synthesized by in situ doping with iron and cobalt using a chemical vapor deposition method [9]. No FeCo clusters and other secondary phases were found in the nanowires. A Curie temperature higher than 300 K was observed from the as-doped nanowires.

Very recently, Seong et al. reported room-temperature ferromagnetic properties in single-crystalline AlGaN:Mn NTs [10]. Room temperature ferromagnetism in Co-doped TiO_2 NTs prepared by sol–gel template synthesis was reported by Huang et al. where the ferromagnetic behavior is related to the oxygen vacancies created by the Co^{2+} substitution of Ti^{4+} site in TiO_2 [11]. The synthesis of room temperature ferromagnetic Co-doped titanate NTs via a simple hydrothermal method was also achieved in another study [12].

As discussed earlier, most efforts have been directed towards the mixing of transition-metal (TM) atoms (such as Fe, Co, Ni, and Mn, which have permanent magnetic moments) into semiconductor devices. To create nanostructures

exhibiting room-temperature ferromagnetism, Krusin-Elbaum et al. synthesized VO_x-alkylamine NTs through a combination of sol–gel and hydrothermal synthesis [13]. They then “doped” the NTs, introducing foreign atoms into the gaps between layers: lithium atoms, which act as electron donors to the vanadium lattice; and iodine atoms, which act as electron acceptors, creating positive charge carriers in the lattice called “holes”. In contrast to the TM devices mentioned earlier (in which a 3d TM atom is added into a nonmagnetic host), here both guest atoms are nonmagnetic but the host is magnetized by the elimination or addition of one extra charge (positive or negative). The bipolar nature of the NTs—the possibility of making them conductors of either electrons or holes through appropriate doping—is important for the fabrication of transistor structures and junctions (p-n junctions).

Experimentally, a carbon NT (CNT) based hybrid nanostructure can be achieved either by filling the NT with foreign materials in its cavity or by coating the materials on the tube surface. CNTs filled with TM have been extensively studied experimentally [14–20]. In some experiments 1D crystal structure actually forms in the cavity of the tube. Coating on the surface of CNTs can also be achieved with a variety of materials. For example, titanium can form stable and continuous structures on the NT surface. Recently, monocrystalline FeCo nanowires encapsulated inside multiwalled carbon NTs was synthesized, which could be used in the fabrication of high-density magnetic storage devices and magnetic composites [21].

10.3 Theoretical Studies

10.3.1 TM-Doped Nanowires

Using density functional theory (DFT), Wang et al. showed that the magnetic coupling of Mn atoms in the nanowires, unlike that in the thin film, is ferromagnetic [22]. This ferromagnetic coupling, brought about because of the confinement of electrons in the radial direction and the curvature of the Mn-doped GaN nanowires' surface, is mediated by N as is evidenced from the overlap between Mn 3d and N 2p states. In addition, the magnitude of the magnetic moments can be tuned by changing the wire thickness. They also carried out a theoretical study of the magnetic properties of Cr-doped GaN nanowires [23]. In contrast to the Mn-doped GaN nanowires, the GaN/Cr nanowire is found to be FM irrespective of the distribution of the Cr atoms. In addition, the binding energy of Cr to the GaN wire is larger than that of Mn, suggesting that it may be possible to dope the GaN nanowire with Cr more easily than with Mn. Thus, the GaN/Cr nanowire could prove to be a robust system for applications. The magnetic moments at the Cr atoms are about 2.5 μ_B and these are coupled antiferromagnetically to a small moment at the N site. The FM coupling results from a charge overlap between the N 2p and Cr 3d states and the coupling is driven by a double exchange mechanism. Schmidt et al. [24] investigated the electronic, structural, and magnetic properties of Mn-doped InP nanowires

along the [111] direction with the dangling bonds on the surface saturated by hydrogen atoms. They found that the most energetically favorable position for the Mn atom is near the surface. When the Mn atoms are in "bulklike" positions, the magnetic Mn–Mn coupling in the nanowire is ferromagnetic. In these cases, their results are consistent with a host-p-Mn-d coupling mechanism. On the other hand, if at least one of the Mn atoms is located near the surface, the coupling is antiferromagnetic.

10.3.2 TM-Doped Nanotubes

10.3.2.1 TM Doped C Nanotubes

Encapsulating ferromagnetic structures inside NTs has become an active research topic. In 2003, Yang et al. [25] found through ab initio calculations that such TM/NT hybrid structures exhibit substantial magnetism. In particular, cobalt atoms packed inside a variety of CNTs offer strong spin polarization at the Fermi level as well as considerable magnetic moments. They considered a (9,0) SWNT with six Co atoms filled inside per unit cell, forming an ABAB staggered triangle packing. The nearest neighboring distances between the Co atoms and C atoms range between 2.167 and 2.245 Å. The calculated magnetic moment for the freestanding Co nanowire with the same configuration is about 2.08 μ_B. And the calculated Co-filled NT has an average magnetic moment of 1.4 μ_B per Co atom. This moment is comparable to that of hcp bulk Co, which is 1.58 μ_B. Define the binding energy as

$$E_b = E(\text{tube}) + E(\text{nanowire}) - E(\text{tube} + \text{nanowire}), \tag{10.1}$$

E_b was found to be 0.16 eV per Co atom. They also performed nonmagnetic calculations for the same system and obtained a binding energy of 0.60 eV per Co atom. Combining this with the substantial charge delocalization of the conduction electrons, an average Co–C bond length of ~2.19 Å, and the observation that the magnetic moment of the hybrid is different from the freestanding wire have led us to the conclusion of a moderate covalent bonding between the Co and C atoms. The reduction of moment of the nanowire inside the tube clearly indicates a strong interaction between the magnetic metal and nonmagnetic carbon. The DOS shows characteristic narrowing of d bands in the nanostructure owing to the reduced coordination number. Band structure analysis shows that there are many more conduction bands crossing the Fermi level for the minority spin than those for the majority spin for the hybrid system. Thus a spin-polarized transport process can be achieved in such hybrid structures. Quantitatively, the calculated spin polarization P (85%) is substantially higher than that calculated for the bulk Co (66%), where the spin polarization P is calculated from the DOS $N(E_F)$ corresponding to the minority (majority) spin at the Fermi level:

$$P = (N_{\downarrow}(E_F) - N_{\uparrow}(E_F))/(N_{\downarrow}(E_F) + N_{\uparrow}(E_F)). \tag{10.2}$$

They observed that the conduction electrons from the majority spin occupy mostly the C sites, while those from the minority spin concentrate on the Co central wire. There is also considerable delocalization of conduction electron density, which indicates strong interaction between the Co and C atoms. Their studies of other similar systems reveal that the qualitative results of magnetism and spin polarization do not depend sensitively on the choice of the magnetic metal, the metal configuration, or the NT chirality. It is noteworthy that both semiconducting and metallic SWNTs are transformed into good spin-polarized conductors with metal filling or coating. Thus, there is no need to separate the semiconducting and metallic NTs in these hybrid structures.

Durgun and Ciraci [26] presented a systematic analysis for the stability, atomic, electronic, and magnetic properties of TM atomic chains adsorbed on the external and internal wall of the (8,0) SWNT. They found that all adsorbed chains have ferromagnetic ground state. The coupling among the adsorbed TM atoms and the charge transfer between adsorbed TM and nearest carbon atom of SWNT play an important role in determining the resulting magnetic moment. Usually, the magnetic moment of the free TM atom is reduced upon the adsorption. And high spin polarization at the Fermi level can be obtained by the adsorption of V and Fe chains on the (8,0) SWNT at specific geometries. Interesting variation of the magnetic moment and binding energy with the number of filled d electrons of the adsorbate have been revealed. The spin-dependent electronic structure and the net magnetic moment calculated for finite-size systems are found to be different from infinite and periodic systems. Their results suggest that these finite-size tubes holding TM atoms can be used as a nanomagnet and can perform as spin-valve or spin-dependent resonant-tunneling devices when they are connected to the metal electrodes from both ends.

Titanium monomers and wires adsorbed on (8,0) CNTs was considered by Fagan et al. [27,28]. The most stable configurations for monomers are found to be over the centre of a C–C bond for inside and over the midpoint of the centre of the hexagonal site for outside. They showed that the most stable configuration is with the wire inside the tube, and the resulting electronic structures show a metallic system with high hybridization between the Ti and C atoms and a large charge transfer from Ti to C atoms. For Ti wire adsorbed inside the tube the low spin configuration is shown to be more stable than high spin configuration and the opposite behavior is observed for the corresponding outside case.

10.3.2.2 TM Doped BN Nanotubes

As shown earlier, while TM nanowires filled CNTs can exhibit substantial magnetism, no HM behavior exists in such systems [25]. Since BN NTs are insulators independent of their chiralities and are more chemically inert than CNTs, they may serve as naturally insulating or protective shields for encapsulating conducting metallic clusters, nanowires, and nanorods [29, 30]. The magnetic nanostructures isolated by a nonmagnetic material, i.e., BN walls, could be efficiently used for high density data storage, without the drawback of particle agglomeration and

magnetic loss attributable to dipolar relaxation. This kind of protection also prevents the oxidation of the metallic clusters, nanowires, and nanorods, which are prone to be oxidized. Recently, BN NTs filled with 3d-TMs such as Fe-Ni Invar alloy, Co nanorods, Mo clusters, Ni and $NiSi_2$ nanowires have been successfully synthesized [31–34]. However, detailed electronic and magnetic properties of these novel nano-structures are far from well understood. And the question how the magnetic properties of TM/BN NTs differ from those of TM/CNTs is open. We performed a comprehensive first principles study on the electronic and magnetic properties for these TM/BN NT hybrid structures. We show that the electronic and magnetic properties of TM/BN NTs differ fundamentally from those of TM/CNTs and HM ferromagnetism could be achieved in TM/BN NTs under appropriate circumstances.

Our theoretical calculations are performed using the Vienna ab initio simulation package (VASP) [67, 68]. We describe the interaction between ions and electrons using the frozen-core projector augmented wave (PAW) approach [35, 69]. The overall framework is spin-polarized DFT [36, 37] in the generalized gradient approximation (PW91) [38, 39]. The basis set cut off is 400 eV. In a typical calculation, a 1D periodic boundary condition is applied along the NT axis with Monkhorst-Pack [40] k-point sampling. During structural relaxation, all atoms except the fixed ones are allowed to relax to reach the minimum energies until the Hellmann-Feynman forces acting on them become less than 0.01 eV/Å. Since most BN NTs are zig-zag type [41, 42], we choose BN zig-zag NTs with a smallest hcp TM nanowire filled inside. Though the most stable bulk phase for Ni is fcc, the stability for Ni nanowires depends not only on the structure, but also on the orientation and radius of the nanowires. For example, the smallest hcp Ni nanowire is found to be more stable by about 0.3 eV per Ni than the smallest fcc Ni nanowire in the [111] orientation. The hcp TM nanowire is composed of six TM atoms per unit cell with ABAB staggered triangle packing. BN(8,0), BN(9,0), and BN(10,0) NTs filled with the Ni hcp nanowire are studied. Different initial guesses are used for the local magnetic moments including ferromagnetic, antiferromagnetic (alternate up-down spins on A and B TM atoms), and nonmagnetic spin configurations, which are then fully relaxed to obtain the final converged structures and spin alignments. The free standing hcp Ni nanowire is also studied for comparison with the hybrid structures.

Figure 10.1 shows the optimized structures for the free standing Ni nanowire and the Ni encapsulated BN NTs. In the optimized structures Ni atoms almost lie in the nitrogen planes of BN NTs, as can be seen from the side view for Ni encapsulated BN(9,0) NT (Fig. 10.1e). This relative position along axis between the BN NT and metal nanowire results from the big electronegativity of the nitrogen atom. The comparative calculation for Ni/C(9,0) shows that Ni atoms in Ni/CNTs do not lie in any carbon planes but in the middle of two adjacent carbon planes since all atoms are the same in carbon NTs. The symmetry of the Ni nanowire changes little after coated by BN NTs. Generally, after being inserted, the Ni nanowire expands a little, e.g., the Ni–Ni distance in a plane (A or B) changes from 2.27 to 2.32 Å in Ni/BN(9,0), and the BN walls expand slightly, 0.01Å for BN(9,0) NT.

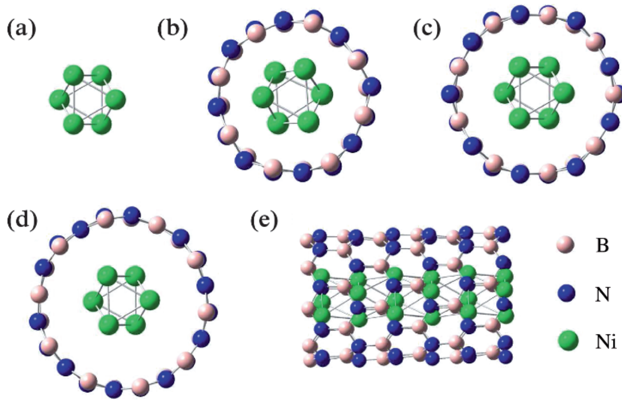

Fig. 10.1 Relaxed structures of the free standing Ni nanowire and Ni/BN NT hybrid structures. (**a**) Top view of the free standing Ni nanowire. (**b**) Top view of Ni/BN(8,0). (**c**) Top view of Ni/BN(9,0). (**d**) Top view of Ni/BN(10,0). (**e**) Side view of Ni/BN(9,0)

Table 10.1 The binding energy (E_b) and total magnetic moment (μ_{tot}) for the free standing Ni nanowire and several Ni encapsulated BN NTs hybrid structures

	E_b (eV)	μ_{tot} (μ_B/unit cell)
Ni nanowire		5.66
Ni/BN(8,0)	−0.88	4.00
Ni/BN(9,0)	0.04	3.49
Ni/BN(10,0)	−0.03	4.53

Refer to the text for the definitions for the binding energy (E_b)

As for the energetics of these hybrid structures, we give the binding energy of the hybrid structures in Table 10.1. And the calculated binding energy for Ni/BN(8,0) is −0.88 eV, which implies the formation of this hybrid structure is endothermic. The absolute value of the binding energy for Ni/BN(9,0) or Ni/BN(10,0) is very small. The slightly favorable energy for Ni/BN(9,0) than that for Ni/BN(10,0) may result from the symmetry matching between the Ni nanowire and NT in Ni/BN(9,0). The positive or small negative binding energy is reasonable since the insulating BN NTs are very stable and inert and there are significant difficulties in wetting a BN graphene-like surface. This also explains that the synthesized BN NTs filled with metals are limited and most of these hybrid structures are produced by a two-stage process [31–33]: first C NTs containing TM nanoparticles at the tube-tips are synthesized, secondly, simultaneous filling NTs with the TM through capillarity and chemical modification of C tubular shells to form BN NTs occur. But once the TM/BN NT hybrid structures are formed, they will be stable because of the large inertia of BN NTs.

Since Ni/BN(9,0) is the most favorable form among the Ni encapsulated BN NTs we studied, we choose it as a typical case for studying the detailed electronic and magnetic properties for Ni/BN NT structures. To serve as a reference, the electronic and magnetic properties for the free standing Ni nanowire are also examined.

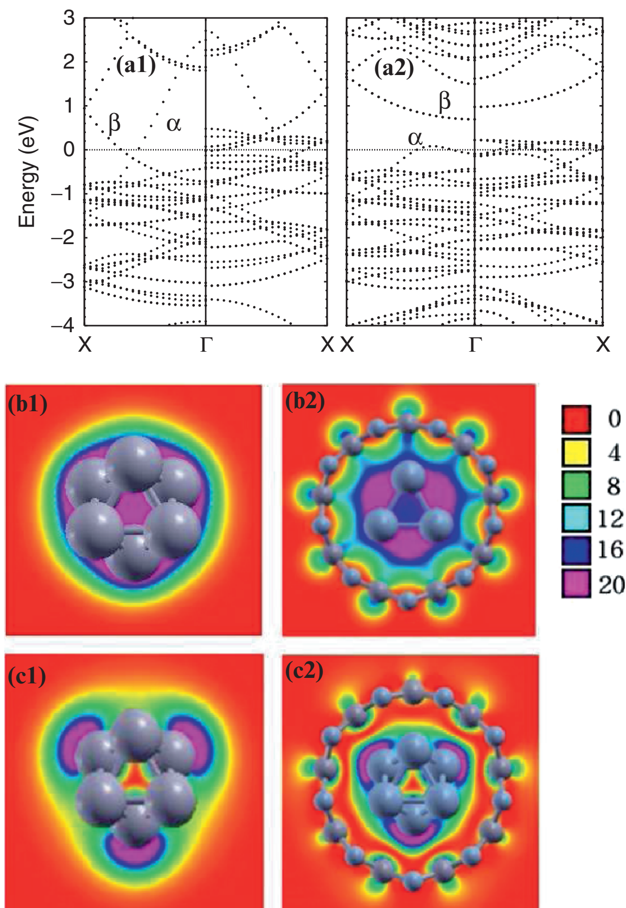

Fig. 10.2 Spin resolved band structures and partial charges of the α and β states for the free standing Ni nanowire and Ni/BN(9,0). (**a1**) and (**a2**) are the band structures for the free standing Ni nanowire and Ni/BN(9,0). The left panel is for the majority spin and the right panel is for the minority spin. (**b1**) and (**b2**) are the partial charges for the α state of the free standing Ni nanowire and Ni/BN(9,0), respectively. (**c1**) and (**c2**) are the partial charges for the β state of the free standing Ni nanowire and Ni/BN(9,0), respectively. The α and β states refer to those marked in panels (**a1**) and (**a2**)

The band structures of the free standing Ni nanowire and Ni/BN(9,0) are shown in Fig. 10.2a1 and a2 respectively. The free standing Ni nanowire is ferromagnetic metal, but not HM or semi-HM, as shown in Fig. 10.2(a1). Similar results for the Co nanowire were obtained by Yang et al. [25]. For the Ni nanowire and Ni/BN(9,0), the DOS around E_{f} is always dominated by the minority spin part. The analysis of the projected density of states (PDOS) for Ni/BN(9,0) shows that the states around the Fermi level are mainly contributed by Ni 3d orbitals. And almost all the spin density is located at the Ni nanowire. So the electronic or spin transport

will occur only in the core metal nanowires. In the spin resolved band structure of Ni/BN(9,0), there is a gap just above the Fermi level for the spin-up component indicating a semi-HM behavior, contrasting sharply with the band structure for the free standing Ni nanowire. It should be emphasized that the semi-HM behavior is found in the stablest ferromagnetic phase of TM/BN(9,0). Singh et al. also found the semi-HM behavior in a Mn-doped Si hexagonal NT, however in the metastable ferromagnetic phase [43]. The ferromagnetic ground state is helpful for application in spin-polarized transport.

So why does the band structure for Ni/BN(9,0) differ so much from that for the free standing Ni nanowire since BN NTs are generally inert? As the semi-HM energy gap arises in the spin majority part, we focus only on the spin majority part. There are two states crossing the Fermi level in the spin majority part in the Ni nanowire, namely a nondegenerate state α and a double degenerate state β, as can be seen from Fig. 10.2(a1). Partial charge analysis shows that the α state mainly distributes in the middle of planes A and B, while the β state almost locates at planes A and B. After the Ni nanowire is inserted into BN NTs, the α state near Γ is shifted to lower energy, on the contrary, the β state near Γ is shifted to higher energy. To see what causes the change of the α and β states upon coated by BN NTs, we plot the partial charges of the α and β states for the free standing Ni nanowire and Ni/BN(9,0) in Fig. 10.2(b) and (c). We can see that the α state becomes more delocalized but the β state becomes more localized after the Ni nanowire is inserted into BN NTs. The different charge distribution between α and β states and the observation that the energy of α state is lower than that of β state in Ni/BN(9,0) suggest that the α state is a bonding orbital and the β state is an antibonding orbital. The bonding and anti-bonding interactions are responsible for the different energy shifts for the α and β states, respectively.

Since low-dimensional HM materials are ideal for spintronic applications, can Ni encapsulated BN NTs become HM? Theoretically, by doping electrons more than 1.4 *e*/unit cell to lift the Fermi level upward about 0.1 eV using some techniques, such as applying gate voltage in a MOSFET like system, Ni/BN(9,0) could become HM. Even a metal to semiconductor transition could occur by doping 4.0 electrons/unit cell to lift the Fermi level upward more than 0.25 eV. On the other hand, seeking intrinsic HM in nanostructures is a more elegant solution to this question. Since the semi-HM in Ni/BN(9,0) results from the hybridization between the Ni nanowire and BN NT, the HM behavior is expected to occur in Ni encapsulated BN NTs with an increased hybridization effect. Two different means are considered to increase the hybridization. First we study the hcp Ni nanowire coated with a smaller BN NT, i.e., BN(8,0) NT. The spin resolved band structure for Ni/BN(8,0) shown in Fig. 10.3(a) obviously indicates a HM behavior. Though the formation of Ni/BN(8,0) is endothermic, Ni/BN(8,0) or other similar hybrid structures could be synthesized at high temperature with some subtle experimental methods, such as mechanic techniques or two-stage process. Second we investigate the Ni encapsulated BN(9,0) NT upon hydrostatic pressure. We simulate the pressure by fixing a homogeneous radial shrunken BN(9,0) NT and then fully relaxing the Ni nanowire. Radial shrinkages to two different levels, 5% and 10%, induced by homogeneous

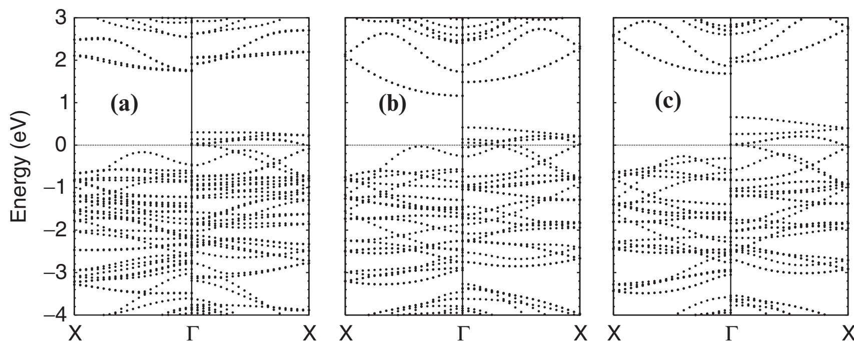

Fig. 10.3 Spin resolved band structures for Ni/BN(8,0) and two radial homogeneously shrunken Ni encapsulated BN(9,0) NT hybrid structures. (**a**) Ni/BN(8,0). (**b**) 5% radial shrinkage. (**c**) 10% radial shrinkage. The left panel is for the majority spin and the right panel is for the minority spin

external pressures 2.6 and 6.7 Gpa respectively, are examined. Here we assume that these external pressures would not cause Ni/BN(9,0) to transform to the oval shape. This is reasonable since the estimated transition pressure is 5.7 Gpa for BN(9,0) if we use the $1/R^3$ relationship between the transition pressure and the radius of the NT, and the fact that BN NTs have similar mechanical properties as carbon NTs, and the transition pressure for C(6,6) (about 4.0 Gpa) [44], moreover, the transition pressure for Ni/BN(9,0) should be larger than this value because of the presence of the core Ni nanowire. The band structures of the Ni encapsulated shrunken BN(9,0) NTs are shown in Fig. 10.3b and c. We can clearly see that an energy gap is induced in the spin majority band of the hybrid structure after a small radial shrinking. Moreover, we find that the HM energy gap increases along with the increase of the shrinkage, as seen from Fig. 10.3 that the HM band gap for 10% shrunken Ni/BN(9,0) is larger than that for 5% shrunken Ni/BN(9,0). The radial shrinkage smaller than 5% would not induce such a semi-HM to HM transition. In the two cases both with a decrease in the radius of the NT and therefore increased hybridization, the bonding and antibonding interactions become stronger. Once the interactions are strong enough, the HM can arise in these hybrid systems. Additionally, we find that the oval deformation could not induce the transition from semi-HM to HM. For the oval deformation, the hybridization between the Ni nanowire and BN NTs is not thorough since the oval deformation only increases the interaction between some Ni atoms and NT, but the interaction between other Ni atoms and NT is weakened.

The results about the total magnetic moment for the free standing Ni nanowire and hybrid Ni/BN NTs are listed in Table 10.2. As we can see, the total magnetic moment are decreased after forming a hybrid Ni/BN NT. This is typically due to the hybridization of the metal 3d states with the 2s and 2p states of boron and nitrogen. Interestingly, the reduction amount does not have a simple relationship with the radius of the BN NTs. When the radius is large enough, the reduction amount decreases with the increase of the NT radius, which can be explained by the weak hybridization effect.

Table 10.2 Calculated lattice constant (c), binding energy (E_b), total magnetic moment per unit cell (M), electronic ground state (GS), and the energy difference between the FM and AFM states for the $[TM(Bz)]_\infty$ sandwich polymers

TM	c (Å)	E_b (eV/TM)	M (μ_B)	GS	ΔE (eV/TM)
Sc	3.78	4.844	0.00	PM metal	/
Ti	3.58	5.317	0.00	AFM metal	0.006
V	3.37	5.334	0.80	FM metal	−0.084
Cr	3.30	2.181	0.00	NM insulator	/
Mn	3.37	1.714	1.00	FM metal	−0.250

TM = Sc, Ti, V, Cr, and Mn; $\Delta E = E(\text{FM}) - E(\text{AFM})$

Though, only Ni encapsulated BN NTs are analyzed in detail in our discussion, the main results for Ni encapsulated BN NTs apply equally to other TM, such as Fe, and Co encapsulated BN NTs. All these three TM/BN(8,0) are HM. The hydrostatic pressure can induce the transition from non-HM to HM for TM/BN NT hybrid systems. By performing a calculation on the Ni nanowire coated by a double-walled BN NT, called BN(8,0)@BN(16,0), we find a HM behavior in such a system, indicating that the speical magnetic properties for TM encapsulated multiwalled BN NTs are mainly dependent on the innermost BN wall. Detailed discussions will appear elsewhere [45]. It is noteworthy that the special magnetic properties are unique for TM/BN NT hybrid structures and are not found in previous studies on TM/C NT hybrid structures [25]. Recently, ferromagnetism in the systems consisting of B, N, and C atoms is also reported [46, 47]. Though the metal-free ferromagnetism is attractive, the energy difference between the ferromagnetic state and the nonmagnetic state is small [47], thus the proposed systems might have low Curie temperature. In contrast, the ferromagnetism in TM/BN NT hybrid structures is due to the strong ferromagnetic metals, and these hybrid structures is expected to have high Curie temperature.

Yang et al. [48] also studied nanocables made of a TM wire and boron nitride sheath. Their calculations indicated that TM wires can be inserted inside a variety of zigzag BN NTs exothermically. In particular a cobalt wire and the BN tube interact just like two giant molecules. The weak interaction between the BN tube and the wire ensures a low binding energy and a high magnetic moment that comes solely from the TM.

Using the DFT, the adsorption of TM atoms on the (8,0) zigzag single-walled BN NT has been systematically studied by Wu and Zeng [49]. Ten 3d TM (from Sc to Zn) and two group-VIIIA elements, Pd and Pt, were considered. They found that most TMs can be chemically adsorbed on the sidewall of BN NT and the adsorption process is typically exothermic. In most cases, the binding energies are less sensitive to the adsorption sites. The TM adsorbed BN NTs are all semiconductors with reduced band gaps except the Fe-adsorbed BN NT (on the bridge site over an axial BN bond), which may result in a half-metal. The adsorption of the TM atoms can give rise to a variety of net magnetic moments, ranging from 5.0 μ_B to 0.

10.3.2.3 Other Nanotubes Doped with TM Atoms

Infinite Si NTs were shown to be stable. TMs have been shown to be particularly important for the stability of metal-encapsulated silicon cage clusters because of their large embedding energies in the silicon cage. Using first-principles DFT calculations, Singh et al. [50] show that hexagonal metallic silicon NTs can be stabilized by doping with 3d TM atoms. Finite NTs doped with Fe and Mn have high local magnetic moments, whereas Co-doped NTs have low values and Ni-doped NTs are mostly nonmagnetic. The infinite $Si_{24}Fe_4$ NT is found to be ferromagnetic with nearly the same local magnetic moment on each Fe atom as in bulk iron. Mn-doped NTs are antiferromagnetic, but a ferrromagnetic state lies only 0.03 eV higher in energy with a gap in the majority spin bands near the Fermi energy. These materials are interesting for silicon-based spintronic devices and other nanoscale magnetic applications.

Singh et al. [51] also studied Mn-doped germanium NTs. They found that pentagonal and hexagonal NTs of Ge can be stabilized in the antiprism structure by doping with Mn atoms. In both cases the infinite NTs are metallic and ferromagnetic. Hexagonal NTs have the highest average magnetic moments of 3.06 μ_B per Mn atom found so far in metal-doped NTs of semiconductors, while the pentagonal NTs show a transition from a ferromagnetic to a ferrimagnetic state upon compression with an abrupt change in the magnetic moments, leading to the possibility of these NTs to act as a nano-piezomagnet.

Wang et al. [52] studied the structure and magnetic properties of Cr-doped GaN NTs. They found the following:

1. a single wall GaN NT constructed from the GaN wurtzite crystal relaxes to a carbon-like zigzag SWNT structure and remains stable at 300 K, while a multiwall GaN NT retains its original wurtzite form.
2. Cr atoms prefer to form clusters and the underlying magnetism depends on the degree of clustering.
3. The coupling between two Cr atoms mediated by the neighboring N is ferromagnetic, but changes to ferrimagnetic as the cluster grows.

First-principles calculations based on spin-polarized DFT were carried out to study the structural, energetic, and magnetic properties of hybrid structures formed by $B_xN_yC_z$ NT encapsulated with TM nanowire [53]. The magnetism of the hybrid structures was found smaller compared to the freestanding TM nanowires. The magnetic moment per TM atom decreases as the diameter of the tube decreases because of stronger interaction between the NT and TM nanowire. Among the four types of NTs considered, i.e., pure carbon, BN, BC_2N, and BC_3, the formation of TM/BC_3 is predicted to be spontaneous, with a negative formation energy. However, the magnetism of the TM/BC_3 structure is the weakest among the four types of structures. When the tube diameter is about 10 Å or larger, the magnetic moment of the hybrid structure saturates to the value of freestanding TM nanowire. Similar to hybrid structures formed with carbon and BN NTs, the TM/BC_2N and TM/BC_3 hybrid structures also show high spin-polarization.

10.3.3 TM-Benzene Sandwich Polymers

Now we turn to the discussion of another interesting HM FM system. A challenge now facing spintronics is transmitting spin signals over long enough distances to allow for spin manipulation. An ideal device for spin-polarized transport should have several key ingredients. First, it should work well at room temperature and should offer as high a magnetoresistance (MR) ratio as possible. In this sense, a half-metallic (HM) ferromagnet with the Curie temperature higher than room temperature is highly desirable since there would be only one electronic spin channel at the Fermi energy [3]. Second, the size or diameter of the materials should be uniform for large scale applications. CNTs were considered as promising one-dimensional (1D) spin mediators because of their ballistic nature of conduction and relatively long spin scattering length (at least 130 nm) [54, 55]. Coherent spin transport has been observed in multiwalled CNT systems with Co electrodes. The maximum MR ratio of 9% was observed in multiwalled CNTs at 4.2 K. However, as the temperature increases to 20 K, the MR ratio goes to zero, preventing any room temperature applications [54]. A theoretical work suggested that the ferromagnetic (FM) TM/CNT hybrid structures may be used as devices for spin-polarized transport to further increase the MR ratio [25]. Unfortunately, although large spin polarization is found in these systems, there is no HM behavior. Another difficulty with CNT is that the devices are unlikely to be very reproducible because of the wide assortment of tube size and helicity that is produced during synthesis. Wide variation in device behavior was reported in the CNT experiment [54].

Recently, an experimental study suggested that the unpaired electrons on the metal atoms couple ferromagnetically in the multidecker organometallic sandwich V-benzene (Bz) complexes, i.e., $V_n(Bz)_{n+1}$ clusters [56]. The FM sandwich clusters are supposed to serve as nanomagnetic building blocks in applications such as recording media or spintronic devices. A subsequent DFT study confirmed the FM coupling in multidecker sandwich $V_n(Bz)_{n+1}$ clusters [57]. Motivated by the earlier-mentioned experimental and theoretical studies, we propose that the 1D organometallic sandwich polymers $[V(Bz)]_\infty$ are the possible candidates for spintronic devices for spin-polarized transport since the polymers with an inherently uniform size are supposed to be also FM.

Metal-ligand molecules have been the subject of many studies in the past decade [58–65]. Especially, TM-Bz complexes ($M_n(Bz)_m$) are the prototypical organometallic complexes for studying the $d-\pi$ bonding interactions. Depending on the metal, there are two types of structures for $M_n(Bz)_m$: Multiple-decker sandwich structures and metal clusters fully covered with Bz molecules (rice-ball structures). The former sandwich structure is characteristic of the complexes for early TMs (Sc-V), whereas the latter is formed for late TMs (Fe-Ni). $Cr(Bz)_2$ and $Mn(Bz)_2$ with a sandwich structure are also observed experimentally [61]. Although the multidecker sandwich $M_n(Bz)_m$ clusters have been extensively studied theoretically [62–65], studies of the 1D $[TM(Bz)]_\infty$ polymers are still very lacking. To our knowledge, only one semiempirical Hückle calculation was performed to examine the thermodynamical stability of the 1D $[TM(Bz)]_\infty$ polymers [58]. The

electronic and magnetic properties of the 1D $[TM(Bz)]_\infty$ polymers remain to be explored using ab initio quantum mechanics methods. Moreover, the differences in bonding, energetics, and magnetic properties between $[TM(Bz)]_\infty$ polymers with different TM atoms are to be clarified since the properties of TM-Bz sandwich clusters depend on the number of the 3d electrons of the TM atoms.

We performed a comprehensive first principles study on the electronic and magnetic properties for the proposed 1D sandwich polymers. Only the $[TM(Bz)]_\infty$ polymers with TM = Sc, Ti, V, Cr, and Mn are considered since Fe, Co, and Ni usually react with Bz to form the rice-ball structures [59, 61]. Our theoretical calculations are performed within spin-polarized DFT with the generalized gradient approximation (GGA) PW91 functional [66]. The Vienna ab initio simulation package (VASP) [67, 68], a plane-wave based program, is used. We describe the interaction between ions and electrons using the frozen-core projector augmented wave approach [69]. The plane-wave basis set cut off is 400 eV. In a typical calculation, a 1D periodic boundary condition is applied along the polymer axis (the z direction) with Monkhorst-Pack [40] k-point sampling.

There are two typical structural configurations for the sandwich polymers. One is a normal sandwich structure with D6h symmetry, in which the TM atom and Bz rings are arranged alternatively, as shown in Fig. 10.4 for the the D6h $[V(Bz)]_\infty$ polymer. The other is a staggered sandwich structure (D6d symmetry) in which one of the Bz rings is rotated by 30% with respect to the other ring. Our preliminary calculations for both D6h and D6d $[V(Bz)]_\infty$ polymer indicate that the electronic and magnetic properties of the D6d conformer differ little from those of the corresponding D6h one. The qualitative similarity between the D6d and D6h configurations is also found in previous study on the sandwich clusters [63]. So hereafter we mainly focus on the polymers with D6h symmetry.

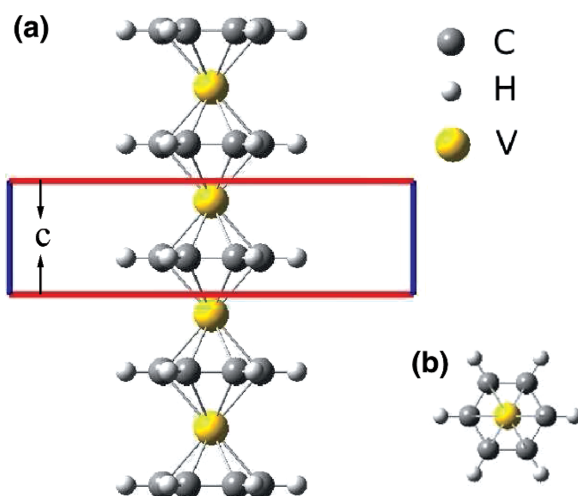

Fig. 10.4 Structure of the D6H $[V(Bz)]_\infty$ sandwich polymer (**a**) side view and (**b**) top view. The enclosed region in panel (**a**) indicates the unit cell of the polymer and c denotes the lattice constant

Our results for different $[TM(Bz)]_\infty$ polymers are summarized in Table 10.2. We can see that the sandwich $[TM(Bz)]_\infty$ polymers display rich electronic and magnetic properties. All $[TM(Bz)]_\infty$ polymers studied here are metallic except that $[Cr(Bz)]_\infty$ is a nonmagnetic (NM) insulator with a 0.71 eV direct energy gap at Γ. $[Sc(Bz)]_\infty$ is paramagnetic (PM). For $[Ti(Bz)]_\infty$, the AFM state is slightly favorable by 6 meV/Ti over the FM state. The ground state for $[V(Bz)]_\infty$ and $[Mn(Bz)]_\infty$ is the robust FM state. The diversity of the magnetic properties for the sandwich clusters with different TM atoms has been found by previous theoretical studies. The NM insulating property for $[Cr(Bz)]_\infty$ accords with the singlet state for $Cr(Bz)_2$ because of the 18-electron rule [62]. For $[V(Bz)]_\infty$ and $[Mn(Bz)]_\infty$, the FM ground state also agrees qualitatively with the doublet ground state for $V(Bz)_2$ and $Mn(Bz)_2$ [62, 64]. However, two distinct cases are Sc and Ti. Previous study showed that $Sc(Bz)_2$ is a doublet state in contrast with the PM state for $[Sc(Bz)]_\infty$ found here. On the other hand, $Ti(Bz)_2$ is a singlet state contrasting sharply to the AFM ground state for $[Ti(Bz)]_\infty$. The binding energy of the $[TM(Bz)]_\infty$ polymers as given in Table 10.2 is defined as: $E_b = E(\mathrm{Bz}) + E(\mathrm{TM}) - E([\mathrm{TM(Bz)}]_\infty)$, where $E(\mathrm{TM})$ is the energy of the isolated TM atom. We can see that $[V(Bz)]_\infty$ has large thermodynamic stability with the largest binding energy (5.334 eV/V atom). The trend of the lattice constant for the $[TM(Bz)]_\infty$ polymers is similar with that of the distance of the TM atoms from the center of the Bz ring in $TM(Bz)_2$ [62]. $[Cr(Bz)]_\infty$ has the the smallest lattice constant (3.30 Å) but not very large binding energy, which might result from the stable $3d^5 4s^1$ valence configuration for the Cr atom.

Since $[V(Bz)]_\infty$ and $[Mn(Bz)]_\infty$ have robust ferromagnetism, which is crucial for practical spintronic applications, the detailed electronic and magnetic properties are examined carefully. The band structures for $[V(Bz)]_\infty$ and $[Mn(Bz)]_\infty$ are shown in Fig. 10.5. For $[V(Bz)]_\infty$, there is a gap just above the Fermi level for the spin-up component indicating a quasi-HM behavior. The V, Mn 4s orbitals lie in the conduction band with very high energy and the bands around the Fermi level are mainly contributed by the TM 3d orbitals. The bands which are mainly composed by the TM 3d orbitals are labeled by their 3d components in Fig. 10.5. In the crystal field of the Bz ligands, the TM 3d bands split into three parts: A two-fold degenerated band D1 contributed mainly by TM $3d_{xy}$ and $3d_{x^2-y^2}$ orbitals, a nonbonding band D2 with TM $3d_{z^2}$ character, and a two-fold degenerated antibonding band D3 because of TM $3d_{xz}$ and $3d_{yz}$. The dispersive D1 band crosses the localized D2 band. And the D3 band with high energy is separated from the other two bands. For $[V(Bz)]_\infty$, in the majority part, the D2 band is fully occupied and there is a small hole in the D1 band, and both D1 and D2 bands are partly filled in the minority part. Such 3d orbitals occupation results in 0.80 μ_B total magnetic moment for $[V(Bz)]_\infty$. Since Mn atom has two valence electrons more than V atom, both D1 and D2 bands are fully occupied in both spin components in $[Mn(Bz)]_\infty$. The remained one valence electron half fills the D3 band in the spin majority part. Such a picture of the orbital occupation leads to the peculiar HM FM behavior in $[Mn(Bz)]_\infty$ with a total magnetic moment 1.00 μ_B.

The earlier-mentioned analysis based on the crystal field theory qualitatively describes the electronic and magnetic properties of the two polymers. However, the large dispersion of the D1 band and the FM mechanism in these systems remain

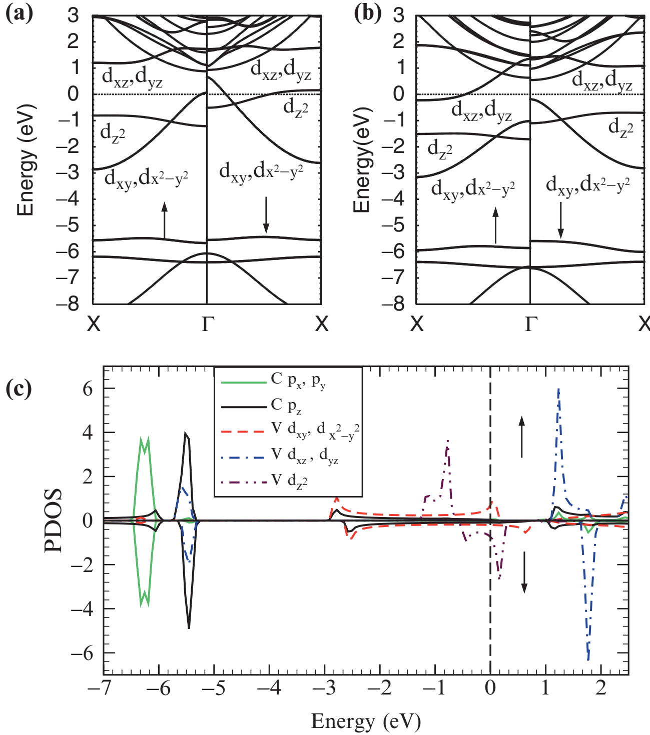

Fig. 10.5 Electronic band structures for (**a**) $[V(Bz)]_\infty$ and (**b**) $[Mn(Bz)]_\infty$. Panel (**c**) shows the C and V PDOS for $[V(Bz)]_\infty$

to be clarified. To penetrate into this problem, we plot the PDOS for $[V(Bz)]_\infty$ in Fig. 10.5c. We can see there is a considerable contribution to the V D1 band near X from C $2p_z$ orbitals; however at Γ the V $3d_{xy}$ and $3d_{x^2-y^2}$ orbitals could only hybrid with C $2p_x$ and $2p_y$ orbitals because of the symmetry matching rule. The C $2p_z$ orbitals of Bz hybrid with V $3d_{xy}$ and $3d_{x^2-y^2}$ orbitals to result in bonding states near X, and antibonding like states near Γ arise because of the weak hybridization between Bz $2p_x$ and $2p_y$ states and these V 3d orbitals. Such hybridization leads to the large dispersion of the D1 band with the highest energy at Γ in the whole Brillouin zone. Clearly, the contribution from Bz orbitals to the states near the Fermi level is very small, and the holes are mainly of TM 3d character, so ferromagnetism in such systems is identified to be due to the double exchange (DE) mechanism [70, 71].

The spin densities for both $[V(Bz)]_\infty$ and $[Mn(Bz)]_\infty$ are shown in Fig. 10.6(a) and (b) respectively. The spin density for $[V(Bz)]_\infty$ clearly indicate the $3d_{z^2}$ character, which is accord with the band structure. Differently, the spin density for $[Mn(Bz)]_\infty$ is mainly due to Mn $3d_{xz}$ and $3d_{yz}$ orbitals, as discussed earlier. An interesting phenomenon should be noted: The spin polarization not only locates around the TM atoms, but also has a small negative contribution from the Bz $2p_z$ orbitals. The spin injection to Bz is due to the hybridization effect. More occupied

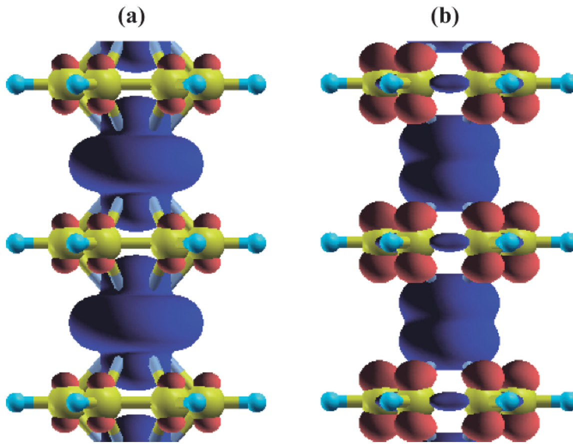

Fig. 10.6 Spin density for (**a**) $[V(Bz)]_\infty$ and (**b**) $[Mn(Bz)]_\infty$. The isovalue for the red and blue isosurfaces is -0.014 and 0.014 e/Å^3, respectively.

hybridized bands will lead to larger spin polarization of Bz. Since the D3 band of the spin up component is also half filled, the spin polarization of Bz in $[Mn(Bz)]_\infty$ is (0.090 μ_B) larger than that (0.067 μ_B) in $[V(Bz)]_\infty$. The spin injection to Bz has also been found by Muhida et al. in the study of $TM(Bz)_2$ (TM = Mn, Fe, and Co) [64]. However, the six C atoms in a Bz ring contribute equally to the spin polarization in both $[V(Bz)]_\infty$ and $[Mn(Bz)]_\infty$, contrasting sharply to their results that two of the C atoms contribute much larger than the others [64].

In the previous paragraphs, we have shown that the ground state of both $[V(Bz)]_\infty$ and $[Mn(Bz)]_\infty$ polymers is FM. We now turn to study the magnetic properties of $[V(Bz)]_\infty$ and $[Mn(Bz)]_\infty$ polymers at finite temperature. Unfortunately, there is no long-range FM or AFM order in any infinite strictly 1D isotropic systems with finite range exchange interaction at any nonzero temperatures [72]. However, there are several mechanisms for the occurrence of FM or AFM order in 1D or quasi-1D systems at finite temperature: Barriers due to the magnetic anisotropy, finite size, and interchain couplings. Large magnetic anisotropy energy can block the thermal fluctuation and stabilize long-range FM order, e.g., 1D monatomic chains of Co constructed on a Pt substrate exhibit long-range FM order below the blocking temperature 15 K [73]. However, our calculated results show that the magnetic anisotropy energy in both $[V(Bz)]_\infty$ and $[Mn(Bz)]_\infty$ polymers is smaller than 0.1 meV/TM, indicating that the ferromagnetism in these polymers might be stabilized only at extremely low temperature by the magnetic anisotropy induced barrier. There are also some reports, indicating the existence of FM in 1D chains with finite length, where the length of the chains is related to the range of the exchange interaction [73]. The most relevant work related to the current study is the discovery of FM in 1D $V_n(Bz)_{n+1}$ sandwich clusters by Miyajima et al. [56] as mentioned earlier. Since here we mainly focus on infinite 1D polymers, thus we will not discuss more on this point. The interchain coupling is found to be an important mechanism to stabilize long-range FM or AFM order in quasi-1D systems. Some quasi-1D systems have

been discovered to display FM [74, 75] or AFM [76] order at finite temperature. Here we study the hexagonal bundles composed by $[V(Bz)]_\infty$ or $[Mn(Bz)]_\infty$ polymers. The optimized distance between the centers of neighbor polymers is about 6.95 Å for both V-Bz and Mn-Bz bundles. Our results indicate that these bundles are energetically more favorable (by about 31 and 17 meV for Mn-Bz and V-Bz bundles respectively) than their corresponding 1D isolated chains. It is well known that there is spin frustration for a AFM spin configuration in a hexagonal lattice. Here we refer to the spin configuration where some neighbor chains couple antiferromagnetically and some neighbor chains couple ferromagnetically as the AFM one. The AFM coupling between V-Bz chains is slightly more favorable by about 3 meV/TM than the FM coupling. In contrast, the interchain coupling in Mn-Bz bundles is found to be FM (with energy about 5 meV/TM lower than the AFM coupling). The different coupling manner between these two cases might originate from the different characters of their spin densities. From the energy difference between the AFM and FM coupling in these bundles, the interchain coupling J is estimated to be about 0.75 or 1.25 meV/TM for V-Bz and Mn-Bz bundles respectively. The interchain coupling should be large enough to stabilize the intrachain FM at finite temperature since it is significantly larger than that in other typical qausi-1D magnetic systems, for example, the interchain coupling J was estimated to be about 0.1 K (0.009 meV) in p-nitrophenyl nitronyl nitroxide (p-NPNN) with a Curie temperature 0.65 K [75].

The intrachain exchange coupling is an important parameter in describing the magnetic properties in quasi-1D magnetic systems. Here we derive the exchange parameters in $[V(Bz)]_\infty$ and $[Mn(Bz)]_\infty$ isolated polymers using total energy calculations for different spin configurations. The intrachain coupling in their bundles is expected to have similar magnitude as that in isolated polymers. Since the distance between a TM atom and its next nearest neighbor TM is larger than 6.0 Å, the magnetic coupling between them should be negligible. Considering only the nearest magnetic coupling, the effective Heisenberg Hamiltonian for the 1D $[TM(Bz)]_\infty$ polymer can be written as $H_{\text{eff}} = -\sum_i J\mathbf{e}_i \cdot \mathbf{e}_{i+1}$, where J is the effective exchange parameter between the nearest neighbor TM atoms, and $\mathbf{e}_i$ is the unit vector pointing in the direction of the magnetic moments at site i. Here we term J as an effective exchange parameter, but not a pure exchange parameter since J also includes the magnitude of the magnetic moment of the TM atoms. One might expect that J could be deduced from the energy difference between the AFM state and FM state. However, we find that the local magnetic moments for V and Mn atoms in the AFM state differ significantly from those in the FM state, so the above method to get J might be questionable. We circumvent this problem by considering another magnetic configuration: The magnetic configuration is $\uparrow\uparrow\downarrow\downarrow$ with the periodicity four times of that for the FM case. In this case, the local magnetic moments for V and Mn atoms are almost the same as those in the FM state. The energy difference between this configuration and the FM state is J per TM atom. The estimated effective exchange parameter for $[V(Bz)]_\infty$ and $[Mn(Bz)]_\infty$ is 24 and 62 meV respectively, which is larger than the intrachain exchange coupling (about 0.4 meV) in p-NPNN [75]. The relatively large effective exchange parameter for $[V(Bz)]_\infty$ and $[Mn(Bz)]_\infty$ is due to the DE mechanism, which usually lead to FM with a relatively high Curie

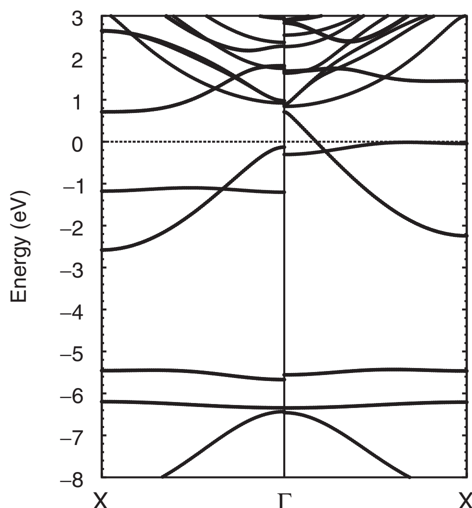

Fig. 10.7 Electronic band structure for $[V(Bz)]_\infty$ with the lattice constant $c = 3.55$ Å. It clearly shows the HM behavior in this system

temperature, e.g., the relative high Curie temperature (about 228–370 K) [77] for Mn-doped GaN is due to the DE mechanism [71, 78].

Pressure is well known to have drastic effect on the electronic and magnetic properties of the magnetic materials [79]. Here, the effect of pressing and stretching on the electronic and magnetic properties of $[V(Bz)]_\infty$ and $[Mn(Bz)]_\infty$ is examined by changing the lattice constant. It is found that the electronic and magnetic properties of $[V(Bz)]_\infty$ and $[Mn(Bz)]_\infty$ change little when they are compressed to a reasonable degree. However, stretching can dramatically change their electronic and magnetic properties. $[V(Bz)]_\infty$ turns into HM FM when the lattice constant is in the range 3.47 to 3.78 Å. To show the HM FM behavior, we plot the band structure of $[V(Bz)]_\infty$ with a lattice constant 3.55 Å in Fig. 10.7. Clearly, the energy gap opens in the spin majority part in the stretched $[V(Bz)]_\infty$ polymer, in contrast to a gap opening in the spin minority part in $[Mn(Bz)]_\infty$. Along with the increase of the lattice constant, the hybridization between TM and Bz is weaken. The band width of the D1 band, especially in the spin majority part, becomes narrower. In the spin majority part the downshift of the D1 band near Γ makes the D1 band fully occupied and the system HM ferromagnetism. We note that turning $[V(Bz)]_\infty$ polymer into HM FM through stretching experimentally the polymer is possible. The stress in a hexagonal bundle composed by $[V(Bz)]_\infty$ polymers with lattice constants $a = 6.95$ Å and $c = 3.55$ Å is about 4.8 GPa, which could be easily realized experimentally. Increasing the lattice constant of $[Mn(Bz)]_\infty$ to a critical value 3.48 Å, the HM behavior disappears. Further increasing the lattice constant of $[Mn(Bz)]_\infty$ up to a second critical value 3.70 Å, a FM metal to AFM insulator transition takes place. The drastic changes of the electronic and magnetic properties of $[Mn(Bz)]_\infty$ is also caused by the reduced hybridization. Although the band narrowing of the D1 band also takes place, the downshift of the D3 band near X in the spin majority part plays a crucial role in

determining the electronic and magnetic properties of $[Mn(Bz)]_\infty$. The disappearance of the HM behavior results from the partly occupying of the D1 band in the spin minority part as a consequence of the downshift of the D3 band in the spin majority part. The FM metal to AFM insulator transition can be reasonably explained. The band narrowing of the D1 band results in smaller DE effect, thus the superexchange AFM interaction can compete with and even overwhelm the DE interaction since the former depends on hopping linearly, and the latter quadratically.

Previous studies indicated that the local density approximation (LDA) and other semilocal GGA functionals fail to describe some conducting polymers. A typical example is the dimerization of trans-polyacetylene: LDA predicts almost no carbon–carbon bond length alternation (BLA), whereas Hartree–Fock (HF) produces a too large BLA [80]. It was shown that hybrid density functional mixed with exact exchange, namely B3LYP [81], provided dimerization parameters close to experiment [80]. Thus it is interesting to know the electronic and magnetic properties of the polymers within the B3LYP formalism. For this, we perform some calculations on these 1D polymers using CRYSTAL03 code [82]. The results show that both $[V(Bz)]_\infty$ and $[Mn(Bz)]_\infty$ are HM FM in their most stable configurations. Although there are some minor differences between the PW91 and B3LYP results, our main conclusions remain valid when using the B3LYP functional. The applicablity of the semilocal GGA functional to the 1D $[TM(Bz)]_\infty$ polymers is not surprising since the current studied systems are not π-conjugated. In fact, LDA has been successfully applied to study the conformation and electronic structure of polyethylene [83].

Maslyuk et al. [84] also studied organometallic V-Bz wire using DFT. They reached essentially the same conclusions. Furthermore, ab initio electron transport calculations reveal that finite size vanadium-benzene clusters coupled to ferromagnetic Ni or Co electrodes will work as nearly perfect spin filters.

Both studies suggest that the 1D $[TM(Bz)]_\infty$ polymers, especially $[V(Bz)]_\infty$ and $[Mn(Bz)]_\infty$ with such peculiar electronic and magnetic properties would be ideal materials for the promising spin-polarized transport.

10.3.4 Transitional-Metal Free Systems

Recent observation of the occurrence of ferromagnetism in materials purely of carbon origin [85] has created enormous interest in these materials as light nonmetallic magnets would be be very promising for many practical applications if Curie point is well above room temperature.

Hydrogenated nanographite can display spontaneous magnetism. Kusakabe and Maruyama [86] proposed that hydrogenation of nanographite is able to induce finite magnetization. Application of the local spin density approximation (LSDA) to the calculation of the electronic band structure of the ribbon, in which each carbon is bonded to two hydrogen atoms at one edge and to a single hydrogen atom at another edge, shows the appearance of a spin-polarized flat band at the Fermi energy. Producing different numbers of monohydrogenated carbons and dihydrogenated carbons can create magnetic moments in nanographite.

Recently, Son et al. [87] predicted half-metallicity in nanometre-scale graphene ribbons by using first-principles calculations. They showed that this phenomenon is realizable if in-plane homogeneous electric fields are applied across the zigzag-shaped edges of the graphene nanoribbons, and that their magnetic properties can be controlled by the external electric fields.

Choi et al. [88] used LSDA calculations to study the occurrence of magnetism in quasi-one dimensional heterostructured C/BN NTs free of metallic impurities. At the zigzag boundary connecting carbon and boron nitride segments of tubes, they found atomiclike states that acquire magnetization when partly filled. Whereas individual C/BN heterojunctions can be used to spin polarize electrons during transport, periodic arrangements of heterojunctions in doped systems can lead to the formation of a one-dimensional itinerant ferromagnetic state.

The geometrical, magnetic, and electronic structures of a series of open BN NTs with different chiralities were examined theoretically [89]. Tremendous spin-splitting (>1 eV) in such a pure sp-electron system were first observed with the appearance of "conjugate", spin-polarized, deep-gap states. They found that the chirality determines the atomic configuration of the mouth, the magnetic character (local magnetic moment), and spin-polarized electronic structure (energy gap and spin-splitting of HOMO states) of the open BN NT. The unpaired electrons of unpaired atoms at the mouth are responsible for the local magnetic moment and the spinpolarized, deep-gap states. Local spin configuration at the tube mouth was found to be stable under the external perturbations (such as strong electric field, doping at the tube body, and interaction with ferromagnetic samples). High spin-polarizations of open B-rich-ended BN NTs, combined with the high stability of their local spin configuration, indicate that they could be used as the promising candidates for nanoscale spin-polarized electron sources in future spintronic devices (such as spin-polarized electron field emitters and SP-STM tips). The spin-polarized electrons might also be emitted from open N-rich-ended BN NTs under near-infrared photon assistance. It is the interaction between the atoms at the mouth that determines the spin configuration of unpaired electrons and their different contributions to the intrinsic magnetism of the open BN NT.

Simeoni et al. studied the electronic and magnetic properties of defective aluminium nitride NTs [90]. Their results showed that, in several defective tubes, a spontaneous spin-polarization arises, due to the presence of spin-split flat bands close to the Fermi level, with a strong localization of the corresponding electronic states and of the magnetic moments. The highest positive spin-magnetization (3 μ_B per cell) is found for the vacancy in the Al site.

10.4 Outlooks

In this Review, the current status of low dimensional nanomaterials for spintronics are surveyed. In order for ferromagnetic nanostructures to have a great impact on technology, the T_C needs to be well above room temperature. Although a number of

systems have been reported to show T_C much higher than 300 K, the details of the material and the mechanism are not fully uncovered, and sometimes the results are not well reproducible. The combination of synthesis and electronic-structure calculations is a powerful tool to identify suitable materials. Half-metallic ferromagnets with high Curie temperatures are important ingredients for spintronics applications. Some proposed systems with half-metallic ferromagnetism were extensively discussed. However, the Curie temperatures of such systems might not be high enough for room temperature applications. Further experimental and theoretical studies should be pursued to obtain low dimensional nanomaterials for spintronics with better performance. Other issues include spin transport and spin dephasing in spintronic materials, the integration of low dimensional nanomaterials for spintronics with current silicon technology. With contributions from a diversity of countries and fields including biology, chemistry, physics, electrical engineering, computer science, and mathematical information theory, the rapidly emerging field of spintronics promises to provide fundamentally new advances in both pure and applied science as well as have a substantial impact on future technology.

Acknowledgments This work is partially supported by the National Natural Science Foundation of China (Nos. 50121202, 20533030, 10474087), by the National Basic Research Program of China (No. 2006CB922004), by the USTC-HP HPC project, and by the SCCAS and Shanghai Supercomputer Center.

References

1. I. Žutić, J. Fabian, S.D. Sarma: Rev. Mod. Phys. 76 (2004) 323
2. S.A. Wolf, D.D. Awschalom, R.A. Buhrman, J.M. Daughton, S. von Molnár, M.L. Roukes, A.Y. Chtchelkanova, D.M. Treger: Science 294 (2001) 1488
3. R.A. de Groot, F.M. Mueller, P.G. van Engen, K.H.J. Buschow: Phys. Rev. Lett. 50 (1983) 2024
4. F.L. Deepak, P.V. Vanitha, A. Govindaraj, C.N.R. Rao: Chem. Phys. Lett. 374 (2003) 314
5. D.S. Han, J. Park, K.W. Rhie, S. Kim, J. Chang: Appl. Phys. Lett. 86 (2005) 032506
6. H.-J. Choi, H.-K. Seong, J. Chang, K.-I. Lee, Y.-J. Park, J.-J. Kim, S.-K. Lee, R. He, T. Kuykendall, P. Yang: Adv. Mater. 17 (2005) 1351
7. M.-H. Ham, J.-M. Myoung: Appl. Phys. Lett. 89 (2006) 173117
8. J. Cui, Q. Zeng, U.J. Gibson: J. Appl. Phys. 99 (2006) 08M113
9. L.Q. Liu, B. Xiang, X.Z. Zhang, Y. Zhang, D.P. Yu: Appl. Phys. Lett. 88 (2006) 063104
10. H.-K. Seong, Y. Lee, J.-Y. Kim, Y.-K. Byeun, K.-S. Han, J.-G. Park, H.-J. Choi: Adv. Mater. 18 (2006) 3019
11. C. Huang, X. Liu, Y. Liu, Y. Wang: Chem. Phys. Lett. 432 (2006) 468
12. D. Wu, Y. Chen, J. Liu, X. Zhao, A. Li, N. Ming: Appl. Phys. Lett. 87 (2005) 112501
13. L. Krusin-Elbaum, D.M. Newns, H. Zeng, V. Derycke, J.Z. Sun, R. Sandstrom: Nature (London) 431 (2004) 672
14. S. Karmakar, S.M. Sharma, P.V. Teredesai, A.K. Sood: Phys. Rev. B 69 (2004) 165414
15. B.C. Satishkumar, A. Govindaraj, P.V. Vanitha, A.K. Raychaudhuri, C.N.R. Rao: Chem. Phys. Lett. 362 (2002) 301
16. C. Guerret-Piécourt, Y.L. Bouar, A. Loiseau, H. Pascard: Nature (London) 372 (1994) 761
17. P.M. Ajayan, C. Colliex, J.M. Lambert, P. Bernier, L. Barbedette, M. Tencé, O. Stephan: Phys. Rev. Lett. 72 (1994) 1722

18. M. Monthioux: Carbon 40 (2002) 1809
19. C. Guerret-Piecourt, Y. Le Bouar, A. Lolseau, H. Pascard: Nature 372 (2002) 761
20. S. Seraphin, D. Zhou, J. Jiao: J. Appl. Phys. 80 (1996) 2097
21. A.L. Elías, J.A. Rodríguez-Manzo, M.R. McCartney, D. Golberg, A. Zamudio, S.E. Baltazar, F. López-Urías, E. Muñoz-Sandoval, L. Gu, C.C. Tang, D.J. Smith, Y. Bando, H. Terrones, M. Terrones: Nano Lett. 5 (2005) 467
22. Q. Wang, Q. Sun, P. Jena: Phys. Rev. Lett. 95 (2005) 167202
23. Q. Wang, Q. Sun, P. Jena, Y. Kawazoe: Nano Lett. 5 (2005) 1587
24. T.M. Schmidt, P. Venezuela, J.T. Arantes, A. Fazzio: Phys. Rev. B 73 (2006) 235330
25. C.-K. Yang, J. Zhao, J.P. Lu: Phys. Rev. Lett. 90 (2003) 257203
26. E. Durgun, S. Ciraci: Phys. Rev. B 74 (2006) 125404
27. S.B. Fagan, A. Fazzio, R. Mota: Nanotechnology 17 (2006) 1154
28. S.B. Fagan, R. Mota, A.J.R.D. Silva, A. Fazzio: Phys. Rev. B 67 (2003) 205414; Microelectron. J. 34 (2003) 481
29. N.G. Chopra, R.J. Luyken, K. Cherrey, V.H. Crespi, M.L. Cohen, S.G. Louie, A. Zettl: Science 269 (1995) 966
30. X. Blase, A. Rubio, S.G. Louie, M.L. Cohen: Europhys. Lett. 28 (1994) 335
31. D. Golberg, F.F. Xu, Y. Bando: Appl. Phys. A 76 (2003) 479
32. Y. Bando, K. Ogawa, D. Golberg: Chem. Phys. Lett. 347 (2001) 349
33. F.F. Xu, Y. Bando, D. Golberg, M. Hasegawa, M. Mitome: Acta Mater. 52 (2004) 601
34. C. Tang, Y. Bando, D. Golberg, X. Ding, S. Qi: J. Phys. Chem. B 107 (2003) 6539
35. G. Kresse, D. Joubert: Phys. Rev. B 59 (1999) 1758
36. P. Hohenberg, W. Kohn: Phys. Rev. 136 (1964) B864
37. W. Kohn, L.J. Sham: Phys. Rev. 140 (1965) A1133
38. J.P. Perdew, Y. Wang: Phys. Rev. B 45 (1992) 13244
39. J.P. Perdew, J.A. Chevary, S.H. Vosko, K.A. Jackson, M.R. Pederson, D.J. Singh, C. Fiolhais: Phys. Rev. B 46 (1992) 6671
40. H.J. Monkhorst, J.D. Pack: Phys. Rev. B 13 (1976) 5188
41. D. Golberg, Y. Bando: Appl. Phys. Lett. 79 (2001) 415
42. M. Terauchi, M. Tanaka, K. Suzuki, A. Ogino, K. Kimura: Chem. Phys. Lett. 324 (2000) 359
43. A.K. Singh, T.M. Briere, V. Kumar, Y. Kawazoe: Phys. Rev. Lett. 91 (2003) 146802
44. X.H. Zhang, D.Y. Sun, Z.F. Liu, X.G. Gong: Phys. Rev. B 70 (2004) 035422
45. H.J. Xiang, J.L. Yang, J.G. Hou, Q.S. Zhu: unpublished
46. S. Okada, A. Oshiyama: Phys. Rev. Lett. 87 (2001) 146803
47. J. Choi, Y.H. Kim, K.J. Chang, D. Tomanek: Phys. Rev. B 67 (2003) 125421
48. C.K. Yang, J. Zhao, J.P. Lu: Phys. Rev. B 74 (2006) 235445
49. X.J. Wu, X.C. Zeng: J. Chem. Phys. 125 (2006) 044711
50. A.K. Singh, T.M. Briere, V. Kumar, Y. Kawazoe: Phys. Rev. Lett. 91 (2003) 146802
51. A.K. Singh, V. Kumar, Y. Kawazoe: Phys. Rev. B 69 (2004) 233406
52. Q. Wang, Q. Sun, P. Jena, Y. Kawazoe: Phys. Rev. B 73 (2006) 205320
53. G.W. Peng, A.C.H. Huan, Y.P. Feng: Appl. Phys. Lett. 88 (2006) 193117
54. K. Tsukagoshi, B.W. Alphenaar, H. Ago: Nature (London) 401 (1999) 572
55. H. Mehrez, J. Taylor, H. Guo, J. Wang, C. Roland: Phys. Rev. Lett. 84 (2000) 2682
56. K. Miyajima, A. Nakajima, S. Yabushita, M.B. Knickelbein, K. Kaya: J. Am. Chem. Soc. 126 (2004) 13202
57. J. Wang, H.P. Acioli, J. Jellinek: J. Am. Chem. Soc. 127 (2005) 2812
58. S. Yabushita, T. Yasuike: J. Phys. Chem. A 103 (1999) 4533
59. P. Jena, B.K. Rao: J. Chem. Phys. 116 (2002) 1343
60. T.D. Jaeger, D. van Heijnsbergen, S.J. Klippenstein, G. von Helden, G. Meijer, M.A. Duncan: J. Am. Chem. Soc. 126 (2004) 10981
61. T. Kurikawa, H. Takeda, M. Hirano, K. Judai, T. Arita, S. Nagao, A. Nakajima, K. Kaya: Organometallics 18 (1999) 1430
62. R. Pandey, B.K. Rao, P. Jena, M.A. Blanco: J. Am. Chem. Soc. 123 (2001) 3799
63. A.K. Kandalam, B.K. Rao, P. Jena, R. Pandey: J. Chem. Phys. 120 (2004) 10414

64. R. Muhida, W.A. Diño, M.M. Rahman, H. Kasai, H. Nakanishi: J. Phys. Soc. Jpn. 73 (2004) 2292
65. W.A. King, S.D. Bella, G. Lanza, K. Khan, D.J. Duncalf, F.G.N. Cloke, I.L. Fragala, T.J. Marks: J. Am. Chem. Soc. 118 (1996) 627
66. J.P. Perdew, J.A. Chevary, S.H. Vosko, K.A. Jackson, M.R. Pederson, D.J. Singh, C. Fiolhais: Phys. Rev. B 46 (1992) 6671
67. G. Kresse, J. Furthmüller: Phys. Rev. B 54 11169 (1996); Comput. Mater. Sci. 6 (1996) 15
68. G. Kresse, J. Hafner: Phys. Rev. B 47 R558 (1993); Phys. Rev. B 49 (1994) 14251
69. P.E. Blöchl: Phys. Rev. B 50 17953 (1994); D. Joubert, G. Kresse: Phys. Rev. B 59 (1999) 1758
70. C. Zener: Phys. Rev. 82 (1951) 403
71. K. Sato, P.H. Dederichs, H. Katayama-Yoshida, J. Kudrnovský: J. Phys.: Condens. Matter 16 (2004) S5491
72. N.D. Mermin, H. Wagner: Phys. Rev. Lett. 17 (1966) 1133
73. P. Gambardella1, A. Dallmeyer, K. Maiti, M.C. Malagoli, W. Eberhardt, K. Kern, C. Carbone: Nature (London) 416 (2002) 301
74. O. Kahn, E. Bakalbassis, C. Mathoniére, M. Hagiwara, K. Katsumata, L. Ouahab: Inorg. Chem. 36 (1997) 1530; A.N. Vasil'ev, O.L. Ignatchik, A.N. Sokolov, Z. Hiroi, M. Isobe, Y. Ueda: JETP Lett. 78 (2003) 551
75. M. Takahashi, P. Turek, Y. Nakazawa, M. Tamura, K. Nozawa, D. Shiomo, M. Ishikawa, M. Kinoshita: Phys. Rev. Lett. 67 (1991) 746
76. See for instance, S.K. Satija, J.D. Axe, G. Shirane, H. Yoshizawa, K. Hirakawa: Phys. Rev. B 21 (1980) 2001
77. M.L. Reed, N.A. El-Masry, M.K. Stadelmaier, M.K. Ritums, M.J. Reed, C.A. Parker, J.C. Roberts, S.M. Bedair: Appl. Phys. Lett. 79 (2001) 3473
78. M. Wierzbowska, D. Sánchez-Portal, S. Sanvito: Phys. Rev. B 70 (2004) 235209
79. W.M. Temmerman, M. Heinemann: Phys. Rev. B 49 4348 (1994); O. Mathon, F. Baudelet, J.P. Itié, A. Polian, M. d'Astuto, J.C. Chervin, S. Pascarelli: Phys. Rev. Lett. 93 (2004) 255503
80. S. Suhai: Phys. Rev. B 51 (1995) 16553
81. C. Lee, W. Yang, R.G. Parr: Phys. Rev. B 37 785 (1988); A.D. Becke: J. Chem. Phys. 98 (1993) 5648
82. V.R. Saunders, R. Dovesi, C. Roetti, R. Orlando, C.M. Zicovich-Wilson, N.M. Harrison, K. Doll1, B. Civalleri, I.J. Bush, Ph. D'Arco, M. Llunell: CRYSTAL2003 User's Manual, University of Torino, Torino, 2003
83. M.S. Miao, P.E. Van Camp, V.E. Van Doren, J.J. Ladik, J.W. Mintmire: Phys. Rev. B 54 (1996) 10430
84. V.V. Maslyuk, A. Bagrets, V. Meded, A. Arnold, F. Evers, M. Brandbyge, T. Bredow, I. Mertig: Phys. Rev. Lett. 97 (2006) 097201
85. P. Esquinazi, R. Hohne: J. Magn. Magn. Mater. 290–291 (2005) 20
86. K. Kusakabe, M. Maruyama: Phys. Rev. B 67 (2003) 092406
87. Y.-W. Son, M.L. Cohen, S.G. Louie: Nature 444 (2006) 347
88. J. Choi, Y.-H. Kim, K.J. Chang, D. Tománek, Phys. Rev. B 67 (2003) 125421
89. S. Hao, G. Zhou, W. Duan, J. Wu, B.-L. Gu: J. Am. Chem. Soc. 128 (2006) 8453
90. M. Simeoni, S. Santucci, S. Picozzi, B. Delley: Nanotechnology 17 (2006) 3166

Chapter 11
One-Dimensional Phase-Change Nanomaterials for Information Storage Applications

Xuhui Sun, Bin Yu, Garrick Ng, and M. Meyyappan

Abstract The electrically operated phase-change random access memory (PRAM) features faster write/read, improved endurance, and much simpler fabrication as compared with the traditional transistor-based nonvolatile semiconductor memories. Low-dimensional phase-change materials in nanoscale dimensions offer advantages over their bulk or thin-film counterparts in several aspects such as reduced programmable volume and reduced thermal energies in phase transition. These features contribute to low-power operation, excellent scalability, and fast write/erase time. In this chapter, we present a general bottom-up synthesis approach and systematic material analysis study of one-dimensional chalcogenide-based phase-change materials including germanium telluride (GeTe), and indium selenide (In_2Se_3) nanowires that are targeted for nonvolatile resistive switching data storage. The phase-change nanowires have been synthesized via thermal evaporation method under vapor–liquid–solid (VLS) mechanism. The morphology, composition, and crystal structure of the synthesized nanowires were investigated by scanning electron microscopy, energy dispersive X-ray spectroscopy, and high-resolution transmission electron microscopy. The as-synthesized nanowires are structurally uniform with single crystalline structures. The one-dimensional phase-change chalcogenide nanowires exhibit significantly reduced melting points, low activation energy, and excellent morphology, making them promising nanomaterials for data storage devices with very low energy consumption and excellent scalability.

11.1 Introduction

Information storage employing alternative, noncharge-based state variables (such as material structural phase and electron spin) represents a major trend in future electronics. Nonvolatile memories are key components of mobile electronics or pervasive computing, as data can be retained even when power is interrupted. Despite great commercial success, the semiconductor industry is searching for

alternative nonvolatile memory technologies with improved performance, reliability, and scalability for high-capacity, low-cost data storage. Phase-change materials (PCMs) are among the most promising media for nonvolatile, rewritable, and highly endurable data storage. The idea to employ material phase change for data storage dates back to the 1960s when Ovshinsky suggested a switch based on material phase transition of multicomponent chalcogenides [1]. This technology was developed into mainstream optical data storage media such as CDs and DVDs that are widely used today [2–7]. The concept has been later extended to develop electrically operated phase-change random access memory (PRAM) [8–13].

Phase-change memories rely on binary or multiple reflective/resistive states of the programmable element to represent logic levels for data storage. The optical reflectivity or electrical resistance in the material is reversibly switched because of thermally-induced transition caused by the application of a short energy stimulus (laser or electrical pulse) between two stable phases: the orderly single crystalline or polycrystalline phase (c-phase) and the less orderly amorphous phase (α-phase). In particular, resistive switching PRAM features faster write/read, improved endurance, and much simpler fabrication process when compared with the traditional transistor-based semiconductor nonvolatile memories such as floating-gate or SONOS-based MOSFETs. Because the data is stored in the form of material phase, PRAM also offers soft-error- or radiation-free operation.

A major issue limiting the extensive use of thin-film-based PRAM, a common way of technological implementation in the semiconductor industry, is the enormous programming current to generate sufficient thermal energy needed for phase change. This is particularly a concern in the crystal-to-amorphous (c-to-α) phase transition, which requires a high current for melting. The Joule heating effect may cause power dissipation issues and intercell thermal interference, preventing memory scaling. The phase-change behavior of chalcogenide materials at nanoscale may overcome these scaling limitations [14, 15] and therefore warrant a detailed investigation.

Low-dimensional nanomaterials are of particular interest as they exhibit anisotropic and dimension-dependent properties, both of which are important attributes in nanodevice design. One-dimensional nanostructures such as wires and tubes have been receiving attention because of their interesting electronic, thermal, and optical properties intrinsically associated with quantum effect, which lead to many potential applications [16]. Inorganic nanowires (NWs) are among the most promising materials for future nanoelectronics applications such as information storage, computing, and sensing. Prototypes of nanowire based diodes, transistors, logic gates, memories, sensors, LEDs, and lasers have been demonstrated [17–24]. Clearly, the behavior and performance of nanodevices depend on the associated properties of the material at the nanoscale.

Recent experimental studies on Ge-doped SbTe "line-cell" fabricated by thin-film deposition and ultrafine photolithography showed nanosecond-level phase switching at low power dissipation, suggesting that nanowire configuration could be ideal for future data storage devices [14]. However, lithography resolution limitation in the traditional top-down process hinders further scaling-down of memory array. Moreover, the exact mechanism of phase transition and the modulation

of thermal properties as functions of material size, especially at nanoscale and low-dimensionality, have not been explored.

Taking chemically synthesized one-dimensional chalcogenide nanowire as an example, it can be shown that phase-change materials at nanoscale exhibit exceptional thermal behavior that may potentially facilitate the effort to surmount the intimidating memory scaling barrier. We begin with a brief discussion of the pros and cons of the "bottom-up" and "top-down" approaches to nanotechnology for memory applications in Sect. 11.2, followed by chemical synthesis, material characterization, and thermal property study of phase-change nanowire materials of common interest, such as GeTe and In_2Se_3, in Sect. 11.3. A summary and future prospects will be given in Sect. 11.4.

11.2 Top-Down vs. Bottom-Up Approaches in Nanotechnology

In principle, there are two strategies for the implementation of nanotechnology or nanofabrication: the *bottom-up* and the *top-down*. The bottom-up approach attempts to build nanodevices via chemical synthesis and self-assembly of nanoscale atomic or molecular components. The top-down approach seeks to fabricate nanodevices using precision tools such as photolithography (e.g., electron-beam, extreme ultraviolet, and X-ray). While the latter has been the choice in semiconductor industry for making microelectronic chips for decades, the core concept of the bottom-up nanofabrication is to employ inexpensive chemistry to assemble the basic building blocks. It contains the following processes: synthesis of nanomaterials, implementation of nanodevice components, and organization/assembly of complex nanosystems.

The pros and cons of the bottom-up and the top-down approaches are matters of debate in the literature. The advancement of top-down semiconductor chip technology has been slowing down owing to increasingly challenging fabrication limitations such as those associated with the resolution capability of the photolithographic tools. In the bottom-up approach, fabrication at both material and device levels are not yet well defined or fully developed. In addition, the connection to the macro world remains an unresolved problem. While each approach has its advantages and disadvantages, future nanotechnology implementations might embrace contributions from both. For example, nanodevices could be made via the bottom-up strategy and assembled in situ (or "grown in place") on a nanochip fabricated via the top-down lithographical techniques with interface to the macro world. This *hybrid* nanotechnology allows integration of the advantageous attributes of both approaches. It is an effective way to investigate the behavior, performance, reliability, and scalability of nanodevices with ultrasmall critical features implemented alternatively by a quick, feasible, and low-cost process, well before the photolithography tool offers competitive patterning capability. In such a sense, nanomaterials made by bottom-up chemical synthesis offer an excellent material platform for advanced scientific research.

11.3 Synthesis and Characterization of Phase-Change Nanowires (PCNWs)

11.3.1 General Synthesis Techniques

One-dimensional inorganic nanowires are potential nanoscale building components in future electronic chip applications. Anisotropic crystal growth (whisker) was found in the ores in 1500s. Laboratory-synthesized 1-D "microwires" (diameter $>1\,\mu m$) were first reported as early as in 1960s by Wagner and Ellis [25]. 1-D "nanowires" (diameter $<100\,nm$) were made possible in the 1990s [26] because of rapid advancement of both nanoscale fabrication and material characterization techniques. For the synthesis of nanowires, it is necessary to restrict the growth of material along the axial direction. A widely used technique is the so-called VLS (vapor–liquid–solid) growth [25]. A schematic diagram of VLS growth via thermal evaporation is shown in Fig. 11.1. Here, a solid–liquid interface is introduced through a

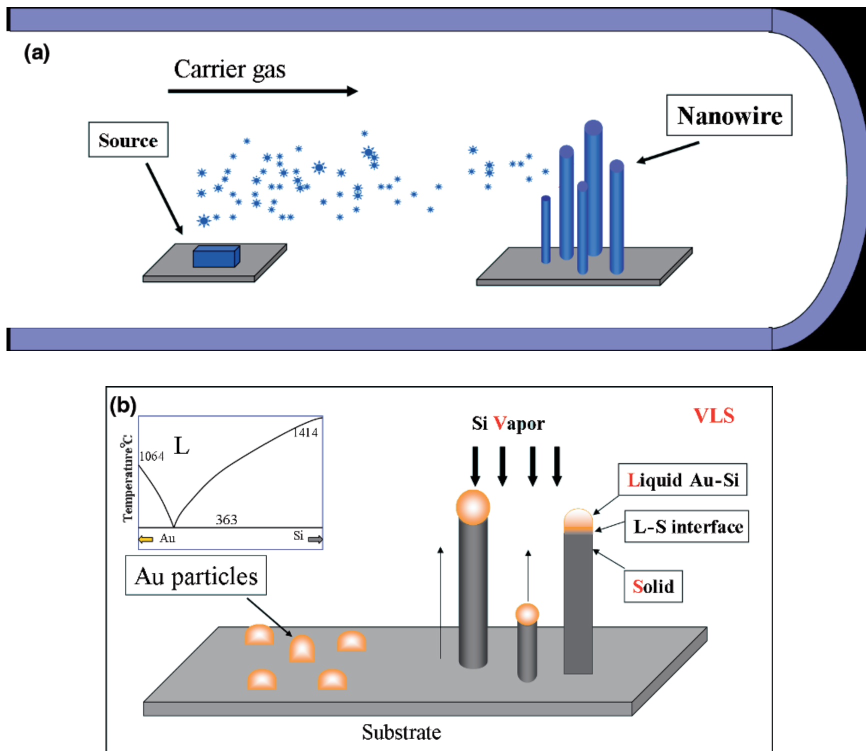

Fig. 11.1 A schematic diagram of thermal-evaporation VLS nanowire growth. (**a**) Thermal evaporation and nanowire growth process. (**b**) Vapor–Liquid–Solid (VLS) mechanism of Si nanowire growth using Au nanoparticles as the catalyst. *Inset*: the phase diagram of Au–Si alloy

metallic nanoparticle serving as catalyst, and the growth occurs only at the solid–liquid interface, promoting directed growth. The material from a gaseous source is "dissolved" in the liquid phase of the metal catalyst in the form of a composite nanoparticle, forming a eutectic mixture. Oversaturated material subsequently crystallizes at the liquid–solid interface, resulting in one-dimensional growth in a continuous manner. Since this method involves three phases, the vapor phase of the material source, the liquid phase of the eutectic mixture droplet, and the solid phase of the nanowire, it is commonly referred to as the VLS growth. This method has been widely used to grow various types of nanowire [16, 27].

In the VLS method, one-dimensional growth is induced and directed by the liquid droplets of the catalyst metal, whose sizes remain essentially unchanged during the entire growth process. Hence, each liquid droplet serves as a virtual template to restrict the lateral growth of an individual wire. Metal nanoparticles of Au, Fe, Ti, In, etc., have been employed as the metal catalysts in nanowire growth [28–32]. Gold is commonly used in nanowire growth because of its inertness and its ability in forming a eutectic with many materials at relatively low temperatures. As many as fifteen metals including gold have been tested for the effectiveness as catalyst in SnO and silicon nanowire growth, which showed an inverse relation between the growth density and melting point of the metal [28]. It should be emphasized that, though often referred to as "catalysts," the metal nanoparticles play more of the role as "initiator" and "director" in the form of a "soft template" for the one-dimensional growth of the nanowires. The advantage of the VLS method is that the diameter of the nanowire can be controlled by the size of catalytic nanoparticles.

Using the thermal evaporation process and gold (Au)-catalyzed VLS growth, reproducible synthesis of high-yield, size-controllable, single crystalline chalcogenide phase-change nanowires on semiconducting (silicon) or insulating (SiO_2) substrates has been demonstrated. The diameter control of the NW was achieved by distinctively selecting the size of Au nanoparticles catalyst or the thickness of Au thin film. The length of NW, depending on the growth time, may extend up to tens of micrometers. The synthesis of nanowires was carried out in a vacuum two-zone furnace synthesis system. A schematic diagram of the system is shown in Fig. 11.2.

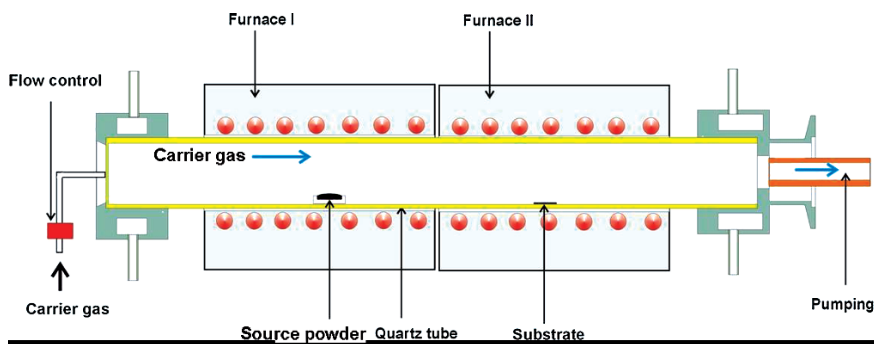

Fig. 11.2 A schematic diagram of a vacuum two-zone nanowire synthesis system

In the setup, the nanowire growth temperature (low) and the source evaporation temperature (high) were separately controlled. The high-purity chalgenide source powders was placed in the high-temperature zone. The silicon or SiO_2-coated silicon substrate, dispersed with gold nanoparticles as catalyst, was loaded downstream in the low-temperature zone as target substrate for NW growth. The reactor tube was evacuated to a base pressure of 10^{-2} Torr prior to the growth experiment. Argon was introduced into the system as a carrier gas during the growth process.

The physical morphology and crystallinity of the as-synthesized NWs was examined by scanning electron microscopy (SEM, Hitachi S-4000 FEG), high-resolution transmission electron microscopy (HR-TEM, Philips CM20, operated at 200 kV) equipped with energy dispersive X-ray spectroscopy (EDX) for chemical composition analysis and selected area electron diffraction (SAED). X-ray photoelectron spectroscopy (XPS) measurement was performed in an SSI S-Probe Monochromatized Spectrometer using Al (ka) radiation (1486 eV) as a probe. The as-grown nanowires were dispersed onto the copper TEM grids (coated with SiO_x or carbon film) for TEM imaging.

11.3.2 Synthesis and Characterization of IV–VI Compound (GeTe) Nanowires

A typical synthesis condition for GeTe nanowires is described as follows. High-purity GeTe powder (99.999%, Aldrich) was placed in the middle of the high-temperature zone. Gold nanoparticles (20 nm) were dispersed as catalyst on thermal SiO_2 coated Si(100) substrate. Argon mixed with hydrogen (20%) as carrier gas was introduced at a flow rate of 25 sccm (standard cubic centimeters per minute) and at a pressure of 200 Torr. The source furnace temperature was maintained at $680 \sim 720°C$ for 1 h and the temperature in the downstream growth zone was $\sim 450°C$.

Figure 11.3 shows a SEM image of the as-synthesized GeTe nanowires showing high-yield nanowire growth. Their diameter is in the range of $40 \sim 80$ nm and length up to tens of micrometers. Gold catalyst beads are visible at the tips of the nanowires, indicating a VLS growth mechanism. Figure 11.4a shows a low-magnification TEM image of a single GeTe nanowire with uniform diameter of about 40 nm along its entire length. Selected Area Electron Diffraction (SAED) pattern taken from the nanowire (shown in the inset) reveals that the nanowire is a single crystal with cubic lattice structure. The EDS analysis of an individual nanowire confirms that the nanowire (shown in Fig. 11.4b) is composed of only germanium and tellurium with an atomic ratio close to 1:1. The trace O peak is from the oxide outer layer, which will be discussed later.

The high-resolution TEM (HR-TEM) image analysis indicates that the as-prepared GeTe nanowires are high-quality single crystals. Figure 11.5a and b show that the GeTe nanowire is structurally uniform and contains no noticeable defects such as dislocations and stacking faults. A layer of 1–3 nm amorphous oxide shell

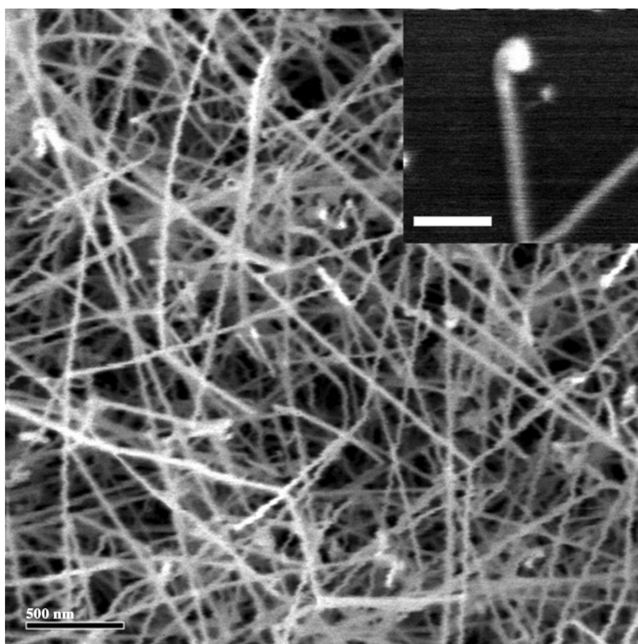

Fig. 11.3 SEM image of as-synthesized GeTe nanowires on SiO_2-coated Si(100) substrate using 20 nm Au nanoparticles as growth catalyst. Scale bar is 1 μm. *Inset*: a close-up view of a catalyst bead at the tip of the single GeTe nanowire. Scale bar (*inset*) is 200 nm

coverings the GeTe nanowire surface and exhibits an atomically sharp interface. It is known that the surface of GeTe is oxidized spontaneously in the presence of atmospheric air to form $GeO_2 \cdot TeO_2$ [33–35]. The lattice spacing of ~3.5 Å in Fig. 11.5a and ~2.1 Å in Fig. 11.5b corresponds to the *d*-spacing of the (111) and (220) crystal planes, respectively, of GeTe with a cubic lattice structure. HR-TEM imaging results and SAED pattern suggest that the GeTe nanowire is single crystal of the cubic structure with lattice constant *a* of ~6.01 Å, which is consistent with the JCPDS PDF 03-065-0415 (cubic structure, Fm3m, a = 6.02 Å). The GeTe nanowires have a preferential growth direction in the <110> crystalline orientation.

At room temperature, the GeTe crystal has rhombohedral structure (R3m), which is transformed to cubic structure (NaCl structure) at high temperatures (~446°C) [36]. The rhombohedral structure can be viewed as a distorted NaCl-type structure. The degree of the distortion from the cubic NaC1-type structure is reflected in the angle $\alpha = 88.35°$ between the axes of the face-centered rhombohedral unit cell, which differs slightly from the undistorted value of 90°. With increasing temperature the angle α increases from the room-temperature value of 88.35° continuously to the undistorted value of 90° at about 446.5°C. The growth temperature of GeTe nanowires is above the transition temperature of GeTe crystal from rhombohedral to cubic structure. Therefore, the nanowires grown at high temperature exhibit cubic structures.

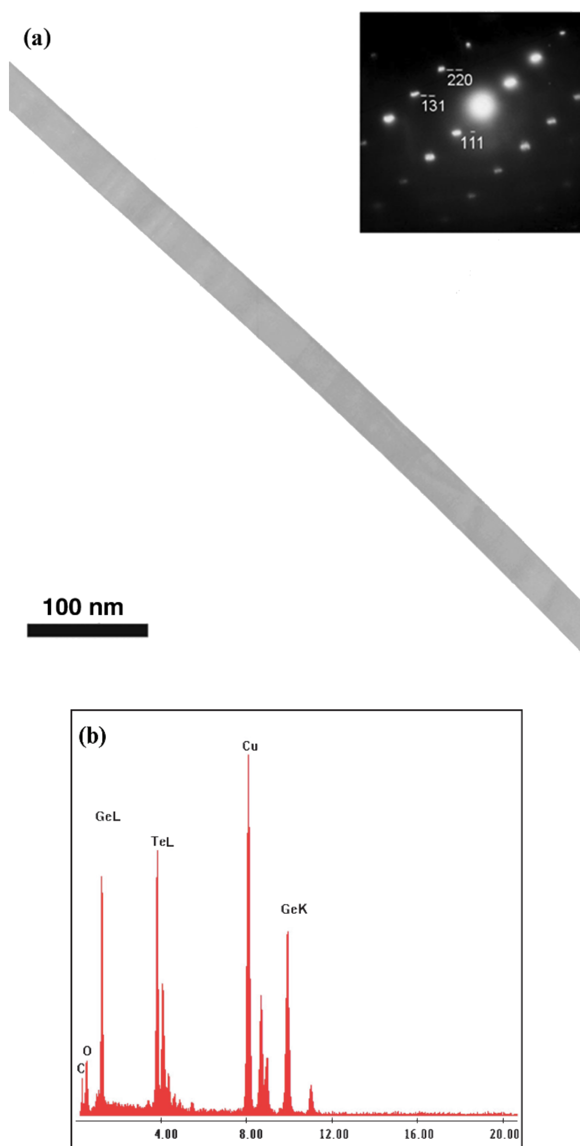

Fig. 11.4 Morphology and composition of germanium telluride nanowire. (**a**) Low-magnification TEM image of an individual GeTe nanowire with a diameter of about 40 nm. The nanowire length is over 5 µm. *Inset*: the SAED pattern of an fcc cubic lattice structure. (**b**) EDS spectrum of the same GeTe nanowire as shown in panel (**a**)

The electronic and chemical state of GeTe nanowires were studied by XPS. Figure 11.6a and b shows the XPS spectra of Ge 3d and Te $3d_{5/2}$, respectively. The binding energies at 30.0 eV in Fig. 11.4a and 572.4 eV in Fig. 11.4b are attributed to Ge 3d and Te $3d_{5/2}$ in GeTe, respectively, which is in agreement with values

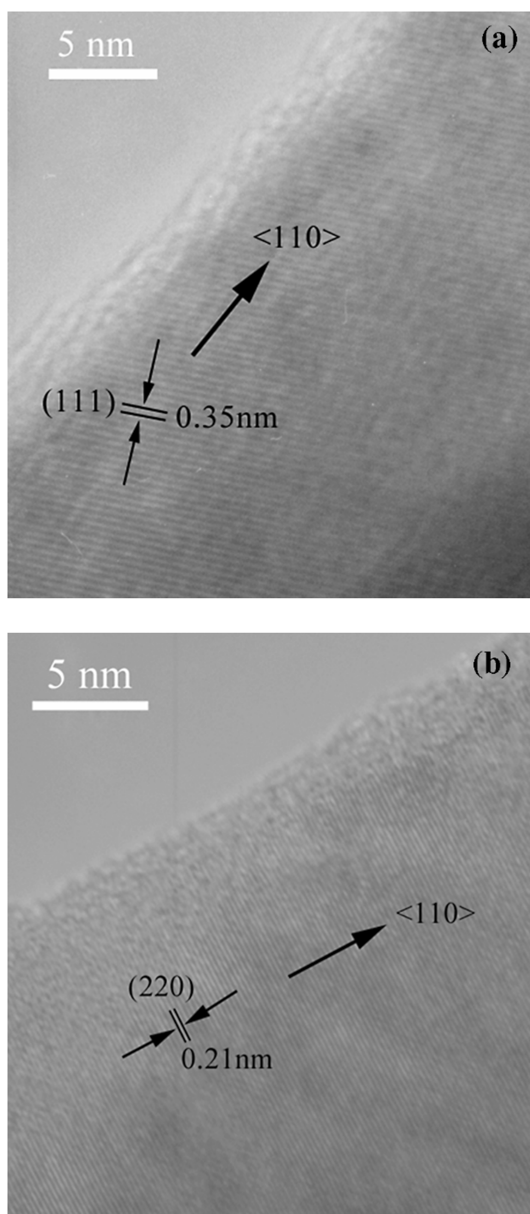

Fig. 11.5 High-resolution TEM images of the crystal structure of germanium telluride nanowires. **(a)** one sample showing (111) planes with an interplane spacing of ∼0.35 nm. **(b)** Another sample of GeTe nanowire shows (220) planes with an interplane spacing of ∼0.21 nm. Both nanowire samples show an elongation along the preferential < 110 > crystalline orientation. A thin (1–3 nm) amorphous oxide layer is observed on the surface in both samples

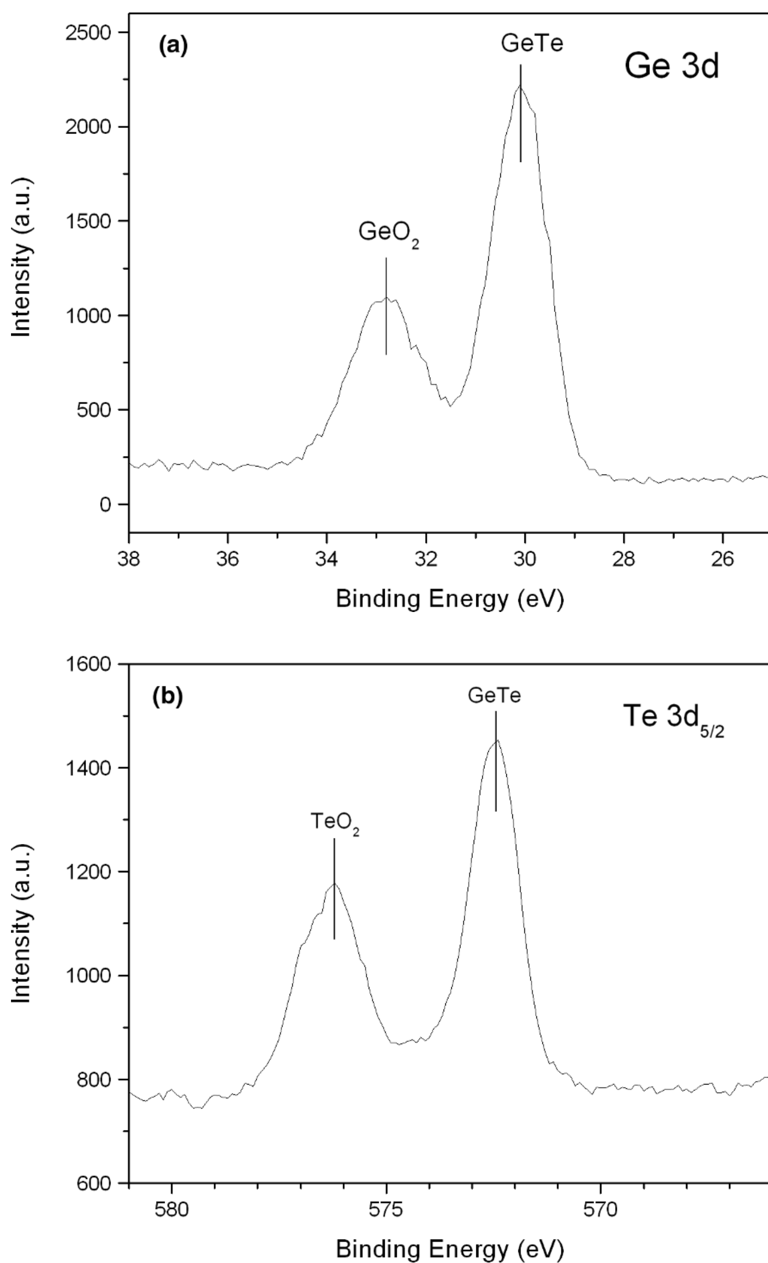

Fig. 11.6 XPS spectra of germanium telluride nanowires with peak representing (**a**) Ge 3d and (**b**) Te $3d_{5/2}$. The binding energy information indicates the existence of GeO_2 and TeO_2 in each case, respectively

reported in the literature [35, 37–39]. The XPS analysis indicates that the nanowires are GeTe compound. The peaks at 32.8 eV in Fig. 11.6a and 576.2 eV in Fig. 11.6b are due to GeO_2 and TeO_2, respectively, from the thin oxide outer layer. Because XPS is a surface sensitive tool with a sampling depth of several nanometers, even 1–3 nm $GeO_2 \cdot TeO_2$ outer layer can be clearly detected. A quantitative analysis from XPS data further confirms that the atomic ratio of Ge and Te is close to 1:1.

11.3.3 Synthesis and Characterization of III–VI Compound (In_2Se_3) *Nanowires*

The compound semiconductor Indium Selenide (In_2Se_3) is of interest due to its polymorphism and the related metal-ion defect structure. It exhibits at least three different crystalline modifications denoted by α, β, and γ with a transition temperature of 200 and 650°C, respectively, for the α–β and β–γ transition [40]. Undoped In_2Se_3 is an n-type semiconductor in the form of hexagonal structure with a direct band gap of 1.7 eV [41]. In_2Se_3 is considered for several applications such as photovoltaic solar cell [42, 43], optoelectronics [44], and ionic battery [45]. In particular, In_2Se_3 has been recently used as a programmable material in phase-change random access memory (PRAM) [46, 47]. In_2Se_3 shows four orders of magnitude higher electrical resistivity than $Ge_2Sb_2Te_5$, a widely used phase-change material for PRAM. Its resistivity can be varied by a factor of 10^5, depending on the degree of crystallization. Highly resistive phase-change materials help to reduce the programming current in PRAM switching activity, especially in the crystal to amorphous (c-to-α) phase transition. The reduced current implies low energy consumption, minimized intercell thermal interference, and improved cell scalability in data storage.

A typical synthesis condition for In_2Se_3 nanowires is described as follows. In_2Se_3 powder (99.999%, Aldrich) was placed upstream in the reactor in the middle of the high-temperature zone. Both Si(111) wafer and 300 Å thermal SiO_2 coated Si(100) wafer, deposited with gold nanoparticles or indium film, were loaded downstream in the low temperature zone as the target substrate for nanowire growth. Argon as the carrier gas was introduced at a flow rate of 25 sccm and pressure of 30$\sim$600 Torr, or at a flow rate of 100 sccm and at atmospheric pressure. The temperatures of the source material and that of the targeted substrate were ramped up to 900–950°C and 650–700°C, respectively, and maintained for 60 min.

The as-grown In_2Se_3 NWs have a diameter in the range of 40–80 nm and are up to 100 μm in length as shown in Fig. 11.7. A representative TEM image (Fig. 11.8a) of an individual In_2Se_3 NW shows that the nanowire has a smooth surface and uniform thickness along the growth direction. The average diameter of the NWs is 60 ± 18 nm. Local EDS analyses (Fig. 11.8b), in which the TEM electron beam is focused on a targeted sample areas as small as 9 nm in diameter, shows that the particle, appeared as a dark-colored ball on the tip of the nanowire, is primarily gold with an indium content below 5 at.% and selenium content below the detection level. The local point EDS analysis on the nanowire (Fig. 11.8c) shows that In and Se

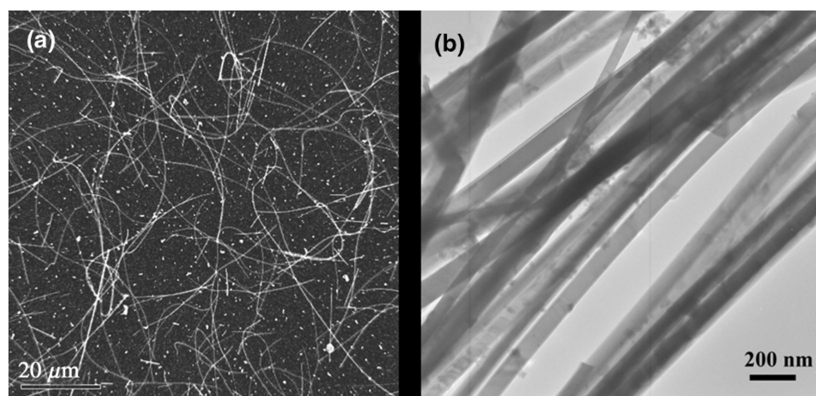

Fig. 11.7 (**a**) SEM image of the as-synthesized In_2Se_3 nanowires on SiO_2-coated Si(100) substrate using 20 nm Au nanoparticles as growth catalyst. (**b**) TEM image of as-synthesized In_2Se_3 nanowires

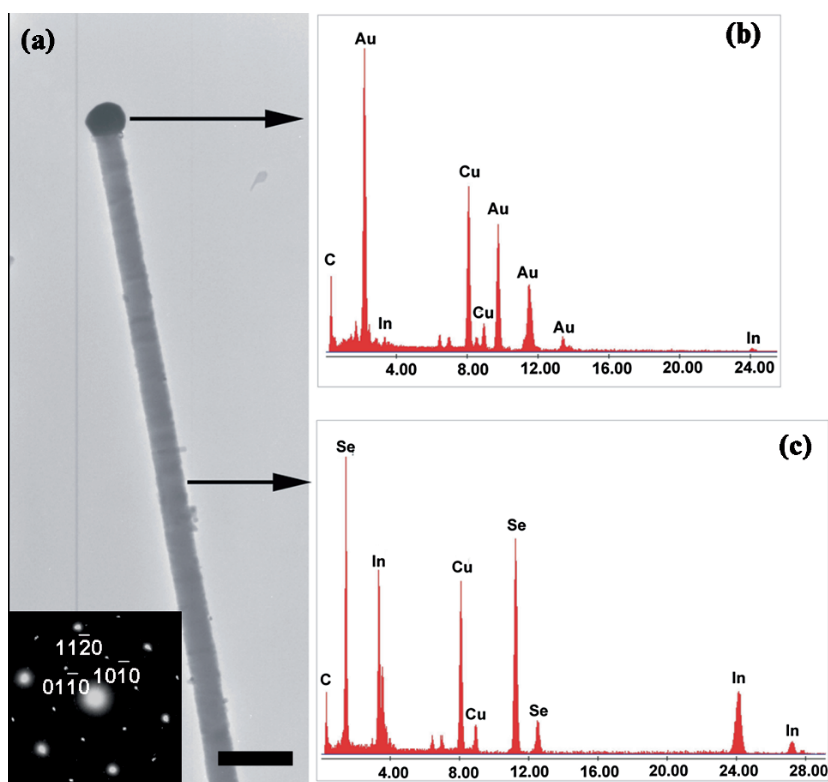

Fig. 11.8 (**a**) TEM image of In_2Se_3 NW grown on SiO_2 substrate using 20 nm gold nanoparticles as catalyst. A metal bead is observed at the tip of the nanowire. Scale bar is 200 nm. SAED pattern taken on the same NW is shown in inset. (**b**) EDS spectrum with locally focused e-beam spot on the bead part (arrow indicated). 5.0 at.% In: 95.0 at.% Au was detected. (**c**) EDS spectrum with locally focused e-beam spot on the nanowire part (arrow indicated)

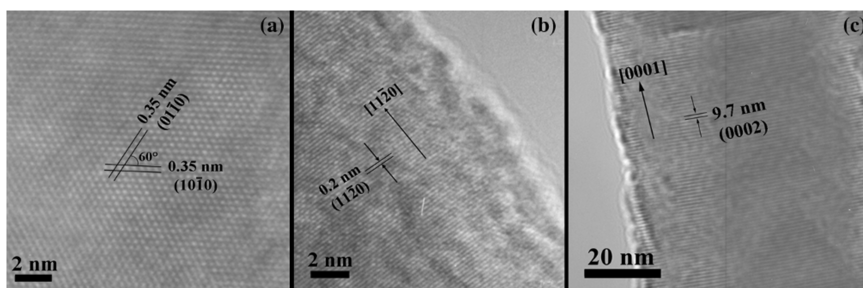

Fig. 11.9 High-resolution TEM images of β-In_2Se_3 NWs with hexagonal structure. (**a**) An individual In_2Se_3 NW sample showing a series of (100) planes with ∼3.5 Å lattice spacing meeting at an angle of 60°. (**b**) (110) planes with ∼2.0 Å lattice spacing of same NW in panel (**a**) is shown by tuning the TEM focus, which demonstrates an elongation along the preferential <110> crystalline orientation. (**c**) An individual In_2Se_3 NW sample showing 9.7 Å lattice spacing of the (002) plane, which has a (001) growth direction. The nanowires were grown on SiO_2 substrate

are present in an approximately 2:3 atomic ratio. The Cu and C signals arise from the carbon-coated copper TEM grid. The selected area electron diffraction (SAED) pattern taken on the same nanowire shows regular spot patterns (Fig. 11.8a inset), which confirms the single crystalline nature of the nanowires. The diffraction spots in the SAED pattern can be indexed to β-phase In_2Se_3 hexagonal structure, and the growth direction of the nanowire is along [110] direction determined together with HR-TEM images analysis as follows.

Figure 11.9a shows the HR-TEM image of an individual In_2Se_3 NW with a lattice spacing of ∼3.5 Å meeting at an angle of 60° that corresponds to *d*-spacing of the $(10\bar{1}0)$ plane of β-phase In_2Se_3 hexagonal structure. The $(11\bar{2}0)$ planes with a lattice spacing of ∼2.0 Å in same nanowire (Fig. 11.9b) can be obtained by tuning the TEM focus. The $(11\bar{2}0)$ planes is perpendicular to the nanowire growth direction, which confirms the nanowires have a preferential growth direction in the $[11\bar{2}0]$ crystalline orientation. In addition to the $[11\bar{2}0]$ growth direction in most nanowires, the [0001] growth direction is also observed by HR-TEM. Figure 11.9c shows the HR-TEM image of an individual In_2Se_3 NW with a large lattice spacing of 9.7 Å that corresponds to *d*-spacing of the (0002) plane of β-phase In_2Se_3 hexagonal structure, which demonstrates the nanowire has [0001] growth direction. The HR-TEM and SAED results from more than 20 nanowires reveal that the synthesized In_2Se_3 NW is a single crystal of the β-phase hexagonal structure with lattice constant a of ∼4.0 Å, and c of ∼19.2 Å, which is consistent with the JCPDS PDF 40–1408 (β-phase hexagonal structure). Only 2 of 20 nanowires (10%) have [0001] growth direction, and the others show $[11\bar{2}0]$ growth direction. The HR-TEM images also show that the nanowires are structurally uniform and contain no noticeable defects such as dislocations or stacking faults. The metal particle on the nanowire tip provides the evidence that the growth process followed VLS mechanism.

In_2Se_3 NWs can also be grown using indium film as growth catalyst using the so-called "self-catalytic" approach. In the Se-In phase diagram, indium can form liquid-phase alloy with In_2Se_3 at a eutectic point of 670°C, which can seed the

In_2Se_3 NW growth. A thick layer of indium (40 nm) was used in these experiments. The physical morphology and crystal structure of the In-catalyzed In_2Se_3 NWs are the same as Au-catalyzed ones, except that no indium bead could be found at the nanowire tip owing to the very low melting point (156°C) of indium. The low melting point is also the reason to use a relatively thick indium film since a significant amount is consumed by evaporation during the pregrowth temperature ramping-up. The self-catalyzed nanowire growth eliminates the potential risk of catalyst contamination from gold and similar metals, which is undesirable in nanoelectronics applications.

Finally, a simple test structure was made by adding metal contacts to an individual In_2Se_3 NW directly synthesized on SiO_2 substrate. Focused Ion Beam was used to pattern the Pt contact lines with between NW and prepatterned Mo pads (Fig. 11.10a). The current–voltage (I–V) characteristics between pairs of contact

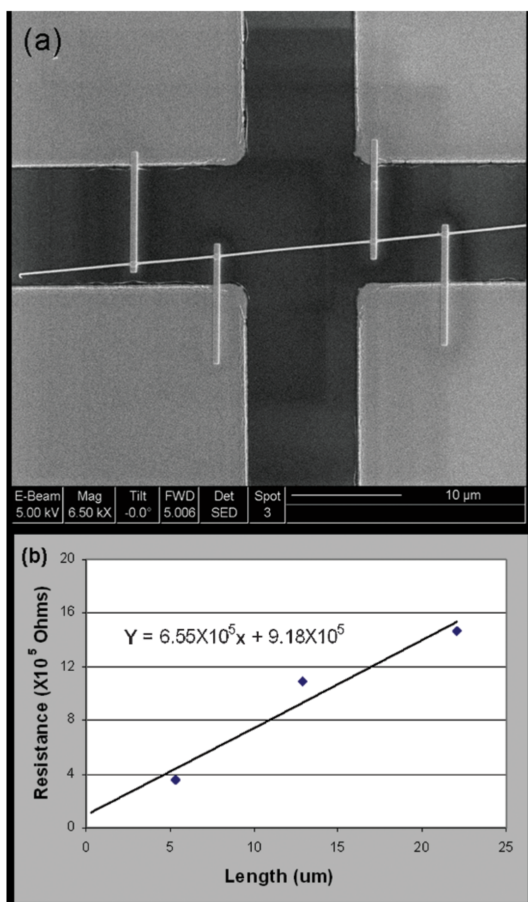

Fig. 11.10 (**a**) SEM top-view image of In_2Se_3 NW contacted by FIB patterned Pt lines between NW and Mo pads. (**b**) The electrical resistances versus the corresponding length of NW

pads in a four terminal device were measured. The resistances were then plotted against the separation distance between contact pads from which they were measured (Fig. 11.10b). From these data points, the total contact resistance, R_c, of the device was estimated by fitting a linear trend line to the data and extrapolating the plot to get the resistance at zero separation distance. The electrical resistivity of the as-synthesized undoped In_2Se_3 NW is estimated to be 8.3 Ωcm at room temperature, which is in close agreement with previously reported value of 6.7 Ωcm at room temperature for bulk In_2Se_3 [48].

11.3.4 Melting Point Measurement

For phase change materials, the melting point (T_m) is an important physical property relevant to the performance of data storage devices. Lower T_m represents that the c-to-α phase transition, corresponding to the memory reset activity, can be executed with a lower thermal energy. An estimate of the melting point of nanowires can be obtained via an in situ heating experiment in a TEM chamber under real-time morphology monitoring. In such a setup, the sample stage was resistively heated at a rate of 10°C/min. The melting temperature of the nanowire is identified as the point at which the electron diffraction pattern disappears and the nanowire starts to melt. The melting and evaporation process of the nanowires was monitored in real time by TEM and recorded by a video camera in the bright-field mode. A reduction in melting point from the bulk value was observed in all as-synthesized chalcogenides nanowires. Later, we use GeTe as an example to describe the details of the measurement and discuss the effect on the future memory devices.

A significant drop in T_m for GeTe nanowire from the bulk value was observed. GeTe nanowires started melting at 390°C, which is 46% less than the bulk melting point of GeTe (725°C). Figure 11.11a shows the TEM image of a single GeTe nanowire before melting with its ED pattern shown in the inset. Upon reaching the T_m(390°C), the contrast of GeTe nanowire abruptly turned dark and the single crystalline electron diffraction pattern disappeared as the material changed from solid crystalline phase to liquid phase (ED data shown in the inset of Fig. 11.11). The molten nanowire further vaporized out from the two open ends of the nanowire and a nanotube structure was left behind. At 460°C, clear evaporation was noticed with the exception of a few very long nanowires in the sample. A TEM image was taken during the evaporation process, as shown in Fig. 11.11b. A GeTe nanowire evaporation process at 420°C was also captured in a video and a few sequences are shown in Fig. 11.12. The very thin wall of the remaining tube, confirmed from EDS analysis, is the GeO_2 oxide outerlayer of GeTe nanowire. Because bulk GeO_2 (T_m : 1115°C) has much higher melting point than that of bulk GeTe and TeO_2 (T_m : 733°C), it turns out that only the GeO_2 shell was left behind when the temperature was increased up to the T_m of GeTe nanowire. Similar melting process and reduction in melting point were also reported for In_2Se_3 nanowires [49] and germanium nanowires [50].

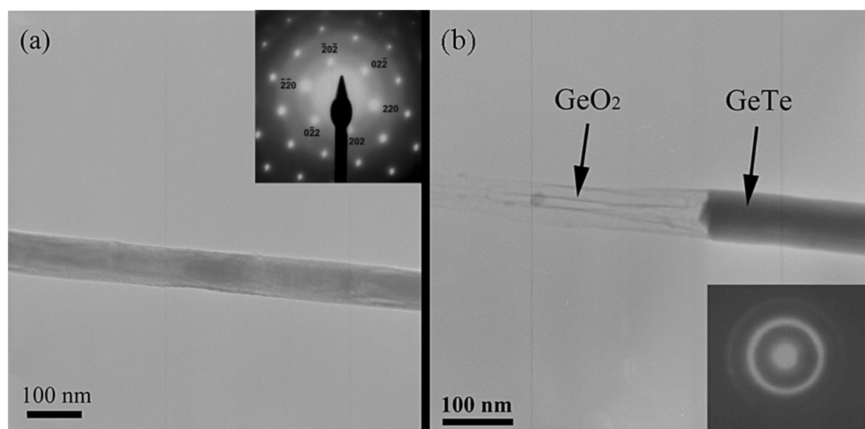

Fig. 11.11 Measurement of the melting point of a single germanium telluride nanowire under real-time TEM morphology monitoring. (**a**) The GeTe nanowire is at room temperature. The inset shows SAED pattern of the crystalline structure with fcc crystal structure. (**b**) The nanowire is molten and its mass is gradually lost through evaporation starting from 390 to 460°C. The remaining oxide nanotube can be clearly seen from the image. The inset shows a SAED pattern of the liquid GeTe NW

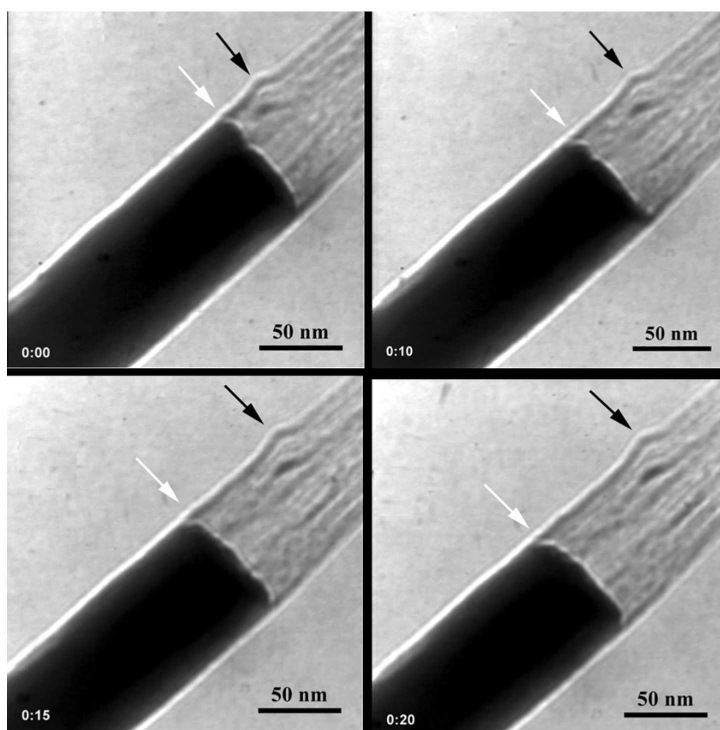

Fig. 11.12 A series of successive frame clips were captured from video which recorded a single GeTe nanowire evaporated at 420°C with the rate of 2 nm s^{-1}. The evaporation rate depends on the temperature and the length of the nanowires

11.4 Conclusions and Future Prospects

Various types of one-dimensional chalcogenide nanowires can be chemically synthesized via the vapor–liquid–solid method. Low-dimensional chalcogenide phase-change nanowires show promise for future-generation information storage applications owing to their superior material scalability, simple chemical synthesis, and low-cost manufacturing. The unique physical properties at the nanoscale such as significantly reduced melting point would enable the design and implementation of nonvolatile phase-change memories with ultra-low thermal programming energy. This in turn would help reduce the device size, intercell thermal interference, and chip power dissipation, leading eventually to ultra-high-density data storage.

Acknowledgments B. Yu and X. Sun are with the University Affiliated Research Center (UARC) at NASA Ames Research Center and their work was supported by a NASA contract to UARC.

References

1. Ovshinsky, S. R. *Phys. Rev. Lett.* 1968, 21, 1450.
2. Adler, D.; Shur, M. S.; Silver, M.; Ovshinsky, S. R. *J. Appl. Phys.* 1980, 51, 3289.
3. Chen, M.; Rubin, K.; Barton, R. *Appl. Phys. Lett.* 1986, 49, 502.
4. Yamada, N.; Ohno, E.; Nishiochi, K.; Akahira, N.; Takao, M. *J. Appl. Phys.* 1991, 69, 2849.
5. Coombs, J.; Jongenelis, A.; van Es-Spiekman, W.; Jacobs, B. *J. Appl. Phys.* 1995, 78, 4906.
6. Volkert, C. A.; Wuttig, M. *J. Appl. Phys.* 1999, 86, 1808.
7. Yamada, N.; Matsunaga, T. *J. Appl. Phys.* 2000, 88, 7020.
8. Lai, S.; Lowrey, T. *IEDM Tech. Dig.* 2001, 803.
9. Lai, S. *IEDM Tech. Dig.* 2003, 255.
10. Pirovano, A.; Lacaita, A. L.; Benvenuti, A.; Pellizzer, S.; Bez, R. *IEEE Trans. Elec. Dev.* 2004, 51, 452.
11. Kotz, J.; Shaw, M. P. *J. Appl. Phys.* 1984, 55, 427.
12. Hwang, Y. N.; Lee, S. H.; Ahn, S. J. *IEDM Tech. Dig.* 2003, 893.
13. Pirovano, A.; Lacaita, A. L.; Benvenuti, A.; Pellizzer, F.; Hudgens, S.; Bez, R. *IEDM Tech. Dig.* 2003, 699.
14. Lankhorst, M. H. R.; Ketelaars, B. W. S. M. M.; Wolters, R. A. M. *Nat. Mater.* 2005, 4, 347–352.
15. Yu, D.; Wu, J. Q.; Gu, Q. A.; Park, H. K. *J. Am. Chem. Soc.* 2006, 128, 8148–8149.
16. Xia, Y. N.; Yang, P. D.; Sun, Y. G.; Wu, Y. Y.; Mayers, B.; Gates, B.; Yin, Y. D.; Kim, F.; Yan, Y. Q. *Adv. Mater.* 2003, 15, 353–389.
17. Cui, Y.; Duan, X. F.; Hu, J. T.; Lieber, C. M. *J. Phys. Chem. B* 2000, 104, 5213–5216.
18. Cui, Y.; Lieber, C. M. *Science* 2001, 291, 851–853.
19. Ng, H.T.; Han, J.; Yamada, T.; Nguyen, P.; Chen, Y. P.; Meyyappan, M. *Nano Lett.* 2004, 4, 1247.
20. Duan, X. F.; Huang, Y.; Lieber, C. M. *Nano Lett.* 2002, 2, 487–490.
21. Duan, X. F.; Niu, C. M.; Sahi, V.; Chen, J.; Parce, J. W.; Empedocles, S.; Goldman, J. L. *Nature* 2003, 425, 274–278.
22. Friedman, R. S.; McAlpine, M. C.; Ricketts, D. S.; Ham, D.; Lieber, C. M. *Nature* 2005, 434, 1085.
23. Zheng, G. F.; Patolsky, F.; Cui, Y.; Wang, W. U.; Lieber, C. M. *Nat. Biotechnol.* 2005, 23, 1294–1301.

24. Chin, A. H.; Vaddiraju, S.; Maslov, A. V.; Ning, C. Z.; Sunkara, M.; Meyyappan, M. *Appl. Phys. Lett.* 2006, 88, 163115.
25. Wagner R. S. and Ellis W. C. *Appl. Phys. Lett.* 1964, 4, 89.
26. Heath J. R. and Legeoues F. K. *Chem. Phys. Lett.* 1993, 208, 263.
27. Law, M.; Goldberger, J.; Yang, P. D. *Annu. Rev. Mater. Res.* 2004, 34, 83.
28. Nguyen, P.; Ng, H. T.; Meyyappan, M. *Adv. Mat.* 2005, 17, 1773.
29. Sun, X.; Calebotta, G.; Yu, B.; Selvaduray, G.; Meyyappan, M. *J. Vac. Sci. Technol. B*, 2007, 25, 415.
30. Gu, Q.; Dang, H. Y.; Cao, J.; Zhao, J. H.; Fan, S. S. *Appl. Phys. Lett.* 2000, 76, 3020.
31. Kamins, T. I.; Williams, R. S.; Basile, D. P.; Hesjedal, T.; Harris, J. S. *J. Appl. Phys.* 2001, 89, 1008.
32. Kamins, T. I.; Li, X.; Williams, R. S. *Appl. Phys. Lett.* 2003, 82, 263.
33. Gogishvili, O. S.; Degaltsev, A. N.; Kononov, G. G.; Lavrinenko, I. P.; Lalykin, S. P. *Inorg. Mater.* 1988, 24, 944.
34. Sheveleva, T. F.; Plaksina, Y. B.; Markholiya, T. P. *Inorg. Mater.* 1976, 12, 791.
35. Yashina, L. V.; Kobeleva, S. P.; Shatalova, T. B.; Zlomanov, V. P.; Shtanov, V. I. *Solid State Ionics* 2001, 141, 513.
36. Chattopadhyayt, T.; Boucherlet, J. X.; von Schnering, H. G. *J. Phys. C* 1987, 20, 1431.
37. Lippens, P. E.; Brousse, E.; Jumas, J. C. *J. Phys. Chem. Solids* 1999, 60, 1663.
38. Shalvoy, R. B.; Fisher, G. B.; Stiles, P. J. *Phys. Rev. B* 1977, 15, 1680.
39. Shevchik, N. J.; Tejeda, J.; Langer, D. W.; Cardona, M. *Phys. Rev. Lett.* 1973, 30, 659.
40. Eddief, M.; Julien, C.; Balkanski, M. *Mater. Lett.* 1984, 2, 432.
41. Bouzouita, H.; Bouguila, N.; Duchemin, S.; Fiechter, S.; Dhouib, A. *Renewable Energy* 2002, 25, 131.
42. Kenawy, M. A.; Zayed, H. A.; El-Soud, A. M. A. *J. Mater. Sci.* 1990, 1, 115.
43. Lakshmikumar, S. T.; Rastogi, A. C. *Sol. Energ. Mat. Sol. C* 1994, 32, 7.
44. Ye, J.; Yoshida, T.; Nakamura, Y.; Nittono, O. *Appl. Phys. Lett.* 1995, 67, 3066.
45. Julien, C.; Hatzikraniotis, E.; Chevy, A.; Kambas, K. *Mater. Res. Bull.* 1985, 20, 287.
46. Lee, H.; Kang, D. H.; L. Tran, *Mater. Sci. Eng. B* 2005, 119, 196.
47. Lee, H.; Kim, Y. K.; Kim, D.; Kang, D. H. *IEEE Trans. Magnet.* 2005, 41, 1034.
48. Julien, C.; Balkanski, M. *Mat. Sci. Eng. B* 1996, 38, 1.
49. Sun, X.; Yu, B.; Ng, G.; Nguyen, T.D.; Meyyappan, M. *Appl. Phys. Lett.* 2006, 89, 233121.
50. Wu, Y.; Yang, P. *Adv. Mater.* 2001, 13, 520.

Chapter 12
Ordering of Self-Assembled Quantum Wires on InP(001) Surfaces

W. Lei, Y. H. Chen, and Z. G. Wang

Abstract InAs/InAl(Ga)As quantum wires (QWRs) have been grown on InP (001) substrates by molecular beam epitaxy (MBE) technology. A modified S-K growth mode has been presented for the formation of InAs QWRs on InAl(Ga)As/InP (001) substrate, in which the effect of lateral composition modulation in InAlAs buffer layers plays an important role. Vertical anticorrelation of InAs quantum wire superlattices has been observed and attributed to the interplay of strain field distribution and alloy phase separation in InAlAs matrix around InAs QWRs. The structural and optical properties of InAs/InAlAs QWR superlattices have also been discussed.

12.1 Introduction

In the past one or two decades, low-dimensional structures, such as quantum wires (QWRs) and quantum dots (QDs), have attracted wide attention because of their fantastic physical properties and potential applications in devices, especially in lasers and photodetectors. Apart from processing techniques involving lithography and etching, the direct growth of these nanostructures *via Stranski–Krastanow* (SK) *mode* has developed as the most promising approach. This kind of SK growth is based on the natural tendency of strained heteroepitaxial layers to spontaneously form *coherent* (i.e., dislocation free) three dimensional (3D) islands after the formation of a uniform 2D wetting layer. The driving force for this SK growth is the strain energy relaxation within the 3D islands due to their lateral expansion or compression in the directions of the free side faces. Under appropriate growth conditions, these self-assembled islands demonstrate sizes in the nanometer range, and when embedded in a higher band-gap matrix, QWRs and QDs with super optical and electronic properties are formed. However, because this SK growth is a kind of random growth process, the nanostructures fabricated show considerable statistical fluctuation in sizes and shapes, which leads to a pronounced inhomogeneous broadening

of the electronic density of states and results in a poorer device performance. So, it is very important to fabricate these nanostructures with high density, homogeneous size, and uniform shape. How can we do to obtain the ordered nanostructures (size uniformity and lateral order)?

There are two main possible ways to solve this problem. One is to optimize the growth parameters, such as, growth rate, deposition amount, and substrate temperatures etc., to grow nanostructures with homogeneous size distribution. The other way is to grow nanostructure superlattices. Both theoretical and experimental work has shown that during multilayer growth the elastic interaction between the nanostructures in different layers can lead to the formation of long-range vertical correlations of the nanostructures which may lead to a lateral ordering and size homogenization of the nanostructures as well. The nanostructures prefer to nucleate and grow at the local minima of the strain energy on the surface which is produced by the nanostructures buried in previous layers. By utilizing these two kinds of methods, big progress has been made in the ordering of In(Ga)As/GaAs and SiGe/Si nanostructures [1–3]. However, as for InP-based nanostructures, which have great potential applications in the long-wavelength (1.55 μm) semiconductor lasers, it presents a challenge to control the shape, size, and distribution of the nanostructures. Especially for InAs/InAlAs/InP(001) nanostructure system, the ordering of the nanostructures is even difficult owing to the phase separation effect in InAlAs layers and the relatively weak driving force for the islands formation associated with low misfit strain (3.2%) [4, 5].

In this chapter, we briefly review the ordered growth of InAs/InAl(Ga)As QWRs on InP(001) substrates by MBE technology. It experimentally demonstrates that the formation of InAs QWRs on InAl(Ga)As/InP(001) substrate is insensitive to the change of growth conditions. On the basis of this experimental phenomenon, a new modified SK growth mode is proposed and confirmed. The structural and optical properties of InAs/InAl(Ga)As QWR superlattices on InP(001) substrate are also summarized here.

12.2 Formation of InAs Quantum Wires on InAlAs/InP(001)

12.2.1 Quantum Wire Formation Insensitive to the Growth Conditions

Usually, the formation of self-assembled nanostructures is very sensitive to growth conditions such as growth rate, deposition amount, As overpressure and substrate temperatures, etc. For example, the size, density, and size distribution of InAs/GaAs QDs are greatly affected by the change of growth conditions [6–8]. However, for InAs/InAlAs QWRs on InP substrates, the change of growth conditions (InAs deposited thickness and InAs growth rate) seems to have little effect on the growth of InAs/InAlAs QWRs [4].

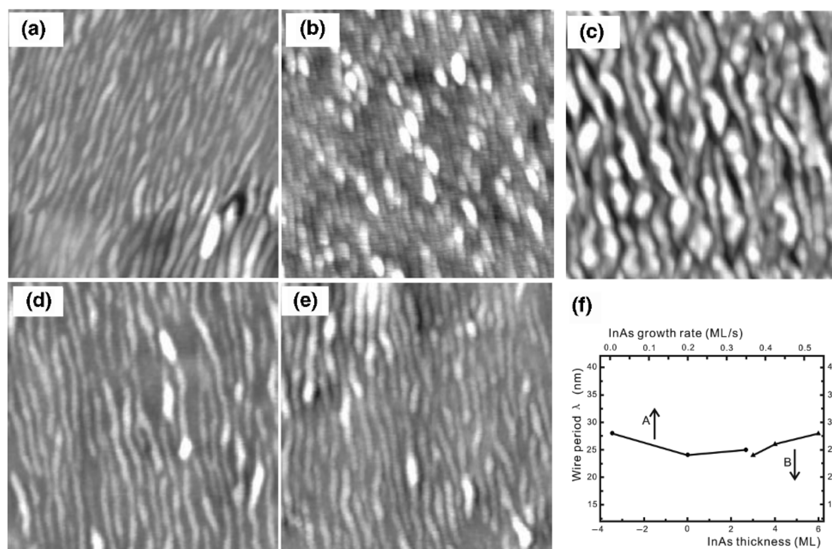

Fig. 12.1 AFM images of InAs nanostructures grown on InAlAs/InP(001). (**a**)–(**c**): as a function of InAs thickness with (**a**) 3 ML, (**b**) 4 ML, and (**c**) 6 ML. The InAs growth rate was 0.2 ML/s; (**d**) and (**e**): as a function of InAs growth rate with (**d**) 0.005 ML/s and (**e**) 0.35 ML/s. The InAs layer thickness was 3 ML/s. The size of the images is 0.5 μm × 0.5 μm. The elongated nanostructures are aligned along the $[1\bar{1}0]$ direction. Panel (**f**) shows the wire period λ as a function of growth rate with InAs coverage of 3 ML (arrow A) and deposition thickness with InAs growth rate of 0.2 ML/s (arrow B)

The atomic force microscopy (AFM) images of the surface of InAs/InAlAs/InP nanostructure samples grown with 3, 4, and 6 monolayer(ML) InAs deposited thickness are shown in Fig. 12.1a–c. The samples consist of 200 nm $In_{0.52}Al_{0.48}As$ buffer layer and InAs layer. The growth rates of InAlAs and InAs layers are 0.7 μm/h and 0.2 ML/s, respectively. As shown in Fig. 12.1a, QWRs aligned along the $[1\bar{1}0]$ direction are formed on the surface of 3 ML-InAs samples. And, a few bright elongated QDs are also formed on the InAs QWRs. When InAs deposited thickness increases to 4 ML, QWRs are also formed along the $[1\bar{1}0]$ direction. Meanwhile, the number of the bright elongated QDs on the QWRs increases a lot, as shown in Fig. 12.1b. With further increasing InAs deposited thickness to 6 ML, as shown in Fig. 12.1c, QWRs with elongated QDs on their top are obtained, which are also oriented along the $[1\bar{1}0]$ direction. It is observed that the lateral size (along the [110] direction) of QWRs in the 6 ML-InAs sample is a little larger than that of QWRs in the 3 and 4 ML samples. And, the size of QDs in the 6 ML-InAs sample is also larger, compared with the QDs obtained in the 3 and 4 ML InAs samples.

Figure 12.1d and e show the surface morphologies of InAs/InAlAs nanostructures grown on InP(001) with different growth rates (0.005 and 0.35 ML/s, respectively). The samples consist of 200 nm $In_{0.52}Al_{0.48}As$ buffer layer and 3 ML InAs layer. The growth rate of InAlAs layer is 0.7 μm/h. As shown in Fig. 12.1a, one can see that all the InAs nanostructures grown with different growth rates have wire

shape oriented along the $[1\bar{1}0]$ direction. Elongated QDs can also be found on some of the InAs QWRs for all the samples, and their lateral size along the [110] direction is a little larger than that of the InAs QWRs.

As shown in the earlier experiments, the change of growth conditions (InAs deposition thickness and growth rate here) have little effect on the morphology and distribution of InAs nanostructures grown on InAlAs/InP(001). Statistics on the average lateral period λ of the QWRs is shown in Fig. 12.1f. It is very interesting that the λ values range from 24 to 28 nm with only a little fluctuation under different growth conditions. Then, what leads to this almost same average lateral period λ? It is well known that the formation of self-organized islands is determined by the epitaxial misfit strain and the accumulation of elastic strain in the epilayer. So, the InAlAs matrix that directly interacts with InAs layer should be taken into account to explain this experimental observation, which will be discussed in the next section.

12.2.2 New Growth Model

Usually, for nanostructures formed by self-organized process, standard SK growth mode works well, which happens on a homogeneous growth plane. However, InAlAs matrix is a kind of immiscible alloy with strong positive mixing parameter (around 3600 cal/mol), which will induce lateral composition modulation (LCM) during the growth of InAlAs layer in order to partially relax the intrinsic alloy strain energy [9]. Indeed, LCM effect exists in the InAlAs layer grown on InP substrate [4].

Figure 12.2 shows bright-field plan-view TEM image of a sample consisting of 500 nm $In_{0.52}Al_{0.48}As$ layer grown on InP(001) substrate. It is observed that there

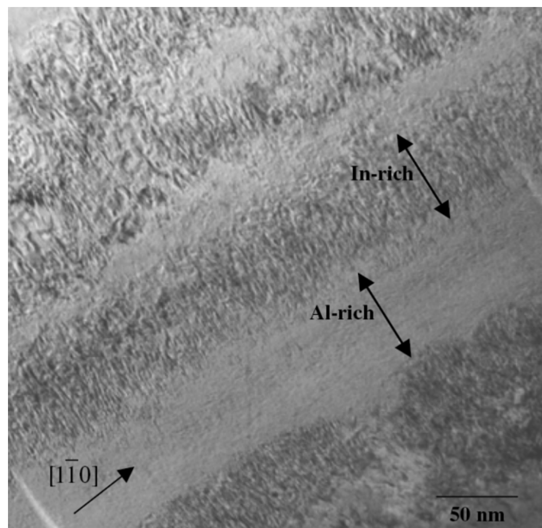

Fig. 12.2 Bright-field plan-view TEM image of an InAlAs layer grown on InP(001) substrate. The darker areas indicate In-rich regions, and the brighter areas indicate Al-rich regions

are well alternate bright/dark contrast regions in the InAlAs layer. These contrast regions are oriented along the $[1\bar{1}0]$ direction and are not very uniform in width, with a contrast modulation wavelength ranging from 45 to 130 nm. Energy dispersive X-ray spectrometry (EDX) is performed to study the origination of this contrast. According to the In atom content obtained from the EDX measurements, the In composition ranges are calculated to be 0.5–0.53 in the darker regions and 0.46–0.48 in the brighter regions. These alternate In-rich and In-poor (Al-rich) bands reveal that the LCM phenomenon has actually occurred in the InAlAs epilayer grown on InP substrate. On the surface of such composition-modulated InAlAs layer, the tensile strain and compressive strain in the In-rich and Al-rich regions will also lead to morphology undulations on the sample surface [10], which has been evidenced by in situ reflection high energy electron diffraction (RHEED) observations. After the deposition of 500 nm-thick InAlAs layer, the RHEED patterns are V-shaped spots along the $[1\bar{1}0]$ direction and the superposition of streaks and spots along the [110] direction. The different RHEED patterns indicate the appearance of an elongated structure along the $[1\bar{1}0]$ direction on the InAlAs surface [11]. Figure 12.3 presents a typical AFM image of the InAlAs surface, which shows obvious morphology undulations aligned along the [110] direction. The undulations are not very uniform, and some undulations might coalesce or bifurcate. The undulation wavelength obtained from the AFM images ranges from 50 to 140 nm, which is approximate to the modulation wavelength obtained from the TEM measurements.

This LCM effect in InAlAs layer is further confirmed by the optical measurements of the InAs/InAlAs/InP QWR samples. As shown by S. Francoeur et al. [12, 13], an important result from LCM in InAlAs layer is the in-plane optical anisotropy between [110] and $[1\bar{1}0]$ in the vicinity of the band gap. Here, reflectance difference spectroscopy (RDS) is taken to measure the reflectance difference of InAlAs epilayers along two perpendicular directions ([110] and $[1\bar{1}0]$) in the surface plane, i.e., $(r_{110} - r_{1\bar{1}0})/(r_{110} + r_{1\bar{1}0})$ [14], where r_{110} and $r_{1\bar{1}0}$ denote the reflectance for light polarized along the [110] and $[1\bar{1}0]$ directions, respectively.

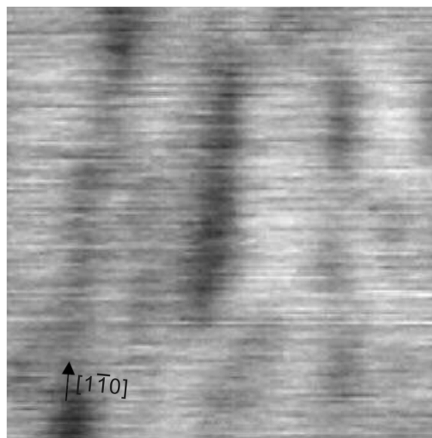

Fig. 12.3 AFM image of an InAlAs surface without InAs deposition. The size of the image is $0.5\,\mu m \times 0.5\,\mu m$

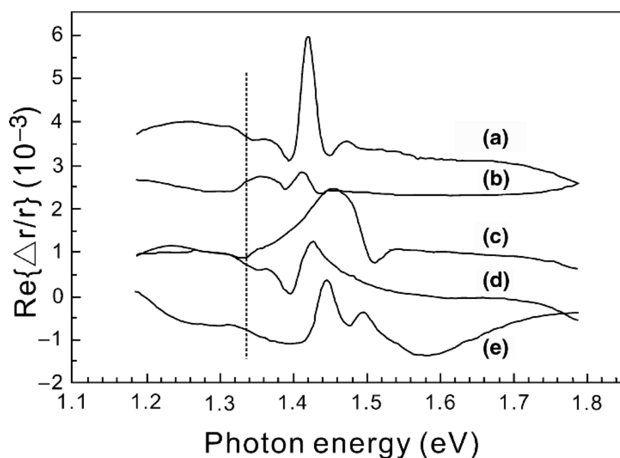

Fig. 12.4 RD spectra of the InAlAs layers measured at room temperature. Spectra (**a**)–(**e**) correspond to InAlAs layer of the samples sequentially shown in Fig. 12.1(**a**)–(**e**)

The RDS results measured at room temperature are shown in Fig. 12.4. Strong resonant structures are observed between 1.38 and 1.52 eV, which can be attributed to the InAlAs band gap. There is also a weak resonant structure at 1.34 eV, indicated by a dashed line, which can be related to the InP band gap. It is known that Cu–Pt ordering can also cause the optical anisotropy between the [110] and $[1\bar{1}0]$ directions [15, 16]. However, TEM and electron diffraction measurements show that there is no Cu–Pt ordering in these InAlAs samples. Therefore, the observed optical anisotropy mainly comes from the LCM effect in InAlAs layers. In the meantime, from AFM and RDS measurements of the samples grown under different growth conditions, a close correlation between the RD intensity of InAlAs and the morphology parameters of InAs nanostructures is established. Figure 12.5 illustrates the ratio of the length to the width of the InAs wire-like structures as a function of the RD intensity of InAlAs layers. Obviously, strong RD intensity of InAlAs layer corresponds to elongated shape of the InAs nanostructures. Because the RD signal is related to the LCM effect in InAlAs layer, this result reveals that the formation of wire-like islands on InAlAs surfaces is related to the LCM effect in InAlAs layers.

Because of the smaller misfit strain energy [10], the regions with tensile strain on the surface of InAlAs layer will provide the preferential nucleation sites for InAs nanostructures. From this point of view, a modified SK growth mode is proposed, as shown in Fig. 12.6. First, at the initial stage of InAs deposition, wire-like wetting layers, instead of a planar wetting layer covering the whole substrate surface, are formed on the In-rich regions. The sizes of the wetting layers might not be uniform because of the nonuniformity of the composition modulation. Then, as more InAs is deposited, the accumulated elastic strain in the wire-like wetting layer becomes strong. SK transition will occur on the wire-like wetting layer forming QDs to relax the excess strain. Meanwhile, the number of QDs will increase with increasing InAs layer thickness. Finally, if the InAs coverage goes on increasing, the initial

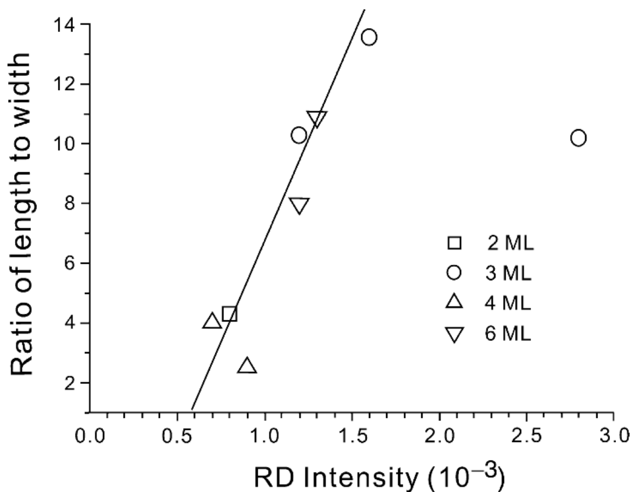

Fig. 12.5 The ratio of the length to the width of the InAs wire-like structures formed under variant InAs deposition thickness as a function of the RD intensity of InAlAs layer underlying the corresponding InAs layer

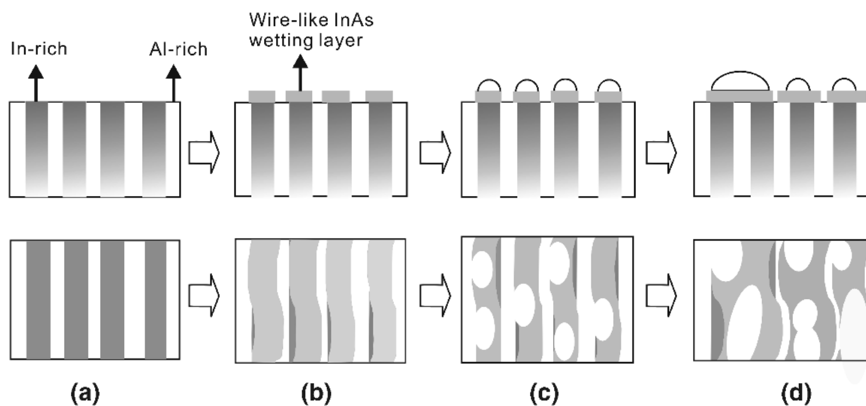

Fig. 12.6 Schematic diagram of the modified SK growth mode that occurs on a composition modulation surface: (**a**) composition-modulated InAlAs layer, (**b**) wire-like InAs wetting layer formed on top of the In-rich areas, (**c**) elongated QDs formed on the wire-like InAs wetting layer, (**d**) coalescence of wire-like wetting layer and QDs respectively. The first row is the cross-section view; the second row is the top view

formed wire-like wetting layer might coalesce and become wider, thus its lateral domination on the QDs is weakened. Here, the newly created QDs on the wider wire-like wetting layer might not be strictly aligned along the $[1\bar{1}0]$ direction. The coalescence of QDs with different orientation on the wires leads to formation of larger and longer dots with irregular shape. This modified SK growth mode is energy favorable if the growth occurs on a composition-modulated layer. In this case, the pitch period λ of the wire-like wetting layer is expected to approximately equal

to the modulation wavelength of the InAlAs layer. However, it is noted that the nonuniform strain distribution of LCM will also lead to a surface undulation, which is indeed observed in our experiments. It is believed that composition modulation can couple with a surface undulation with identical wavelength or one half wavelength [17]. The combined effect of the LCM and surface undulation will probably lead to the formation of InAs QWR with the pitch period λ to be one half of the wavelength of the LCM. That is probably the reason for the discrepancy between the λ value of the InAs QWRs, about 25 nm for all samples, and the wavelength of LCM ranging from 45 to 130 nm.

This modified SK growth mode is further confirmed by the growth of InAs nanostructures on InAlAs layers with strengthened and weakened LCM effect in it [18, 19]. Figure 12.7 shows the $[1\bar{1}0]$ and [110] cross-sectional dark-field (DF) TEM images of InAs/InAlAs nanostructures grown on normal and misoriented (8° off (001) toward (111)) InP(001) substrates [18]. The samples are composed of a 300 nm-$In_{0.5}Al_{0.5}As$ buffer layer, six periods of 4 ML-InAs/15 nm-$In_{0.5}Al_{0.5}As$ and an 80 nm-$In_{0.5}Al_{0.5}As$ cap layer. Both the DF TEM images are obtained with $g = 002$ reflection, which is more sensitive to composition than strain. So, the contrast is mainly attributed to the composition difference. The bright and dark regions in InAlAs buffer layers in Fig. 12.7 correspond to In-rich and Al-rich regions, respectively. As shown in Fig. 12.7a, there are some LCM effect existed in the InAlAs buffer layer, which leads to the formation of InAs QWRs in the sample. However, it is observed that the LCM effect in the InAlAs buffer layer grown on the misoriented

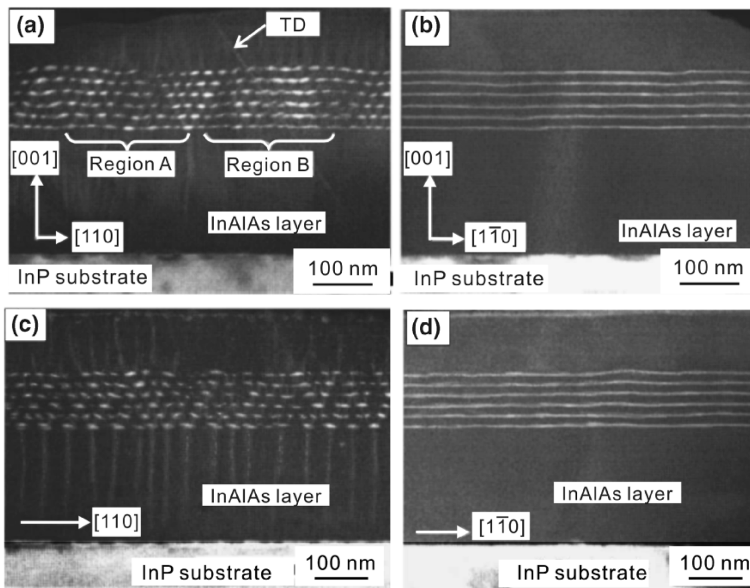

Fig. 12.7 $g = 002$ dark-field $[1\bar{1}0]$ and [110] cross-sectional TEM images for the sample grown on normal InP(001) ((**a**) and (**b**)) and misoriented InP(001) substrate ((**c**) and (**d**)). Note that within the epilayer in Fig. 12.7(**a**), threading dislocation (TD) is visible as indicated by the arrow

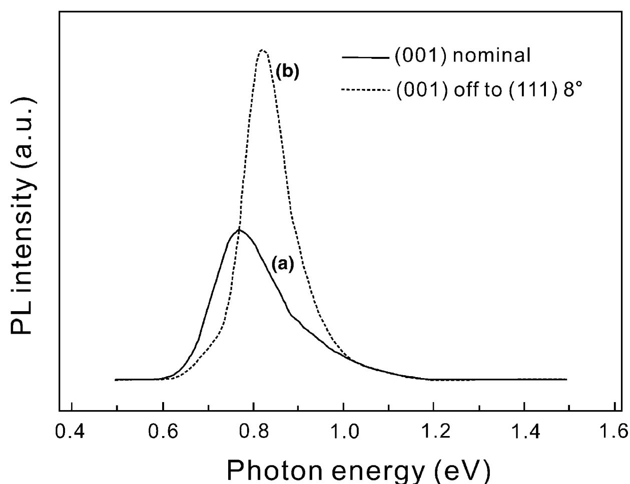

Fig. 12.8 The 77 K PL spectra of the as-grown samples. Curves (**a**) and (**b**) correspond to the samples grown on the normal and misoriented InP(001), respectively

InP substrate is greatly strengthened. As shown in Fig. 12.7c, well alternate In-rich and Al-rich bands are developed in the InAlAs buffer layer. This reveals that obvious LCM along the [110] direction has occurred in the InAlAs buffer layer. These In-rich bands are perpendicular to the growth surface and extend along the $[1\bar{1}0]$ direction. The width and period of these In-rich bands are about 10 and 40 nm, respectively. The origin of this strong LCM effect in the InAlAs buffer layer can be mainly attributed to the bunching of surface steps, which has been discussed by Wang et al. [18]. Because of the small misfit-energy, the In-rich bands will provide the preferential nucleation sites for InAs nanostructures. So, these well alternate In-rich and Al-rich regions provide a good growth template for the InAs nanostructures, which greatly reduces the random nature of SK growth model and leads to a very homogeneous size distribution for InAs QWRs. Figure 12.8 shows the 77 K photoluminescence (PL) spectra of InAs QWRs grown on the nominal and misoriented InP(001) substrates. And, the full widths at half maximum (FWHMs) of the PL spectra are 182 and 123 meV for InAs QWRs grown on the nominal and misoriented InP substrates, respectively. The small PL FWHM of InAs QWRs grown on the misoriented InP substrate indicates a homogeneous size distribution for InAs QWRs, which further confirms the important role of the LCM in InAlAs layer. In addition, the linear density of the second-period InAs QWRs is approximately two times of that of the first-period InAs QWRs, which is mainly induced by the very large lateral period of In-rich bands in InAlAs buffer layer. Usually, because of the small misfit strain energy the meeting point of the V-like In-rich arms in InAlAs spacer layers will provide preferential nucleation sites for the InAs QWRs in the subsequent layer. For the certain angle $(\sim 61^\circ)$ between the In-rich arms and the (001) surface here, the V-like In-rich arms in InAlAs spacer layer originated from the first-period InAs QWRs will meet about 30 nm above the first-period InAs

QWRs because of the larger lateral period of In-rich bands in the InAlAs buffer layer ($\sim$33 nm). So, if the InAlAs spacer layer thickness were 30 nm, the density of the second-period InAs QWRs would be the same as that of the first-period InAs QWRs. However, because the InAlAs spacer layer thickness here is only 15 nm, the V-like In-rich arms in InAlAs spacer layer will not meet on the surface of the first-period InAlAs spacer layer. Like the meeting point of the V-like In-rich arms, the unmet In-rich arms in the InAlAs spacer layer will also provide preferential sites for InAs QWRs in the next layer, resulting in the double density for the second period InAs QWRs.

In the meantime, the LCM effect in InAlAs layer can also be weakened by growing As-pressure-modulated (As-rich and As-poor) InAlAs multilayer structure (AM-InAlAs-MLS) [19]. The structure and growth details of the sample investigated have been reported elsewhere [19]. Figure 12.9 shows the AFM images of the InAs nanostructures grown on InAlAs buffer layers with different periods of AM-InAlAs-MLS. As shown in Fig. 12.9a, InAs QWRs along the $[1\bar{1}0]$ direction are formed on conventional InAlAs buffer layer. When two periods of AM-InAlAs-MLS are inserted before the InAs deposition, InAs QWRs and some QDs were obtained, as shown in Fig. 12.9b. As show in Fig. 12.9c, the introduction of four-period AM-InAlAs-MLS leads to the formation of elliptical dots elongated along

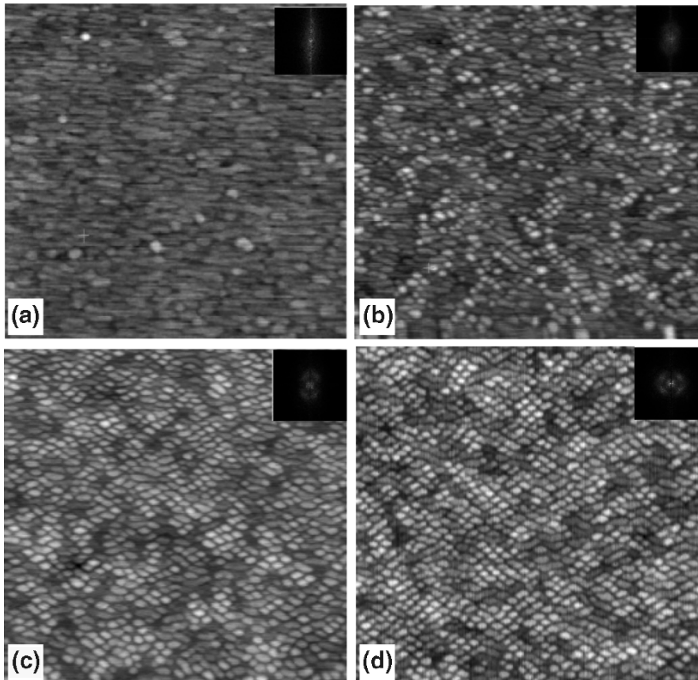

Fig. 12.9 1 μm × 1 μm AFM images of InAs nanostructures grown on AM–InAlAs multilayer structures with the period number of (**a**) 0, (**b**) 2, (**c**) 4, (**d**) 6. The insets show the Fourier transform spectra of AFM images

the $[1\bar{1}0]$ direction, with the average lateral size and height of the dots being 32.4 and 4.18 nm, respectively, and the density being $9.21 \times 10^{10}\,cm^{-2}$. In Fig. 12.9d, the use of six period AM-InAlAs-MLS produces circular InAs QDs, the average width and height of the InAs QDs being 30.5 and 3.77 nm, and the density of the QDs being about $1.16 \times 10^{11}\,cm^{-2}$. It is obvious that, with increasing the AM-InAlAs-MLS period number, the morphology of the InAs nanostructures changes from QWRs into mixed nanostructures including QDs and QWRs, then elliptical QDs, and finally circular QDs. Meanwhile, the nanostructure size becomes smaller and their density gets higher. These results reveal that the As-lacking InAlAs layers can suppress the formation of wire-like nanostructures and favor the formation of high-density InAs QDs. Then, what leads to this interesting experimental phenomenon? An important factor, LCM effect, should be considered. As discussed earlier, the LCM effect in InAlAs layer can cause the morphological undulations and anisotropic strain field on the surface of InAlAs layer [20, 21], which could lead to the transition from QWRs into QDs. As shown by Priester et al. [22], the phase separation can be affected by the surface ridges of the buffer layer. The InAlAs layers grown under normal As-rich conditions by MBE have a surface with (2×4) reconstruction [23]. And, the InAlAs surface contains As dimers and tiny ridges aligned along the $[1\bar{1}0]$ direction [9], which will induce the LCM in InAlAs layer with In-rich regions oriented along the $[1\bar{1}0]$ direction. So, When InAs layer is deposited, In adatoms diffuse preferentially along the $[1\bar{1}0]$ direction and InAs QWRs are formed [9], which is demonstrated in Fig. 12.9a. However, the InAlAs layers grown under As-poor conditions show a surface with (4×2) reconstruction [23]. This (4×2) surface reconstruction will create As dimers [24] and surface ridges [25, 26] along the [110] direction, which will result in a morphology undulation and strain field along the [110] direction. As a result, on (4×2) reconstructed surface, the InAs islands will prefer nucleation and growth along the [110] direction. Hence, by inserting several AM-InAlAs-MLS layers before the deposition of InAs layers, one can balance the effect of the two kinds of surface reconstruction ((2×4) and (4×2)), which leads to the formation of InAs QDs. In our case, with increasing the number of AM-InAlAs-MLS period, when the effect of the As-lacking InAlAs layers is strong enough compared with that caused by the As-rich InAlAs layers, InAs QDs are obtained, as shown in Fig. 12.9c.

All the earlier-mentioned experimental results and analysis demonstrate that the LCM in InAlAs layers plays a very important role in the formation of InAs/InAlAs nanostructures on InP(001) substrate, which further confirms the modified SK growth mode proposed.

12.3 Spatial Correlation of InAs Quantum Wire Superlattices

For practical device applications, vertical stacking of layers containing nanostructures (nanostructure superlattices) is usually used instead of single layer nanostructures. For nanostructure superlattices, the spatial correlation of the nanostructures is very important, which may influence their structural, optical, and electrical properties.

12.3.1 Vertical Anticorrelation of InAs Quantum Wire Superlattices

For InAs/GaAs QDs system [27], InAs QD superlattices demonstrate vertical correlation, as shown in Fig. 12.10. This vertical correlation of InAs/GaAs QD superlattices can be explained by elastic strain field distribution on the surface of spacer layers [27, 28].

However, InAs/InAlAs QWR superlattices show a special spatial correlation, which is completely different from that of InAs/GaAs QD superlattices. Figure 12.11 shows the typical $[1\bar{1}0]$ cross-sectional TEM images of a sample with $InAs/In_{0.52}Al_{0.48}As$ QWR superlattices grown on InP(001) substrate [29]. It is observed that InAs QWRs are diagonally aligned along the [001] growth direction in the InAs/InAlAs QWR superlattices. InAs QWRs in the upper layer are centered in the interstice of QWRs of previous layer, which forms so-called "vertical anticorrelation" [30, 31]. From the point of experiments, this vertical anticorrelation is caused by the LCM in InAlAs spacer layer. As shown in Fig. 12.11, there is obvious LCM effect in the InAlAs spacer layers. The LCM in the InAlAs spacer layers forms V-like In-rich InAlAs arms above the QWRs, which has also been observed in other researches [5, 18]. The meeting points of these V-like In-rich arms will provide adequate nucleation sites for new InAs QWRs in the next plane of stacked structure, taking into account the smaller misfit strain energy, leading to the vertical anti-correlation of QWR superlattices.

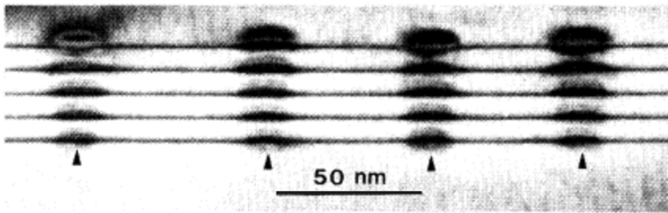

Fig. 12.10 Typical $g = 200$ dark-field cross-sectional TEM images of a sample with five sets of InAs QDs separated by 36 ML GaAs spacer layer

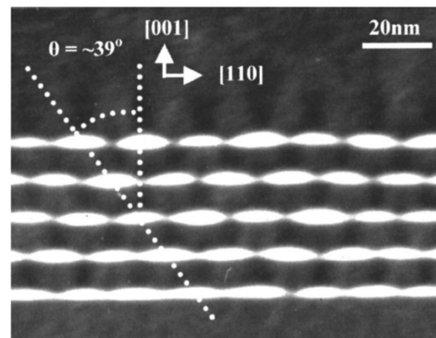

Fig. 12.11 Typical $g = 002$ dark-field $[1\bar{1}0]$ cross-sectional TEM image of a sample with InAs/InAlAs QWR superlattices grown on InP (001) substrate

Theoretically, such vertical anticorrelation in InAs/InAlAs QWR superlattices may be explained with numerically calculation of the strain distribution around an InAs wire using finite element method based on a simple model [30]. From the cross-sectional TEM images shown in Fig. 12.11, it can be seen that the width-to-height ration of the InAs wire can be around 3–5 or even larger, and its effect on strain distribution may be similar to that produced by an elastically strained ribbon in far regions in the matrix. Therefore, in the calculation, the wire section is approximated with a line segment of L_0 in original length in an isotropic two-dimensional matrix of indefinite dimension. The line segment in the figure is homogeneously stretched by 3% in length, which is equal to the mismatch between InAs and $In_{0.52}Al_{0.48}As$ matrix as well as InP substrate, and the region surrounding the line is elastically distorted to some extent. The calculated angular distribution of the elastic distortion above the stretched line segment is shown in Fig. 12.12. Figure 12.12a and b show the calculated elastic distortion d_x and d_y around the line segment with 3%

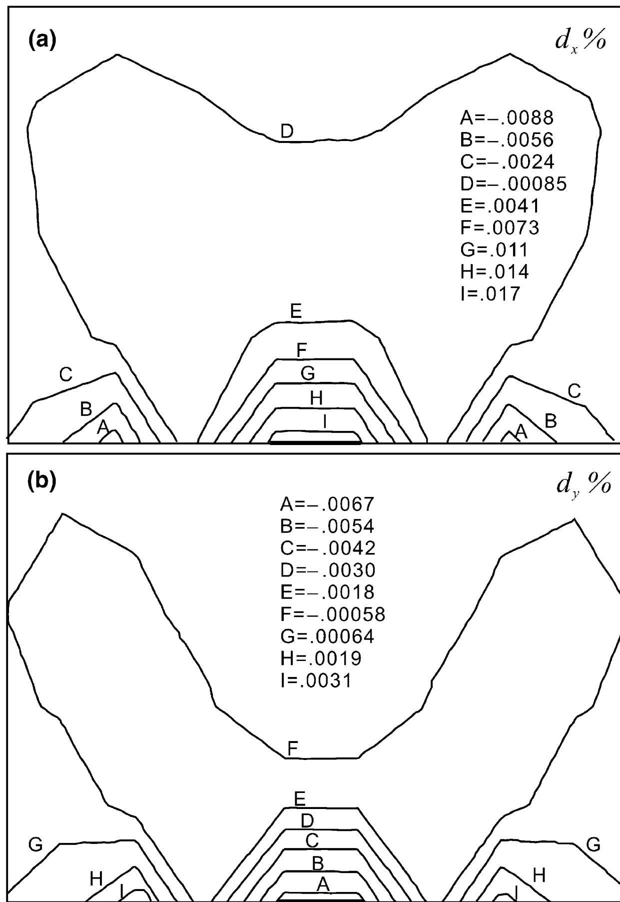

Fig. 12.12 Calculated elastic distortion d_x and d_y around the QWR. (**a**) d_x, distortion in the x-direction; (**b**) d_y, distortion in the y-direction. The thick short lines represent the QWR

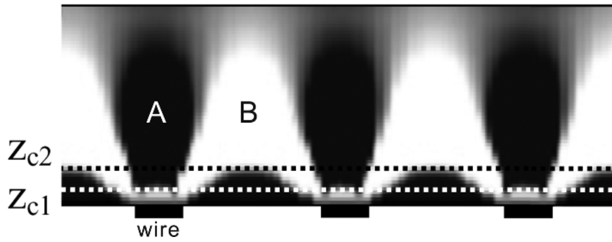

Fig. 12.13 Distribution of the strain component ε_{xx} in a two-dimensional (2D) QWR array calculated with $w = d/4$ in isotropic medium, where w and d are the width and lateral period of the QWRs, respectively. The dark denotes compressive region while the white denotes tensile region. The rectangles represent the 2D QWRs schematically

elastic extension in the matrix. The figures show that the maximum elastic distortion is not directly above the wire but staggers away, and the strain angular distribution is skew away from the wire's top. Although the calculation is performed for the matrix with infinite dimension, the results may be appropriate to the practical situation if the influences of the boundary and the interaction between the extended segments are not significant. During the epitaxial growth of strained InAs film on InAlAs spacer layer, QWRs will nucleate and grow in the region where the values of the components of the elastic strain field are maximum. As calculated, the strain maximum in each InAs layer is staggeringly arranged and, as experimentally observed, the InAs QWRs are indeed diagonally arranged in the multilayer structure [18, 29–31]. Therefore, the calculation is consistent with the experimental observation.

The strain distribution around an embedded quantum wire was also calculated using the Airy stress function, and Fig. 12.13 shows the calculated distribution of strain components ε_{xx} around InAs QWRs, where x is the direction along the array of QWRs [32, 33]. It can be seen from the figure that with the increase in the distance away from the QWR array, the material in the region A is first laterally stretched ($\varepsilon_{xx} > 0$) and then becomes laterally compressed ($\varepsilon_{xx} < 0$). There exists a critical value z_{c1} at which the strain ε_{xx} changes from tensile to compressive. In contrast, the material in the region B is first laterally compressed and then becomes laterally stretched. Another critical value z_{c2} can be defined in this region. The calculated strain distribution implies that when it is buried deeply enough, the 2D QWR array will produce compressive surface regions right above the QWRs and stretched surface regions above the interstices between QWRs, resulting in the vertical anticorrelation of QWRs in a multiple layer structure.

12.3.2 Effect of Growth Mode on the Symmetry of Wire Arrangement

As for the growth of self-assembled InAs QWRs on InP substrate, the deposition of InAs layers can be performed in both conventional MBE and Migration enhanced epitaxy (MEE) growth modes. The distinction between these two epitaxial modes

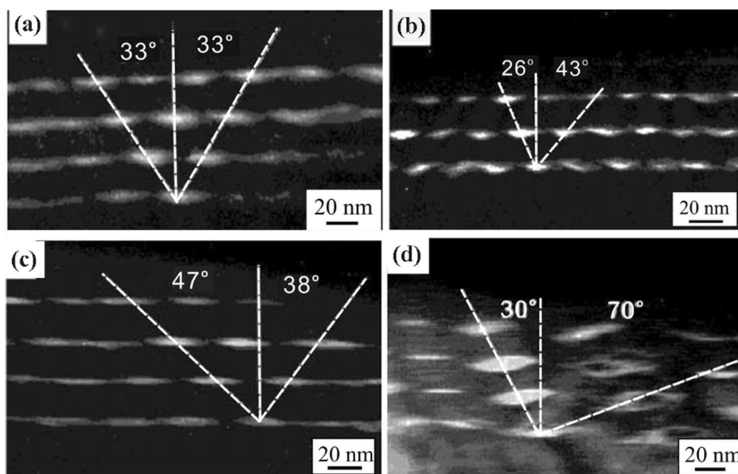

Fig. 12.14 Dark-field [1$\bar{1}$0] cross-sectional TEM images of InAs/InAlAs QWRs: (**a**) MBE, 8 ML InAs on InP(001); (**b**) MBE, 8 ML InAs on InP mis-oriented from (001) by 6°; (**c**) MEE, 8 ML InAs on InP(001); (**d**) MEE, 10 ML InAs on InP(001)

is that for the MBE mode the group III and V elements are deposited simultaneously on the growing surface, while for the MEE mode the group III element and the group V element are deposited in succession to enhance the migration of the group III adatoms on the growing surface [34]. Such an enhancement in migration is generally believed to improve the surface morphology of the flat epitaxial film. Growth mode has some influence on the structural properties of QWR array in InAs/InAlAs/InP(001) system [35]. Figure 12.14 shows the [1$\bar{1}$0] cross-sectional TEM images of InAs QWRs array grown by both MBE and MEE modes. The images of MBE-grown InAs/InAlAs QWR array on InP(001) are shown in Fig. 12.14a, where the deposited thickness of InAs-layer is 8 ML. The InAs QWRs in the array are stacked along the direction away from the [001] growth direction on either side by about 33°, and the QWR array is symmetrical about the [001] growth direction. However, such symmetry in the MBE-grown QWR array on InP(001) is disrupted when the InAs/InAlAs QWRs are grown on a misoriented substrate or grown with MEE mode on InP (001) substrate. Figure 12.14b shows the image of the unsymmetrical InAs wire array grown on the InP substrate with 6°-misoriented from (001) towards (111) by MBE mode. And, the angles between the growth direction and wire alignment are 26° and 43° on the two sides in the figure, respectively. Figure 12.14c is the unsymmetrical MEE-grown InAs(8 ML)/InAlAs(15 nm) wire array on InP(001) substrate, and the angles between (001) and the wire alignment are 47° and 38°, respectively, on the two sides. Figure 12.14d shows the unsymmetrical MEE-grown InAs(10 ML)/InAlAs(15 nm) wire array, and the slanting angles are 30° and 70°, respectively. Obviously, as the thickness of InAs layer is increased from 8 to 10 ML, the asymmetry in the MEE InAs wire alignment is enhanced.

In addition, the QWR cross-section shape in Fig. 12.14d is apparently distorted from a symmetrical one about the [001] growth direction.

The [001] direction is symmetrical in bulk crystallography and it is easy to understand that the MBE-grown InAs QWR array on InP(001) substrate is symmetrical about the growth direction and that the symmetry is disrupted when the material is grown on misoriented InP(001) substrate. However, the asymmetry in the alignment of the MEE-grown InAs QWR array on the exact InP(001) substrate is worth of some discussion.

The main difference between MBE and MEE growth modes is that the surface atomic diffusion during growth is significantly enhanced in MEE mode relative to that in MBE mode. The asymmetry in the MEE-grown InAs QWR array may be related to the enhanced diffusion kinetics, and the mechanism is proposed as follows.

Figure 12.15 presents a schematic cross-section of an InAs QWR under self-assembling during MBE epitaxial growth. The hills at both side A and side B in the figure are built up with terraces and steps in atomic scale. Uphill migration of adatoms randomly deposited on the growing surface is necessary for the QWR to self-organize and the driving force for adatom's ascending motion is strain energy, as an In atom incorporated on a atop site would be in a more relaxed strain state. If the terraces and steps on sides A and B are different from each other in the atomic structure, the energy barriers for the ascending adatoms will be different and the upwards motion is biased with more adatoms migrating up the hill from the side with the smaller energy barrier. This biased uphill motion of adatoms may lead to the asymmetry in the MEE-grown InAs QWR array on the exactly (001) oriented substrate.

Indeed, the steps on the hills A and B are different from each other in atomic structure. Figure 12.16 demonstrates a structural model of the (2×4) GaAs(001) reconstructed surface in α-phase [36]. The reconstructed InAs surface may be

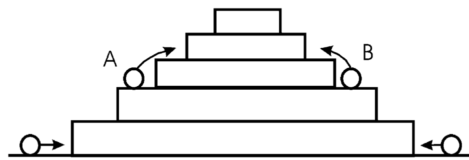

Fig. 12.15 Schematic cross-section of an InAs wire

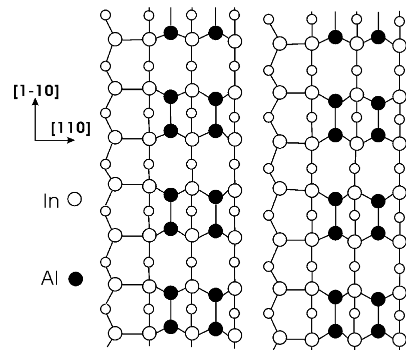

Fig. 12.16 Structural model of the (2×4) reconstructed GaAs surface

similar to the (2×4) GaAs(001) reconstructed surface in atomic structure [35]. A long terrace of 1 ML height along the $[1\bar{1}0]$ direction should be formed with the complete (2×4) unit cells to keep charge neutral. Therefore, the two edges of a terrace should be different from each other in atomic structure due to surface reconstruction, resulting in different energy barriers for ascending atoms up hills A and B. With more adatoms ascending up the hill from the side with the smaller energy barrier, the wire cross section would be distorted from the symmetrical one and the resulting angular distribution of the mismatch strain is not symmetrical about the growth direction. Eventually, the asymmetrical strain distribution produces the asymmetry for the InAs QWR array on the InP(001) substrate.

For the MBE growth mode, the atomic diffusion is greatly reduced compared with that in the MEE mode and the effect proposed above may be neglected. So, the MBE InAs wire array seems symmetrical about the [001] growth direction.

12.3.3 Uniform InAs Quantum Wires Formed by Using Strain Compensating Technique

Generally, for InAs/InAlGaAs/InP nanostructure system, the generated tensile strain due to the deposition of InAs layer cannot be compensated completely by the growth of spacer layers lattice matched to InP substrate, which may influence the quality of InAs nanostructures growing in the subsequent layer. By introducing compressive InAlGaAs spacer layer whose lattice constant is slightly smaller than that of InP substrate, it would be possible to compensate the residual strain. Therefore, by adjusting the composition of InAlGaAs spacer layer, the quality of InAs QWRs can be greatly enhanced and a uniform InAs QWRs array may be achieved [37].

Figure 12.17 shows the AFM image of InAs nanostructures grown on InAlGaAs matrix with appropriate composition. The sample structure and growth details have been reported elsewhere [37]. As shown in Fig. 12.17, high quality InAs QWRs are

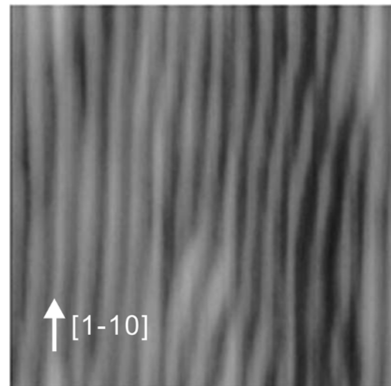

Fig. 12.17 Typical 0.4 μm × 0.4 μm AFM image of InAs QWRs grown on InAlGaAs/InP(001)

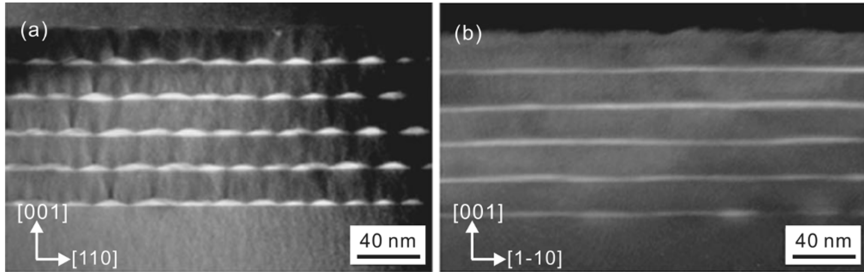

Fig. 12.18 $g = 002$ dark-field $[1\bar{1}0]$ and [110] cross-sectional TEM images of InAs QWRs grown on InAlGaAs/InP(001)

formed on the sample surface, which are aligned along the $[1\bar{1}0]$ direction. These QWRs demonstrate a uniform width, and most of them are more than 500 nm long. This high quality InAs QWRs is difficult to obtain by conventional growth methods.

The $g = 002$ DF cross-sectional TEM images of the sample is shown in Fig. 12.18. Obviously, the InAs/InAlGaAs QWR superlattices also present a vertical anticorrelation, which is the same as that of InAs/InAlAs QWR system. This kind of vertical anticorrelation can also be attributed to the LCM in the InAlGaAs spacer layers. As shown in Fig. 12.18a, there is obvious LCM in the InAlGaAs spacer layers, which is indicated by variation in contrast (where bright and dark regions correspond to In-rich and Al- or Ga-rich regions). The LCM also forms V-like In-rich InAlGaAs arms above the InAs QWRs in InAlGaAs spacer layer. Because of the smaller misfit strain energy, the meeting points of these V-like In-rich arms will provide adequate nucleation sites for new InAs QWRs in the next layer of the stacked structure, leading to the formation in vertical anti-correlation in InAs/InAlGaAs QWR superlattices.

12.3.4 Effect of Alloy Phase Separation in Spacer Layers on Spatial Correlation

As discussed earlier, the spatial correlation of InAs/InAlAs QWR superlattices is mainly determined by the LCM effect in InAlAs spacer layers. So, different LCM effect in the InAlAs spacer layers can lead to different spatial correlation for InAs/InAlAs nanostructure superlattices [38].

Figure 12.19 shows the $g = 002$ DF cross-sectional TEM images of InAs/InAlAs nanostructures obtained under different As overpressure (1×10^{-5}, 5×10^{-6}, and 2.5×10^{-6} Torr) during the MBE growth of InAs layers. The samples are composed of a 200 nm-$In_{0.52}Al_{0.48}As$ buffer layer, six periods of 3 ML-InAs/15 nm-$In_{0.52}Al_{0.48}As$ and an 80 nm-$In_{0.52}Al_{0.48}As$ cap layer. All the InAlAs layers are grown under an As overpressure of 5×10^{-6} Torr. As shown in Fig. 12.19, the shape of the InAs islands is quite different depending on the As overpressure during the growth of InAs layers. For the InAs layers grown under 1×10^{-5} Torr As

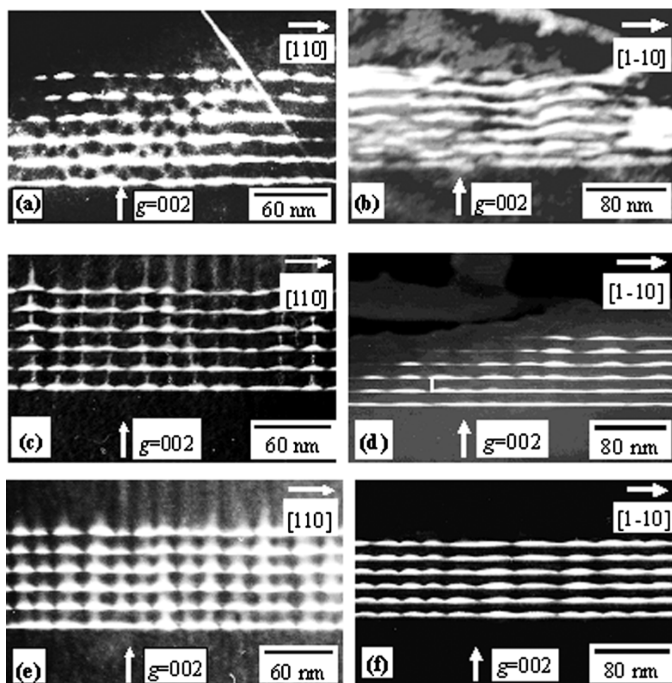

Fig. 12.19 $g = 002$ dark-field $[1\bar{1}0]$ and [110] cross-sectional TEM images of the samples. (**a**) and (**b**) for the sample in which InAs nanostructures are grown under 1×10^{-5} Torr As overpressure; (**c**) and (**d**) for the sample in which InAs nanostructures are grown under 5×10^{-6} Torr As overpressure; (**e**) and (**f**) for the sample in which InAs nanostructures are grown under 2.5×10^{-6} Torr As overpressure

overpressure, InAs QWRs oriented along the $[1\bar{1}0]$ direction are formed. When the As overpressure is decreased to 5×10^{-6} or 2.5×10^{-6} Torr, InAs QDs elongated along the $[1\bar{1}0]$ direction are obtained. In the meantime, as the As overpressure is decreased, the size of InAs nanostructures along the $[1\bar{1}0]$ direction is decreased from $\sim$200 to $\sim$25 nm, while their [110]-oriented sizes are kept around 16–18 nm. It seems that the As overpressure has little effect on the base width and lateral periodicity along the [110] direction of the InAs islands here. This is in contrast to the InAs/GaAs QD system, where As overpressure exhibited significant influence on the size and density of the islands [39]. This insensitivity can also be attributed to the LCM effect in the InAlAs buffer layer [4]. This experiment further confirms the modified SK growth mode proposed.

As shown in Fig. 12.19, quite different spatial correlations of the InAs nanostructure superlattices are observed for the samples. For InAs nanostructures grown under 1×10^{-5} Torr As overpressure, the InAs/InAlAs QWR superlattices show strong vertical anticorrelation, i.e., the QWRs of upper layer are centered in the interstices of QWRs of the previous layer. As to InAs nanostructures grown under 5×10^{-6}

and 2.5×10^{-6} Torr, the InAs/InAlAs QD superlattices exhibit vertical correlation, i.e., the QDs of upper layer are located just above QDs of the previous layer.

Previous works based on elastic properties (anisotropic/isotropic) of the matrix material predict that spatial correlation of QWR superlattices can be turned from vertical anticorrelation to vertical correlation by changing space layer thickness or island size [28, 40]. However, the vertical correlation in InAs/InAlAs QWR superlattices is not observed experimentally despite the endeavor of Li et al. and Brault et al. [5, 41]. As for the spatial correlation of InAs/InAlAs nanostructure superlattices, it is determined not by the elastic properties of matrix, but mainly by the alloy decomposition in space layers [5, 42]. The TEM results shown in Fig. 12.19 confirm the close relation between the alloy phase separation and the spatial correlation of nanostructures. From Fig. 12.19a, c, and e, one can observe the fine alternate bright/dark contrast regions in the InAlAs spacer layers, which reveals a LCM along the [110] direction. And, the brighter/darker regions are In-rich and Al-rich, respectively. For InAs nanostructures grown under 1×10^{-5} Torr As overpressure, the LCM in InAlAs space layers forms V-like In-rich InAlAs arms above the QWRs. The meeting points of these V-like In-rich arms will provide preferential nucleation sites for new InAs QWRs in the next plane of stacked structure taking into account the smaller misfit strain energy [5, 29, 43], leading to the formation of vertical anticorrelation for QWR superlattices. However, as to InAs nanostructures grown under 5×10^{-6} and 2.5×10^{-6} Torr, the alloy phase separation in InAlAs space layers forms I-like In-rich arms just above the QDs. These I-like In-rich arms originate from each InAs QD and align along the [001] direction, as shown in Fig. 12.19c and (e). Similar to the V-like In-rich arms in InAlAs space layers of InAs nanostructures grown under 1×10^{-5} Torr As overpressure, these I-like In-rich arms will also provide preferential nucleation sites for new InAs QDs in the subsequent plane of the stacked structure, resulting in the vertical spatial correlation.

In addition, the alloy phase separation triggered by the InAs QWRs and QDs can extend long distance along the growth direction. Figure 12.20 shows the $g = 002\mathrm{DF}[1\bar{1}0]$ cross-sectional TEM images of typical In-rich regions in InAlAs cap layer of the sample in which InAs nanostructures are grown under 2.5×10^{-6} Torr. It is observed that the In-rich bands extend to the sample surface, which is 80 nm away from the topmost InAs layer. This indicates that the vertical correlation of QD superlattices can be kept when space-layer is thinner than 80 nm. Though In-rich regions in InAlAs cap layer of the QWR superlattices cannot be observed clearly in Fig. 12.19a, our previous work on InAs/InAlAs QWR superlattices shows that the V-like In-rich region can extend at least 35 nm along the growth direction [44].

12.3.5 Dislocations in Quantum Wire Superlattice

Lei et al. [45] has discussed the dislocation in QWR superlattices consisting of six layers of InAs separated by 15 nm $In_{0.52}Al_{0.48}As$ space layers with the InAs deposition thickness of 2, 4, and 6 ML. No threading dislocations are observed

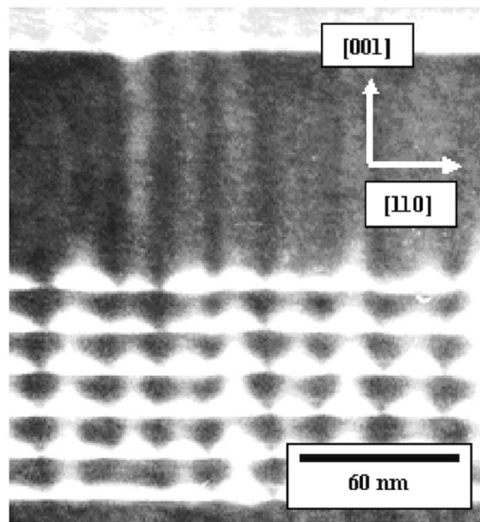

Fig. 12.20 $g = 002$ dark-field $[1\bar{1}0]$ cross-sectional TEM images of typical In-rich regions in InAlAs cap layer of the sample in which InAs nanostructures are grown under 2.5×10^{-6} Torr As overpressure. The image contrast has been enhanced to see the In-rich regions more clearly

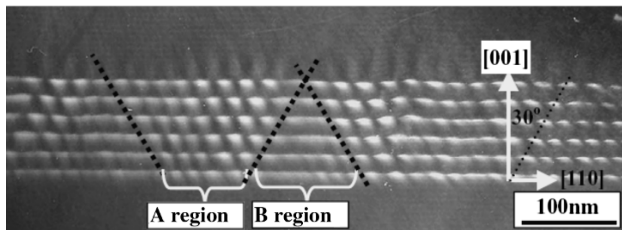

Fig. 12.21 $g = 002$ dark-field $[1\bar{1}0]$ cross-sectional TEM image of the InAs(4 ML)/$In_{0.52}Al_{0.48}As$ (15 nm) QWR superlattices

in the 2 ML and 4 ML-InAs samples, whereas some threading dislocations aligned along the $[11\bar{1}]$ direction are clearly observed in the 6 ML-InAs sample, which were introduced by the large strain accumulated. However, edge dislocations extending along the $[1\bar{1}0]$ direction with the Burgers vector [001]/2 in InAs layer have been observed in the 4 ML-InAs sample by high resolution transmission electron microscopy (HRTEM) [46].

Figure 12.21 shows the $g = 002$ DF cross-sectional TEM image of InAs/InAlAs QWR superlattices. The InAs nanostructures are divided into two regions, A and B, as shown in Fig. 12.21. In the region A, InAs wires are self-assembled along the $[1\bar{1}0]$ direction and the elastic strain due to the 3% mismatch between InP and InAs are partially relaxes along the [110] direction, while the strain components along the $[1\bar{1}0]$ direction are reserved. While in the region B, no InAs wires are formed, and all the components of mismatch strain are stored in the InAs layers.

Figure 12.22 shows the HR chemical lattice fringe image of region A and B in the InAs layer in (1–10) cross-section. The image contrast is obtained mainly by interference between (002) reflection and undeviated beam. The periodic lattice

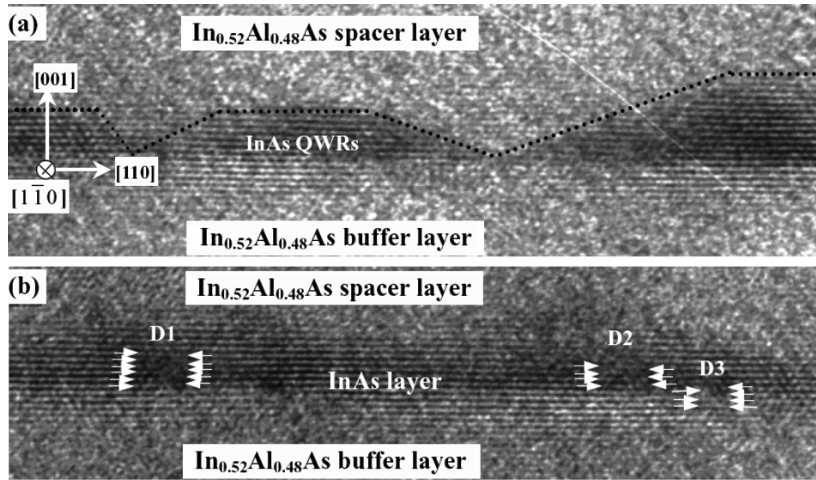

Fig. 12.22 HR chemical lattice images of InAs layer; (**a**) the first period partial InAs nanostructures in region A; (**b**) the first period partial InAs nanostructures in region B, Arrows D1, D2, and D3 point to [001]/2 edge dislocations

fringes correspond to InAs layer, and the amorphous-like region corresponds to InAlAs layer. Figure 12.22a is the HR chemical lattice image of the InAs layer in the first InAs/InAlAs period in region A marked out in Fig. 12.21. It can be seen that defect-free InAs QWRs are bounded by certain growth facets (as indicated by dot-line in Fig. 12.22a). Figure 12.22b is the HR chemical lattice fringe image of the InAs layer in the first InAs/InAlAs period in region B. No wire-like structures are formed in region B. The InAs layer clearly shows quantum well-like structure. However, edge dislocations with the Burgers vector of $[001]/2$ are observed. The edge dislocations are indicated by the arrows and signed as D1, D2, D3, respectively, in Fig. 12.22b. The dislocation lines lie in the (110) plane and extend along the $[1\bar{1}0]$ direction. These dislocations can be identified by counting the number of lattice fringes on each side of the dislocation core.

Burger's vector of $[001]/2$ of the edge dislocations in the InAs layer are along the [001] growth direction and have no component parallel with the interface. Therefore, these edge dislocations make no contribution to the relaxation of elastic strain. Formally, the edge dislocation is formed by inserting an extra half (001) plane into the crystal. The end of the inserted plane in the crystal is the core of the edge dislocation. If the edge dislocations were developed in the elastic strained InAs layer during the nucleation growth process, the material in one side of the dislocation core would be compressed and on another side the material tensioned. The two actions may cancel with each other and no change occurs in the strain energy. However, if the edge dislocations are introduced in the MBE depositing process, the situation will be quite different.

To interpret the presence of the edge dislocations with Burger's vector [001]/2 and extending along the $[1\bar{1}0]$ direction, the following mechanism is proposed for the formation of the edge dislocations here. With the successive deposition of InAs layers during the epitaxial process, the elastic strain in the epilayer is increased to such a high extent that the adatoms are deregistered into the two dimensional growth islands to form the edge dislocation core. All the atomic bonds near the core can be extended to some extent and the mismatch strain is relaxed.

12.4 Optical Properties of Self-Assembled Quantum Wires on InP

12.4.1 Optical Anisotropy

One of the important optical properties of the QWRs is their optical anisotropy, i.e. the optical absorption and/or emission are different for light polarized parallel to or perpendicular to QWRs. For a QWR structure, the optical anisotropy is introduced mainly by a valence-band mixing due to quantum confinement in the lateral direction. Other factors, such as anisotropic strain and anisotropic interface roughness, also contribute to the optical anisotropy of QWRs [47]. The degree of linear polarization P is defined by $p = \frac{I_P - I_\perp}{I_P + I_\perp}$, where $I_P(I_\perp)$ is the intensity of the luminescence polarizing along $[1\bar{1}0]$ ([110]). For self-assembled QWRs formed on the (001) surface, the axis of the wires are usually along the $[1\bar{1}0]$ direction. In this case, the $\perp$ direction is along the [110] direction. Figure 12.23 shows the polarized PL spectra of an InAs/InAlAs/InP(001) QWR sample, which is composed of six layers of InAs (2 ML) separated by 15 nm $In_{0.52}Al_{0.48}As$ spacer layers [48]. The inset shows the DF plane-view TEM image of the sample. Clearly, QWRs aligned along the $[1\bar{1}0]$ direction are formed in the sample. As shown in Fig. 12.23, the degree of linear polarization of the PL peak at 1.12 eV is around 44%, demonstrating the strong optical anisotropy of the QWRs.

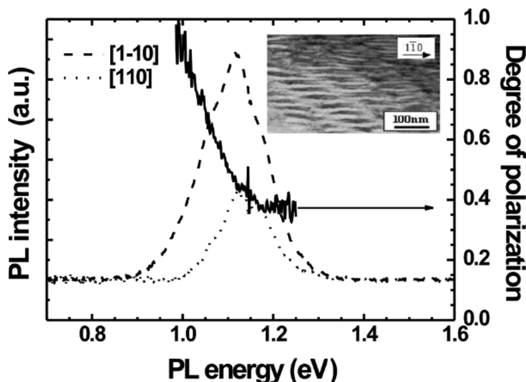

Fig. 12.23 Polarized PL spectra of the sample taken at 77 K. The inset shows the plan-view dark-field TEM images of the sample

12.4.2 Anomalous Temperature Dependence of Interband Transition

Theoretical and experimental investigations show that the magnitude of temperature effect on the band-gap energy of a biaxially strained heterostructure is about the same as that of bulk material. For QDs or QWRs, the PL peak usually shows a fast red-shift with increasing temperature due to the carrier redistribution among the QDs (QWRs) with different sizes [49, 50]. However, a temperature insensitive PL wavelength was observed for some special QWRs structures. Wohlert et al. reported a temperature insensitive PL wavelength for InGaAs/InP strained wires formed by the strain induced lateral-layer ordering (SILO) process [51]. And, the multiaxial strain field in the InGaAs/InP QWRs induced by SILO process was proposed as the possible explanation for the temperature insensitivity of the PL wavelength. The self-assembled InAs/InAlAs QWR nanostructure also exhibit such kind of behavior. Figure 12.24 shows PL spectra of an InAs/InAlAs/InP QWR sample at different temperatures [52]. The sample consists of six layers of InAs QWRs (3 ML) separated by 15 nm $In_{0.52}Al_{0.48}As$ barrier layers. Clearly, the PL spectra are all composed of two dominant peaks. The inset shows the typical AFM image of a sample grown under the same growth condition, in which wire-like InAs structures are clearly observed. Comparing with PL spectra and AFM image, the higher energy PL peaks are attributed to the thin wire-like structures, while the lower energy PL peaks are attributed to the thick wire-like structures. The latter usually locate at the places where two or three thin wires joint.

Figure 12.25 summarizes the shifts of the two PL peaks. With increasing temperature, the higher energy peak shows a red-shift faster than InAs bulk materials,

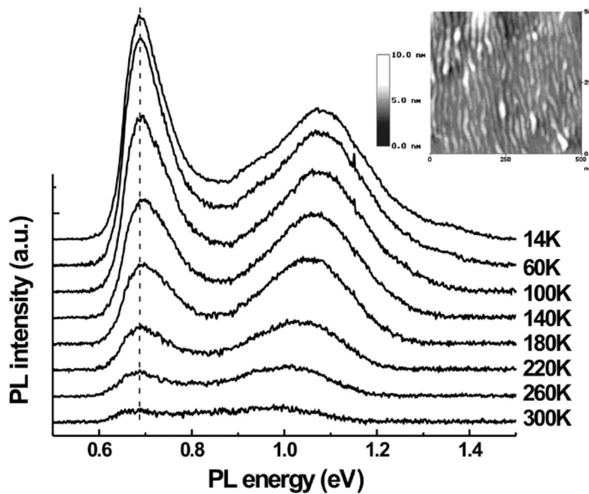

Fig. 12.24 Temperature dependent PL spectra of the sample. The inset shows the typical AFM image of a sample grown under the same growth condition as that of the sample. The size of the AFM image is 0.5 μm × 0.5 μm

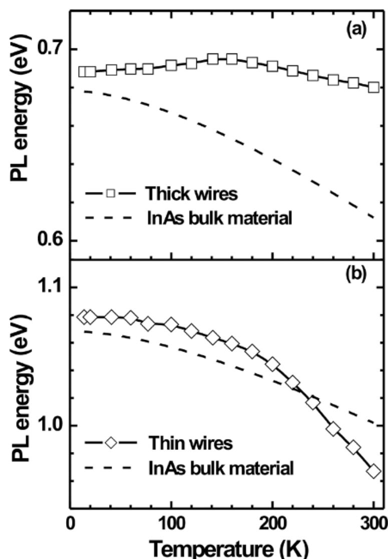

Fig. 12.25 Temperature dependence of the PL peak energies of the thick wires (**a**) and thin wires (**b**) in the sample

which is the common character of the QDs (QWRs) structures and can be attributed to the carriers redistribution among the QWRs with different sizes. As a comparison, the lower energy peak is almost fixed at 0.68 eV. This unusual shift of PL peak is assumed to be related to the thermal strain. Because the linear thermal expansion coefficient of $In_{0.52}Al_{0.48}As$ (4.85×10^{-6} Å/K at 300 K) is larger than that of InP (4.5×10^{-6} Å/K at 300 K) [53], a net thermal compressive strain will be introduced in the InAlAs layers as the temperature increases. This compressive strain in the InAlAs layers is passed to the InAs nanostructures buried in the InAlAs matrix. As shown in the inset of Fig. 12.24, the thick wires, which contribute to the lower energy PL peak, are usually centered at the places where two or three thin wires joint. It means the thick wires can serve probably as the concentrations of force, i.e. the stress transferred through the thin InAs wires can be amplified at the thick wires. In addition, this thermal strain in the thick wires should have a multiaxial nature due to the asymmetric distribution of the surrounding thin InAs wires. It has been reported that the multiaxial asymmetric lattice distortion does not change linearly with temperature and the linear thermal expansion coefficient should also be considered in precise treatment [51, 54]. Therefore, the amplified multiaxial compressive strain can induce a large blue-shift for the PL peak of the thicker wires, which compensates the red shift induced by the increase in temperature.

12.4.3 Phonon Vibration Property

Phonons are important for the carrier relaxation process of QWRs (QDs), especially when the splitting of the energy levels in QWRs (QDs) matches a multiple

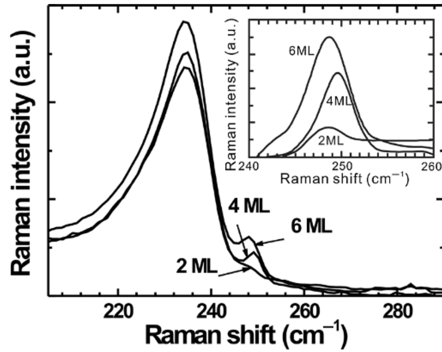

Fig. 12.26 Raman spectra of the samples grown with 2, 4, and 6 ML InAs measured under the $z(x',x'+y')\bar{z}$ configuration. The inset shows the QWR LO phonon peaks after subtraction of the InAs-like background

of the QWR (QD) phonon energy. Because of the two dimensional confinement, QWRs may show vibrational properties different from those of QDs and quantum wells (QWs). So, the knowledge of the phonons in QWRs will be helpful for the understanding of fundamental physics in low dimensional system and their device applications.

Figure 12.26 shows the Raman spectra of InAs/InAlAs/InP(001) QWR samples grown with 2, 4, and 6 ML InAs deposited thickness measured under the $z(x,x+y)\bar{z}$ configuration ($x \| [100], y \| [010], z \| [001], x' \| [1\bar{1}0], y' \| [110]$) [55]. The samples consist of six layers of InAs separated by 15 nm $In_{0.52}Al_{0.48}As$ spacer layers. As shown in Fig. 12.26, all the Raman spectra display one intense peak centered at 235 cm^{-1}, which corresponds to the InAs-like LO mode in the InAlAs matrix [56–58]. Above the InAs-like LO mode peak, the Raman spectra of the samples all display an additional peak whose frequency depends on the sample (249, 250, and 249 cm^{-1} for the sample with 2, 4, and 6 ML InAs deposited thickness, respectively). These three peaks can be attributed to the LO phonon of the InAs QWRs [59]. The QWR LO phonon peak increases in intensity with increasing the InAs deposited thickness due to the increase of In-As bonds in the QWRs. The different frequency shift of the QWR LO phonon peak can be understood by the different strain in the QWRs grown with different InAs deposited thickness [55].

The polarized Raman spectra of the samples are shown in Fig. 12.27 [55]. The QWR LO phonons show an obvious polarization dependence as they are observed in the $z(x',x')\bar{z}$ configuration, but not in the $z(x',y')\bar{z}$ configuration, as shown in Fig. 12.27a and b. This demonstrates that the QWR LO phonons follow the selection rule of the LO phonons in the bulk zinc-blende semiconductors, which is similar to the Raman scattering results on InAs/GaAs QDs [59]. As shown in Fig. 12.27c, the QWR LO phonons and the InAs-like LO phonons in InAlAs matrix of the sample with 6 ML InAs deposited thickness also appear in the $z(x',y')\bar{z}$ polarization configuration, which can be ascribed to the threading dislocations in the sample. The threading dislocations may relax the selection rule of the phonons in both the InAs wires and InAlAs matrix, leading to the appearance of LO phonons in the $z(x',y')\bar{z}$ polarization configuration [55].

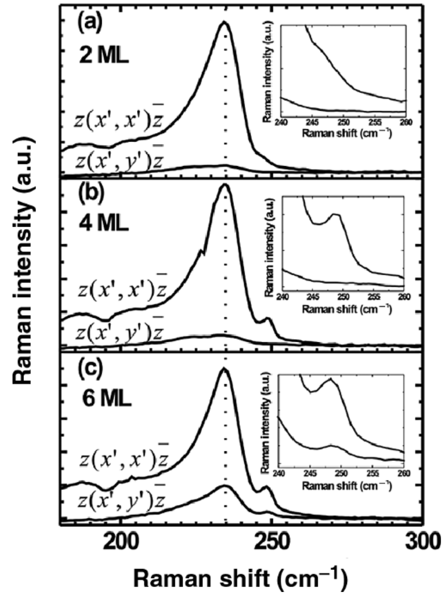

Fig. 12.27 Polarized Raman spectra of the samples: (**a**) the sample grown with 2 ML InAs, (**b**) the sample grown with 4 ML InAs, (**c**) the sample grown with 6 ML InAs. The insets show the partially zoom-in images of the Raman spectra of the samples

12.4.4 Intraband Photocurrent

Theoretically, QWRs allow the absorption of normal-incidence radiation due to their special selection rule of intraband transition [1, 60]. So, QWRs can be used for fabricating infrared photodetectors with normal incidence, which takes advantage of the intraband transition in QWRs. Here, the intraband transition in QWRs is investigated with photocurrent (PC) spectroscopy [61]. Two kinds of infrared light sources (tungsten lamp and globar lamp) are used in the PC measurements. Lateral electrodes with 1.5 mm spacing in between are obtained by alloying the Indium stripe in the sample surface. The electrical fields are applied along the [110] direction. When the PC measurements are performed with a globar lamp, a solid-state laser (532 nm) is used as the pump light source for optical pumping. All photocurrent spectra are measured in a normal incidence configuration.

Figure 12.28 shows the 14 K PL and PC spectra of an InAs/InAlAs/InP(001) QWR sample measured with tungsten lamp. The sample consists of six layers of InAs QWRs (3 ML) separated by 15 nm $In_{0.52}Al_{0.48}As$ barrier layers. The 15 nm InAlAs barriers are composed of 4 nm undoped InAlAs, 2 nm Si-doped InAlAs $(1 \times 10^{18}\,cm^{-3})$ and 9 nm undoped InAlAs. The inset of Fig. 12.28a shows the typical AFM image of a sample grown under the same growth condition, in which wire-like InAs structures are observed. Comparing with PL spectra and AFM image, the higher energy PL peak is attributed to the thin wire-like structures, while the lower energy PL peak is attributed to the thick wire-like structures.

Compared with the PL spectrum, more features are revealed in the PC spectrum, as shown in Fig. 12.28b. The PC features centered at 1.55 and 1.42 eV are from the

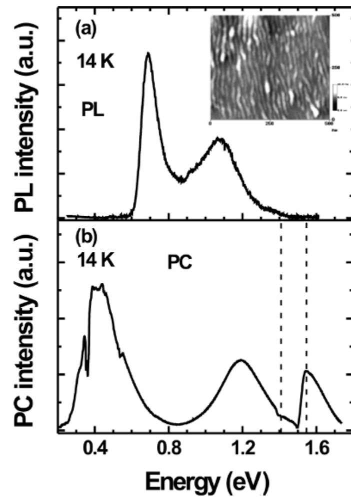

Fig. 12.28 PL (**a**) and PC (**b**) spectra of the sample measured at 14 K. The inset in panel (**a**) shows the typical AFM image of a sample grown under the same condition without cap layer. The size of the AFM image is 0.5 μm × 0.5 μm

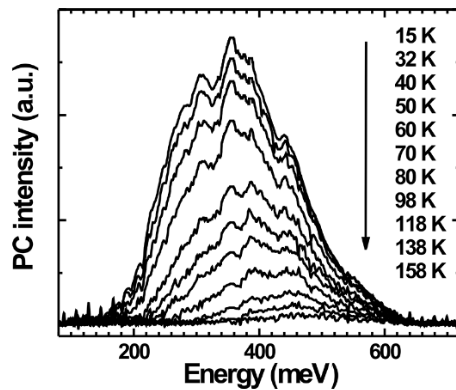

Fig. 12.29 Temperature dependent intraband PC spectra of the sample measured with a globar lamp under a steady interband excitation

interband transition of the InAlAs matrix and InP substrate, respectively. The PC signal ranging from 0.6 to 1.4 eV can be ascribed to the interband transitions of the wire-like InAs structures. Because of the large size distribution of the nanostructures, a large Stokes shift is observed between PL and interband PC peaks of the nanostructures [62]. Besides these PC peaks, there is a broad PC peak located around 0.41 eV, which can be attributed to the intraband transition from the bound states of the InAs wire-like structures to the continuum states of the InAlAs barriers [61]. It should be pointed out that the intraband PC signal in Fig. 12.28b can be observed only when there is an interband excitation (the illumination of the tungsten lamp serves as the interband excitation in Fig. 12.28b), which may be due to the possible deep traps in the sample structure and can be improved by growing high quality sample [61].

For infrared photodetectors, one important parameter is their operation temperature. Figure 12.29 shows the temperature dependent intraband PC spectra of the sample measured with a globar lamp under steady interband excitation. It is

observed that the intraband PC signal decreases with increasing temperature, which can be attributed to the decrease of the lifetime and mobility of electrons and the thermal escape of electrons. In addition, the linewidth of the intraband PC signal decreases and the low energy cut-off of the inraband PC peak shifts to higher energy gradually when the temperature is increased. These changes mainly arise from the thermal ionization of electrons from the thinner InAs wires. Clearly, the intraband PC signal of the InAs QWRs can be observed up to about 160 K, indicating their great potential applications in infrared photodetectors.

12.4.5 Quantum Wire Lasers

Lasers based on self-assembled InAs QWRs or quantum dashes (QDash) grown on InP(001) substrates can extend the lasing wavelength up to 1.55 μm and even above, which is important for the long-wavelength optical fiber communication. The InP-based InAs QWRs or QDashes laser was first reported by Wang et al. in 2001 [63]. In this device the InAs QDash layers were embedded in a compressively strained InAlGaAs waveguides, and then surrounded by InAlAs cladding layers lattice matched to InP substrate. The laser worked in a pulsed mode at room temperature with a ground state lasing wavelength of 1.6 μm and the threshold current density of $410\,\mathrm{A/cm^2}$. By using a dash-in-well structure, in which the InAs QDashes were inserted in a compressively strained InGaAs QWs, the lasing wavelength was extended up to 2.03 μm at room temperature [64]. Room temperature continuous wave (CW) working of the InAs QDash laser was achieved in 2004 [65]. The threshold current density of the laser was below $1.2\,\mathrm{kA/cm^2}$, and the lasing wavelength was about 1.57 μm with a output power of 50 mW per facet and no degradation was found at 10 mW/facet output for over 6500 hours in the aging test [66]. The room temperature CW operating of InAs QWR laser was demonstrated in 2006 [67]. In this QWR laser device, the ground state lasing wavelength was about 1.73 μm and the threshold current showed obvious dependence on the laser cavity orientation. The threshold current of the laser with cavity along the [1–10] direction was larger than that with cavity along the [110] direction, which could be attributed to the different optical gain for different electric field polarization.

12.5 Summary

In this chapter, we briefly present the recent advance in the ordering of InAs QWRs on InP(001) substrates. As reviewed earlier, considerable progress has been made in this field. By tuning the LCM effect in InAlAs spacer layer, the island shape, island density, and spatial correlation can be controlled to a certain extent. And, uniform InAs QWRs with high quality can be achieved by using the strain compensating technology. However, the growth control and optical properties of these QWRs are

still not satisfying and need to be improved further for their device applications, which presents a big challenge to us. To achieve the ideal QWRs, we have a lot of work to do!

Acknowledgments This work was supported by the 973 program (2006CB604908) and the National Natural Science Foundation of China (60390074, 60625402).

References

1. D. Bimberg, M. Grundmann and N.N. Ledentsov, *Quantum Dot Heterostructures*, Wiley, New York, 1999.
2. G. Springholz, V. Holy, P. Mayer, M. Pinczolits, A. Raab, R.T. Lechner, G. Bauer, H. Kang, L. Salamanca-Riba, *Mater. Sci. Eng. B* 88, 143 (2002).
3. Vitaliy A. Shchukin and Dieter Bimberg, *Rev. Mod. Phys.* 71, 1125 (1999).
4. F.A. Zhao, Y.H. Chen, X.L. Ye, P. Jin, B. Xu, Z.G. Wang and C.L. Zhang, *J. Phys: Condens. Matter*. 16, 7603 (2004).
5. J. Brault, M. Gendry, O. Marty, M. Pitaval, J. Olvares, G. Grenet and G. Hollinger, *Appl. Surf. Sci.* 162/163, 584 (2000).
6. D.I. Westwood, Z. Sobiesierski and C.C. Matthai, *Appl. Surf. Sci.* 144/145, 484 (1999).
7. P.B. Joyce, T.J. Krzyzewski, G.R. Bell, T.S. Jones, S. Malik, D. Childs and R. Murray, *J. Cryst. Growth* 227/228, 1000 (2001).
8. R. Songmuang, S. Kiravittaya and O.G. Schmidt, *J. Cryst. Growth* 249, 416 (2003).
9. T. Hashizume, Q.K. Xue, A. Ichimiya and T. Sakurai, *Phys. Rev. B* 51, 4200 (1995).
10. D.E. Wohlert, K.Y. Cheng, K.L. Chang and K.C. Hsieh, *J. Vac. Sci. Technol. B* 17, 1120 (1999).
11. B.H. Koo, T. Hanada, H. Makino, J.H. Chang and T. Yao, *J. Cryst. Growth* 229, 142 (2001).
12. S. Francoeur, Y. Zhang, A.G. Norman, F. Alsina, A. Mascarenhas, J.L. Reno, E.D. Jones, S.R. Lee and D.M. Follstaedt, *Appl. Phys. Lett.* 77, 1765 (2000).
13. S. Francoeur, M.C. Hanna, A.G. Norman and A. Mascarenhas, *Appl. Phys. Lett.* 80, 243 (2002).
14. D.E. Aspnes, J.P. Harbison, A.A. Studna and L.T. Folrez, *J. Vac. Sci. Technol. A* 6, 1327 (1988).
15. L.C. Su, I.H. Ho, N. Kobayashi and G.B. Stringfellow, *J. Cryst. Growth* 145, 140 (1994).
16. P. Ernst, Y. Zhang, F.A.J.M. Driessen, A. Mascarenhas, E.D. Jones, C. Geng, F. Scholz and H. Schweizer, *J. Appl. Phys.* 81, 2815 (1997).
17. F. Glas, *Phys. Rev. B* 62, 7393 (2000).
18. Y.L. Wang, P. Jin, X.L. Ye, C.L. Zhang, G.X. Shi, R.Y. Li, Y.H. Chen and Z.G. Wang, *Appl. Phys. Lett.* 88, 123104 (2006).
19. X.R. Yang, B. Xu, L.Y. Liang, C.G. Tang, Y.Y. Ren, X.L. Ye and Z.G. Wang, *Nanotechnology* 18, 215302 (2007).
20. B. Shin, A. Lin, K. Lappo and R.S. Goldman, *Appl. Phys. Lett.* 80, 3292 (2002).
21. R.S. Goldman, B. Shin and B. Lita, *Phys. Status Solidi a* 195, 151 (2003).
22. C. Priester and G. Grenet, *J. Vac. Sci. Technol. B* 16, 2421 (1998).
23. J.P. Praseuth, L. Goldstein, P. Henoc and J. Primot, *J. Appl. Phys.* 61, 215 (1987).
24. Q. Xue, T. Hashizume, J.M. Zhou, T. Sakata, T. Ohno and T. Sakurai, *Phys. Rev. Lett.* 74, 3177 (1995).
25. Z.H. Zhang and K.Y. Cheng, *Appl. Phys. Lett.* 83, 3183 (2003).
26. A. Konkar, A. Madhukar and P. Chen, *Appl. Phys. Lett.* 72, 220 (1998).
27. Q. Xie, A. Madhukar, P. Chen and N.P. Kobayashi, *Phys. Rev. Lett.* 75, 2542 (1995).
28. G. Springholz, M. Pinczolits, P. Mayer, V. Holy, G. Bauer, H.H. Kang and L. Salamanca-Riba, *Phys. Rev. Lett.* 84, 4669 (2000).

29. Z. Sun, S.F. Yoon, J. Wu and Z. Wang, *J. Appl. Phys.* 91, 6021 (2002).
30. J. Wu, B. Xu, H.X. Li, Q.W. Mo, Z.G. Wang, X.M. Zhao and D. Wu, *J. Cryst. Growth* 197, 95 (1999).
31. H.X. Li, J. Wu, Z.G. Wang and T. Daniels-Race, *Appl. Phys. Lett.* 75, 1173 (1999).
32. Y.H. Chen, J. Wu, Z.Z. Sun and Z.G. Wang, unpublished.
33. D.A. Faux and J. Haigh, *J. Phys: Condens. Matter* 2, 10289 (1990)
34. Y. Horikoshi, M. Kawashima and H. Yamaguchi, *Jpn. J. Appl. Phys.* 25, L868 (1986).
35. Z.G. Wang and J. Wu, *Microelectron. J.* 34, 379 (2003).
36. H.H. Farrell, C.J. Palmstrom, *J. Vac. Sci. Technol. B* 8, 903 (1990).
37. X.Q. Huang, Y.L. Wang, L. Li, L. Liang and F.Q. Liu, *Appl. Phys. Lett.* 87, 083108 (2005).
38. W. Lei, Y.H. Chen, P. Jin, X.L. Ye, Y.L. Wang, B. Xu and Z.G. Wang, *Appl. Phys. Lett.* 88, 063114 (2006).
39. H. Yasuda, F. Matsukura, Y. Ohno and H. Ohno, *Appl. Surf. Sci.* 166, 413 (2000).
40. V.A. Shchukin, D. Bimberg, V.G. Malyshkin and N.N. Ledentsov, *Phys. Rev. B* 57, 12262 (1998).
41. H. Li, T. Daniels-Race and M.-A. Hasan, *Appl. Phys. Lett.* 80, 1367 (2002).
42. C. Priester and G. Grenet, *Phys. Rev. B* 64, 125312 (2001).
43. M. Gendry, J. Brault, B. Salem, G. Bremond and O. Marty, *Physica E* (Amsterdam) 17, 505 (2003).
44. Y.L. Wang, Y.H. Chen, J. Wu, Z.G. Wang and Y.P. Zeng, *Superlattices Microstruct.* 38, 151 (2005).
45. W. Lei, Y.H. Chen, Y.L. Wang, X.Q. Huang, Ch. Zhao, J.Q. Liu, B. Xu, P. Jin, Y.P. Zeng, Z.G. Wang, *J. Cryst. Growth* 286, 23 (2006).
46. Y.L. Wang, J. Wu, Y.H. Chen, Z.G. Wang, 13th International Conference on Semiconducting and Insulating Materials, Beijing, China, 2004.
47. Y. Masumoto and T. Takagahara, *Semiconductor Quantum Dots*, Springer-Verlag, Berlin/Heidelberg, 2002.
48. W. Lei, Y.H. Chen, Y.L. Wang, X.L. Ye, P. Jin, B. Xu, Yi Ping, Zeng, Z.G. Wang, *Materials Science Forum*, 475–479, 1897 (2005).
49. Z.Y. Xu, Z.D. Lu, X.P. Yang, Z.L. Yuan, B.Z. Zheng, J.Z. Xu, *Phys. Rev. B* 54, 11528 (1996).
50. S. Sanguinetti, M. Henini, M. Grassi Alessi, M. Capizzi, P. Frigeri, S. Franchi, *Phys. Rev. B* 60, 8276 (1999).
51. D.E. Wohlert, S.T. Chou, A.C. Chen, K.Y. Cheng, K.C. Hsieh, *Appl. Phys. Lett.* 68, 2386 (1996).
52. W. Lei, Y.H. Chen, B. Xu, P. Jin, Y.L. Wang, Ch. Zhao and Z.G. Wang, *Solid State Commun.* 137, 606 (2006).
53. O. Wada, H. Hasegawa, *InP-based Materials and Devices: Physics and Technology*, Wiley, New York, 1999, p. 80.
54. K. Mukai, M. Sugawara, *Appl. Phys. Lett.* 74, 3963 (1999).
55. W. Lei, Y.H. Chen, B. Xu, X.L. Ye, Y.P. Zeng and Z.G. Wang, *Nanotechnology* 16, 1974 (2005).
56. J.E. Maslara, P.W. Bohnb, S. Agarwala, I. Adesidab, C. Caneau and R. Bhat, *Appl. Phys. Lett.* 64, 3575 (1994).
57. L. Pavesia, R. Houdrk, P. Giannozzi, *J. Appl. Phys.* 78, 470 (1995).
58. S. Tripathy, Thwin-Htoo and S.J. Chua, *J. Vac. Sci. Technol. A* 22, 111 (2004).
59. L. Artus, R. Cusco, S. Hernandez, A. Patane, A. Polimeni, M. Henini and L. Eaves, *Appl. Phys. Lett.* 77, 3556 (2000).
60. V. Ryzhii and I. Khmyrova, *Proc. SPIE* 4986, 190 (2003).
61. W. Lei, Y.H. Chen, B. Xu, P. Jin, Ch. Zhao, L.K. Yu and Z.G. Wang, *Nanotechnology* 16, 2785 (2005).
62. A. Patane, A. Levin, A. Polimeni, L. Eaves, P.C. Main and M. Henini, *Phys. Rev. B* 62, 11084 (2000).
63. R.H. Wang, A. Stintz, P.M. Varangis, T.C. Newell, H. Li, K.J. Malloy and L.F. Lester, *IEEE Photon. Technol. Lett.* 13, 767 (2001).

64. T.J. Rotter, A. Stintz, K.J. Malloy, Long wavelength quantum dash lasers grown on InP substrates, OSA trends in optics and photonics (TOPS), *Conference on Lasers and Electro-Optics 2003*, 88, 1498 (2003)
65. P. Resneau, M. Calligaro, S. Bansropun, O. Parillaud, M. Krakowski, R. Schwertberger, A. Somers, J.P. Reithmaier and A. Forchel, *Proc SPIE* 5452, 22 (2004).
66. P. Resneau, M. Calligaro, S. Bansropun, O. Parillaud, M. Krakowski, R. Schwertberger, A. Somers, J.P. Reithmaier, and A. Forchel, High power, very low noise and long term ageing 1.55μm InP-based Fabry-Perot quantum dash lasers under CW operation, *Conference on Lasers and Electro-Optics 2005*, 3, 1805 (2005).
67. X.R. Yang, B. Xu, Z.G. Wang, P. Jin, P. Liang, Y. Hu, H. Sun, Y.H. Chen and F.L. Liu, *Electron. Lett.* 42, 757 (2006).

Index

A

AAM. *See* Anodic alumina membranes
AAO template, 34
Al-decorated nanotubes, 235
Amorphous materials, 167
Anisotropic crystal growth, 276
Anisotropic scatterers, 135
Anisotropic surface energy, 194
Anodic alumina membranes, 34
Antenna-like plasmon resonances, 177
Antenna resonances, 176, 183, 200–202. *See also* Particle excitations
Arc discharge process, 21–23
Atomic configurations
  of GaN nanotube, 114–115, 118, 119
  slabs, 104
  of stretching tube 2, 113
Au-Ga alloy, 6
Au-In alloy
  liquid-like migration of, 7, 8
  oxidation of, 4–5
Au-In eutectic temperature, 2
Au-In tip, 2, 4, 7
Au nanoparticles
  in InAs nanowire growth, 8, 10
  in optical lithography-patterned substrate, 84
  in Si nanowire growth, 3
  on SiO_2 surface, 86
Auxiliary differential equation method
  for studying dispersion properties, 150–151

B

Ballistic electron transport, 218
BDT temperature, 113
  of cubic GaN, 118
  and nanotube thickness, 116
  and rate of applied loading, 117
Binary system, metallic
  Ga(In) content in Au-Ga(Au-In), 10
  melting point depression of, 7–8
Birefringence, 134
  angular dependent reflection and transmission, 137
  long nanowires, 139–141
  parameter estimation
    in ensembles of aligned nanowires, 137
    of layers of GaP nanowires, 142
    Maxwell–Garnett approximation, anisotropic media, 136
    short nanowires, 141–143
Birefringent layer, single transmission, 138
BN nanotube sheath, 46
Bond length alternation (BLA), 267
Bottom-up chemical synthesis, 275
Boundary element method (BEM)
  for solving Maxwell's equations, 183
Brittle to ductile transition temperature. *See* BDT temperature
Buckling behavior, GaN nanostructures
  critical stress and strain, 121–122
  stress-strain response, 118–119
  temperature and strain rate effects on, 119–120
  tube length effect on, 121
Bulk GaN, potential energy variation, 102

C

Carbon-coated copper TEM grid, 285
Carbon nanotube (CNT), 217. *See also* Multi-walled nanotubes (MWNTs); Single-walled nanotubes (SWNTs)
  confined reaction, 20–21

fabrication with contact engineering, 227–231
metal clusters effects on, 233–238
metal oxidation effects on, 219–223
pressure and interfacial contact effects on, 223–227
projected density of states of, 223–224
quantum interference patterns observed in, 218
semiconducting, 220
Channel-decorated devices, 233
Chemical sensors, 233
Chemical vapor deposition
for formation of nanostructures, 25
for growth of semiconductor nanowires, 128
Si substrate
β-SiC nanowires, 25–26
SiC nanorods, 26
Coaxial nanocables, 38
Copper nanowires. *See also* Nanowire
electrical transport properties of, 192
electrochemically deposition of, 191
Core shell heterostructures, 94
Core-shell p-n junctions, fabrication of, 69
Core-shell SiC/SiO2 nanowires
field-emission currents, 42
Young's modulus for, 48
Critical points models, 153
used in conjunction with Drude model, 155–156
Cu-silicide/Si/oxide nanochains, 67
CVD. *See* Chemical vapor deposition

D
Data storage devices, performance of, 287
Debye model, 154
Density-functional theory (DFT) method, 219
Diameter fluctuations, SiC nanowires
as fractal, 73–74
mono-affinity and multiaffinity, 74–75
as random walk, 75–76
Diluted magnetic semiconductor (DMS) nanowires, 248
Dipolar resonance, 179
Dipole discrete dipole approximation (DDA), 183
Dispersion models, combinations of, 156–157, 159
Dispersive materials
FDTD method for modeling, 148
studied using Debye, Drude, or Lorentz models, 153
Drude–Lorentz model, 166, 205
Drude model, 154
combination with Lorentz model, 156–157
for studying dispersion properties, 150

E
Electric-field assisted assembly technique, 82
Electromagnetic boundary conditions, 131
Electromagnetic nanowire resonances, 177
Electromagnetic waves scattering, by metal objects, 179
Electron-beam lithography (EBL), 187, 194–196
Electron-ion interactions, 219
Energy dispersive X-ray spectrometry (EDX), 278, 295

F
Fermi level, 220, 225
Ferromagnetic semiconductor nanostructures, 248
Fe-silicide nanowires
β-$FeSi_2$ nanowires
Au/Si templates, annealing, 72
cooling process, 73
fabrication of, 71
α-$FeSi_2$ and ε-FeSi nanowires, 71
Finite density of states (DOS), 248
Finite-Difference Time-Domain (FDTD) method
antenna modes, existence of, 179
calculation of SERS gains using, 205
elecromagnetic phenomena, for modeling of, 148
for plasmonic structures' design and optimization, 147
Fowler–Nordheim relationship, 41–42

G
GaAs nanowires, growth of, 6–7
Gallium nitride, 98
SW potential for, 101
GaN nanotubes
buckling behavior of, 118–122
construction, 98–100
hexagonal structure of, 100
melting processes, simulation of, 101–102
melting temperature dependence on thickness, 106
potential energy variation of, 104–105
snapshots of, 105
tensile behavior of, 112–118
thermal conductivity of, 106–111
GaN nanowires, 250
GaP nanowires
birefringence parameter, 142, 143
cross-sectional SEM images of, 130, 142

refractive indexes of ensembles of epitaxially grown, 141
transmission and reflection measurements, 138, 140
Ge nanowires, melting point reduction in, 9
GeTe nanowires, 278
EDS spectrum of, 280
evaporation rate, 288
high-resolution TEM images of crystal structure of, 281
melting point, measurement of, 288
SEM image of, 279
Giant birefringence, 141–143
Giant magnetoresistance (GMR), 247
Gibbs–Thomson effect, 7–9
Gold, thin films of, 129

H
Half-metallic (HM) ferromagnet, 260
Hard disk drive (HDD), 247
Heisenberg Hamiltonian, 265
High-density magnetic storage devices, 250
High-frequency induction heating furnace, components of, 30
Hybrid nanostructure, 250

I
InAs/InAl(Ga)As QWR superlattices, 292
InAs nanostructures, nucleation sites for, 299
InAs nanowires
growth of, 2
effect of oxygen on, 4–5
effect of SiO_x on, 10–13
melting point depression, Au–In tip, 7–8
InAs quantum wires
formation on InAlAs/InP(001), 292
superlattices
spatial correlation of, 301
vertical anticorrelation of, 302
Indium phosphide nanowire, 128
Indium titanium oxide (ITO), 195
Infrared reflection-absorption spectroscopy (IRRAS), 210
InP nanowires, 129
photoluminescence spectra of, 132, 133
In_2Se_3 nanowires
SEM image of, 284
on SiO_2 substrate, 286
β-In_2Se_3 nanowires, high-resolution TEM images of, 285
Interband transition, anomalous temperature dependence of, 314
Intraband photocurrent, 317
Ion beam alignment, 84, 91
Isopropanol (IPA), 195

K
Kohn–Sham single-electron equations, 219

L
Laser-ablation technique, 23–24
Laser beam depolarization, 204
Lateral composition modulation (LCM), 294
Liquid metal alloy droplet, 3
Liquidus depression, 9–10
Local density approximation (LDA), 267
Local spin density approximation (LSDA), 267
Lorentz Model, 155
combination with Drude model, 156–157
Lorentz oscillator, 161
LSP resonance, 178, 200, 205
Luebbers coefficients, 156

M
Magnetic anisotropy, 249, 264
Magnetoresistance (MR) ratio, 260
Magnetoresistive random access memory (MRAM), 247
Maxwell–Garnett effective medium approximation, 136
Maxwell's equations, 148, 178
for metallic nanorods, 180
techniques to solve, 183
MD simulations, GaN nanotubes
compressive behavior of, 121–122
melting processes of, 102–103
thermal conductivity, 107–110
Melting point depression, Gibbs–Thompson effect, 7–9
Melting temperature
bulk GaN, 102–103
GaN nanotubes, 105–106
GaN slabs, 103–104
metal cluster, 101
Mercury-cadmium telluride (MCT) detector, 196
Metal alloy tip
liquid state of, 1
solid state of, 2, 6, 10
Metal-carbon nanotube, 219
Metal cluster decoration, for sensing characteristics of SWNT-FETs, 234
Metal-CNT interfaces, 227
Metal-film morphology, 207
Metal-induced gap state (MIGS), 223
Metallic nanoparticles
study of, 162
surface plasmon resonances of, 176, 200
Metallic nanorods, Maxwell's equations for, 180

Metallic nanostructures, 167
Metallic nanowires, 160, 166
factors governing optical response of, 178
prepared by growth in ion tracks, 196
Metal-nanoparticle films, 208
Metal-nanotube tunneling barrier, 243
Metal NWs, fabrication of, 81
Metal-organic vapor-phase epitaxy (MOVPE) system, 129
Methylisobutylketon (MIBK), 194
Microsampling, of SiGe needle, 68, 70
Mie resonances, 176, 178
Migration enhanced epitaxy (MEE) growth modes, 304
Mn-Mn coupling, 251
Molecular dynamics simulations, GaN nanotubes. *See* MD simulations, GaN nanotubes
Mono-affine and multi-affine nanowires. *See* Diameter fluctuations, SiC nanowires
Mono-affinity, 74
Monocrystalline nanostructure, 167
Monocrystalline silver nanowire. *See* Silver nanowire
Multiple multipole expansion (MMP) techniques, 183
Multi-walled nanotubes (MWNTs), 217

N
Nanoantennas, 176, 181
Nanocables
β-SiC-SiO_2-BN/C, structure of, 37
coaxial, 38
PL spectra of SiC, 44, 45
SiC/SiO_2, 32
ZnS/SiC, 39
Nanofabrication, top-down *vs.* bottom-up, 275
Nanometer Pattern Generation System (NPGS), 195
Nano-optic simulation, fabrication process in, 167
Nano-piezomagnet, 259
Nanoribbons, SiC-shelled ZnS, 39
Nanoscale structures, fabrication process of, 167
Nanosphere lithography, 203
Nano-spintronics, 248–249. *See also* Spintronics
Nanosprings, SiC/SiO_2
applications, 32–33
TEM images of, 33
Nanotubes
TM doped BN, 252–258
TM doped C, 251–252
Nanowhiskers
3C-SiC, 26
high-resolution TEM image of, 26
photoluminescence spectra, 28
Nanowire. *See also* Specific nanowires
crystallinity and crystallographic orientation, study of, 191
electronic properties, factors affecting, 81
fabrication methods
electron-beam lithography, 194–196
wire growth in ion tracks of membranes, 187–194
flowers
components of, 28–29
growth, Si substrate, 29–30
growth mechanisms
oxide assisted (OA), 1
oxygen, inhibiting effect, 4
using metal catalysts, capabilities, 6
vapor-liquid-solid (VLS), 1–2
layer, thickness of, 138
magnetic alignment of, 82
plasmon modes, factors governing, 180
resonances
basics of, 178–180
spectroscopy of, 196
Near-field optical transmittance, 161
Nondispersive media, 156

O
One-dimensional semiconductor nanostructures, 17, 83
One-dimensional SiC nanostructures, 20–21
Optical anisotropy, 313
Optical phonons, 218
Orient SiC nanowire arrays, 34–35
Oxidation and nanowire growth, 4–5

P
Particle excitations, 176
PCNWs. *See* Phase-change nanowires
Periodic diameter modulation, 64–65
Permeability, 134
Permittivity tensor, 134–135
Phase-change materials (PCMs), 274
Phase-change nanowires
melting point measurement, 287–288
synthesis and characterization of
III-VI compound (In_2Se_3) nanowires, 283–287
IV-VI compound (GeTe) nanowires, 278–283
vapor-liquid-solid (VLS) growth mechanism of, 276–27

Phase-change random access memory, 274
Phosphate buffered saline (PBS), 238
Photocurrent (PC) spectroscopy, 317
Photolithographic tools, advancement of, 275
Photoluminescence, polarization anisotropy of, 129, 131
Photonic structures, 176
Plasmon hybridization, 186
Plasmonic Fabry–Perot cavity, 162
Polarization anisotropy, 132
  absorption, 131–132
  emission, 132–134
Polyethyleneimine (PEI)-starch functionalization, 234
Polymer-matrix composites, tensile stress-strain curves of, 50
Polymethyl methacrylate (PMMA), 194
Potential energy, variation
  bulk GaN, 101–102
  GaN nanotubes, 104–105
  slabs, 103–104
PRAM. *See* Phase-change random access memory
Projected density of states (PDOS), 224, 255
Projector augmented wave (PAW), 253
Protein nanoparticles, contact engineering with, 238–242

Q
Quantum computation, 248
Quantum dashes (QDash), 319
Quantum wire lasers, 319
Quantum wire superlattice, dislocations in, 310–313
Quartz tube, 4, 30

R
Raman signal enhancement, 203
Rayleigh instability, 194
Recursive accumulator, 153
Recursive convolution method, for studying dispersion models, 150, 152–153
Reflectance difference spectroscopy (RDS), 295
Reflection high energy electron diffraction (RHEED), 295

S
Schottky barriers
  to electron transport, 233
  at metal-nanotube contact, 240
  of SWNT-FETs, 227
Selected-area electron diffraction (SAED), 191, 285
Self-affine patterns, 73
Self-assembled monolayers (SAM)
  of molecules containing thiol group, 227
  preparation of, 208
Self-assembled quantum wires
  anomalous temperature dependence of interband transition, 314
  optical properties of, 313
Semiconductor materials, nanorods of, 185
Semiconductor nanowires, 131
  coherent propagation of light, 134
  growth of, 128–130
  incident wave onto, 131
  Maxwell–Garnett permittivity of, 136
  photoluminescence, polarization anisotropy of, 131
  polarization anisotropy, 132
  propagation of light, 129
Semiconductor NWs
  alignment during growth, 82–83
  fabrication of, 81
Shape memory synthesis, 21
Si-assisted growth mechanism
  of InAs nanowires, 10
    oxide layer effects on, 11–12
    via In diffusion, 13
SiC
  crystalline structure of, 18
  nanostructures, 28–29
  nanotubes
    hydrogen storage in, 52–53
    interlayer spacing, 36
    synthesis apparatus, 35–36
  photodegradation rates, 52
  PL spectra of, 44
  properties of, 19
SiC/BN nanowires, electrical transport of, 46
SiC-CNT junctions, 38–39
SiC nanorods
  optical properties of, 44
  strengths of, 48
  synthesis of
    arc-discharge process, 22–23
    by floating catalyst methods, 30
    by hot filament CVD, 26
    sol-gel and carbothermal reduction, 24–25
    with thermally annealing singlewalled carbon nanotube sheets, 21, 22
    two-step reaction process, 20
SiC nanowires
  Al-doped, 27–28
  alignment during growth, 82–83
  arrays, oriented, 34–35
    fabrication process, 84–87
    zigzagging behavior, 87, 90

BN-sheathed, synthesis of, 38–39
crystalline quality of, 87
postgrowth process effects, 93
diameter fluctuations in
fractal, 73–75
random walk, 75–76
EDS analysis of, 28
electrical contacts, 91
electrical transport in, 46
fabrication process, 83
catalyst site, 86, 87
EBL and metal deposition processes, 86
Si wafer, 84
in vertical metal-organic chemical vapor deposition reactor, 86
field-effect transistor
carrier mobility, 48
drain current, 47–48
electronic measurement configuration for, 46–47
I_{ds}–V_{ds} characteristic of, 47
field-emission measurements
Fowler–Nordheim (FN) theory, 41–42
setup for, 40–41
single-crystal, 42–43
hydrogen storage properties, 52–53
ion-beam alignment, 90–91
I–V curves, 46
I–V measurement of, 93
kinking of, 87, 88
mechanical properties measurements
flexural properties, 49–50
Young's modulus, 48–49
photocatalytic activity of, 51, 52
postgrowth alignment, 83
postgrowth assembly process, 82
properties of, 17–18
Raman spectra of, 44
randomly oriented, on Au islands, 84
response to, DC electric field set up, 82–83
synthesis methods
arc-discharge process, 21–22
bottom-up approach, 81
comparison of, 33–34
direct current magnetron sputtering methods, 27
laser-ablation technique, 23–24
microwave plasma CVD, 25–26
top-down semiconductor processing, 80–81
zigzagging behavior, 87, 90
ZnO nanorod fabrication on, 39
β-SiC nanowires
IR spectrum of, 44, 45
synthesis by
high-frequency induction heating, 30–33
sol-gel and carbothermal reduction, 24
thermal evaporation, 33
SiCNTs. *See* SiC nanotubes
SiCNW composites, tensile stress-strain curves of, 50
Si core-shell needles, sulfur-assisted growth of, 68
SiC whiskers, 20
arc-discharge process, 21–23
SiC/ZnO shell–core nanostructures, 39–40
SiGe core-shell needles, sulfur-assisted growth of
Ge/Si atomic ratio, 69–70
microsampling, 68
VLS growth, 69
Silicon carbide nanorods. *See* SiC nanorods
Silver nanowire, 162, 171
influence of mean free path on guiding efficiency for, 168–170
Si nanochains
discovery of, 62
formation mechanism, 63
periodic diameter modulation, 64–65
surface oxidation, 65–66
TEM micrographs of, 63
as templates, Cu-silicide/Si/oxide nanochain fabrication, 67
Si nanowires, 2
Ti-catalyzed, growth of, 6, 10
Single-crystalline wurtzite GaN nanotubes. *See* GaN nanotubes
Single-crystal SiC nanowires, field-emission of, 42–43
Single plasmonic nanowires, near-field optical properties of, 160–161
Single silver nanowire. *See* Silver nanowire
Single-spin transistor, 248
Single-walled nanotubes (SWNTs), 217
fabrication of *n*-Type transistors with Al decoration, 232–233
Sol-gel and carbothermal reduction processing, 24–25
Sol-gel template synthesis, 249
Spherical nanoparticles, resonances of, 176
Spin-based electronics. *See* Spintronics
Spin-dependent resonant tunneling devices, 252
Spin-injection devices, 249
Spin-magnetization, 268
Spin-polarized carriers, 248

Spin-polarized conductors, 252
Spin polarized electrons, 248
Spintronics
application in quantum computation, 248
impact on HDD industry, 247
Stillinger-Weber potential, 100–101
Strain induced lateral-layer ordering (SILO) process, 314
Surface charge density, 185
Surface enhanced infrared absorption (SEIRA), 177, 181
application to, 207–210
Surface enhanced Raman scattering (SERS), 177, 181
application to, 202–207
Surface oxidation, 65–66
Surface plasmon
modes, role in single elongated nanoparticles, 147
propagation, 162
resonators, 160, 185

T
Tensile behavior, GaN nanotubes
critical stress, 113–114
strain-stress simulations, 112–113
Thermal conductivity
bulk GaN, MD simulations, 108–111
estimation methods, 107
T-NFRC, flexural properties of, 49
Transitional-metal free systems, 267–268
Transition-metal (TM) atoms, 249
benzene sandwich polymers, 260–267
doping
BN nanotubes, 252–258
C nanotubes, 251–252
nanowires, 250–251
Transversal polarizations, 181
Trimethylindium (TMI), 129
Turn-on field
of carbon-coated SiC nanowires, 43
definition of, 41
of pure BN nanotubes, 42

U
Uniaxial birefringent material, 135
UNI-LAC linear accelerator, 188

V
Vacuum two-zone nanowire synthesis system, 277
Vapor-liquid-solid growth mechanism, 2
oxygen effects on, 4–5
schematics of, 129
SiGe core-shell needles, 69
of Si nanowires, 3
and VSS growth mechanism, 6–10
Vapor-solid growth, 61
of nanowire, 62
Vienna ab initio simulation package (VASP), 219, 253, 261
VLS growth mechanism. *See* Vapor-liquid-solid growth mechanism
VLS nanowire growth, 276
VSS growth mechanism
metallic binary system, melting point depression of, 7–8
Ti-catalyzed Si nanowire, 6

W
Whiskers, of single crystalline Si
growth mode of, 61
periodic instability in, 64
Wire growth, in ion tracks of membranes, 187–194
Wrapping method, 98

Y
Young's modulus
for core–shell SiC/SiO2 nanowire, 48
GaN nanotube, 121
SiC–SiO_x nanowires, 49

Z
ZnO nanorods, 39
Z-transform method, for modeling of gold films properties, 151–152